Davis, E. E., Mottl, M. J., Fisher, A. T., et al., 1992
Proceedings of the Ocean Drilling Program, Initial Reports, Vol. 139

7. SITE 857[1]

Shipboard Scientific Party[2]

HOLE 857A

Date occupied: 27 July 1991

Date departed: 28 July 1991

Time on hole: 1 day, 1 hr, 45 min

Position: 48°26.495′N, 128°42.803′W

Bottom felt (drill-pipe measurement from rig floor, m): 2429.1

Distance between rig floor and sea level (m): 10.80

Water depth (drill-pipe measurement from sea level, m): 2418.3

Total depth (rig floor, m): 2541.30

Penetration (m): 112.20

Number of cores (including cores with no recovery): 14

Total length of cored section (m): 112.2

Total core recovered (m): 94.72

Core recovery (%): 85

Oldest sediment cored:
Depth below seafloor (m): 112.20
Nature: silty clay
Earliest age: Pleistocene (13X-2, 68–72 cm)
Measured velocity (km/s): 1.602

HOLE 857B

Date occupied: 28 July 1991

Date departed: 28 July 1991

Time on hole: 7 hr, 30 min

Position: 48°26.490′N, 128°42.804′W

Bottom felt (drill-pipe measurement from rig floor, m): 2429.1

Distance between rig floor and sea level (m): 10.80

Water depth (drill-pipe measurement from sea level, m): 2418.3

Total depth (rig floor, m): 2459.60

Penetration (m): 30.50

Number of cores (including cores with no recovery): 3

Total length of cored section (m): 22.40

Total core recovered (m): 23.34

Core recovery (%): 104

Oldest sediment cored:
Depth below seafloor (m): 30.50
Nature: silty clay
Earliest age: Pleistocene

Comments: Only Core 1H split. Cores 2H and 3H saved for special studies.

HOLE 857C

Date occupied: 28 July 1991

Date departed: 9 August 1991

Time on hole: 7 days, 17 hr (first time); 11 hr, 30 min (second time)

Position: 48°26.485′N, 128°42.682′W

Bottom felt (drill-pipe measurement from rig floor, m): 2432.5

Distance between rig floor and sea level (m): 10.80

Water depth (drill-pipe measurement from sea level, m): 2421.7

Total depth (rig floor, m): 3000.20

Penetration (m): 567.70

Number of cores (including cores with no recovery): 68

Total length of cored section (m): 514.70

Total core recovered (m): 169.04

Core recovery (%): 32

Oldest sediment cored:
Depth below seafloor (m): 549.00
Nature: sulfide siltstone
Earliest age: Pleistocene (40R-CC)
Measured velocity (km/s): 2.361

Hard rock:
Depth below seafloor (m): 561.23
Nature: diabase
Measured velocity (km/s): 4.320

Comments: First time: 1100 hr, 28 July, to 0400 hr, 5 August. Second time: 0330 to 1500 hr, 9 August.

HOLE 857D

Date occupied: 5 August 1991

Date departed: 3 September 1991

Position: 48°26.517′N, 128°42.651′E

Bottom felt (drill-pipe measurement from rig floor, m): 2431.5

Distance between rig floor and sea level (m): 10.90

Water depth (drill-pipe measurement from sea level, m): 2420.6

Total depth (rig floor, m): 3367.70

Penetration (m): 936.20

Number of cores (including cores with no recovery): 37

Total length of cored section (m): 354.70

Total core recovered (m): 37.36

Core recovery (%): 10

Oldest sediment cored:
Depth below seafloor (m): 927.00
Nature: claystone, siltstone, sandstone
Earliest age: no fossil data
Measured velocity (km/s): 3.457 (31R)

---

[1] Davis, E. E., Mottl, M. J., Fisher, A. T., et al., 1992. *Proc. ODP, Init. Repts.,* 139: College Station, TX (Ocean Drilling Program).
[2] Shipboard Scientific Party is as given in the list of participants preceding the contents.

Hard rock:
Depth below seafloor (m): 581.50
Nature: diabase
Measured velocity (km/s): 5.597 (35R)

Comments: Reentry hole; no coring done the first time. Coring done the second time. First time: 0400 hr, 5 August, to 0330 hr, 9 August. Second time: 1700 hr, 23 August, to 1730 hr, 3 September.

Principal results: Site 857 is located 5.2 km west of the normal-fault scarp that forms the eastern topographic and hydrologic boundary of Middle Valley, and about 1.5 km east of the sediment-buried fault that forms the current structural boundary of the central part of the rift. The primary objective of drilling at this site was to penetrate into "hydrologic basement" at a point well away from areas of either recharge or discharge, in order to (1) test the hypothesis that there is a thermally and chemically well-mixed hydrothermal "reservoir" beneath the sediments of the valley, (2) characterize the physical and chemical nature of water-rock interaction within high-temperature basement, and (3) determine how efficiently the fluids can be delivered to seafloor vents several kilometers away.

The site lies over a major thermal anomaly, where the seafloor heat flow exceeds 0.8 W/m^2 over an area extending 10 km in a rift-parallel direction. Heat flow increases to the north from the site, toward a hydrothermal vent field 1.6 km away, where heat flow exceeds 4 W/m^2 and fluids discharge at the seafloor at temperatures up to 276°C (the planned location of Site 858).

Coring operations began with advanced piston corer/extended core barrel (APC/XCB) in Hole 857A (see Table 1 for coring summary), which was drilled slightly west of the peak of the heat flow anomaly in order to avoid intersecting a bright reflector, inferred to be a sill, at 400 milliseconds (ms) two-way traveltime (TWT) in seismic reflection records. This hole was drilled to 112 mbsf. An adjacent Hole 857B was drilled with the APC to 30 mbsf, in order to provide a mudline core and additional temperature data within the upper sediment section. From these and thermal conductivity data we determined that heat flow at this location is conductive at a value of 0.709 W/m^2, somewhat lower than we had targeted for this deep-penetration site. For this reason we offset 180 m to the east to drill the exploratory Hole 857C with the rotary core barrel (RCB). The conductive temperature gradient measured over the upper 80 m of Hole 857C indicates a heat flow of 0.803 W/m^2.

The sediment section comprises Holocene through interbedded hemipelagic mud and turbiditic silt and sand. The fraction of coarse material increases with depth in the section, as does the sedimentation rate, estimated in the upper tens of meters from two clear biostratigraphic markers, and in the lower part of the section from the inferred age of igneous basement. The sediment becomes increasingly indurated with depth. The induration is caused primarily by the high thermal gradient and the accompanying diagenetic alteration and metamorphism, and in part by metasomatism resulting from diffuse fluid flow. At depths less than about 250 mbsf, carbonate concretions and diagenetic pyrite are common. This assemblage gives way with depth to carbonate-cemented clastic sediment, then to pervasively cemented fine and coarse-grained sediment, and ultimately to ferroan carbonate. Below 400 mbsf, detrital feldspar is altered to clay minerals and magnetite is pyritized by H_2S. At shallow depths, the magnetic susceptibility is highly variable; susceptibility peaks result from magnetite concentrated in the basal, sandy parts of turbidite layers. A 3- to 5-m-thick unit at 15 mbsf bears distinctively low susceptibility, and is strikingly similar to intervals seen at Sites 856 and 858; the cause of this shallow interval of susceptibility is at this point unknown. On average, the susceptibility decreases steadily from 150 to 250 mbsf and remains low at greater depths because of the increasing alteration of magnetite to iron sulfide minerals.

The first of a series of sills, interbedded with indurated sediment, was penetrated at 471 mbsf. The sills are basaltic in composition, with plagioclase and pyroxene phenocrysts set in a fine-grained, hydrothermally altered groundmass, and are properly described as metadiabase. The dominant alteration assemblage consists of chlorite, epidote, and actinolite. The sills are subvertically fractured and cut with veins of epidote, chlorite, carbonate, pyrite, chalcopyrite, and sphalerite. Hole 857D, a deep reentry hole, was drilled 50 m north of Hole 857C to a total depth of 936 mbsf. The altered sill/sediment sequence intersected in Hole 857C continues with remarkably little systematic change in composition or degree of alteration to the bottom of Hole 857D.

Physical properties reflect clearly the high degree of induration of the sediment. Porosity measured on cored material decreases systematically with depth, from normal values of about 65% near the seafloor to as low as 25% at a depth of 450 m, and there is a corresponding increase in seismic velocity over this same depth interval, from about 1550 meters per second (m/s) to 3000–3500 m/s. The average velocity of the full section of sediment down to the first sill, defined by the 470 mbsf depth to the top of the first sill and the traveltime to the first reflector of 480 ms TWT, is 1980 m/s. Velocities measured transverse to core axes are higher than vertical velocities; anisotropy increases with depth from about 5% in the upper part of the section to 25% at 400–500 mbsf (horizontal values are quoted above). Velocity in the igneous units ranges from 4500 to 6500 m/s. The intrinsic porosity of the igneous rock is low, typically 5% and less, although mineralized and open subvertical fractures are present in the cores. Fractures are also observed commonly in formation microscanner images of Hole 857D. Remanent magnetic intensity of the igneous rocks is low, averaging about 20 mA/m, as is magnetic susceptibility, which averages about 0.5×10^{-3} SI.

On the basis of variations in drilling rate, it was inferred that thick intervals of sediment were interbedded with the intrusive layers below 471 mbsf, but recovery in the sedimentary intervals was generally poor. Induction, porosity, lithodensity, sonic, natural gamma, and formation microscanner logs run in Holes 857C and 857D reveal the lithologic structure clearly and confirm this inference. Numerous igneous units are imaged clearly in all logs; these range from 1 to 25 m in thickness. The range of thickness of sedimentary interbeds is similar, and the volumetric proportion of igneous to sedimentary rocks is roughly 2:3. *In-situ* sonic velocities determined by the logs are similar to the vertical-component velocities measured on samples. Electrical resistivity of the sediment ranges from about 0.4 to 0.6 ohm-m, and of the igneous layers from 3 to 20 ohm-m. Average values within individual igneous units are resolvably different, and there is a tendency for resistivity to increase into the sill interiors. There is also some tendency for the contrast in physical and electrical properties to be sharper at the bases of the sills than at the tops. The logging data also reveal the thicker layers of sandy and silty turbidites clearly. Further analysis should provide an accurate measurement of the proportions and frequency of the large turbidite layers.

In spite of low porosities, pore waters were extracted from all parts of the section. Higher porosity material was squeezed in the normal manner. Lithified sediment and porous igneous rocks were first shattered, then ground with a quantity of distilled water equivalent to the pore volume, and finally squeezed. Profiles of composition vs. depth reflect mainly reaction and diffusion, although lateral flow is indicated by the occurrences of broad maxima and minima of various chemical species in the vicinity of 300 mbsf. Concentrations of sodium, potassium, and calcium are remarkably similar to those found in vent fluids at the location of Site 858.

Temperature measurements in the open Hole 857C were made while the hole was still recovering from drilling disturbance. A temperature of 222°C measured at 476 mbsf thus provides a minimum estimate for the formation temperature at this depth. An extrapolation of the conductive gradient measured higher in the section provides a maximum estimate of about 260°C for this same depth. Temperatures in the cased section of Hole 857D, measured 14.5 days after drilling and before the casing shoe was drilled out, showed clear indications of fluid flow down the annulus around the outside of the casing and into the sediment section. Temperatures were much lower than 100°C in the upper part of the hole, and were close to those measured in Hole 857C only below 300 mbsf. This implies that much of the cement used to grout the casing was lost to the formation, and that the sediment was sufficiently permeable to accept downhole flow to 300 mbsf.

Hydrologic properties of the formation were determined in the section of hole below the casing in Hole 857D. Packer injection tests, along with a flowmeter log, showed the formation to be extremely permeable. Virtually all of the pressure losses occurred in the pipe and through the packer itself; formation pressures rose little, even at the maximum injection rate of 3000 L/min (150 strokes/min). Much of the flow entered the formation in two discrete zones which were conspicuous in electrical resistivity and spontaneous potential logs. A packer test in the formation below the deeper zone yielded more "normal" behavior, with pressures responding smoothly during and following injection intervals, although even in this deepest interval, the permeability is high. Formation pressures measured while the packer was seated confirmed the high differential pressure that was indicated by loss of circulation pressure during drilling; pressure measured in the formation was over 1 MPa lower than that in the cold hole. Under this differential pressure, the less restricted flow into the formation with the packer released was found to be over 10,000 L/min.

Final operations in Hole 857D involved setting an instrumented reentry cone seal (CORK), which included a 300-m-long, 10-thermistor temperature-sensor string, a pressure sensor, and plumbing for fluid sampling. This will allow pressure and temperature to be monitored as the formation returns to equilibrium conditions.

BACKGROUND AND OBJECTIVES

Site 857 is located over a part of Middle Valley where the sediment cover is thick and locally continuous, and the heat flow is high, typically over 0.8 W/m^2. The site is located 1.6 km away from a large hydrothermal vent field, where fluids discharge through the seafloor at temperatures up to 276°C. Because the sediment cover is thick, it was anticipated that the heat transfer at this site should be dominantly conductive, and thus at this level of heat flow, the depth at which hydrothermally high (300°–350°C) temperatures are present could be reached with only a few hundred meters of drilling.

The highest priority objective at this site was to penetrate through the sediment fill of the valley into what may be a regional "reservoir" where high-temperature fluids reside in the upper igneous crust, chemically interact with their permeable host rocks, and supply fluid to remote areas of focused discharge where local permeable conduits allow fluids to penetrate the otherwise thick and impermeable sediment section. Drilling at this site would test this conceptual model for the thermal and hydrologic regime in this sedimented rift, and allow the chemical composition of the water-rock system, and the hydrologic and thermal properties of the sediment and permeable basement to be determined. This was to be accomplished through a combination of direct sampling of the rock and fluids at various levels in the formation, discrete and continuous downhole measurements and logging, formation permeability testing, and long-term observations of temperatures and pressures in the formation.

Other objectives at this site included the determination of (1) the degree of alteration of organic and inorganic constituents of the sediment column which probably have been exposed to high temperatures but relatively minor amounts of pore-fluid flux, (2) the effect of high-temperature alteration on the physical and magnetic properties of sediment and upper igneous crustal rocks, (3) the composition and physical nature of the volcanic rock that comprises igneous basement in this sedimented rift.

SITE GEOPHYSICS AND GEOLOGY

Site 857 is located just outside the primary structural boundary of the current center of rifting in Middle Valley (Fig. 1; see also maps and profiles included in the back pocket of this volume). The age of the igneous crust beneath the site, as estimated from the combination of the distance to the eastern edge of the Brunhes magnetic chron and the spreading rate for the ridge, is about 250,000 yr (Davis and Villinger, this volume). The structural boundary that separates the site from the valley axis is a large-offset syn-sedimentary normal-fault zone. The offset of the basement surface defined by seismic reflection data is at least several hundred meters (Fig. 1). Seafloor relief associated with the fault near Site 857 has been modified some by local erosion (Johnson et al., in press), but in total is only a few tens of meters (Figs. 2 and 3). Offsets across the fault of the seafloor and of the basement surface decrease to the south; to the north, the offsets increase and ultimately form the major topographic boundary of the valley (Davis and Villinger, this volume).

At the latitude of Site 857, the fault bounds a back-tilted block to the east (Fig. 3), considered here to be the foot-wall block, and a down-dropped hanging-wall block that dips to the west toward the axis of the rift (Fig. 1). The drilling site is located on the uplifted foot-wall block, roughly 1.5 km east of, and thus well away from, the normal-fault zone. The seafloor in the vicinity of the site dips steadily from a depth of 2435 m near the fault down to a depth of 2480 m over a distance of about 3 km. This gentle dip of just under 1° mimics the dip of shallow seismic stratigraphic horizons. Below about 100 ms TWT, the structure becomes more localized; fault blocks of smaller size (1–2 km) can be seen that appear to have behaved independently at earlier times. These appear to have become "fused," and the block between the current rift-bounding fault and the valley-bounding fault appears to be currently behaving as an integral unit. Lack of recent motion on local faults is confirmed by the side-scan acoustic imagery of the area, in which no small surface offsets are seen (Fig. 2B and map in back pocket of this volume), with the exception of a very faint surface trace seen just west of the Site 857 holes in Figure 4. Site 857 is located approximately midway between two of the buried faults (Fig. 5).

The seismic stratigraphy of the section locally beneath Site 857 is shown in Figures 5 and 6 (see also Davis and Villinger, this volume). Sediment cover in this part of Middle Valley is continuous across the full width of the valley, from the normal-fault scarp where Site 855 is located, to the opposite side of the valley 15 km to the west (Fig. 1). Sediment thickness is variable, ranging from up to 1.0 s TWT in the central part of the rift axis, down to about 0.5 s in the vicinity of Site 857, and to a few hundred milliseconds in the outer parts of the valley. The sediment section contains numerous coherent, low-amplitude reflectors (Fig. 5). One of the strongest of these (at 3490 ms, or 200 ms bsf) produces a reflection of roughly half the amplitude of the seafloor reflection (Fig. 6). A very bright, singular, and horizontally discontinuous reflection occurs at 3690 ms (400 ms bsf). Its signature is very similar to the seafloor reflection signature, except that it is reversed in polarity, and considerably higher in amplitude. This reflection is interpreted to be from the base of a sill. Site 857 was located just west of the termination of this reflection in order to avoid any possible drilling difficulties that might be associated with it. Below 3770 ms (480 ms bsf) a 200-ms-thick reverberant series of high-amplitude, spatially coherent reflections is present that probably indicates the presence of interbedded sediment and igneous rock. Along parts of the line, this reverberant character persists for up to 400 ms.

The thermal structure near Site 857 is well characterized by numerous heat flow measurements in this part of the valley (Fig. 7; Davis and Villinger, this volume). The site is located over a linear thermal anomaly that parallels the rift valley about 1 km east of the primary rift-bounding fault. Values within the anomaly are typically 0.8–1.0 W/m^2; values outside the anomaly vary between 0.4 and 0.6 W/m^2. The anomaly is continuous along strike for about 12 km, and is several hundred meters to 1 km wide. About 2 km north of Site 857, heat flow increases to over 5 W/m^2 at a hydrothermal vent field at Site 858. Temperatures of the section beneath the location of Site 857, estimated by extrapolating measured seafloor gradients through the estimated thickness of the sediment section, suggest that the sediment/basement interface is about 300°C. This appears to be true beneath much of Middle Valley, and much of the heat flow variability appears to be caused simply by variations in sediment thickness over a roughly uniform-temperature, permeable hydrothermal "reservoir." If this is true, Site 857 provides one of the best opportunities for reaching "permeable basement" at a location well away from an area of discharge with a modest amount of drilling.

High regional basement temperatures are also suggested by the magnetic field anomaly pattern over the valley. Middle Valley is

Table 1. Site 857 coring summary.

Core	Date (1991)	Time (UTC)	Depth (mbsf)	Cored (m)	Recovered (m)	Recovery (%)
139-857A-						
1H	27 July	0650	1.9–11.4	9.5	9.67	102.0
2H	27 July	0730	11.4–20.9	9.5	9.80	103.0
3P	27 July	0900	20.9–21.9	1.0	0.05	5.0
4H	27 July	1025	21.9–31.4	9.5	10.31	108.5
5H	27 July	1130	31.4–40.9	9.5	10.13	106.6
6H	27 July	1315	40.9–50.4	9.5	9.89	104.0
7H	27 July	1600	50.4–59.9	9.5	7.30	76.8
8H	27 July	1635	59.9–69.4	9.5	10.19	107.2
9H	27 July	1800	69.4–78.9	9.5	10.08	106.1
10H	27 July	1915	78.9–86.9	8.0	8.31	104.0
11X	27 July	2015	86.9–91.9	5.0	0.61	12.2
12X	27 July	2245	91.9–101.5	9.6	0.36	3.8
13X	28 July	0000	101.5–111.2	9.7	7.46	76.9
14P	28 July	0115	111.2–112.2	1.0	0.56	56.0
			Coring totals	110.3	94.72	85.9
			Drilled	0.00–1.9 mbsf		
139-857B-						
1H	28 July	0415	0.0–3.4	3.4	3.36	98.8
2H	28 July	0515	3.4–12.9	9.5	9.92	104.0
3H	28 July	0640	21.0–30.5	9.5	10.16	106.9
			Coring totals	22.4	23.44	104.6
			Washed	12.9–21.0 mbsf		
139-857C-						
1R	28 July	2000	0.0–3.5	3.5	3.59	102.0
2R	29 July	0235	56.5–66.5	10.0	2.38	23.8
3R	29 July	0335	66.5–76.1	9.6	4.40	45.8
4R	29 July	0550	76.1–82.1	6.0	0.05	0.8
5R	29 July	0650	82.1–86.2	4.1	0.59	14.4
6R	29 July	0750	86.2–95.2	9.0	3.25	36.1
7R	29 July	1015	95.2–104.9	9.7	0.08	0.8
8R	29 July	1115	104.9–114.5	9.6	0.12	1.3
9R	29 July	1205	114.5–124.1	9.6	1.32	13.7
10R	29 July	1315	124.1–133.8	9.7	0.99	10.2
11R	29 July	1415	133.8–143.5	9.7	1.76	18.1
12R	29 July	1515	143.5–153.1	9.6	2.68	27.9
13R	29 July	1615	153.1–162.8	9.7	4.24	43.7
14R	29 July	1715	162.8–172.5	9.7	3.30	34.0
15R	29 July	1825	172.5–182.2	9.7	6.90	71.1
16R	29 July	1930	182.2–191.9	9.7	0.81	8.4
17R	29 July	2130	191.9–201.6	9.7	3.65	37.6
18R	30 July	0100	201.6–211.3	9.7	3.43	35.3
19R	30 July	0235	211.3–220.9	9.6	2.96	30.8
20R	30 July	0350	220.9–230.6	9.7	0.00	0.0
21R	30 July	0510	230.6–240.3	9.7	4.12	42.5
22R	30 July	0635	240.3–249.9	9.6	1.82	18.9
23R	30 July	0805	249.9–259.2	9.3	0.71	7.6
24R	30 July	1000	259.2–268.8	9.6	2.72	28.3
25R	30 July	1145	268.8–274.5	5.7	1.00	17.5
26R	30 July	1415	274.5–284.1	9.6	1.86	19.4
27R	30 July	1930	284.1–293.8	9.7	2.80	28.8
28R	30 July	2055	293.8–303.4	9.6	4.44	46.2
29R	30 July	2210	303.4–313.1	9.7	2.42	24.9
30R	30 July	2330	313.1–322.7	9.6	4.69	48.8
31R	31 July	0040	322.7–327.6	4.9	3.55	72.4
32R	31 July	0145	327.6–332.4	4.8	4.38	91.2
33R	31 July	0305	332.4–336.5	4.1	4.19	102.0
34R	31 July	0415	336.5–341.3	4.8	3.95	82.3
35R	31 July	0530	341.3–346.1	4.8	4.70	97.9
36R	31 July	0650	346.1–350.8	4.7	4.03	85.7
37R	31 July	0810	350.8–355.8	5.0	3.43	68.6
38R	31 July	0930	355.8–360.4	4.6	2.96	64.3
39R	31 July	1100	360.4–365.4	5.0	3.97	79.4
40R	31 July	1210	365.4–374.9	9.5	2.56	26.9
41R	31 July	1345	374.9–379.7	4.8	4.01	83.5
42R	31 July	1510	379.7–384.7	5.0	3.57	71.4
43R	31 July	1630	384.7–389.7	5.0	4.19	83.8
44R	31 July	1755	389.7–394.3	4.6	3.13	68.0
45R	31 July	1900	394.3–399.0	4.7	2.44	51.9
46R	31 July	2015	399.0–404.0	5.0	3.42	68.4

Table 1 (continued).

Core	Date (1991)	Time (UTC)	Depth (mbsf)	Cored (m)	Recovered (m)	Recovery (%)
47R	31 July	2130	404.0–408.7	4.7	2.38	50.6
48R	31 July	2245	408.7–413.7	5.0	2.82	56.4
49R	1 Aug.	0015	413.7–418.3	4.6	3.31	71.9
50R	1 Aug.	0130	418.3–423.4	5.1	2.49	48.8
51R	1 Aug.	0255	423.4–427.8	4.4	2.99	67.9
52R	1 Aug.	0440	427.8–432.8	5.0	2.61	52.2
53R	1 Aug.	0555	432.8–437.0	4.2	1.25	29.7
54R	1 Aug.	0720	437.0–442.0	5.0	0.18	3.6
55R	1 Aug.	0855	442.0–446.5	4.5	0.40	8.9
56R	1 Aug.	1005	446.5–451.7	5.2	0.28	5.4
57R	1 Aug.	1145	451.7–461.5	9.8	0.20	2.0
58R	1 Aug.	1340	461.5–471.1	9.6	0.23	2.4
59R	1 Aug.	1715	471.1–480.8	9.7	4.84	49.9
60R	1 Aug.	1940	480.8–490.5	9.7	2.08	21.4
61R	1 Aug.	2120	490.5–500.0	9.5	1.91	20.1
62R	1 Aug.	2315	500.0–509.7	9.7	1.86	19.2
63R	2 Aug.	0050	509.7–519.4	9.7	0.55	5.7
64R	2 Aug.	0240	519.4–529.1	9.7	2.37	24.4
65R	2 Aug.	0410	529.1–538.8	9.7	0.34	3.5
66R	2 Aug.	0630	538.8–548.4	9.6	1.00	10.4
67R	2 Aug.	0820	548.4–558.0	9.6	0.54	5.6
68R	2 Aug.	1045	558.0–567.7	9.7	2.85	29.4
			Coring totals	514.7	169.04	32.8
Washed between Cores 139-857C-1R and -2R (3.5–56.6 mbsf)						
139-857D-						
1R	24 Aug.	1830	581.5–589.6	8.1	1.80	22.2
2R	24 Aug.	2130	589.6–599.3	9.7	1.26	13.0
3R	25 Aug.	0015	599.3–608.9	9.6	2.08	21.6
4R	25 Aug.	0245	608.9–618.6	9.7	1.73	17.8
5R	25 Aug.	0650	618.6–627.9	9.3	0.14	1.5
6R	25 Aug.	0930	627.9–637.6	9.7	0.11	1.1
7R	25 Aug.	1245	637.6–647.3	9.7	0.30	3.1
8R	25 Aug.	1645	647.3–656.9	9.6	0.88	9.2
9R	25 Aug.	1900	656.9–666.6	9.7	0.94	9.7
10R	25 Aug.	2045	666.6–676.2	9.6	0.30	3.1
11R	25 Aug.	0240	676.2–685.9	9.7	0.40	4.1
12R	26 Aug.	0130	685.9–695.5	9.6	1.25	13.0
13R	26 Aug.	0330	695.5–705.1	9.6	0.15	1.6
14R	26 Aug.	0540	705.1–714.8	9.7	0.12	1.2
15R	26 Aug.	0740	714.8–724.5	9.7	0.75	7.7
16R	26 Aug.	1010	724.5–733.9	9.4	2.00	21.3
17R	26 Aug.	1330	733.9–743.6	9.7	3.47	35.8
18R	26 Aug.	1630	743.6–752.8	9.2	2.17	23.6
19R	26 Aug.	1945	752.8–762.5	9.7	0.28	2.9
20R	26 Aug.	2245	762.5–772.2	9.7	1.01	10.4
21R	27 Aug.	0140	772.2–781.8	9.6	1.72	17.9
22R	27 Aug.	1825	781.8–791.5	9.7	0.70	7.2
23R	27 Aug.	2135	791.5–801.2	9.7	0.89	9.2
24R	28 Aug.	0030	801.2–810.8	9.6	2.39	24.9
25R	28 Aug.	0415	810.8–820.3	9.5	0.66	7.0
26R	28 Aug.	0640	820.3–829.6	9.3	0.72	7.7
27R	28 Aug.	0850	829.6–838.9	9.3	0.86	9.3
28R	28 Aug.	1245	838.9–848.4	9.5	0.64	6.7
29R	28 Aug.	1545	848.4–858.9	10.5	1.73	16.5
30R	28 Aug.	1800	858.9–868.5	9.6	0.46	4.8
31R	28 Aug.	2030	868.5–878.1	9.6	0.76	7.9
32R	28 Aug.	2315	878.1–887.8	9.7	0.35	3.6
33R	29 Aug.	0120	887.8–897.5	9.7	0.70	7.2
34R	29 Aug.	0405	897.5–907.2	9.7	0.70	7.2
35R	29 Aug.	0645	907.2–916.9	9.7	1.12	11.5
36R	29 Aug.	1000	916.9–926.5	9.6	1.50	15.6
37R	29 Aug.	1245	926.5–936.2	9.7	0.32	3.3
			Coring totals	354.7	37.36	10.5

inferred to lie fully within the Brunhes magnetic chron. However, a large-amplitude negative magnetic anomaly is centered over the axis of the valley (see Davis and Villinger, this volume). This is inferred to be caused by low magnetization and susceptibility of the basement rock, which is hot and possibly highly altered (Davis and Lister, 1977; Levi and Riddihough, 1986).

OPERATIONS

Operations Outline

To reach the desired objectives at this site required a single deep hole penetrating through the sediment section and as deeply as possible into permeable basement as time would permit. This entailed drilling, in the normal sequence, an APC/XCB hole (two nearly co-located holes were completed, 857A and 857B), an RCB exploratory hole (857C, which was logged and later cemented off to prevent a possible thermal, chemical, and hydraulic "short circuit" from the seafloor to any permeable formation below the sediment section), and an RCB reentry hole (857D). After the reentry cone was washed in Hole 857D, the hole was drilled about 100 m into an interbedded diabase sill/sediment complex to a total depth of 568 m, then cased and grouted. The hole was left with the casing shoe intact to thermally re-equilibrate while initial operations at Site 858 were carried out.

After a period of two weeks, Hole 857D was reentered, and a temperature log was completed. The casing shoe was then drilled out and the hole was deepened with two bits to a total depth of 936 mbsf. This deepened hole was then logged with the JAPEX temperature tool, a seismic stratigraphy tool string, and a formation microscanner. At the end of the formation microscanner run, the tool became stuck as it was pulled into the end of the drill string. Following the pipe trip that was required to retrieve this tool, a packer/flowmeter experiment and a final logging run with the lithoporosity tool string were completed. This completed all drilling and downhole measurements this hole, and an instrumented CORK was set in the reentry cone.

Hole 857A

The initial seafloor APC core was "shot" from 2431 to 2440.5 m on the basis of a depth of 2435 m obtained with the precision depth recorder (PDR). A full core barrel was recovered which appeared to include the seafloor interface. Continuous APC coring therefore continued, with the depth set at 2431 m. The pressure core sampler (PCS) was lowered for its first field trial at 19 mbsf following recovery of the second APC core. The sampler recovered a small amount of core but failed to retain pressure in the core chamber. A successful water-sampler temperature probe (WSTP) run was made at 50 mbsf. Cores 139-857-9H and -10H failed to achieve complete stroke, and the switch to XCB coring was made at 85 mbsf.

XCB cores were taken to 111 mbsf, where a second PCS run was made. The PCS recovered a good core, but the ball-valve mechanism malfunctioned. A good WSTP temperature measurement was made at 90 mbsf. A final WSTP attempt at 110.1 mbsf resulted in a flooded pressure case and no data. The sediments were considered firm enough for RCB coring at that point, and operations were terminated in preparation for the deeper RCB exploratory hole.

Hole 857B

Closer inspection of Core 139-857A-1H (after the liner was opened) revealed that the sediment/water interface had not been recovered. A second "mudline" core was therefore requested to obtain the valuable uppermost sediments. In addition, better temperature data were needed from the upper 30 m of sediment to resolve the geothermal gradient.

When the bit had been pulled above the seafloor, an APC core was taken from 2423 to 2432.5 m. The core liner contained 3.4 m of sediment, this time definitely including seafloor sediment. The seafloor depth was redefined as 2429.1 m. As a result, all below-seafloor depth data for Hole 857A were adjusted by adding 1.9 m.

Core 139-857B-2H was then taken for a temperature-shoe measurement at 13 mbsf. The bit was "washed" ahead to 21 mbsf for Core 139-857-3H and a temperature-shoe reading at 30.5 mbsf. The data were of good quality and the drill string again was pulled clear of the seafloor.

Hole 857C

The position of Hole 857A (and 857B) over the peak of the heat flow anomaly in this part of Middle Valley had been compromised slightly in an attempt to avoid having to drill through a sill (a bright reflector) present part way down through the sediment section not far to the east of these holes. The heat flow determined from the temperature measurements in Holes 857A and 857B indicated that we would be required to drill considerably deeper than planned to reach our "hydrothermal basement" objective; to reduce this requirement, it was decided that the reentry hole should be located closer to the peak heat flow, despite the potential difficulty of drilling through the sill. The position for the reentry site was therefore moved 180 m to the east. Following the round trip for the RCB bottom-hole assembly (BHA), a jet-in test was begun to determine the casing point for the reentry installation. Unfortunately, the jet-in test was begun before the offset was made, resulting in a loss of 2.5 hr.

When the required move had been completed, Hole 857C was spudded with a seafloor "punch" core that established the seafloor at 2432.5 m. The second jet-in test was then started. At 37.5 mbsf, the test was interrupted for a temperature probe measurement. The jet-in test then continued to 56.5 mbsf, where increasingly firm sediment signaled the limit for jetting in casing. Following a second temperature probe run at that depth, continuous RCB coring began.

Hole conditions and rate of penetration (ROP) remained good through the sedimentary section, although core recovery was disappointing. Penetration was locally slower in the interval from 167 to 187 mbsf. At 230 mbsf, core length was reduced to half the normal interval in an effort to increase recovery. The sediment became firmer at about the same depth, so it was not clear which factor had more effect on the dramatically increased core recovery, which rose from about 35% to about 90%.

Coring operations were interrupted at 202 and 285 mbsf for bottom-hole temperature tests with the GRC self-contained temperature-recording tool, which was deployed on the coring line through the RCB bit. The first run was completed with the tool run fully into the fill in the bottom of the hole, and the second with the tool in the water above the bottom. Neither provided reliable estimates for formation temperature; the records indicated that in both cases, temperature was recovering rapidly from drilling disturbance, but not rapidly enough to allow a 1- to 2-hr post-drilling measurement to be meaningful. The measurements were useful, however, in showing that seawater circulation was even more effective at keeping the hole and BHA cool than had been anticipated.

Below 435 mbsf, sediments became more highly indurated and brittle, and recovery again decreased. At 471 mbsf, an altered basaltic sill was encountered. Though the sill appeared to be a good casing seat, coring continued to 568 mbsf through a series of variably altered sills and interbedded, altered sediment to confirm that the hole was stable below the sill. No hole trouble of any kind had been experienced during the drilling down to that depth, so preparations for logging began.

A wiper trip was made to 75 mbsf to confirm the hole's suitability for logging and to condition it. Though the pipe initially was free in the hole, the trip was "wet" to 228 mbsf, where overpull to 40,000 lb was required. After that point, the pipe was dry and free in the hole. The bit was then run back to total depth, where only 2 m of fill were found. A 40-barrel (bbl) sweep of drilling mud was then pumped through the annulus to clean the loose material from the hole. Following the mud sweep, the running/setting tool (RST) was run twice on the coring line, first to release the bit and then to downshift the internal sleeve of the mechanical bit release (MBR). The open-ended pipe then was pulled back to 75 mbsf for logging operations.

The new conical side-entry sub (SES) was employed to provide the capability of cooling the hole with pump circulation to protect the logging tools and cable. It was the inaugural deployment of the SES by the rig crew. The deployment went smoothly and the first logging run with a seismic stratigraphy tool string began.

As measurements of temperature in the bottom of the hole were planned as a final operation following the logging runs, the drill pipe was not run to total depth; a 20 m section above the bottom of the hole was kept as a thermal "sanctuary." The circulating head was then rigged to initiate circulation for the logging operation with the bottom of the pipe at this depth. As soon as pumping began, the drill string

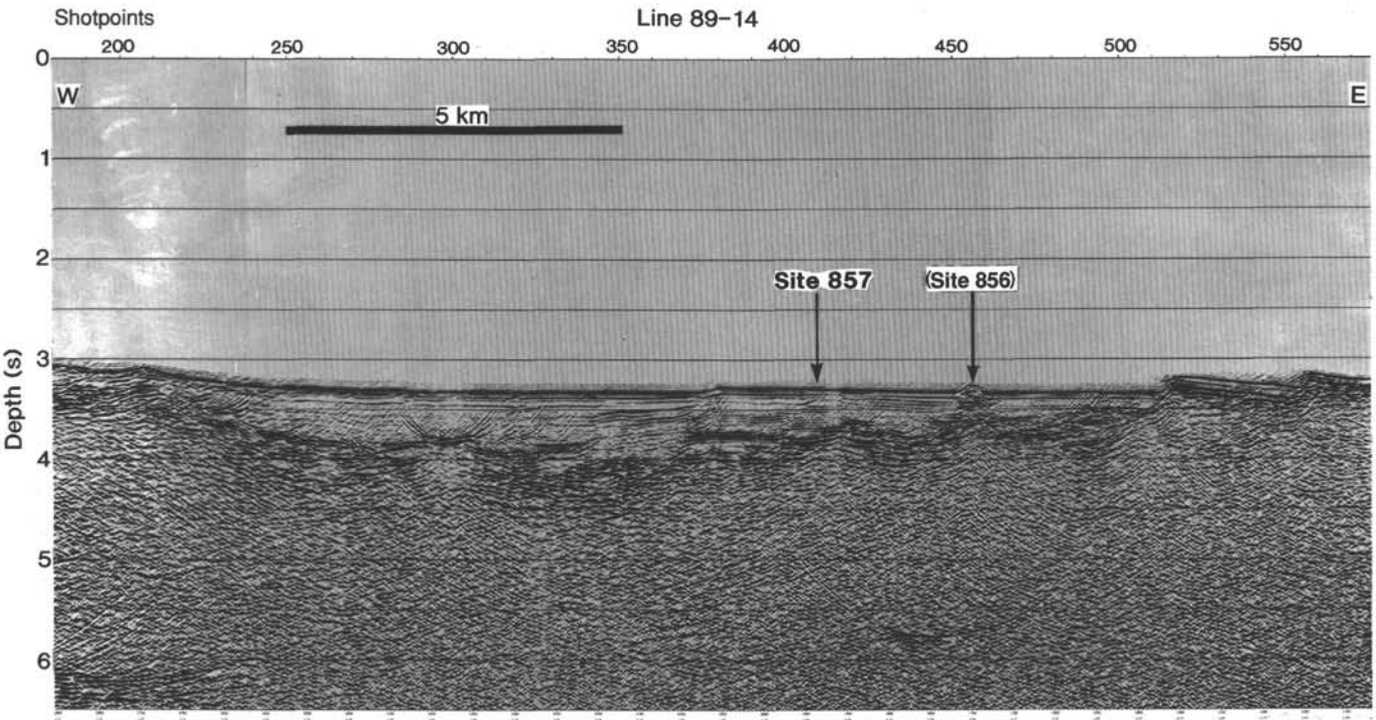

Figure 1. Multichannel seismic reflection profile 89-14, crossing Middle Valley and Site 857 (from Rohr et al., 1992). The location of Site 856 is shown for reference.

became "packed off" and stuck. Circulation was regained and the pipe was free to be raised after about 30 min, but the logging tool entered open hole only to stop on fill 26 m short of total depth, and 6 m short of the targeted logging depth. The log then proceeded without incident, except that minor sticking tendencies persisted each time a stand of pipe was raised ahead of the logging tool.

The lithoporosity tool combination was run next. The drill string was lowered to 527 mbsf for circulation leaving a few meters of open hole undisturbed for later temperature logging. Circulation was maintained for about 30 min while the logging tool was lowered to that depth, after which the pipe was withdrawn, leaving the tool in open hole. A good log then was recorded without incident.

The same technique was used for the third logging attempt, with the formation microscanner (FMS). All seemed routine until the drill string was raised to permit open-hole logging. When this was done, the logging wire went slack, indicating that the tool was stuck in the bottom of the string. A partial sediment plug in the pipe was suspected, and increased pump circulation was tried in an attempt to wash out the sediment and free the tool. Circulation pressure was noted to be too low for the length of the drill string. Concurrently, attempts to free the tool with the logging winch resulted in the tool becoming stuck in both directions. The most reasonable explanation for the low circulating pressure was that the oilsaver packoff in the SES had become unseated. It was also suspected that the logging cable had become knotted at the SES due to excess slack and that the knot had unseated the packoff. The drill string and stuck logging cable then were raised simultaneously until the SES reached the moonpool. The packoff was indeed found to be unseated, along with the "stinger" that holds the float valve away from the logging line. The cable was straight and undamaged through the SES, however, and the unlatching of the oilsaver was unexplained. It was reseated and circulation was established, but efforts to free the stuck tool were unsuccessful. Readings from the tool's sensors indicated that the FMS arms near the bottom of the tool were in open hole while the gamma-ray portion, higher up, was inside the BHA. When all measures to recover the tool had failed, the only reasonable option open was to crimp and cut the logging cable near the cablehead and to recover the stuck tool with the drill string.

Because plans for the completion of Hole 857C included temperature logging and plugging with cement, and because of a possible need to fish for the logging tool if it dropped from the BHA after the cable was cut, a free-fall reentry funnel (FFF) was rigged around the drill string and dropped into place as soon as the severed logging cable was retrieved. The vibration isolated television (VIT) was also deployed so that the pipe could be observed as it cleared the FFF, in order to see if the logging tool extended below the BHA. Though the withdrawal from the cone was observed and videotaped, limited visibility and perspective prevented a clear view or indication of whether the tool was present.

The pipe trip out of the hole was slowed by the electromagnetic inspection of the BHA connections, which was considered necessary because of high stresses imposed by operations at Sites 855 and 856 and because of the heavy loads and high investment of the subsequent reentry installation. When the MBR top connector cleared the moonpool, the lower portion of the logging tool was seen to be extending about 1.5 m below the pipe. After the lower stand of the BHA had been broken down, the Kinley tools were removed and the logging tool was extricated from the outer core-barrel assembly. A small amount of cable was found to have been kinked or knotted into the cavity of the top sub and fouled between the cablehead and the latch sleeve of the outer core barrel. Despite the abuse the tool had suffered during recovery, it was in excellent condition.

Hole 857D

A string of four joints of 16-in. casing was made up to the casing hanger and hung off in the reentry cone held in the moonpool. The lower BHA was assembled and attached to the casing string. The entire installation then was latched into the lower cone, which was lowered through the moonpool, and the pipe trip to the seafloor continued with construction of the upper BHA. A very long and heavy BHA was required for this hole because of anticipated hard-rock drilling with the 14-3/4-in. bit.

A

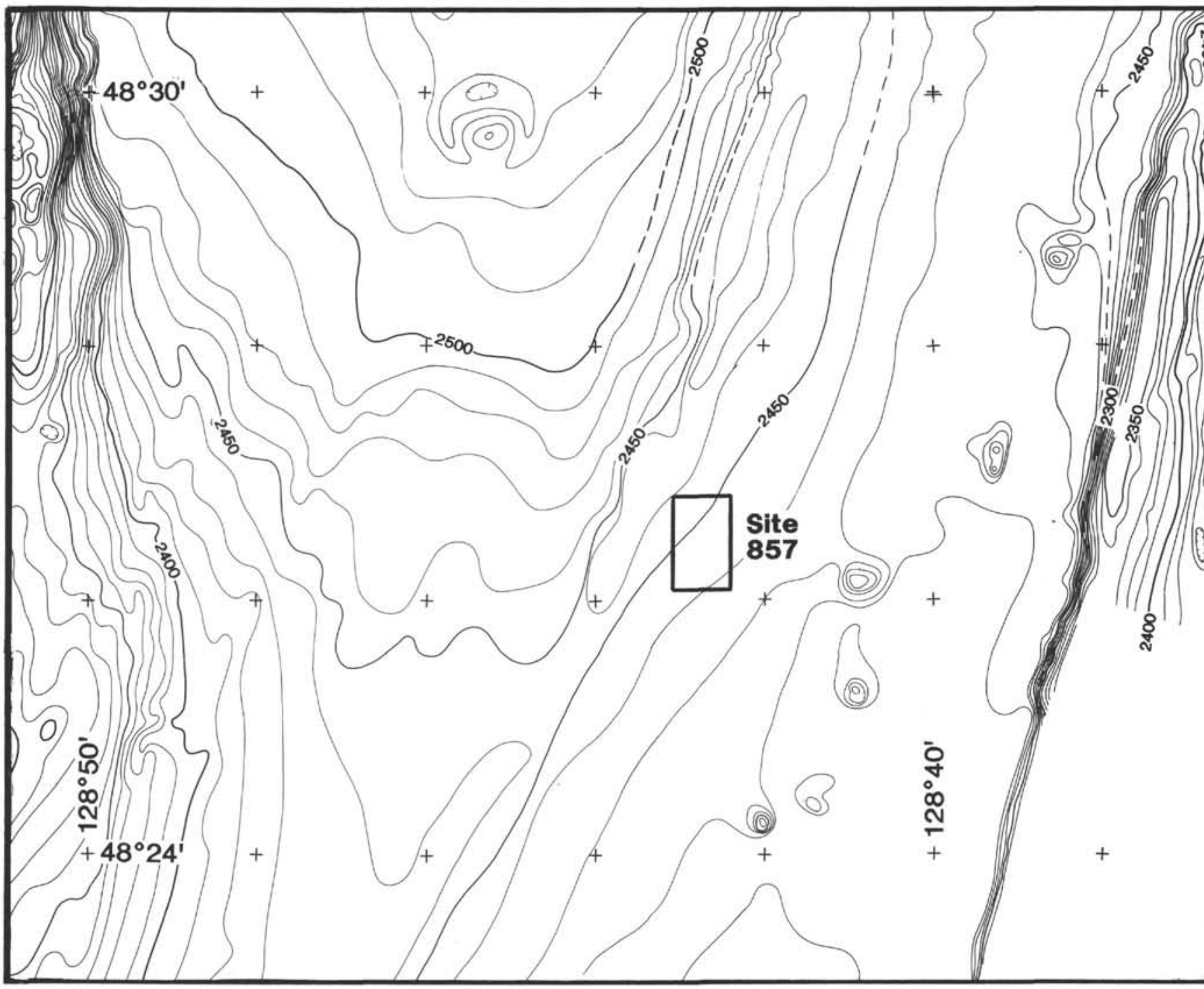

Figure 2. **A.** Bathymetry of the part of Middle Valley occupied during Leg 139, based on continuous SeaBeam swath soundings. Depths are computed using a sonic velocity of 1500 m/s and contoured at 10-m intervals. The area of Site 857 included in Figure 4 is outlined. **B.** SeaMARC II acoustic imagery of the same area that is shown in (A).

Hole 857D was spudded on 5 August at 0930 hr at a position 50 m north-northeast of Hole 857C. The casing shoe was jetted to 2480.2 m, where the rate of penetration abruptly dropped. The distance from the casing shoe to the mud plate of the reentry cone was 48.7 m, and thus the seafloor depth was set at 2431.5 m. A wireline run with the RST released the cone/casing assembly.

Drilling then proceeded toward the total depth of Hole 857C. Since caliper logs had shown intervals of oversized hole to be present well below the upper intrusive unit and between several sills near total depth, plans were made to set the casing through the entire section. Hard drilling was first encountered at 2895 m, about 8 m higher than in Hole 857C. As drilling proceeded, the detailed correlation of drilling rate vs. depth between the holes did not improve. A strong drilling break occurred just before the planned total depth of 3000 m for the 14-3/4-in. hole, indicating the presence of soft and possibly unstable sediment. As several meters of fast drilling were involved, drilling continued to 3012 m (580.5 mbsf) so that an additional joint of casing could be set to isolate the soft interval. The drilling rate at that depth continued to indicate that sedimentary material was being penetrated, but it was firm and uniform compared to the interval near 3000 mbsf. The entire section was drilled in 26 rotating hr. A satisfactory ROP was achieved in the hardest material with only 35,000 lb of bit weight, so it was not necessary to apply the weight of much of the long string of unstabilized 8-1/4-in. drill collars.

The hole was then flushed with 65 bbl of high-viscosity drilling mud before the pipe trip began. No significant overpull was encountered as the bit was pulled toward the seafloor, and other hole-cleaning measures, such as a wiper trip, were judged unnecessary. Upon recovery of the bit, preparations were made for running the 11-3/4-in. surface casing string. Weather conditions began to deteriorate as the operation progressed, and wind gusts to 66 knots produced vessel-motion conditions that approached operational limits. Nevertheless, the entire casing operation, including construction of the drill-pipe "stinger," was completed in just 18-3/4 hr despite the adverse conditions. The 580-m string included 47 joints of range-3 casing, an expansion joint, and the casing hanger.

Although the weather had improved as the casing job neared completion, it deteriorated again as the casing string was run toward

B

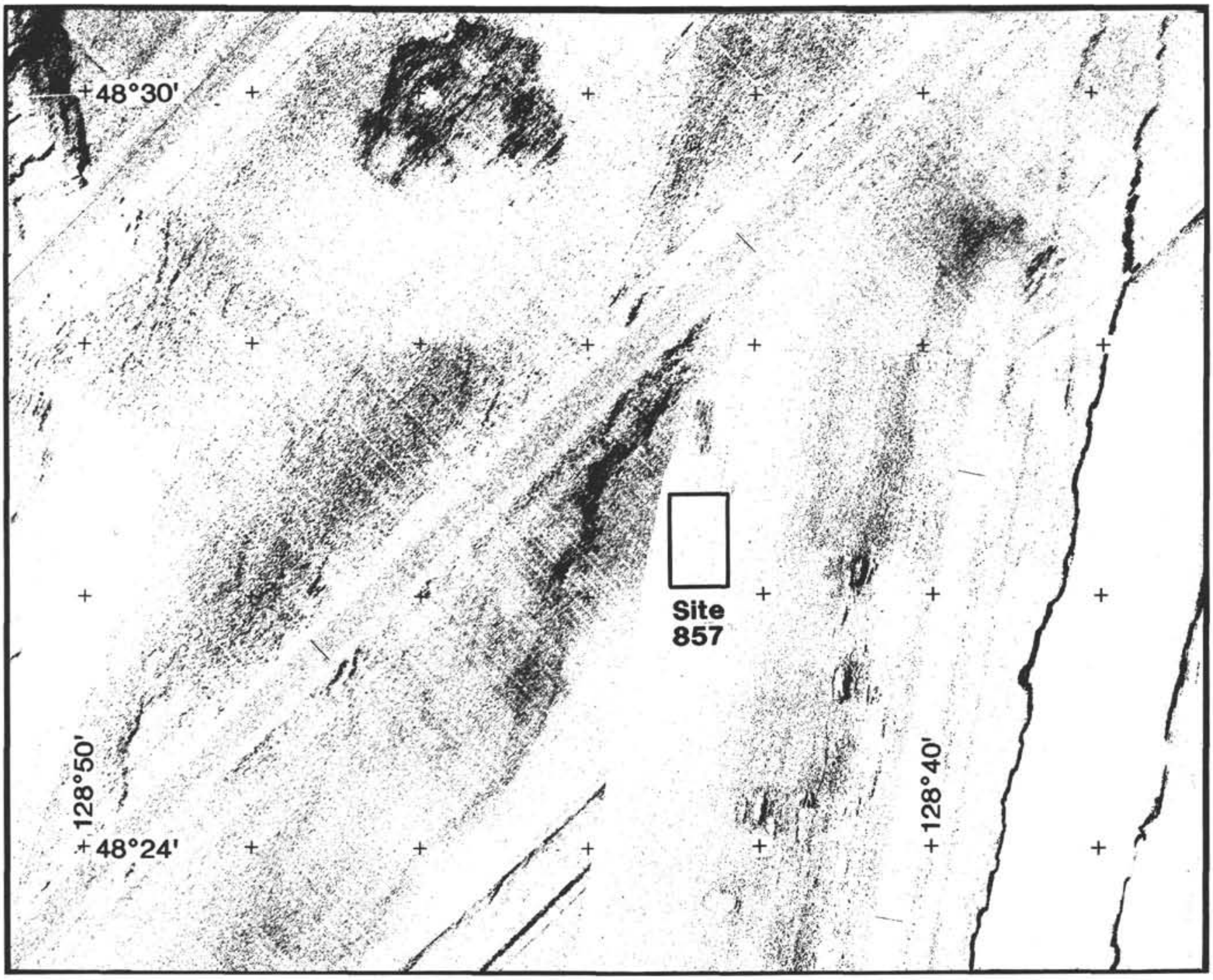

Figure 2 (continued).

the seafloor on drill pipe. The wind increased to gusts of 55 knots and combined sea/swell waves reached 20 ft. Dynamic positioning (DP) operators reported currents in excess of 2 knots at high angles to wind and seas—a condition that made station-keeping of the precision required for reentry an impossibility. The pipe trip continued until the casing shoe was three stands above the seafloor, and heavy "knobby" pipe was picked up to minimize bending stresses on the string at the ship. Conditions were improving rapidly at that time and, after only an hour of delay, the VIT frame was put into the water and started down the pipe. As the VIT approached reentry depth, the knobbies were removed and the final pipe was added to the string.

Reentry maneuvering required an hour before the stab could be made, due to a combination of difficult surface environment for positioning, unresponsiveness of the casing string to vessel moves, and heave motion to 10 ft. The rim of the cone was contacted twice before a successful reentry was made, and then the casing nearly heaved back out of the cone before enough pipe could be lowered to keep it in.

When the casing shoe had been lowered to 300 mbsf, the top drive was deployed so that circulation could be used to cool the seals in the float valve and seal nipple during the remainder of the trip.

The hole apparently remained in good condition and no resistance was noted until the casing took weight about 13 m from the expected latch-in point. The obstruction seemed to be a ledge or hard, rocky fill, but increased circulation and one or two setdowns easily moved the casing an additional 3 m. Solid resistance to lowering then was felt. A successful latch-in of the hanger was indicated, but the possibility of a stuck casing could not be eliminated, especially as the depth was 10 m short of the latch-in point indicated by the pipe tally. Because the discrepancy was almost exactly equal to the length of a joint of pipe, the tally was checked and rechecked—with no mathematical error found. It was considered probable that the casing was latched in, but if the string was stuck and released with the hanger above the cone, further reentries would be virtually impossible and the entire expenditure of time and hardware would be a waste. After some discussion, the conservative approach was taken, and the VIT was lowered for a TV inspection of the cone. The running tool and its centralizer sleeve were out of sight down the throat of the cone and the string was latched in. Later investigation revealed that, while the math was right, the tally for the 5-1/2-in. drill pipe had been used instead of the one for the 5-in. pipe that was actually run, and the 10 m was the difference in the two string lengths.

When the VIT had been recovered and the string could be rotated, the releasing operation began. Much difficulty was experienced in finding the neutral point and achieving rotation of the drill string to

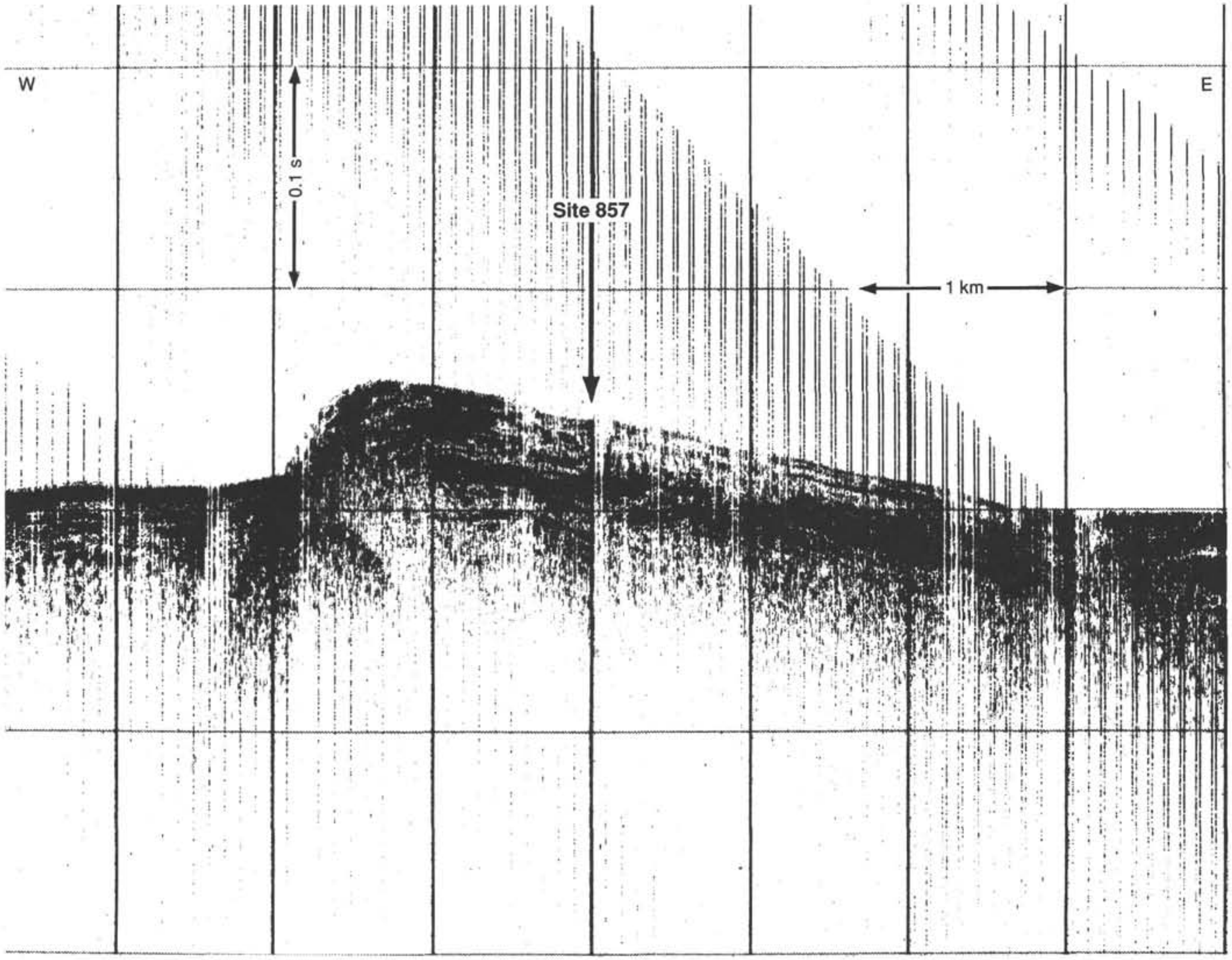

Figure 3. The 3.5-kHz profile crossing Site 857. The vertically exaggerated profile illustrates well the back-tilting of the fault block into which the holes of Site 857 were drilled.

effect release. The problem was exacerbated by vessel heave, which still amounted to several meters, and probably by friction of the centralizer sleeve against the inside of the lower cone. After several cycles of increasing and decreasing drill-string weight while holding torque with the top drive, enough rotations of the string were made to release the casing.

The cementing operation then commenced, but was slowed by difficulties in shipping the bulk cement from the surge tank to the mixing unit. As a result, some of the slurry was mixed lighter than had been desired. Care was taken, however, to insure that dense slurry was emplaced around the casing shoe. About 650 sacks of Class G cement (40% silica flour blend) were used. The slurry was displaced with seawater until the latch-down top plug landed at the shoe. The drill string then was raised until the seal nipple unseated from the shoe and loss of pressure signaled that the plug had cleared. The stinger was pulled above the reentry cone at 2030 hr on 8 August.

Hole 857C (Return)

During the next hour, the drill string was flushed of residual cement while the ship was offset the 50 m back to Hole 857C. A routine reentry was made into the FFF, though the lightweight stinger lagged behind the ship. The stinger was run to 94 mbsf, where the Sandia temperature tool was run on the coring line for an attempt to log the undisturbed water in the hole. The logging tool was stopped by a bridge or other obstruction at 192 mbsf and had to be retrieved. The pipe then was "washed" to 274 mbsf, where a second run with the Sandia tool was attempted—but the tool descended only to 299 mbsf before coming to a halt. A third attempt was made at 474 mbsf, but the logging tool stopped only 1 m below the seal nipple. Logging attempts were then abandoned, but the maximum recorded temperature of over 200°C appeared to confirm that there was no strong downflow of seawater into the hole.

A 30-bbl plug of neat cement slurry then was mixed and spotted at approximately 474–408 mbsf to guard against any potential fluid communication between 857C and the 857D reentry hole. The drill string was pulled clear of the seafloor at 2030 hr on 8 August, flushed out, then tripped for the assembly of the coring BHA to be used at Site 858. The Site 857 beacon was switched to standby mode and we moved to the next site, leaving the cased and grouted Hole 857D to begin thermal re-equilibration.

Hole 857D (Return)

After completing initial operations at Site 858, the DP move was completed and the Site 857 beacon was activated at 0745 hr on 23

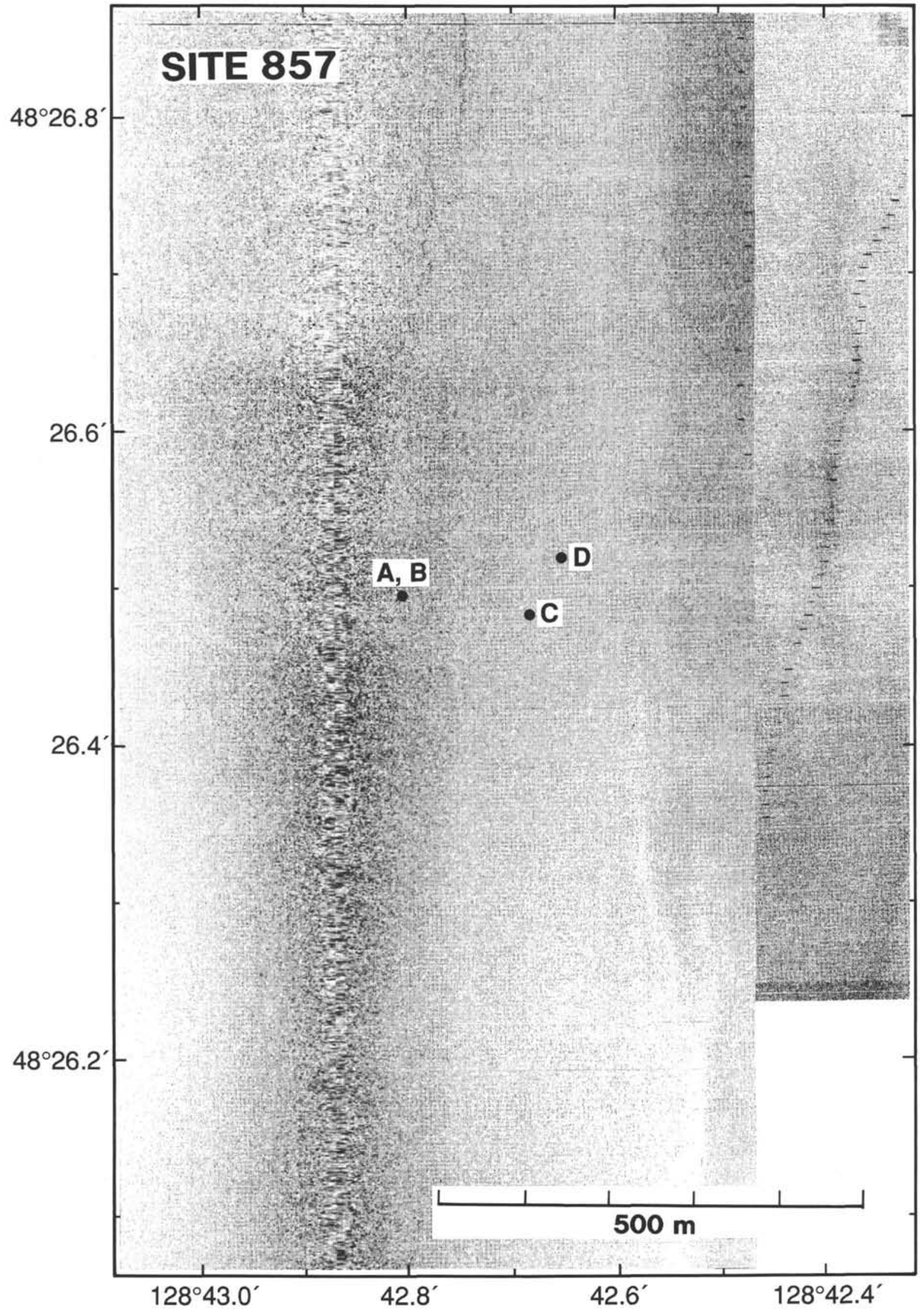

Figure 4. SeaMARC I side-scan acoustic image of the seafloor in the vicinity of Site 857 from Johnson et al. (in press), showing individual hole locations.

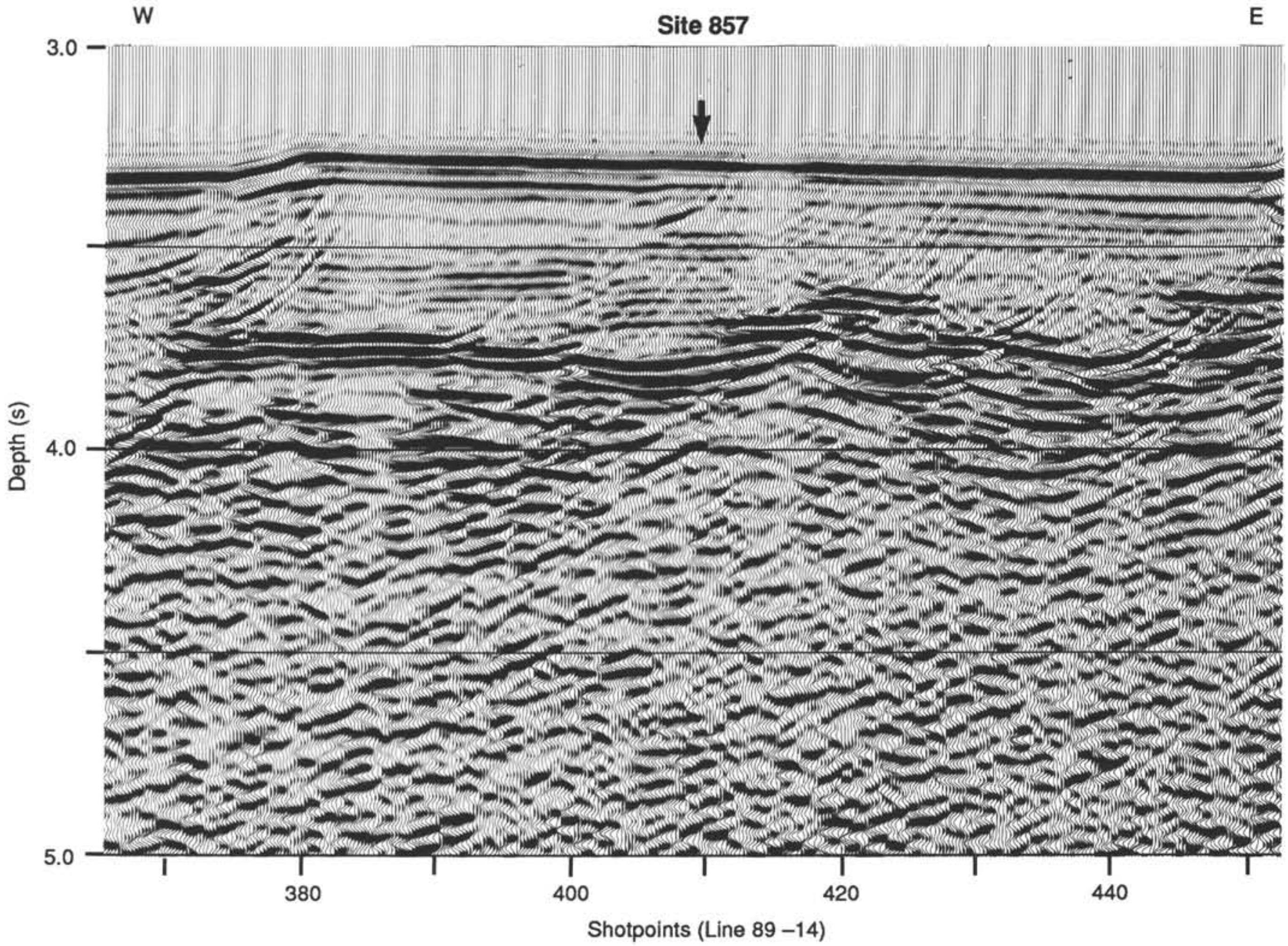

Figure 5. Details of seismic reflection profile 89-14, showing structure in the vicinity of Site 857. Shotpoints are spaced 50 m apart.

August. The signal was usable but too weak for confidence in beginning operations in a fairly deep reentry hole. A new beacon was launched at 1045 hr and the original was switched back to standby to be used as a backup for the duration of site occupancy.

The VIT was deployed and was run down the drill string while a drilling line cut-and-slip operation was performed. With the core bit in reentry position, the logging sheaves were rigged and the JAPEX PTF logging tool was made up with a modified inner core barrel. The pipe was fortuitously positioned exactly over the reentry cone as lowering of the logging tool began, so reentry was made immediately.

Temperatures were logged both on the trips down and up in the cased hole. Logging stopped at 510 mbsf where the tool apparently landed on cement. The temperature was 235°C.

When the bit had been lowered to 300 mbsf (about 145°C), the top drive was deployed so that seals in the bit, float valve, and jars could be cooled by circulation. Solid cement was contacted in the casing at 552 mbsf and was drilled easily to the plug and shoe at 573 mbsf. More than 3 hr were required to drill the shoe, but no other problems were experienced as the rathole was cleaned to total depth and 1 m of new hole was made.

Continuous RCB coring then began, and a mud flush was circulated to clean out any debris from the shoe while the initial core was being cut. The lithology comprised alternating highly altered diabase units and metamorphosed siltstone/claystone strata. Core recovery was fair to poor, particularly in the sedimentary parts of the section.

A particularly hard igneous unit was penetrated at 607–613 mbsf, followed by a sharp drilling break and rapid drilling from about 614–619 mbsf. Low circulating pressure was noted when the subsequent core barrel was pumped down the pipe. When the process of recovering the barrel was begun to check for proper latch-in, it was noted that the fluid level was far down the pipe and that the pipe was "under vacuum" when broken. The driller also noted an apparent gain in string weight of 10,000–12,000 lb, with no associated torquing or sticking tendencies of the drill string. As the phenomena apparently indicated a change in hydrologic conditions in the borehole, there was interest in measuring the actual fluid level in the drill string. A swab was rigged on the coring line with some of the lower cups inverted. The swab gave a clear weight indication when it reached the air/water interface at 135 m below the dual elevator stool (124 m below sea level).

One interpretation for the negative head of 124 m of seawater was that a sudden major influx of hot formation water displaced the cold drilling water from the annulus and created a "U" tube effect. Calculations showed that the drawdown was the amount that would exist if the entire annular length were filled with water of about 250°C average temperature and the entire drill string were filled with cold water. An alternative explanation was a gas flow that coincidentally produced the same loss of head as the hot-water case. The third possibility was that a layer had been penetrated that had sufficient permeability to allow a high rate of flow downhole driven by the density contrast between the cold seawater in the hole and the hot

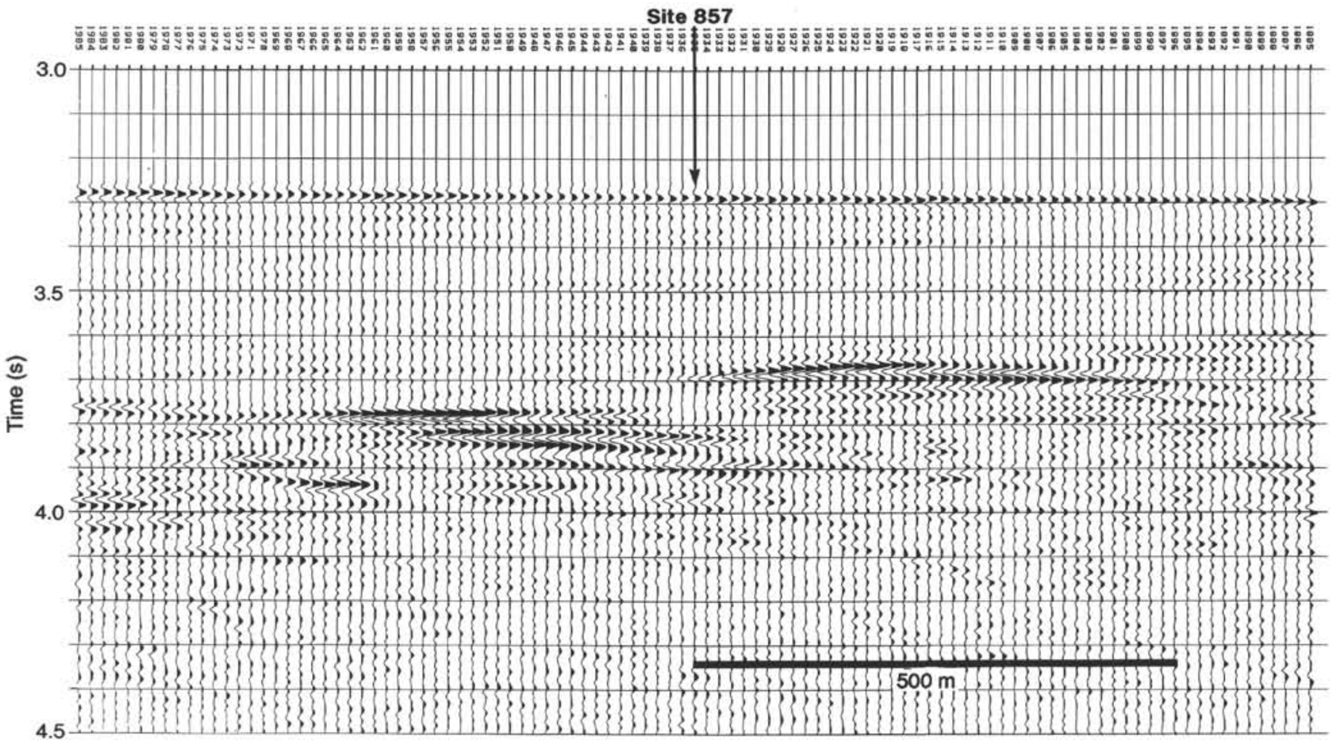

Figure 6. Near-trace display of multichannel seismic reflection line 89-14. Individual traces are spaced 12.5 m apart.

fluids in the formation. Swab soundings were taken every few hours and showed progressive reduction in the head loss as the hole was deepened below the permeable horizon.

Core recovery improved somewhat below about 725 mbsf. Accompanying lower drilling rates supported the appearance of reduced fracturing in the alternating sediments and sills. Coring was interrupted for a bit change at 782 mbsf. The bit had accrued 34-1/2 rotating hr. As the Security roller-bearing bits had no "track record" for longevity in Ocean Drilling Program (ODP) drilling, a conservative approach was taken and the bit was retired about 10 rotating hr sooner than a standard journal-bearing bit would have been.

The round trip and reentry were routine and consumed only 13 hr. The bit was found to have two fairly loose cones, indicating a rather advanced degree of bearing failure and that the trip had not been premature. Hole conditions were excellent, with no "drag" and only 2 m of fill upon the return to total depth.

Coring resumed at 0800 hr on 27 August. There was little change in lithology, drilling parameters, or core recovery from the preceding interval. ROP varied from 5 to 8 m/hr and average recovery was 9% for the bit run. Hole conditions remained excellent, but there were continued signs of hydrostatic drawdown in the drill string. Coring operations were terminated at 3367.7 m (936.2 mbsf), as there was no sign that the fraction of sediment was decreasing and operating time was running out.

After the final core, the hole was flushed with viscous mud and the bit was pulled inside casing for a JAPEX PTF log to check temperature. The tool logged a maximum temperature of 130°C at total depth. Extremely low temperatures higher in the hole indicated a flow of seawater down the bore. The drill string then was recovered to change over to an open-ended logging BHA. Upon recovery, the bit was in excellent condition (after 25 rotating hr), though the effectiveness of two of the cone seals was questionable.

The round trip was made in gale-force winds and heavy seas, but the reentry was accomplished without undue difficulty and with only about one-half hour of maneuvering time. The SES was rigged with the end of the pipe about 85 mbsf, and the seismic stratigraphy logging combination was assembled.

Pump circulation and the SES were used to cool the hole and to obtain a log essentially from total depth into casing. Log quality was fairly good despite vessel heave of 2–3 m. Because temperature sensors on the first logging tool indicated slow thermal recovery in the hole, the second logging suite, the FMS, was lowered into open hole without being accompanied by the pipe for cooling (though deployed through the SES in case of need). Two open-hole runs were made with the FMS, with spurious caliper readings beginning on the second run. When the tool was retrieved to the end of the drill pipe, it could not be pulled into the end of the pipe. Surface indications showed the problem to be at the location of the caliper/pad arms.

When 2 hr of effort failed to induce the tool to enter the pipe, the Kinley crimper/cutter tools were employed for the second time on Site 857. The operation again was hampered by the presence of the SES and by rough (though moderating) sea conditions, but otherwise was routine and the crimp and cut were made as planned. The severed logging cable was recovered, and the drill string was retrieved to recover the FMS tool. Again, the VIT was deployed so that pullout from the cone could be observed; the end of the FMS was visible. The tool was held tightly between the crimped line, with the crimper landed on a landing/saver sub, and a damaged FMS pad, which was wedged into the reentry/cleanout bit. It was necessary to cut the damaged caliper arm with a cutting torch so that the tool could be pulled up and out of the BHA. Three FMS pads had been lost in the hole.

Though the planned logging operations were only half complete, further logging was held in abeyance pending completion of packer permeability tests. The BHA was modified for packer work by adding one stand of drill collars, removing the landing/saver sub, and installing the dual-element TAM straddle packer (TSP) at the bottom. After a routine trip and reentry, the packer was run into the cased hole about 96 m to provide lateral support for the drill collars above it.

The first two attempts to set the packer were unsuccessful, apparently because too little weight was applied to the packer element after

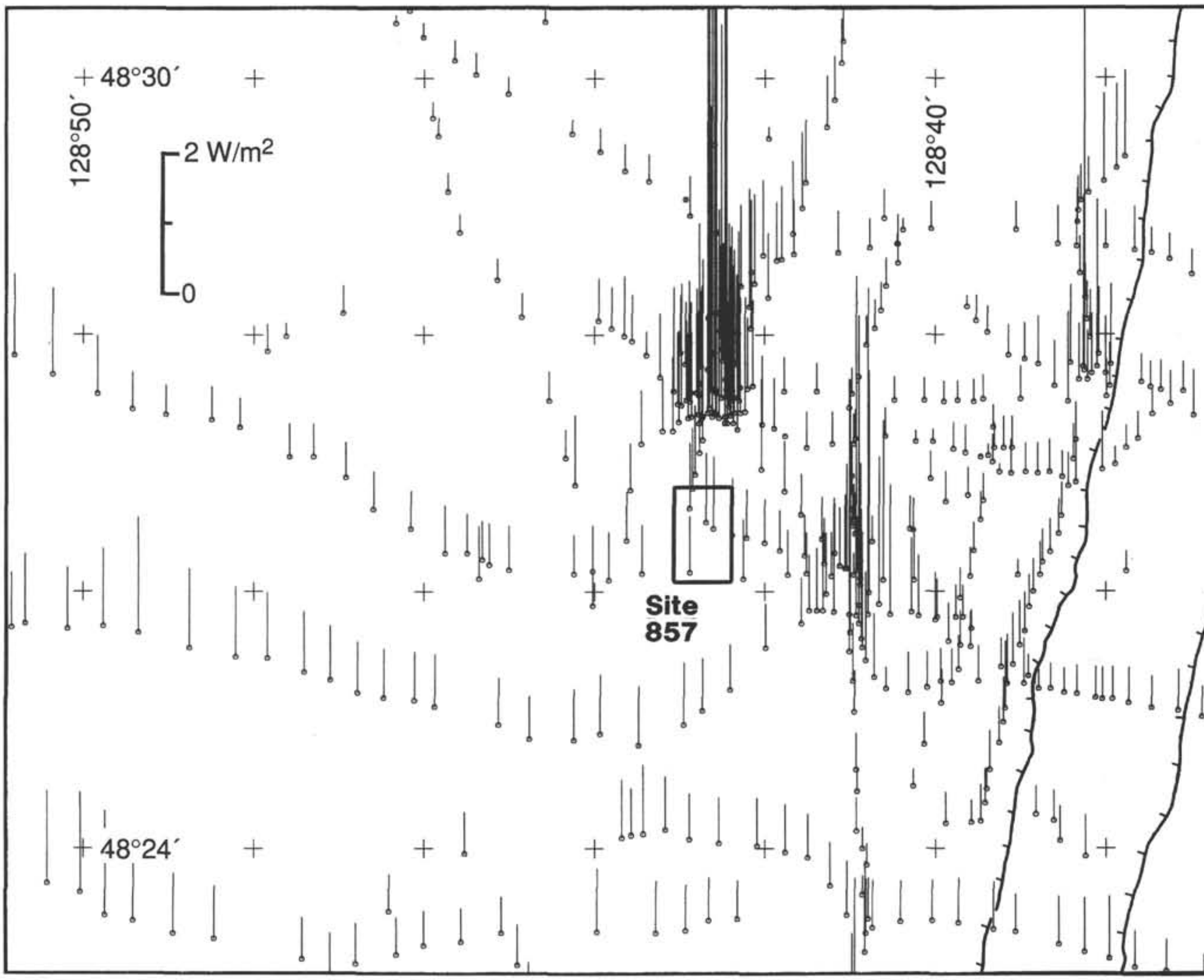

Figure 7. Heat flow in the part of Middle Valley occupied by Leg 139 (the same area as in Fig. 2). The area of Site 857 (shown in Fig. 4) is outlined.

inflation and vessel heave shifted the deflate sleeve. No further setting problems occurred after collar weight of 25,000–30,000 lb was used. Also, sea conditions were improving rapidly.

Pulse tests then were attempted for permeability determination but were unsuccessful because an accumulation of pipe rust blocked the flow passages of the go-devil. It was necessary to recover and redress the go-devil before tests could proceed. While the go-devil was out of the hole, a plastic pig was pumped down the pipe to remove as much additional rust scale as possible. Pulse-test efforts then were repeated, but pressure bled off immediately when the packer element was isolated and a satisfactory pressure buildup could not be achieved on attempts to induce a pulse. The high-permeability alternative, a constant-rate injection test, then was tried. Circulation rates were increased, stepwise, to 720 gpm, but surface pressure indications appeared to be only those imposed by fluid friction in the drill string and bleedoff was immediate. The packer was unseated and the go-devil was recovered so that flowmeter tests could proceed.

The flowmeter tool and special wireline-deployed go-devil were run to the packer on the logging cable. The packer was reset and the go-devil was run down the cased portion of the hole. The flowmeter was calibrated in casing with pump rates of up to 770 gpm before being lowered into open hole. The open-hole section then was logged with the flowmeter, but all indication of flow was lost when the instrument passed the suspected permeable zone at about 614 mbsf. With the flowmeter back inside casing, the packer was unseated and the flowmeter jumped to about triple the rate recorded at the highest pump rate. A repeat log with uncontrolled flow showed flow into a second zone about 50 m below the first, but no reading was obtained below that. The flowmeter and go-devil then were retrieved.

After the packer had been lowered to 756 mbsf, it was reset to isolate the lowermost 180 m of "tight" hole. Pulse tests again bled off quickly, but two successful constant-rate tests were conducted at reasonable pumping rates. With packer tests complete, the go-devil was retrieved and the drill string was pulled back to about 120 mbsf for additional logging.

An electrical problem had been identified with one of the conductors in the logging cable and was estimated to be 2500–3000 m above the downhole end of the cable. After several alternatives had been considered, the decision was to cut off the lower portion of the cable, including the 2000-m high-temperature section, rehead the cable, and use the remainder of the (standard grade) logging line for the balance of the leg. With the drill string hung off in casing, the lower 3000 m of cable was spooled onto the draw-works sand reel for temporary storage. The remaining cable then was reheaded and the lithoporosity tool combination was attached.

The logging tool then was lowered to total depth in the hole, and the signal was lost as logging was to begin. Upon recovery of the logging tool, the lower 100 m of cable was found to be severely heat-damaged. The polypropylene conductor insulation had melted and extruded through the armor. The tool was checked out and found to be undamaged, however. The lowermost 200 m of cable was cut off, a new head was attached, and a second attempt was made to run the lithoporosity combination tool, this time staying above the permeable zones that were drawing in cold water. Unfortunately, a bad conductor in the cablehead prevented the caliper pad from extending, and the formation density log was of little value. The neutron porosity log was good, however.

With the allotted time for logging expired, a round trip was made for installation of the CORK and data logger. The CORK and its special BHA were assembled and run in without incident, except that the pipe trip was interrupted for over an hour for replacement of a broken skate wire on the piperacker. A routine reentry was made, and the drill-collar "stinger" of the CORK assembly was run a few meters into the casing.

The CORK was left suspended above the reentry cone while the 300-m thermistor and fluid-sampling string was deployed, attached to the data logger package, lowered, and landed in the CORK by means of the coring line. When the coring line had been recovered, the CORK was landed in the 11-3/4-in. casing hanger and latched in hydraulically by means of a pump-down ball. With the drill string still attached, a special submersible/ROV landing platform was bolted around the drill string and free-dropped to land on the reentry cone. The VIT was lowered for inspection of the platform and CORK installation and for observation of the release from the drill string. The latch mechanism was "unjayed" at 0545 hr on 3 September.

After the VIT and most of the drill string had been recovered, the positioning beacon was released and recovered. While the BHA was recovered and the drilling line was cut and slipped, the rig was offset to Site 856, where the beacon used earlier at that site also was released and retrieved. Offsetting continued to Site 858 as the new RCB-coring BHA was assembled. The beacon left in standby 11 days earlier was reactivated by acoustic command at 1130 hr.

LITHOSTRATIGRAPHY AND SEDIMENTOLOGY

Site 857 is situated about 5 km west of the eastern boundary fault of Middle Valley and about 2 km south of an active vent field. Holes 857A, 857B, 857C, and 857D were spudded in at water depths of 2418.3, 2418.3, 2421.7, and 2420.6 m, respectively. Hole 857A was drilled by APC/XCB to a depth of 112.2 mbsf with 85.9% recovery. Although the mudline was missed in Core 139-857A-1H, recovery in this hole was nearly perfect in the upper 10 cores and coring disturbance was minimal. Thus, Hole 857A probably provides the best "background" record of Holocene and upper Pleistocene sedimentation collected during Leg 139. Hole 857B was offset a few meters and drilled by APC to 30.5 mbsf primarily to recover a mudline core and to measure the sediment temperature. Only the mudline core, 139-857B-1H, was split and described aboard the ship. The identification of mudline in Core 139-857B-1H caused all sub-bottom depths in Hole 857A to be increased by 1.90 m.

Additional comparison of Cores 139-857A-1H and -857B-1H suggests that there is an actual vertical offset of 1.63 m between the two cores, close to the 1.90 m offset which has been used officially throughout Hole 857A. Hole 857C was located 180 m east of Holes 857A and 857B and drilled by RCB to a depth of 567.7 mbsf with 32.8% recovery. Reentry Hole 857D was spudded 50 m north-northeast of Hole 857C. It was drilled without coring and cased to 581.5 mbsf, and then cored by RCB to a completion depth of 936.2 mbsf with 10.5% total recovery.

As at other drill sites in Middle Valley, interbedded turbidites and hemipelagic sediment comprise by far the largest fraction of the sediments. These sediments at Site 857 are divided into two lithostratigraphic units which are defined in a similar manner to lithologic Units I and II at Sites 856 and 858 (Table 2 and Fig. 8).

Lithologic Unit I

Sections 139-857A-1H-1, 0 cm, to -4H-3, 30 cm (0 to 25.20 mbsf); Sections 139-857B-1H-1, 0 cm, to -1H-CC, 22 cm (0 to 3.36 mbsf); Sections 139-857C-1R-1, 0 cm, to -1R-CC, 16 cm (0 to 3.59 mbsf); Holocene–late Pleistocene.

Lithologic Unit I is a Holocene to upper Pleistocene olive gray (5Y 5/2) to greenish gray (5GY 5/1) silty clay. The unit is primarily hemipelagic (by volume) but contains several thin (0.1 to 1.0 cm thick), dark gray (N4), quartz silty layers which are presumed to be turbidites. The base of the unit was sampled only in Hole 857A and is marked by the uppermost occurrence of coarser grained (fine sand) and thicker (>1 cm thick) turbidites.

Biogenic components in the sediment of lithologic Unit I include abundant and well-preserved foraminifers and nannofossils, as well as diatoms, radiolarians, and sponge spicules. Biogenic silica is particularly abundant in Core 139-857A-2H and at the top of Core 139-857A-4H.

Pale gray (N 5/) streaks of disseminated pyrite are common throughout the unit. In smear slides, pyrite crystals have a spherical shape, implying a framboidal habit. The coarse-grained, turbiditic silt often contains minor amounts of pyrite. This pyrite may account for the dark color of the silt. Numerous pale green (5GY 6/1) laminations, which may represent altered ash horizons or some other concentration of authigenic clay, are also present in this unit.

A distinctive stratigraphic marker bed which has previously been observed in piston-cored sediments throughout Middle Valley (W. Goodfellow, pers. comm., 1991) occurs in Section 139-857A-1H-4, 36–74 cm. The "*Zoophycus* marker bed" is 38 cm thick in Hole 857A and occurs about 6.5 mbsf. This bed is distinguished by its slightly maroonish gray (5Y 5/1) color and its distinctive *Zoophycus* burrow traces. The same bed was recognized in Holes 858C and 858D at sub-bottom depths of 5.33 and 6.70 mbsf and thicknesses of 41 and 45 cm, respectively (see "Lithostratigraphy and Sedimentology" section, "Site 858" chapter, this volume).

The age of the base of lithologic Unit I (25.20 mbsf) is bracketed by the base of the *Emiliani huxleyi* Acme Zone (approximately 73 ka at 17.66 mbsf; see "Biostratigraphy" section, this chapter) and the tentatively identified base of the planktonic foraminiferal Zone CD3 (approximately 125 ka at about 27.2 mbsf). By linear interpolation, we place the base of lithologic Unit I at approximately 114 ka.

Lithologic Unit II

Lithologic Unit II is characterized by interbedded hemipelagic and turbiditic sediments. At Site 857 this unit is subdivided into three subunits based on the relative degrees of induration and hydrothermal alteration. Sediments of Subunit IIA exhibit little to no induration. Sediments of Subunit IIB are moderately to well indurated. Sediments of Subunit IIC are well indurated and hydrothermally altered and are interbedded with mafic igneous rocks. The contact between Subunits IIA and IIB is gradational. The contact between Subunits IIB and IIC is placed at the uppermost occurrence of igneous rock.

Subunit IIA

Sections 139-857A-4H-3, 30 cm, to -12X-CC, 36 cm (25.20 to 92.26 mbsf); Sections 139-857C-2R-1, 0 cm, to -8R-CC, 12 cm (56.50 to 105.02 mbsf); late Pleistocene.

Sediment from Subunit IIA consists of greenish gray (5GY 5/1) silty clay interbedded with dark greenish gray (5Y 4/1) micaceous silty sand (Fig. 9). These interbedded lithologies are interpreted as

Table 2. Lithostratigraphic units for Site 857.

Unit	Description (age)	Interval	Top (mbsf)	Bottom (mbsf)	Thickness (m)
I	Fine-grained hemipelagic sediments with minor fine-grained turbidites (Holocene–late Pleistocene)	857A-1H-1, 0 cm, to 4H-3, 30 cm 857B-1H-1, 0 cm, to 1H-CC, 22 cm 857C-1R-1, 0 cm, to 1R-CC, 16 cm	0.00 0.00 0.00	25.20 3.36 3.59	25.20 3.36 3.59
IIA	Interbedded hemipelagic and turbiditic sediments, non- or weakly indurated (late Pleistocene)	857A-4H-3, 30 cm, to 12X-CC, 36 cm 857C-2R-1, 0 cm, to 8R-CC, 12 cm	25.20 56.50	92.26 105.02	67.06 48.52
IIB	Interbedded hemipelagic and turbiditic sediments, moderately to well-indurated (late Pleistocene to Pleistocene?)	857A-13X-1, 0 cm, to 14P-1, 56 cm 857C-9R-1, 0 cm, to 58R-1, 23 cm	101.50 114.50	111.86 461.73	10.36 347.23
IIC	Interbedded mafic igneous rock and silicified and hydrothermally altered, interbedded hemipelagic and turbiditic strata (Pleistocene?)	857C-59R-1, 0 cm, to 68R-3, 36 cm 857D-1R-1, 0 cm, to 37R-1, 36 cm	471.10 581.50	571.06 936.20	99.96 354.70

stacked, fining-upward turbidites. The turbidites commonly have multiple scoured basal contacts within the sandy intervals, suggesting either multiple phases of deposition of coarse-grained intervals with little or no intervening hemipelagic sedimentation, or erosion of hemipelagic sediment deposited between turbidite pulses. The sandy intervals commonly exhibit parallel laminations and convolute bedding. Bioturbation is more evident (more pervasive?) in the finer grained portion of each sequence than in the coarser grained portion. Pyrite-filled burrows are common throughout the subunit.

Biogenic components present in Subunit IIA include common and well-preserved foraminifers and nannofossils. These calcareous microfossils decrease in preservation and abundance near the base of the subunit (about 80 mbsf; see "Biostratigraphy" section, this chapter). Locally, foraminifers occur in small (millimeters in diameter) patches (e.g., Cores 139-857A-6H to -10H). Biogenic silica is abundant down to about 40 mbsf. Sections 139-857A-5H-5 to -7H-7 contain small (several millimeters in diameter) patches of siliceous spiculite which also contain abundant radiolarians and silicoflagellates.

Diagenetic carbonate occurs in Subunit IIA in the form of carbonate nodules and carbonate cement. The shallowest occurrence of diagenetic carbonate is in a thin layer of calcite(?) in interval 139-857A-6H-4, 65–66 cm (46.1 mbsf). The shallowest carbonate nodule occurs in interval 139-857A-6H-5, 138–144 cm (48.3 mbsf). Large noncalcitic carbonate nodules (probably dolomite) occur in Sections 139-857C-7R-CC (95.2 mbsf) and -8R-CC (105.0 mbsf). The shallowest occurrence of carbonate cement, as differentiated from carbonate nodules, is in Section 139-857A-11X-CC (87.5 mbsf). The increased induration of Subunit IIB relative to Subunit IIA is due to selective carbonate cementation.

Disseminated and nodular pyrite are common throughout much of the subunit. The pyrite commonly occurs as euhedral crystals filling burrows. As in lithologic Unit I, pale green laminations are numerous in some intervals (e.g., Core 139-857A-8H) and may represent altered ash or some other concentration of authigenic clay. Barite rosettes are present in several of the samples that were washed for micropaleontological analysis: intervals 139-857C-3R-2, 98–100 cm (74.2 mbsf), -5R-1, 24–28 cm (82.3 mbsf), and -6R-2, 86–88 cm (88.5 mbsf). Anhydrite(?) crystals are present in similar samples from Section 139-857C-7R-CC (104.9 mbsf), as well as in Subunit IIB from Sections 139-857C-9R-CC (124.1 mbsf) and -12R-2, 31–33 cm (145.3 mbsf).

Subunit IIB

Sections 139-857A-13X-1, 0 cm, to -14P-1, 56 cm (101.50 to 111.86 mbsf); Sections 139-857C-9R-1, 0 cm, to -58R-1, 23 cm (114.50 to 461.73 mbsf); late Pleistocene to Pleistocene?

Sediment from Subunit IIB consists of interbedded gray (N 5/) siltstone and fine sandstone and darker gray (N 4/) silty claystone. The gradational transition from Subunit IIA to Subunit IIB is defined by an increase in induration. As mentioned previously, this induration appears to be largely the result of carbonate cementation. In the upper part of Subunit IIB, carbonate cementation is concentrated near the base of the sandstone beds; most of the silty claystone is noncalcareous.

The sediments in this subunit are interpreted as turbidites. Massive or convolute beds of sandstone often have sharp bases and scoured (or multiply scoured) basal contacts. These are typically overlain by parallel- to ripple-laminated siltstone and grade upward to massive or bioturbated silty claystone (Figs. 10 and 11). Flame structures and other evidence of soft-sediment deformation are common. There is a general increase in the sand fraction with depth (Table 3), particularly below Core 139-857C-26R (about 284 mbsf). Sandstone intervals with recovered thicknesses greater than 50 cm occur in Sections 139-857C-28R-3 (298 mbsf), -49R-2 (416 mbsf), and -50R-1 (418 mbsf). These sandstone beds are very porous and probably highly permeable.

Disseminated pyrite is common throughout Subunit IIB. The pyrite is typically concentrated in the sandstone and siltstone beds. Pyrite-filled burrows and pyrite nodules are also present. In addition, pyrite occurs within authigenic calcite nodules and fracture fills (e.g., Section 139-857C-36R-1, 352 mbsf) and as a rim on other carbonate nodules (e.g., interval 139-857C-51R-1, 41–42 cm, 423.8 mbsf). Fragments of massive sulfide-containing pyrite, pyrrhotite, and sphalerite are present at the base of a turbiditic sequence in Section 139-857C-43R-3 (388 mbsf). A slickensided fracture in interval 139-857C-52R-1, 135–150 cm (429.2 mbsf) is lined with pyrrhotite, chalcopyrite, and sphalerite. Most rocks below this depth emit an odor of hydrogen sulfide when freshly cut or broken.

Carbonate occurs predominantly as cement throughout the entire depth range of Subunit IIB, but there are several other modes of carbonate occurrence. Locally, concentrically zoned carbonate nodules which contain euhedral carbonate that fills internal dilation fractures (Fig. 12). Elsewhere, concentrically zoned carbonate nodules

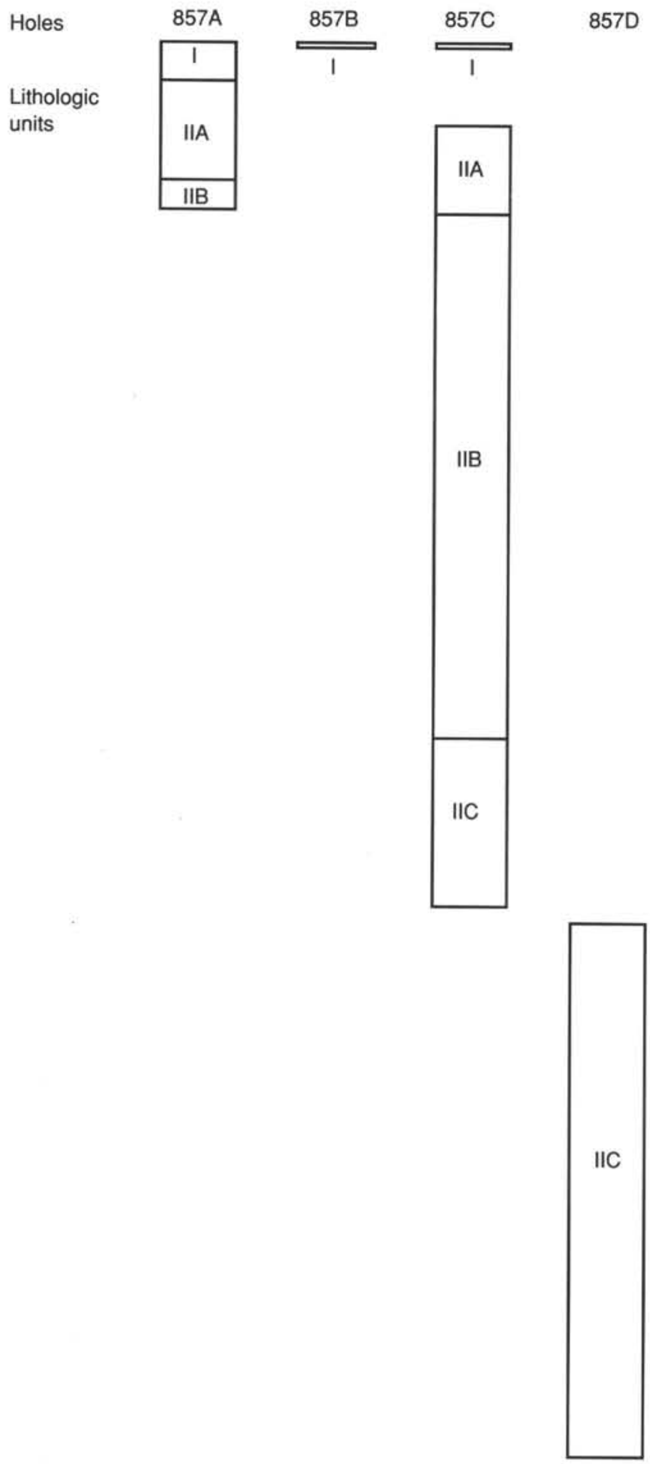

Figure 8. Hole-to-hole correlation of lithostratigraphic units at Site 857.

appear to have ferroan calcite rims (e.g., Sections 139-857C-39R-1 and -39R-2; 361 to 363 mbsf). Beds of crystalline carbonate cement (Fig. 13) and veins filled with crystalline calcite (Fig. 14) also occur. In addition, some bizarre, crab-shaped fracture-fills of authigenic calcite (Fig. 15) are found in several sections. Small amounts of biogenic calcite (foraminifers and nannofossils) remain in the sediment in Hole 857C as deep as 394 mbsf. The deepest occurrence of carbonate cement observed at Site 857 is in Section 139-857C-58R-1 (461 mbsf).

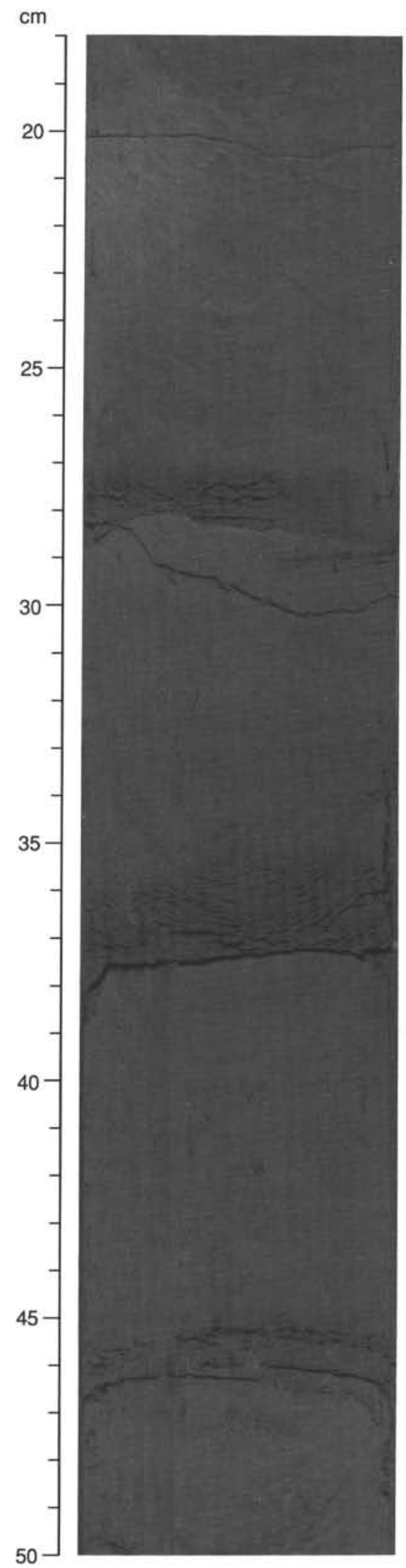

Figure 9. Close-up photo of interval 139-857A-4H-5, 18–50 cm. Three fine sand layers typical of the turbidites in the upper portion of Subunit IIA. Note the sharp basal contacts and gradational upper contacts and the bioturbation of sand into the overlying clay. In this shallow part of Unit II, the sands are darker than adjacent clays. At greater depth, sands become lighter than adjacent, finer grained sediments.

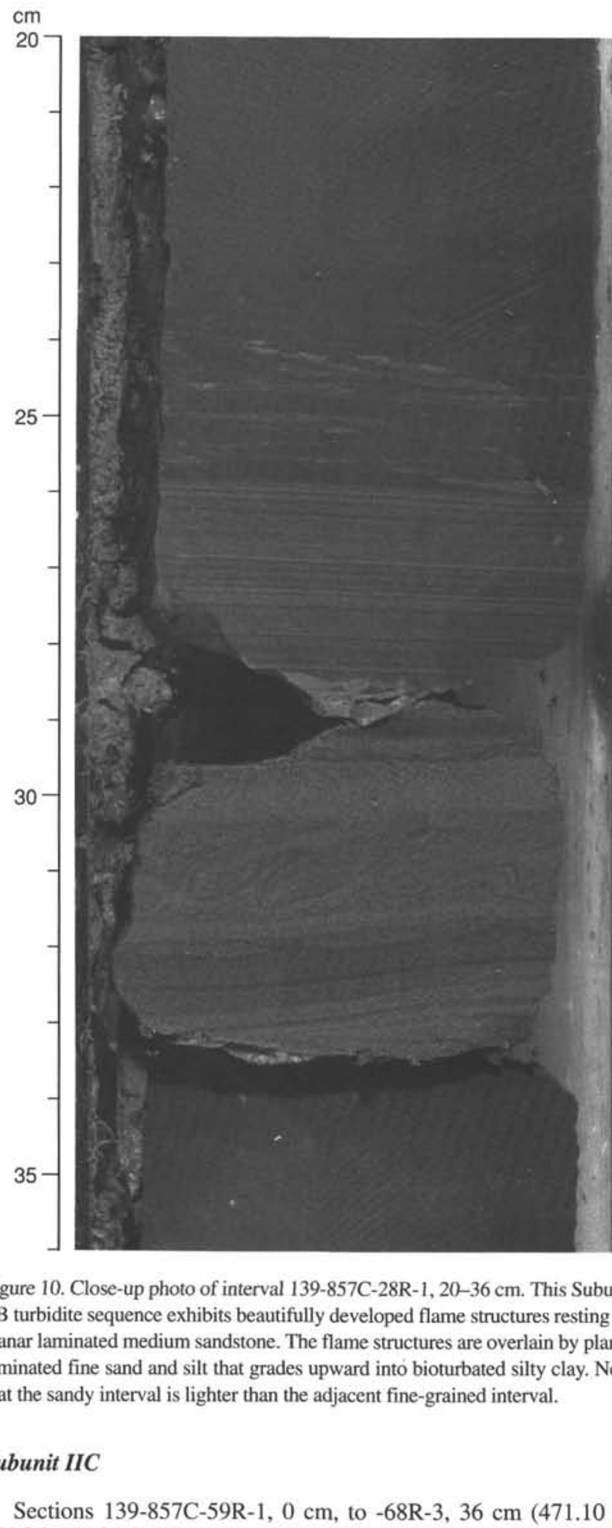

Figure 10. Close-up photo of interval 139-857C-28R-1, 20–36 cm. This Subunit IIB turbidite sequence exhibits beautifully developed flame structures resting on planar laminated medium sandstone. The flame structures are overlain by planar laminated fine sand and silt that grades upward into bioturbated silty clay. Note that the sandy interval is lighter than the adjacent fine-grained interval.

Subunit IIC

Sections 139-857C-59R-1, 0 cm, to -68R-3, 36 cm (471.10 to 571.06 mbsf); Sections 139-857D-1R-1, 0 cm, to -37R-1, 36 cm (581.5 to 936.2 mbsf); Pleistocene(?).

The shallowest mafic intrusive rock at Site 857 was recovered in Section 139-857C-59R-1, 0 cm (471.1 mbsf). Hole 857D, only 50 m distant, the first mafic intrusive rock was recovered (cored) in Section 139-857D-1R-1 (581.5 mbsf). From these depths to the bottoms of the respective holes, silicified, hydrothermally altered, and metamorphosed interbedded turbidites and hemipelagic sediment alternate with mafic intrusive rocks. The latter are described in the "Igneous Petrology" section (this chapter).

The sedimentary protoliths of the altered strata in Subunit IIC were gray (N 5/ to N 6/) siltstone and fine- to medium-grained sandstone and dark gray (N 4/) silty claystone. These strata are most commonly quartz-cemented; no carbonate was observed within Subunit IIC. Primary sedimentary structures include well-preserved load casts, convolute bedding, planar and cross-laminations, bioturbation, and mud rip-up clasts.

The sedimentary rocks of Subunit IIC have undergone a large range of deformation. Structures resulting from this deformation include soft sediment deformation (Fig. 16), high-angle normal and reverse microfaults (Fig. 16), tight isoclinal folds and evidence of plastic flow (Fig. 17), and nearly vertical or overturned bedding (Fig. 18).

A variety of fracture-fill mineral assemblages is present: quartz with pyrite (Cores 139-857D-4R, 610 mbsf; -13R, 696 mbsf; -17R, 772 mbsf; -24R, 801 mbsf; -28R, 840 mbsf; -34R, 898 mbsf), quartz and chlorite with pyrite and pyrrhotite (Cores 139-857D-5R, 619 mbsf; -15R, 715 mbsf; -16R, 725 mbsf), quartz (Core 139-857D-11R, 676 mbsf), epidote and chlorite (Core 139-857D-12R, 686 mbsf), pyrite (Cores 139-857D-22R, 782 mbsf; -31R, 869 mbsf), quartz plus pyrite and sphalerite (Core 139-857D-27R, 830 mbsf), and quartz and zeolite with zoisite, pyrite, minor epidote, and trace sphalerite (Core 139-857D-30R, 859 mbsf). Disseminated pyrite is also present in the silty claystone.

Near the base of Hole 857D (from Cores 139-857D-29R, 849 mbsf, to -37R, 927 mbsf) the sandstone and silty sandstone is grayish yellow green (10Y 7/2) to yellowish gray (10Y 7/1). This color reflects an increased abundance of epidote contained within these rocks. Near the contact zones and between the sills, the sandstones contain more epidote.

BIOSTRATIGRAPHY

Four holes were cored at Site 857. Hole 857A was cored continuously to 111.2 mbsf. Hole 857B was cored discontinuously to 30.5 mbsf with no coring between 12.9 and 21.0 mbsf. Hole 857C consists of a mudline core which bottoms at 3.5 mbsf, a washed interval from 3.5 to 56.5 mbsf, and a continuously cored interval from 56.5 to 567.7 mbsf, in which a complex of basaltic sills and intercalated sediment lies below 471.1 mbsf. Reentry Hole 857D recovered cores from 581.5 to 936.2 mbsf. The sedimentary sequences consist of turbiditic and hemipelagic sediments which are strongly affected by thermal alteration at depth. Recovery of sediment was generally poor below about 85 mbsf (see "Lithostratigraphy and Sedimentology" section, this chapter).

Foraminifers

In Holes 857A, 857B, and 857C, foraminifers are abundant to common in number and moderately to well preserved in sediment shallower than approximately 83 mbsf (Samples 139-857A-9H-CC and 139-857C-4H-CC), and moderately to poorly preserved and rare to few in number in the foraminifer-bearing samples below 83 mbsf (Tables 4 and 5). Thirty-two of 58 samples below 83 mbsf are barren. Two extensive barren intervals characterize Hole 857C: one from 240.3 to 327.6 mbsf, and one from 394.3 to 471.1 mbsf (Samples 139-857C-21R-CC to -31R-CC and 139-857C-44R-CC to -58R-CC). The two barren intervals are separated by a fossiliferous zone of recrystallized, golden brown foraminifers from 327 to 390 mbsf. Foraminifers are absent from Hole 857D, in which coring began at 581.5 mbsf. No samples from this hole were prepared for foraminifers, but the highly lithified sedimentary intervals were inspected carefully for sand-size fossils with a hand lens.

The planktonic foraminiferal fauna (Table 5) bears species typical of subarctic waters and includes *Globigerina bulloides* d'Orbigny, *Globigerinita glutinata* (Egger), *Globigerinita minuta* (Natland), *Globigerinita uvula* (Ehrenberg), sinistral and dextral *Neogloboquadrina pachyderma* (Ehrenberg), and *Turborotalita quinqueloba*

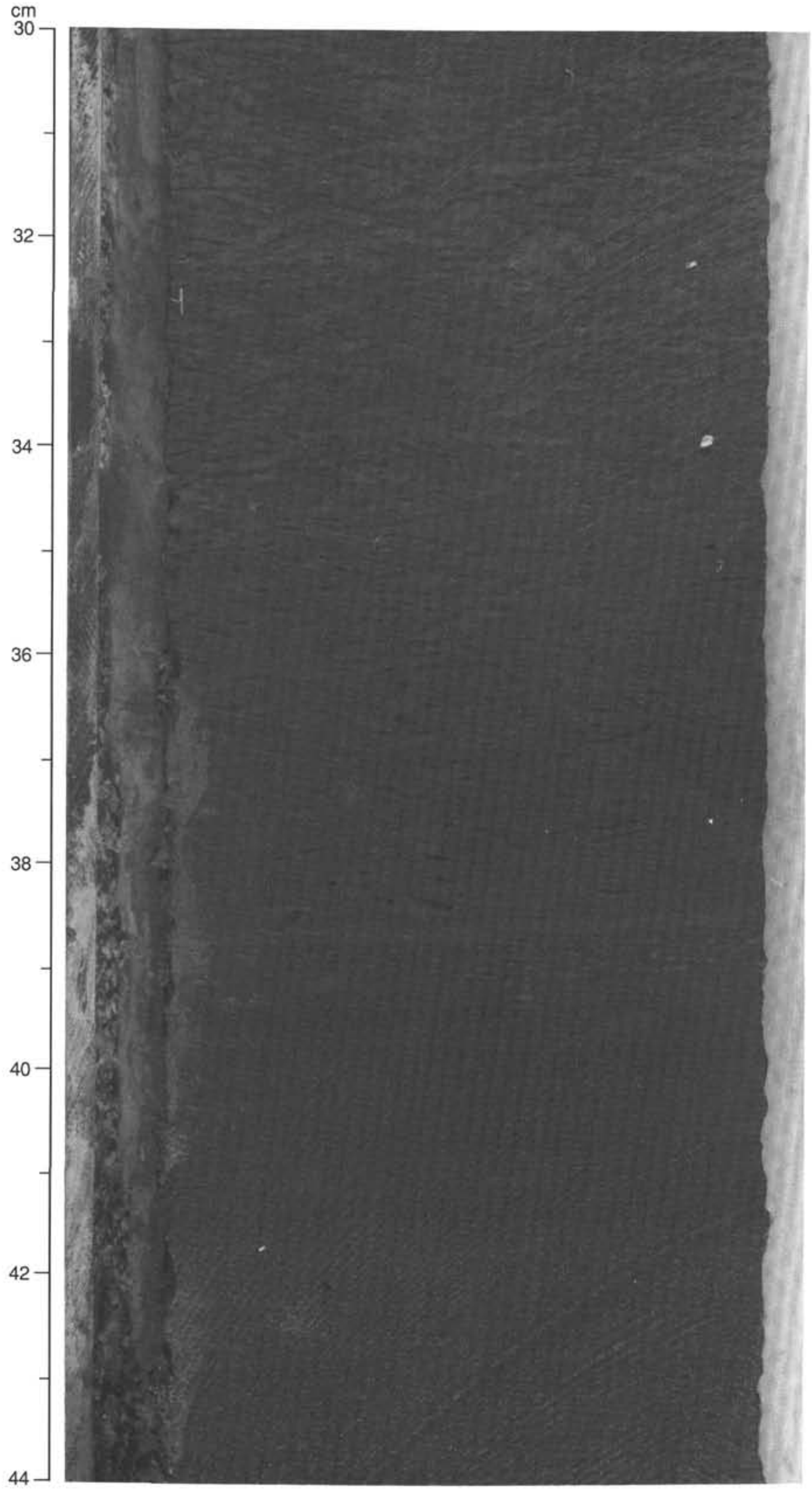

Figure 11. Bioturbated zone in Subunit IIB at interval 139-857C-35R-1, 30–44 cm.

Table 3. Volume percentage of sand and silt in the total thickness of recovered core in lithologic Unit I and Subunits IIA and IIB in Holes 857A and 857C.

Core	Sand content (%)
139-857A-	
1H	7
2H	7
3P	n.r.
4H	13
5H	13
6H	24
7H	30
8H	30
9H	18
10H	43
11R	15
12R	6
13R	25
14R	13
15R	13
16R	p.r.
17R	32
18R	31
19R	17
20R	8
21R	3
22R	4
23R	p.r.
24R	10
25R	42
26R	18
27R	44
28R	30
29R	54
30R	26
31R	23
32R	17
33R	14
34R	16
35R	35
36R	28
37R	23
38R	13
39R	14
40R	32
41R	24
42R	8
43R	28
44R	28
45R	40
46R	34
47R	27
48R	21
49R	31
50R	31
51R	23
52R	8
53R	31
54R	p.r.
55R	p.r.
56R	p.r.
57R	p.r.
58R	p.r.

Notes: Percentages were estimated by examination of core photographs and visual core description forms. The abbreviations "p.r." and "n.r." mean poor recovery and no recovery, respectively.

(Natland). The transitional species are few to rare in abundance in the sequences and include *Orbulina universa* d'Orbigny and *Globorotalia scitula* (Brady). Three subtropical species occur at the site: few *Globorotalia theyeri* in Sample 139-857A-1H-CC and single specimens of *Globorotaloides hexagonus* (Natland) and *Neogloboquadrina dutertrei* (d'Orbigny) in Samples 139-857A-1H-1, 0–1 cm, and 139-857C-1R-1, 0–1 cm, respectively).

Sediment of Holocene age was found at the seafloor in all three holes and was recognized from the relative frequency of dextral to sinistral *Neogloboquadrina pachyderma* (Bandy, 1960) (Table 5). Dextral coiling forms are greater in frequency than sinistral forms in this region of the North Pacific Ocean during interglacial climatic intervals. The dextral form occurs commonly relative to the sinistral form in Samples 139-857A-1H-1, 0–1 cm, 139-857B-1H-1, 0–1 cm, and 139-857C-1H-1, 0–1 cm. The samples are assigned to Zone CD1 of Lagoe and Thompson (1988). The Holocene-Pleistocene boundary lies within the first core of each hole, and in Hole 857B lies above 3.4 mbsf, the depth of the core-catcher sample (Table 6).

A sample that might be from the penultimate interglacial (approximately equivalent to oxygen isotopic stage 5e) was recognized from Hole 857A. Sample 139-857A-4H-4, 49–51 cm, contains abundant planktonic foraminifers, and 50% of the *Neogloboquadrina pachyderma* are the dextral form. The sample is tentatively assigned to Zone CD3 of Lagoe and Thompson (1988). Shore-based work will reveal the extent of the zone in Hole 857A and whether it occurs in Hole 857B.

The remainder of the samples were tentatively assigned to the late Pleistocene Zones CD2 or CD4, or they could not be assigned to a zone. All samples from Hole 857A within Core 857A-1H to Sample 857A-4H-3, 115–117 cm, are assigned to Zone CD2 of Lagoe and Thompson (1988), and samples below Core 857A-4H are tentatively assigned to Zone CD4 (Table 6). One barren sample at the base of the section remains unzoned. All other samples that bear few to abundant planktonic foraminifers in Holes 857B and 857C are tentatively assigned to Zone CD2 or Zone CD4 (Lagoe and Thompson, 1988) depending on whether they lie above or below 27 mbsf, the approximate depth of Zone CD3 in Hole 857A. All barren samples or those with fewer than 10 specimens remain unzoned.

The benthic assemblage consists of species from depth zones ranging from neritic to lower bathyal (Table 5). Lower and lower-middle bathyal species dominate most samples in which foraminifers are common to abundant at the top of the three holes. Prominent members of the *in-situ* depth fauna include *Cibicides wuellerstorfi, Gyroidina altiformis, Gyroidina planulata, Hoeglundina elegans, Melonis pompilioides, Pullenia bulloides, Sphaeroidina bulloides, Uvigerina dirupta,* and *Uvigerina senticosa.* Species from neritic and upper bathyal depths (Bergen and O'Neil, 1979; R. Patterson, unpubl. data, 1991) persist in minor amounts in samples dominated by middle and lower bathyal species. Upper bathyal species include *Stainforthia complanata, Globobulimina affinis, Bulimina barbata,* and *Bolivina pacifica.* Neritic taxa include *Cribroelphidium foraminosum, Globobulimina pacifica, Nonion, Nonionella, Pullenia salisburyi, Elphidium, Buliminella elegantissima,* and *Rosalina.* The trace amounts of shallow-water taxa may have been mixed into the hemipelagic units from adjacent turbidites by bioturbation. Neritic and upper bathyal species are most abundant in turbiditic core-catcher samples below 40 mbsf in Hole 857A and below 86 mbsf in Hole 857C, indicating a shelf source and a pathway down the slope for this interval of common turbidite deposits.

Sorting during turbidite transport and deposition strongly affected foraminiferal associations. Abundant, small, and delicate specimens dominate the benthic foraminiferal population in mica-rich turbiditic samples (for example, Samples 139-857A-6H-CC, -7H-CC, -8H-CC, and -10H-CC) and evidently were deposited with the medium-size silt fraction. In contrast, foraminiferal abundance is low in well-sorted, fine-sand turbidites (for example, Samples 139-857A-11H-CC and -12H-CC). The mature foraminiferal tests acted hydraulically like particles of coarse silt and were winnowed from the sand during turbidite emplacement. Paleoceanographic and biostratigraphic interpretations made from turbidite assemblages must be viewed with caution.

Calcareous Nannofossils

Calcareous nannofossils are present in three holes drilled at Site 857. Of the 113 samples examined, 31 are completely barren of

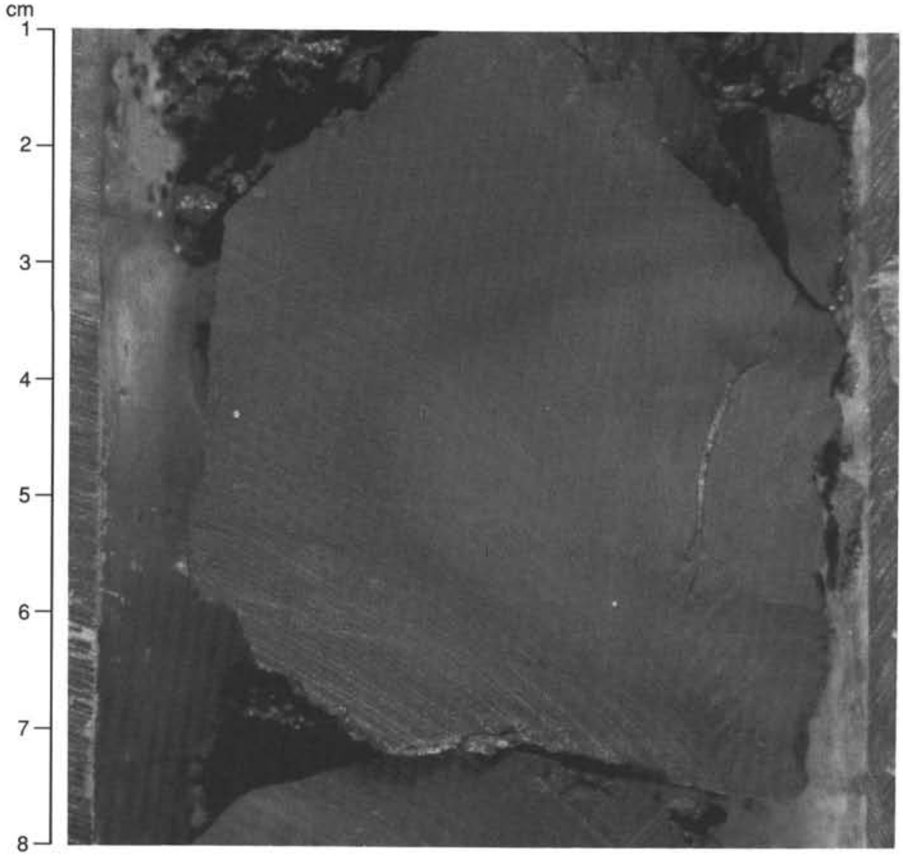

Figure 12. Close-up photo of interval 139-857C-30R-3, 1–8 cm. This large, zoned, incipient carbonate nodule from Subunit IIB has carbonate cement filling an internal dilational crack.

nannofossils; nannofossils are rare to abundant in the remaining 82 samples. Hole 857A has the most diverse fossil assemblage with more than 12 species; Hole 857C, which is the deepest hole, contains nannofossils to the greatest depth (389.7 mbsf); and Hole 857B, which extends to only 30.5 mbsf, is fossiliferous throughout its length (Table 7). No samples from Hole 857D were prepared for calcareous nannofossils.

Preservation is generally poor at Site 857, and nannofossils in most samples exhibit some degree of etching and dissolution. Moderate preservation occurs only in a few samples from the upper part of the section (for example, Sample 139-857A-4H-CC), and preservation is quite poor

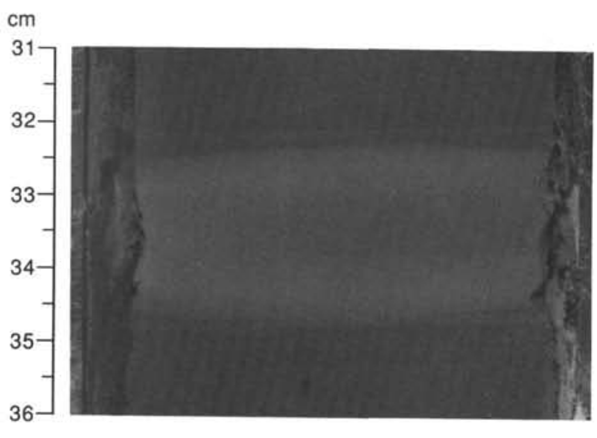

Figure 13. Close-up photo of interval 139-857C-24R-1, 31–36 cm. This is a bedding-parallel, incipient carbonate nodule in silty claystone of Subunit IIB.

in the deeper sections, reflecting the gradient in thermal alteration between the top and bottom of the sequence. The structure of nannofossils is different from taxa to taxa, and their resistance to etching, dissolution, and thermal alteration, therefore, varies. The first stage of dissolution and thermal alteration was detected in *Gephyrocapsa* by absence of its central bridge and *Coccolithus pelagicus* by calcite replacement of the original laths forming the central area, so that the edges of the central area appear incomplete and ragged. The next stage of thermal alteration was marked by calcite overgrowth of the proximal shield of *Coccolithus pelagicus* in samples from the lower sections of Holes 857A and 857C (for example, Sample 139-857A-6H-CC). *Coccolithus pelagicus* proved to be the strongest species in terms of resistance to thermal alteration; it is the only species that occurs deep in the sequence in Hole 857C (Sample 139-857C-43R-CC) at 389.7 mbsf, where thermal alteration was great.

Nannofossil abundance generally decreases with depth, probably due to both thermal alteration, which dissolved the nannofossils after deposition, and the low carbonate content of seawater at the time of sedimentation. Hole 857C offers examples of the relationship between the downhole decline in abundance and the two causes mentioned above. Nannofossils are very rare where they occur below Sample 139-857C-18R-CC, where the first thermally indurated sediments are encountered. At this level, *Coccolithus pelagicus* is the only species in the nannofossil flora. Its preservation is poor, exhibiting strong dissolution and calcite overgrowth, apparently resulting from thermal alteration. The abundance of nannofossils abruptly increases from rare to few in Sample 139-857C-40R-CC, in which the carbonate content is high compared with samples from above and below. Nannofossils were not found in samples below Core 139-857C-43R, where carbonate content is low and where thermal alteration was most intense.

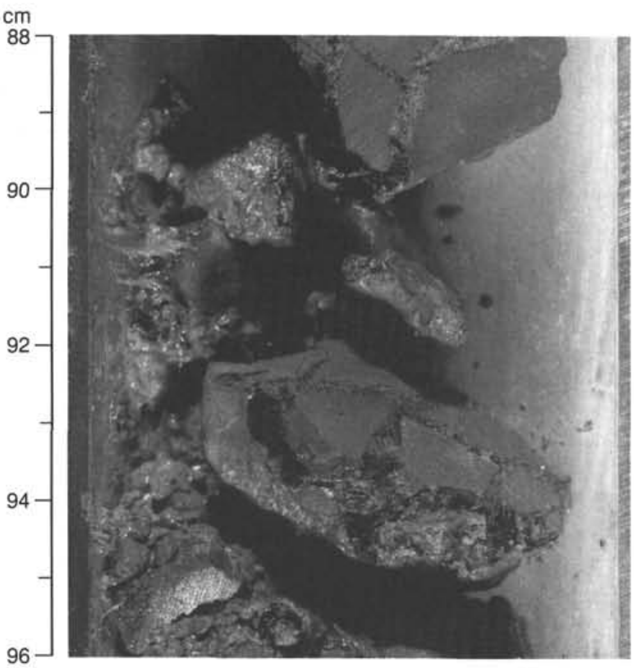

Figure 14. Close-up photo of interval 139-857C-29R-1, 88–96 cm. Black calcite fills dilational cracks in claystone forming an *in-situ* breccia in Subunit IIB.

The *Emiliania huxleyi* Acme Zone was recognized in all three holes of Site 857. In Hole 857A, *Emiliania huxleyi* occurs in all samples but one (Sample 139-857A-13X-CC), and the nannofossil assemblage from the interval from Core 139-857A-1H to Sample 139-857A-13X-2, 68–72 cm, was therefore assigned to Zone NN21 (Martini, 1971). The base of the *Emiliania huxleyi* Acme Zone (Gartner, 1977) was placed between Samples 139-857A-2H-5, 22 cm (17.62 mbsf) and -2H-5, 28 cm (17.68 mbsf). The age of the base of the *Emiliania huxleyi* Acme Zone is about 80 ka in the tropics to 73 ka in the high latitudes (Verbeek, 1990). The average accumulation rate during the latest Pleistocene to Holocene estimated by age divided by sediment thickness is 24.17 ± 0.04 cm/k.y. or 241.7 ± 0.4 m/m.y. Small *Gephyrocapsa* usually dominate the nannofossil assemblages from this hole. *Emiliania huxleyi* and *Coccolithus pelagicus* occur commonly in most samples, whereas the other nine species occur only in samples in which nannofossils are abundant (Table 7).

Emiliania huxleyi was encountered in all samples from Hole 857B, and the Acme Zone of this species was identified between Samples 139-857B-2H-CC and -3H-CC (Table 7). The average accumulation rate during the last 73 ka for Hole 857B was between 1.77 to 4.15 mm/yr (17.7 to 41.5 cm/k.y.), which brackets that for Hole 857A. Like Hole 857A, small *Gephyrocapsa, Emiliania huxleyi,* and *Coccolithus pelagicus* occur in all samples, and small *Gephyrocapsa* are always the dominant form in the nannofossil assemblages.

Calcareous nannofossils from Hole 857C occur mainly in 19 samples from the upper part of the section which also contains *Emiliania huxleyi.* The nannofossil assemblage from this interval was therefore assigned to Zone NN21 (Martini, 1971). The *Emiliania huxleyi* Acme Zone was recognized in the uppermost three samples (Table 5). The accumulation rate during the last 73 ka cannot be estimated because 53 m of Hole 857C was washed between Cores 139-857C-1R and -2R. The base of the Acme Zone is probably within the washed interval. Samples below Core 139-857C-13R yield very rare calcareous nannofossils that are poorly preserved because of etching and dissolution combined with some overgrowth. Except for one of 19 samples, only one to eight specimens of *Coccolithus pelagicus* in 100 fields were encountered. In Sample 139-857C-40-CC, however, one specimen of *Coccolithus pelagicus* was encountered within every two fields. As for *Gephyrocapsa,* the ubiquitous and most abundant genus of the Pleistocene nannofossil assemblage, only one to two specimens were detected in Samples 139-857C-17R-CC and -18R-CC. The 15 samples from the lowermost part of the section (below Core 139-857C-44R) are completely barren of nannofossils. The age of the interval between Samples 139-857C-13R-CC and -18R-CC can be dated questionably as Pleistocene by the presence of *Gephyrocapsa,* while that of the interval below Sample 139-857C-18R-CC cannot be determined due to the lack of marker species or any nannofossils.

Sedimentation Rates

We estimated the sedimentation rate from three paleontologic datums and compared the result to the sedimentation rate estimated from geophysical observations. Three datums were located in our shipboard study with varying stratigraphic error (Table 8). The base of planktonic foraminiferal zone, CD1, which is equivalent to the Holocene-Pleistocene boundary in the North Pacific Ocean (Bandy, 1960), lies between 0.6 mbsf in Hole 857C and 5.13 mbsf in Hole 857A, so the depth is crudely estimated at 2.88 ± 2.25 mbsf (Table 8). The base of the *Emiliania huxleyi* Acme Zone lies between 17.62 and 17.68 mbsf in Hole 857A, so the depth is well constrained to 17.65 ± 0.03 mbsf. The base of the planktonic foraminiferal zone, CD3, lies between 26.90 and 27.47 mbsf in Hole 857A, so the depth is fairly well constrained to 27.19 ± 0.29 mbsf. The sedimentation rates for the three stratigraphic intervals from the shallowest to the deepest are 28.8 cm/k.y., 23.5 cm/k.y., and 18.2 cm/k.y., respectively. The average is about 22 cm/k.y., which is notably faster than the Holocene to latest Pleistocene rate of 11.5 ± 0.3 and 5.65 ± 0.15 cm/k.y. estimated from ^{14}C dates by Goodfellow and Blaise (1988), and similar to average rates calculated for the Pleistocene portion of Deep Sea Drilling Project (DSDP) Site 174 on Astoria Fan.

The age of basement calculated from spreading rates and other geophysical considerations is about 250,000 yr (see Davis and Villinger, this volume, and "Site Geophysics and Geology" section, this chapter). This result suggests that the sedimentation rate for the sequence below the 125,000 yr datum must be substantially faster than that above the datum. The minimum sedimentation rate for the total sediment stack is 190 cm/k.y., which is calculated from the depth of the shallowest sill. A better estimate of sedimentation can be made once the thickness of sediment below the first sill is estimated from logs and the amount compaction is considered. This, too, will be a minimum estimate because basement lies below the maximum depth of Hole 857D at 936.2 mbsf.

The sedimentation rate based on geophysical observations is very fast compared to that estimated from biostratigraphic observations at the top of the sequence. The difference in estimates suggests two extreme possibilities or a situation between the two: (1) the age of the basement is older than 250,000 yr, perhaps an order of magnitude older, and the sedimentation rate deep in the section is similar to that in the upper 27 m of the sequence, or (2) the age of the basement is about 250,000 yr old; Middle Valley was a subsiding basin capturing all turbidites that flowed to the region, and at some time before 125 ka, sedimentation slowed to present rates at Site 857, when uplift and rotation raised the site above sedimentary base level.

Magnetic Susceptibility Quiet Zone

A dramatic magnetic susceptibility quiet zone (see "Paleomagnetism" and "Physical Properties" sections, this chapter) ranges in depth from about 16 to 22 mbsf in Hole 857A. The top of the zone lies about 1.7 m above the base of the *Emiliania huxleyi* Acme, and the base of the zone lies about 5.2 m above the base of Zone CD3. The top and bottom of the magnetic susceptibility quiet zone are about 70 and 95 ka, respectively and span the top of the penultimate interglacial period and the base of the last glaciation. These age

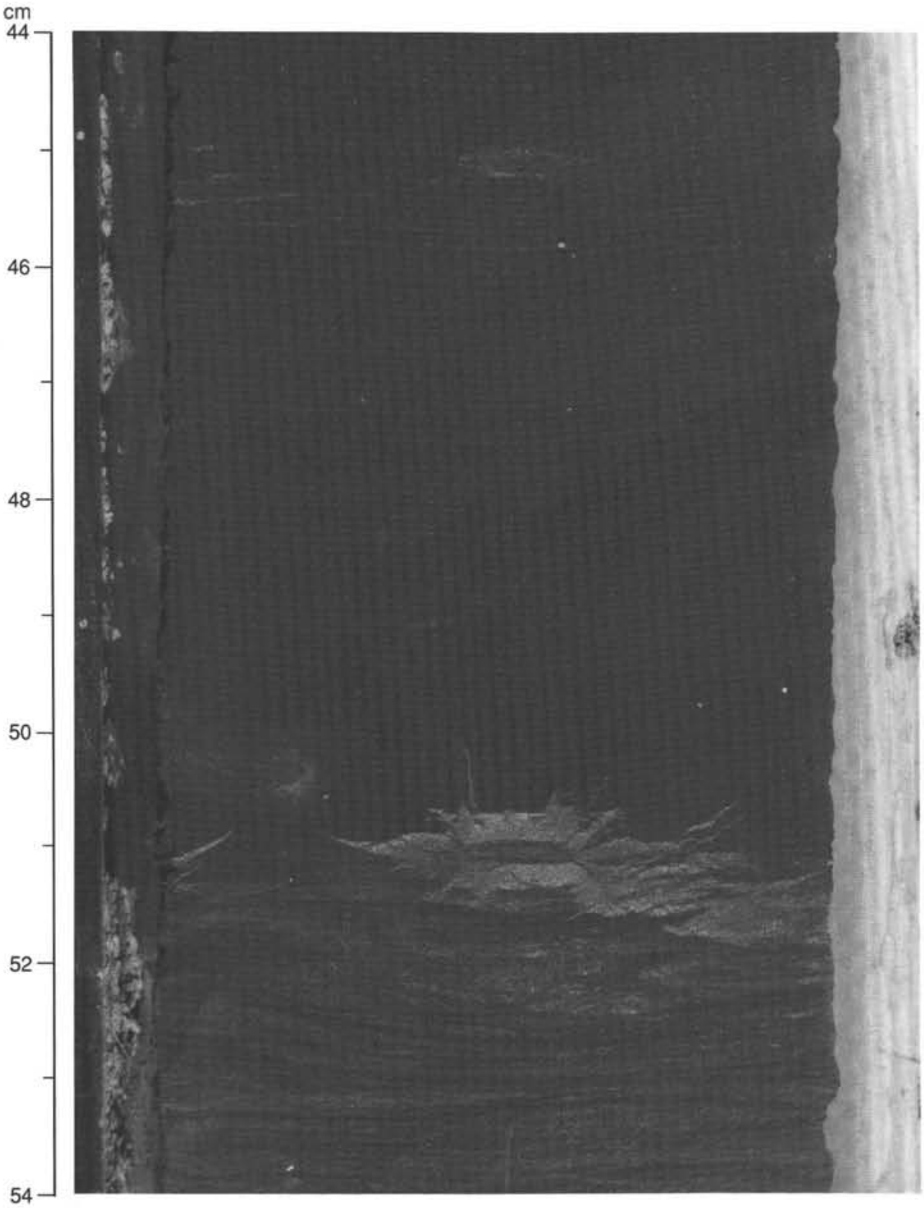

Figure 15. Close-up photo of interval 139-857C-36R-1, 44–54 cm. This crab-shaped calcite growth occurs in silty claystone and siltstone of Subunit IIB.

estimates are crude and will be revised after shore-based work. A similar susceptibility quiet zone was detected in Hole 856A (see "Lithostratigraphy and Sedimentology" section, "Site 856" chapter, this volume). Shore-based work will determine if these intervals are correlative and result from the same depositional event or if they are due to postdepositional alteration.

PALEOMAGNETISM

One of the most important goals of paleomagnetic studies on igneous rocks collected during Leg 139 was to quantify the effect of intense hydrothermal alteration on magnetic properties of oceanic crust. The magnetic anomaly pattern indicates that Middle Valley is centered on the Brunhes normal polarity chron, although the magnetic field anomaly has negative values locally over Middle Valley (Raff and Mason, 1961). There are other examples of young oceanic crust produced at spreading centers which is not accompanied by a positive magnetic anomaly: Guaymas Basin of the Gulf of California (Larson et al., 1972; Bischoff and Henyey, 1974), the Paul Revere Ridge and Winona Basin (Davis and Riddihough, 1982), and the Escanaba Trough on the southern Gorda Ridge (Raff and Mason, 1961). The lack of a coherent central positive anomaly is believed to be the result of high temperatures and high degree of alteration of the sediment-sealed oceanic crust (Davis and Lister, 1977; Levi and Riddihough, 1986).

Of the four holes drilled at Site 857, Hole 857B was the shallowest at only 30 m deep and was washed down from 12.9 to 21.0 mbsf. Paleomagnetic studies were carried out on core samples from Holes 857A, 857C, and 857D. Hole 857A was cored by APC/XCB to 112 mbsf, Hole 857C was cored by RCB to 567.7 mbsf, and Hole 857D was cored by RCB from 581.5 to 936.2 mbsf. The latter two holes intersected interbedded sills and sediments below 471 mbsf.

The natural remanent magnetization (NRM) and the magnetization after alternating field (AF) demagnetization were measured on archive halves of cores from Holes 857A, 857C, and 857D, using the pass-through cryogenic magnetometer at 10-cm intervals. Most of the samples were demagnetized in a 5- and 15-mT alternating field.

Figure 16. Close-up photo of Section 139-857D-28R-1, Piece 11. Planar laminated siltstone surrounds an interval of soft-sediment deformation in this sample from Subunit IIC. The sample is cut by high-angle apparent normal and reverse microfaults with less than 1 cm offset. It occurs in Subunit IIC.

Figure 17. Close-up photo of Section 139-857D-24R-1, Piece 10. Tight isoclinal fold of interlaminated siltstone and claystone occurs in Subunit IIC. Internal deformation was apparently ductile.

Measurements after 15-mT AF demagnetization on cores from Hole 857A were carried out at intervals of 2 cm. Thirteen discrete samples of sediment were taken from the working half of the cores from Hole 857A, nine from Hole 857C, and seven from Hole 857D. Fifteen discrete samples of igneous rock were taken from Hole 857C and 12 from Hole 857D. These samples were progressively demagnetized in 7–12 steps using the Schonstedt AF demagnetizer and were measured with the Molspin spinner magnetometer. One sample was taken of igneous rock from Hole 857D for a progressive thermal demagnetization experiment, and was heated stepwise up to 600°C in the Schonstedt thermal demagnetizer. Thirty-six samples of sediment were taken from Hole 857C and their NRM was measured. These samples have weak magnetization intensity, so they will be progressively demagnetized and measured as part of a shore-based study.

The volume magnetic susceptibility of all the cores was measured on the multisensor track (MST) at 2-cm intervals before splitting. The volume magnetic susceptibility of all the discrete samples was measured by a susceptibility meter with a 36-mm dual frequency loop in the low frequency mode, and the Koenigsberger (Q) ratio was calculated for samples from sill complexes.

Magnetism of Sediment

Hole 857A

The NRM of Hole 857A ranges from 4 mA/m to 4000 mA/m and the average value is about 340 mA/m. Core samples seem to be overprinted by drilling-induced remanence, which was partly removed by AF demagnetization. After AF demagnetization at 15 mT, intensities fall to 1–100 mA/m (Fig. 19). The intensity of magnetization is about 70 mA/m from 0 to 15.5 mbsf, drops abruptly at 15.5 mbsf from 100 mA/m to 4 mA/m, then increases near 24 mbsf to about 40 mA/m. Below 24 mbsf, intensity fluctuates between 10 mA/m and 200 mA/m. This change in magnetization intensity is also apparent in the results of progressive AF demagnetization on discrete samples (Fig. 20).

Figure 18. Close-up photo of Section 139-857D-16R-2, Pieces 1 and 2. Ductile deformation of interlaminated siltstone and claystone from Subunit IIC.

Susceptibility also shows an abrupt decrease at 16–24 mbsf from 4×10^{-3} to 3×10^{-4} SI. This low intensity zone is thought to correspond to an interval of low susceptibility and low intensity of magnetization that was also found at Site 856 (see "Paleomagnetism" section, "Site 856" chapter). This low intensity zone seems to correspond to a biogenic silica-rich zone found in Core 139-857A-2H and in the top of Core 139-857A-4H, which might lower the relative concentration of magnetic minerals (see "Lithostratigraphy and Sedimentology" section, this chapter). In general, the large-scale variations in magnetization intensity correlate well with volume magnetic susceptibility.

The stable inclination of discrete samples from Hole 857A is shown in Figure 21, along with results from measurements on archive halves. Archive half measurements show scattered negative inclination values around 16–24 mbsf, 46–58 mbsf, and 84–86 mbsf. However, all discrete samples taken from the working half show stable positive inclination after AF demagnetization. The results of progressive AF demagnetization are shown in Figure 22A. The difference in AF demagnetization characteristics between archive-half and discrete samples is thought to be due to strong drilling remanence in the outer rim of the core. The results of progressive AF demagnetization for discrete samples show relatively high median destructive field (MDF) from 4 to 40 mT (Table 9). Three discrete samples (139-857A-4H-2, 42–44 cm; -7H-2, 77–79 cm; and -7H-3, 58–60 cm) indicate low MDF, but these values are thought to be artificially lowered by strong drilling remanence.

Hole 857C

Figure 23 shows paleomagnetic results after AF demagnetization at 15 mT from Hole 857C. Because this hole was drilled by rotary coring and the recovery was poor, paleomagnetic results from archive halves show scattered directions. Progressive AF demagnetization measurements on discrete samples gave mostly stable results (Fig. 22). Stable inclination data from discrete samples and archive halves are plotted in Figure 21. All the stable inclinations are positive and their average is 51° (±15°). This value is lower than that expected from the axial dipole field (67°). The magnetization intensity of the sediment decreases with depth (Fig. 20), which is thought to result from increasing alteration (see "Lithostratigraphy and Sedimentology" section, this chapter). The magnetization intensity is 50 mA/m at about 100 mbsf, decreases continuously from around 150 mbsf to about 0.5 mA/m at 250 mbsf, then stays constant to the bottom of the sediments. One sample (139-857C-53R-1, 60–62 cm; 433 mbsf) has high intensity compared with other samples from nearly the same depth, but the magnetization and inclination are not stable (Table 9). Susceptibility shows the same decreasing pattern from 200 to 300 mbsf. These gradual decreases in magnetization intensity and susceptibility are assumed to result from alteration of detrital magnetite.

Magnetism of Igneous Rock

Hole 857C

Table 10 shows the paleomagnetic inclination of stable components, intensity of NRM, median destructive field, susceptibility, and Q-ratio of igneous rock samples from Hole 857C. The intensity of magnetization tends to decrease sharply below the top of the sill complex from 100 mA/m at the top of the sills to about 10 mA/m below, and the average intensity is 53 mA/m (Fig. 24). Sample 139-857C-66R-1, 38–40 cm, is extremely altered igneous rock and its NRM is 0.39 mA/m. This intensity of magnetization is extremely low compared with that typical for young oceanic basalt (0–1 Ma: $J_0 = 5.1$ A/m; Bleil and Petersen, 1983). It is low even compared with the intensity of hydrothermally altered sheeted dikes from DSDP Hole 504B, which averages 0.74 A/m (Smith and Banerjee, 1986). We measured one sample from the sediments between sequences of sills (139-857C-66R-1, 12–14 cm); the measured intensity is 0.39 mA/m, which is comparable to the value obtained from sediments above the sills. Progressive AF demagnetization results show that the samples from 470 to 480 mbsf are unstable and were overprinted by secondary remanence suspected to result from drilling (Fig. 22). Other samples show relatively stable characteristics and MDFs that are low for 470–480 mbsf (4–26 mT) but increase with depth to 26–64 mT. The average stable inclination is 60° (±8°), which is consistent with the magnetic anomally pattern indicating the Brunhes normal polarity chron.

Susceptibility of igneous rocks is also highest above 480 mbsf and ranges from 9.3×10^{-4} to 15.4×10^{-4} SI. Below 480 mbsf, susceptibility ranges from 4×10^{-4} to 6×10^{-4} SI. These values are all low compared with that obtained from the hydrothermally altered transition

Table 4. Comparison of abundances of calcareous nannofossils, planktonic foraminifers, and benthic foraminifers to lithology of sample.

Sample (cm)	Lithology	Nannofossil abundance	Benthic foraminifer abundance	Planktonic foraminifer abundance
139-857A-				
1H-1, 0–1	Silty clay	C	C	A
1H-3, 10–13	Silty clay	A	C	A
1H-CC	Silty clay	C	C	A
2H-1, 45–48	Silty clay	—	C	A
2H-1, 105–107	Silty clay	—	C	A
2H-2, 20–22	Silty clay	—	C	A
2H-2, 129–131	Silty clay	—	C	A
2H-3, 48–50	Silty clay	—	C	A
2H-3, 129–131	Silty clay	—	C	A
2H-4, 12–14	Clay with biogenic silica	—	C	A
2H-4, 17–19	Clay with biogenic silica	C	A	A
2H-4, 127–129	Clay with biogenic silica	—	C	A
2H-5, 19–21	Silty clay	C	—	—
2H-5, 22–24	Silty clay	C	A	A
2H-5, 28	Silty clay	C	—	—
2H-5, 31	Silty clay	A	—	—
2H-5, 42	Silty clay	A	—	—
2H-5, 114–116	Silty clay	F	—	—
2H-5, 118–120	Silty clay	—	A	C
2H-6, 4–6	Silty clay	F	—	—
2H-6, 9–11	Silty clay	—	F	A
2H-6, 112–114	Silty clay	—	F	A
2H-7, 48–50	Silty clay	—	A	C
2H-CC	Silty clay	F	A	C
3P-CC	No description of pressure core	R	A	C
4H-1, 16–18	Silty clay with biogenic silica	F	—	—
4H-1, 22–24	Silty clay with biogenic silica	—	C	F
4H-1, 99–101	Silty clay with biogenic silica	F	—	—
4H-1, 104–106	Silty clay with biogenic silica	—	A	C
4H-2, 31–33	Silty clay with biogenic silica	F	—	—
4H-2, 37–39	Silty clay with biogenic silica	—	A	R
4H-2, 99–101	Silty clay with biogenic silica	F	—	—
4H-2, 105–107	Silty clay with biogenic silica	—	C	F
4H-2, 140–142	Silty clay with biogenic silica	F	F	F
4H-3, 37–39	Silty clay with biogenic silica	—	C	F
4H-3, 110–112	Silty clay with biogenic silica	R	—	—
4H-3, 115–117	Silty clay with biogenic silica	—	C	C
4H-4, 32–34	Silty clay	F	—	—
4H-4, 49–51	Silty clay	—	A	A
4H-4, 106–108	Silty clay	C	—	—
4H-4, 111–113	Top of graded silt	—	C	A
4H-5, 60–62	Silty clay	F	—	—
4H-5, 71–73	Silty clay	—	C	A
4H-5, 127–129	Silty clay	—	C	A
4H-6, 86–88	Graded silt	—	C	A
4H-CC	Disturbed clay with sand	A	C	A
5H-4, 9–13	Laminated mud	F	C	C
5H-CC	Silty clay and clay	A	F	A
6H-5, 45–49	Clay	C	R	R
6H-CC	Silty sand	C	C	C
7H-4, 1–5	Silty clay	A	C	A
7H-CC	Sand	F	A	F
8H-5, 114–118	Silty clay	C	C	A
8H-CC	Silt laminations and clay	F	C	R
9H-5, 79–84	Silty clay	C	C	A
9H-CC	Silty clay	F	F	A
10H-2, 12–14	Silty clay	C	F	A
10H-CC	Silty sand	F	C	C
11X-CC	Graded sand	R	F	F
12X-CC	Sand?	R	R	F
13X-2, 68–72	Graded silty sand	R	B	B
13X-CC	Laminated mud	B	B	B
139-857B-				
1H-1, 0–1	Clay	C	A	C
1H-CC	Clay	R	F	C
2H-CC	Core not split	C	A	A
3H-CC	Core not split	C	A	A
139-857C-				
1R-1, 0–1	Clay	C	C	A

Table 4 (continued).

Sample (cm)	Lithology	Nannofossil abundance	Benthic foraminifer abundance	Planktonic foraminifer abundance
1R-1, 61–65	Disturbed	C	C	A
1R-CC	Disturbed	C	C	A
2R-2, 67–70	Laminated silty clay	C	C	A
2R-CC	Clay	C	C	F
3R-2, 98–100	Silty clay	–	F	A
3R-CC	Laminated silty clay	C	C	A
4R-CC	Silty claystone	F	C	A
5R-1, 24–28	Laminated siltstone	F	F	F
5R-CC	No description	R	F	F
6R-2, 86–88	Disturbed	F	F	A
6R-CC	Disturbed	B	R	R
7R-CC	Siltstone with a nodule	F	B	B
8R-CC	Carbonate nodule	F	R	F
9R-1, 62–64	Drilling slurry	B	R	R
9R-CC	Siltstone	R	R	R
10R-1, 33–35	Drilling slurry	F	B	R
10R-CC	Silt laminations and slurry	F	F	F
11R-1, 52–54	Silty clay	F	R	R
11R-CC	Silty clay	F	C	R
12R-2, 31–33	Silty clay	R	F	B
12R-CC	No description	R	R	C
13R-CC	Laminated silty clay	R	R	R
14R-CC	Silty clay	R	F	F
15R-CC	Silty clay	B	B	B
16R-CC	Laminated silty clay	R	B	R
17R-CC	Medium-size sand	R	R	R
18R-CC	Fine sand	R	R	R
19R-CC	Silty clay	R	F	R
21R-CC	Disturbed	R	B	B
22R-CC	Calcite nodule	B	B	B
23R-CC	Drilling slurry	B	B	B
24R-CC	Silty claystone	B	B	B
25R-CC	No description	B	B	B
26R-CC	Sandy siltstone	R	B	B
27R-CC	Claystone	B	B	B
28R-CC	Sandstone	B	—	—
29R-CC	Sandstone	B	B	B
30R-CC	Laminated silty claystone	R	B	B
31R-CC	Silty claystone	B	B	B
32R-CC	Laminated silty claystone	R	R	B
33R-CC	Laminated silty claystone	R	R	B
34R-CC	Silty claystone	B	B	B
35R-CC	Laminated silty clay	B	R	B
36R-CC	Laminated silty clay	B	R	B
37R-CC	Clayey siltstone	R	F	R
38R-CC	Laminated silty claystone	R	F	B
39R-CC	Claystone	R	F	B
40R-CC	Turb. claystone	F	B	A
41R-CC	Laminated silty claystone	R	B	B
42R-CC	Laminated silty claystone	R	F	B
43R-CC	Laminated silty claystone	R	R	B
44R-CC	Laminated silty claystone	B	B	B
45R-CC	No description	B	B	B
46R-CC	Laminated silty claystone	B	B	B
47R-CC	Silty claystone	B	B	B
48R-CC	Laminated siltstone	B	B	B
49R-CC	Laminated siltstone	B	B	B
50R-CC	Silty claystone	B	B	B
51R-CC	Silty claystone	B	B	B
52R-CC	Silty claystone	B	B	B
53R-CC	Silty claystone	B	B	B
54R-CC	Sandstone	B	B	B
55R-CC	Sandstone	B	B	B
56R-CC	Sandstone	B	B	B
57R-CC	Sandstone	B	B	B
58R-CC	Silty claystone	B	B	B

Note: A = abundant, C = common, F = few, R = rare, B = barren, — = sample not prepared.

Table 5. Range chart of planktonic and benthic foraminifers and their abundance and preservation, and abundance of other major constituents of the sand-size fraction.

Sample (cm)	Abundance of benthic foraminifers	Abundance of planktonic foraminifers	Preservation of foraminifers	*Globigerina bulloides*	*Globigerinita glutinata*	*Globigerinita minuta*	*Globigerinita uvula*	*Globorotalia scitula*	*Globorotalia theyeri*	*Globorotaloides hexagona*	*Neogloboquadrina pachyderma* (dex.)	*Neogloboquadrina pachyderma* (sin.)	*Orbulina universa*	*Tenuitella iota*	*Turborotalita quinqueloba*	*Agglutinated taxa*	*Eggerella bradyi*	*Karreriella* sp. A	*Martinottiella* sp. A	*Spirosigmoilinella* (?)	*Textularia* sp. A	Miliolids	*Miliolina* spp.	*Pyrgo murrhina*	*Pyrgo* spp.
139-857A-																									
1H-1, 0	A	A	G	A	C	·	·	R	·	R	C	A	R	·	C	·	·	·	·	·	·	X	·	X	·
1H-3, 1	C	A	G	A	·	A	F	F	·	·	·	A	·	·	C	·	X	·	·	·	·	·	·	·	·
1H-CC	C	A	G	A	C	R	R	F	F	·	R	A	·	·	C	·	·	·	·	X	·	·	·	·	X
2H-1, 45	C	A	G	A	X	X	·	·	·	·	·	A	·	·	X	·	·	·	·	·	·	·	·	X	·
2H-1, 105	C	A	M	A	·	R	·	·	·	·	·	A	·	·	X	·	·	·	·	X	·	·	·	·	·
2H-2, 20	C	A	M	A	X	·	·	X	·	·	R	A	·	·	C	·	·	·	·	·	X	·	·	·	·
2H-2, 129	C	A	M	A	C	F	X	·	·	·	R	A	·	·	C	·	X	·	·	X	·	·	·	X	·
2H-3, 48	C	A	M	A	·	·	·	·	·	·	·	A	·	·	·	·	·	X	·	·	X	·	·	X	·
2H-3, 129	C	A	M	A	X	X	·	X	·	·	R	A	·	·	X	·	·	·	·	X	·	·	·	X	·
2H-4, 12	A	A	M	A	X	·	·	·	·	·	·	A	·	·	X	·	X	·	·	X	X	·	·	X	·
2H-4, 17	A	A	M	A	·	·	·	F	·	·	·	A	·	·	C	X	·	·	·	·	·	·	X	·	·
2H-4, 127	C	A	M	A	X	·	·	·	·	·	·	A	·	·	X	·	·	·	·	·	·	·	·	·	·
2H-5, 22	A	A	M	A	X	·	·	·	·	·	·	A	·	·	X	·	X	·	·	X	X	·	·	X	·
2H-5, 118	A	C	P	X	·	·	·	·	·	·	·	X	·	·	X	·	·	·	·	·	·	·	·	·	·
2H-6, 9	F	A	M	A	·	·	X	·	X	·	·	A	·	X	X	·	·	·	·	X	·	·	·	·	·
2H-6, 112	F	A	M	A	X	·	·	X	·	·	·	A	·	·	X	·	·	·	X	·	X	·	·	·	X
2H-7, 48	A	C	P	X	X	·	·	·	·	·	·	X	·	·	X	·	·	·	·	·	·	·	·	·	·
2H-CC	A	C	M	·	·	·	·	·	·	·	·	C	·	·	C	·	·	·	·	·	·	·	·	·	·
3H-CC	A	C	P	C	R	·	·	·	·	·	·	C	·	·	R	·	·	·	·	·	·	·	·	·	X

Note: A = abundant, C = common, F = few, R = rare, B = barren, G = good preservation, M = moderately good preservation, P = poor preservation, X = present.

Table 5 (continued).

Sample (cm)	*Globobulimina pacifica*	*Globocassidulina* spp.	*Gyroidina altiformis*	*Gyroidina gemma*	*Gyroidina planulata*	*Gyroidina* sp. A	*Gyroidina* spp.	*Hoeglundina elegans*	Lagenids	*Melonis barleeanum*	*Melonis guadalupe*	*Melonis pompilioides*	*Nodosarids*	*Nonion labradorica*	*Nonion* spp.	*Nonionella digitata*	*Oridorsalis tener*	*Pullenia bulloides*	*Pullenia salisburyi*	*Pullenia* spp.	*Rosalina* sp. A	*Rutherfordoides* sp. A	*Sphaeroidina bulloides*	*Stainforthia complanata*	*Stainforthia* spp.
139-857A-																									
1H-1, 0	X	X	·	·	X	X	X	X	X	·	·	·	X	·	·	·	·	·	·	·	·	·	X	·	·
1H-3, 1	·	X	·	·	·	X	·	·	X	·	·	X	·	·	·	·	X	·	·	X	·	·	·	X	·
1H-CC	·	X	X	·	X	X	·	·	·	X	·	X	·	·	·	·	·	X	X	·	X	·	·	X	·
2H-1, 45	·	X	X	·	X	X	·	·	·	X	·	X	·	·	·	·	X	X	·	·	·	·	·	·	X
2H-1, 105	X	·	·	·	X	X	·	·	X	X	·	X	·	·	·	·	·	·	X	·	·	·	·	X	X
2H-2, 20	X	·	X	·	X	X	·	·	·	X	·	X	·	·	·	·	·	·	·	·	·	·	·	X	·
2H-2, 129	·	X	X	·	X	X	·	·	X	X	·	·	·	·	·	·	X	X	·	·	·	·	·	X	·
2H-3, 48	·	·	X	·	·	·	·	·	X	·	X	X	·	·	·	·	·	X	·	·	·	·	·	X	·
2H-3, 129	·	X	X	·	X	X	·	·	X	X	·	X	X	·	·	·	X	X	·	·	·	·	·	X	·
2H-4, 12	·	·	X	·	·	X	X	·	X	X	X	X	X	·	·	·	·	·	·	·	X	·	·	·	·
2H-4, 17	·	X	X	·	X	X	·	·	X	·	·	X	·	·	·	·	·	X	·	·	·	·	·	X	·
2H-4, 127	X	X	·	·	X	·	·	·	X	X	·	X	·	·	·	·	·	·	X	·	·	·	·	X	X
2H-5, 22	·	·	X	·	·	X	X	·	X	X	X	X	X	·	·	·	·	·	·	·	X	·	·	·	·
2H-5, 118	X	·	·	·	X	·	·	·	·	·	·	X	·	·	·	·	·	X	·	·	·	·	·	X	·
2H-6, 9	·	·	·	X	·	X	·	·	X	·	·	X	·	X	·	X	·	·	·	·	·	·	·	X	X
2H-6, 112	·	X	·	·	·	X	·	·	X	·	X	X	·	·	·	·	·	·	·	·	·	·	·	·	·
2H-7, 48	·	X	·	X	·	X	·	·	X	·	·	X	·	·	·	·	·	X	X	·	·	·	·	X	X
2H-CC	X	X	·	·	·	·	X	·	X	·	·	X	·	·	·	·	X	X	X	·	·	X	·	X	·
3H-CC	·	·	·	·	·	·	·	·	X	·	·	X	·	·	X	·	X	·	X	·	X	·	·	·	·

Table 5 (continued).

Sample (cm)	*Quinqueloculina akneriana*	*Quinqueloculina* spp.	*Triloculina* sp. A	*Bolivina pacifica*	*Bolivina seminuda*	*Bulimina barbata*	*Bulimina* cf. *B. inflata*	*Bulimina rostrata*	*Buliminella tenuata*	*Cassidulina laevigata carinata*	*Cassidulinoides* spp.	*Chilostomella oolina*	*Chilostomella ovoidea*	*Chilostomellina fimbriata* (?)	*Cibicides kullenbergi*	*Cibicides lobatula*	*Cibicides wuellerstorfi*	*Cibicidina* cf. *C. basiloba*	*Cibicidoides* sp. A	*Cribroelphidium foraminosum*	*Dentalina frobisherensis*	*Elphidium* spp.	*Eponides turgida*	*Globobulimina affinis*	*Globobulimina ovula*
139-857A-																									
1H-1, 0	·	·	·	X	X	X	·	X	·	X	·	·	·	·	·	·	X	·	·	·	·	·	X	X	·
1H-3, 1	·	·	X	·	X	·	·	·	·	·	·	·	·	·	·	·	X	·	·	·	·	·	·	X	·
1H-CC	·	·	X	·	·	·	X	·	·	X	·	X	·	·	X	·	X	·	·	X	·	·	X	X	·
2H-1, 45	·	·	·	·	·	·	·	·	·	X	·	X	·	·	·	·	X	·	X	X	·	·	X	·	·
2H-1, 105	·	·	·	·	·	·	·	·	·	·	·	X	·	X	·	X	X	·	X	·	·	·	·	X	X
2H-2, 20	·	·	X	X	X	·	·	·	·	X	·	X	·	X	X	·	X	·	X	·	·	·	X	X	X
2H-2, 129	·	·	X	X	·	·	·	·	·	·	·	X	·	·	·	·	X	·	·	·	·	·	·	X	X
2H-3, 48	·	X	X	·	·	·	·	·	·	X	·	·	·	·	X	·	·	·	·	·	·	·	X	X	X
2H-3, 129	·	·	X	X	·	X	·	·	·	X	·	X	·	·	X	·	X	·	·	·	·	·	X	X	·
2H-4, 12	·	·	X	·	·	·	·	·	·	X	·	·	·	·	X	·	X	X	·	·	·	·	·	·	X
2H-4, 17	·	·	X	X	·	·	·	·	·	·	·	X	·	X	·	·	X	·	X	·	·	·	X	X	X
2H-4, 127	X	X	X	·	·	·	·	·	·	X	·	X	·	X	·	·	·	·	X	·	·	·	X	X	X
2H-5, 22	·	·	X	·	·	·	·	·	·	X	·	·	·	·	X	·	X	X	·	·	·	·	·	·	X
2H-5, 118	·	·	·	·	X	·	·	·	·	·	·	·	·	·	·	·	X	·	X	·	·	·	X	X	X
2H-6, 9	·	·	·	X	X	·	·	·	·	·	·	·	·	·	X	·	X	·	·	·	·	·	X	X	X
2H-6, 112	·	·	X	X	X	·	·	·	·	·	·	·	·	X	·	·	X	·	·	·	X	·	X	·	·
2H-7, 48	·	X	X	X	X	·	·	·	X	·	·	·	X	·	X	·	X	·	·	·	·	·	X	X	·
2H-CC	·	·	X	·	X	·	·	·	X	·	·	X	·	·	·	·	X	·	·	·	·	·	·	X	X
3H-CC	·	·	·	X	·	·	·	·	X	·	X	X	·	·	·	·	X	·	·	·	·	X	·	X	·

Table 5 (continued).

Sample (cm)	*Strebloides* sp. A	*Uvigerina dirupta*	*Uvigerina hispida*	*Uvigerina senticosa*	*Uvigerina* cf. *U. juncea*	*Valvulineria inequalis*	*Valvulineria laevigata*	*Valvulineria* cf. *V. inequalis*	*Valvulineria* sp. A	*Valvulineria* spp.	Indeterminate	Clay lumps	Diatoms	Mica	Ostracodes	Pyrite tubes	Radiolarians	Recrystallized foraminifers	Sponge spicules	Sulfides	Test fragments
139-857A-																					
1H-1, 0	·	X	·	X	·	X	X	·	·	·	·	·	·	·	·	·	·	·	·	·	·
1H-3, 1	·	·	·	X	·	·	X	X	·	·	·	·	·	·	·	·	·	·	·	·	A
1H-CC	·	X	·	X	·	·	·	·	·	·	·	·	·	·	·	F	C	·	·	·	·
2H-1, 45	X	·	X	X	·	·	X	·	X	·	·	·	·	·	·	·	X	·	·	·	·
2H-1, 105	·	X	·	X	·	·	·	·	·	·	·	·	·	·	R	·	C	·	C	·	A
2H-2, 20	·	·	·	X	·	·	·	·	·	·	·	·	·	·	·	·	·	·	·	·	·
2H-2, 129	·	·	·	X	·	·	·	·	·	·	·	·	·	·	R	·	R	·	·	·	A
2H-3, 48	·	·	·	X	X	·	·	·	·	·	·	·	·	·	·	·	R	·	·	X	A
2H-3, 129	·	·	·	X	·	·	·	·	·	·	·	·	·	·	·	F	C	·	·	·	A
2H-4, 12	·	·	·	X	·	·	·	·	·	·	·	·	A	·	·	F	C	·	·	·	·
2H-4, 17	·	X	X	X	·	·	·	X	·	·	X	·	·	·	·	·	·	·	·	·	·
2H-4, 127	·	X	·	X	·	·	·	·	X	·	·	·	A	·	·	C	A	·	·	·	·
2H-5, 22	·	·	·	X	·	·	·	·	·	·	·	·	A	·	·	F	C	·	·	·	·
2H-5, 118	·	·	·	X	X	·	·	·	·	·	·	·	·	·	·	F	A	·	·	·	A
2H-6, 9	·	·	X	X	·	·	·	·	X	·	·	·	·	·	·	·	A	·	·	A	·
2H-6, 112	·	·	·	·	X	·	·	·	·	X	·	C	·	·	·	F	C	·	·	·	·
2H-7, 48	X	·	·	·	·	X	·	·	·	·	·	·	·	A	R	F	C	X	·	C	·
2H-CC	·	·	·	·	·	X	·	·	·	·	·	·	·	A	·	A	A	·	·	·	·
3H-CC	·	X	·	X	·	X	·	·	·	·	·	·	·	·	·	X	X	·	·	·	·

Table 5 (continued).

Sample (cm)	Abundance of benthic foraminifers	Abundance of planktonic foraminifers	Preservation of foraminifers	*Globigerina bulloides*	*Globigerinita glutinata*	*Globigerinita minuta*	*Globigerinita uvula*	*Globorotalia scitula*	*Neogloboquadrina dutertrei*	*Neogloboquadrina pachyderma* (dex.)	*Neogloboquadrina pachyderma* (sin.)	*Orbulina universa*	*Turborotalia quinqueloba*	*Eggerella bradyi*	*Eggerella parkerae*	*Eggerella* spp.	*Karreriella* sp. A	*Spirosigmoilina tenuis*	*Spirosigmoilinella* (?)	*Textularia* sp. A	*Miliolina* spp.	*Pyrgo murrhina*	*Pyrgo* spp.	*Quinqueloculina* spp.	*Triloculina* sp. A
139-857A-																									
4H-1, 22	C	F	G	A	X	·	·	X	·	R	A	·	·	·	·	·	·	·	·	·	·	·	·	·	·
4H-1, 104	A	C	B	F	F	·	·	·	·	R	F	·	·	·	·	·	·	·	·	·	X	·	·	·	·
4H-2, 37	A	R	M	R	·	·	·	·	·	·	·	·	·	·	·	·	·	·	·	·	·	·	·	·	·
4H-2, 105	C	F	M	F	·	·	·	·	·	R	F	·	·	·	X	·	·	·	·	·	·	·	·	·	X
4H-2, 140	F	F	M	X	·	·	·	·	·	·	X	·	·	·	·	·	·	·	·	·	·	·	·	·	·
4H-3, 37	C	F	M	X	X	·	·	·	·	·	X	·	·	·	·	·	·	·	·	·	·	·	·	·	X
4H-3, 115	C	C	M	X	·	·	·	·	·	·	X	·	·	·	X	·	·	·	·	·	·	·	·	·	X
4H-4, 49	A	A	G	A	X	·	·	·	R	A	A	·	X	·	·	·	·	·	·	·	·	·	·	·	·
4H-4, 111	C	A	M	A	X	·	·	X	·	·	A	·	X	X	·	·	·	·	X	·	·	·	·	·	X
4H-5, 71	C	A	M	A	X	·	·	·	·	·	A	·	·	·	·	·	·	·	·	·	X	·	·	·	X
4H-5, 127	C	A	M	A	X	X	·	·	·	F	A	·	X	X	·	·	·	·	·	·	·	·	·	X	X
4H-6, 86	C	A	G	A	X	X	·	·	·	F	A	·	X	·	·	·	·	·	X	X	·	X	·	·	X
4H-CC	F	A	G	A	·	F	R	R	·	R	A	R	A	·	·	·	·	·	·	·	·	·	X	·	X
5H-4, 9	C	C	M	C	X	·	·	·	·	·	C	·	·	X	X	X	·	·	·	·	·	·	·	·	·
5H-CC	C	A	M	A	F	F	·	F	·	·	A	R	F	·	·	·	·	·	·	·	·	·	·	·	·
6H-5, 45	R	R	M	X	·	X	·	·	·	·	X	·	X	·	·	·	·	·	·	·	·	·	·	·	·
6H-CC	C	C	G	R	·	C	·	·	·	·	R	·	R	·	·	·	·	·	·	·	·	·	·	·	·
7H-4, 1	C	A	M	A	X	·	X	X	·	·	A	·	X	X	·	·	·	·	·	X	X	X	X	·	·
7H-CC	A	R	M	·	·	F	·	·	·	·	R	·	F	·	·	·	·	·	·	·	·	·	·	·	·
8H-5, 114	C	A	G	A	X	X	X	X	·	·	A	·	·	·	·	·	X	·	·	X	·	·	·	·	X
8H-CC	C	R	M	·	·	·	·	·	·	·	R	·	R	·	·	·	·	·	·	·	·	·	·	·	·
9H-5, 79	C	A	G	A	X	X	·	·	·	·	A	·	X	X	·	·	·	·	·	X	·	·	·	·	X
9H-CC	F	A	P	A	R	R	R	R	·	·	A	·	F	X	·	·	·	·	·	·	·	·	·	·	·
10H-2, 12	F	A	M	A	·	·	X	·	·	R	A	·	X	·	·	·	·	·	·	X	·	·	·	·	X
10H-CC	C	C	G	·	·	C	·	R	·	·	C	·	R	·	·	·	·	·	·	·	·	·	·	·	·
11X-CC	F	F	G	·	·	·	R	·	·	·	F	·	·	·	·	·	·	X	·	·	·	·	·	·	·
12X-CC	R	F	P	F	·	·	·	·	·	·	F	·	·	·	·	·	·	·	·	·	·	·	·	·	·
13X-2, 68	B	B	·	·	·	·	·	·	·	·	·	·	·	·	·	·	·	·	·	·	·	·	·	·	·
13X-CC	B	B	·	·	·	·	·	·	·	·	·	·	·	·	·	·	·	·	·	·	·	·	·	·	·

zone of extrusive rock to dikes in Hole 504B (3.4×10^{-3} SI; Smith and Banerjee, 1986). The Q-ratio of igneous rocks from Hole 857C is generally >1 above 480 mbsf and <1 below this depth.

Hole 857D

The results of paleomagnetic measurements on archive halves are very scattered (Figs. 20 and 21). Table 11 shows results from progressive AF demagnetization and thermal demagnetization. We characterize these samples as having four types of demagnetization behavior: (A) intensity following the maximum demagnetization level was insufficient for the spinner magnetometer; (B) two components of magnetization were observed separately in lower and higher demagnetization steps; (C) two overlapped components were observed but cannot be separated; and (D) unstable. Stable inclinations are calculated from only two sediment samples and two igneous rock samples; the average inclination is 57° (Fig. 21). Most of the other samples show gradual change in direction and the trace on a Schmidt net defines part of a great circle (Fig. 22D; 139-857D-3R-2, 67–69 cm), which means that two components of magnetization were demagnetized simultaneously. The lower-coercivity component of type B samples is thought to be caused by drilling, and the higher one is probably the primary component. During coring, rock samples might be rapidly cooled by up to 200°C by circulating drilling fluid, in the distorted strong magnetic field generated at the end of the core barrel, and may then acquire a strong, stable thermoremanent magnetization.

The magnetization intensity of sediments from Hole 857D ranges from 0.3 mA/m to 3.4 mA/m and averages 1.4 mA/m; this result is consistent with the intensity from 250 mbsf to the bottom of Hole 857C (Fig. 20). The magnetization of igneous rocks ranges from 0.2 mA/m to 100 mA/m and averages 25 mA/m, consistent with the igneous rocks of Hole 857C. The MDF of igneous rocks ranges from 4 mT to 78 mT and the average is 20 mT. The MDF of sediments ranges from 9 mT to 60 mT and averages 28 mT. Some of the MDF of igneous rocks and sediments were affected by changes in magnetic direction during demagnetization. The susceptibility of igneous rocks ranges from 300 to 1000×10^{-6} SI and that of sediments from 160 to 500×10^{-6} SI. The Q-ratio is generally low and ranges from 0.02 to 0.3 for sediments and from 0.02 to 2.3 for igneous rocks.

A thermal demagnetization experiment was carried out on Sample 139-857D-3R-2, 89–91 cm (Fig. 25). Although we could not get a primary direction from the result, we can say that the polarity is normal and the Curie temperature may be higher than 500°C. Polished thin-section Sample 139-857D-3R-2, 70–71 cm, contains many altered titanomagnetite grains (see "Igneous Petrology and Geochemistry" section, this chapter).

The Middle Valley Magnetic Anomaly

The low magnetic anomaly over Middle Valley could be explained by the combination of low intensity of magnetization and low suscep-

Table 5 (continued).

Sample (cm)	*Baggina* sp. A	*Bolivina pacifica*	*Bolivina seminuda*	*Bolivina* spp.	*Buccella* sp. A	*Bulimina barbata*	*Buliminella elegantissima*	*Buliminella tenuata*	*Cassidulina laevigata carinata*	*Cassidulinoides* spp.	*Chilostomella oolina*	*Chilostomella ovoidea*	*Chilostomellina fimbriata* (?)	*Cibicides kullenbergi*	*Cibicides lobatula*	*Cibicides mckannai*	*Cibicides wuellerstorfi*	*Cibicidoides* sp. A	*Cribroelphidium foraminosum*	*Cribroelphidium subarcticum*	*Elphidium excavatum*	*Elphidium* spp.	*Eponides turgida*	*Globobulimina affinis*	*Globobulimina ovula*
139-857A-																									
4H-1, 22	·	·	·	·	·	·	·	X	·	X	·	X	·	·	·	·	·	·	·	·	·	·	·	X	·
4H-1, 104	·	·	X	·	·	·	·	X	·	·	·	·	·	·	·	·	X	·	X	·	·	·	·	·	X
4H-2, 37	·	·	·	·	·	·	·	X	·	·	·	X	·	·	·	·	X	·	X	·	·	·	·	X	X
4H-2, 105	·	X	·	·	·	·	·	X	·	X	·	·	·	X	X	X	X	·	·	·	·	·	X	·	X
4H-2, 140	·	·	·	·	·	·	X	·	·	X	·	·	X	·	·	·	X	·	·	·	·	·	·	X	·
4H-3, 37	·	·	·	·	·	·	·	X	·	X	·	X	·	·	·	X	X	X	·	·	·	·	·	X	·
4H-3, 115	·	·	·	·	·	·	·	X	·	·	·	·	X	·	·	·	·	·	·	·	·	·	X	X	·
4H-4, 49	·	·	X	·	·	X	·	X	·	X	·	X	·	·	·	·	X	·	·	·	·	·	X	X	X
4H-4, 111	·	·	·	·	·	·	·	·	X	·	X	·	·	·	·	·	X	·	·	·	·	·	X	X	X
4H-5, 71	·	·	X	·	·	·	·	·	·	·	X	·	·	·	·	·	·	·	·	·	·	·	X	·	X
4H-5, 127	·	·	·	·	·	·	·	·	·	·	X	·	X	·	·	·	X	·	·	·	·	·	X	X	·
4H-6, 86	·	X	·	·	·	X	·	·	X	·	X	·	X	·	X	·	X	·	·	·	·	·	X	X	X
4H-CC	X	·	·	·	·	·	·	·	X	·	·	·	·	·	X	·	·	·	·	·	·	·	·	·	·
5H-4, 9	·	·	·	X	·	·	·	·	·	·	·	·	·	X	X	·	X	·	·	·	·	·	X	X	·
5H-CC	·	X	X	·	·	·	·	·	X	X	·	·	·	·	·	·	X	·	·	·	·	·	X	X	·
6H-5, 45	·	·	·	·	·	·	·	·	·	·	·	·	·	·	·	·	·	·	·	·	·	X	·	·	·
6H-CC	·	X	X	·	·	·	·	·	·	·	·	·	·	·	·	·	·	·	·	X	·	·	·	·	·
7H-4, 1	·	·	·	·	·	·	·	·	·	·	X	·	X	·	·	·	X	·	·	·	·	·	X	X	X
7H-CC	·	·	·	·	·	·	·	·	·	·	·	·	·	·	·	·	·	·	·	·	·	·	·	·	·
8H-5, 114	·	X	·	·	·	·	·	·	X	·	·	·	·	·	X	·	X	·	·	·	·	·	X	·	·
8H-CC	·	·	·	·	·	·	·	·	·	·	·	·	·	·	·	·	·	·	·	·	·	·	·	·	·
9H-5, 79	·	·	·	·	·	·	·	·	·	·	·	·	·	X	·	·	X	·	·	·	·	·	·	X	·
9H-CC	·	·	·	X	·	·	·	·	·	·	·	·	·	·	·	·	·	·	·	·	·	·	·	·	·
10H-2, 12	·	·	·	·	·	·	·	·	·	·	·	·	·	·	·	·	X	·	·	·	·	·	·	X	X
10H-CC	·	X	·	·	X	·	X	·	·	·	·	·	·	·	·	·	·	·	·	·	·	X	·	·	·
11X-CC	·	·	·	·	·	·	X	·	·	·	·	·	·	·	·	·	·	·	·	·	X	·	·	·	·
12X-CC	·	·	·	·	·	·	·	·	·	·	·	·	·	·	·	·	·	·	·	·	·	·	·	·	·
13X-2, 68	·	·	·	·	·	·	·	·	·	·	·	·	·	·	·	·	·	·	·	·	·	·	·	·	·
13X-CC	·	·	·	·	·	·	·	·	·	·	·	·	·	·	·	·	·	·	·	·	·	·	·	·	·

tibility of the sills, which may be intensely hydrothermally altered. The measured NRM intensity of the sills is almost the same as that of the upper part of the overlying sediment. Whether the Curie temperature is higher or lower than the temperature of sills is critical for estimation of *in-situ* magnetization. The estimated temperature in the sills could be >300°C (see "Heat Flow" section, this chapter). The Curie temperature of titanomagnetite in oceanic basalt changes with composition and degree of low-temperature oxidation from 150°C to 460°C (Petersen et al., 1979). Also high-temperature oxidation of titanomagnetite (>600°C) causes exsolution of ilmenite lamellae to form magnetite (Curie temperature; 580°C). We could not find evidence for high-temperature oxidation in polished thin sections. However, Smith and Banerjee (1986) suggested the possibility of high-temperature deuteric oxidation, which does not produce observable exsolution lamellae below 600°C. The progressive thermal demagnetization experiment is consistent with the possibility that these samples have a high Curie temperature. In order to clarify the possible oxidation mechanism of titanomagnetite, the Curie temperature of Site 857 igneous rocks will be measured as part of a shore-based study.

FLUID GEOCHEMISTRY

Pore waters were extracted from all four holes drilled at Site 857, which is located about 5 km west of Site 855, where bottom seawater is flowing into basement along the rift-boundary fault, and about 1.5 km south of Site 858, where chemically altered seawater exits at temperatures up to 276°C in the central rift of Middle Valley. These pore waters were analyzed to characterize (1) their interaction with sediment and altered basaltic sills at temperatures approaching 350°C, and (2) the composition of seawater that supplies the hydrothermal system located in the central rift.

Hole 857A was drilled to 112 mbsf at a location where the heat flow is about 0.7 W/m^2; several hundred meters to the east, heat flow approaches 1 W/m^2. Hole 857B was drilled about 10 m from Hole 857A to define better the upper 30 m of the sediment column. Hole 857C was drilled 180 m east of Holes 857A and 857B at a location where the heat flow is about 0.8 W/m^2. This hole was drilled to 568 mbsf, at which depth the temperature is estimated to be greater than 250°C. Several sills were penetrated in Hole 857C, the shallowest at 471 mbsf. Hole 857D was drilled 50 m north-northeast of Hole 857C. Coring began at 581 mbsf and encountered silicified sediment interlayered with altered mafic sills. The hole bottomed in altered sediment at 936 mbsf.

Methods of Pore-water Extraction

Pore water was obtained from Holes 857A and 857B by squeezing whole-rounds samples. The same technique succeeded in recovering water from highly altered sediment and diabase to a depth of 501 mbsf in Hole 857C and from a single sample from 604 mbsf in Hole 857D. Pore waters also were obtained by squeezing sediment recovered with

Table 5 (continued).

Sample (cm)	*Globobulimina pacifica*	*Globocassidulina* spp.	*Gyroidina altiformis*	*Gyroidina planulata*	*Gyroidina quinqueloba*	*Gyroidina* sp. A	*Gyroidina* spp.	Lagenids	*Lenticulina*	*Melonis barleeanum*	*Melonis guadalupe*	*Melonis pompilioides*	Nodosarids	*Nonion labradorica*	*Nonion* spp.	*Nonionella* cf. *N. miocenica*	*Nonionella digitata*	*Nonionella turgida*	*Nonionella* spp.	*Oridorsalis tener*	*Pullenia bulloides*	*Pullenia quinqueloba*	*Pullenia salisburyi*	*Rosalina* sp. A	*Rutherfordoides* sp. A
139-857A-																									
4H-1, 22	X	X	·	·	·	X	·	X	·	·	·	X	·	·	·	·	·	·	·	·	X	·	X	X	·
4H-1, 104	·	X	·	X	·	·	·	X	·	·	·	X	·	·	·	·	·	·	·	·	X	·	X	·	·
4H-2, 37	·	X	·	·	·	·	·	X	·	·	·	X	·	·	·	·	·	·	·	·	X	·	X	·	·
4H-2, 105	·	X	·	·	·	X	·	X	·	·	·	X	·	·	·	·	·	·	·	·	X	·	X	·	·
4H-2, 140	·	·	·	·	·	X	·	·	·	·	·	X	·	·	·	·	X	·	·	·	·	·	·	·	·
4H-3, 37	·	X	·	·	·	·	·	X	·	·	·	X	·	·	·	·	X	·	·	X	·	·	X	·	·
4H-3, 115	·	X	·	X	·	X	·	X	·	·	X	X	·	·	·	·	·	·	·	·	·	·	·	·	·
4H-4, 49	·	·	X	X	·	·	·	X	·	·	·	X	·	X	·	·	·	·	·	X	X	·	X	·	·
4H-4, 111	·	X	X	X	·	X	·	X	·	X	·	·	·	X	·	·	·	·	·	·	X	·	·	·	·
4H-5, 71	·	X	·	·	·	X	·	X	·	X	·	X	·	X	·	·	·	·	·	·	X	·	·	·	·
4H-5, 127	·	X	·	·	·	X	X	X	·	X	·	X	·	·	·	·	·	·	·	·	·	·	·	·	·
4H-6, 86	·	X	X	X	·	X	·	X	X	X	·	X	·	·	·	·	·	·	·	X	X	·	X	·	·
4H-CC	X	X	·	·	·	X	·	·	·	·	·	X	·	·	X	·	·	·	·	·	X	·	·	X	·
5H-4, 9	X	·	·	·	X	X	·	X	·	·	·	·	·	·	·	·	·	·	·	X	X	·	·	·	·
5H-CC	X	·	·	·	·	X	·	X	·	·	·	·	·	·	·	X	·	·	·	X	·	X	·	X	·
6H-5, 45	·	·	·	·	·	·	·	·	·	·	·	·	·	·	·	·	·	·	·	·	·	·	·	·	·
6H-CC	·	X	·	·	·	·	·	·	·	·	·	·	·	·	·	·	·	·	X	·	·	·	·	·	X
7H-4, 1	·	X	·	·	·	X	·	X	·	·	·	·	·	·	·	·	·	·	·	·	X	·	·	·	·
7H-CC	·	·	·	·	·	·	·	·	·	·	·	·	·	·	·	·	·	·	·	·	·	·	·	·	·
8H-5, 114	·	X	·	X	·	X	·	X	·	X	·	X	X	·	·	·	·	·	·	·	X	·	·	·	·
8H-CC	·	·	·	·	·	·	·	·	·	·	·	·	·	·	·	·	·	·	·	·	·	·	·	·	·
9H-5, 79	·	X	·	X	·	X	·	X	·	·	X	·	·	·	·	·	·	·	·	·	X	·	·	·	·
9H-CC	·	X	·	·	·	X	·	X	·	·	·	X	·	·	·	·	·	·	·	·	·	·	·	·	·
10H-2, 12	·	·	·	·	·	·	X	X	·	·	·	·	·	·	·	·	·	X	·	·	X	·	·	·	·
10H-CC	·	X	·	·	·	·	·	·	·	·	·	·	·	·	·	X	·	·	·	·	·	·	·	·	·
11X-CC	·	·	·	·	·	·	·	·	·	·	·	·	·	·	·	·	·	·	·	·	·	·	·	·	·
12X-CC	·	·	·	·	·	·	·	·	·	·	·	·	·	·	·	·	·	·	·	·	·	·	·	·	X
13X-2, 68	·	·	·	·	·	·	·	·	·	·	·	·	·	·	·	·	·	·	·	·	·	·	·	·	·
13X-CC	·	·	·	·	·	·	·	·	·	·	·	·	·	·	·	·	·	·	·	·	·	·	·	·	·

the pressure core barrel (Section 139-857A-3P-1) (see "Explanatory Notes" chapter, this volume) and by using the water-sampler temperature-probe (WSTP) (Sections 139-857A-7I-1 and -12I-1). In addition, 14 samples of indurated sediment and altered diabase and gabbro from Hole 857C and 26 samples from Hole 857D were treated by the GRIND (ground rock interstitial normative determination) technique to estimate the chemical composition of pore water (see "Fluid Geochemistry" section, "Explanatory Notes" chapter, this volume). Interstitial water from six samples was obtained both by squeezing and by the GRIND technique. The two techniques produced waters of similar compositions, when adjusted to the same chlorinity, indicating that the GRIND technique produces water of representative composition.

The composition of the pore water is listed in Tables 12 and 13. Several samples have anomalously high concentrations of calcium and a corresponding anomaly in either sulfate or alkalinity. These anomalous values are artifacts of sample handling and are adjusted in Figures 26 to 28 for dissolution of anhydrite or calcium carbonate upon retrieval, or eliminated if alkalinity was not measured.

Results and Discussion

Concentrations of chemical species in pore water change from bottom-seawater values as a result of bacterial degradation of organic matter, reaction with detrital silicates and basaltic sills, recrystallization of biogenic carbonates and silicates, hydration of silicates, and transport processes. Profiles of pore-water chemistry from Site 857 are generally controlled within the upper 100 mbsf by bacterial degradation of organic matter, and at greater depths by water-rock reactions. Because the profiles from each of the holes at this site are similar, and because no samples were taken from the upper 3 to 57 mbsf in Hole 857C nor from the upper 582 mbsf in Hole 857D, the following discussion will incorporate data from all of the holes into a unified interpretation for each chemical species.

Profiles of chlorinity increase from the value in bottom seawater at the sediment-water interface to a local maximum about 85 mbsf in Hole 857A and 145 mbsf in Hole 857C (Fig. 26). The maximum in Hole 857A is 565 mmol/kg, about 10 mmol/kg lower than the maximum in Hole 857C; at a given depth in the upper 100 mbsf, however, the chlorinity is greater in Hole 857A than in Hole 857C. Between about 150 to 200 mbsf chlorinity decreases, but then it increases again to about 590 mmol/kg at 400 mbsf. The shape of the chlorinity profile requires either two sources and one sink at steady state, or a non-steady-state condition. The deeper source, below about 400 mbsf, probably results from hydration of silicate minerals in the sediment and basaltic sills. Alternative explanations include dissolution of chloride-bearing minerals, and phase separation followed by segregation of the gas and brine phases, but these processes are unlikely to occur at this site, as no stable chloride-bearing minerals have been observed and estimated temperatures at 150 mbsf are too low to cause phase separation.

Table 5 (continued).

Sphaeroidina bulloides	*Stainforthia complanata*	*Stainforthia rotunda*	*Stainforthia* spp.	*Streblodes* sp. A	*Suggrunda eckisi*	*Uvigerina dirupta*	*Uvigerina senticosa*	*Valvulineria inequalis*	*Valvulineria laevigata*	*Valvulineria* cf. *V. inequalis*	*Valvulineria* sp. A	*Valvulineria* spp.	Indeterminate	Clay lumps	Diatoms	Mica	Mineral grains	Ostracodes	Pine pollen	Pyrite tubes	Radiolarians	Recrystallized foraminifers	Sponge spicules	Sulfides	Test fragments	Very small rotalids
·	X	·	·	X	·	·	·	X	·	·	·	·	·	·	A	A	·	·	·	·	A	·	·	A	·	·
·	X	·	·	X	·	·	·	X	·	·	·	·	·	·	A	A	·	·	·	·	A	·	·	·	·	·
·	D	X	·	X	·	·	·	X	·	·	·	X	·	·	A	A	·	·	R	·	A	·	A	X	·	·
·	·	·	·	X	·	·	·	X	·	·	·	·	X	·	A	A	·	·	·	·	A	·	A	A	·	·
X	·	·	·	·	·	·	X	·	·	·	·	·	X	·	F	A	A	·	·	·	F	·	F	X	·	·
·	·	·	·	X	·	·	·	X	·	·	·	·	X	·	A	A	·	·	·	R	A	·	·	A	·	·
·	X	X	X	X	·	·	·	·	·	·	·	·	·	·	A	A	·	·	·	·	A	·	·	A	·	·
·	·	·	·	X	·	·	X	·	·	·	·	·	X	·	·	·	·	·	·	·	A	·	·	A	·	·
·	X	·	·	X	·	·	·	X	·	·	X	·	·	·	·	·	·	·	·	·	A	·	·	A	·	·
X	X	·	·	X	·	X	·	X	·	·	·	X	·	·	·	·	A	·	·	·	A	·	·	A	·	·
·	X	X	·	X	·	·	·	X	·	·	·	·	·	·	·	A	A	R	·	F	A	·	·	A	·	·
·	X	·	·	·	·	X	X	·	·	·	·	·	·	·	·	·	·	F	·	·	C	·	·	·	A	·
·	·	·	·	·	·	·	X	·	·	·	·	·	·	·	·	·	·	·	·	·	·	·	·	·	·	·
X	X	·	·	·	·	·	X	·	·	X	·	·	·	·	·	·	·	·	·	·	A	·	·	A	·	·
·	X	·	·	·	·	·	X	·	X	·	·	·	·	·	·	A	·	·	·	·	·	·	·	·	·	·
·	·	·	·	·	·	·	·	·	·	·	·	·	·	·	·	·	X	·	·	·	·	·	·	X	·	·
·	X	·	·	·	X	·	·	·	·	·	·	X	·	·	·	A	·	·	·	A	·	·	·	·	·	·
X	X	·	·	·	·	X	X	·	·	·	·	·	·	·	·	·	·	R	·	·	·	R	·	·	·	·
·	·	·	·	·	·	·	·	·	·	·	·	·	·	·	·	A	A	·	·	A	·	·	·	·	·	A
·	X	X	·	·	·	X	·	·	·	·	X	·	X	·	·	·	·	·	·	·	·	R	·	·	·	·
·	·	·	·	·	·	·	·	·	·	·	·	·	·	·	·	A	A	·	·	C	·	·	·	·	·	X
·	X	·	·	·	·	·	·	·	X	·	X	X	X	·	·	·	A	R	·	·	·	·	·	A	·	·
·	X	·	·	·	·	·	·	·	·	·	·	·	·	·	·	·	·	·	·	A	·	·	·	·	A	·
X	X	·	·	·	·	·	X	·	·	·	·	·	·	·	·	·	·	R	·	·	·	·	·	·	A	·
·	·	·	·	·	X	·	·	·	·	·	·	·	·	·	·	A	A	·	·	·	·	·	·	·	·	X
·	·	·	·	·	·	·	·	·	·	·	·	·	·	·	·	A	A	·	·	X	·	·	·	·	·	·
·	·	·	·	·	·	·	·	·	·	·	·	·	X	·	·	A	A	·	·	A	·	·	·	·	·	·
·	·	·	·	·	·	·	·	·	·	·	·	·	·	A	·	A	A	·	·	·	·	·	·	A	·	·
·	·	·	·	·	·	·	·	·	·	·	·	·	·	·	·	A	A	·	·	F	·	·	·	·	·	·

If steady state exists and there is no lateral fluid flow, then the shallower source at about 150 mbsf could likewise be attributed to hydration of silicates and the sink at about 200 mbsf could be dehydration. This scenario is unlikely because there are no distinct mineralogical differences in the sediment between 100 and 200 mbsf. Thus, transport or non-steady-state processes or both must control these profiles. Transport of the glacial-to-interglacial change in the chlorinity of bottom seawater cannot explain the shape of the upper 200 m of the chlorinity profile, because the measured change in chlorinity is almost twice the change that occurred during the last glacial-to-interglacial period. Therefore, either two fluids with different chlorinities are flowing laterally at 150 and 200 mbsf, possibly at steady state, or a recent event has caused a lower-chlorinity fluid to flow laterally through the sediment at about 200 mbsf. Flow in the latter, non-steady-state case would disrupt what was once a diffusive profile. We prefer the non-steady-state explanation, but cannot discount lateral flow at 150 and at 200 mbsf. None of the other chemical species measured at this time enables us to distinguish between these two explanations, either because the imprecision of the analysis is greater than 3%, or because the concentration increases between 150 and 200 mbsf by tens of percent.

At depths below 415 mbsf, only two pore-water samples were recovered by squeezing. One sample was recovered from highly altered metadiabase basalt at 501 mbsf (Section 139-857C-62R-1) and has a chlorinity of 604 mmol/kg. This measurement implies either that chlorinity increases with depth to about 650 mmol/kg at 1000 mbsf, based on a linear extrapolation of chlorinity from about 400 mbsf, or that the chlorinity measured in this sample reflects a local zone where hydration is occurring. Because the concentration of chloride is about 590 mmol/kg in the second squeezed sample, from 604 mbsf (Section 139-857D-12R-1), and in nine other samples from 350 to 415 mbsf, we suggest that the profile of chlorinity is uniform with depth below 415 mbsf, and we have adjusted all GRIND samples to a chlorinity of 590 mmol/kg in Figures 26 to 28. Even if the chlorinity increases to 650 mmol/kg at 1000 mbsf, concentrations of other species in GRIND samples would be at most 10% greater than the values plotted in these figures. This small difference would not alter our interpretations. For comparison, the chlorinity of the 276°C vent water at Site 858 is about 600 mmol/kg.

The concentration of calcium is similar to that in bottom seawater in the upper 50 mbsf, then increases with depth to about 285 mbsf (Fig. 27). The nearly uniform concentration in the upper 50 mbsf probably reflects a balance between release of calcium to pore water during alteration of detrital silicates, and uptake of calcium from pore water during authigenic formation of calcium carbonate. A similar trend is observed in profiles from Sites 855 and 856. The profile of alkalinity is consistent with this interpretation: it shows about a five-fold increase in the upper 37 mbsf that results from microbial degradation of organic matter, and then decreases to the bottom-seawater value by 80 mbsf (Fig. 26). Carbonate must be precipitating

Table 5 (continued).

Sample (cm)	Abundance of benthic foraminifers	Abundance of planktonic foraminifers	Preservation of foraminifers	*Globigerina bulloides*	*Globigerinita glutinata*	*Globigerinita minuta*	*Globigerinita uvula*	*Globorotalia scitula*	*Neogloboquadrina pachyderma* (dex.)	*Neogloboquadrina pachyderma* (sin.)	*Orbulina universa*	*Turborotalita quinqueloba*	Agglutinated taxa	*Ammodiscus incertum*	*Eggerella bradyi*	*Hormosina* sp. A	*Karreriella* sp. A	*Martinottiella* sp. A	*Saccammina* sp. A	*Spirosigmoilinella* (?)	Miliolids	*Miliolina* spp.	*Pyrgo murrhina*	*Triloculina* sp. A	*Bolivina pacifica*
139-857B-																									
1H-1, 0	A	C	G	C	F	·	·	R	C	C	R	F	X	X	X	X	·	·	X	·	·	·	X	X	X
1H-CC	R	C	M	C	R	R	·	·	R	C	·	R	·	·	·	·	·	·	·	·	·	·	·	·	·
2H-CC	A	A	G	A	F	F	F	·	·	A	·	F	·	·	·	·	X	·	·	X	X	X	·	X	·
3H-CC	A	A	G	A	R	·	·	·	C	A	·	C	·	·	·	·	·	X	·	X	·	·	·	X	X

Table 5 (continued).

Sample (cm)	*Pullenia salisburyi*	*Rosalina* sp. A	*Sphaeroidina bulloides*	*Stainforthia complanata*	*Stainforthia rotunda*	*Uvigerina dirupta*	*Uvigerina senticosa*	*Valvulineria laevigata*	*Valvulineria* cf. *V. laevigata*	Indeterminate	Diatoms	Ostracodes	Radiolarians
139-857B-													
1H-1, 0	·	·	X	·	X	X	X	X	·	·	A	·	A
1H-CC	·	·	·	·	·	·	·	·	·	·	·	·	·
2H-CC	X	X	·	X	·	X	X	X	·	X	·	·	·
3H-CC	X	·	·	X	·	X	·	·	X	X	·	R	·

throughout this interval, as the amount of alkalinity produced by bacterial degradation should be twice the observed decrease in sulfate of about 10 mmol/kg:

$$2\ CH_2O + SO_4^{2-} = H_2S + 2\ HCO_3^{2-}.$$

In the absence of precipitation of calcium carbonate, the alkalinity would rise to about 23 meq/kg, or about 10 meq/kg greater than the measured value. The increase in the concentration of calcium between 50 and 285 mbsf is a product of continued alteration of silicates coupled with transport of calcium; together these processes produce calcium in excess of that being removed by precipitation of calcium carbonate or calcium sulfate. Over this interval, the alkalinity generally remains less than 1 meq/kg.

From 285 to 400 mbsf the average concentration of calcium is about 83 mmol/kg, about 2 mmol/kg greater than the projected end-member concentration of water that discharges at 276°C from the vents at Site 858, about 1.5 north of Site 857 (J. Lydon, pers. comm., 1991). At depths greater than 400 mbsf, the concentration of calcium from GRIND samples decreases to about 50 mmol/kg at 936 mbsf. The alkalinity of interstitial water below 100 mbsf is generally less than that in bottom seawater, but because of the present lack of data, no comparison can be made with the alkalinity of hot water venting at Site 858.

Profiles of sulfate in pore water show two depth intervals where sulfate is being consumed and one interval that requires a source of sulfate. Sulfate is consumed during bacterial degradation of organic matter, which we infer to be occurring in the upper 53 mbsf in Hole 857A and in the upper 70 mbsf in Hole 857C. Degradation of organic matter utilizing sulfate as the oxidant is consistent with downhole increases in the concentrations of alkalinity, phosphate, and ammonium. The concentration of sulfate decreases from that in bottom seawater to a minimum of about 18 mmol/kg at 53 mbsf in Hole 857A and about 21 mmol/kg at 70 mbsf in Hole 857C. At depths below this minimum, the concentration of sulfate increases and thus requires a source. This source could be dissolution of sulfate-bearing minerals such as anhydrite, which was observed in the interval from 90 to 140 mbsf, and barite, which was observed in the interval from 70 to 100 mbsf. Another possible source is inorganic oxidation of sulfide minerals by oxygen that is introduced during retrieval and squeezing; however, the only sulfide mineral that was detected in this interval is pyrite, which would lower the pH of pore water if it readily oxidized. Between the interval from about 100 to 200 mbsf, concentrations of sulfate decrease to about 5 mmol/kg. This decrease requires a sink, which may be bacterial degradation of organic matter, or precipitation of sulfate-bearing minerals, or both. Based on a simple estimate of activity coefficients and the concentrations of calcium and sulfate, the pore water is estimated to be saturated or supersaturated with anhy-

Table 5 (continued).

Sample (cm)	*Bolivina seminuda*	*Cassidulina laevigata carinata*	*Cassidulinoides* spp.	*Chilostomella oolina*	*Cibicides kullenbergi*	*Cibicides mckannai*	*Cibicides wuellerstorfi*	*Cibicidoides* sp. A	*Eponides turgida*	*Globobulimina affinis*	*Globobulimina ovula*	*Globobulimina pacifica*	*Globocassidulina* spp.	*Gyroidina altiformis*	*Gyroidina planulata*	*Gyroidina* sp. A	*Gyroidina* spp.	Lagenids	*Melonis barleeanum*	*Melonis guadalupe*	*Melonis pompilioides*	*Nonion labradorica*	*Nonion* spp.	*Oridorsalis tener*	*Pullenia bulloides*
139-857B-																									
1H-1, 0	X	·	·	X	X	·	X	·	X	X	X	X	X	X	·	·	X	·	·	·	X	·	·	·	·
1H-CC	·	·	X	·	·	·	·	·	X	·	·	X	·	·	·	·	·	·	·	·	X	·	·	·	·
2H-CC	·	X	·	X	·	X	·	·	X	X	X	·	X	X	X	X	·	X	X	·	X	·	X	·	X
3H-CC	·	·	·	·	X	·	·	X	·	·	·	·	X	X	X	X	·	·	X	X	X	X	·	X	X

drite and gypsum throughout this interval. Lateral flow of seawater in the interval from about 150 to 200 mbsf may control the shape of the chlorinity profile, but has no apparent influence on profiles of sulfate, as indicated by the observed decrease. Below 200 mbsf the concentration of sulfate in pore water generally decreases to about 2 mmol/kg at the base of Hole 857D.

Hydrogen sulfide was detected by smell during handling of samples that were retrieved from below 350 mbsf, but these samples yielded too little fluid to analyze.

Bacterial degradation of organic matter and adsorption and exchange reactions probably control the shape of the phosphate and ammonium profiles (Fig. 28). The concentration of phosphate increases 15-fold in the upper 11 mbsf as a result of oxidation of organic matter, but it virtually disappears by 70 mbsf. The decrease in phosphate presumably results from precipitation with carbonates and sorption on manganese- and iron-oxide surfaces. The depth at which pore water is depleted of phosphate corresponds to the depth of the local minimum in sulfate and the depth at which the concentration of calcium begins to increase above that in bottom seawater. The lack of dissolved phosphate below 70 mbsf suggests that the decrease in sulfate between 100 and 200 mbsf may not result from degradation of organic matter; however, concentrations of ammonium increase over the interval from 150 to 200 mbsf, consistent with this process. Other potential sources of ammonium include thermal maturation of organic matter (as suggested by the light hydrocarbon data), exchange with clays, and reduction of dissolved nitrogen. The concentration of ammonium is as large as 2 mmol/kg at about 290 mbsf.

The concentration of magnesium in the upper 50 mbsf is about equal to that in bottom seawater (Fig. 27). Below about 50 mbsf, it decreases to a minimum of about 3 mmol/kg at about 193 mbsf, probably by reaction with the turbidite sediment. At depths below 193 mbsf, the concentration of magnesium generally increases to about 15 mmol/kg at 963 mbsf. The source of magnesium over this interval is uncertain, but may reflect water-rock equilibrium with a different mineral assemblage as temperature increases, or diffusive exchange with interstitial water from below the sampled section. This water must have a higher concentration of magnesium than the pore water at 400 mbsf. The scatter in the GRIND samples is probably an artifact of the analytical method, in which magnesium is detected by difference from titrations of total alkaline earths and calcium (see "Fluid Geochemistry" section, "Explanatory Notes" chapter, this volume). Because of the lower concentration and small sample size, greater error is introduced in both the alkaline earth and calcium measurements of GRIND samples. Shore-based measurements using an inductively coupled plasma (ICP) technique may resolve the scatter in the GRIND data.

The concentration of potassium in the upper few meters of the sediment column is greater than that of bottom seawater (Fig. 27). This increase is an artifact of sampling and squeezing techniques. The concentration of potassium decreases from the sediment-water interface to a minimum concentration of about 3 mmol/kg at about 100 mbsf in Hole 857A and at about 145 mbsf in Hole 857C. We attribute this decrease to low-temperature reactions in which potassium and magnesium are taken up by sediment undergoing alteration and calcium is released to the pore water, as is commonly observed in laboratory experiments at temperatures below 150°C (Seyfried and Bischoff, 1979). The estimated temperature range at the minimum in potassium is about 80° to 120°C (see "Heat Flow" and "Downhole Logging" sections, this chapter). The depths of the two minima correspond to those of the chlorinity maxima, but this correspondence does not provide evidence for the processes that control the profiles of chlorinity. At depths below the minimum concentration of potassium, potassium increases to about 20 mmol/kg at about 350 mbsf. This increase is attributed to water-rock reaction at temperatures greater than about 150°C. From 350 to 430 mbsf the average concentration of potassium is about 20 mmol/kg, about 2 mmol/kg greater than the concentration of potassium in the 276°C water that vents near Site 858. The concentration of potassium generally decreases below 430 mbsf to about 14 mmol/kg at 936 mbsf. The depth interval of the required sink for potassium is the same as that which must be a sink for calcium and a source for magnesium and sulfate.

The concentration of sodium generally ranges from 460 to 480 mmol/kg in the upper 175 mbsf, then decreases to about 385 mmol/kg at about 300 mbsf (Fig. 27). This decrease is a product of albitization or zeolite formation in the sediment and corresponds to an increase in the concentration of sodium in the sediment. From 300 to 400 mbsf the concentration of dissolved sodium is uniform and about 10% lower than the concentration of 430 mmol/kg measured in the 276°C water that vents at Site 858. Within about the same depth interval, the concentration of sodium in the sediment is uniform with depth at a value that is about twice as high as that in the upper 200 m. To produce this large an increase in the concentration of sodium in the sediment requires long-lived lateral fluid flow and albitization, but not necessarily at the present time. At depths below about 400 mbsf, the concentration of dissolved sodium generally increases to about 460 mmol/kg at 963 mbsf. The change in the concentration of dissolved sodium below 400 mbsf is probably related to the changes in calcium, magnesium, sulfate, and potassium.

Table 5 (continued).

Sample (cm)	Abundance of benthic foraminifers	Abundance of planktonic foraminifers	Preservation of foraminifers	*Globigerina bulloides*	*Globigerinita glutinata*	*Globigerinita minuta*	*Globigerinita uvula*	*Globorotalia scitula*	*Neogloboquadrina dutertrei*	*Neogloboquadrina pachyderma* (dex.)	*Neogloboquadrina pachyderma* (sin.)	*Orbulina universa*	*Turborotalita quinqueloba*	*Eggerella bradyi*	*Karreriella* sp. A	*Spirosigmoilinella* (?)	*Textularia* sp. A	*Miliolina* spp.	*Pyrgo murrhina*	*Quinqueloculina* spp.	*Triloculina* sp.A	*Bolivina pacifica*	*Bolivina seminuda*	*Bulimina rostrata*	*Bulimina* cf. *B. inflata*
139-857C-																									
1R-1, 0	A	A	G	A	·	·	·	R	R	A	C	R	F	·	·	·	·	·	X	·	X	·	·	X	·
1R-1, 61	C	A	G	X	X	X	·	X	X	X	X	X	X	·	·	·	·	·	X	X	·	X	X	·	X
1R-CC	C	A	M	A	F	F	·	R	·	·	A	·	·	·	·	·	·	·	X	X	·	X	·	·	·
2R-2, 67	C	A	M	A	F	F	·	·	·	R	A	·	C	X	·	X	·	X	·	·	·	X	·	·	·
2R-CC	C	F	G	R	·	F	·	R	·	·	R	·	R	·	·	·	·	·	·	·	·	X	·	·	·
3R-2, 98	F	A	M	C	X	·	·	·	·	·	A	·	X	·	·	X	X	·	·	·	·	·	X	·	·
3R-CC	C	A	G	A	A	C	·	·	·	·	A	·	A	·	X	·	X	·	·	·	·	·	·	·	·
4R-CC	C	A	G	A	·	R	R	R	·	R	A	·	R	X	·	·	·	·	·	·	·	·	·	·	·
5R-1, 24	F	F	P	X	·	·	·	·	·	·	X	·	·	·	·	·	·	·	·	·	X	·	·	·	·
5R-CC	F	F	M	F	R	·	·	R	·	·	F	·	R	X	·	·	X	·	·	·	X	X	X	·	·
6R-2, 86	F	A	M	A	X	X	X	·	·	·	A	·	A	·	·	·	·	·	·	·	X	X	·	·	·
6R-CC	R	R	P	·	·	·	·	·	·	·	R	·	·	·	·	·	·	·	·	·	·	·	·	·	·
7R-CC	B	B	·	·	·	·	·	·	·	·	·	·	·	·	·	·	·	·	·	·	·	·	·	·	·
8R-CC	R	F	M	F	R	·	·	·	·	·	F	·	R	·	·	·	·	·	·	·	·	·	·	·	·
9R-1, 62	R	R	P	X	·	·	·	·	·	·	X	·	·	·	·	·	·	·	·	·	·	·	·	·	·
9R-CC	R	R	M	R	·	·	·	·	·	·	R	·	·	·	·	·	·	·	·	·	·	·	·	·	·
10R-1, 33	B	R	P	·	·	·	·	·	·	·	X	·	·	·	·	·	·	·	·	·	·	·	·	·	·
10R-CC	F	F	P	·	·	R	·	·	·	·	F	·	·	·	·	·	·	·	·	·	·	·	·	·	·
11R-1, 52	R	R	P	·	·	·	·	·	·	·	X	·	·	·	·	·	·	·	·	·	·	·	·	·	·
11R-CC	C	R	P	·	·	·	·	·	·	·	·	·	·	·	·	·	·	·	·	·	·	·	·	·	·
12R-2, 31	F	B	P	·	·	·	·	·	·	·	·	·	·	·	·	·	·	·	·	·	·	·	·	·	·
12R-CC	R	C	P	C	R	·	·	R	·	R	C	·	R	·	·	·	·	·	·	·	·	·	·	·	·
13R-CC	R	R	P	·	·	·	·	·	·	·	R	·	·	·	·	·	·	·	·	·	·	·	·	·	·
14R-CC	F	F	P	R	·	R	·	·	·	·	R	·	·	·	·	·	·	·	·	·	X	·	·	·	·
15R-CC	B	B	·	·	·	·	·	·	·	·	·	·	·	·	·	·	·	·	·	·	·	·	·	·	·
16R-CC	B	R	P	·	·	·	·	·	·	·	R	·	·	·	·	·	·	·	·	·	·	·	·	·	·
17R-CC	R	R	P	·	·	X	·	·	·	R	R	·	·	·	·	·	·	·	·	·	·	·	·	·	·
18R-CC	R	R	P	R	·	·	·	·	·	·	·	·	·	·	·	·	·	·	·	·	·	·	·	·	·
19R-CC	F	R	P	·	·	·	·	·	·	R	·	·	·	·	·	·	·	·	·	·	·	·	·	·	·
21R-CC	B	B	·	·	·	·	·	·	·	·	·	·	·	·	·	·	·	·	·	·	·	·	·	·	·
22R-CC	B	B	·	·	·	·	·	·	·	·	·	·	·	·	·	·	·	·	·	·	·	·	·	·	·
23R-CC	B	B	·	·	·	·	·	·	·	·	·	·	·	·	·	·	·	·	·	·	·	·	·	·	·
24R-CC	B	B	·	·	·	·	·	·	·	·	·	·	·	·	·	·	·	·	·	·	·	·	·	·	·

The concentration of dissolved silica increases in the upper 40 mbsf to a maximum of about 1 mmol/kg (Fig. 28). The source for silica in this interval is believed to be dissolution of amorphous silica. At depths below this maximum, concentrations decrease to about 0.3 mmol/kg at about 80 mbsf. This decrease may reflect equilibrium with a different silica phase. Below 80 mbsf the concentration of dissolved silica is generally uniform with depth, but on the basis of the estimated temperature profile, it should increase with depth. Some of the GRIND samples yielded concentrations of dissolved silica as high as 4 mmol/kg. These samples are usually from altered basalt and produce measured chlorinities that are less than about 65 mmol/kg, because of the dilution inherent in the GRIND technique.

The pH of the pore water is scattered between 7.6 and 8 in the upper 100 to 200 mbsf (Fig. 26). Profiles of pH generally decrease with depth, but pH remains above 7.2 in the sampled section. The pH of some GRIND samples was measured but these data are not plotted in Figure 26.

Conclusions

The chemical composition of pore water from Site 857 has been changed from that of bottom seawater by early diagenetic processes as well as by water-rock reactions at temperatures that exceed 250°C. These processes produce a pore water in the depth interval from 300 to 400 mbsf that closely resembles the 276°C water that vents at Site 858 about 1.5 km away in its concentrations of chlorinity, sodium, potassium, and calcium. This depth interval may represent one in which pore water is well mixed and flows laterally. It is interesting to note that this depth interval lies above the uppermost sill.

Pore water in this interval is most likely a source for the vents, rather than effluent from the hydrothermal system at Site 858, because sulfate and magnesium are present in the pore water and not in the vent water, and sources of these ions at 200° to 300°C are highly unlikely. Other evidence that lateral flow at Site 857 is toward rather than away from the vents includes the increase in the concentration of sodium in the sediment throughout this interval. This increase is also unlikely to occur with a hydrothermal fluid that has already had sodium removed by high-temperature water-rock reactions.

Lateral flow of pore water also may exist in the interval from 150 to 200 mbsf, but there is no evidence for vertical fluid flow through any of the holes at Site 857. Below 400 mbsf, the composition of the pore water tends toward that of seawater. This trend may reflect changes in the rate or type of water-rock reactions with depth, or may reflect a less altered seawater that exists below the sampled interval.

Table 5 (continued).

Sample (cm)	*Buliminella relegantissima*	*Cassidulina laevigata carinata*	*Cassidulinoides* spp.	*Chilostomella oolina*	*Chilostomella fimbriata* (?)	*Cibicides kullenbergi*	*Cibicides* spp.	*Cibicides wuellerstorfi*	*Cibicidoides* sp. A	*Cibicidoides* spp.	*Elphidium* spp.	*Epistominella* cf. *E. vitrea*	*Epistominella pacifica*	*Eponides turgida*	*Globobulimina affinis*	*Globobulimina ovula*	*Globobulimina pacifica*	*Globobulimina* cf. *G. pacifica*	*Globocassidulina* spp.	*Gyroidina altiformis*	*Gyroidina planulata*	*Gyroidina* sp. A	*Gyroidina* spp.	*Hoeglundina elegans*	Lagenids
139-857C-																									
1R-1, 0	·	X	·	X	·	X	·	X	·	·	·	·	·	X	·	·	X	·	X	X	X	·	·	·	X
1R-1, 61	·	·	·	X	·	·	·	X	·	·	·	·	X	X	X	X	·	·	X	X	X	X	·	X	·
1R-CC	·	·	·	X	·	·	·	X	·	·	·	X	·	·	X	·	·	·	X	X	X	X	·	·	X
2R-2, 67	·	·	·	·	·	·	·	·	·	·	X	·	X	·	X	X	·	·	X	·	·	X	·	·	·
2R-CC	·	·	·	·	·	·	·	·	·	·	·	·	·	·	·	·	·	X	X	·	·	·	·	·	X
3R-2, 98	·	·	·	·	·	·	·	·	·	·	·	·	·	·	·	X	·	·	X	·	·	X	·	·	·
3R-CC	·	·	·	·	·	·	·	X	·	·	X	X	·	X	·	·	X	·	X	X	·	X	X	·	X
4R-CC	·	·	·	·	·	·	X	X	·	·	X	·	·	X	·	·	X	·	·	X	·	X	·	·	X
5R-1, 24	·	·	·	·	·	·	·	X	·	·	·	·	·	·	·	·	·	·	X	·	·	·	·	·	·
5R-CC	·	·	·	·	·	·	·	X	·	·	·	·	·	X	·	X	·	·	·	X	·	X	·	·	X
6R-2, 86	·	·	·	·	·	·	·	X	·	·	·	·	·	·	·	·	·	·	·	·	·	·	·	·	X
6R-CC	·	·	·	·	·	·	·	·	·	X	·	·	·	·	·	·	·	·	·	·	·	·	·	·	·
7R-CC	·	·	·	·	·	·	·	·	·	·	·	·	·	·	·	·	·	·	·	·	·	·	·	·	·
8R-CC	·	·	·	·	·	·	·	·	·	·	·	·	·	·	·	·	·	·	·	·	·	·	·	·	·
9R-1, 62	·	·	·	·	·	·	·	·	·	·	·	·	·	·	·	X	·	·	·	·	·	·	·	·	·
9R-CC	·	·	·	·	·	·	·	X	·	·	·	·	·	·	·	X	·	·	·	·	·	·	·	·	·
10R-1, 33	·	·	·	·	·	·	·	·	·	·	·	·	·	·	·	·	·	·	·	·	·	·	·	·	·
10R-CC	·	·	·	·	·	·	·	·	·	·	X	·	·	·	·	·	·	·	X	·	·	·	·	·	X
11R-1, 52	·	·	·	·	·	·	·	·	·	·	·	·	·	·	·	·	·	·	·	·	·	·	X	·	·
11R-CC	·	·	·	·	·	·	·	·	X	·	·	·	·	X	·	X	·	·	·	·	·	·	·	·	·
12R-2, 31	·	·	·	·	X	·	·	·	·	·	·	·	·	·	·	·	·	·	·	·	·	·	·	·	·
12R-CC	·	·	·	·	·	·	·	·	·	·	·	·	·	·	·	·	·	·	·	·	·	·	·	·	·
13R-CC	·	·	·	·	·	·	·	·	·	·	·	·	·	·	·	·	·	·	·	·	·	·	·	·	·
14R-CC	X	·	X	·	·	·	·	·	·	·	X	X	·	·	·	·	X	·	X	·	·	·	·	·	·
15R-CC	·	·	·	·	·	·	·	·	·	·	·	·	·	·	·	·	·	·	·	·	·	·	·	·	·
16R-CC	·	·	·	·	·	·	·	·	·	·	·	·	·	·	·	·	·	·	·	·	·	·	·	·	·
17R-CC	·	X	·	·	·	·	·	·	·	·	·	·	X	·	·	·	·	·	X	·	·	·	·	·	·
18R-CC	·	·	·	·	·	·	·	·	·	·	·	X	·	·	·	·	·	·	·	·	·	·	·	·	·
19R-CC	·	·	·	·	·	·	·	X	·	·	X	X	·	·	·	·	·	·	X	·	·	·	X	·	X
21R-CC	·	·	·	·	·	·	·	·	·	·	·	·	·	·	·	·	·	·	·	·	·	·	·	·	·
22R-CC	·	·	·	·	·	·	·	·	·	·	·	·	·	·	·	·	·	·	·	·	·	·	·	·	·
23R-CC	·	·	·	·	·	·	·	·	·	·	·	·	·	·	·	·	·	·	·	·	·	·	·	·	·
24R-CC	·	·	·	·	·	·	·	·	·	·	·	·	·	·	·	·	·	·	·	·	·	·	·	·	·

ORGANIC GEOCHEMISTRY

The shipboard organic geochemical analyses of sediment samples from Holes 857A, 857B, and 857C included inorganic carbon; total carbon, hydrogen, nitrogen and sulfur; volatile hydrocarbon and nonhydrocarbon gases; organic matter fluorescence estimation; and total hexane-soluble lipid/bitumen analysis. Instrumentation, operating conditions, and procedures are summarized in the "Organic Geochemistry" section, "Explanatory Notes" chapter (this volume).

Volatile Gases

Volatile gases (hydrocarbons, CO_2, H_2S, and N_2) were continuously measured in the sediments at Site 857 as part of the shipboard safety and pollution monitoring program. Results are listed in Table 14. Methane concentrations in the headspace volumes range between 3 and 80,000 ppm (volume/volume, or v/v). Concentrations were low in Hole 857A (Fig. 29), similar to those found at Site 856. In Hole 857C, methane increased exponentially with increasing depth and temperature to about 300 mbsf (Fig. 30). Concentrations then remained roughly constant and high from 300 to 400 mbsf, followed by a gradual minor decrease to the bottom of the hole. Above 200 mbsf ethane and propane were either absent or present in only trace amounts. Both compounds then increased exponentially with depth and have profiles similar to that of methane (Fig. 30), but with concentrations of 100 to 1000 times less. C_1/C_2 ratios in Hole 857C are irregular but appear to decrease somewhat with depth, especially below 400 mbsf, which is typical of the normal trend with increasing geothermal gradient at numerous DSDP sites (Claypool, 1975). The lower C_1/C_2 ratios from 120 to 180 mbsf and from 280 to 320 mbsf correspond approximately to zones of low corrected-gamma-ray (CGR) values, possibly representing sandy and more porous layers in the sediment column (see "Downhole Logging" section, this chapter), where lateral fluid flow might cause preferential depletion of the lighter C_1 over the heavier C_2.

As discussed previously for Sites 855 and 856, the overall low methane content in sections of Holes 857A and 857C shallower than 100 mbsf suggests that the environmental conditions were not favorable for methanogenesis. The exponential increase in methane, ethane, and propane which occurs from 200 to 300 mbsf is consistent with a thermogenic source either *in situ* or at depth. The interval of 200 to 300 mbsf in Hole 857C (Fig. 30) corresponds to a present-day temperature range of about 150° to 200°C, estimated from surface heat flow (see "Heat Flow" section, this chapter, and approximate temperatures indicated at various depths in Fig. 31). This temperature

Table 5 (continued).

Sample (cm)	*Melonis barleeanum*	*Melonis guadalupe*	*Melonis pompilioides*	*Nonion labradorica*	*Nonion* spp.	*Oridorsalis tener*	*Pullenia bulloides*	*Pullenia quinqueloba*	*Pullenia salisburyi*	*Rosalina* sp. A	*Rutherfordoides* sp. A	*Sphaeroidina bulloides*	*Stainforthia complanata*	*Stainforthia rotunda*	*Stainforthia* spp.	*Suggrunda eckisi*	*Uvigerina dirupta*	*Uvigerina hispida*	*Uvigerina senticosa*	*Valvulineria inequalis*	*Valvulineria laevigata*	*Valvulineria* cf. *V. laevigata*	*Valvulineria* sp. A	*Valvulineria* spp.
139-857C-																								
1R-1, 0	·	·	X	·	·	·	·	X	·	·	·	X	·	·	·	·	X	·	X	·	·	·	·	·
1R-1, 61	·	·	X	·	·	·	·	·	·	·	·	·	·	·	·	·	·	X	X	·	·	·	X	·
1R-CC	X	X	X	·	·	X	·	·	X	X	·	X	X	·	·	·	·	·	X	·	·	·	·	·
2R-2, 67	·	·	X	·	·	X	X	·	·	·	X	·	·	·	X	·	·	·	X	·	·	·	·	X
2R-CC	·	·	·	·	·	·	·	·	·	·	·	·	X	·	·	·	·	·	·	·	·	X	·	·
3R-2, 98	·	·	X	·	·	·	X	·	·	·	·	·	X	·	X	·	·	·	·	·	·	·	·	·
3R-CC	·	·	X	·	·	·	X	·	X	X	·	X	X	X	·	·	X	·	X	·	·	·	X	·
4R-CC	·	·	X	X	·	·	X	·	·	·	·	X	X	X	·	·	·	·	X	·	·	·	·	X
5R-1, 24	·	·	·	·	·	·	·	·	·	·	·	X	X	·	·	·	·	·	·	X	·	·	·	·
5R-CC	·	·	X	·	·	X	X	·	·	X	·	X	X	·	·	·	·	·	X	X	·	·	·	·
6R-2, 86	·	·	X	X	·	·	·	·	·	·	·	·	X	·	·	·	·	·	·	·	·	·	X	·
6R-CC	·	·	·	·	·	·	·	·	·	·	·	·	·	·	·	·	·	·	·	·	·	·	·	·
7R-CC	·	·	·	·	·	·	·	·	·	·	·	·	·	·	·	·	·	·	·	·	·	·	·	·
8R-CC	·	·	·	·	·	·	·	·	·	·	X	·	X	·	·	·	·	·	·	·	X	·	·	·
9R-1, 62	·	·	·	·	·	·	·	·	·	·	·	·	·	·	·	·	·	·	·	X	·	·	·	·
9R-CC	·	·	·	·	·	·	X	·	·	·	·	·	·	·	·	·	·	·	·	·	·	·	·	·
10R-1, 33	·	·	·	·	·	·	·	·	·	·	·	·	·	·	·	·	·	·	·	·	·	·	·	·
10R-CC	·	·	·	·	·	·	·	·	·	·	·	·	·	·	·	·	·	·	·	·	·	·	·	·
11R-1, 52	·	·	·	·	·	·	·	·	·	·	·	·	·	·	·	·	·	·	·	·	·	·	·	·
11R-CC	·	·	·	·	·	·	·	·	·	·	·	·	X	·	X	·	·	·	·	·	·	·	X	·
12R-2, 31	·	·	·	X	·	·	·	·	·	·	X	·	·	·	·	·	·	·	·	·	·	·	·	·
12R-CC	·	·	·	·	X	·	·	·	·	·	·	·	X	·	·	·	·	·	·	X	·	·	·	·
13R-CC	·	·	·	·	·	·	·	·	·	·	·	·	·	·	·	·	·	·	·	·	·	·	·	·
14R-CC	·	·	·	·	·	·	·	·	·	·	·	·	X	·	·	X	·	·	·	X	X	·	·	·
15R-CC	·	·	·	·	·	·	·	·	·	·	·	·	·	·	·	·	·	·	·	·	·	·	·	·
16R-CC	·	·	·	·	·	·	·	·	·	·	·	·	·	·	·	·	·	·	·	·	·	·	·	·
17R-CC	·	·	·	·	·	·	·	·	·	·	·	·	·	·	·	·	·	·	·	·	·	·	·	·
18R-CC	·	·	·	·	·	·	·	·	·	·	·	·	·	·	·	·	·	·	·	·	·	·	·	·
19R-CC	·	·	·	·	·	·	·	·	·	·	·	·	X	·	·	·	·	·	·	·	·	·	·	·
21R-CC	·	·	·	·	·	·	·	·	·	·	·	·	·	·	·	·	·	·	·	·	·	·	·	·
22R-CC	·	·	·	·	·	·	·	·	·	·	·	·	·	·	·	·	·	·	·	·	·	·	·	·
23R-CC	·	·	·	·	·	·	·	·	·	·	·	·	·	·	·	·	·	·	·	·	·	·	·	·
24R-CC	·	·	·	·	·	·	·	·	·	·	·	·	·	·	·	·	·	·	·	·	·	·	·	·

range falls within the gas generation portion of the petroleum thermal window (Hunt, 1979) and, therefore, is consistent with an *in-situ* thermal source from kerogen for these gases. The total organic carbon (TOC) for Holes 857A and 857B, which ranges from about 0.3% to 0.55% (Table 15), supports this interpretation. These organic carbon concentrations, which are more than sufficient to generate the small concentrations of gas observed, are too low for efficient petroleum generation and primary expulsion, as discussed previously (see "Organic Geochemistry" section, "Site 856" chapter). Under these circumstances, the generated but unexpelled oil or bitumen, which forms in the temperature range of about 50° to 150°C (Hunt, 1979), plus any residual kerogen, would remain dispersed in the sediments and would be expected to undergo further cracking to gas at higher temperatures, consistent with the downhole profiles observed in Figure 30.

According to this scenario, the leveling out of the amounts of methane, ethane, and propane observed from about 300 to 450 mbsf in Hole 857C (Fig. 30) could be caused by (1) a depletion of the gas generation capability of the *in-situ* kerogen and bitumen, (2) a steady-state condition where the rates of gas generation and expulsion into shallower zones from a specific depth interval are approximately equaled by the rate of upward gas migration from deeper and hotter zones, or (3) a decrease in geothermal gradient in deeper intervals, where the temperature either remains constant or decreases below 300 mbsf. The present-day temperatures estimated from surface heat flow and the downhole temperature data do not support the latter interpretation (see "Heat Flow" section, this chapter). However, support for this possibility is provided by the presence of measurable amounts of C_{14+} bitumens to the bottom of Hole 857C, the presence of recognizable foraminifers which still contain calcium carbonate in Section 139-857C-42R-CC at 375 mbsf (see "Biostratigraphy" section, this chapter), and some deeper intervals containing mineral assemblages which do not appear to be thermally altered (see "Lithostratigraphy and Sedimentology" section, this chapter).

Alternatively, the methane profile in Figure 30 (but not ethane or propane) is similar to that of calcium, so that diffusional processes could be important, as postulated for calcium and sodium (see "Inorganic Geochemistry" section, this chapter). Further shore-based research will be required to distinguish among these possibilities.

Carbon dioxide occurs at levels between about 1000 and 10,000 ppm in these sediments (Figs. 29 and 30). The profiles are very irregular and show no obvious correlation with those of C_1, C_2, or C_3, nor with TOC (Figs. 29 and 30).

Table 5 (continued).

Sample (cm)	Indeterminate	Anhydrite and/or gypsum	Barite roses	Clay lumps	Diatoms	Dolomite nodule	Flattened foraminifers	Mica	Mineral grains	Ostracodes	Pine pollen	Pyrite tubes	Radiolarians	Recrystallized foraminifers	Sponge spicules	Sulfides	Test fragments	Very small rotalids
139-857C-																		
1R-1, 0	X	·	·	·	A	·	·	·	·	·	·	·	A	·	·	·	·	·
1R-1, 61	·	·	·	·	·	·	·	·	·	·	·	·	C	·	·	·	A	·
1R-CC	X	·	·	·	·	·	·	·	·	·	·	·	A	·	·	·	·	·
2R-2, 67	·	·	·	·	·	·	·	A	A	R	·	·	·	·	·	A	A	·
2R-CC	X	·	·	·	·	·	·	·	·	·	·	·	·	·	·	·	·	·
3R-2, 98	X	·	F	·	·	·	·	·	·	·	·	·	·	·	·	A	·	·
3R-CC	X	·	·	·	·	·	·	A	A	·	·	·	·	·	·	·	·	·
4R-CC	·	·	·	·	·	·	·	·	·	·	·	·	·	·	·	·	·	·
5R-1, 24	·	·	R	·	·	·	·	·	·	·	·	·	·	·	·	A	·	·
5R-CC	X	·	F	·	·	·	·	·	·	·	·	·	·	·	·	·	·	·
6R-2, 86	X	·	R	·	·	·	·	·	·	R	·	·	·	·	·	·	·	·
6R-CC	·	·	·	·	·	·	·	A	·	·	·	F	·	·	·	·	·	·
7R-CC	·	A	·	·	·	X	·	·	·	·	·	·	·	·	·	·	·	·
8R-CC	·	·	·	·	·	X	·	A	A	·	·	C	·	·	·	·	·	·
9R-1, 62	·	·	·	·	·	·	·	A	·	·	R	·	·	·	·	A	·	·
9R-CC	·	R	·	A	·	·	·	·	·	·	·	A	·	·	·	·	·	·
10R-1, 33	·	·	·	·	·	·	·	·	·	·	·	C	·	·	·	·	·	·
10R-CC	·	·	·	·	·	·	·	A	A	·	·	A	·	·	·	·	·	·
11R-1, 52	·	·	·	·	·	·	·	A	A	·	·	·	·	·	·	·	·	X
11R-CC	·	·	·	·	·	·	·	A	A	·	·	X	·	X	·	·	·	·
12R-2, 31	X	X	·	·	·	·	·	·	·	·	·	·	·	X	·	·	·	·
12R-CC	X	·	·	A	·	·	F	·	·	·	·	A	·	·	·	·	·	·
13R-CC	X	·	·	A	·	·	·	·	·	·	·	·	·	·	·	·	·	·
14R-CC	X	·	·	·	·	·	·	A	A	·	·	R	·	·	·	·	·	·
15R-CC	·	·	·	·	·	·	·	·	·	·	·	·	·	·	·	·	·	·
16R-CC	·	·	·	·	·	·	·	·	A	·	·	·	·	·	·	·	·	·
17R-CC	X	·	·	·	·	·	·	A	A	·	·	·	·	·	·	·	·	·
18R-CC	·	·	·	A	·	·	·	A	A	·	·	·	·	·	·	·	·	·
19R-CC	X	·	·	A	·	·	·	A	A	·	·	·	R	·	R	·	·	·
21R-CC	·	·	·	·	·	·	·	A	A	·	·	A	·	·	·	·	·	·
22R-CC	·	·	·	·	·	X	·	·	A	·	·	A	·	·	·	·	·	·
23R-CC	·	·	·	·	·	·	·	·	·	·	·	·	·	·	·	·	·	·
24R-CC	·	·	·	·	·	·	·	·	A	·	·	·	·	·	·	·	·	·

Fluorescence

The extract colors ranged from yellow-green to pale yellow to a depth of 60 mbsf in Hole 857A and colorless for the remaining samples analyzed to 111 mbsf. The extracts of all samples from Hole 857C were colorless. Holes 857A and 857C had yellow fluorescence to 41 and 153 mbsf, respectively, and white fluorescence down to 111 and 297 mbsf, respectively. The yellow fluorescence is interpreted as thermal maturation of bitumen to the mature stage (i.e., exposed to temperatures of at least 50° to 90°C over geologic times or even higher temperatures for short times) and white fluorescence is overmature bitumen enriched in polynuclear aromatic hydrocarbons (PAH, i.e., sediments heated to temperatures of at least 150°C over geologic times or even much higher for brief periods; Curray, Moore, et al., 1982). Thus, in Hole 857C, the yellow fluorescence occurs in all sediments down to 153 mbsf, corresponding to a maximum temperature of about 110°C, while white fluorescence is observed down to 297 mbsf, corresponding to present-day temperatures of approximately 200°C, as estimated from surface heat flow (see "Heat Flow" section, this chapter). The concentration levels of extractable organic matter are extremely low and uniform throughout both holes based on the color and fluorescence intensities.

Bitumen Analyses

Aliquots of the hexane/isopropanol or methanol extracts of the samples from the fluorescence assessment or subsamples of freeze-dried sediment were concentrated under a stream of nitrogen to about 10–40 μL. Equal volumes of sediment and solvent were prepared for extraction so that the relative concentrations of the lipids/bitumen could be estimated vs. depth. The extract concentrates were analyzed by high-resolution gas chromatography. Examples of traces are shown in Figure 32. Yields of extractable organic matter are low throughout both holes and show a trend of gradually decreasing amounts vs. sub-bottom depth (Figs. 31 and 33). This low yield together with low TOC values (see Figs. 29 and 30 and discussion below) indicates that migrated bitumens are probably not important and the hydrocarbon signatures can be utilized as indicators for *in-situ* alteration conditions (cf. previous discussion in the "Organic Geochemistry" section, "Site 856" chapter). The gradual concentration decrease vs. depth may indicate thermal alteration (oxidation) of the organic matter, possibly to CO_2.

The dominant compound series in the total extracts are hydrocarbons ranging from n-C_{14} to n-C_{35}, with pristane ($C_{19}H_{40}$, Pr) and phytane ($C_{20}H_{42}$, Ph) as the major isoprenoid alkanes (Fig. 32A, 32B).

Table 5 (continued).

Sample (cm)	Abundance of benthic foraminifers	Abundance of planktonic foraminifers	Preservation of foraminifers	*Globigerina bulloides*	*Neogloboquadrina pachyderma* (dex.)	*Neogloboquadrina pachyderma* (sin.)	*Buliminella elegantissima*	*Chilostomella oolina*	*Elphidium* spp.	*Epistominella* spp.	*Globocassidulina* spp.	*Nonionella* spp.	*Rosalina* sp. A	*Stainforthia complanata*	*Valvulineria* spp.	Indeterminate	Clay lumps	Mineral grains	Pyrite tubes	Recrystallized foraminifers
139-857C-																				
25R-CC	B	B	·	·	·	·	·	·	·	·	·	·	·	·	·	·	A	·	·	·
26R-CC	B	B	·	·	·	·	·	·	·	·	·	·	·	·	·	·	A	·	·	·
27R-CC	B	B	·	·	·	·	·	·	·	·	·	·	·	·	·	·	·	·	·	·
29R-CC	B	B	·	·	·	·	·	·	·	·	·	·	·	·	·	·	·	·	·	·
30R-CC	B	B	·	·	·	·	·	·	·	·	·	·	·	·	·	·	·	·	·	·
31R-CC	B	B	·	·	·	·	·	·	·	·	·	·	·	·	·	·	·	·	·	·
32R-CC	R	B	·	·	·	·	·	·	·	·	·	·	·	·	·	X	·	·	·	X
33R-CC	R	R	P	R	·	R	·	X	·	·	·	·	·	X	·	·	·	·	·	·
34R-CC	B	B	·	·	·	·	·	·	·	·	·	·	·	·	·	·	A	·	X	·
35R-CC	R	B	P	·	·	·	·	X	·	·	·	X	·	·	·	·	A	·	·	R
36R-CC	R	R	P	·	·	·	·	·	·	·	·	·	·	·	·	X	A	·	·	X
37R-CC	F	R	·	·	·	·	X	·	X	X	·	·	·	·	X	X	A	·	·	F
38R-CC	F	B	P	·	·	·	·	·	·	·	·	·	X	·	·	X	A	·	·	F
39R-CC	F	B	P	·	·	·	·	·	·	·	·	·	·	·	·	X	A	·	·	F
40R-CC	B	A	·	A	A	·	·	·	·	·	·	·	·	·	·	X	A	·	·	A
41R-CC	B	B	·	·	·	·	·	·	·	·	·	·	·	·	·	·	A	·	·	·
42R-CC	F	B	P	·	·	·	·	·	·	·	X	·	·	X	·	X	A	·	·	F
43R-CC	R	B	·	·	·	·	·	·	·	·	·	·	·	X	X	X	A	·	·	R
44R-CC	B	B	·	·	·	·	·	·	·	·	·	·	·	·	·	·	A	·	·	·
45R-CC	B	B	·	·	·	·	·	·	·	·	·	·	·	·	·	·	A	·	·	·
46R-CC	B	B	·	·	·	·	·	·	·	·	·	·	·	·	·	·	A	·	·	·
47R-CC	B	B	·	·	·	·	·	·	·	·	·	·	·	·	·	·	A	·	·	·
48R-CC	B	B	·	·	·	·	·	·	·	·	·	·	·	·	·	·	A	·	·	·
49R-CC	B	B	·	·	·	·	·	·	·	·	·	·	·	·	·	·	A	·	·	·
50R-CC	B	B	·	·	·	·	·	·	·	·	·	·	·	·	·	·	A	·	·	·
51R-CC	B	B	·	·	·	·	·	·	·	·	·	·	·	·	·	·	A	·	·	·
52R-CC	B	B	·	·	·	·	·	·	·	·	·	·	·	·	·	·	A	·	·	·
53R-CC	B	B	·	·	·	·	·	·	·	·	·	·	·	·	·	·	A	·	·	·
54R-CC	B	B	·	·	·	·	·	·	·	·	·	·	·	·	·	·	A	·	·	·
55R-CC	B	B	·	·	·	·	·	·	·	·	·	·	·	·	·	·	A	·	·	·
56R-CC	B	B	·	·	·	·	·	·	·	·	·	·	·	·	·	·	A	·	·	·
57R-CC	B	B	·	·	·	·	·	·	·	·	·	·	·	·	·	·	·	A	·	·
58R-CC	B	B	·	·	·	·	·	·	·	·	·	·	·	·	·	·	A	·	·	·

The bitumen parameters for maturation and organic matter sources which were measured on the ship are listed in Table 16. The *n*-alkanes $>C_{26}$ have a significant predominance of odd carbon numbers (carbon preference index, CPI, >1.0) and carbon number maximum (C_{max}) at C_{27} or C_{29} in the upper sections of both holes, typical for immature hydrocarbons with an origin from terrestrial higher plants (Fig. 32A, 32B; Simoneit, 1977, 1978). The *n*-alkane patterns $<C_{24}$ with the unresolved complex mixture (UCM) of branched and cyclic compounds and the C_{max} at C_{17} are typical for autochthonous marine bitumen derived from alteration of microbial lipids (Fig. 32A, 32B, Table 16; Simoneit, 1977, 1978).

The CPI (range C_{26}–C_{35}) for Hole 857A decreases gradually to one below 100 mbsf (Fig. 33), indicative of enhanced diagenesis/maturation due to high regional heat flow. The CPI profile for Hole 857C also decreases to values of one (e.g., Fig. 31) and then to <1 below 320 mbsf, consistent with increasing thermal stress vs. depth, together with a source of alkanes with an even predominance (Fig. 32). The variability of the surficial CPI values in both holes reflects different source inputs of marine and terrestrial organic matter. The CPI <1 in the lower sections of Hole 857C (e.g., Fig. 32D) is of interest. This even-carbon-number predominance of *n*-alkanes has been described for DSDP sediments from Legs 5 and 18 in the northeast Pacific to the south of this region (Simoneit, 1977) and for sediments from other geographic areas (Grimalt and Albaiges, 1987). Thermal maturation generally does not produce CPI values of less than one, so that the decrease in CPI with depth in this hole must be partially source-related. Since maturation in these sediments begins with immature organic matter that has not completed diagenetic alteration, the *n*-alkanols from terrestrial plant waxes (Simoneit, 1978) may be the source of the even-chain alkanes $>C_{24}$. This would require alteration by dehydration and double bond reduction of the *n*-alkanols, as discussed previously ("Organic Geochemistry" section, "Site 856" chapter).

Maturation is not evident in the isoprenoid to normal hydrocarbon ratios (Pr/*n*-C_{17} and Ph/*n*-C_{18}) for Hole 857A (Fig. 33) and a slight trend is observed below 170 mbsf of Hole 857C (Fig. 31). Low Pr/*n*-C_{17} and Ph/*n*-C_{18} values (<0.5) are characteristic of basin sediments which, at some time in their geologic history, have been heated to temperatures greater than 50°C, at the beginning of the oil thermal window ("Organic Geochemistry" section, "Site 855" chapter, this volume). Pr/Ph, which has been reported to be influenced both by source and by maturation (cf. "Organic Geochemistry" section, "Site 856" chapter), generally shows fluctuating values in the range of 0.6 to 2.5 for both holes (Figs. 31 and 33). This may reflect the organic

Table 6. Comparison of sequences zoned by calcareous nannofossils (Martini, 1971; Gartner, 1977) and planktonic foraminifers (Lagoe and Thompson, 1988).

Hole 857A Sample (cm)	Depth (mbsf)	Age	Foraminifer zone	Nannofossil zone	
1H-1, 0–1	0.0	Holo.	CD1	NN 21	E. huxleyi Acme
1H-3, 10–13	5.12	late Pleistocene	CD2		
1H-CC	11.4				
2H-1, 45–48	11.87				
2H-1, 105–107	12.45				
2H-2, 20–22	13.11				
2H-2, 129–131	14.20				
2H-3, 48–50	14.89				
2H-3, 129–131	15.70				
2H-4, 12–14	16.03				
2H-4, 17–19	16.08				
2H-4, 127–129	17.18				
2H-5, 19–21	17.6				
2H-5, 22–24	17.62				
2H-5, 28	17.68				*Emiliania huxleyi*
2H-5, 31	17.71				
2H-5, 42	17.82				
2H-5, 114–116	18.56				
2H-5, 118–120	18.59				
2H-6, 04–06	18.95				
2H-6, 9–11	19.00				
2H-6, 112–114	20.03				
2H-7, 48–50	20.89				
2H-CC	20.9				
3P-CC	21.9				
4H-1, 16–18	22.07				
4H-1, 22–24	22.13				
4H-1, 99–101	22.9				
4H-1, 104–106	22.95				
4H-2, 31–33	23.72				
4H-2, 37–39	23.78				
4H-2, 99–101	24.4				
4H-2, 105–107	24.46				
4H-2, 140–142	24.81				
4H-3, 37–39	25.28				
4H-3, 110–112	26.01				
4H-3, 115–117	26.06				
4H-4, 32–34	26.73				
4H-4, 49–51	26.90		CD3		
4H-4, 106–108	27.47		CD4		
4H-4, 111–113	27.52				
4H-5, 60–62	28.51				
4H-5, 71–73	28.62				
4H-5, 127–129	29.18				
4H-6, 86–88	30.27				
4H-CC	31.4				
5H-4, 9–13	36.02				
5H-CC	40.9				
6H-5, 45–49	47.36				
6H-CC	50.4				
7H-4, 1–5	55.0				
7H-CC	59.9				
8H-5, 114–118	67.05				
8H-CC	69.4				
9H-5, 79–84	76.22				
9H-CC	78.9				
10H-2, 12–4	80.54				
10H-CC	80.9				
11X-CC	91.8				
12X-CC	101.5				
13X-2, 68–72	103.7				
13X-CC	111.2		?		

Hole 857B Sample (cm)	Depth (mbsf)	Age	Foraminifer zone	Nannofossil zone	
1H-1, 0-1 cm	0.0	Holo.	CD1	NN21	E. huxleyi Acme
1H-CC	3.4	late Pleist.	CD2		
2H-CC	12.9				
3H-CC	30.5		CD4 ?		E. huxleyi

Hole 857C Sample (cm)	Depth (mbsf)	Age	Foraminifer zone	Nannofossil zone	
1R-1, 0–1	0.0	Holo.	CD1	NN21	E. huxleyi Acme
1R-1, 61–65	0.6				
1R-CC	3.5	late Pleistocene	CD2		
2R-1, 67–70	57.6		CD4 ?		*Emiliania huxleyi*
2R-CC	66.5				
3R-CC	76.1				
4R-CC	82.1				
5R-1, 24–28	82.3				
5R-CC	86.2				
6R-2, 86–88	88.5				
6R-CC	95.2				
7R-CC	104.9				
8R-CC	114.5				
9R-1, 62–64	115.1				
9R-CC	124.1				
10R-1, 33–35	124.4				
10R-CC	133.8				
11R-1, 52–54	134.3				
11R-CC	143.5				
12R-2, 31–33	145.3				
12R-CC	153.1				
13R-2, 25–29	154.8	Pleistocene		NN19–21 or NN21 ?	
13R-CC	162.8				
14R-1, 115–119	163.9				
14R-CC	172.5				
15R-1, 120–124	173.7				
15R-CC	182.2				
16R-CC	191.9				
17R-CC	201.6				
18R-CC	211.3				
19R-CC	220.9				
21R-CC	240.3	Pleistocene ?	?	?	
22R-CC	249.9				
23R-CC	259.2				
24R-CC	268.8				
25R-CC	274.5				
26R-CC	284.1				
27R-CC	293.8				
28R-CC	303.4				
29R-CC	313.1				
30R-CC	322.7				
31R-CC	327.6				
32R-CC	332.4				
33R-CC	336.5				
34R-CC	341.5				
35R-CC	346.1				
36R-CC	350.8				
37R-CC	355.8				
38R-CC	360.4				
39R-CC	365.4				
40R-1, 138–141	366.8				
40R-CC	374.9				
41R-CC	379.7	?			
42R-CC	384.7				
43R-CC	389.7				
44R-CC	394.3				
45R-CC	399.0				
46R-CC	404.0				
47R-CC	408.7				
48R-CC	413.7				
49R-CC	418.3				
50R-CC	423.4				
51R-CC	427.8				
52R-CC	432.8				
53R-CC	437.0				
54R-CC	442.0				
55R-CC	446.5				
56R-CC	451.7				
57R-CC	461.5				
58R-CC	471.1				

Table 7. Range chart of calcareous nannofossils and their abundance and preservation.

Hole 857A Sample (cm)	Depth (mbsf)	Age		Nannofossil zonation	Abundance	Preservation	*Braarudosphaera bigelowii*	*Calcidiscus leptoporus*	*Coccolithus pelagicus*	*Emiliania huxleyi*	*Emiliania pujosae*	*Gephyrocapsa oceanica*	*Gephyrocapsa caribbeanica*	*Gephyrocapsa* sp.	*Pontosphaera japonica*	*Rhabdosphaera claveger*	*Syrocosphaera pulchra*	*Thoracosphaera* sp.	*Umbilicosphaera mirabilis*	*Helicosphaera carteri*
1H-1,0–1	0.0	late Pleistocene – Holocene	NN21	*Emiliania huxleyi* Acme	C	M	R	R	C	C	R	C	R		C	R	R	R	R	
1H-3,10–13	5.12				A	M			C	C	R	A			R					
1H-CC	11.4				C	P			C	C	R	C	R		R		R	R		
2H-4,17–19	16.081				C	M			F	C	R	C			R					
2H-5,19–21	7.6				C	M	R		F	C	R	C			R					
2H-5, 22	17.62				C	P		F	C	C		C		F						
2H-5, 28	18.55			*Emiliania huxleyi*	C	P			C	F		C		F						
2H-5, 31	17.68				A	P			C	F		C		C						
2H-5, 42	17.71				A	M		R	C	F		M		C	R					
2H-5,114–116	17.82				F	P			R	R		F								
2H-6, 4–6	18.95				F	P		R		R		F								
2H-CC	20.9				F	P			R	F		F	R		R					
3P-CC	21.9				R	P				R		R								
4H-1, 16–18	22.07				F	P	R		R	F		F		F						
4H-1, 99–101	22.9				F	P		R	R	F		F								
4H-2, 31–33	23.72				F	P		R		R		F								
4H-2, 99–101	24.4				F	P		R		R		F								
4H-2, 140–142	24.81				F	P			R	R	R	F								
4H-3, 110–112	26.01				R	P				R		R								
4H-4, 32–34	26.73				F	P				F		F								
4H-4,106–108	27.47				C	P	R		R	F		F		R						
4H-5, 60–62	28.51				F	P			R	R		F								
4H-CC	31.4				A	M	R	R	F	F	R	A	F					F	R	R
5H-4, 09–13	36.02				F	M		R	F	F	R	R								
5H-CC	40.9				A	M	C		C	F	F	A					R			R
6H-5, 45–49	47.36				C	P			R	R		C			R					
6H-CC	50.4				C	P	R		R	R		C								
7H-4, 1–5	55.0				A	M	R		F	F		A			R					
7H-CC	59.9				F	P	R		R	R		F								
8H-5, 114–115	67.05				C	P	R		F	R	R	C	R		R		R			
8H-CC	69.4				F	P	R	R	R	R		F								
9H-5, 79–84	76.22				C	P			F	F		C								
9H-CC	78.9				F	P			F	R		F								
10H-2, 12–14	80.54				C	P			R	R		C								
10H-CC	80.9				F	P			R	R		F								
11H-CC	91.8				R	P						R								
12X-CC	101.5				R	P				R		F								
13X-2, 68–72	103.7				R	P				R		R								
13X-CC	111.2				B	—														

Hole 857B Sample (cm)	Depth (mbsf)	Age		Nannofossil zonation	Abundance	Preservation	*Calcidiscus leptoporus*	*Coccolithus pelagicus*	*Emiliania huxleyi*	*Emiliania pujosae*	*Gephyrocapsa oceanica*	*Gephyrocapsa caribbeanica*	*Pontosphaera japonica*	*Syrocosphaera pulchra*
1H-1, 0–1	1.0	l. Pleis. – Holocene	NN21	*Emiliania huxleyi* Acme	C	M	F	R	C		C	R		R
1H-CC	3.4				R	P		R	R		R			
2H-CC	12.9				C	M		F	C	R	C			
3H-CC	30.5			*E. huxleyi*	C	P	R	R	F	R	C	R	R	

Note: A = abundant, C = common, F = few, R = rare, B = barren, G = good preservation, M = moderately good preservation, P = poor preservation.

matter sources rather than maturation. Furthermore, the black carbonaceous residue from the kerogen (cf. "Organic Geochemistry" section, "Site 856" chapter) is not found in Hole 857A, and only in minor amounts at depths >350 mbsf in Hole 857C, suggesting that full maturation has not occurred.

The overall hydrocarbon signatures of the surficial intervals of these sediments are quite similar to those of Site 856 and of shallow gravity cores taken near the Middle Valley hydrothermal vents (Simoneit et al., in press). The hydrocarbons in the deeper intervals indicate rapid maturation by accelerated diagenesis, probably resulting from high regional heat flow rather than from hydrothermal alteration.

If correct present-day subsurface temperatures can be extrapolated from the surface heat flow curves (see "Heat Flow" section, this chapter), then the approximate present-day temperatures of the samples shown in Figures 31 to 33 can be estimated. A surprising result from this estimate is that the higher molecular weight compounds (>C_{14}) are surviving in these sediments to temperatures considerably beyond those considered normal for the oil generation window. For

Table 7 (continued).

Hole 857C Sample (cm)	Depth (mbsf)	Age	Nannofossil zonation		Abundance	Preservation	*Braarudosphaera bigelowii*	*Calcidiscus leptoporus*	*Coccolithus pelagicus*	*Emiliania huxleyi*	*Emiliania pujosae*	*Gephyrocapsa oceanica*	*Gephyrocapsa caribbeanica*	*Pontosphaera japonica*	*Reticulofenestra* sp.	*Syrocosphaera pulchra*
1R-1, 0–1	0.1	late Pleistocene – Holocene	NN21	*E. huxleyi* Acme	C	M		F	F	C		C				R
1R-1, 61–65	0.6				C	P			F	R		C				
1R-CC	3.5				C	M	R	R	F	C	R	C	R	R		R
2R-2, 67–70	57.6			*Emiliania huxleyi*	C	P			F	F		C				
2R-CC	66.5				C	P	R		R	F		C	R			
3R-CC	76.1				C	P			F	R		F				
4R-CC	82.1				F	P			F	R		F				
5R-1, 24–28	82.3				F	P			R	R		F				
5R-CC	86.2				R	P			R	R		R				
6R-2, 86–88	88.5				F	P			F							
6R-CC	95.2				B	—										
7R-CC	104.9				F	P						F				
8R-CC	114.5				F	P			R			R				
9R-1, 62–64	115.1				B	—										
9R-CC	124.1				R	P			R			R				
10R-1, 33–35	124.4				F	P			R	F		F	R	R		
10R-CC1	133.8				F	M			R	R						
1R-1, 52–54	134.3				F	P			R	R		R				
11R-CC	143.5				F	P			R	R		R				
12R-2, 31–33	145.3				R	P			R	R		R			R	
12R-CC	153.1				R	P			R	R		R				
13R-2, 25–29	154.8	Pleistocene	NN19–21 or NN21 ?		B	—										
13R-CC	162.8				R	P			R							
14R-1, 115–119	163.9				R	P										
14R-CC	172.5				R	P			R							
15R-1, 120–124	173.7				R	—			R							
15R-CC	182.2				B	—										
16R-CC	191.9				R	P			R							
17R-CC	201.6				R	P			R			R				
18R-CC	211.3				R	P			R			R				
19R-CC	220.9	?	?		R	P			R							
21R-CC	240.3				R	P			R							
22R-CC	249.9				B	—										
23R-CC	259.2				B	—										
24R-CC	268.8				B	—										
25R-CC	274.5				B	—										
26R-CC	284.1				R	P			R							
27R-CC	293.8				B	—										
28R-CC	303.4				B	—										
29R-CC	313.1				B	—										
30R-CC	322.7				R	P			R							
31R-CC	327.6				B	—										
32R-CC	332.4				R	P			R							
33R-CC	336.5				R	P			R							
34R-CC	341.5				B	—										
35R-CC	346.1				B	—										

example, small quantities of long-chain hydrocarbons used in making the CPI determination are still measurable at 433 mbsf in Hole 857C (Fig. 31), corresponding to an estimated present-day temperature of 270°C, considerably beyond the maximum range of 135° to 150°C normally considered to be the end of the oil window in conventional basins (Hunt, 1979). In addition, the CPI is not decreasing to a value of one, diagnostic of maturation, until these sediments reach temperatures above 150°C at depths below 230 mbsf. Thus, the thermal alteration/destruction of these typical aliphatic petroleum hydrocarbons is not complete up to temperatures of 270°C at 433 mbsf in Hole 857C. Their gradual thermal destruction together with that of the remaining residual kerogen is a potential source for the C_1 to C_3 hydrocarbons (Fig. 30). It is possible that survival of C_{14+} hydrocarbons to depths and temperatures well beyond those generally considered "normal" for the oil window is due to the young age of the sediments (about 250,000 yr or less; see "Site Geophysics and Geology" section, this chapter). Both time and temperature must be considered in maturation processes, which respond exponentially to temperature and linearly to time. Alternatively, the cumulative organic geochemical data suggest that the actual maximum temperatures experienced by sediments below 300 mbsf in Hole 857C are less than the values estimated from the surface heat flow.

Molecular Stratigraphy

Molecular stratigraphy using the long-chain ketones (C_{37} and C_{38} alkenones) as markers for coccolithophorids was described earlier ("Organic Geochemistry" section, "Site 856" chapter). The alkenones were only detectable in the bitumen extracts of sediments from Holes 857A and 857C to a depth of about 80 mbsf and not in the deeper section (Table 16). Their presence to that depth in these holes parallels the occurrence of *Emiliania huxleyi* ("Biostratigraphy" section, this chapter), although the molecular fossils disappear before the fossil tests, probably due to decomposition with increasingly higher temperatures. Since the alkenones are apparently not stable under significant thermal stress their distribution is consistent with the current thermal regime (see "Site Geophysics and Geology" section, this chapter). The ketone unsaturation index (U^K_{37}; Marlowe et al., 1984; Brassell et al., 1986; Prahl and Wakeham, 1987) was calculated for sediments from this site as:

Table 7 (continued).

Hole 857C Sample (cm)	Depth (mbsf)	Age	Nannofossil zonation	Abundance	Preservation	*Coccolithus pelagicus*
36R-CC	350.8			B	—	
37R-CC	355.8			R	P	R
38R-CC	360.4			R	P	R
39R-CC	365.4	?	?	R	P	R
40R-1, 138–141	366.8			R	P	R
40R-CC	374.9			F	P	F
41R-CC	379.7			R	P	R
42R-CC	384.7			R	P	R
43R-CC	389.7			R	P	R
44R-CC	394.3			B	—	
45R-CC	399.0			B	—	
46R-CC	404.0			B	—	
47R-CC	408.7			B	—	
48R-CC	413.7			B	—	
49R-CC	418.3			B	—	
50R-CC	423.4			B	—	
51R-CC	427.8	?	?	B	—	
52R-CC	432.8			B	—	
53R-CC	437.0			B	—	
54R-CC	442.0			B	—	
55R-CC	446.5			B	—	
56R-CC	451.7			B	—	
57R-CC	461.5			B	—	
58R-CC	471.1			B	—	

$$U^K_{37} = [C_{37:2}]/([C_{37:2}] + [C_{37:3}])$$

The results are plotted in Figure 34 and show slightly warmer sea-surface conditions (5°–6°C) in the upper 50 mbsf than in deeper sections (average 3°C). Whether this is a significant difference in seawater temperature of the photic zone will have to be calibrated by shore-based studies. The U^K_{37} in the depth interval below 55 mbsf is variable due to the low alkenone concentrations. Examples of this ratio with surface sea water temperatures for alkenones in surficial sediment from the more tropical Site 658 on Walvis Ridge (Poynter et al., 1989) and Site 686 on the Peru Margin (Farrimond et al., 1990) are also shown.

Elemental Analyses

Downhole profiles for weight percentage of C, H, N, and S are shown in Table 15 and in Figures 35 and 36. Total carbon varies from about 0.5% to 1% in Hole 857A and 0.4% to 0.7% in Hole 857C, comparable to the general range observed at Sites 855 and 856. The total carbon is generally about equally divided between organic and inorganic carbon (Table 15; Figs. 29 and 30). Exceptions occur in three sections which are slightly enriched in carbonate: in Hole 857A at 11 and 63–69 mbsf (Fig. 29) and in Hole 857C at 80 mbsf. (The low TOC observed at 63–69 mbsf in Hole 857A is an artifact of the calculation method, where subtraction of large values of carbonate carbon from total carbon results in high errors in the differences which are the TOC values.)

Nitrogen occurs in low concentrations, 0.02% to 0.06% in Hole 857A and in intervals of Hole 857C deeper than 82 mbsf (Table 15; Figs. 35 and 36). In Hole 857C, an exponential decrease in nitrogen occurs between 57 and 82 mbsf (Fig. 36, Table 15). This decrease occurs in an interval where the sulfur concentration drops to zero and the hydrogen concentration shows a maximum. On the basis of shipboard analyses, the reason for these changes is not immediately obvious—no apparent changes in mineralogy were observed in this zone. The same is true for the inverse correlation between S and H from 15 to 45 mbsf in Hole 857A (Fig. 35). The process of pyrite formation could cause this trend. However, pyrite formation occurs throughout both Holes 857A and 857C (see "Lithostratigraphy and Sedimentology" section, this chapter), so that the reason for these localized features in Hole 857A is currently unknown.

Large decreases in C, H, N, and TOC are observed in Hole 857C below 450 mbsf in a series of interbedded sills and sediments (Figs. 30 and 36). A series of maxima and minima in the H, N, and S curves can also be observed below 300 mbsf in Hole 857C. This is about the same depth where the concentrations of the gases, C_1–C_3, stopped decreasing and leveled off (Fig. 30) and where a maximum is observed in pore water calcium (see "Inorganic Geochemistry" section, this chapter). It is suggested that all of these phenomena may be related to lateral fluid flow at this depth and below, possibly associated with the sills.

Percentages of inorganic carbon and TOC are plotted along with the gases, methane, and carbon dioxide for Hole 857A (Fig. 29) and for Hole 857C (Fig. 30). The gas profiles were obtained from different samples and depth intervals than the inorganic carbon and the TOC profiles; therefore, only general trends may be meaningful. Nevertheless, in Hole 857A, a broad peak in CO_2 from 50 to 70 mbsf does encompass a zone of higher inorganic carbon from about 65 to 70 mbsf (Fig. 29). In Hole 857C, a small decrease in methane and CO_2 below 450 mbsf is associated with a significant decrease in inorganic carbon and TOC as the sills are penetrated (Fig. 30). Shore-based studies on carbon isotopes of the gases will be carried out to determine if a genetic relationship exists between the gases, inorganic carbon, and TOC.

There is some suggestion of an inverse correlation between the concentrations of H and S from 0 to 40 mbsf in Hole 857A (Fig. 35) and from 50 to 150 mbsf in Hole 857C (Fig. 36), possibly related to deposition of sulfide minerals in more permeable intervals, which would be sandy and hence relatively poor in clay minerals. The clay minerals contain most of the bound water in these sediments (see "Sediment Alteration and Geochemistry" and "Lithostratigraphy and Sedimentology" sections, this chapter).

SEDIMENT ALTERATION AND GEOCHEMISTRY

Sediment was sampled from three holes at Site 857 for geochemical analysis (Tables 17 and 18). Analyzed samples from Hole 857A were collected at 4.2–105.7 mbsf, from Hole 857C at 57.2–548.9 mbsf, and from Hole 857D at 582.8–926.7 mbsf. Holes 857C and 857D are located approximately 180 m east of Hole 857A. Sediment from below 471 m in Hole 857C and all sediment samples from Hole 857D occur in interlayered with diabase sills. Because of the proximity of these holes to each other, the geochemical data from Site 857 are shown together on plots of chemical variation vs. depth. Downcore variation in sediment mineralogy was determined for selected

Table 8. Paleontologic datums and estimated sedimentation rates at Site 857.

Datum	Age (ka)	Shallowest depth (mbsf)	Greatest depth (mbsf)	Average depth (mbsf)	Stratigraphic error (mbsf)	Sedimentation rate (cm/k.y.)
Base of Zone CD1	10	0.63	5.13	2.88	± 2.25	28.8
Base of *E. huxleyi* Acme	73	17.63	17.68	17.66	± 0.03	23.5
Base of Zone CD3	125	26.90	27.47	27.19	± 0.29	18.3

Note: The rates are calculated for the age intervals 0 to 10 ka, 10 to 73 ka, and 73 to 125 ka.

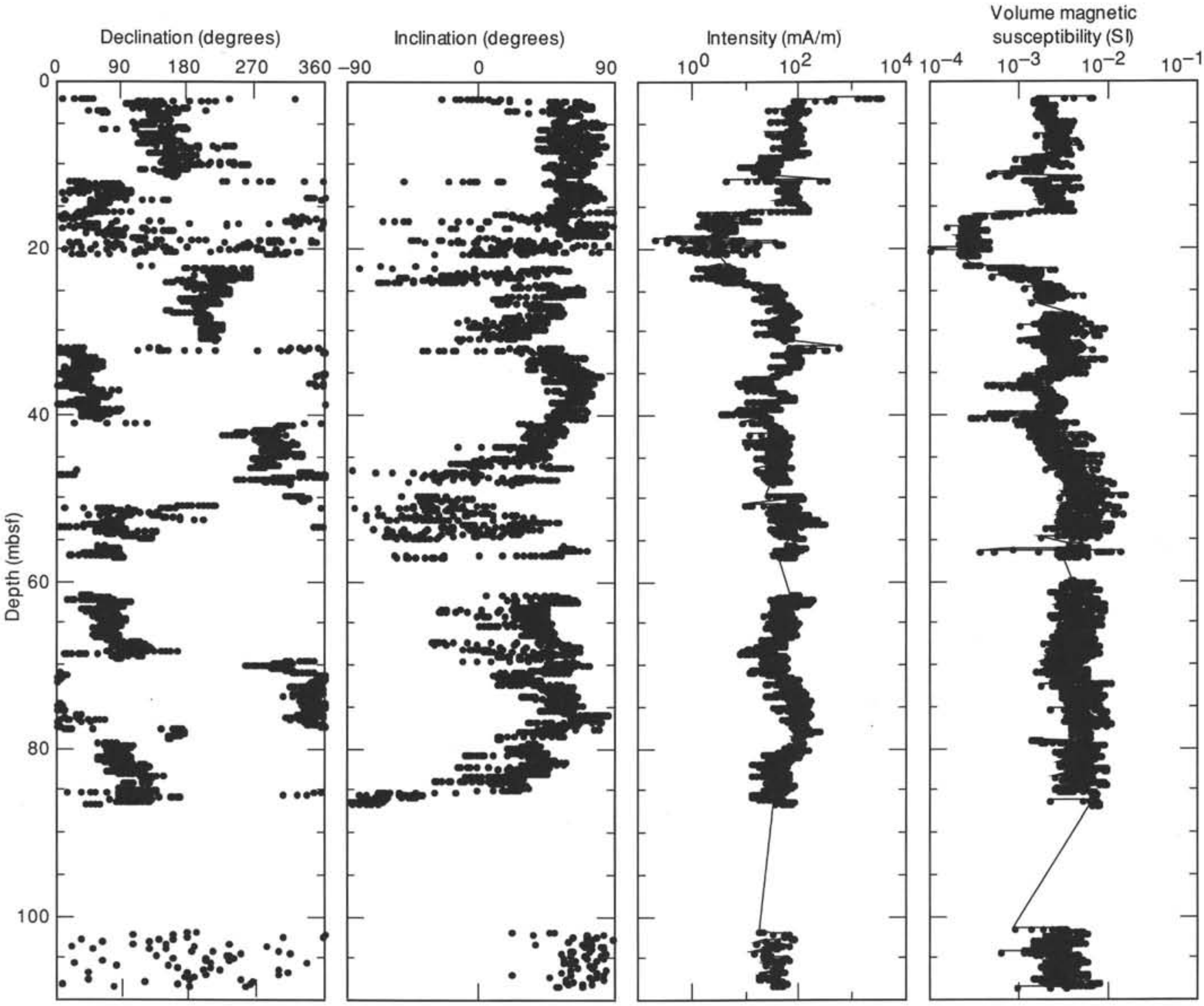

Figure 19. Declination, inclination, intensity after 15-mT AF demagnetization, and susceptibility vs. depth for Hole 857A.

samples by X-ray diffraction (XRD), as given in Tables 19 to 21. Variation in the chemical composition of sediment samples at Site 857 is mainly attributable to two factors: (1) original compositional differences that are primarily a function of grain size and (2) the effects of hydrothermal metamorphism, which increase abruptly in intensity below 400 mbsf.

Compositional differences related to grain size are similar to those described for sediment in Holes 855A–855C and Hole 856A (see "Sediment Alteration and Geochemistry" sections, "Site 855" and "Site 856" chapters). Chemical covariation in Holes 857A and 857B at depths shallower than approximately 400 mbsf is dominated by two factors: (1) a coarse-clastic component related to quartz and plagioclase feldspar content that is manifest by covariation of SiO_2, CaO, and Na_2O, and (2) a clay component related to illite and chlorite abundance that is manifest by covariation of TiO_2, Al_2O_3, Fe_2O_3, MgO, K_2O, loss on ignition (LOI), Rb, Cu, and Zn. Original chemical variation of the sediment related to grain size difference is relatively minor compared with increasing hydrothermal metamorphism of the sediment with depth. However, because of selective recovery of more indurated, coarser grained sediment at depth in Holes 857C and 857D, the proportion of silt and sand samples analyzed, relative to clay samples, increases with depth at Site 857. It is therefore important to consider the magnitude of the original chemical variations with grain size before discussing the effects of hydrothermal metamorphism.

Figures 37 and 38 show plots of the content of Al_2O_3 and TiO_2 in sediment against depth, with samples differentiated by grain size. Al_2O_3 and TiO_2 are strongly correlated with the clay component of the sediment (see "Sediment Alteration and Geochemistry" section, "Site 855" chapter). Variations in Al_2O_3 and TiO_2 at depths less than approximately 400 m at Site 857 are typical of the variations observed at the other Middle Valley drill sites. Silt and sand samples tend to have lower contents of Al_2O_3 and TiO_2 than samples of clay taken at similar depth. The elements identified above as enriched in the clay fraction of the sediment show similar behavior at depths shallower than approximately 400 m. Samples from below this depth show a systematic change that is larger in magnitude than is typical for unaltered sediment at Middle Valley, and cannot be explained by the increase of grain size. These chemical variations are attributed to enhanced thermal diagenesis and/or hydrothermal metamorphism of the sediment. The chemical change is considered to be of fundamental

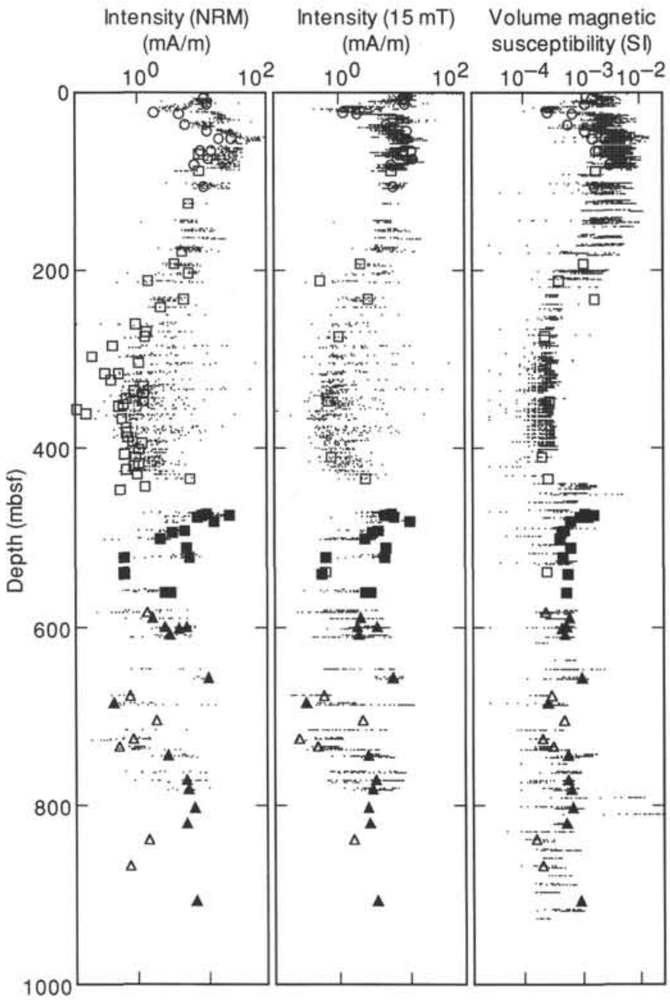

Figure 20. Volume magnetic susceptibility and magnetization intensity plots vs. depth for Holes 857A, 857C, and 857D before and after AF demagnetization. Open and solid squares (and open and solid triangles) denote sediment samples and igneous rock samples, respectively, from Hole 857C (and Hole 857D). Dots are inclination after 15-mT demagnetization of archive halves from Holes 857A, 857C, and 857D. Results after 20-mT AF demagnetization are plotted for discrete measurements and after 15-mT AF demagnetization for whole-core measurements.

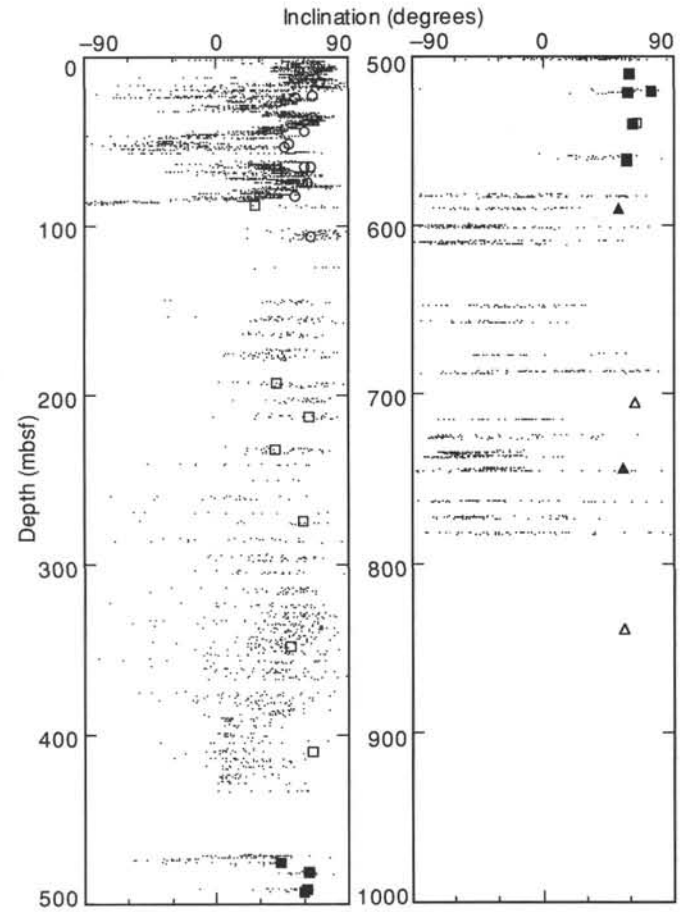

Figure 21. Inclination vs. depth for Holes 857A, 857C, and 857D. Open circles indicate discrete samples of Hole 857A. Symbols are as in Figure 20.

importance in describing the sediment from this site and the section below approximately 400 mbsf is referred to in the discussion below as the zone of hydrothermal metamorphism.

Vertical profiles of SiO_2 and Al_2O_3 (Figs. 39 and 40) show antithetic covariation in the zone of hydrothermal metamorphism, similar to the sediment above, but also show an increase and decrease, respectively, relative to the overlying unaltered sediment. Quantitative element-flux calculations require consideration of density changes. The apparent decrease in Al_2O_3 of the sediment may be attributed to an increase in grain density (and decrease in LOI, Fig. 41), and dilution by addition of silica to the sediment; thus, the apparent Al_2O_3 decrease should not be interpreted as requiring mobility of Al_2O_3 out of the sediment.

Bulk-sediment X-ray diffraction indicates a relative increase in the amount of chlorite with depth at Site 857. Chlorite alteration of basaltic rock generally conserves Al_2O_3 and involves Mg-Fe metasomatism and/or silica loss. In contrast, although the sediment MgO content may increase slightly with depth (Fig. 42), presumably due to changes in grain density, Fe_2O_3 appears to decrease slightly with depth (Fig. 43). MgO and Fe_2O_3 show positive covariation, even in the zone of hydrothermal metamorphism. Silica content of the sediment increases in the zone of chlorite formation, and XRD data suggest addition of quartz. Therefore, chlorite formation in the sediment appears to proceed by recrystallization of clay without major additions or depletions of the chemical constituents that compose chlorite.

The behavior of K_2O contrasts sharply with the chemical components that form chlorite. K_2O is nearly completely leached from the sediment in the zone of hydrothermal metamorphism (Fig. 44). This suggests that chlorite may be forming by alteration of illitic clay and release of K to a fluid phase. Surprisingly, the XRD data show that a 10-Å mica peak persists, as a minor component, in bulk sediment samples from the zone of hydrothermal metamorphism. The vertical profile of Rb content (Fig. 45) parallels that of K_2O, indicating near quantitative removal of Rb from this zone.

Compositional controls on sediment Na_2O content are clearly different from K_2O. Na_2O content variation in sediment above the zone of hydrothermal metamorphism is mainly controlled by the abundance of detrital plagioclase feldspar, which is enriched in the coarser grained fraction. There is near mirror image antithetic variation of Na_2O and K_2O in the upper sedimentary section (Figs. 44 and 46). Although alkali depletion is common in hydrothermally altered rocks, the strong K_2O depletion in the zone of hydrothermal metamorphism is not seen in the Na_2O data. Intersill sand and silt is relatively depleted in Na_2O at the bottom of Hole 857D, but is not depleted at shallower depths in the sediment from the lower part of Hole 857C. Interestingly, the sediment from approximately 200 m to 400 mbsf in Hole 857C, immediately above the zone of hydrothermal metamorphism, appears to be relatively enriched in Na_2O.

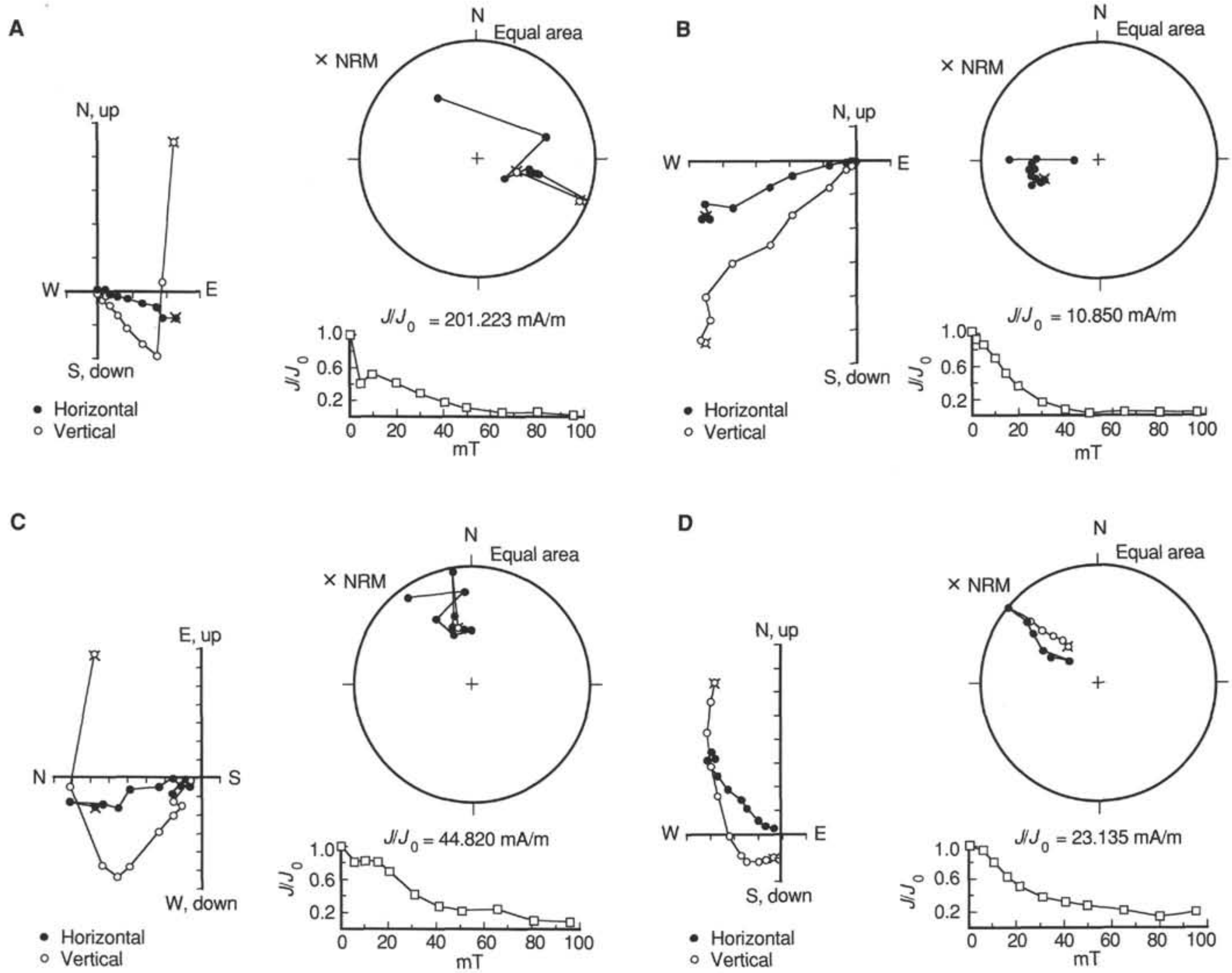

Figure 22. Representative examples of Zijderveld plot (left), equal-area projection (right), and intensity decay plot (lower right) as function of AF demagnetization field (0 to 95 mT) for sediments from Holes 857A and 857C and for igneous rocks from Holes 857C and 857D. **A.** Sample 139-857A-7H-3, 58–60 cm, scale = 40.00 mA/m per division. **B.** Sample 139-857C-17R-1, 67–69 cm, scale = 1.50 mA/m per division. **C.** Sample 139-857C-59R-3, 105–107 cm, scale = 5.00 mA/m per division. **D.** Sample 139-857D-3R-2, 67–69 cm, scale = 3.00 mA/m per division.

Plagioclase feldspar is detected as a major phase in bulk sediment XRD throughout this interval as well as throughout the deeper zone cored in Hole 857D. If plagioclase feldspar is the dominant Na_2O reservoir in the sediment, than CaO content may be expected to co-vary with Na_2O. If the relative increase in sediment Na_2O content in the interval from approximately 200 to 400 mbsf is caused by an increase in the plagioclase feldspar component, then CaO should correlate with Na_2O and should increase in the same interval, assuming that the Na/Ca ratio of the detrital plagioclase is constant.

There are no geochemical or sedimentological data that suggest a major change in sedimentary source composition for this interval ("Lithostratigraphy and Sedimentology" section, this chapter). Alternatively, the Na_2O increase could be due to albitization of detrital plagioclase, in which case CaO content should vary antithetically with Na_2O and be relatively depleted in this interval.

Interpretation of the CaO variation in the sediment requires consideration of the CO_2 content because calcite is detected in bulk sediment XRD, and authigenic carbonate nodules and calcite cement occur in Hole 857C throughout the interval of Na_2O enrichment ("Lithostratigraphy and Sedimentology" section, this chapter). Figure 47 is a plot of "silicate" CaO with depth, where "silicate" CaO is calculated by subtracting an amount of CaO equivalent to the molar abundance of CO_2 in the sediment. The calculated "silicate" CaO may be too low due to the presence of noncalcite carbonate minerals, or too high because CaO in anhydrite, which also occurs as an authigenic phase in this interval ("Lithostratigraphy and Sedimentology" section, this chapter), is not similarly subtracted. Figure 47 shows that CaO content of the sediment is relatively constant throughout the interval of Na_2O enrichment. These data suggest that Na_2O enrichment in this zone occurs independently of detrital feldspar addition or alteration. Addition of an Na_2O-rich authigenic phase, such as albite or analcime, also seems unlikely, as this process should result in a correlation between Na_2O and Al_2O_3, which is not apparent in the data.

An alternate, though speculative, explanation for the Na_2O increase is that illitic clay is being replaced by paragonite. This reaction could account for the mirror image Na_2O increase and K_2O decrease, and the presence of a 10-Å mica XRD peak in samples that have been nearly completely stripped of K_2O. This speculation should be investigated by more detailed XRD analysis of sediment samples from Hole 857D and the lower part of Hole 857C.

Although CaO content is relatively constant in the shallower zone of Na_2O enrichment, CaO content of the sediment does increase dramatically in the zone of hydrothermal metamorphism (Fig. 47).

Table 9. Inclination of stable component (I), intensity of natural remanent magnetization (J_0), median destructive field (MDF), and volume magnetic susceptibility (χ_0) for sediment samples from Holes 857A and 857C.

Core, section, interval (cm)	Depth (mbsf)	I (°)	J_0 (mA/m)	MDF (mT)	χ_0 ($\times 10^{-4}$ SI)	Lithology
139-857A-						
1H-4, 26–28	6.66	70	74	37	15.8	Silty clay
2H-3, 35–37	14.75	71	91	33	11.5	Silty clay
4H-1, 95–97	22.85	66	2.9	18	2.6	Silty clay
4H-2, 42–44	23.82	54	15	4	7.0	Silty clay
5H-4, 20–22	36.10	66	23	35	5.8	Silty clay
6H-3, 20–22	44.10	60	92	33	11.9	Silty clay
7H-2, 77–79	51.49	50	455	4	25.4	Silty clay
7H-3, 58–60	52.80	47	201	4	15.4	Silty clay
8H-4, 127–129	65.67	65	117	35	18.1	Silty clay
8H-4, 130–132	65.70	60	61	40	20.0	Silty clay
9H-4, 56–60	74.46	62	98	40	48.0	Silty clay
10H-3, 31–33	82.21	54	40	30	31.8	Silty clay
13X-3, 130–132	105.80	65	73	15	17.1	Silty clay
139-857C-						
6R-2, 11–13	87.81	26	52	22	18.1	Silty claystone
17R-1, 67–69	192.57	41	11	15	11.1	Silty clay
19R-1, 126–128	212.56	64	2.0	13	4.1	Silty clay
21R-2, 35–37	232.45	40	20	13	16.6	Silty claystone
26R-1, 11–13	274.61	59	1.6	29	2.3	Claystone
36R-2, 22–24	347.82	51	1.4	10	2.8	Silty claystone
48R-2, 24–26	410.44	66	0.90	28	2.1	Silty claystone
53R-1, 60–62	433.40	Unstable	28	10	2.6	Silty claystone
66R-1, 12–14	538.92	64	0.39	34	2.5	Siltstone

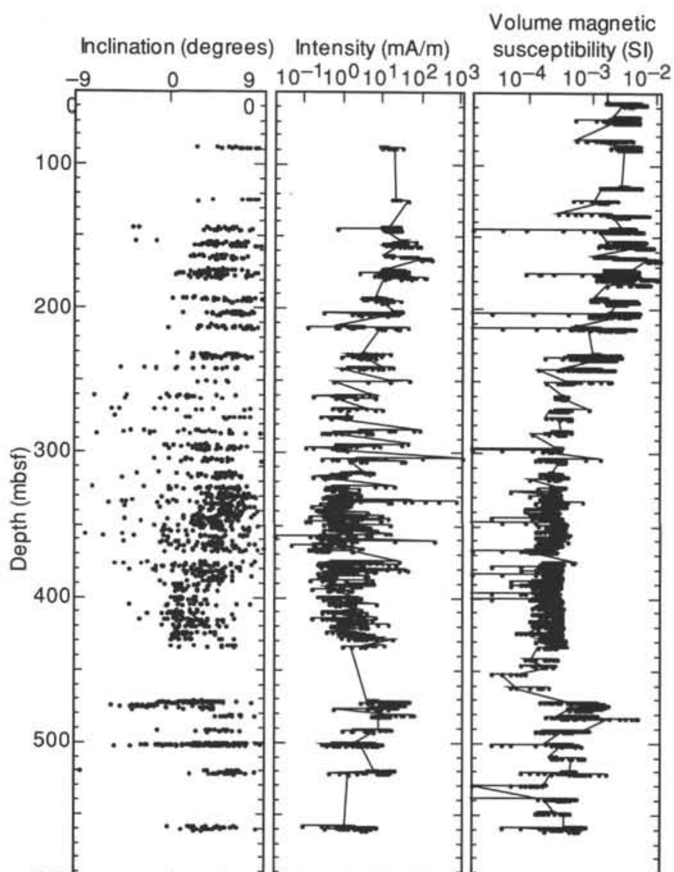

Figure 23. Inclination, intensity after 15-mT AF demagnetization, and susceptibility vs. depth for Hole 857C.

This zone of increased CaO content correlates with both visual and XRD identification of epidote as a major alteration mineral in silty and sandy sediment. Epidote occurs with quartz and feldspar, presumably albite, and locally with the Ca-rich zeolite wairakite. The quartz-albite-epidote (± wairakite) alteration represents significant CaO and SiO_2 addition to the sediment, accompanied by significant loss of K_2O and Rb. Ba (Fig. 48) and Cu (Fig. 49) are also generally depleted in the zone of hydrothermal metamorphism, although some samples have high concentrations of Cu, presumably due to the presence of secondary Cu-sulfide phases in the sediment. Surprisingly, Zn content of the sediment (Fig. 50) does not show the strong depletion seen in the Cu data. Lower relative mobility of Zn relative to Cu in this hydrothermal environment should be considered as a possible contributing factor in the relatively low Zn/(Zn + Cu) of the massive sulfide deposit drilled at Site 856 ("Sulfide Petrology and Geochemistry" section, Site 856).

IGNEOUS PETROLOGY AND GEOCHEMISTRY

Igneous rock was recovered at from Holes 857C and 857D as a series of mafic sills, 1–25 m thick, interlayered with sediment. The primary purpose of drilling at this site was to penetrate into and characterize a hydrothermal reservoir. The goals of petrographic and geochemical analyses of the igneous rocks are to (1) assess the relationship of the sill complex to the other rocks in Middle Valley in terms of petrogenesis, (2) document any stratigraphic changes in extent or grade of metamorphism in the rocks, (3) assess whether the metamorphism preserved within the igneous units represents a regional hydrothermal reaction zone for nearby hydrothermal vent fluids.

Lithology and Units

Hole 857C

In Hole 857C, mafic sills interlayered with sediment were encountered between 471.1 and 567.7 mbsf; a total of 20.6 m of igneous rock were recovered (Table 22; Fig. 51). Many of the cored sills are

Table 10. Inclination of stable component (I), intensity of natural remanent magnetization (J_0), median destructive field (MDF), magnetic susceptibility (χ_0), and Q-ratio for igneous rock samples from Hole 857C.

Core, section, interval (cm)	Depth (mbsf)	I (°)	J_0 (mA/m)	MDF (mT)	χ_0 ($\times 10^{-4}$ SI)	Q-ratio	Lithology
139-857C-							
59R-1, 102–104	472.12	Unstable	78	15	11.1	1.65	Fine-grained diabase
59R-2, 91–93	473.51	Unstable	353	3	10.7	5.15	Fine-grained diabase
59R-3, 33–35	474.17	Unstable	59	8	15.4	1.19	Coarse-grained diabase
59R-3, 88–90	474.90	Unstable	45	—	9.3	1.08	Coarse-grained diabase
59R-3, 105–107	475.07	43	45	26	12.1	0.83	Coarse-grained diabase
60R-1, 17–19	480.97	63	127	26	6.3	4.54	Fine- to medium-grained diabase
61R-1, 62–64	491.12	61	19	25	5.0	0.85	Medium- to fine-grained diabase
61R-2, 45–47	492.31	59	9	64	4.3	0.45	Medium- to coarse-grained diabase
62R-1, 42–44	500.42	Unstable	4.2	55	4.1	0.23	Coarse-grained diabase
63R-1, 56–58	510.62	59	22	34	6.2	0.81	Fine-grained diabase
64R-1, 68–70	520.08	74	27	27	4.7	1.28	Highly felsic dioritic gabbro
64R-2, 38–40	521.28	58	0.42	61	4.7	0.02	Medium-grained diabase
66R-1, 38–40	539.18	61	0.39	33	5.4	0.02	Heavily altered igneous rock
68R-2, 58–60	560.08	57	8	44	5.3	0.34	Diabase
68R-3, 23–25	561.23	57	5	57	5.1	0.24	Fine-grained diabase

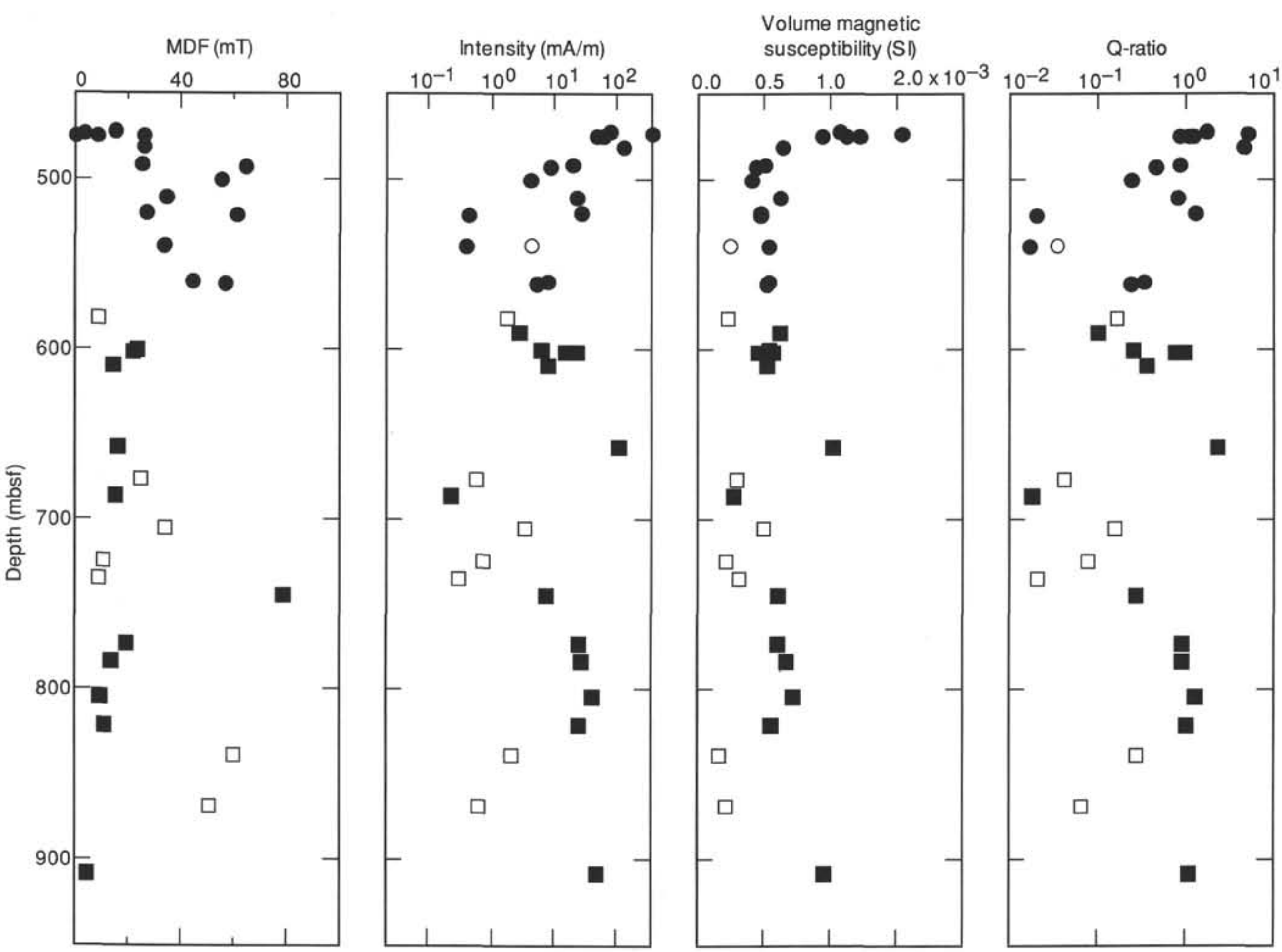

Figure 24. Median destructive field, intensity of NRM, susceptibility, and Q-ratio vs. depth from sill complexes of Holes 857C and 857D. Open circles and squares and solid circles and squares represent sediments and igneous rocks, respectively, from Holes 857C and 857D.

Table 11. Inclination of stable component (I), intensity of natural remanent magnetization (J_0), median destructive field (MDF), magnetic susceptibility (χ_0), and Q-ratio for discrete samples from Hole 857D.

Core, section, interval (cm)	Depth (mbsf)	Type	I (°)	J_0 (mA/m)	MDF (mT)	χ_0 ($\times 10^{-4}$ SI)	Q-ratio	Lithology
139-857D-								
1R-1, 125–127	582.75	A	Unstable	1.7	9	2.3	0.17	Silty claystone
2R-1, 73–75	590.33	B	53	2.8	—	6.1	0.10	Porphyritic diabase
3R-1, 130–132	600.60	C	Positive	6.0	23	5.3	0.25	Diabase
3R-2, 67–69	601.44	C	Positive	23	22	5.7	0.92	Diabase
3R-2, 89–91	601.66	D	Unstable	15	ThD	4.6	0.75	Diabase
4R-1, 88–90	609.78	A	Unstable	7.9	14	5.1	0.35	Hydrothermal breccias
9R-1, 32–34	657.22	C	Positive	102	16	10.1	2.26	Fine-grained diabase
11R-1, 47–49	676.67	A	Unstable	0.58	25	3.1	0.042	Silty claystone
12R-1, 31–33	686.21	A(C)	Positive	0.21	15	2.7	0.018	Fine-grained diabase
14R-1, 18–20	705.28	B	63	3.4	34	5.0	0.15	Clayey siltstone
16R-1, 75–77	725.25	A	Unstable	0.73	11	2.1	0.078	Siltstone
17R-1, 122–124	735.12	A	Unstable	0.29	9	3.1	0.021	Siltstone
18R-1, 59–61	744.19	B	56	7.3	78	6.0	0.27	Diabase
21R-1, 65–67	772.85	C	Positive	25	19	6.1	0.91	Medium-grained diabase
22R-1, 89–91	782.69	C	Positive	27	13	6.7	0.90	Fine-grained diabase
24R-2, 32–34	803.02	C	Positive	40	9	7.1	1.25	Medium-grained diabase
26R-1, 10–12	830.40	C	Not oriented	24	11	5.5	0.99	Medium-grained diabase
28R-1, 33–35	839.23	B	56	2.1	60	1.6	0.29	Siltstone
31R-1, 27–29	868.77	D	Not oriented	0.62	51	2.1	1.08	Siltstone
35R-1, 70–72	907.90	C	Positive	46	4	9.5	0.066	Altered diabase

Notes: Type classification is based on demagnetization characteristics: A = intensity following the maximum demagnetization level was insufficient for the spinner magnetometer, B = separated two components, C = mixed two components, and D = unstable. Sample 139-857D-3R-2, 67–69 cm, was demagnetized by thermal demagnetization experiment.

characterized by chilled margins against the adjacent sedimentary units, and by a gradual change in grain size from fine-grained margins to coarse-grained interiors. The chilled margins are frequently extensively metamorphosed and the adjacent fine-grained rock is typically heavily veined and vesicular.

Igneous rock was first encountered in Core 139-857C-59R (Unit 1), the top of which is fine-grained diabase. The rock changes to very coarse-grained microgabbro in Sections 139-857C-59R-2 and -59R-3. The grain size systematically decreases in Section 139-857C-59R-4, although no chill or sediments were observed in this core. The top of Core 139-857C-60R (Unit 2) contains a chilled margin and fine-grained diabase which coarsens conspicuously in the lower half of Section 139-857C-60R-1. The upper 20 cm of Section 139-857C-60R-2 systematically decreases in grain size to a well-preserved basal contact with sediment at 25 cm. Diabase is again present in interval 139-857C-60R-2, 49–142 cm (Unit 3), mostly as small unoriented pieces, which include some very coarse-grained samples. Phyric diabase continues to Section 139-857C-61R-1, 100 cm (Unit 4), where there is a sharp contact with sediment. The top of Section 139-857C-61R-2 is a fine-grained contact to a phyric diabase, which comprises the remainder of Core 139-857-61R (Unit 5).

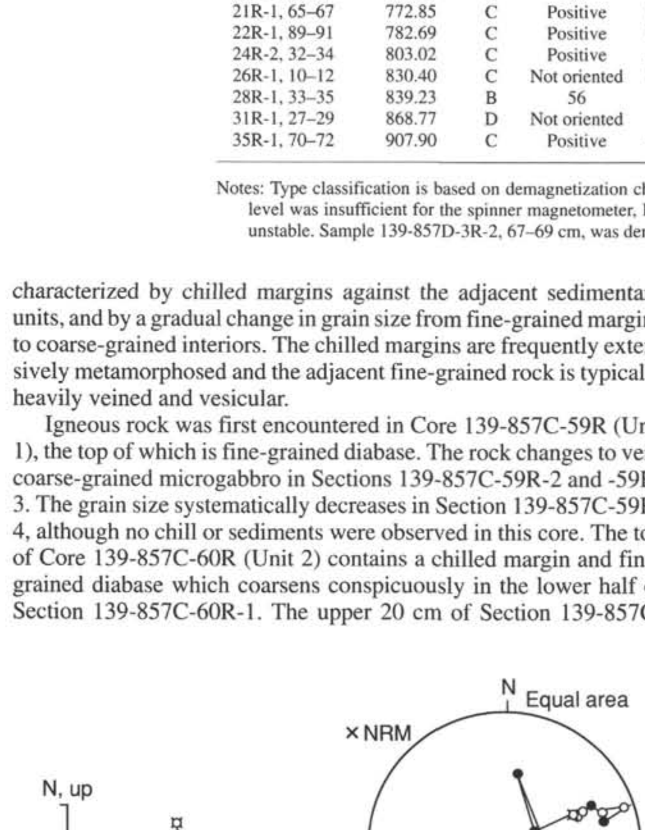

Figure 25. Zijderveld plot (left), equal-area projection (right), and intensity decay plot (lower right) of progressive thermal demagnetization (0 to 600 mT) for igneous rock Sample 139-857D-3R-2, 89–91 cm. Scale = 3.00 mA/m per division.

Core 139-857C-62R is composed of coarse-grained diabase to microgabbro with macroscopically conspicuous laths of ilmenite and no contacts with sediment or reduction in grain size (Unit 6). The top of Core 139-857C-63R, however, is metamorphosed sediment with a diabase contact within a gravel horizon composed of mixed sediment and vesicular igneous fragments. The remainder of Core 139-857C-63R is poikilitic microgabbro with ilmenite laths (Unit 7). Core 139-857C-64R is similarly coarse-grained diabase to microgabbro (Unit 8) with a slight decrease in grain size at the bottom of Section 139-857C-64R-2.

Fine-grained basalt is found as a few centimeter-sized fragments in gravel in the upper 5 cm of Section 139-857C-65R-1 (Unit 9), in contact with a sedimentary horizon. Sedimentary rocks also comprise the upper 24 cm of Core 139-857C-66R. A baked sediment contact above a highly altered basaltic horizon was found in the remainder of Section 139-857C-66R-1. This basaltic horizon (Unit 10) is unique in that it is a vertical contact between a basaltic intrusion and sediment. The basaltic rock of this unit is almost totally replaced by magnesian chlorite, yet the texture of the quench margin and the variolitic zone are recognizable (Fig. 52). The vertical orientation of the contact suggests that this is either a late cross-cutting dike or the toe of a sill. It contains olivine and plagioclase phenocrysts, most of which are altered. A similar metabasalt fragment is present at the top of Core 139-857C-67R above a sedimentary horizon.

Eighteen centimeters of plagioclase phyric diabase comprise the bottom of Core 139-857C-67R below the sedimentary horizon (Unit 11). Core 139-857C-68R (Unit 12) is composed of coarse-grained poikilitic diabase unbroken by any chilled contacts. Chlorite-rich, fine-grained material is present in some pieces, as well as sharp changes in color due to variable replacement of the matrix by chlorite. These variations likely reflect alteration fronts rather than variations

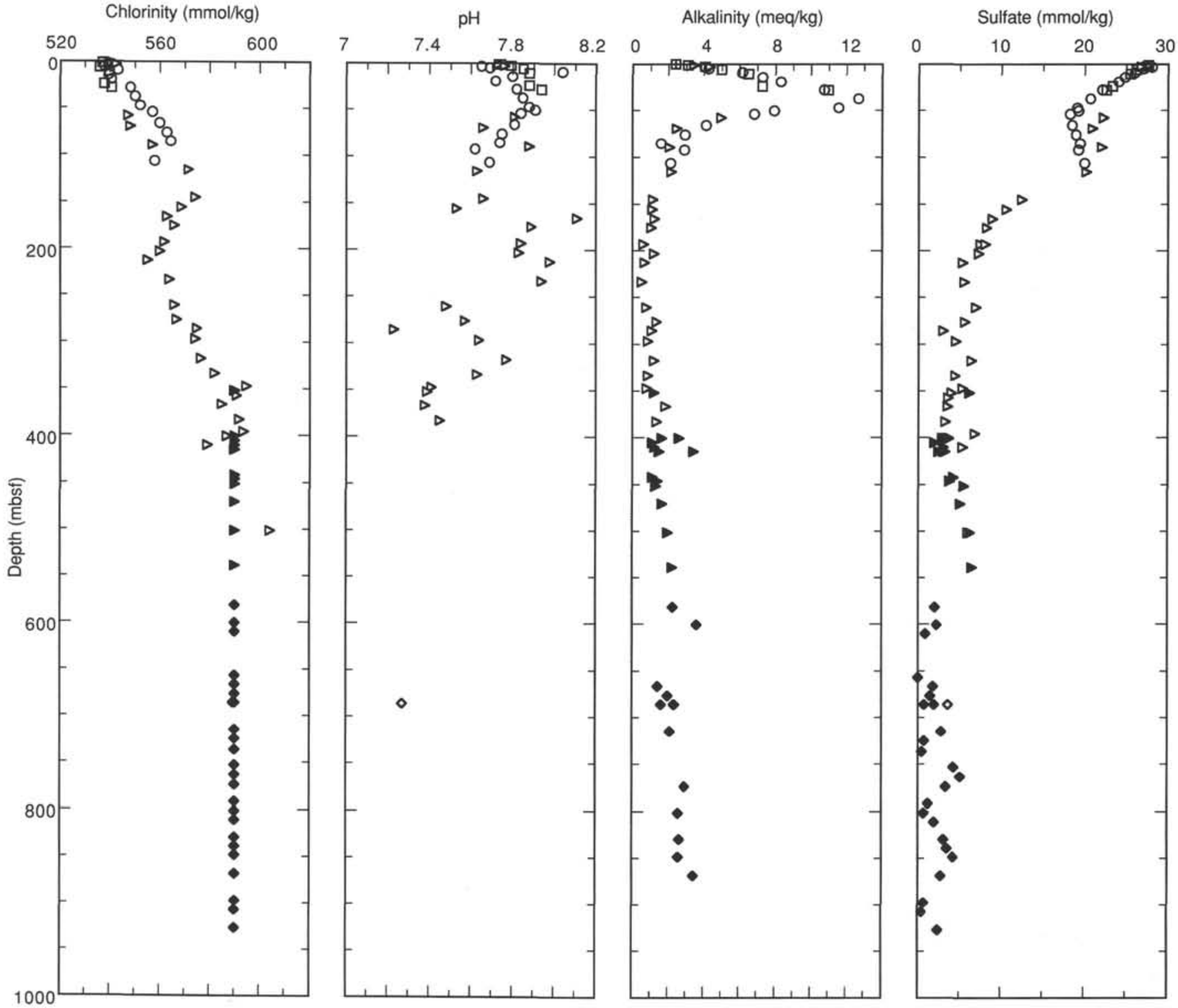

Figure 26. Composition of pore water from sediment and diabase at Site 857. The plus inside a square at 0 mbsf denotes bottom seawater. GRIND samples have been adjusted to a chlorinity of 590 mmol/kg. Samples denoted by open circles (Hole 857A), open squares (Hole 857B), open triangles (Hole 857C), and open diamonds (Hole 857D). GRIND samples denoted by solid triangles (Hole 857C) and solid diamonds (Hole 857D).

in the primary lithology, although this latter possibility could not be completely ruled out. The number of cooling units identified thus far are a minimum; almost every sill contained rubble or veined breccia layers that could indicate a missing section. A resistivity log from this hole (Fig. 52; "Downhole Logging" section, this chapter) reveals conspicuous resistivity highs associated with the sills and resistivity lows associated with sediment. Comparison between the resistivity log and the recovered basalt is quite good and suggests that the sill complexes are well represented in the recovered core (Fig. 53).

Hole 857D

In Hole 857D, mafic sills and interlayered sediment were cored between 581.1 and 936.2 mbsf (Fig. 51). In this hole, recovery of the sills from contact to interior was less complete than in Hole 857C. The average thickness of the assigned units is greater for Hole 857D than for Hole 857C, although the individual subunits are thinner. Each unit or subunit is bounded by chilled margins or sedimentary horizons. Subunits share a common lithology, although they may represent different cooling units. Very coarse-grained horizons are fewer in number than were recovered in Hole 857C, once again suggesting thinner, more numerous cooling units, although the results from downhole logging indicate two thick units between 740 and 840 mbsf. In addition, several units are composed of only a few pieces of rubble within a mostly sedimentary interval. It is not known whether these isolated pieces represent low recovery of an igneous unit, or pieces imported from shallower in the hole during drilling; they are all included as separate units (Table 23).

The top 110 cm of Section 139-857D-1R-1 (Unit 13) is a fine-grained, leucocratic diabase, which terminates with a chilled contact against sediments. Unit 14 is a fine-grained, plagioclase-phyric diabase with a clear upper contact with sediment at Section 139-857D-1R-2, 65 cm. This unit coarsens slightly in grain size within Section 139-857D-2R-1. A few pieces of sedimentary rubble and a chilled contact at Section 857D-2R-1, 47 cm, separate Subunits 14A and 14B, which are lithologically identical. This fine- to medium-grained pla-

Table 12. Composition of pore water from sediment and one sample of metadiabase from Site 857.

Sample[a]	Core, section, interval (cm)	Depth (mbsf)	Volume (mL)	Squeeze pressure (psi)	Salinity[b] (‰)	pH	Alkalinity (meq/kg)	Chlorinity (mmol/kg)	Sulfate (mmol/kg)	Na[c] (mmol/kg)	K (mmol/kg)	Mg[d] (mmol/kg)	Ca[d] (mmol/kg)	Si (µmol/kg)	NH_4 (µmol/kg)	Phosphate (µmol/kg)
Surface seawater (9 August 1991)								497.6	25.73	426.5	9.5	48.25	9.36	0	0	0.0
Bottom seawater (collected by *Alvin*, 6 August 91)								540.2	27.73	461.1	10.5	52.95	10.24	183	0	2.5
	139-857A-															
IW-1	1H-1, 144–150	3.37	50	5,000	35.5	7.65	4.049	539.4	28.10	466.7	12.0	50.38	9.96	480	190	12.7
IW-2	1H-2, 144–150	4.87	50	5,000	34.5	7.69	4.273	537.8	27.11	463.4	10.2	51.09	10.09	534	283	18.0
IW-3	1H-5, 144–150	9.37	15	10,000	34.0	8.04	6.167	543.2	26.06	467.9	11.7	50.44	10.22	626	551	30.4
IW-4	2H-2, 140–150	14.35	50	5,000	35.5	7.80	7.302	539.7	24.91	462.8	10.5	51.08	10.31	636	673	21.8
IW-5	2H-5, 140–150	18.85	50	8,000	35.5	7.72	8.356	540.6	24.12	464.0	9.5	51.22	10.28	732	698	18.6
PO-6	3P-1, 0–100	21.40	800	—	35.0	7.84	2.080	504.6	25.56	431.5	9.0	49.32	9.31	3	<10	0.0
IW-7	4H-4, 140–150	27.85	50	5,000	35.5	7.82	10.772	548.4	22.17	471.1	7.8	51.54	10.28	823	912	21.9
IW-8	5H-4, 140–150	37.35	50	7,000	35.5	7.85	12.700	550.3	20.73	472.8	8.1	51.10	10.19	986	937	17.8
IW-9	6H-4, 140–150	46.85	50	15,000	35.5	7.88	11.577	552.3	19.12	470.3	8.0	50.99	10.40	568	956	4.3
BC-10	7I-1, 74–97	50.40	10	—		7.91	7.976	612.1	19.31	532.9	10.7	47.91	9.66	504		1.9
[e]BO-10	7I-1, 74–97		110	—				285.7	25.16		10.7	54.66	11.49	341		0.0
IW-11	7H-2, 140–150	53.35	50	20,000		7.84	6.837	557.1	18.27	472.1	6.8	50.18	10.16	507	941	0.5
IW-12	8H-4, 140–150	65.85	50	12,000		7.81	4.126	560.0	18.50	473.2	5.7	44.66	15.91	426	1024	0.6
IW-13	9H-4, 140–150	75.35	47	20,000	35.5	7.75	2.966	562.9	18.98	474.1	5.0	43.51	18.31	370	1029	0.0
IW-14	10H-4, 140–150	84.85	30	20,000	36.0	7.74	1.623	564.5	19.48	474.7	4.0	41.23	21.44	248	1049	0.0
BC-15	12I-1, 74–97	91.90	10	—		7.62	2.912	587.9	19.31	512.6	4.7	32.75	22.64	623	1337	0.1
[e]BO-15	12I-1, 74–97		300	—		7.72	3.573	453.2	20.41	520.1	6.4	35.83	17.08	594		0.0
IW-16	13R-3, 140–150	105.95	22	20,000	36.0	7.69	2.139	558.0	20.05	474.6	3.0	34.67	26.09	322	1063	0.0
	139-857B-															
IW-1	1H-1, 144–150	1.47	50	10,000	35.5	7.74	3.081	536.9	27.62	461.8	12.2	50.69	9.85	496	78	10.6
IW-2	1H-2, 144–150	2.97	50	10,000	35.8	7.79	4.039	539.7	27.33	465.8	12.0	50.29	9.94	482	185	12.4
IW-3	2H-2, 140–150	6.35	50	6,000	36.0	7.85	4.980	535.9	26.23	462.3	10.7	49.97	9.97	540	405	21.4
IW-4	2H-5, 140–150	10.85	50	6,000	36.0	7.88	6.502	539.7	25.50	461.9	11.0	51.54	10.28	737	610	38.0
IW-5	3H-2, 140–150	23.95	50	5,000	35.0	7.88	7.273	537.8	23.35	458.1	10.2	51.15	10.14	722	844	26.1
IW-6	3H-5, 140–150	28.45	50	5,000	35.5	7.94	10.989	540.7	22.62	464.0	10.0	50.75	10.22	883	922	20.6
	139-857C-															
IW-1	1R-1, 144–150	1.47	36	10,000	35.5	7.73	3.428	540.7	27.70	466.5	11.5	50.83	9.85	452	98	6.9
IW-2	1R-2, 144–150	2.97	50	10,000	35.5	7.76	4.320	542.6	26.85	467.7	10.2	51.12	10.09	544	288	24.6
IW-3	2R-1, 140–150	57.95	50	12,000	35.0	7.81	4.969	547.4	22.31	465.3	6.7	46.12	16.05	371	732	0.1
IW-4	3R-2, 140–150	69.45	44		35.5	7.66	2.493	548.4	20.95	460.1	5.1	43.21	20.22	332	766	0.0
IW-5	6R-2, 140–150	89.15	40	25,000	36.0	7.88	2.074	557.1	22.08	465.4	4.8	36.90	29.23	224	883	0.0
IW-6	9R-1, 109–114	115.62	18	25,000	36.0	7.63	2.179	571.5	20.22	480.1	4.2	20.39	43.95	374	1185	0.5
IW-7	12R-2, 0–10	145.05	21	26,000	36.0	7.66	1.153	574.4	12.51	471.8	3.0	11.40	50.97	278	1039	0.0
IW-8	13R-2, 140–150	156.05	28	27,000	35.0	7.53	1.107	568.7	10.59	471.5	4.5	9.09	47.79	285	1190	0.0
IW-9	14R-3, 0–10	165.85	17	28,000	35.0	8.11	1.261	562.9	8.95	443.8	6.0	6.84	58.49	359	1566	0.9
IW-10	15R-3, 0–10	175.55	27	22,000		7.89	1.064	565.8	8.25	475.5	6.5	4.10	45.87	282	1385	0.1
IW-11a	17R-1, 135–150	193.33	22	25,000	35.0			561.9	7.48	(457.9)	7.2	2.93	52.69	239	1551	0.1
IW-11b	17R-1, 135–150	193.33	20	25,000	35.0	7.84	0.621	561.9	8.10	458.6	7.7	2.83	52.60	229	1571	0.0
IW-12	18R-2, 0–15	203.18	30	25,000	35.5	7.83	1.218	560.0	7.31	448.8	7.2	3.51	55.62	260	1512	0.1
IW-13	19R-2, 0–15	212.88	40	25,000	35.5	7.98	0.677	555.2	5.37	427.4	8.1	3.12	61.55	284	1707	0.0
IW-14	21R-2, 135–150	233.53	24	25,000	34.5	7.94	0.537	563.8	5.53	424.5	11.0	5.27	63.81	316	1668	
IW-15	24R-2, 0–10	260.75	13	27,000	36.0	7.48	0.774	565.8	6.95	411.4	14.6	5.95	70.34	241	1805	0.0
IW-16	26R-1, 135–150	275.93	13	27,000	35.5	7.57	1.354	566.7	5.59	405.6	13.0	7.61	71.78	375	1834	
IW-17	27R-1, 135–150	285.53	6	27,000	37.0	7.23	1.093	574.9	3.05	389.0	14.8	4.00	84.18	307	1946	
IW-18	28R-3, 0–15	296.88	20	30,000	36.0	7.64	0.874	574.4	4.55	388.5	15.8	5.95	83.27	325	1620	0.0

Table 12 (continued).

Sample[a]	Core, section, interval (cm)	Depth (mbsf)	Volume (mL)	Squeeze pressure (psi)	Salinity[b] (‰)	pH	Alkalinity (meq/kg)	Chlorinity (mmol/kg)	Sulfate (mmol/kg)	Na[c] (mmol/kg)	K (mmol/kg)	Mg[d] (mmol/kg)	Ca[d] (mmol/kg)	Si (μmol/kg)	NH_4 (μmol/kg)	Phosphate (μmol/kg)
IW-19	30R-3, 134–150	317.52	9	33,000	36.5	7.77	1.205	576.4	6.44	395.5	16.5	10.44	78.07		1444	
IW-20	33R-1, 135–150	333.83	6	37,000	37.0	7.63	0.875	582.1	4.46	387.2	18.4	7.61	84.78	286	1600	0.1
IW-21	36R-2, 3–18	347.71	7	38,000	36.0	7.41	0.812	594.7	5.34	399.9	15.8	8.10	86.44		1376	
IW-22	37R-1, 140–150	352.25	5	28,000		7.39	0.440	589.9	4.04	394.1	18.5	7.32	85.57			
IW-23	38R-2, 0–15	357.38		40,000				590.8	3.64	(397.3)	18.4	6.15	85.56			
IW-24	40R-1, 121–136	366.69	16	37,000	36.0	7.38	1.885	585.0	3.53	396.9	22.9	6.05	80.09	673	1951	0.6
IW-25	42R-3, 0–15	382.78	5	38,000		7.45	1.380	591.8	3.28	401.7	20.8	6.05	81.76	348	1600	
IW-26	45R-2, 0–15	395.88	1	37,000				593.7	6.83	(417.3)	19.5	11.02	74.74			
IW-27	46R-2, 0–15	400.58	1	40,000				587.0	3.73	(390.7)	20.1	8.20	84.11			
IW-28	48R-1, 132–147	410.10	0.5	40,000				579.3	5.34	(405.5)	18.3	10.54	72.29		1478	
IW-29	49R-1, 135–150	415.13	2.5	39,000				589.9	2.99	(402.0)	22.7	6.15	79.90	347		
[f]IW-30	62R-1, 142–150	501.46	3.0					604.3	6.01	(348.5)	17.0	8.59	117.31			
	139-857D-															
IW-1	12R-1, 16–20	686.08	1.2	40,000		7.27	2.367	589.5	3.64	355.0	12.0	13.81	102.25	160		

Note: Sample 139-857C-62R-1, 142–150 cm, is a highly altered metadiabase. All other samples are sediment.
[a]IW = squeezed interstitial water sample; BC = interstitial water sample taken *in situ* with the WSTP; BO = overflow aliquot from the WSTP (diluted with distilled water); PO = overflow aliquot from pressure core sampler.
[b]By refractive index.
[c]Concentrations of Na in parentheses were calculated assuming an alkalinity of 1 meq/kg.
[d]Ca and Mg have been corrected using the equations of Gieskes and Peretsman (1986).
[e]Concentrations in mmol/kg measured in overflow aliquots have been adjusted to the chlorinity of the prime aliquot.
[f]Sample is highly altered metadiabase. All other samples are sediment.

gioclase-phyric diabase extends to the bottom of Core 139-857D-3R. Unit 15 in Core 139-857D-4R is a heavily veined metagabbro that is bounded by sedimentary horizons, but no chilled contacts were recovered. The large grain size suggests that this interval is from the center of a large sill.

The lithology of the igneous intervals in Cores 139-857-7R to -9R is a fine- to medium-grained sparsely phyric diabase. This interval comprises Subunits 16A–C, which are separated by a chilled margin (Section 139-857D-8R-1, 0 cm) and a small piece of sediment rubble (Section 139-857D-8R-1, 66–71 cm), respectively. Of interest is a partially lithified sedimentary inclusion in the diabase at Section 139-857D-8R-1, 34 cm (Fig. 54). These units may comprise a single intrusion.

The top of Subunit 17A is a distinctive chilled and massively altered margin at Section 139-857D-12R-1, 21 cm, that continuously grades into plagioclase-phyric fine to medium-grained diabase. This same rock type is found in Subunit 17B, composed of a single piece of rubble within sedimentary horizons. Short intervals of fine-grained metadiabase and metabasalt within Sections 139-857D-15R-1 and -16R-2 comprise Subunits 18A and 18B, respectively.

The top of Unit 19 (Section 139-857D-17R-3) is distinctive in the abundance of large sulfide-filled vesicles or vugs within a leucocratic, fine-grained diabase. This is the thickest unit in this hole, extending through Core 139-857D-20R, which contains melanocratic microgabbro and gabbro. These coarse-grained rocks must be from the center of a thick intrusive body.

Igneous rock recovered from Sections 139-857D-21R-1 to -24R-1 (Subunits 20A–D) are leucocratic fine- to medium-grained diabase with local concentrations of plagioclase phenocrysts. Short sedimentary intervals separate the subunits; otherwise they appear to be lithologically identical. These subunits, taken together, show a gradual increase in grain size and alternation of melanocratic and leucocratic mineralogy, characteristics which suggest local fractionation and layering.

Unit 21 extends from the bottom of Core 139-857D-24R to the bottom of Core 139-857D-26R. Except for a fine-grained contact, this unit is dominantly medium-grained, leucocratic, plagioclase-phyric diabase. It is notable in the abundance of round or equant vesicles, vugs or cavities filled with chlorite, epidote, and sulfide. Many of these vesicles are zoned. The base of this unit is melanocratic.

An extensively metamorphosed fine-grained contact zone for Unit 22 is contained within Section 139-857D-27R-1. This unit is composed of veined and mineralized basaltic rubble. Some pieces are very coarse-grained and presumably come from highly altered centers of large (fractured?) sills. Section 139-857D-29R-1 (Subunit 23A) is a highly epidotized diabase that systematically increases in grain size from top to bottom. It is associated with intervals of epidote-rich sandstone. Cores 139-857D-30R to -32R (Subunits 23B–G) are similar epidotized and chloritized fine-grained diabase, with intervening sediment and bleached metabasalt contact zones separating subunits. The pieces are small and discontinuous and may be a series of thin, highly fractured sills.

A conspicuous quenched margin for Unit 24 was observed in Section 139-857D-33R-1, with a bleached contact zone and inner vesicle-rich zone that grades rapidly into a medium-grained diabase. Subunit 25A is a single piece of variolitic basalt. Subunits 25B and 25C are similarly locally variolitic, fine-grained diabase: they increase in grain size and becomes more mafic toward their bases. Unit 26 is a small, single piece of epidotized diabase within a sedimentary interval.

Petrography

The igneous rocks recovered at this site vary from fine-grained basalt at sill margins to coarse-grained, isotropic gabbro in the sill interiors. Superimposed upon this textural variation is variable alteration, which will be discussed in the next section. The two types of petrographic variation are not independent, however. Marginal rocks

Table 13. Composition of water extracted from lithified sediment and diabase or gabbro from Site 857 using the GRIND technique.

Sample	Core, section, interval (cm)	Depth (mbsf)	Volume (mL)	Squeeze pressure (psi)	pH	Alkalinity (meq/kg)	Chlorinity (mmol/kg)	Sulfate (mmol/kg)	Na[a] (mmol/kg)	K (mmol/kg)	Mg[b] (mmol/kg)
	139-857C-										
G-5	37R-1, 140–150	352.25	5.5	25000	7.61	0.590	284.3	2.96	188.7	15.4	7.18
G-2	46R-2, 0–15	400.58	8	5000	7.31	0.478	170.9	0.83	120.6	6.8	4.42
G-1	46R-2, 0–15	400.58	7.5	2000	7.91	0.581	131.3	0.78	95.3	5.0	1.77
G-3	46R-2, 0–15	400.58	3	10000			273.2	1.48	189.8	10.1	5.92
G-7	47R-1, 135–150	405.43	3.9	30000	7.52	0.526	273.2	0.90	184.6	10.5	5.10
G-4	48R-1, 132–147	410.10	4.2	25000	7.71	0.557	266.0	1.38	181.2	12.0	5.44
G-6	49R-1, 135–150	415.13	4.2	25000	7.73	0.755	294.5	1.20	201.8	11.7	6.20
G-21	49R-1, 135–150	415.13	5.5	15000	7.63	1.483	258.7	7.55	176.9	12.0	8.07
G-8	55R-1, 36–38	442.37	5.2	12000	7.80	0.556	290.6	2.08	205.9	9.7	9.30
G-9	56R-1, 10–14	446.62	4.5	20000	7.69	0.640	268.4	1.70	188.8	9.1	7.02
G-10	57R-1, 0–20	451.80	4.2	20000	7.82	0.622	281.9	2.62	203.0	9.3	8.93
G-11	58R-CC, 0–22	471.00	4.6	30000	7.72	0.786	275.2	2.37	194.8	9.4	8.73
G-19	62R-1, 142–150	501.46	5	25000	7.34	7.988	196.2	2.08	142.1	6.0	3.48
G-12	66R-1, 4–9	538.87	4.5	30000	7.90	0.952	251.1	2.78	187.1	6.2	9.16
139-857D-											
G-1	1R-2, 5–12	583.09	3	10000	7.29	0.830	216.1	0.75	156.2	5.2	7.84
[c]G-3	3R-2, 0–7	600.84	3	30000	7.42	0.607	99.1	0.38	73.9	2.0	2.14
G-2	4R-2, 68–72	611.10	2.5	25000			113.1	0.17	85.5	2.2	3.13
[c]G-4	9R-1, 33–36	657.25	2.5	35000			58.5	0.00	46.0	1.0	1.00
G-6	10R-1, 19–21	666.82	4	10000	7.33	0.584	238.4	0.74	173.1	6.2	7.12
G-9	11R-1, 20–23	676.42	3.5	30000	7.34	0.649	191.9	0.48	140.4	4.8	5.91
G-5	12R-1, 16–20	686.08	4	12000	7.26	0.631	160.1	0.52	118.3	4.3	3.13
G-7	12R-1, 16–20	686.08	4	15000	7.20	0.436	157.0	0.20	107.9	4.6	3.20
G-11	15R-1, 10–14	714.92	4	35000	7.34	0.679	187.7	0.89	139.3	5.0	5.87
G-8	16R-1, 8–11	724.60	3.5	25000			165.0	0.22	122.4	3.7	4.28
G-10	17R-2, 109–111	736.50	3	35000			141.5	0.12	109.5	2.8	3.68
[c]G-12	19R-1, 18–19	752.99	3	25000			56.6	0.41	46.9	1.6	0.53
[c]G-13	20R-1, 90–92	763.41	2.8	25000			40.3	0.35	34.0	1.2	0.24
G-14	21R-2, 30–34	774.02	3.5	15000	7.50	1.154	230.9	1.31	173.4	5.0	9.66
[c]G-15	23R-1, 10–11	791.61	2.5	35000			46.5	0.09	37.1	1.1	0.40
G-16	24R-1, 66–69	801.88	3	30000	7.26	0.644	146.3	0.16	109.3	3.3	4.72
[c]G-17	25R-1, 41–42	811.22	3	35000			44.6	0.15	35.9	0.9	0.61
G-18	27R-1, 28–32	829.90	3.5	15000	7.44	0.920	205.7	1.08	154.8	2.9	6.14
G-20	28R-1, 10–14	839.02	3	35000			116.0	0.69	88.4	3.6	2.28
G-22	29R-1, 4–8	848.46	4	25000	7.44	0.945	215.6	1.56	165.4	5.1	9.06
G-23	31R-1, 5–7	868.56	4.5	30000	7.28	1.171	201.4	0.95	156.9		6.36
G-24	34R-1, 5–7	897.56	3	35000			138.8	0.16	112.2		3.59
[c]G-25	35R-1, 5–10	907.28	3	35000			64.1	0.05	52.2		0.89
G-26	37R-1, 36–37	926.87	3.2	35000			187.1	0.76	148.9		5.01

Note: Concentrations are those measured on the diluted samples.
[a]In calculating Na, alkalinity was assumed to be 0.5 meq/kg if not measured.
[b]Ca and Mg have been corrected using the equations of Gieskes and Peretsman (1986).
[c]Diabase or gabbro. All other samples are indurated sediment.

frequently suffered massive metamorphic recrystallization, obscuring original texture and mineralogy. Sill interiors frequently appear fresh except for complete replacement of mesostasis by fine-grained secondary minerals. Mafic phenocrysts are all replaced by chlorite, so their original identity is inferred from shape and association only. The only primary variation in the mineralogy of the sills is the presence of plagioclase and rare mafic phenocrysts whose identity is thus ambiguous. The most interesting petrographic features of both holes follow, with no attempt to exhaustively describe each unit.

Hole 857C

Several samples selected for petrographic study from Hole 857C were phyric, with examples from Cores 139-857C-60R, -61R, and -68R (Table 24). Plagioclase is the primary phenocryst phase and is locally present in abundances up to 10% (Sample 139-857C-60R-1, Piece 1, 13–15 cm), but is more commonly present in abundances of 1%–3%. The smaller (<1 mm) plagioclase phenocrysts are typically elongate tabular, while the larger plagioclase phenocrysts are columnar. The latter type frequently are found as broken glomerocrystic aggregates with concentric extinction and sodic rims. Plagioclase phenocrysts are most conspicuous in the fine-grained marginal rocks, as the distinction between phenocryst and groundmass diminishes with increasing grain size. No systematic difference in chemistry was observed between phenocrysts and groundmass in the few samples where they could be compared. Plagioclase compositions for both populations average An_{60}, with variation from An_{50}–An_{70} and with plagioclase megacrysts as calcic as An_{72}. One sample (139-857C-63R-1, Piece 4, 51–53 cm) contains sparse, ovoid, chloritized pseudomorphs after a mafic mineral, which is postulated to have been clinopyroxene or olivine.

Groundmass minerals always include plagioclase, regardless of the grain size. The groundmass in the fine-grained marginal rocks is solely composed of plagioclase microlites and glassy (always altered) mesostasis. The mesostasis is typically spherulitic with secondary minerals mimicking the primary texture (e.g., Sample 139-857C-61R-1, Piece 8A, 97–100 cm). Such cryptocrystalline rocks were not present in great volumes, as the groundmass grain size was typically microcrystalline to microlitic in texture within 10 cm of a contact.

The groundmass texture varies systematically as a sill margin is approached. Just inside the altered, chilled margin, both lath-like plagioclase and spherulitic clinopyroxene are recognizable in the groundmass. The morphology of the plagioclase varies from needle-

Table 13 (continued).

Sample	Core, section, interval (cm)	Ca[b] (mmol/kg)	Si (μmol/kg)
	139-857C-		
G-5	37R-1, 140–150	36.19	167
G-2	46R-2, 0–15	18.42	133
G-1	46R-2, 0–15	14.83	133
G-3	46R-2, 0–15	32.47	170
G-7	47R-1, 135–150	35.16	163
G-4	48R-1, 132–147	32.61	153
G-6	49R-1, 135–150	35.86	175
G-21	49R-1, 135–150	35.11	178
G-8	55R-1, 36–38	30.54	84
G-9	56R-1, 10–14	30.29	100
G-10	57R-1, 0–20	28.80	100
G-11	58R-CC, 0–22	29.53	112
G-19	62R-1, 142–150	26.67	178
[c]G-12	66R-1, 4–9	23.04	123
139-857D-			
G-1	1R-2, 5–12	20.69	90
G-3	3R-2, 0–7	10.12	83
G-2	4R-2, 68–72	9.98	72
[c]G-4	9R-1, 33–36	5.00	76
G-6	10R-1, 19–21	23.42	82
G-9	11R-1, 20–23	18.20	83
G-5	12R-1, 16–20	16.46	96
G-7	12R-1, 16–20	19.44	80
G-11	15R-1, 10–14	17.09	98
G-8	16R-1, 8–11	15.62	82
G-10	17R-2, 109–111	11.28	71
[c]G-12	19R-1, 18–19	4.18	244
[c]G-13	20R-1, 90–92	2.90	278
G-14	21R-2, 30–34	18.48	59
[c]G-15	23R-1, 10–11	4.12	98
G-16	24R-1, 66–69	12.62	69
[c]G-17	25R-1, 41–42	3.70	126
G-18	27R-1, 28–32	19.39	98
G-20	28R-1, 10–14	10.64	190
G-22	29R-1, 4–8	15.52	76
G-23	31R-1, 5–7	17.45	68
G-24	34R-1, 5–7	10.10	62
[c]G-25	35R-1, 5–10	5.32	76
G-26	37R-1, 36–37	15.10	76

like microlites to small, euhedral, twinned laths. The clinopyroxene morphology varies from spherulitic (radial aggregates of thin prismatic crystals) to granular intergrowths with plagioclase. Some samples exhibit spectacular spherulitic texture in pyroxene, with length to width ratios greater than 5:1, and individual crystals several millimeters in length (Sample 139-857C-68R-2, Piece 1, 8–10 cm; Fig. 55). Oxide (presumably titanomagnetite) is present as small anhedral grains occupying interstitial areas or as small crystallites within mesostasis. Mesostasis with altered glass or cryptocrystalline minerals are present in all but the coarsest intervals. These are dominantly altered and are characterized by a fine-grained mesh of secondary minerals that forms a honeycomb texture through the mass of the rock. As the grain size increases, the quantity of mesostasis declines.

In the coarser grained intervals found in the center of the thicker sills, textures are heterogeneous and microgabbroic to gabbroic. The plagioclase crystals are broader in dimension, having a columnar shape, and typically contain concentric zonation (An_{50-70}). Small plagioclase crystals are present as inclusions in clinopyroxene oikocrysts. Clinopyroxene is anhedral and fills the space between euhedral plagioclase to form a poikilitic texture (Fig. 56). Euhedral laths of ilmenite (up to 1 mm long) and anhedral grains of magnetite are present in abundances up to 5%. In spite of these features, the texture is not cumulate. Both poikilitic and spherulitic textures can be found in a single thin section due to local variations in cooling. The textures are most similar to the "isotropic" gabbro found at high levels in ophiolites at the boundary between sheeted dikes and cumulates.

Hole 857D

Representative modal analyses from seven of the 26 samples selected for petrographic analyses are provided in Table 25. The textural variations described for Hole 857C are also observed in Hole 857D, with textural types varying from intersertal to poikilitic. A different texture was also observed in Hole 857D: a highly phyric fine- to medium-grained diabase with an intersertal to intergranular texture, typified by Sample 139-857D-3R-1, Piece 2B, 25–27 cm. This sample contains 25% large (1–2 mm) plagioclase phenocrysts observed as embayed, glomerocrystic aggregates (Fig. 57). These large crystals are broken, corroded, strongly zoned (An_{65-80}) and have sodic overgrowths (An_{40}), all characteristic of xenocrysts. In addition there are a few small square minerals tentatively identified as euhedral spinel. The phenocrysts or xenocrysts are contained in a fine-grained intersertal matrix of small plagioclase laths, spherulitic clinopyroxene, and up to 10% altered mesostasis.

Of the samples selected for petrographic description, all but one of the fine- to medium-grained rocks contain such large calcic plagioclase xenocrysts (up to An_{88}), mostly in abundances of 1%–5%. They are present even in samples that contain skeletal, microlitic, and lantern-shaped plagioclase (An_{65-70}) in the groundmass (Sample 139-857D-1R-2, Piece 11D, 81–82 cm). Two fine-grained samples have small crystals that may be chromian spinel. Glomerocrysts of clinopyroxene and plagioclase were observed in Sample 139-857D-9R-1, Piece 16, 88–90 cm. Two other fine-grained samples contain pseudomorphs of mafic phenocrysts that could have been olivine or clinopyroxene.

The second contrast between the textures observed in samples from Holes 857C and Hole 857D is the paucity of spherulitic clinopyroxene in the latter. In Hole 857D, fine-grained rocks contain spherulitic plagioclase with abundant mesostasis or granular clinopyroxene. Local poikilitic textures, with anhedral clinopyroxene enclosing plagioclase laths, are very common.

Alteration

The alteration observed in Holes 857C and 857D can be separated into three categories: (1) static replacement of phenocrysts and mesostasis material, (2) veins and associated wall-rock alteration, and (3) deposition of sulfide minerals. Clearly the paragenesis of the secondary minerals requires that the processes for all three categories overlap, and thus these divisions are solely for descriptive purposes. Generalizations about both holes are as follows. Fine-grained quenched sill margins exhibit intense hydrothermal recrystallization and probably metasomatism. Such margins are bleached to a pale gray and are almost completely replaced by pale magnesian chlorite (Fig. 58). Included microlites and phenocrysts are replaced, dominantly by green chlorite and epidote. The most abundant and largest vein networks cross-cut these highly altered margins and extend into the fresher rock slightly farther than the extent of the chill. Many of the veins exhibit complete zonation and some show "crack and fill" textures. Typical vein fillings include chlorite, sulfide minerals, quartz, zeolites (most notably wairakite) (Fig. 59), and epidote. The chill and interval immediately adjacent typically are vesicle-rich. The vesicles are almost uniformly filled, most frequently with chlorite but also with quartz, epidote, prehnite, smectite, or sulfide minerals.

The second most intensely metamorphosed intervals are the gabbroic to microgabbroic rocks from the sill centers. This alteration is best developed in Hole 857D. The least altered rocks are fine- to medium-grained diabase not associated with chilled margins. The alteration in these rocks is limited to replacement of the sparse amounts of mesostasis material. A summary of specific features of each hole is given here.

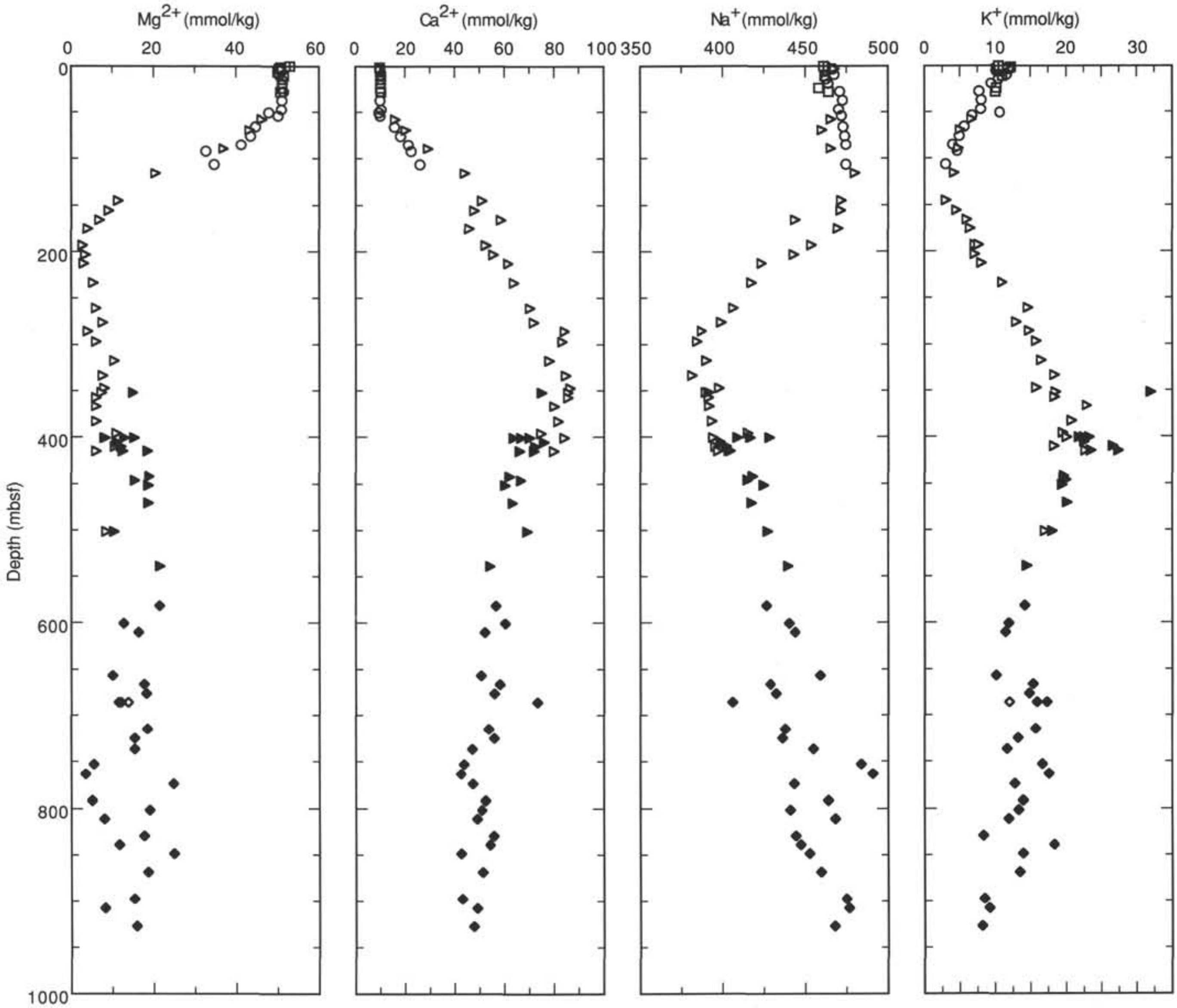

Figure 27. Composition of pore water from sediment and diabase at Site 857. The plus inside a square at 0 mbsf denotes bottom seawater. GRIND samples have been adjusted to a chlorinity of 590 mmol/kg. Samples denoted by open circles (Hole 857A), open squares (Hole 857B), open triangles (Hole 857C), and open diamonds (Hole 857D). GRIND samples denoted by solid triangles (Hole 857C) and solid diamonds (Hole 857D).

Hole 857C

Mesostasis in all samples studied from Hole 857C is completely altered to fine-grained meshes of chlorite and epidote. Fresh ilmenite laths and white skeletal plagioclase are morphologically preserved within the replacement minerals. These crystalline phases show little evidence of replacement. The replacement of the mesostasis produces a network of fine-grained alteration minerals throughout the bulk of the rock, and gives the rock a green color. A similar honeycomb of chlorite and epidote replacement is observed in the coarse-grained rocks. In this latter case, the plagioclase or clinopyroxene are likely being replaced by the secondary minerals. Truncated and embayed plagioclase crystals and rare pyroxene relicts within the secondary minerals support this model. The embayed plagioclase phenocryst typically have strong zonation and sodic rims (to An_{30}).

Euhedral pale epidote crystals can be identified as inclusions in larger plagioclase crystals. Smaller grains of epidote are associated with chlorite in plagioclase pseudomorphs. Epidote was present in small but conspicuous amounts (3%–5%) throughout Cores 139-857C-59R, -60R, -62R, and -68R. It was only observed in trace amounts or was not present in the samples from other cores. Chlorite is the dominant secondary mineral in this hole, and was present in every sample studied. Chlorite replaces mesostasis, plagioclase, and pyroxene. This static replacement was typically by pale green to brown magnesian chlorite. Green ferroan chlorite was observed to fill veins and vesicles and to be consistently associated with the appearance of sulfide. Other secondary minerals include small amounts (<2%) of blue-green actinolite present as stubby prismatic crystals replacing pyroxene. Actinolite is also occasionally present as tiny needles with chlorite in the altered mesostasis. Plagioclase pseudomorphs and some altered grains include a white albite. Trace amounts of sphene were observed associated with some grains of altered ilmenite.

Most of the veins observed in this hole are 1–3 mm wide and filled with chlorite. Larger veins are frequently zoned and contain a variety of minerals. A complex vein from the uppermost sill (Sample 139-

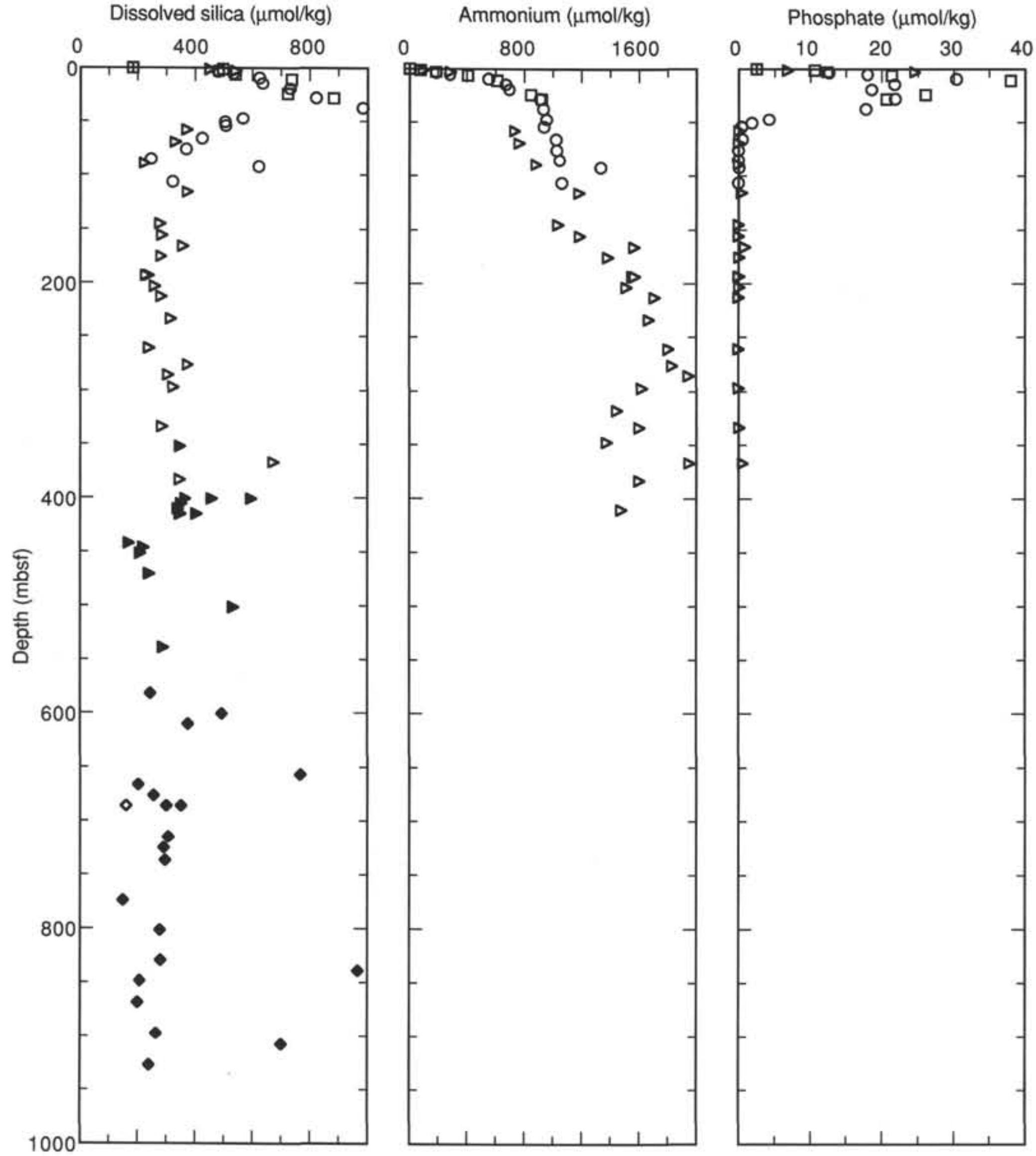

Figure 28. Composition of pore water from sediment and diabase at Site 857. The plus inside a square at 0 mbsf denotes bottom seawater. GRIND samples have been adjusted to a chlorinity of 590 mmol/kg. Samples denoted by open circles (Hole 857A), open squares (Hole 857B), open triangles (Hole 857C), and open diamonds (Hole 857D). GRIND samples denoted by solid triangles (Hole 857C) and solid diamonds (Hole 857D).

857C-59R-1, Piece 1B, 26–28 cm) contains euhedral sphalerite and comb-texture quartz in its center. Surrounding this is wairakite containing tiny epidote laths. The lining along the diabase wall rock contains disseminated pyrite, quartz, epidote, and chlorite. Epidote, chlorite, and sulfide are frequently associated in veins (Sample 139-857C-60R-1, Piece 1, 13–15 cm). Less common is the association seen in Sample 139-857C-64-2, Piece 7, 70–72 cm, in which a large vein contains sphalerite, chalcopyrite, wairakite, and euhedral quartz.

Sulfide was most frequently observed filling veins and healed microfractures. The thinnest cracks commonly contain pyrite. Pyrite is also a common vesicle filling and coats fracture surfaces (Fig. 60) Sulfide minerals disseminated within the matrix of the rock are ubiquitous in these rocks. Sulfide is found as small interstitial grains, "porphyroblasts" indiscriminately replacing mesostasis or crystals and ovoid aggregates. Although sulfide and chlorite are frequently associated, the presence of sulfide within the rock mass does not appear to be dependent on the extent of metamorphism. The textural relationships suggest that the metamorphism of the rock matrix and the formation of the disseminated sulfide may be decoupled processes.

Hole 857D

Within Hole 857D, both chlorite and epidote are consistently present, and they are typically in greater abundances than observed in Hole 857C. These minerals replace the same phases as in Hole 857C, plagioclase and mesostasis, and are the dominant vein minerals. White sodic rims and mottled extinction in the plagioclase phenocrysts suggests that these are partially replaced by albite. Prehnite appears in Core 139-857D-3R, both filling veins and replacing plagioclase. Green actinolitic hornblende and acicular actinolite are common replacements of clinopyroxene, especially in the upper half of the hole. An interesting texture is observed in Core 139-857D-18R, where poikilitic plagioclase and

Table 14. Composition of headspace gases for sediment from Holes 857A, 857B, and 857C.

Sample (cm)	Type[a]	Depth (mbsf)	Methane (ppm)	Ethane (ppm)	Propane (ppm)	Butane (ppm)	CO_2 (ppm)	C_1/C_2
139-857A-								
1H-3, 0–4	HS	4.90	3.0	0.0	0.0	0.0	2787	—
5H-2, 145–150	HS	34.35	7.0	0.0	0.0	0.0	1131	—
6H-6, 0–5	HS	48.40	9.3	0.0	0.0	0.0	921	—
7H-2, 0–5	HS	51.90	5.7	0.0	0.0	0.0	4298	—
8H-5, 0–5	HS	65.90	6.9	0.0	0.0	0.0	2878	—
9H-2, 0–5	HS	70.90	6.0	0.0	0.0	0.0	3215	—
10H-5, 0–4	HS	84.90	6.3	0.0	0.0	0.0	374	—
13X-4, 0–2	HS	106.00	4.1	0.0	0.0	0.0	306	—
9H-1, 131	V	70.70	9.1	0.0	0.0	0.0	4790	—
139-857B-								
1H-2, 0–5	HS	1.50	3.0	0.0	0.0	0.0	2241	—
2H-3, 0–5	HS	6.40	3.8	0.0	0.0	0.0	4907	—
3H-3, 0–5	HS	24.00	2.7	0.0	0.0	0.0	5014	—
139-857C-								
1R-2, 0–5	HS	1.50	2.7	0.0	0.0	0.0	1122	—
2R-2, 0–5	HS	58.00	6.3	0.0	0.0	0.0	2878	—
3R-3, 0–5	HS	69.50	8.9	0.0	0.0	0.0	1413	—
3R-CC	HS	82.00	7.2	0.0	0.0	0.0	4298	—
5R-1, 0–3	HS	82.10	7.0	0.0	0.0	0.0	1033	—
6R-2, 0–5	HS	87.70	11.2	0.0	0.0	0.0	2114	—
9R-1, 0–25	HS	114.50	28.3	0.0	0.0	0.0	956	—
10R-1, 79–84	HS	124.89	73.0	1.0	0.0	0.0	n.d.	73
11R-1, 145–150	HS	135.25	49.0	1.0	0.0	0.0	3637	49
12R-2, 0–5	HS	145.00	43.0	0.7	0.0	0.0	279	61
13R-3, 0–3	HS	156.10	65.0	1.1	0.0	0.0	n.d.	59
13R-3, 0–3	HS	156.10	51.0	1.1	0.0	0.0	2923	46
14R-CC	HS	172.40	61.0	1.0	0.0	0.0	667	61
15R-4, 0–2	HS	177.00	63.0	1.0	0.0	0.0	n.d.	63
16R-1, 0–2	HS	182.20	43.0	0.8	0.0	0.0	921	54
17R-2, 0–2	HS	193.40	139	1.3	0.0	0.0	8739	107
18R-2, 0–2	HS	203.10	352	2.5	0.5	0.0	6409	141
19R-1, 0–2	HS	211.30	125	1.6	0.5	0.0	6409	78
19R-1, 148–150	HS	212.78	354	3.0	0.5	0.0	2023	118
21R-2, 130–132	HS	233.40	762	8.9	5.1	0.0	267	86
22R-1, 149–150	HS	241.79	1,477	12.0	5.9	0.0	n.d.	123
23R-1, 68–71	HS	250.58	1,738	18.0	14.0	0.0	1687	97
24R-2, 15–20	HS	260.85	3,238	28.0	16.0	25.0	n.d.	116
25R-1, 0–5	HS	268.80	2,814	25.0	15.0	0.0	5733	113
26R-1, 15–17	HS	274.65	5,909	102	27.0	0.0	n.d.	58
27R-1, 131–132	HS	285.41	4,042	156	64.0	25.0	n.d.	26
27R-1, 138–140	HS	285.48	5,500	247	49.0	0.0	689	22
28R-3, 0–15	HS	296.80	4,850	109	35.0	0.0	238	44
29R-CC	HS	313.00	7,899	272	131	0.0	4255	29
30R-1, 5–10	HS	313.15	27,600	313	50.0	0.0	779	88
30R-4, 0–5	HS	317.60	21,200	236	37.0	0.0	588	90
31R-2, 0–1	HS	324.20	22,696	237	34.0	0.0	666	96
32R-2, 0–2	HS	329.10	34,440	329	40.0	0.0	n.d.	105
33R-1, 130–133	HS	333.70	31,110	311	42.0	19.0	3729	100
34R-3, 0–1	HS	339.50	24,730	232	35.0	26.0	780	107
35R-2, 0–1	HS	342.80	33,045	346	44.0	0.0	n.d.	96
36R-3, 0–1	HS	349.10	26,568	305	49.0	0.0	2950	87
37R-1, 145–150	HS	352.25	38,763	346	38.0	16.0	3252	112
39R-2, 148–150	HS	363.38	42,802	412	47.0	0.0	4762	104
40R-2, 0–5	HS	366.90	32,381	223	27.0	0.0	6815	145
41R-3, 0–5	HS	377.90	37,940	381	44.0	0.0	3735	100
42R-2, 0–2	HS	381.20	14,007	174	24.0	0.0	2674	81
43R-1, 141–142	HS	386.11	38,037	280	33.0	0.0	3195	136
44R-1, 0–3	HS	389.70	32,251	302	42.0	0.0	5729	107
45R-1, 148–150	HS	395.78	60,645	456	47.0	0.0	2524	133
46R-CC	HS	404.00	77,883	479	48.0	0.0	259	163
47R-1, 135–150	IW	405.35	233,266	1626	51.0	0.0	n.d.	143
46R-CC	HS	404.00	70,832	640	158	0.0	n.d.	111
47R-CC	HS	408.70	38,228	334	44.0	0.0	2909	114
47R-CC	HS	408.70	56,960	548	102	0.0	n.d.	104
48R-CC	HS	413.70	36,853	314	44.0	0.0	6855	117
48R-CC	HS	413.70	54,840	383	46.0	0.0	n.d.	143
49R-1, 135–150	IW	415.05	200,000	1735	128	0.0	n.d.	115
49R-CC	HS	418.30	35,695	289	38.0	0.0	1129	124
49R-CC	HS	418.30	32,658	385	52.0	0.0	n.d.	85
50R-CC	HS	423.40	35,233	278	34.0	0.0	3163	127
51R-1, 149–150	HS	424.89	31,468	485	149	0.0	3482	65

Table 14 (continued).

Sample (cm)	Type[a]	Depth (mbsf)	Methane (ppm)	Ethane (ppm)	Propane (ppm)	Butane (ppm)	CO_2 (ppm)	C_1/C_2
52R-2, 0–1	HS	429.30	30,231	319	40.0	0.0	3532	95
52R-CC	HS	432.80	37,821	494	130	0.0	n.d.	77
53R-CC	HS	437.00	32,838	226	26.0	0.0	3699	145
53R-CC	HS	437.00	41,628	434	50.0	0.0	n.d.	96
54R-CC	HS	442.00	37,711	384	49.0	0.0	2184	98
55R-CC	HS	446.50	6,460	192	67.0	0.0	4424	34
56R-CC	HS	451.70	16,327	164	24.0	0.0	3706	100
57R-1, 0–1	HS	461.50	8,197	166	38.0	0.0	4354	49
58R-CC	HS	471.10	31,874	283	34.0	0.0	5408	113
64R-2, 0–1	HS	529.10	8,907	96.0	22.0	0.0	1033	93
65R-1, 0–1	HS	538.80	10,449	221	62.0	0.0	4472	47
66R-1, 0–1	HS	548.38	9,654	107	21.0	0.0	596	90
67R-1, 0–1	HS	548.40	5,095	46.0	18.0	0.0	1856	111
68R-1, 0–1	HS	558.00	1,753	18.0	7.6	0.0	1108	97

Notes: Concentrations of gases are in parts per million (ppm) by volume. n.d. = not determined, — = not applicable.
[a]HS = headspace; V = vacutainer.

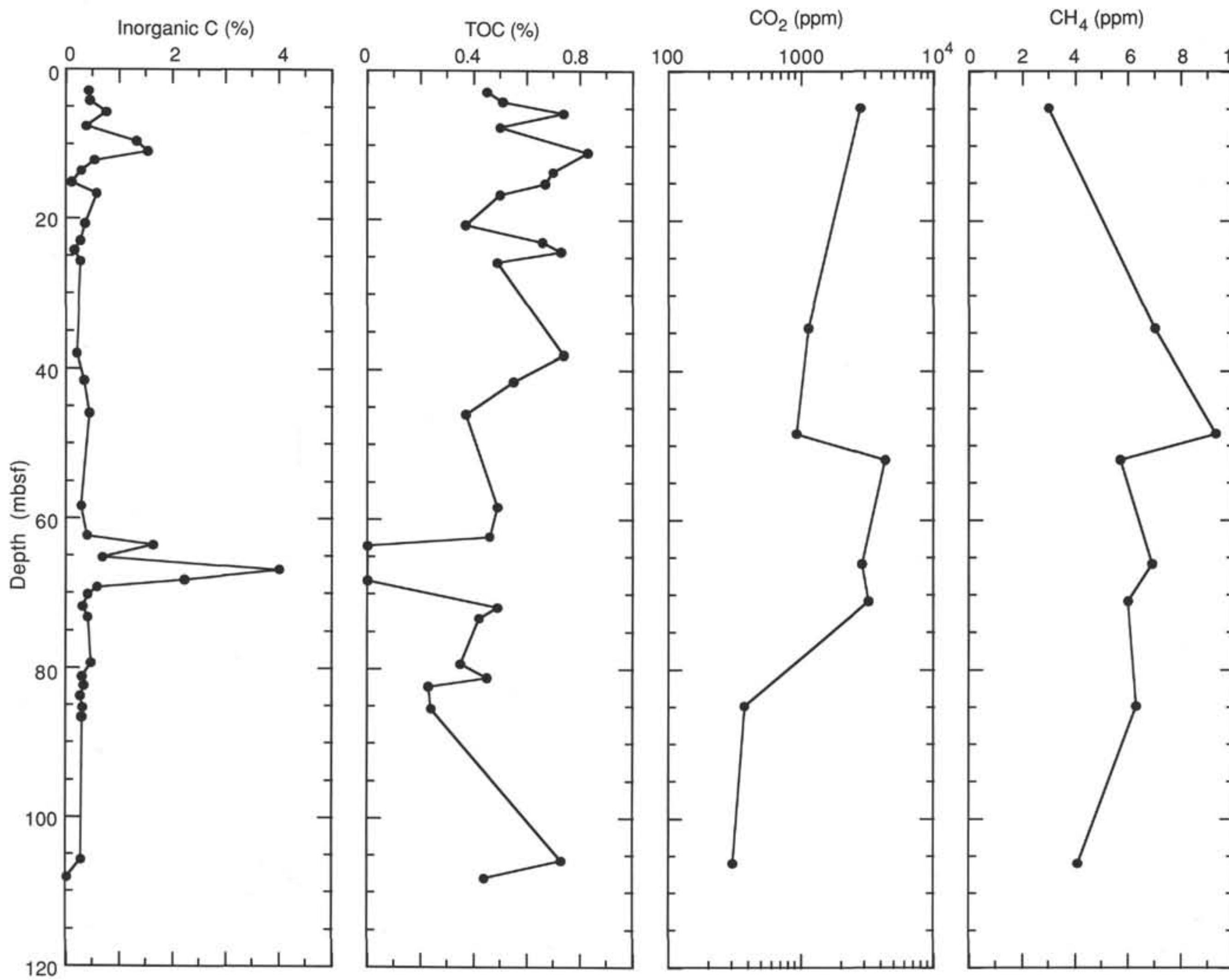

Figure 29. Concentrations of inorganic and total organic carbon, carbon dioxide, and methane vs. depth in Hole 857A.

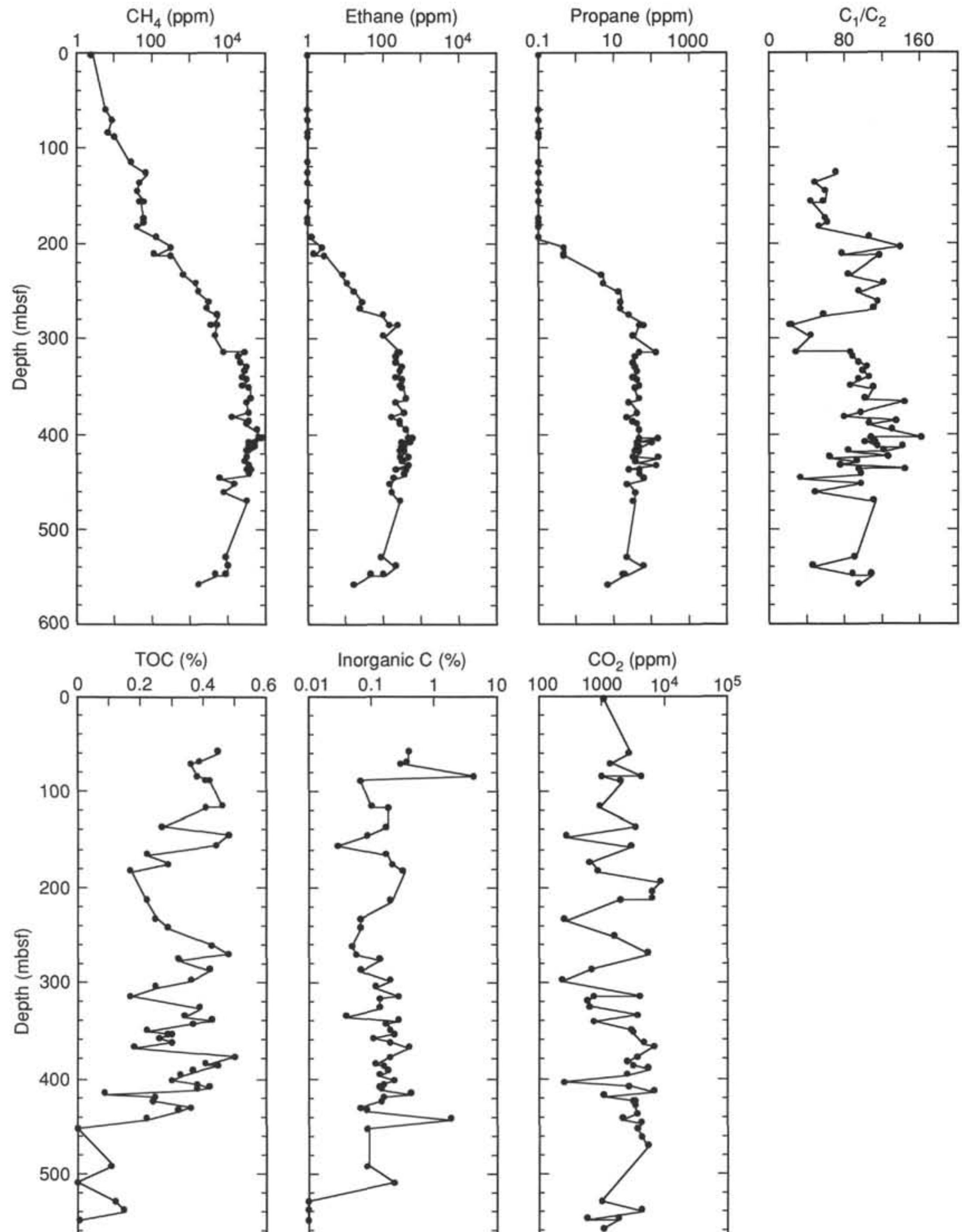

Figure 30. Gas concentrations (v/v), C_1/C_2 ratio, and weight percentages of total organic and inorganic carbon and carbon dioxide vs. depth in Hole 857C.

pyroxene have been perfectly pseudomorphed by prehnite and epidote, respectively. A major difference in the metamorphism between Holes 857C and 857D is that in the latter, pyroxene, is replaced in equal or greater proportions than plagioclase. In Hole 857C, in contrast, plagioclase was preferentially replaced by chlorite.

Wairakite, chlorite, and chalcopyrite are observed to be associated in a vein at the top of the hole (Sample 139-857D-1R-1, Piece 8D, 68–70 cm) and wairakite alone is found in a vein in Core 139-857D-12R. Epidote, pyrite, and chalcopyrite fill two of the large veins. The abundance of veins decreases downcore, from about Core 139-857D-21R, except for rare sulfide-epidote-prehnite-wairakite veins. The veins typically have a 1–2 cm epidote- and chlorite-rich aureole (Fig. 61) in the host. The vein abundance in Hole 857D is much less than what is observed in Hole 857C.

Sulfide, dominantly pyrite, is most abundant as vesicle fillings and porphyroblasts. These latter interstitial aggregates of crystals

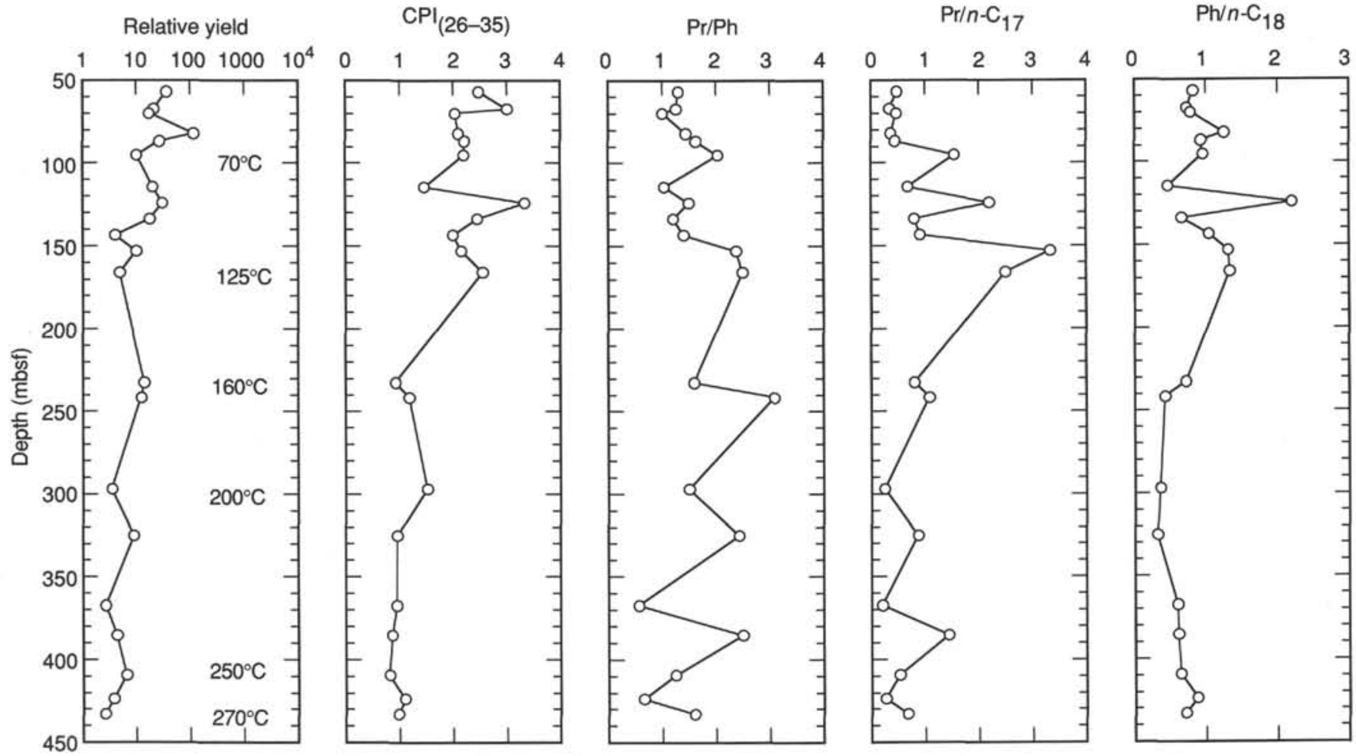

Figure 31. Plots of bitumen maturity parameters vs. depth for sediment in Hole 857C.

can be up to 0.5 cm across. They appear to replace phases in the matrix of the rock, including pyroxene, mesostasis or even plagioclase. Vein sulfide systematically extends beyond the wall of the vein through replacement of the adjacent host rock. The porphyroblasts are typically ovoid in shape and can be dendritic or filled. They occasionally include feldspar or epidote grains.

Sulfide Mineralization

Three distinct habits of sulfide minerals are evident in the sills: disseminated sulfide aggregates, iron sulfide-chlorite ± epidote veins, and zeolite–chlorite–epidote–base metal sulfide veins. The first two types occur throughout the holes, whereas the third type has a more confined spatial distribution.

The sills contain abundant vein-filled fractures in Hole 857C (Cores 139-857C-59R to -68R) and in the upper part of Hole 857D (Cores 139-857D-1R through -15R). Below a thick sediment section (Cores 139-857D-14R, -15R, and -16R, and the top half of Core 139-857D-17R), the fractures and veins are much narrower and occur only rarely. The veins in the highly fractured areas have two predominant orientations, subparallel to (usually about 20°) and perpendicular to (80°–90°) the core axis. The two vein sets are contemporaneous, and where they occur in the same sample (for example, 139-857D-12R-1, Pieces 8A and 8B; 139-857D-8R-1, Piece 5), the same alteration and zoning pattern is associated with both; no cross-cutting relationships could be defined.

Large Veins

The veins in Sample 139-857D-8R-1, Piece 5 (Fig. 54), are typical of the largest veins. They are about 8 to 15 mm wide, extend the length of the piece, and pinch and swell irregularly. These all have a similar zoning pattern, usually with a dark green chloritic border, 1 to 2 mm wide, enclosing a narrow zone of lighter green mineral aggregate (chlorite-amorphous silica) and a central zone filled with discrete patches of epidote, quartz, quartz-zeolite, pyrite, and, in some samples (e.g., 139-857D-1R-1, Piece 8), sphalerite and chalcopyrite. The zeolite is identified (by XRD) as wairakite, the calcium analogue of analcite. In the veins containing sphalerite and chalcopyrite, pyrite is usually absent. Sphalerite in these veins is a distinctive red to light brown, low-iron variety. Both sphalerite and chalcopyrite form 10- to 15-mm anhedral masses that locally fill the vein. They, along with the wairakite and euhedral quartz, appear to be the latest vein filling. In base metal-poor veins, pyrite occurs as a minor phase, usually as a late, central or marginal infilling; or cross-cutting all other vein minerals, as well as the wall rocks. In this habit, pyrite forms discrete elongate blebs. Many of these large veins, particularly those with epidote, quartz-zeolite, and base metal sulfide minerals, contain medial crystal-lined vugs (Fig. 61), attesting to the open, high-permeability structure that these veins impart to the sills.

Adjacent to the veins, diabase is distinctly altered (Fig. 61). The alteration zone is usually about twice the width of the vein, and consists of a bleached zone (silification) near the vein, and chloritization grading outward into the less altered groundmass.

Chlorite-Pyrite ± Epidote Veins

These veins are very common in the highly fractured parts of Holes 857C and 857D, and occur throughout the diabasic rocks of both holes as well as (less commonly) within the sediments. They vary from microscopic, filled fractures to 2-mm-wide veins. They are mineralogically simple, filled with dark green to black chlorite, and more locally, pyrite. In the deeper sections of Hole 857D, some of these veins contain both pyrite and pyrrhotite. A few of these contain epidote as a minor constituent. Epidote typically cross-cuts chlorite, but itself is cut by pyrite. Some veins are zoned, with a silica-rich margin, 0.5 mm wide. Pyrite forms large, flattened subhedral aggregates in the larger veins; these pyrite aggregates are typical 1 to 2 cm in width, and are coarse grained (Fig. 60). Wall-rock alteration is not prominent; petrographic examination reveals some chloritization of

Table 15. Weight percentages of C, H, N, S, inorganic carbon, and organic carbon (TOC) for sediment from Holes 857A and 857C.

Core, section, interval (cm)	Depth (mbsf)	C (%)	H (%)	S (%)	N (%)	C/H[a]	C/N[a]	C/S[a]	Inorganic carbon (%)	TOC (%)
139-857A-										
1H-1, 99–103	2.89	0.88	0.54	0.13	0.045	1.63	20	6.77	0.43	0.45
1H-2, 80–84	4.20	0.96	0.54	0.00	—	1.78	—	—	0.45	0.51
1H-3, 84–88	5.74	1.50	0.48	0.00	—	3.13	—	—	0.76	0.74
1H-4, 125–129	7.65	0.88	0.48	0.00	—	1.83	—	—	0.38	0.50
1H-6, 23–27	9.63	—	—	—	—	—	—	—	1.33	—
1H-7, 10–14	11.00	2.37	0.58	0.04	—	4.09	—	57.80	1.54	0.83
2H-1, 82–85	12.22	—	—	—	—	—	—	—	0.54	—
2H-2, 73–75	13.63	0.99	0.61	0.06	—	1.62	—	16.50	0.29	0.70
2H-3, 79–81	15.19	0.78	0.54	0.04	—	1.44	—	18.14	0.11	0.67
2H-4, 79–81	16.69	1.08	0.42	0.64	0.044	2.57	25	1.69	0.58	0.50
2H-7, 32–34	20.72	0.73	0.32	0.59	—	2.28	—	1.24	0.36	0.37
4H-1, 111–114	23.01	0.93	0.47	0.42	0.056	1.98	17	2.21	0.27	0.66
4H-2, 86–90	24.26	0.89	0.47	0.37	—	1.89	—	2.41	0.16	0.73
4H-3, 84–88	25.74	0.76	0.38	0.53	—	2.00	—	1.43	0.27	0.49
5H-5, 63–67	38.03	0.94	0.59	0.31	—	1.59	—	3.03	0.20	0.74
6H-1, 67–71	41.57	0.89	0.50	0.17	—	1.78	—	5.24	0.34	0.55
6H-4, 54–58	45.94	0.81	0.48	0.00	—	1.69	—	—	0.44	0.37
7H-3, 69–73	54.09	0.89	0.50	0.24	0.055	1.78	16	3.71	—	—
7H-3, 81–85	54.21	0.71	0.37	0.40	0.030	1.92	24	1.78	—	—
7H-3, 81–85	54.21	0.62	0.55	0.19	0.042	1.13	15	3.26	—	—
7H-6, 48–52	58.38	0.78	0.45	0.14	0.034	1.73	23	5.57	0.29	0.49
8H-2, 95–99	62.35	0.86	0.47	0.00	—	1.83	—	—	0.40	0.46
8H-3, 70–74	63.60	0.88	0.51	0.11	0.039	1.73	23	8.00	1.64	0.00
8H-4, 88–92	65.28	—	—	—	—	—	—	—	0.69	—
8H-5, 97–101	66.87	—	—	—	—	—	—	—	4.01	—
8H-6, 83–87	68.23	0.75	0.51	0.21	0.042	1.47	18	3.57	2.23	0.00
8H-7, 33–37	69.23	—	—	—	—	—	—	—	0.59	—
9H-1, 84–88	70.24	—	—	—	—	—	—	—	0.41	—
9H-2, 93–98	71.83	0.81	0.57	0.00	—	1.42	—	—	0.32	0.49
9H-3, 86–90	73.26	0.83	0.53	0.00	—	1.57	—	—	0.41	0.42
10H-1, 44–46	79.34	0.82	0.50	0.09	0.031	1.64	26	9.32	0.47	0.35
10H-2, 79–81	81.19	0.75	0.39	0.26	—	1.92	—	2.88	0.30	0.45
10H-3, 50–52	82.40	0.57	0.30	0.13	0.021	1.90	27	4.38	0.34	0.23
10H-4, 44–46	83.84	—	—	—	—	—	—	—	0.27	—
10H-5, 47–49	85.37	0.56	0.30	0.08	0.020	1.87	28	7.18	0.32	0.24
10H-6, 26–28	86.66	—	—	—	—	—	—	—	0.29	—
10H-6, 28–30	86.68	—	—	—	—	—	—	—	0.30	—
13X-3, 122–124	105.72	1.02	0.43	0.78	—	2.37	—	1.31	0.29	0.73
13X-5, 62–64	108.12	0.46	0.42	0.34	0.033	1.10	14	1.35	0.02	0.44
139-857C-										
2R-1, 63–67	57.13	0.86	0.43	0.43	0.340	2.00	3	2.0	0.41	0.45
3R-1, 90–92	67.40	0.78	0.40	0.24	0.160	1.95	5	3.3	0.39	0.39
3R-3, 38–40	69.34	0.66	0.45	0.02	0.130	1.47	5	41.3	0.30	0.36
5R-1, 4–8	82.14	4.99	0.34	0.00	0.056	14.68	89	—	4.61	0.38
6R-1, 33–35	86.53	0.48	0.55	0.03	0.066	0.87	7	15.0	0.07	0.41
6R-1, 66–68	86.86	0.49	0.57	0.00	0.069	0.86	7	—	0.07	0.42
9R-1, 27–30	114.77	0.56	0.48	0.04	0.085	1.17	7	15.1	0.10	0.46
9R-1, 31–34	114.81	0.60	0.43	0.08	0.091	1.40	7	7.7	0.19	0.41
11R-1, 124–126	135.04	0.45	0.26	1.30	0.061	1.73	7	0.4	0.18	0.27
12R-1, 80–83	144.30	0.57	0.59	0.20	0.058	0.97	10	2.9	0.09	0.48
13R-2, 48–51	155.08	0.47	0.58	0.12	0.071	0.81	7	3.9	0.03	0.44
14R-2, 27–29	164.57	0.40	0.32	0.05	0.049	1.25	8	7.8	0.18	0.22
15R-1, 93–95	—	—	—	—	—	—	—	—	0.26	—
15R-2, 97–99	174.97	0.51	0.38	0.43	0.039	1.34	13	1.2	0.22	0.29
17R-1, 82–86										—
16R-1, 15–17	182.35	0.50	0.29	0.22	0.017	1.72	29	2.3	0.33	0.17
18R-1, 76–80	202.36	0.40	0.51	0.20	0.044	0.78	9	2.0	—	—
19R-2, 78–82	213.58	0.43	0.35	0.21	0.023	1.23	19	2.1	0.21	0.22
21R-1, 129–131	231.89	0.32	0.31	0.30	0.026	1.03	12	1.1	0.07	0.25
22R-1, 124–127	241.54	0.36	0.37	0.25	0.039	0.97	9	1.4	0.07	0.29
24R-2, 33–37	261.03	0.48	0.42	0.35	0.052	1.14	9	1.4	0.05	0.43
25-1, 51–54	269.31	0.54	0.39	0.31	0.051	1.38	11	1.7	0.06	0.48
26R-1, 66–68	275.16	0.46	0.39	0.07	0.056	1.18	8	6.4	0.14	0.32
27R-2, 87–90	286.47	0.49	0.50	0.37	0.062	0.98	8	1.3	0.07	0.42
28R-3, 27–29	297.07	0.56	0.42	0.22	0.042	1.33	13	2.6	0.20	0.36
29-1, 58–61	303.98	0.37	0.36	0.24	0.047	1.03	8	1.5	0.12	0.25
30R-1, 28–31	313.38	0.45	0.28	0.14	0.014	1.61	32	3.2	0.28	0.17
30R-2, 74–77	315.34	—	—	—	—	—	—	—	0.14	—
31R-2, 102–105	325.22	0.53	0.42	0.24	0.041	1.26	13	2.2	0.14	0.39
33R-2, 71–73	334.61	0.38	0.47	0.24	0.048	0.81	8	1.6	0.04	0.34
34R-2, 97–100	338.97	0.70	0.35	0.50	0.050	2.00	14	1.4	0.27	0.43
35R-1, 124–127	342.54	0.55	0.35	0.45	0.046	1.57	12	1.2	0.18	0.37

Table 15 (continued).

Core, section, interval (cm)	Depth (mbsf)	C (%)	H (%)	S (%)	N (%)	C/H[a]	C/N[a]	C/S[a]	Inorganic carbon (%)	TOC (%)
36R-3, 83–87	349.93	0.42	0.50	0.19	0.042	0.84	10	2.2	0.20	0.22
37R-2, 115–119	353.45	0.53	0.44	1.03	0.056	1.20	9	0.5	0.24	0.29
37R-2, 115–119	353.45	0.54	0.45	0.85	0.055	1.20	10	0.6	0.24	0.30
38R-2, 69–71	357.99	0.37	0.47	0.14	0.038	0.79	10	2.6	0.11	0.26
39R-2, 48–50	362.38	0.51	0.41	0.28	0.033	1.24	15	1.8	0.21	0.30
40R-2, 48–51	367.38	0.58	0.27	0.49	0.020	2.15	28	1.2	0.40	0.18
41R-2, 89–91	377.29	0.70	0.51	0.29	0.069	1.37	10	2.4	0.20	0.50
43R-1, 66–70	385.36	0.53	0.44	0.42	0.046	1.20	12	1.3	0.12	0.41
43R-2, 9–12	386.29	0.62	0.50	0.34	0.068	1.24	9	1.8	0.17	0.45
44R-2, 27–31	391.47	0.56	0.48	0.19	0.050	1.17	11	3.0	0.19	0.37
45R-2, 42–44	396.22	0.47	0.48	0.22	0.035	0.98	13	2.1	0.14	0.33
46R-2, 142–146	401.92	0.54	0.49	0.21	0.032	1.10	17	2.6	0.24	0.30
47R-2, 5–8	405.55	0.54	0.46	0.25	0.042	1.17	13	2.2	0.16	0.38
48R-1, 73–75	409.43	0.56	0.47	0.25	0.044	1.19	13	2.2	0.14	0.42
48R-2, 116–119	411.36	0.53	0.48	0.22	0.045	1.10	12	2.4	0.15	0.38
49R-2, 45–47	415.65	0.52	0.32	0.17	0.010	1.63	51	3.1	0.43	0.09
50R-1, 121–123	419.51	0.41	0.43	0.23	0.016	0.95	26	1.8	0.16	0.25
51R-1, 28–30	423.68	0.39	0.43	0.56	0.046	0.91	8	0.7	0.15	0.24
52R-CC, 10–12	430.41	0.43	0.45	0.22	0.038	0.96	11	2.0	0.07	0.36
53R-1, 24–26	433.04	0.41	0.44	0.22	0.033	0.93	12	1.9	0.09	0.32
55R-1, 25–27	442.25	2.10	0.22	0.00	0.005	9.55	389	—	1.88	0.22
57R-1, 16–18	451.86	0.05	0.22	0.50	0.003	0.25	18	0.1	0.09	0.00
61R-1, 113–115	491.63	0.20	0.32	1.00	0.003	0.63	69	0.2	0.09	0.11
63R-1, 13–16	509.83	0.11	0.32	0.00	0.000	0.34	—	—	0.24	0.00
65R-1, 15–17	529.25	0.13	0.28	0.73	0.054	0.46	2	0.2	0.01	0.12
66R-1, 15–17	538.95	0.16	0.36	0.35	0.029	0.44	6	0.5	0.01	0.15
67R-1, 55–57	548.95	0.02	0.32	0.26	0.046	0.07	0	0.1	0.01	0.012
Hole 857C black soot	2.51	0.93	0.34	0.068	2.70	37	7.38	—	—	—

Note: — = not determined.
[a]Calculated as percent ratios.

immediately adjacent rock. Overall, these veins are remarkably similar in mineral content and zonation to the vesicle filling that is prominent in the chilled margins of the sills.

Disseminated Sulfide

Disseminated pyrite is pervasive throughout virtually all of the units described above. It typically forms about 1% of the rock. It occurs as discrete aggregates, usually about 2 to 3 mm in diameter, and is evenly distributed. Petrographic examination reveals that the aggregates consist of a very fine-grained network of pyrite, both surrounding and cross-cutting virtually all groundmass silicate minerals. Pyrite has grown poikiloblastically, displacing grain boundaries and filling microfractures. Where it has grown in the mesostasis, alteration (to chlorite) seems prominent. However, where it has formed in the granular groundmass, it incorporates both feldspar and pyroxene grains with no alteration. Remnants of silicate grains retain their optical continuity through the pyrite. Precipitation seems to have occurred primarily by grain-boundary and fracture displacement.

Some of the lowermost sections of Hole 857D have intimately intergrown pyrite and pyrrhotite forming intergranular sulfide aggregates. A few grains of chalcopyrite are also present in these lower sections.

Geochemistry

The chemical data for the samples from Holes 857C and 857D are considered together (Tables 26 and 27). The series of sills penetrated by these holes is an almost continuous representation of magmatic activity at this site, with no overlap. Samples from the 26 units listed in Tables 22 and 23 include both fine-grained chilled margins and the coarser interiors of sills. Although the majority of the samples were chosen to represent the freshest possible material, several samples are from altered margins of some sills.

Cumulative frequency diagrams are used to divide the data into "altered" and "less altered populations" (Fig. 62). The selected elements typically are mobile (or, for LOI elements, added in part metasomatically), and their distribution is noticeably affected by alteration. Each plot in Figure 62 demonstrates a distinctive bimodal distribution of data. MgO is typically very sensitive to alteration, and in this set of plots, has the largest number of samples in its uppermost population. The lower population, representing about 75% of the data, forms a linear unimodal distribution; these are the "normal," unaltered (actually less altered) rocks. The upper population illustrates that up to 4% of additional MgO was added during alteration. These samples almost all come from near the margins of the sills or from heavily veined samples.

The two sample populations were separated and compared with Ni and Cr distributions. The lower, normal group has a strong correlation between Ni and Cr (R = 0.75), reinforcing the argument that these data represent variations in the primary igneous composition of the sills; Ni and Cr are not correlated in the upper group (R = –0.04). The upper population of MgO data do not correlate well with Cr and Ni. These latter elements are usually immobile during alteration, and further demonstrate that the variation in MgO above about 11% is due to alteration and not primary igneous processes.

Loss on ignition data show a similar trend. The population represented by the lower linear trend indicates hydration of the primary igneous minerals, whereas the second population (above 3.75%) indicates a gain of sulfide and hydrous clay and sulfide minerals. MgO is strongly correlated with LOI in the latter population (R = 0.92), and only moderately well correlated with the lower group (R = 0.57). The moderate correlation of LOI and MgO in the lower, less altered group reflects in part the preferential hydration of ferromagnesian minerals.

The Fe_2O_3 data illustrate another aspect of alteration. The data are distributed into three distinct populations. The lower linear trend represents a normal variation in the primary igneous composition of

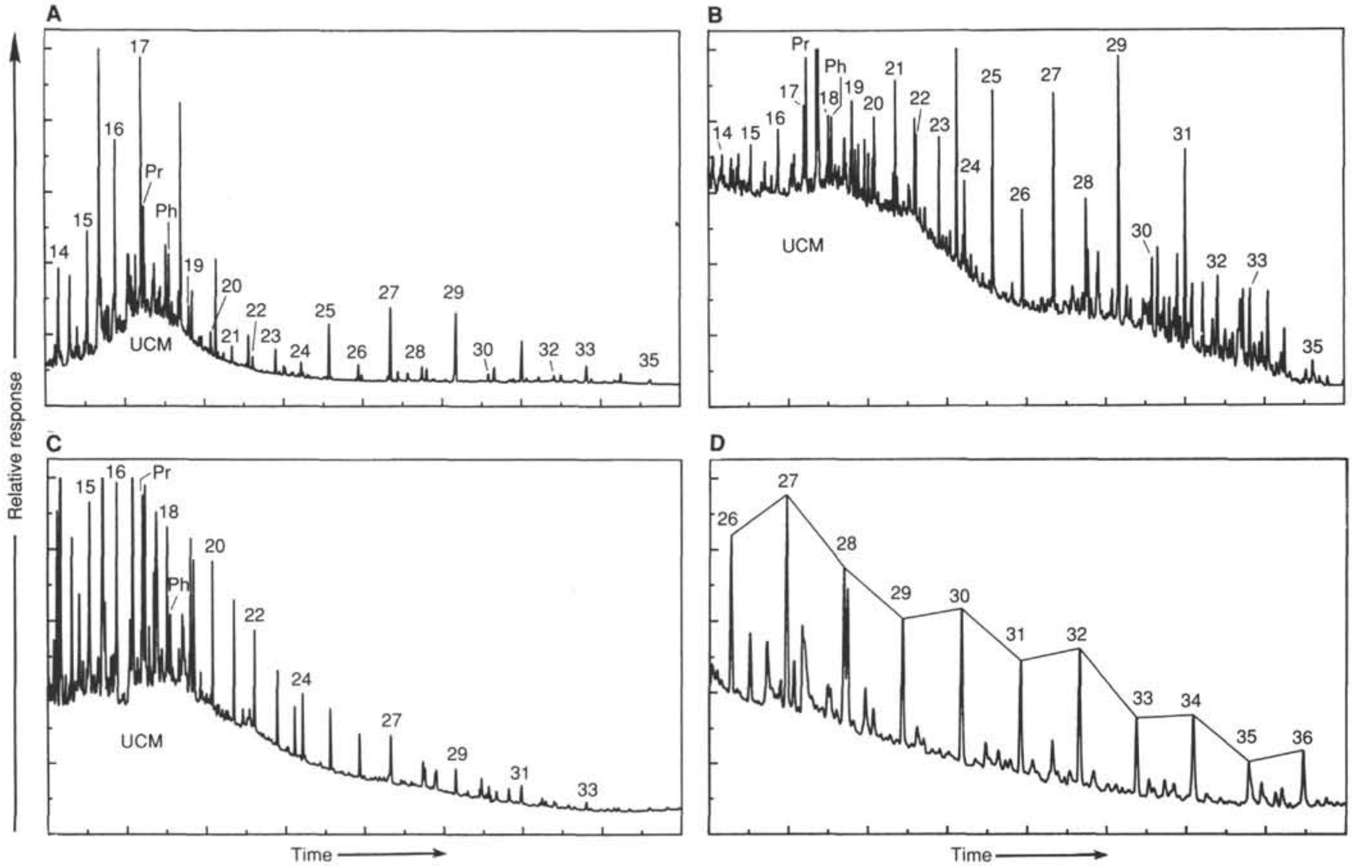

Figure 32. Examples of gas chromatographic traces of the bitumen (hexane-soluble matter) in sediment from Site 857. **A.** Sample 139-857A-4H-2, 86–90 cm, carbon preference index (CPI) = 3.95. **B.** Sample 139-857C-6R-CC, CPI = 2.21. **C.** Sample 139-857C-22R-1, 124–127 cm, CPI = 1.19. **D.** Sample 139-857C-48R-1, 73–75 cm, CPI = 0.81. Numbers refer to carbon chain length of *n*-alkanes. Pr = pristane, Ph = phytane, UCM = unresolved complex mixture of branched and cyclic compounds.

the sills (between about 9 and 12% Fe_2O_3). The other two groups of data probably represent the addition of iron sulfide to the sills. This indicates that Fe addition, and not just sulfur metasomatism, has been effective in forming at least some of the almost ubiquitous iron sulfide.

The data for silica illustrate a lower anomalous population (below 48.0% SiO_2). Again, this population is correlated with the high MgO, Fe_2O_3, and LOI data, which indicates either that silica has been lost from the most intensely altered margins and veined parts of the sills, or that the addition of pyrite and ferromagnesian clay minerals has had a profound effect on the mass or volume of the altered rock.

Other major changes in chemical composition that reflect alteration are (1) a major gain in zinc and copper during alteration (370 ppm Zn and 130 ppm Cu average in altered rocks, 90 ppm Zn and 90 ppm Cu in unaltered rocks), (2) loss of Na_2O in some altered samples, (3) a pronounced loss of CaO and Sr in the altered rocks (an average of 6.59% in altered rocks vs. 11.95% in the unaltered group), (4) an apparent (relative) gain in alumina and titania during alteration. The normative mineral abundances (Table 26) reflect the complexity of the total mass balance changes during alteration. The bleached margins have high normative abundances of ilmenite and anorthite due to the refractory concentration of Ti and Al. Samples with high MgO and LOI also contain large abundances of normative hyperthene from the net addition of Mg. Without an examination of mass balance effects, no additional treatment of the altered rocks is warranted.

The remainder of the examination of chemical data is devoted to the less altered suite of samples. For comparison with other sites and other areas of the Juan de Fuca Ridge, these data include only those samples with less than 11.0% MgO and 3.75% LOI.

The sills have compositions, including their Mg numbers (average 60.8 ± 2.3, 1 s.d.), that are typical of normal mid-ocean ridge basalt (MORB). They have a considerable compositional range, with silica varying from 46.3% to 52.2% and Al_2O_3 from 14.2% to 18.5%. Their Cr contents have a large range (153 to 597 ppm) compared with normal MORB; for example, all but two samples from Endeavour Ridge (Karsten et al., 1990) vary from 53 to 330 ppm. The larger variation in the sills for Site 857 may be due to fractional crystallization, or to a parental component of more primitive basaltic melt.

The plots of immobile element data (Figs. 63 and 64) indicate a much greater variability in composition within the sills than is evident in the volcanic rocks of the Juan de Fuca Ridge (Karsten et al., 1990). For example, on Figure 63, the data all lie within the "ocean floor basalt" field, but spread across the field in comparison with the tight cluster of data from Site 855. On a plot of Ti vs. Zr (Fig. 64), the data lie only partially within the field of ocean floor basalt; they extend to much higher Ti contents than are normal for basalt. On the latter plot, the data display a moderately well-defined linear trend with a positive slope. The sills have compositions that clearly resemble ocean-floor basalt, but appear to have been extensively fractionated. The bulk samples include abundant crystalline phases, whose accumulation will also impact these chemical trends.

In order to examine the possible effects of fractionation, the variation in Ti vs. Mg number and the ratio of CaO to Al_2O_3 vs. Mg number are shown in Figures 65 and 66. Both diagrams illustrate the broad compositional range of these sills. The very high Ti contents of a few samples of the sills, and their generally high content of Ti relative to the Endeavour samples, as well as those from Site 855,

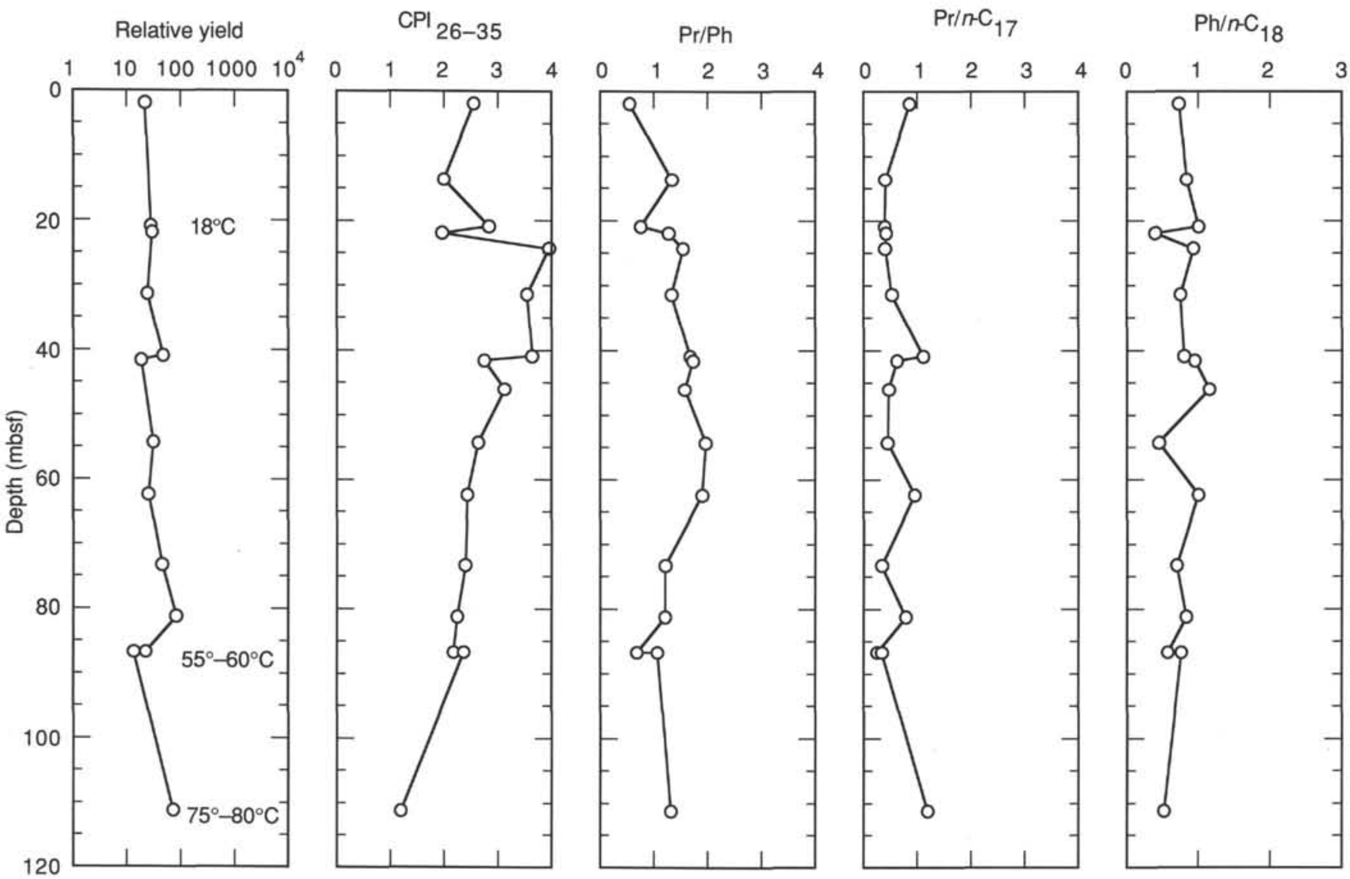

Figure 33. Plots of bitumen maturity parameters vs. depth for sediment in Hole 857A.

indicate moderately strong fractionation of the parent melts to these sills as well as ilmenite accumulation. The data form a broadly linear array with a negative slope (Fig. 65), which indicates both plagioclase and olivine fractionation. On the latter plot, some of the compositions lie well outside the fields for basalt from the Juan de Fuca and Endeavour ridges, again indicative of fractional crystallization of crystal accumulation. Fractionation probably occurred at a high crustal level, and in part within the sills themselves. Zoned plagioclase phenocrysts (noted petrographically) and an increase in abundance of ferromagnesian minerals with depth both reflect fractional crystallization within the thicker sills. In all of the plots, the sills are compositionally more evolved than the intrusions at Site 856.

Finally, we undertook a cursory examination of the variations in composition of the sills with depth below seafloor (Fig. 67). Variations within individual thick sills are seen to be as great as the variability between sills. Chilled margin samples were conspicuously altered, rendering the use of even their "immobile element" contents suspect, pending mass balance studies. Nevertheless, some broad trends are apparent. The CaO/Al_2O_3 ratio decreases somewhat with depth to about 650 mbsf. The Cr content decreases downward to about 600 mbsf and Zr increases upward from the same depth, suggesting that the lower sills in this interval may be less fractionated.

The variations in composition below 650 mbsf are more complex. The CaO/Al_2O_3 ratio has a slight upward increase. The Cr and Zr contents are both low, relative to the lower (for Cr) and upper (for Zr) parts of the higher interval, respectively. The variations in composition for the sills may indicate crystal fractionation within the sill complex.

Conclusions

Coring at Site 857 recovered igneous rock from a series of mafic sills. For many of the intrusive units, a fine-grained chilled margin and coarse-grained interior can be readily identified in the core. The sill margins are extensively chemically modified by alteration and replacement by magnesian chlorite. The interiors of the larger sills are extremely coarse grained and composed of poikilitically intergrown plagioclase and clinopyroxene with ilmenite, magnetite, and residual mesostasis. Mesostasis and plagioclase and show extensive metamorphic recrystallization to epidote, chlorite, albite, and actinolite.

The sills at Site 857 are the products of extensive fractionation and crystal accumulation from a normal MORB parent melt. All of the sills were probably derived from a similar magmatic source.

The exceptional amount of upper-zeolite to greenschist alteration, accompanied by zinc and, to a lesser extent, copper deposition, may indicate that a weakly metalliferous hydrothermal fluid penetrated the sills during cooling. This fluid was not likely a high-temperature ore-forming type. The pervasive Mg-enrichment accompanying metal deposition could not have been derived from the highly evolved (and therefore Mg-depleted) type of hydrothermal fluid observed in volcanic-dominated ridge crests. Relatively cool, unmodified seawater would provide the best source of Mg. Loss of CaO and Na_2O from these rocks probably occurred during destruction of feldspar and mesostasis in glassy rocks. Feldspar is usually removed under high water/rock ratio, low-pH alteration conditions, typified by zones of hydrothermal upwelling (Franklin, 1986). The highly fractured nature of the sills in the upper part of the sequence indicates that they were highly permeable. The dominance of Mg-rich alteration minerals that fill these fractures and replace the margins of the sills indicates that unevolved seawater penetrated the fractures, was probably rapidly heated, lost magnesium and removed Ca, Na, and Si.

The abundant disseminated pyrite that is a pervasive alteration of the sills (and sediment; see "Lithostratigraphy and Sedimentology" section, this chapter) throughout the cored interval of Holes 857C and 857D is somewhat enigmatic. It is associated with a pronounced zinc

Table 16. Various parameters for the solvent-soluble organic matter in sediment from Site 857.

Core, section, interval (cm)	Depth (mbsf)	Relative yield (×10^6)	Carbon maxima[a]	$CPI_{(26-35)}$	Pr/Ph	Pr/n-C_{17}	Ph/n-C_{18}	U^K_{37}
139-857A-								
1H-1, 0–1	1.90	21.8	27, 21	2.55	0.55	0.86	0.73	0.28
2H-2, 73–75	13.64	39.6	17, 27	1.99	1.33	0.40	0.83	0.15
2H-CC	20.90	27.7	27, 17	2.83	0.75	0.39	1.00	0.29
3H-CC	21.90	29.2	17, 25	1.96	1.27	0.42	0.40	0.26
4H-2, 86–90	24.28	57.8	17, 27	3.95	1.54	0.40	0.93	0.31
4H-CC	31.40	24.0	27, 17	3.54	1.33	0.53	0.75	0.29
5H-CC	40.90	46.7	29, 17	3.63	1.67	1.11	0.80	0.26
6H-1, 67–71	41.60	18.5	17, 29	2.74	1.72	0.62	0.95	na
6H-4, 54–58	45.96	44.3	17, 29	3.12	1.57	0.47	1.15	0.30
7H-3, 81–85	54.23	31.1	17, 27	2.63	1.96	0.45	0.45	0.26
8H-2, 95–99	62.37	25.3	17, 29	2.43	1.90	0.95	1.00	0.18
9H-3, 86–90	73.28	45.1	17, 27	2.39	1.21	0.34	0.70	0.18
10H-2, 79–81	81.20	82.2	17, 27	2.24	1.20	0.79	0.83	0.26
10H-6, 26–28	86.67	22.2	17, 27	2.17	0.68	0.25	0.57	nd
10H-6, 28–30	86.67	13.3	17, 27	2.36	1.06	0.34	0.76	nd
13X-CC	111.20	73.2	18, 27	1.19	1.31	1.19	0.52	nd
139-857C-								
2R-1, 63–67	57.16	36.9	17, 18	2.48	1.30	0.48	0.82	0.16
3R-1, 90–92	67.41	21.3	17, 29	3.01	1.26	0.34	0.73	0.27
3R-3, 38–40	69.89	17.3	17, 27	2.04	1.00	0.47	0.78	0.19
5R-1, 4–8	82.16	115.9	17, 27	2.10	1.44	0.36	1.25	0.32
6R-1, 66–68	86.87	27.1	17, 29	2.22	1.63	0.44	0.93	na
6R-CC	95.20	10.3	29, 21	2.21	2.04	1.55	0.96	nd
8R-CC	114.50	20.3	20, 25	1.47	1.04	0.68	0.47	nd
9R-CC	124.10	30.8	29, Pr	3.34	1.50	2.20	2.20	nd
10R-CC	133.80	18.0	20, 29	2.46	1.21	0.80	0.66	nd
11R-CC	143.50	4.1	25, 17	2.00	1.40	0.91	1.04	nd
12R-CC	153.10	10.1	Pr, 29	2.16	2.38	3.33	1.31	nd
14R-3, 0–3	165.83	5.0	Pr, 27	2.56	2.50	2.50	1.33	nd
21R-2, 37–38	232.48	14.1	16, 27	0.93	1.59	0.80	0.72	nd
22R-1, 124–127	241.55	12.4	14, 27	1.19	3.09	1.08	0.43	nd
28R-3, 0–15	296.87	3.5	17, 18	1.52	1.50	0.24	0.36	nd
31R-2, 102–105	325.24	9.0	18, 27	0.96	2.43	0.87	0.32	nd
40R-2, 48–51	367.40	2.7	17, 27	0.95	0.56	0.20	0.60	nd
43R-1, 66–70	385.38	4.3	Pr, 27	0.86	2.50	1.43	0.61	nd
48R-1, 73–75	409.44	6.5	17, 27	0.81	1.24	0.52	0.64	nd
51R-1, 28–30	423.69	3.8	17, 27	1.10	0.65	0.26	0.87	nd
53R-1, 24–26	433.05	2.6	27, 17	0.98	1.60	0.67	0.71	nd

Notes: n.a. = not analyzed; n.d. = not determined because compounds not present.
[a]Major homologs are listed in decreasing order of intensity.

anomaly and a much less pronounced copper anomaly. The metal/base metal ratio of the alteration and the prevalence of pyrite (rather than pyrrhotite) indicate that deposition occurred from a moderate-temperature iron- and sulfur-bearing fluid. The rather irregular association of pyrite alteration with Mg metasomatism may indicate that the processes leading to these two alteration assemblages are somewhat independent. Separation of these two alteration mechanisms is further indicated by the late deposition of pyrite relative to chlorite in the veins, the lack of a ubiquitous association of chlorite and pyrite, and the distribution of the two assemblages; pyrite occurs in the coarsest interiors as well as the fine-grained chilled margins of the sills, but Mg-enrichment is confined primarily to the sill margins. Both are related to a hydrothermal "system," but the pyrite-base metal alteration may have formed through cooling of a low-pH metalliferous fluid (a collapsing high-temperature hydrothermal system?) whereas the Mg-rich alteration formed from progressive heating of downdrawn seawater. The latter probably was voluminous, and may have become sufficiently acid to leach and transport metals that eventually were the source of the pyrite-base metal alteration.

The sulfide mineral assemblages are probably polygenetic, however. The wairakite-chalcopyrite-sphalerite veins are notably deficient in iron sulfide. Wairakite can be deposited only from a high-pH fluid (Steiner, 1955). Higher pH, lower temperature fluids enhance bisulfide, rather than chloride transport of metals. Such transport conditions mitigate against iron transport. The coexistence of only copper and zinc sulfide and zeolite minerals in this category of veins is consistent with high-pH, low-temperature transport of metals. This distinctive, very late vein set is probably genetically unrelated to the formation of either the pyrite or chlorite alteration types.

PHYSICAL PROPERTIES

Physical properties measurements were made on hemipelagic and turbiditic sediment in Hole 857A, drilled with the APC/XCB system to 112 mbsf, and on sediment and relatively fresh to altered diabase drilled to 568 mbsf with the RCB system in Hole 857C. Site 857 was revisited after six holes were drilled at Site 858; reentry Hole 857D was drilled and cased to 581.5 mbsf and cored through the sill complex first encountered in Hole 857C to 936.2 mbsf. Measurements were made only on two of the three APC cores recovered from Hole 857B; hence the following discussion will focus on shipboard analytical results from Holes 857A, 857C, and 857D. APC cores recovered from Hole 857A were subjected to whole-round volume magnetic susceptibility (VMS), gamma-ray attenuation porosity evaluator (GRAPE), and compressional wave velocity (*P*-wave logger, or PWL) analyses on the multisensor track (MST) up to Core 139-857A-13X, where GRAPE and PWL scans were discontinued.

VMS and GRAPE analyses were made on all RCB cores from Hole 857C for hole-to-hole correlation and to test how whole-round

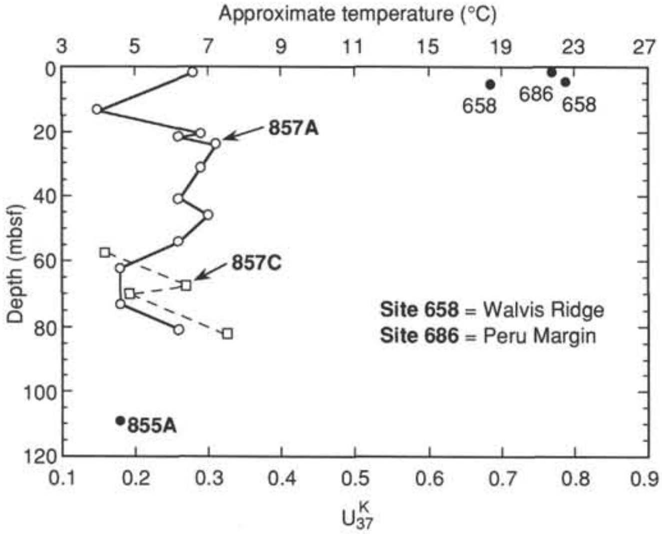

Figure 34. C_{37} alkenone parameter (U^K_{37}) and temperature estimate of the ocean surface water vs. depth below seafloor in Holes 857A and 857C. Other more tropical sites are also shown for comparison.

density measurements compare with discrete sample data; both analyses were also made for Hole 857D but were not as successful. Thermal conductivity was measured with the full-space method on cores from Holes 857A and 857B and with both the full-space and half-space methods from Holes 857C and 857D. Velocities at both deeper holes were obtained with the digital sound velocimeter (DSV) and Hamilton frame velocimeter (HFV). Electrical resistivities were measured on all APC cores and on Core 139-857A-12X from Hole 857A, and on nine cores from Hole 857C; formation factors were calculated for use by the pore-water geochemists. Index properties samples were taken at or adjacent to other measurement locations whenever possible and at a typical frequency of two to three per core, depending on recovery. Volume magnetic susceptibility data are given in SI and have not been corrected for either the coil-to-inner core liner diameter ratio of 0.825 or the effects of partially filled liners. None of the physical properties data have been corrected for *in-situ* temperature, *in-situ* pressure, or rebound effects.

Volume Magnetic Susceptibility

Sediments at Site 857 are composed of hemipelagic mud intercalated with silty to sandy turbidites. Good core recovery in the upper 87 mbsf of Hole 857A resulted in the collection of high-quality VMS data (Fig. 68); the data from Hole 857B are also of good quality

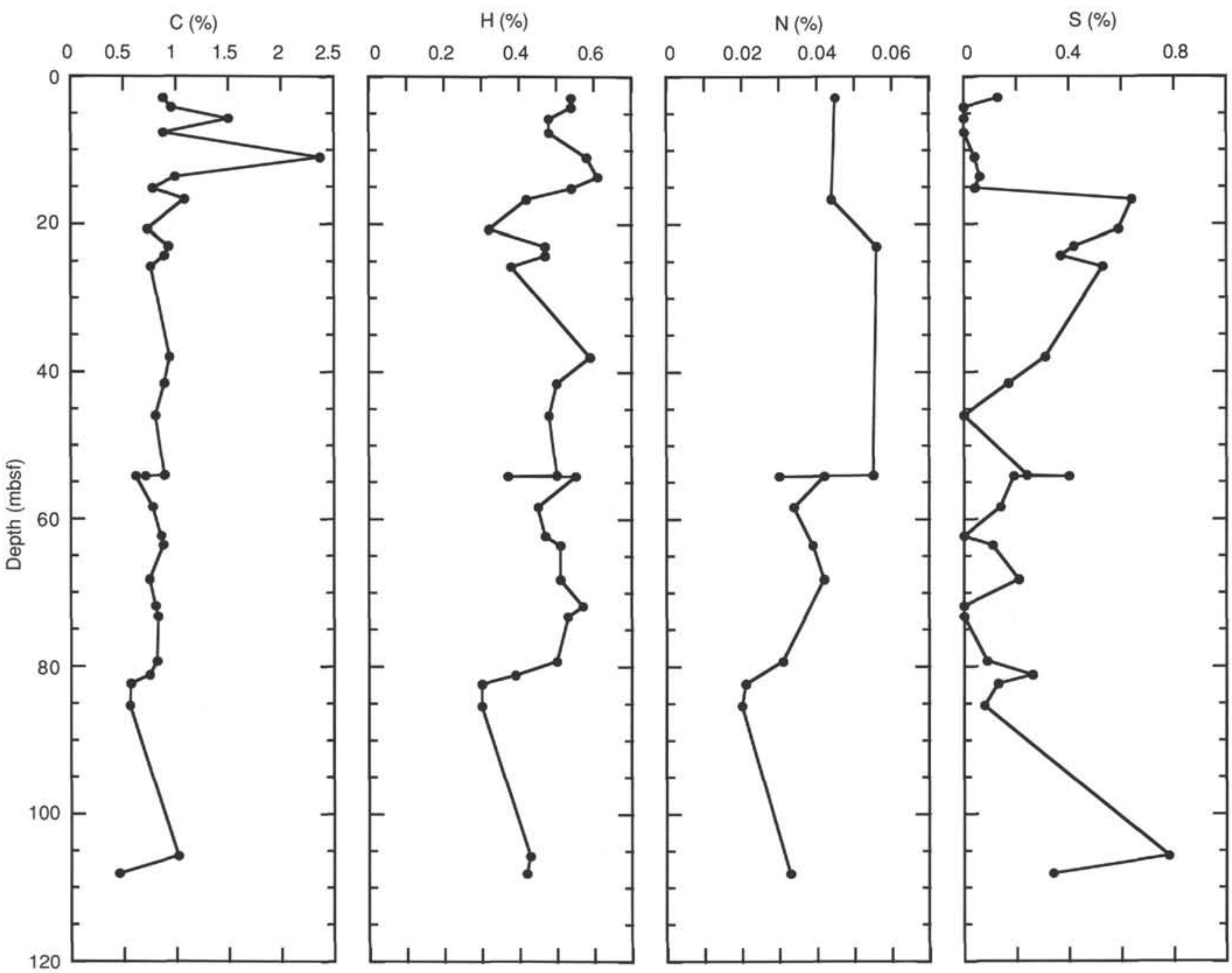

Figure 35. Weight percentages of C, H, N, and S vs. depth in sediment from Hole 857A.

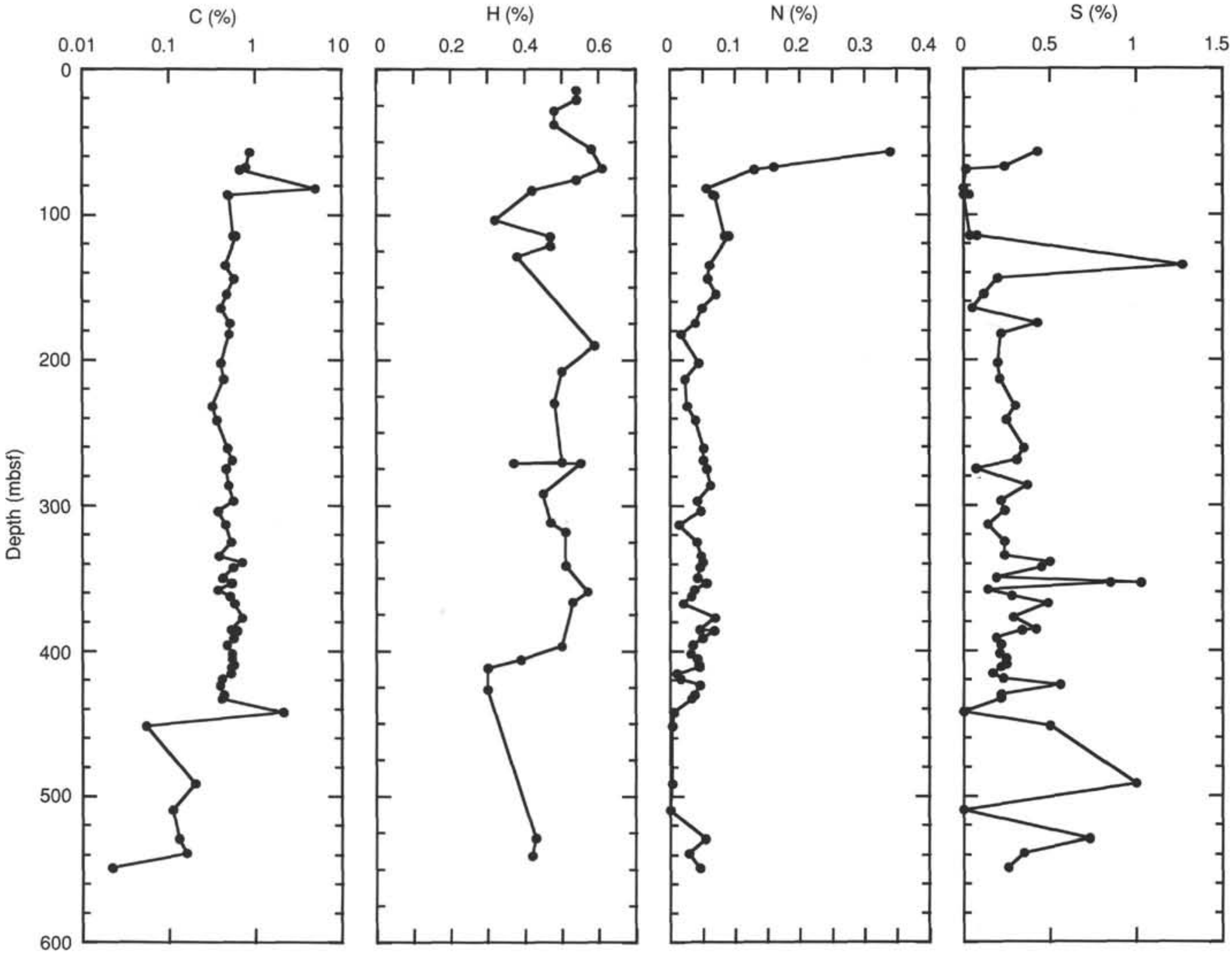

Figure 36. Weight percentages of C, H, N, and S vs. depth in sediment from Hole 857C.

(Fig. 69). Washing from 3.5 to 56.6 mbsf and spotty core recovery in Hole 857C resulted in gaps in the whole-round analysis records and precluded correlation with Holes 857A and 857B (Fig. 70).

The bases of turbidites are well defined by the VMS data, probably because of the higher magnetite content in their coarse-grained sediment; similar observations are discussed in detail in the "Physical Properties" sections, "Site 855" and "Site 856" chapters. The generally high VMS values in the sediment, which range from 0.0015 to 0.002 in the upper 36 mbsf in Hole 857A and the upper 30.5 mbsf of Hole 857B, may reflect the mineralogy of the sediment. Bulk geochemical analyses of sediment from all three sites reveal a mean of 0.87 weight percent TiO_2 ("Sedimentary Geochemistry and Alteration" sections in this chapter and in the "Site 855" and "Site 856" chapters). Although much of this oxide may be present in rutile, enough TiO_2 could be contained within ilmenite-magnetite to produce the relatively high VMS values observed in the cores (see "Igneous Petrology and Geochemistry" section, this chapter).

A significant excursion in these data in Hole 857A, to a lower average value of 0.00025 to 0.0003, occurs at 15.5–21.0 mbsf, where the sediments are dominantly hemipelagic clay (Fig. 68). This interval falls at or just below the acme zone (the base of which is estimated between 11.4 and 16.1 mbsf) of *Emiliana huxleyii* (see "Biostratigraphy" section, this chapter) from the last glacial period. Unfortunately, Hole 857B was washed from 12.9 to 21 mbsf, and the low VMS zone was not cored. However, data from the upper sections of Core 139-857B-3H (21.0–24.0 mbsf) exhibit the same increasing trend with depth as do cores below the "quiet zone" from Hole 857A; in fact, the correlation in the shallow section between these two holes is very good in all sections where there is overlap.

A region of lower amplitude data variation, with VMS values from 0.002 to 0.0025, was identified from about 36.5 to 39.5 mbsf in Hole 857A (Fig. 68). This depth corresponds to a zone where few turbidites were found in the split cores (see "Lithostratigraphy and Sedimentology" section, this chapter). Another turbidite-poor interval was seen from about 77.3 to 79.0 mbsf.

VMS decreases with depth in the disseminated pyrite-enriched, silty claystone interbedded with siltstone and sandstone in Hole 857C, to about 0.00025 at 297.0 mbsf, and remains at this low level through 434.0 mbsf (Fig. 70). Below this depth, VMS values decrease again to about 0.0001 at 462.0 mbsf, although data are sparse due to low recovery. This systematic decrease in volume magnetic susceptibility may reflect the diagenetic alteration of magnetite to iron sulfide due to H_2S flux through the sediments (see "Organic Geochemistry" and "Fluid Geochemistry" sections, this chapter). The destruction of magnetic minerals in this hydrothermal regime can occur via oxidization or pyritization (see "Igneous Petrology and Geochemistry" section, this chapter).

The first of several sills encountered in Hole 857C was penetrated at 471.1 mbsf. Susceptibility generally decreases with depth from unit to unit. Metadiabase samples have a high VMS of 0.009 to 0.017 from

Table 17. Major oxide and element composition (in wt%) of sediment samples from Site 857.

Core, section, interval (cm)	Depth (mbsf)	Grain size	SiO_2	TiO_2	Al_2O_3	Fe_2O_3	MnO	MgO	CaO	Na_2O	K_2O	P_2O	LOI	Total	H_2O	CO_2	Organic C	S	N
139-857A-																			
1H-2, 80–84	4.20	Clay	57.07	0.91	16.96	8.22	0.09	3.56	2.85	2.06	2.88	0.21	5.20	100.53	4.86	1.65	0.51	0.00	
2H-2, 73–75	13.63	Clay	56.40	0.87	16.31	8.56	0.11	4.24	3.22	2.43	2.12	0.19	5.53	100.51	5.49	1.06	0.70	0.06	
4H-2, 86–90	24.26	Clay	56.57	0.84	13.79	11.67	0.08	3.20	2.73	2.02	1.92	0.16	7.02	99.87	4.23	0.59	0.73	0.37	
5H-3, 78–82	35.18	Clay	57.23	0.86	17.34	7.57	0.11	4.01	2.96	1.97	2.99	0.19	4.77	99.58		0.92			
6H-4, 54–58	45.94	Clay	58.11	0.90	16.78	7.00	0.12	3.63	3.56	2.05	2.70	0.22	4.93	99.16	4.32	1.61	0.37	0.00	
7H-3, 69–73	52.91	Clay	57.48	0.88	15.98	8.84	0.12	3.70	3.90	2.31	2.42	0.25	4.13	98.39	4.50	1.83	0.39	0.24	0.055
8H-2, 95–99	62.35	Clay	57.01	0.94	15.80	7.85	0.11	4.09	4.47	2.74	1.87	0.23	4.89	99.58	4.23	1.47	0.46	0.00	
9H-2, 93–98	71.83	Clay	56.73	0.90	16.00	8.13	0.11	4.45	3.34	2.15	2.53	0.23	5.44	99.55	5.13	1.17	0.49	0.00	
10H-2, 79–81	81.19	Clay	61.33	0.87	15.42	6.73	0.09	3.36	3.70	2.59	1.91	0.22	3.77	99.07	3.51	1.10	0.45	0.26	
13X-3, 122–124	105.72	Silt	59.43	0.90	16.21	7.25	0.08	4.07	2.90	2.58	2.18	0.19	4.21	100.01	3.87	1.06	0.73	0.78	
139-857C-																			
2R-1, 63–67	57.13	Clay	57.49	0.93	16.05	7.89	0.10	4.54	3.73	2.60	2.03	0.22	4.43	99.86	3.87	1.50	0.45	0.43	0.340
3R-3, 38–40	69.88	Clay	55.56	0.86	15.88	7.95	0.13	4.46	4.38	2.17	2.52	0.23	5.85	100.16	4.05	1.10	0.36	0.02	0.130
5R-1, 4–8	82.14	Clay	57.28	0.86	16.76	7.91	0.10	4.97	2.43	2.53	2.15	0.23	4.78	100.43	3.06	16.90	0.38	0.00	0.056
6R-1, 33–35	86.53	Clay	57.51	0.93	17.04	8.02	0.10	4.57	2.17	2.44	2.25	0.19	4.78	99.83	4.95	0.26	0.42	0.03	0.069
6R-1, 66–68	86.86	Clay	55.15	0.89	16.70	8.62	0.09	5.06	2.00	3.07	2.32	0.19	5.91	101.61	5.13	0.26	0.42	0.00	0.069
9R-1, 27–30	114.77	Clay	58.06	0.93	16.60	7.66	0.10	4.60	2.39	2.72	2.49	0.18	4.28	100.09	4.32	0.37	0.46	0.04	0.085
11R-1, 124–126	135.04	Clay	61.93	0.88	15.14	7.88	0.08	3.30	3.24	2.86	1.73	0.20	2.77	99.35	2.34	0.66	0.27	1.27	0.061
12R-1, 80–83	144.30	Clay	56.66	0.96	17.13	8.72	0.10	5.15	2.14	2.17	2.23	0.23	4.52	100.49	5.31	0.33	0.48	0.20	0.058
13R-2, 48–51	155.08	Clay	55.42	0.96	17.20	9.17	0.11	5.40	2.03	2.32	2.25	0.23	4.91	100.37	5.22	0.11	0.44	0.12	0.071
14R-2, 27–31	164.57	Silt	59.02	0.89	16.00	7.52	0.11	4.34	3.48	3.14	1.70	0.22	3.58	99.86	2.88	0.48	0.27	0.05	0.049
15R-1, 93–95	173.43	Clay	58.70	0.96	16.98	7.41	0.11	4.31	2.60	3.13	2.08	0.23	3.48	99.15	4.05	0.95	0.22	0.00	0.020
16R-1, 15–17	182.35	Clay	62.32	0.92	14.87	6.39	0.11	3.17	4.19	3.21	1.43	0.22	3.17	100.32	2.61	1.21	0.17	0.22	0.017
17R-1, 82–86	192.72	Clay	60.02	0.88	14.19	7.29	0.12	6.72	0.72	2.85	0.20	0.20	6.80	100.08	3.42	7.19	0.40	0.00	0.031
18R-1, 76–80	202.36	Clay	56.75	0.93	17.25	8.74	0.12	5.03	1.89	3.25	2.17	0.19	3.68	99.78	4.59	0.26	0.33	0.20	0.044
19R-2, 78–82	213.58	Silt	60.32	0.90	15.85	7.25	0.11	3.92	2.55	3.47	1.89	0.20	3.55	99.57	3.15	0.77	0.22	0.21	0.023
21R-1, 129–131	231.89	Clay	61.35	0.87	15.85	6.70	0.09	3.41	2.38	4.44	1.75	0.22	2.95	100.66	2.79	0.26	0.25	0.30	0.026
22R-1, 124–127	241.54	Silt	59.17	0.91	16.52	7.58	0.11	3.88	2.28	4.19	1.76	0.22	3.38	101.17	2.25	0.26	0.29	0.25	0.039
24R-2, 33–37	261.03	Clay	56.44	0.96	17.37	8.64	0.11	4.36	1.91	3.94	2.17	0.22	3.88	100.39	3.78	0.18	0.43	0.35	0.052
25R-1, 51–54	269.31	Clay	56.28	0.94	17.85	8.76	0.11	4.35	1.73	3.73	1.92	0.21	4.14	100.28	3.51	0.22	0.48	0.31	0.051
26R-1, 66–68	275.16	Clay	56.19	0.97	17.18	8.63	0.11	4.55	2.10	4.20	1.76	0.22	4.09	100.79	3.51	0.40	0.35	0.07	0.056
27R-2, 87–90	286.47	Clay	54.40	0.97	17.94	9.29	0.12	4.96	1.86	3.66	1.97	0.22	4.62	100.67	4.50	0.26	0.42	0.37	0.062
28R-3, 27–29	297.07	Clay	55.80	0.96	17.04	8.54	0.12	4.67	2.55	4.06	1.70	0.22	4.36	99.76	3.78	0.73	0.36	0.22	0.042
29R-1, 58–61	303.98	Silt	60.27	0.94	15.92	7.31	0.10	3.79	2.28	4.27	1.50	0.21	3.41	100.88	3.24	0.44	0.25	0.24	0.047
30R-2, 74–77	315.34	Silt	60.85	0.90	15.72	7.07	0.11	3.73	2.26	3.90	1.72	0.26	3.47	100.62		0.51			
31R-2, 102–105	325.22	Clay	55.88	0.93	17.41	8.53	0.11	4.46	2.23	3.58	2.05	0.23	4.58	100.66	3.78	0.51	0.39	0.24	0.041
33R-2, 71–73	334.61	Clay	55.63	0.96	17.66	9.07	0.13	4.97	1.74	3.73	2.01	0.21	3.89	99.95	4.23	0.15	0.34	0.24	0.048
35R-1, 124–127	342.54	Silt	63.03	0.91	15.19	6.56	0.10	3.13	2.20	3.35	1.84	0.19	3.49	99.98	3.15	0.66	0.37	0.45	0.046
37R-2, 115–119	353.45	Silt	57.30	0.90	16.72	9.00	0.11	4.34	2.29	3.12	2.17	0.22	3.84	99.74	3.96	0.70	0.34	1.03	0.056
39R-2, 48–50	362.38	Clay	56.97	0.99	16.39	8.26	0.11	4.45	2.58	3.20	1.85	0.21	5.00	101.07	3.69	0.77	0.30	0.28	0.033
41R-2, 89–91	377.29	Silt	53.83	1.00	18.02	8.94	0.16	5.09	2.44	2.65	2.47	0.21	5.18	100.43	4.59	0.73	0.50	0.29	0.069
43R-2, 9–12	386.29	Clay	56.21	0.96	17.50	8.40	0.13	4.53	2.34	2.56	2.37	0.21	4.80	100.44	4.50	0.62	0.45	0.34	0.068
45R-2, 42–44	396.22	Clay	54.83	1.00	17.44	9.12	0.10	5.37	2.20	2.91	2.23	0.21	4.60	100.64	4.32	0.51	0.33	0.22	0.035
47R-2, 5–8	405.55	Clay	56.12	0.94	17.31	8.51	0.11	5.13	2.33	2.70	2.22	0.22	4.43	100.09	4.14	0.59	0.38	0.25	0.042
49R-2, 45–47	415.65	Sand	65.43	0.54	14.67	3.55	0.07	1.44	6.34	2.69	0.79	0.09	4.39	100.80	2.88	1.58	0.09	0.17	0.010
51R-1, 28–30	423.68	Clay	56.31	0.99	16.88	9.22	0.12	5.19	2.56	3.02	2.00	0.22	3.49	99.80	3.87	0.55	0.24	0.56	0.046
53R-1, 24–26	433.04	Clay	55.83	0.97	17.58	9.01	0.11	4.93	2.50	3.25	1.78	0.21	3.82	100.61	3.96	0.33	0.32	0.22	0.033
55R-1, 25–27	442.25	Silt	54.93	0.78	13.21	5.27	0.17	2.22	11.48	3.44	0.49	0.20	7.82	99.80	1.98	6.89	0.22	0.00	0.005
61R-1, 113–115	491.63	Silt	62.43	0.76	14.30	7.63	0.13	5.36	2.48	3.72	0.06	0.17	2.95	100.58	2.88	0.33	0.11	1.00	0.003
63R-1, 13–16	509.83	Silt	59.42	0.90	15.84	7.52	0.17	4.33	5.90	3.12	0.04	0.21	2.54	100.58	2.88	0.88	0.00	0.00	0.000
65R-1, 15–17	529.25	Silt	63.06	0.84	14.81	6.21	0.09	3.90	3.75	3.61	0.05	0.18	3.49	100.52	2.52	0.04	0.12	0.73	0.054
66R-1, 15–17	538.95	Silt	61.37	0.86	14.71	7.01	0.14	5.02	3.97	2.95	0.03	0.18	3.75	100.19	3.24	0.04	0.15	0.35	0.029
67R-1, 55–57	548.95	Silt	72.39	0.61	10.10	5.21	0.12	4.10	1.94	2.10	0.06	0.12	3.24	100.71	2.88	0.04	0.01	0.26	0.046
139-857D-																			
1R-1, 128–130	582.78	Silt	71.64	0.47	9.11	7.30	0.14	6.21	0.81	1.36	0.00	0.12	2.84	101.33					
31R-1, 95–98	869.45	Sand	67.29	0.54	12.51	6.18	0.11	0.00	11.72	0.16	0.00	0.12	1.38	100.74	0.85	0.95	0.00	0.00	0.001
37R-1, 21–23	926.71	Sand	63.91	0.67	14.96	6.81	0.11	1.66	8.10	2.52	0.00	0.17	1.10	100.17	1.53	1.21	0.00	0.60	0.001

471.0 to 482.0 mbsf that decreases to a relatively steady range of 0.003 to 0.009 below 490.0 mbsf. This lower range of values is one to two orders of magnitude lower than the susceptibility (10^{-2}) of typical mid-ocean ridge basalts (Carmichael, 1982). Six thermally altered, mostly turbiditic sediment packages, often associated with baked margins, were identified within the sill sequence between Cores 139-857C-59R and -68R (471.1–558.0 mbsf). The drilled sediment sequences range in thickness from about 0.25 to 0.55 m (and can be identified by their spiky VMS character and low values, which range from 0.0004 to 0.002). Their true thicknesses cannot be estimated from recovered core but can be determined from borehole logs. Very low VMS distinguishes the sediment immediately above and below the sills. The sediment interbeds exhibit even lower VMS than does the sediment well above the sill complex, possibly due to the effects of higher temperature alteration near the intrusions.

VMS data from Hole 857D are not plotted because they are of poor quality and lack depth control, but the trend of decreasing susceptibility with depth appears to hold. The percentage of core

Table 18. Minor and trace element composition (in ppm) of sediment samples from Site 857.

Core, section, interval (cm)	Depth (mbsf)	Ba	Ce	Cr	Cu	Nb	Ni	Rb	Sr	V	Y	Zn	Zr
139-857A-													
1H-2, 80–84	4.20	662	26	80	48	12	42	91	271	162	26	106	173
2H-2, 73–75	13.63	663	8	106	62	10	68	65	266	182	22	123	140
4H-2, 86–90	24.26	742	14	103	45	11	56	68	276	160	22	118	190
5H-3, 78–82	35.18	891	14	103	47	13	61	104	244	157	21	130	147
6H-4, 54–58	45.94	763	24	111	48	14	56	95	285	150	23	122	168
7H-3, 69–73	52.91	852	69	100	56	17	64	80	279	152	22	115	131
7H-3, 81–85	53.03	712	10	110	40	12	57	66	337	148	23	95	191
8H-2, 95–99	62.35	508	6	94	53	10	49	57	269	179	25	101	164
9H-2, 93–98	71.83	646	12	106	55	12	61	74	270	174	23	121	161
10H-2, 79–81	81.19	601	10	104	41	10	49	57	319	158	23	87	188
13X-3, 122–124	105.72	548	15	94	44	11	46	68	230	163	25	98	171
139-857C-													
2R-1, 63–67	57.13	655	9	108	54	12	75	71	292	171	23	134	165
3R-2, 90–92	68.90	705	71	94	54	17	48	71	265	153	22	97	140
3R-3, 38–40	69.88	515	10	105	52	10	50	61	250	187	25	102	152
5R-1, 4–8	82.14	345	6	67	35	6	30	42	229	113	16	57	102
6R-1, 66–68	86.86	546	6	102	57	9	58	66	215	187	22	115	133
9R-1, 27–30	114.77	618	5	91	58	11	46	78	248	188	22	121	154
9R-1, 31–34	114.81	703	58	87	61	15	44	65	231	184	25	109	121
11R-1, 124–126	135.04	495	8	97	32	9	49	45	344	151	21	89	192
12R-1, 80–83	144.30	608	7	108	57	10	59	62	215	199	24	114	140
13R-2, 48–51	155.08	529	14	103	58	9	59	61	219	190	22	122	131
14R-2, 27–31	164.57	541	5	77	40	9	33	41	385	165	21	84	167
15R-1, 93–95	173.43	515	4	95	52	9	48	56	272	186	22	103	145
16R-1, 15–17	182.35	497	4	96	33	9	36	36	352	157	23	63	202
17R-1, 82–86	192.72	597	5	86	48	9	49	56	234	165	24	101	120
18R-1, 76–80	202.36	552	6	104	55	10	59	63	228	185	22	121	138
19R-2, 78–82	213.58	530	14	99	43	11	47	57	251	171	23	100	163
21R-1, 129–131	231.89	532	5	98	36	10	41	48	252	156	23	87	122
22R-1, 124–127	241.54	529	17	104	41	10	47	49	230	166	24	102	159
24R-2, 33–37	261.03	517	13	108	55	10	60	55	189	191	24	122	142
25R-1, 51–54	269.31	535	16	111	52	10	62	64	187	187	22	125	141
26R-1, 66–68	275.16	471	12	96	56	9	55	50	168	184	24	121	136
27R-2, 87–90	286.47	535	10	110	60	10	65	58	167	206	24	141	136
28R-3, 27–29	297.07	487	9	99	57	10	52	50	185	188	25	123	142
29R-1, 58–61	303.98	470	16	90	47	10	39	40	200	168	23	86	164
30R-2, 74–77	315.34	558	19	99	35	11	46	50	208	163	25	92	186
31R-2, 102–105	325.22	616	10	108	57	10	58	61	200	189	24	117	137
33R-2, 71–73	334.61	609	11	106	53	10	61	59	196	189	23	123	132
35R-1, 124–127	342.54	488	20	105	26	12	40	59	194	150	23	75	193
37R-2, 115–119	353.45	537	21	118	47	11	66	67	176	163	22	104	160
39R-2, 48–50	362.38	509	20	113	52	11	47	57	312	270	24	81	161
41R-2, 89–91	377.29	596	14	113	47	11	54	74	161	213	24	94	136
43R-2, 9–12	386.29	546	9	115	50	10	55	69	156	193	24	107	137
45R-2, 42–44	396.22	494	9	132	38	10	67	64	166	206	24	91	140
47R-2, 5–8	405.55	471	7	124	39	8	77	53	158	163	20	84	122
49R-2, 45–47	415.65	408	0	37	8	4	9	18	277	105	13	17	154
51R-1, 28–30	423.68	570	7	122	41	10	57	52	201	197	25	90	150
53R-1, 24–26	433.04	536	2	116	51	9	63	48	229	206	25	106	146
55R-1, 25–27	442.25	181	8	89	25	7	34	13	296	130	24	52	178
57R-1, 16–18	451.86	72	18	93	7	8	45	1	266	141	21	58	149
61R-1, 113–115	491.63	281	13	72	6	7	21	4	359	107	18	49	223
63R-1, 13–16	509.83	38	17	90	9	8	38	1	408	177	23	66	178
65R-1, 15–17	529.25	68	28	85	8	10	38	1	341	144	23	51	211
66R-1, 15–17	538.95	73	24	94	28	9	42	1	341	173	22	91	185
67R-1, 55–57	548.95	54	24	61	11	6	16	1	154	105	14	63	155
139-857D-													
1R-1, 128–130	582.78	7	7	46	5	5	21	0	57	93	14	57	100
3R-2, 125–127	602.02	32	14	87	7	8	47	1	279	170	23	77	141
4R-2, 58–60	610.98	9	16	83	12	7	40	0	311	174	20	59	141
10R-1, 19–21	666.79	37	16	74	11	8	30	1	309	127	21	44	192
15R-1, 76–78	715.56	59	17	78	7	9	37	1	318	169	25	71	177
16R-1, 77–79	725.27	77	29	86	7	9	29	1	313	150	23	77	186
17R-3, 11–13	736.95	46	16	139	7	9	81	1	346	0	22	60	179
24R-1, 54–56	801.74	60	17	90	12	9	38	1	318	145	23	72	205
24R-2, 100–103	803.70	35	0	274	22	6	57	0	228	270	28	41	129
26R-1, 16–19	820.46	26	0	302	163	6	63	1	168	295	29	56	126
28R-1, 20–23	839.10	66	15	99	5	9	44	1	256	186	29	54	201
29R-1, 30–33	848.70	20	10	61	8	6	16	1	304	132	15	30	165
31R-1, 95–98	869.45	37	55	50	11	5	0	0	646	166	16	0	175
34R-1, 44–48	897.94	75	11	83	83	9	4	1	371	198	24	110	150
37R-1, 21–23	926.71	26	8	66	10	5	20	1	359	143	18	23	157

Table 19. X-ray diffraction mineralogy for bulk samples from Hole 857A.

Core, section, interval (cm)	Quartz	Feldspar	Hornblende	Chlorite	Mica	Calcite
139-857A-						
1H-2, 80–84	***	*	*	*	*	*
2H-2, 73–75	***	*	*	*	*	*
4H-2, 86–90	***	*	*	*	*	
5H-3, 78–82	***	*	*	*	*	
7H-3, 81–85	******	**	*	*	*	*
8H-2, 95–99	***	*	*	*	*	*
9H-2, 93–98	***	*	*	*	*	*
10H-2, 79–81	******	***	*	*	*	*
13X-3, 122–124	***	***	*	*	*	*

Notes: Relative mineral abundances were determined by peak heights and are indicated as follows: * = trace, *** = minor, and ****** = major. Because peak heights are determined by mineral morphology in addition to mineral abundance, this table cannot be used to quantitatively determine the relative abundances of different minerals. See "Sediment Geochemistry and Alteration" section, "Explanatory Notes" chapter (this volume), for a description of X-ray diffraction methods.

Table 20. X-ray diffraction mineralogy for bulk samples from Hole 857C.

Core, section, interval (cm)	Quartz	Feldspar	Hornblende	Chlorite	Mica	Calcite
139-857C-						
2R-1, 63–67	***	***	*	*	*	*
3R-3, 38–40	***	***	*	*	*	*
5R-1, 4–8	***	*	*	*	*	********
5R-1, 59–61	***	***		*	*	
6R-1, 66–68	***	*		*		
9R-1, 27–30	***	***		*	*	
9R-1, 31–34	***	***		*	*	
11R-1, 124–126	******	**		*	*	*
12R-1, 80–83	***	*		*	*	
13R-2, 48–51	***	***		*	*	
14R-2, 27–31	******	******		*	*	
15R-1, 93–95	***	***		*	*	*
15R-2, 97–99	******	******		*	*	*
16R-1, 15–17	******	******		*	*	*
17R-1, 82–86	***	***		*	*	******
18R-1, 76–80	***	***		*	*	
19R-2, 79–82	******	******		*	*	
21R-1, 129–131	***	******		*	*	
22R-1, 124–127	***	******		***	*	
24R-2, 33–37	***	******		***	*	
25R-1, 51–54	***	******		***	*	
26R-1, 66–68	***	******		***	*	
27R-2, 87–90	***	******		***	*	
28R-3, 24–29	***	******		*	*	
30R-2, 74–77	***	******		*	*	*
31R-2, 102–105	***	******		*	*	
33R-2, 71–73	***	******		***	*	
35R-1, 124–127	******	******		*	*	*
37R-2, 115–119	***	******		*	*	*
39R-2, 48–50	***	******		***	*	*
41R-2, 89–91	***	******		***	*	*
43R-2, 9–12	***	******		***	*	*
44R-1, 41–43	***	******		******	*	
44R-2, 27–31	***	******		***	*	*
45R-1, 23–25	***	******		***	*	*
45R-2, 42–44	***	******		***	*	*
46R-1, 94–97	***	******		***	*	
46R-2, 142–146	***	***		***	*	
47R-1, 43–45	***	******		******	*	*
47R-2, 60–63	***	******		***	*	
48R-1, 73–75	***	******		******	*	
48R-2, 116–119	***	******		***	*	
49R-1, 123–125	***	******		***	*	*
50R-1, 121–123	***	***		***	*	
51R-1, 28–30	***	******		***	*	
52R-CC, 10–12	***	******		******	*	
53R-1, 24–26	***	******		***	*	
55R-1, 25–27	******	******		***	*	******
57R-1, 16–18	******	********		***	*	
61R-1, 113–115	******	******		***		
63R-1, 13–16	***	***		***		

Notes: Relative mineral abundances were determined by peak heights and are indicated as follows: * = trace, *** = minor, ****** = major, and ******** = dominant. Because peak heights are determined by mineral morphology in addition to mineral abundance, this table cannot be used to quantitatively determine the relative abundances of different minerals. See "Sediment Geochemistry and Alteration" section, "Explanatory Notes" chapter (this volume), for a description of X-ray diffraction methods.

recovered was lower than that from Hole 857C; usually only one section per core was available for whole-round analyses. Also, the scans were made on uncurated sections, which rendered them uncorrelatable with other measurements made on samples from the curated working halves (plastic spacers were inserted between each piece during curation, increasing total recovered length). The MST data were used only as a qualitative indicator of, for example, the sudden appearance of fresh basalt in an otherwise altered sequence.

GRAPE Bulk Density

GRAPE wet-bulk density data from whole-round sections are shown in Figures 68, 69, and 70 for Holes 857A, 857B, and 857C, respectively. Both GRAPE and PWL measurements were discontinued after Core 139-857A-10H.

An overall increase in GRAPE wet-bulk density with depth is observed in Hole 857A (Fig. 68). Density averages 1.70 g/cm^3 from 2.0 to 20.0 mbsf, increases to 1.80–1.85 g/cm^3 by 36.0 mbsf and remains at 1.85–1.90 g/cm^3 from 43.0 to 56.0 mbsf. Average values of 1.90 to 1.95 g/cm^3 are observed throughout the remainder of the hole. Several excursions to lower densities are apparent. The zones of less scatter in the VMS record (correlated with regions of few to no turbidites in the core descriptions) are also recognizable in the GRAPE record. Intervals from 36.5–40.0 mbsf and 77.5–79.0 mbsf seem to exhibit less scatter in density than do turbidite-rich zones.

GRAPE densities in Hole 857B increase rapidly from a mudline value of 1.35 g/cm^3 to 1.55 g/cm^3 at 1.5 mbsf and stay at this value until 8.0 mbsf. Values decrease to 1.55 g/cm^3 at 11.0 mbsf and increase again to 1.70 g/cm^3 at 12 mbsf. A decrease in densities to 1.65 g/cm^3 follows; the next cored interval, from 21.0 to 30.5 mbsf, has GRAPE densities of 1.65 g/cm^3 to 1.80 g/cm^3 at 30 mbsf. The data generally agree quite well with trends observed in the upper 30 m of Hole 857A.

Poor core recovery throughout most of Hole 857C resulted in a spotty GRAPE wet-bulk density record. These data were also degraded due to RCB coring but still show density trends with depth. After the mudline core was collected, Hole 857C was washed to 56.5 mbsf. Densities ranged from 1.60 to 1.90 g/cm^3 to about 115.0 mbsf and become more variable with increasing depth. The overall trend reveals low density values of 1.60–1.65 g/cm^3, increasing gradually with depth, and local maxima of 2.10–2.15 g/cm^3, which may correlate with the bases of turbidites. The highest value of 2.15 g/cm^3 occurs at 385.0 mbsf, and is followed by low values of 1.80–2.00 g/cm^3. Values increase steadily with depth from about 1.90 to 2.05 g/cm^3 at 440.0 mbsf. The sill complex is characterized by densities of 2.30–2.55 g/cm^3 in the upper section; values decrease steadily to 2.20–2.40 g/cm^3 by 520.0 mbsf. A sharp decrease in density to less than 2.20 g/cm^3 is seen at 530.0–545.0 mbsf, the location of a fairly thick sediment interbed.

GRAPE data from Hole 857D are not plotted for reasons discussed previously in the magnetic susceptibility section. However, a very general trend of lower densities in the sediment and higher densities in the igneous rock was observed.

PWL Velocity

P-wave logger velocity data from whole-round sections are shown in Figures 68 (Hole 857A) and 69 (Hole 857B). Whole-core compressional wave velocities in Hole 857A show an increase with depth that is commensurate with the GRAPE wet-bulk density trend. Velocity increases from about 1480 m/s at the top of the hole to 1530–1540 m/s at 50.0 mbsf. A relatively sharp increase to a velocity of 1600 m/s occurs at 87.0 mbsf. More scatter in the data is apparent in the deeper part of the section than in the upper 30 m.

Table 21. X-ray diffraction mineralogy for bulk samples from Hole 857D.

Core, section, interval (cm)	Quartz	Feldspar	Chlorite	Actinolite	Epidote
139-857C-					
1R-1, 128–130	******	***	******		
3R-2, 125–127	******	******	***		
4R-2, 58–60	******	*	*		
10R-1, 19–21	******	******	******		******
15R-1, 76–78	******	******	******		
16R-1, 77–79	******	******	******		
17R-3, 11–13	******	******	***		******
21R-1, 130–132	******	******	******		
24R-1, 54–56	******	******	******		
28R-1, 20–23		**********	*	******	
29R-1, 30–33	******	******	******		******
34R-1, 47–48	***	******	***		
36R-1, 26–28	***	********	******		
37R-1, 21–23	******	******	*		******

Note: Symbols same as in Table 20.

The PWL record in Hole 857B extends from 0.0 to 30.5 mbsf and shows an increase in velocity from 1480 m/s at 0.0–5.0 mbsf to about 1510 m/s at 25.0 mbsf. Velocity drops back to 1495 m/s by 30.0 mbsf.

Index Properties

Index properties data for Site 857 samples are given in Tables 28–32 and Figure 71 (Hole 857A), and Tables 33–34 and Figure 71 (Hole 857B), Tables 35–39 and Figure 72 (Hole 857C), and Tables 40–42 and Figure 73 (Hole 857D). Limited samples were taken from Hole 857B; velocity and thermal conductivity data from Hole 857B are plotted with Hole 857A data.

Wet-bulk density values in Hole 857A average 1.58 g/cm^3 in the upper 18.2 mbsf and then increase to 1.81 g/cm^3 by 77.6 mbsf. The data from 77.6 to 105.6 mbsf exhibit more scatter and have an average of 1.86 g/cm^3. Grain densities average 2.74 g/cm^3 to 46.0 mbsf and increase to 2.75 g/cm^3 by 105.6 mbsf. Porosity and water content trends follow each other well with depth. The average porosity is 70% in the upper 18.2 m of the hole and decreases to 59% at 46.0 mbsf. Values of 58% exist from 52.9 mbsf to 105.6 mbsf.

Hole 857C wet-bulk densities increase steadily with depth from 1.64 g/cm^3 at 57.2 mbsf to 2.23 g/cm^3 at 261.1 mbsf. Values increase more gradually with depth to 2.35 g/cm^3 over 402.0–451.8 mbsf. The sill complex from 471.1 to 560.1 mbsf is characterized by higher bulk densities of 2.50 g/cm^3 in the two samples obtained from a major sediment interbed to 2.88 g/cm^3 in the diabase; the basement data show more scatter than the sediment values. Recovery of sediment was very low in contrast to the amount of igneous rock cored. Grain densities are remarkably uniform with depth and average 2.79 g/cm^3 to 451.8 mbsf. Values decrease slightly, to 2.75 g/cm^3, between 144.2 and 269.3 mbsf. Higher grain densities of 2.94 g/cm^3 characterize the diabase sills; interbedded sediments have lower values. Both porosity and water content decrease with depth in a complementary manner throughout the sedimentary section. Porosity of 62.5% from 57.2 to 86.5 mbsf decrease sharply to 34% at 114.9 mbsf and then averages 47.6% by 261.1 mbsf. The trend flattens out at 39% from 261.1 to 304.0 mbsf and decreases to 30.1% just above the base of the sediment section. Porosities in the sill complex are 3.9% at 472.1 mbsf and increase to 8.9% by 520.1 mbsf. The higher values at 538.9 and 539.2 mbsf are from the sediment interbed.

The ratio of recovery of sediment to igneous material increased for Hole 857D; the cores contained roughly 50% of each rock type. A more detailed study of the variation in index properties was thus possible. The range of wet-bulk density values with depth was very constant throughout the hole, with sediments having a mean density

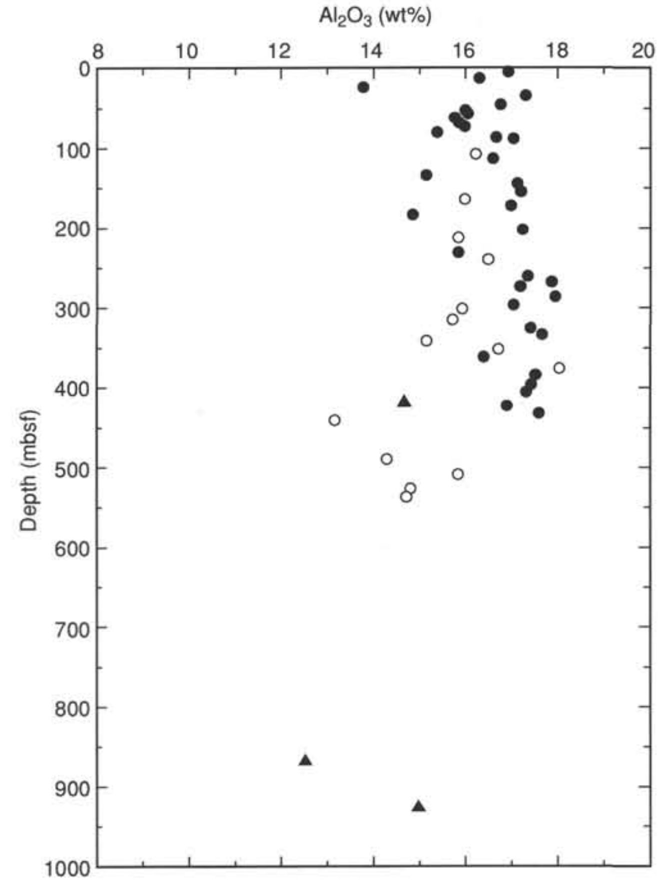

Figure 37. Weight percentages of Al_2O_3 vs. depth of sediment from Holes 857A, 857C, and 857D. Samples that are predominantly clay and silty clay are shown by filled circles, silt samples are shown by open circles, and sand samples are shown by triangles. Samples from depths less than approximately 400 m show variations with grain size that are typical of Middle Valley sediment. Larger variations at depths below approximately 400 m are related to hydrothermal metamorphism of the sediment. Sediment below approximately 470 m is interlayered with igneous sills of basaltic composition.

of 2.58 g/cm^3 and sills averaging 2.95 g/cm^3. These values agree well with those in the upper section of the sill complex cored from Hole 857C. Grain densities of the sediment, which average 2.76 g/cm^3, are more variable than in the upper part of the sequence. The average value for igneous rock of 2.94 g/cm^3 is similar to that seen in Hole 857C. Porosities throughout the section cored from Hole 857D generally decrease with depth and average 14.5% overall in the sediments; they are very consistent, with a mean value of 5.4%, in the sills. A sharp increase in porosity and water content is seen in the sediment data from 676.7 to 686.2 mbsf. Porosities in the sediments average 12.9% thereafter.

Thermal Conductivity

Thermal conductivity data for Holes 857A, 857B, 857C, and 857D are listed in Tables 31, 33, 38, and 42, respectively, and are shown in Figures 71E (for both Holes 857A and 857B), 72D, and 73D. The average thermal conductivity in the indurated sediments in Hole 857A is 1.0 W/(m·K) in the upper 15.5 mbsf and increases steadily to 1.17 W/(m·K) by 53.9 mbsf. A slight increase to 1.21 W/(m·K) is observed by 81.0 mbsf. Data between 82.7 to 108.0 mbsf have average values of 1.44 W/(m·K). Conductivities in the upper 12.7 m of Hole 857B were slightly higher, at 1.08 W/(m·K), and increase locally to 1.55 W/(m·K) by 30.3 mbsf.

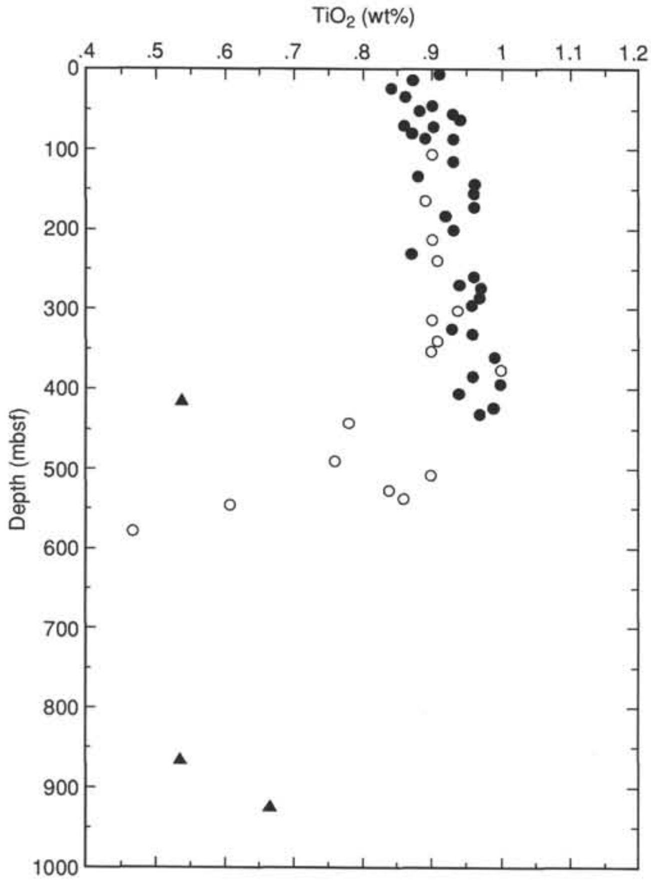

Figure 38. Weight percentages of TiO_2 vs. depth of sediment from Holes 857A, 857C, and 857D. Samples that are predominantly clay and silty clay are shown by filled circles, silt samples are shown by open circles, and sand samples are shown by triangles. Samples from depths less than approximately 400 m show variations with grain size that are typical of Middle Valley sediment. Larger variations at depths below approximately 400 m are related to hydrothermal metamorphism of the sediment. Sediment below approximately 470 m is interlayered with igneous sills of basaltic composition.

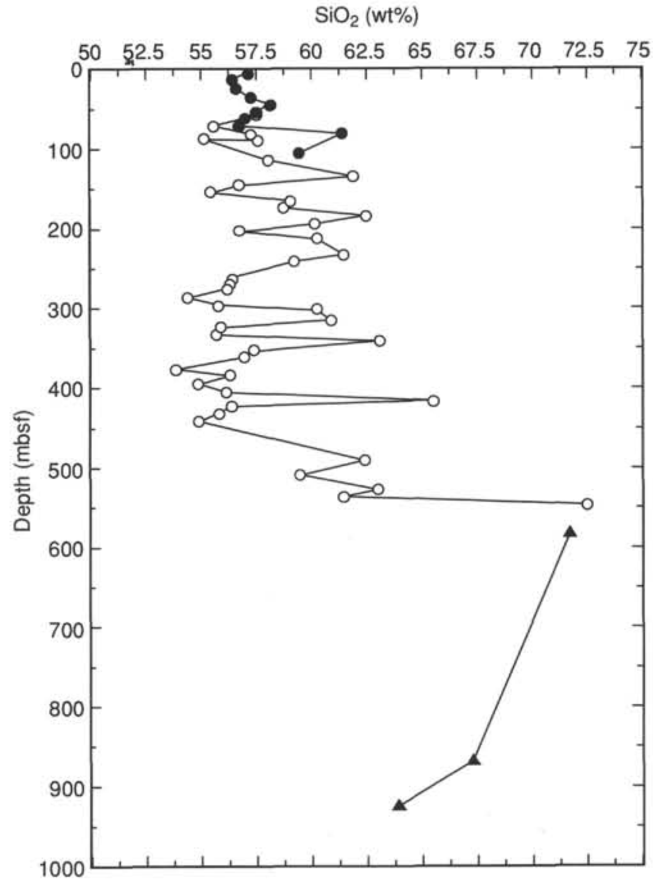

Figure 39. Vertical profile of SiO_2 content of sediment at Site 857. SiO_2 generally shows positive covariation with CaO and Na_2O and negative covariation with TiO_2, Al_2O_3, Fe_2O_3, MgO, K_2O, loss on ignition (LOI), Rb, Cu, and Zn in the shallow sediment (approximately 400 mbsf) above the zone of hydrothermal metamorphism. SiO_2 has been added to sediment in the zone of hydrothermal metamorphism. Symbols as in Figure 37.

Hole 857C sediment conductivity varies between 1.05 and 1.44 W/(m·K) from 0.0 to 88.0 mbsf and then increases to 1.66 W/(m·K) at 115.5 mbsf. Full-space measurements were discontinued at 157.0 mbsf due to lithification of the cores and the half-space technique was used for the remainder of the hole. Data scatter is accentuated from 155.7 to 202.3 mbsf, with values ranging from 0.94 to 1.79 W/(m·K); thermal conductivity increases steadily with depth below 202.3 mbsf to 1.95 W/(m·K) from 401.8 to 442.0 mbsf. The increase in thermal conductivity with depth correlates with decreases in porosity and water content. The indurated sediments have conductivities similar to those of the underlying igneous rock (1.91 W/(m·K), Fig. 72D); these sediments have high conductivities due to low porosities and perhaps due to high-temperature diagenetic cementation of clay and coarser grained material.

Figure 74 shows thermal conductivity vs. porosity for sediment from Holes 857A and 857C. The relationship between these parameters can be described by the geometric mean of two end-members, solid grains, and seawater, assuming a constant grain thermal conductivity (see "Physical Properties" sections, "Site 855" and "Site 856" chapters). A best-fit grain thermal conductivity for Site 857 sediment samples is 3.12 W/(m·K). This value fits the data from Hole 857C quite well but is arguably low for data from Hole 857A. The grain thermal conductivity may be uniformly higher in Hole 857A (i.e., in the upper part of the section). The sediment grain conductivity is considerably lower than the values calculated for Sites 855 (3.5 W/[m·K]) and 856 (3.64 W/[m·K]) for reasons not yet understood; the higher heat flow/thermal gradient at Site 857 may play a role. The three values determined for igneous rock were excluded from this fitting process.

The sill complex in the lower 96 m of Hole 857C is characterized by an average thermal conductivity of 1.91 W/(m·K) with a range of 1.59–2.21 W/(m·K). There is little contrast in thermal conductivity between the sediment and igneous rock at this level (Fig. 72D). Sediment and igneous rock values show more contrast deeper in the sequence, as shown in Figure 73D for Hole 857D. The average thermal conductivity of the sediment interbeds is 2.37 W/(m·K); the sills have a mean conductivity of 1.97 W/(m·K). The sediment data are more variable and suggest a gradual increase in conductivity with depth.

Compressional Wave Velocity

The high degree of sediment induration at Site 857 is apparent in the velocities measured by the PWL in whole-round scans and by the DSV and HFV on discrete samples. Velocity profiles are presented in Figures 68 and 71A for Hole 857A, Figures 69 and 71A for Hole 857B (plotted with Hole 857A data), Figure 75A for Hole 857C and Figure

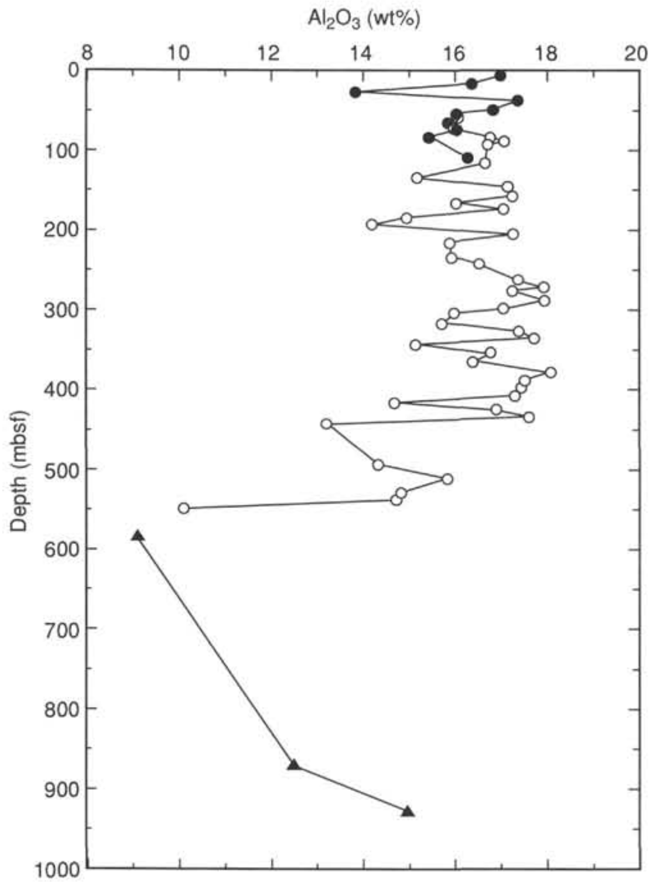

Figure 40. Vertical profile of Al_2O_3 content of sediment at Site 857. Variations in the Al_2O_3 content of sediment primarily reflect changes in the clay content and changes in sediment bulk density as the sediment becomes increasingly indurated at depth. Symbols as in Figure 37.

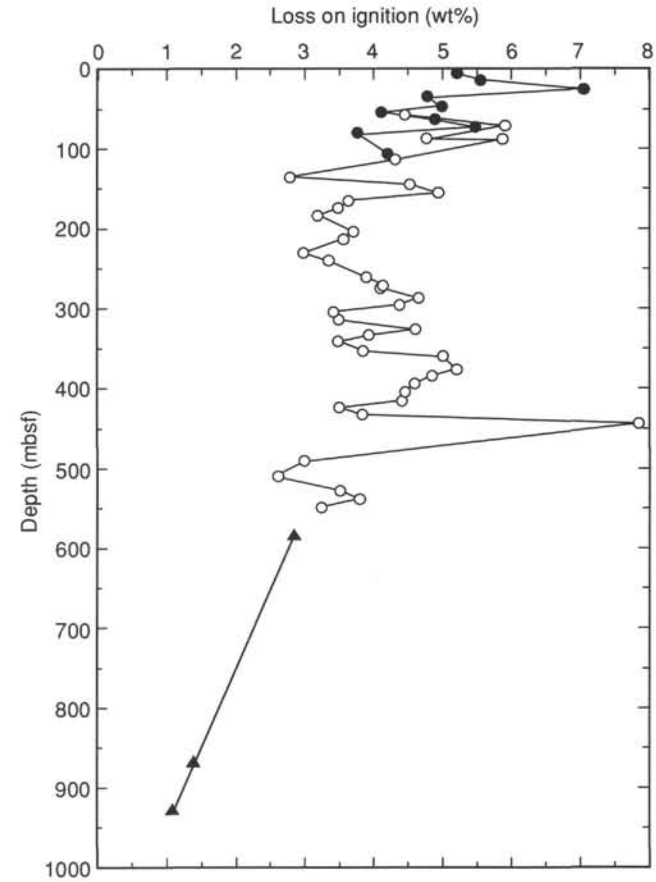

Figure 41. Vertical profile of LOI content of sediment at Site 857 showing both a relative decrease in the clay component with depth and the effects of increasing lithification of the sediment. Symbols as in Figure 37.

76A for Hole 857D. Velocity measurements are also listed in Tables 29 and 30 (Hole 857A), Table 34 (Hole 857B), Tables 36 and 37 (Hole 857C), and Table 41 (Hole 857D).

The DSV was used from Hole 857A until sediments became too lithified for blade penetration at 92.2 mbsf. An average velocity of 1521 m/s was observed from 0.0 to 20.6 mbsf. The interval from 22.7 to 29.1 mbsf is a turbidite/ hemipelagic clay sequence with velocities of 1557 m/s in the clay to 1715 m/s in the turbidite sand; the high value was confirmed by measurement on a sample in the same lithologic unit with the HFV (Fig. 71A). Other basal turbidite sample velocities were measured at 60.9 mbsf (1667 m/s) and at 86.8 mbsf (1673 m/s). DSV velocities in the clay gradually increase with depth in response to lithification and average 1645 m/s over 76.2–85.7 mbsf.

HFV velocities in Hole 857A are highly variable, ranging from 1541 m/s (92.2 mbsf) to 1677 m/s (106.3 mbsf). Sandy parts of turbidites are probably under-represented in XCB cores in comparison to APC cores from similar depths in nearby holes. Analysis of core photos and visual core descriptions from 92.2–108.1 mbsf shows that XCB cores are seriously disturbed by drilling (see "Lithostratigraphy and Sedimentology" sections in this chapter and in the "Site 855" and "Site 856" chapters). Data from Core 139-857A-12X (92.2 mbsf) and Sections 139-857A-13X-2 (104.3 mbsf) and -13X-3 (105.6 mbsf) were likely influenced by drilling disturbances. If the data obtained from disturbed samples are disregarded, the average velocity increases and is consistent with those obtained for clay and sandy turbidite samples in the interval from 50.2 to 86.8 mbsf. This velocity trend also is consistent with the trends of porosity, water content, wet-bulk density, and grain density at the same depths.

Only three measurements were made with the DSV in Core 139-857B-1H. Velocities increased from 1504 m/s in soupy mud at 1.0 mbsf to 1543 m/s at 2.5 mbsf.

Compressional wave velocities increase throughout Hole 857C, as shown in Figure 75A. All data were collected with the HFV perpendicular to the axis of the core (in the transverse, or "c," direction) using half-round core pieces until 153.5 mbsf, where the sediment became lithified enough for cubes to be cut. Velocities were then measured both in the transverse direction on half-round pieces of rock and in all three directions ("a" is parallel to core axis; "b" and "c" are perpendicular to core axis) on cube samples. As the cores were not oriented in space in an absolute sense, the measurements in the b- and c-directions were combined as the mean horizontal velocity, v_H.

The upper 56.5 mbsf in Hole 857C were washed so no data are available. The shallowest horizontal velocities, from 57.2 to 87.9 mbsf, average 1645 m/s. Velocities begin to increase at 114.9 mbsf, below which they increase to 2210 m/s at 241.5 mbsf. Velocities in the vertical direction increase also, but at a lesser rate of from 1943 m/s at 269.3 mbsf to 2665 m/s at 399.9 mbsf. Vertical velocities decrease to 2468 by 442.0 mbsf. The increase in velocity with depth in the sediments from Hole 857C may result from compaction due to burial and induration due to the high thermal gradient, which also promotes diagenetic cementation. Although the dominant (>50%) lithology is claystone, the percentages of siltstone and sandstone increase with depth (see "Lithostratigraphy and Sedimentology" section, this chapter). These coarser sequences are progressively cemented with carbonate, especially near nodule-rich zones at depths less than 250 mbsf. Feldspar grains in the clastic sediment are transformed into clay minerals below 400 mbsf. The velocity signature

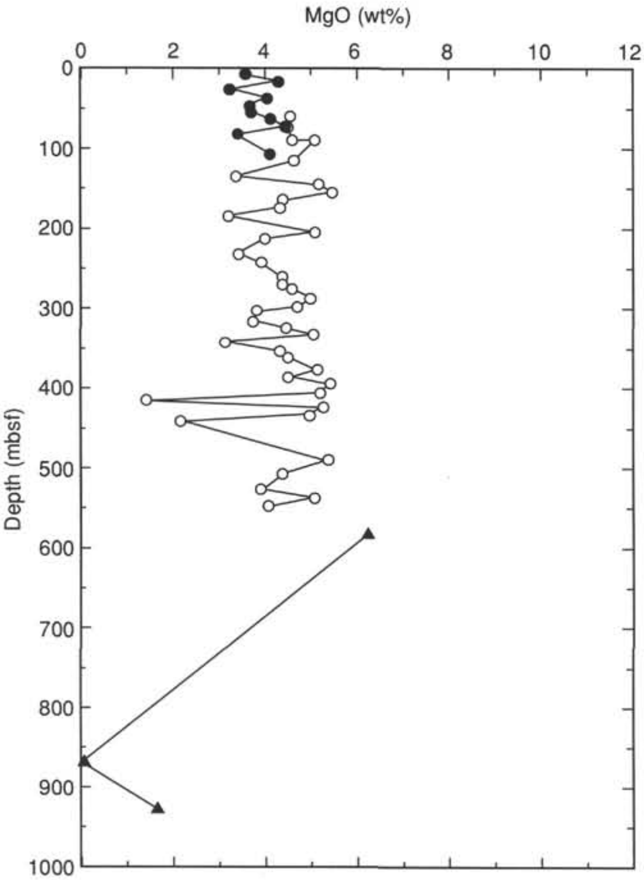

Figure 42. Vertical profile of MgO content of sediment at Site 857. MgO is relatively constant or increases slightly with depth. MgO shows positive covariation with Fe_2O_3, Al_2O_3, and TiO_2, suggesting control by the content of detrital chlorite in the sediment. Symbols as in Figure 37.

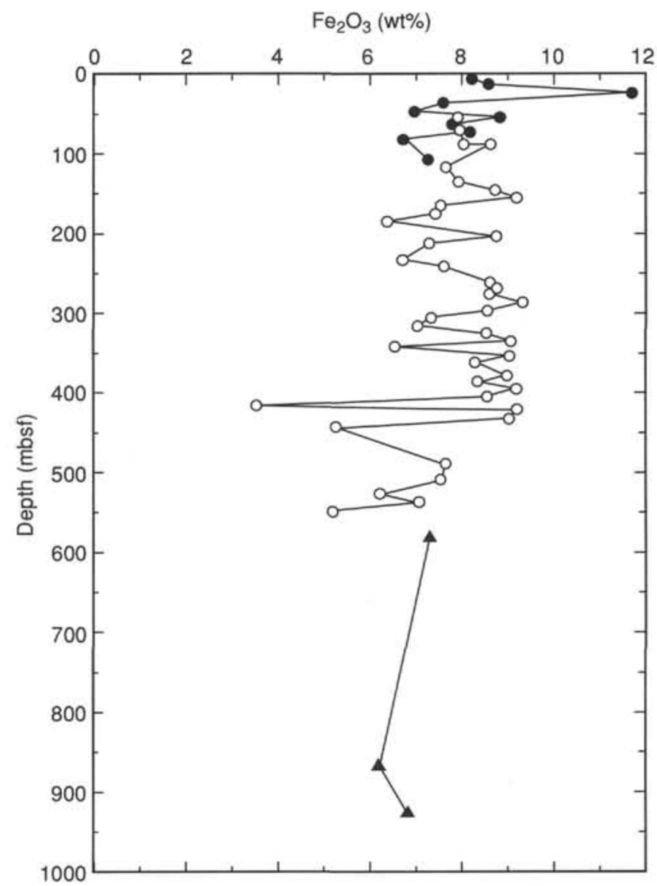

Figure 43. Vertical profile of Fe_2O_3 content of sediment at Site 857, which is approximately constant with depth. Symbols as in Figure 37.

may be due less to compaction and dewatering of clay and more to recrystallization of clay under high temperatures. An explanation for the locally slower velocities in all directions at 367.7–385.3 mbsf is not apparent; these occur below a zone of no core recovery. Slight changes in the trends of wet-bulk density, porosity, and water content data can be seen as well below the data gap; no change in the grain density profile is apparent.

The range in horizontal velocities obtained with both measurement techniques in the igneous rocks of the sill complex was large, from 4500 m/s to 5200 m/s just below 472 mbsf and decreasing to 4500 m/s at 520 mbsf and 3900 m/s at 560 mbsf (Fig. 76A). Velocities from sediment cubes are lower and appear more variable in the horizontal direction, averaging 3345 m/s, than in the vertical direction, where the mean velocity is 3132 m/s. The average horizontal velocity from half-round pieces is 3079 m/s; these data may not be as reliable as cube data due to irregular sample geometry and the possible presence of hidden fractures. The scatter in the velocity data is most likely due to variations in porosity and density in the diabase and the interbedded sediment, and the presence of alteration and open and filled fractures; the sill interbeds are pervasively cemented with silica (see "Lithostratigraphy and Sedimentology" and "Igneous Petrology and Geochemistry" sections, this chapter).

Velocity in both the sediments and igneous rocks increases with depth in Hole 857D (Fig. 76A); the average velocities for both measured near the top of the cored section (581.5 mbsf) are considerably higher than those at the bottom of Hole 857C at 561.3 mbsf. Sediment and igneous-rock velocities measured on working-half pieces and cubes generally fall into two distinct velocity populations. Vertical sediment velocities range from 4080 m/s at 582.8 mbsf to an average of 4087 m/s between 839.2 and 868.8 mbsf; vertical velocities in the sills increase to 5626 m/s at 907.9 mbsf from an average of 5004 m/s in the upper 10 m of the complex (590.3–600.6 mbsf). Average horizontal velocities are 4057 m/s for sediment cubes and 5513 m/s for igneous rock cubes. Horizontal values from working-half samples have means of 3831 m/s for sediments and 5104 m/s for the sills; the differences in the data ranges can be explained by the difference in sample size and geometry and the discrimination techniques used to select cube samples (i.e., no obvious surficial microcracks).

Some of the apparent scatter in Figure 76A is related to measurement error; however, close inspection of detailed measurements between, for example, 730.0 and 750.0 mbsf reveals the inherent variation of velocities within a cored section of igneous rock and sediment (Fig. 76B). Sediment velocity variability is greater than that in the sills throughout the sill complex.

Velocity Anisotropy in Hole 857C

Velocity anisotropy was calculated as the difference between the horizontal velocity (v_H: average of v_b and v_c) and the vertical velocity (v_a) divided by the average velocity (see "Physical Properties" section, "Explanatory Notes" chapter, this volume). Transverse velocities are, on average, about 20% higher than vertical velocities in the sedimentary section of Hole 857C above the sills; anisotropy reaches 24% to 28% below 400.0 mbsf. Anisotropy data for the lower 175 m of sediments and the sill complex from 471.1 to 561.4 mbsf are shown in Figure 75B. The variation in anisotropy between sediment and igneous rock is more apparent for Hole 857D (Fig. 76C) due to the greater recovery of sediment relative to sill material.

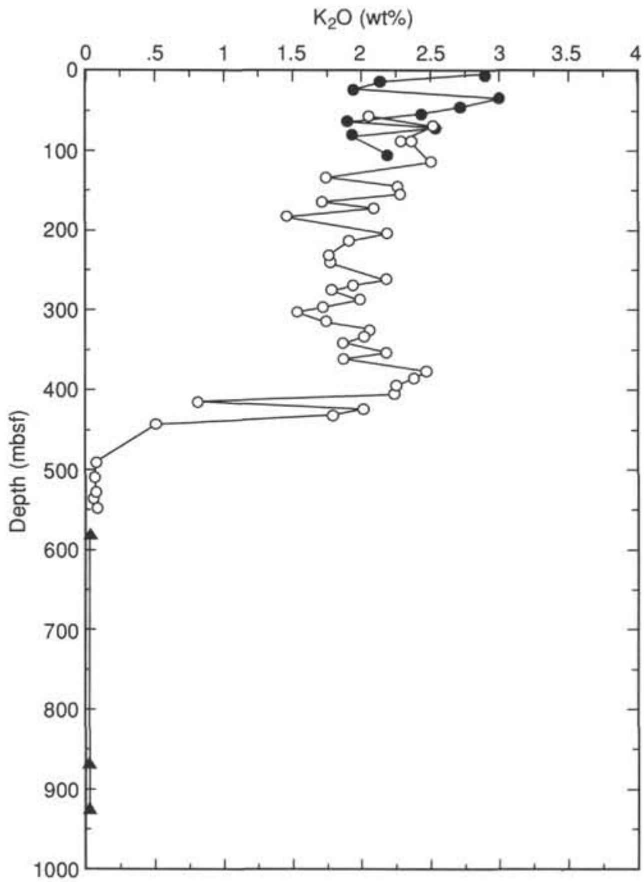

Figure 44. Vertical profile of K_2O content of sediment at Site 857. K_2O variation is inverse to Na_2O variation. K_2O is strongly depleted in the zone of hydrothermal metamorphism below approximately 400 mbsf. Symbols as in Figure 37.

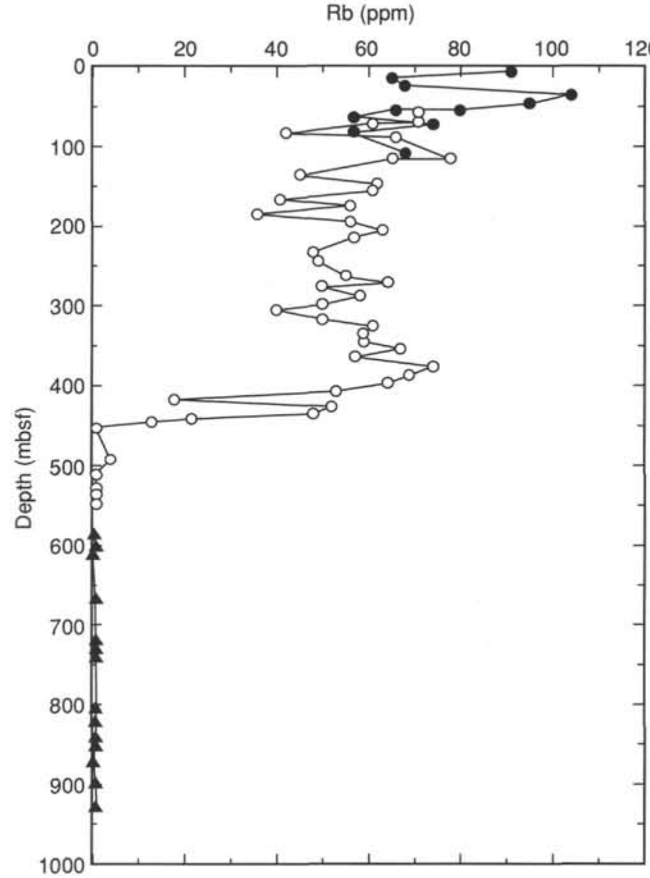

Figure 45. Vertical profile of Rb content of sediment at Site 857, which is similar to that for K_2O. Symbols as in Figure 37.

The variability in sediment anisotropy can be attributed to lithologic variation, compaction with increasing depth and diagenetic alteration at high temperatures. Claystone samples have the widest range of velocity anisotropy, as is expected due to preferential alignment of grains in response to overburden pressure. Siltstone values are less variable, as are siltstone/sandstone samples. Most of the extreme anisotropy values (i.e., greater than the average sediment anisotropy of 18%–20%) were measured on claystone or siltstone samples. Only two massive sandstone samples from the basal sections of turbidites at depths of 350.0 and 440.0 mbsf were analyzed; their anisotropies were a surprising 20% and 26%. These values are much higher than anisotropies expected for coarse-grained material. We have as yet no explanation for these results, which will be analyzed along with all shipboard velocity data in post-cruise study.

The average anisotropy of the two adjacent sediment cubes (from 538.9 to 539.2 mbsf) cut from sill complex cores drilled in Hole 857C is 7.2%; the individual values were –0.7% and 15.0%. The mean anisotropy of sediments recovered from Hole 857D is the same (7.2%); there is no indication of a decrease in anisotropy with depth due to closing of pores and cracks.

Anisotropy in the igneous rock recovered from Hole 857C ranges from –1.9% to 8.9% and averages 3.5%; the mean anisotropy in the sills from Hole 857D is –2.8% and the data range, from –8.3% to 5.6%, is greater. The range of anisotropy in the igneous rock may be due to the presence of open and mineralized vugs or fractures within the cube samples; small negative values in three sill samples from Hole 857C may be due to measurement errors and may not represent a true negative anisotropy. However, the numerous negative values for samples from Hole 857D appear real and indicate much higher vertical than horizontal velocities. These data could be explained by the presence of subvertical microcracks in the formation that could be related to the cooling history of the sills. Detailed analyses of the formation microscanner (FMS) log for Hole 857D should provide data on whether preferred orientation of discontinuities exists within the borehole walls.

Comparison of Laboratory Data with 857C Downhole Logs

The excellent induction, porosity, lithodensity, sonic, and natural gamma logs obtained in Hole 857C provide valuable *in-situ* information on lithologic variation and physical properties that could not be obtained in the laboratory due to poor core recovery and measurements made at atmospheric pressure and temperature. Details about the different logs and shipboard processing of these data can be found in the "Downhole Logging" section (this chapter) and in the "Explanatory Notes" chapter (this volume). Additional processing, correction, and correlation of log and laboratory data will be a major focus of post-cruise research.

Initial comparisons of raw borehole data and shipboard laboratory results can be made for velocity, density, and porosity. A plot of smoothed velocities from the long-spaced sonic (LSS) tool and compressional wave velocities measured on cubes in the laboratory vs. depth is shown in Figure 77A. Raw borehole velocity data within the sill complex are very noisy and unreliable and are excluded from this discussion; these data may be restored by post-cruise processing. Figure 77B presents lithodensity (HLDT) tool data and laboratory wet-bulk densities vs. depth and Figure 77C shows the variation vs.

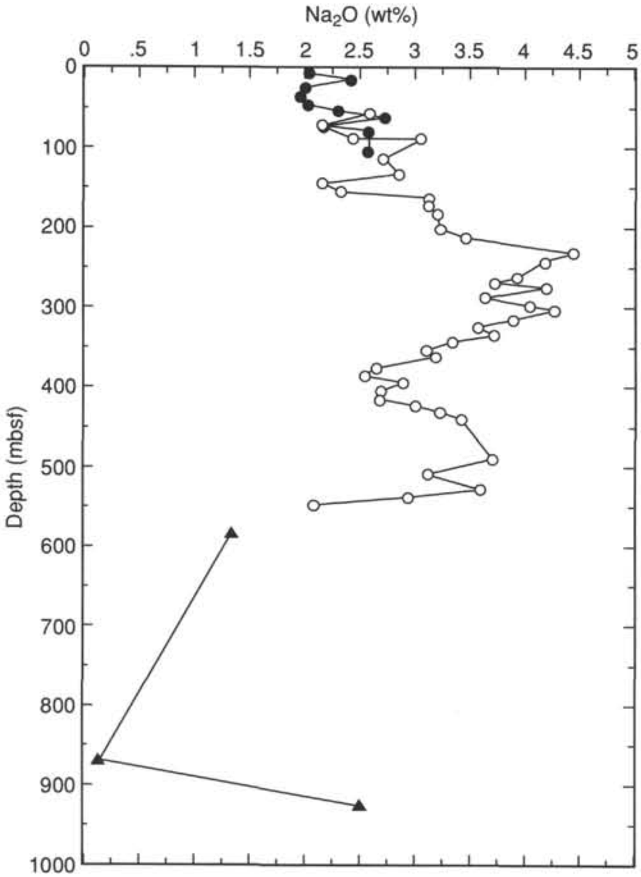

Figure 46. Vertical profile of Na_2O content of sediment at Site 857. Na_2O content of the sediment is in the interval between approximately 200 to 400 mbsf, immediately above the zone of hydrothermal metamorphism. Symbols as in Figure 37.

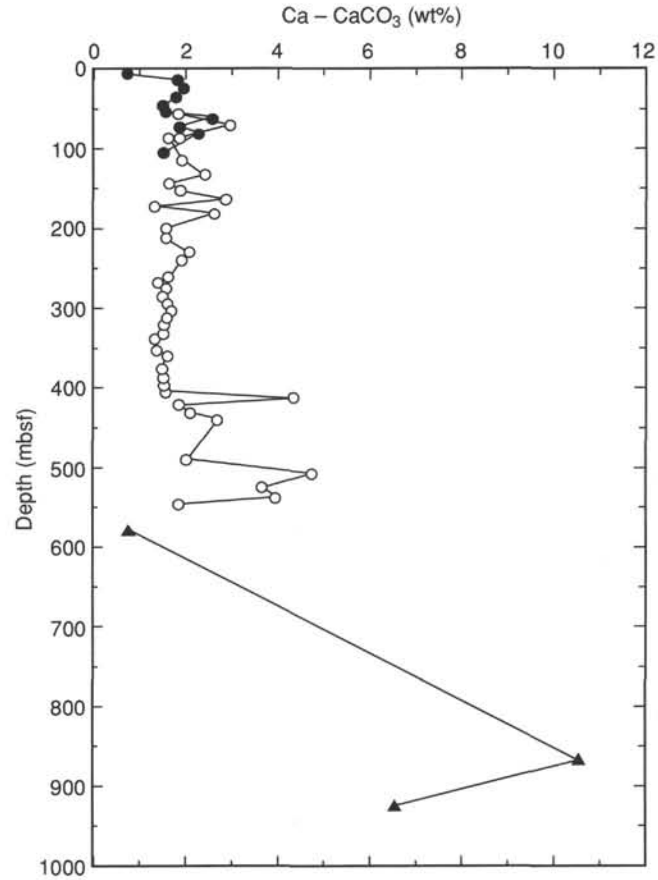

Figure 47. Vertical profile of "silicate" CaO content of sediment at Site 857. Silicate CaO was calculated by subtracting an amount of CaO equivalent to the molar content of CO_2 from the measured CaO content, assuming that all CO_2 in the sample was present as $CaCO_3$. Symbols as in Figure 37.

depth of borehole porosities measured by the compensated neutron (CNT) porosity tool and laboratory porosity data.

Agreement exists in the general trends of *in-situ* sonic velocities and laboratory compressional wave velocities measured in the vertical direction in the upper part of the sedimentary section. The profiles begin to diverge below 361.2 mbsf, with the laboratory velocities having 10% to 12% higher velocities. The sharp reduction in lab velocities at 367.7–385.3 mbsf discussed earlier in this section does not appear in the log profile; this reduction does correlate with the base of a 5- to 6-m-long zone of less variable velocities in the log data (Fig. 77A). The disparity between the two types of velocity data below 350.0 mbsf could be attributed to lithologic variation as well as pressure and temperature effects, and may also be due to a bias in selection of discrete samples. We specifically excluded in our sampling rocks with fractures or veins visible on the planar surface of the working half; occasional samples did reveal discontinuities after being cut into cubes. The logging tool, on the other hand, samples over a range of about 1 m into the formation surrounding the borehole and includes open or filled fractures and veins. These macroscale fractures would lower borehole velocities relative to laboratory velocities. Thus the depth at which log and laboratory velocities diverge may represent a depth below which fracturing of the indurated sediments is pervasive.

Densities from borehole and laboratory data compare favorably to a depth of about 240.0 mbsf (Fig. 77B). Below this depth, borehole densities seem to be systematically lower by about 10%; this also holds for densities in the sill complex below 471.1 mbsf.

Porosities decrease with depth in both the laboratory and borehole profiles (Fig. 77C). *In-situ* values, measured by the neutron porosity tool, are persistently 10% to 13% higher than discrete sediment sample values below 155.4 mbsf. Calculated porosities derived from the density log, presented in the "Downhole Logging" section (this chapter) are consistently lower than neutron porosities. The neutron tool is sensitive to all H^+ atom ions present in formation, including bound water residing in clay interstices, and will therefore record higher porosities (and water contents). Variability in the borehole data increases dramatically below 471.1 mbsf in the complex of sills and interbedded sediments. The borehole porosity range of 28% to 50% in this section seems unrealistically high relative to our laboratory data. In addition to pressure and temperature effects and the sampling bias discussed in the previous section, small amounts of evaporation from samples before measurement of the wet weights and volumes that are incorporated into index properties calculations could introduce a significant systematic error into the measurement of porosity. Chip and cube samples, especially from diabase, were resaturated in salt water. However, samples of more massive, coarse-grained sandstone from turbidite sequences almost certainly drained after coring; porosities measured in the laboratory probably do not indicate their natural values.

DOWNHOLE LOGGING

Logging at Site 857 was carried out in several stages. Temperature logs were run before and after running the conventional strings. Hole

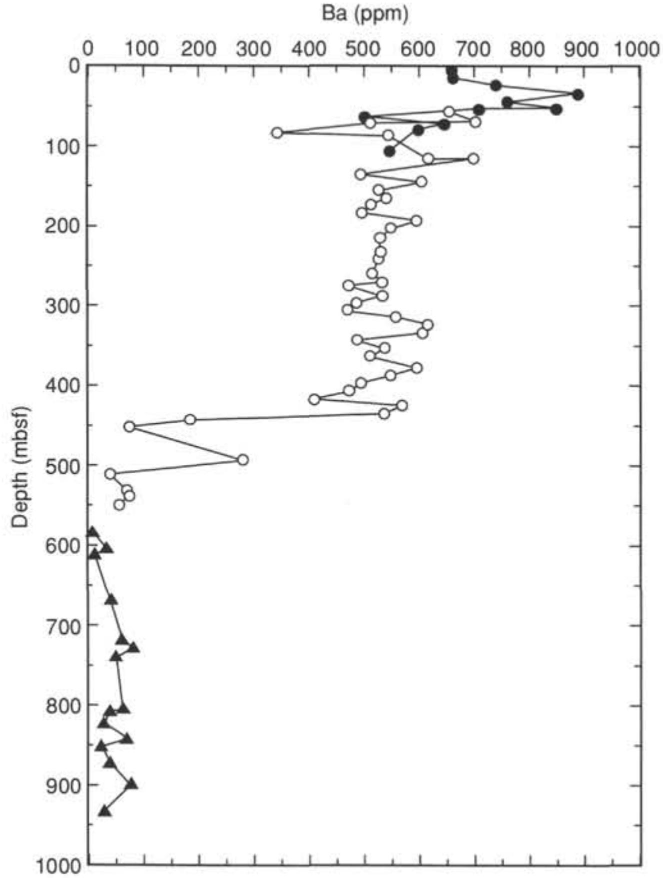

Figure 48. Vertical profile of Ba content of sediment at Site 857 showing strong depletion in the zone of hydrothermal metamorphism. Symbols as in Figure 37.

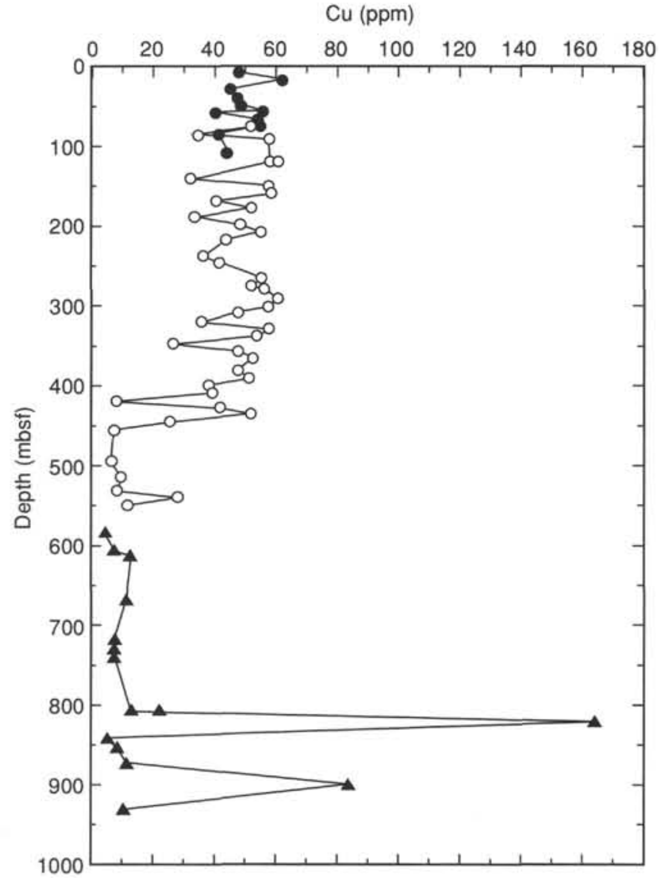

Figure 49. Vertical profile of Cu content of sediment at Site 857 showing strong depletion in the zone of hydrothermal metamorphism, with the exception of local enrichment interpreted to result from addition of secondary Cu sulfide phases. Symbols as in Figure 37.

857C was logged with the seismic stratigraphy and lithoporosity strings on 2 and 3 August (Table 43). We had intended to run the formation microscanner and geochemical strings in Hole 857C as well; however, the FMS string became wedged in the bottom of the pipe, which required us to sever the logging cable just above the tool string and pull the pipe up to retrieve it. As a result, we ended logging operations in Hole 857C without running either the FMS or the geochemical string. The logs that were obtained in Hole 857C are generally of very good quality and appear at the end of this chapter.

Hole 857D was prepared as a reentry hole between 4 August and 8 August. Casing was installed in this hole and cemented into igneous sills at about 574 mbsf. The cement was not drilled out so that water filling the casing was hydraulically isolated from the surrounding sediments and rock. The next stage in the logging program began 23 August, when the *JOIDES Resolution* returned to reentry Hole 857D and made a measurement of the temperature profile in the water in the casing which had been left undisturbed for 14 days (Table 44). Subsequently, Hole 857D was deepened to 936 mbsf, and a second temperature profile was measured to the bottom of the hole on 29 August, approximately 6 hr after drilling and coring in Hole 857D were completed. Schlumberger logs were run in the open hole below 574 mbsf with the seismic stratigraphy string, the formation microscanner string, and a modified lithoporosity string (Table 44).

Temperature Measurements

During the drilling of Hole 857C coring was interrupted twice to measure bottom-hole temperatures with the self-recording GRC high-temperature tool. These measurements were made with two objectives: the first was to determine if there was water at formation temperatures entering the hole at a high enough rate to displace the cold borehole water, and the second was to see if, during an interruption in drilling, a reasonable estimate of the equilibrium bottom-hole temperature could be made with an hour-long record. For these measurements the drill bit was raised about 30 m above the bottom of the hole, and the temperature tool was lowered into open hole below the bit. Two temperature records were obtained (Figure 78A). On run 1 the probe penetrated loose sediment at the bottom of the hole at 202 mbsf, and was left undisturbed for 1 hr. The temperature rose after penetration to 84°C before the tool was retrieved. Run 2 was made after drilling to a depth of 282 mbsf. On this run the tool was held for 1 hr in the water just above the bottom of the hole. The temperature during this period rose at a nearly uniform rate and reached 59°C, which is 25°C lower than the maximum temperature recorded on run 1, 80 m higher in the drilled section. The low and slowly increasing temperatures observed on both runs are inferred to be the result of conductive thermal recovery from drilling disturbance and to indicate that there was no significant flux of hot formation water into the bottom of the hole.

Figure 78B shows portions of the records of runs 1 and 2 plotted vs. the reciprocal of time since circulation of drill fluids stopped. This type of plot is often used as a method for extrapolating transient cylindrical probe histories to equilibrium (see "Heat Flow" section, "Explanatory Notes" chapter, this volume). The curve of run 1 appears to follow a normal conductive recovery from the drilling disturbance, and is quite linear during the last half hour of the observation in fill. A linear extrapolation to $1/t = 0$ yields an estimate of the equilibrium temperature of about 115°C. It will be shown later that this value is in reasonable accord

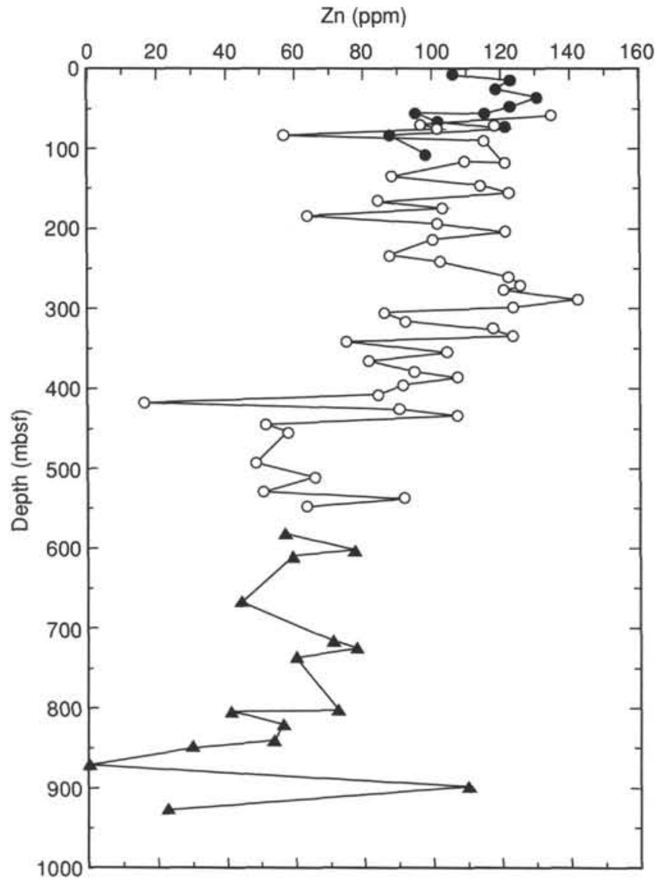

Figure 50. Vertical profile of Zn content of sediment at Site 857. Zn is not strongly depleted in the zone of hydrothermal metamorphism, and appears to be locally enriched due to addition of secondary Zn sulfide. Symbols as in Figure 37.

with other estimates of the equilibrium temperature profile in Hole 857C. Temperatures recorded during run 2 shown on the same plot have significant curvature, which indicates that water in the bottom of the hole is not recovering in accord with simple cylindrical theory.

Temperature runs 3, 4, and 5 in Hole 857C were made 4 days after coring in the hole was completed. Consequently, there had been no circulation in Hole 857C for about 96 hr. We tried to make a continuous log of temperature from top to bottom in the open hole, but each time the tool was lowered it was stopped by obstructions in the hole. When an obstruction was encountered we retrieved the temperature

Table 22. Extent of igneous units observed in Hole 857C.

Unit	Top of section (cm)	Bottom of section (cm)	Thickness (cm)
	139-857C-		
1	59R-1, 0	59R-4, 139	581
2	60R-1, 0	60R-2, 31	169
3	60R-2, 49	60R-2, 142	93
4	61R-1, 0	61R-1, 100	100
5	61R-2, 0	61R-2, 82	82
6	62R-1, 0	62R-2, 79	227
7	63R-1, 34	63R-1, 73	39
8	64R-1, 0	64R-2, 133	283
9	65R-1, 0	65R-1, 5	5
10	66R-1, 24	67R-1, 5	127
11	67R-1, 58	67R-1, 76	18
12	68R-1, 0	68R-3, 36	336

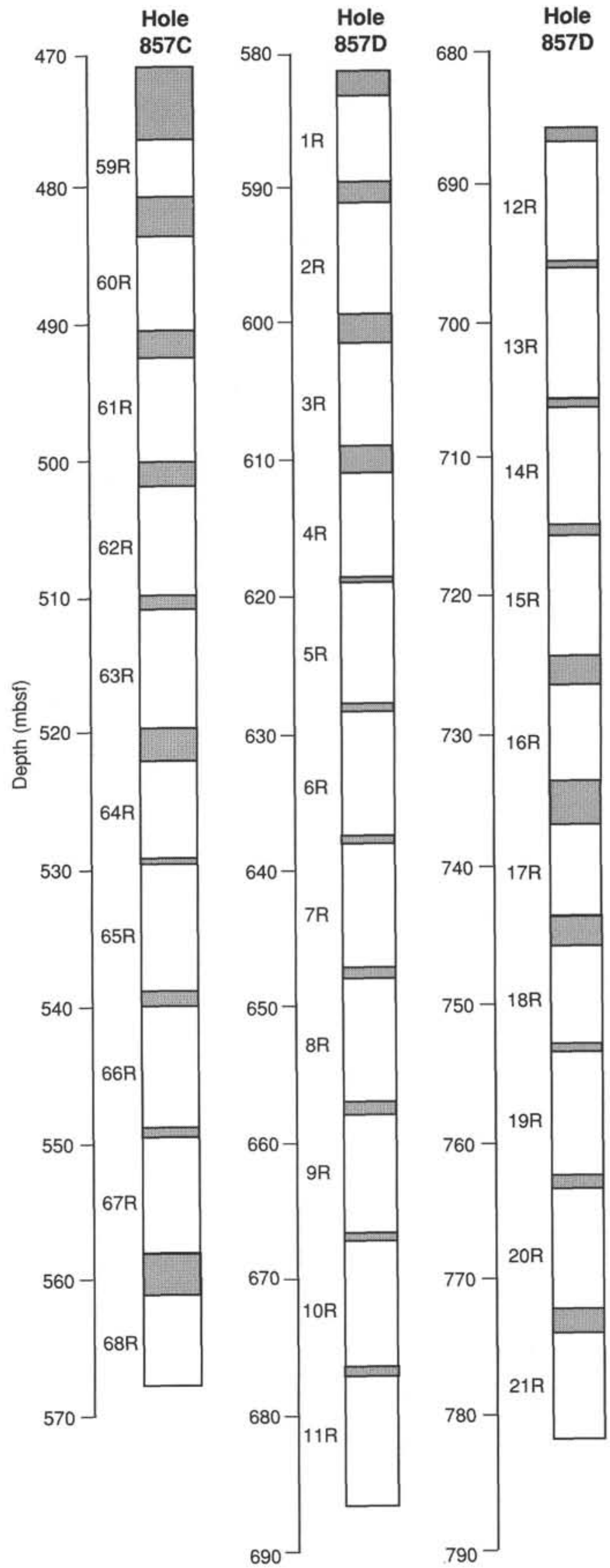

Figure 51. Lithostratigraphic columns for Holes 857C and 857D, showing cored intervals and recovery. Unit designations are listed in Tables 22 and 23.

Figure 52. Close-up photograph of Section 139-857C-66R-1, Piece 5B, showing vertical chilled contact and highly bleached and altered basalt.

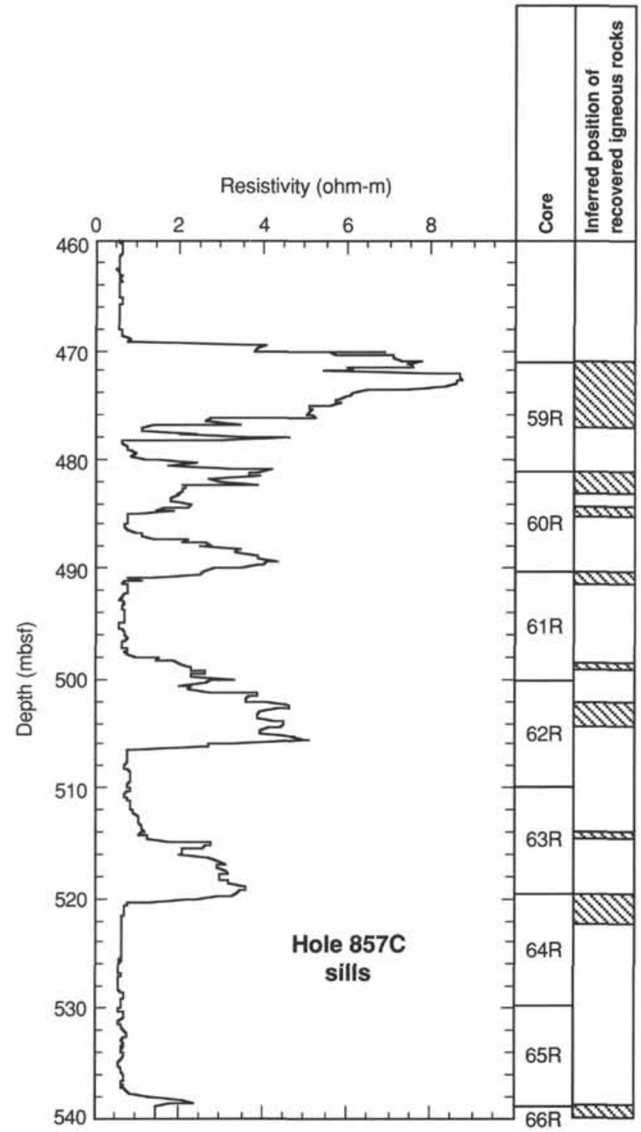

Figure 53. Resistivity log from the bottom of Hole 857C compared to recovery of igneous rocks. Resistivity highs are believed to be associated with igneous rocks and resistivity lows with sediments. Position of igneous recovery within each core has been shifted to correspond to resistivity highs.

tool, lowered the drill pipe until it penetrated past the obstruction, and then made another temperature run. Run 3 resulted in a temperature vs. depth profile between 107 and 193 mbsf. Runs 4 and 5 added two bottom-hole temperatures at depths of 321 and 476 mbsf (Fig. 79).

As described above, a temperature profile in the casing was measured in Hole 857D on 23 August, which was 15 days after the casing was installed. Figure 80 shows temperatures from various sources plotted vs. depth. Figure 80 includes an extrapolation of the two WSTP measurements using the calculated heat flow, 803 mW/m^2, (see "Heat Flow" section, this chapter), and a linear fit to the thermal conductivity values of core samples between 100 and 450 mbsf ("Physical Properties" section, this chapter). This extrapolation thus gives an estimate of the temperature profile if vertical heat transfer is by conduction only. The estimated equilibrium temperature from run 1 falls closest to the conductive profile. The measurements made on runs 3–5 all fall below the conductive profile, probably because the hole was still recovering from the drilling disturbance 4 days before. However, the temperature gradient defined by these points is in reasonable agreement with the extrapolated conductive profile, which suggests that conductive heat transfer predominates in the upper 500 m of the section penetrated by Holes 857C and 857D.

The temperature profile measured in Hole 857D inside the casing 15 days after it was installed (small solid squares in Fig. 80) is hard to understand. The very low gradient in the upper 250 m is typical of deep-sea drill holes where there is a flow of bottom water into the hole (see "Downhole Logging" section, "Site 856" chapter). Cementing the bottom of the casing and the annulus between the casing and the wall of the hole should have prevented drawdown (see "Operations" section, this chapter); however, the temperature profile indicates that the seal between the casing and the hole wall may have been incomplete and allowed a downward flow of cold seawater in the annulus between the hole wall and the outside of the casing to a depth of about 300 mbsf.

Between 23 and 29 August, reentry Hole 857D was deepened to 936 mbsf and a temperature profile to the bottom of the hole was measured soon after it was completed (Fig. 81). This profile indicated a strong downflow of bottom water. The temperature gradient that existed in the cased hole on 23 August (Fig. 80) had been completely wiped out, and on 29 August temperatures in the deepened hole were isothermal to a depth of 620 mbsf. Flowmeter measurements in the hole indicated a drawdown of over 10,000 L of water per minute, or a downward flow of nearly 2.5 m/s (see "Special Downhole Experi-

Table 23. Extent of igneous units observed in Hole 857D.

Unit	Top of section (cm)	Bottom of section (cm)	Thickness (cm)
	139-857D-		
13	1R-1, 0	1R-1, 110	110
14A	1R-2, 65	2R-1, 38	71
14B	2R-1, 47	3R-2, 123	349
15	4R-1, 7	4R-2, 47	190
16A	7R-1, 0	7R-1, 52	52
16B	8R-1, 0	8R-1, 66	66
16C	8R-1, 71	9R-1, 122	151
17A	12R-1, 21	12R-2, 48	79
17B	13R-1, 7	13R-1, 12	5
18A	15R-1, 35	15R-1, 63	28
18B	16R-2, 55	16R-2, 65	10
19	17R-3, 48	20R-1, 119	442
20A	21R-1, 18	21R-1, 115	97
20B	21R-1, 135	21R-1, 140	5
20C	22R-1, 0	22R-1, 14	14
200	22R-1, 31	24R-1, 12	193
21	24R-1, 104	26R-1, 96	415
22	27R-1, 17	28R-1, 7	102
23A	29R-1, 32	29R-2, 44	162
23B	30R-1, 16	30R-1, 19	3
23C	30R-1, 25	30R-1, 36	11
230	30R-1, 39	31R-1, 4	39
23E	31R-1, 53	31R-1, 91	38
23F	31R-1, 91	31R-1, 108	17
23G	32R-1, 0	32R-1, 65	65
24	33R-1, 18	33R-1, 98	80
25A	34R-1, 88	34R-1, 95	7
25B	35R-1, 0	36R-1, 22	166
25C	36R-1, 32	36R-1, 43	111
26	37R-1, 17	37R-1, 20	3
Total			30.87 m

ments" section, this chapter). Much of this flow of water was diverted into the formation between 610 and 620 mbsf. The temperature profile shows a small gradient in temperature below 620 mbsf, indicating that there is a significant reduction of the rate of downflow of water at that depth in the hole. The flowmeter measurements indicated a second zone of influx of seawater into the formation between 680 and 695 mbsf where the temperature profile again shows another increase in gradient. Another break to a higher gradient occurs at 835 mbsf, which suggests that there may be a third zone of inflow at that level. If a downward flow continued below 700 mbsf it was not rapid enough to be detected by the flowmeter measurements, the resolution of which was limited by large heave of the ship and the threshold of sensitivity of the flowmeter instrument.

The temperature tool was held at the bottom of Hole 857D for 40 min. Comparison of the profiles made during lowering and hoisting of the tool show that the temperatures in the bottom 100 m of the hole were rising rapidly; however, the drawdown of water apparently prevented thermal recovery of the hole above about 800 m.

Schlumberger Logging Results in Hole 857C

Density and Porosity

Hole 857C penetrated a 469 m section of sediment composed mainly of hemipelagic claystone with numerous layers of turbiditic silt and sand. The sediments are increasingly lithified with depth. The hole bottomed in a sequence of interbedded volcanic sills and sediments. Profiles of porosity, velocity, resistivity, and density in the sedimentary section between 130 and 460 mbsf are shown in Figures 82A and 82B. All of the data shown are raw uncorrected values. Strong correlations between these properties can be seen especially between 130 and 330 mbsf. The zones of high resistivity, velocity,

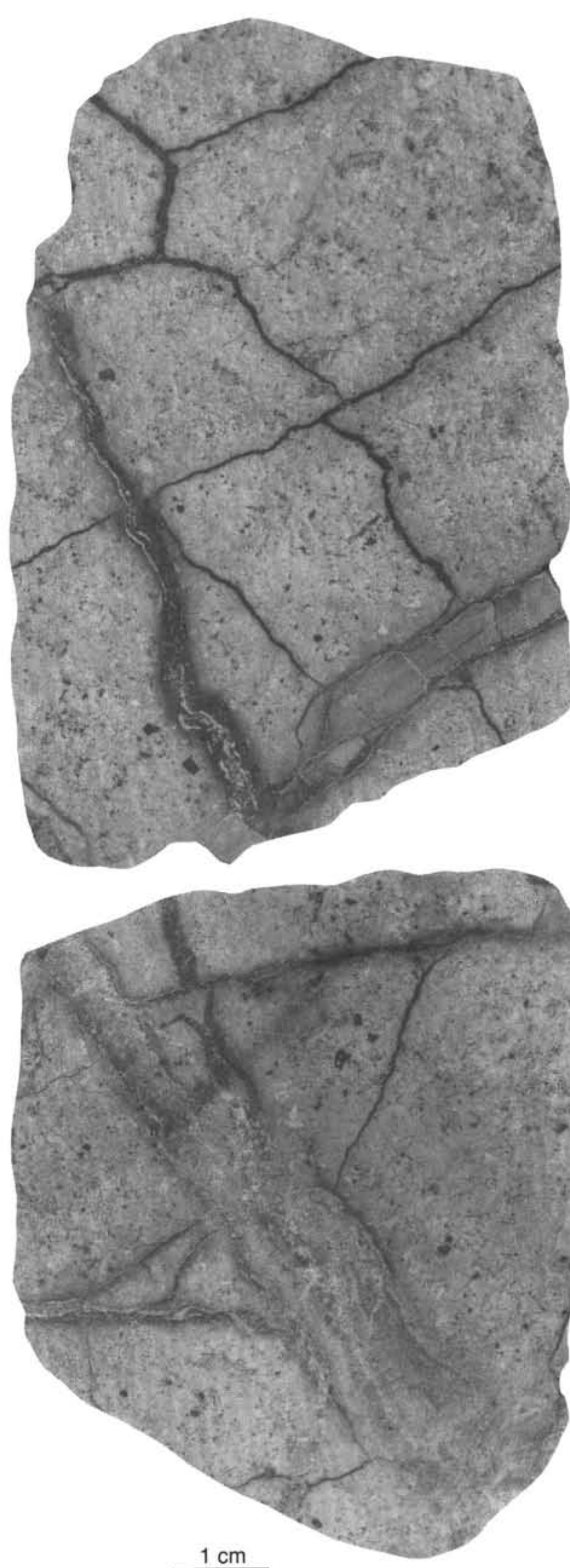

Figure 54. Close-up photograph of Sample 139-857D-8R-1, Piece 5, 31–46 cm. Distinctly veined and altered chilled margin of a sill. The veins are rimmed with chlorite and their centers are filled with quartz, epidote, and pyrite. Note an unusual inclusion of chert (similar to altered sediment) in the upper part of Piece 8A. This may be a stoped block or a vein filled with rapidly deposited silica.

Table 24. Visual estimates of modal proportions in thin sections from Hole 857C.

Core, section:	59R-1	59R-3	60R-1	61R-1	61R-1	68R-1	68R-2
Interval (cm):	106–108	100–102	13–15	97–100	70–71	22–24	8–10
Piece number:	8	5	1	8A	5	4	1
Texture:	Fine-grained	Poikilitic	Ophitic	Chill	Ophitic	Intersertal	Spherulitic
Primary minerals (%)							
Plagioclase	35	38	40	10	40	40	35
Clinopyroxene	38	37	38		44	25	40
Oxide	1	3	2	1	3		
Spinel							
[a]Mesostasis	o.p.	o.p.	3	27	9	o.p.	o.p.
Secondary minerals (%)							
Smectite	tr	tr		1		tr	
Chlorite	20	15	8	50	3	25	15
Sulfides	1	1	5	10	<1	1	1
Actinolite		tr				tr	1
Epidote	5	4	5				5
Sphene							tr
Zeolites		1					

Notes: tr = trace; o.p. indicates that phase was originally present, now totally replaced. Some of the plagioclase occur as phenocrysts.
[a]Interstitial or matrix glass.

density, and low porosity probably correspond to relatively thick silty and sandy turbidite layers in the sediment sequence.

Two porosity curves are displayed in Figure 82; one is based on measurements with the compensated neutron porosity tool and the other is the porosity derived from the density measured by the lithodensity tool and an assumed grain density. Neutron porosity is a measure of the abundance of hydrogen atoms in the formation and it will overestimate the porosity in marine clay, because the water incorporated into the structure of clay will be interpreted as free pore water. The density-derived porosity, ϕ, was calculated using the relation

$$\phi = (\rho_g - \rho_b)/(\rho_g - \rho_w),$$

where ρ_g is the mean grain density (2780 kg/m^3) of core samples (see "Physical Properties" section, this chapter), ρ_w is the density of seawater (1027 kg/m^3), and ρ_b the bulk density measured by the lithodensity tool. The density-derived porosities provide the better estimate of the *in-situ* values, and are in good agreement with the shipboard measurements (Fig. 83). The difference between the two porosity curves gives an estimate of the amount of water that is bound up in clay minerals. The difference should be least in the lower porosity turbidites and consequently should correspond to layers of higher resistivity. This association is tested in Figure 84 where the difference between the two porosity curves is compared with the resistivity profile. The correlation is generally good except for an 8-m-thick layer of sediment of higher density, resistivity, and velocity between 160 and 170 mbsf, where the difference between the porosities remains high. Core recovery from this interval was about 30% (Cores 139-857C-13R and -14R) and neither the visual descriptions nor the core photographs reveal anything remarkable about this zone, which is composed of indurated claystone and siltstone with stringers of sand.

Velocity

The velocity profile (Fig. 82) shows a general increase with depth due to increasing compaction, but the increase is not monotonic. In some zones the velocity gradient is low or even negative; see, for example, 240–270, 325–350, and 370–390 mbsf. The correlation between resistivity and velocity at a scale <10 m is clear and positive; however, there is only a small increase in resistivity (0.45 to 0.55 ohm-m) over the entire sedimentary section between 130 and 460 mbsf despite a 20% decrease in porosity. The effects of compaction are probably counterbalanced by the decrease in resistivity that results from the large temperature increase with depth. The correlation between velocity and density is positive for depths less than 260 mbsf. At depths greater than 260 mbsf the correlation in some zones is negative (e.g., the zone from 265 to 300 mbsf).

Comparisons of discrete measurements of physical properties made on core samples with measurements made downhole are described in the "Physical Properties" section in Figure 77A–C (this chapter). The agreement between logging measurements and shipboard measurements of velocity in the vertical direction is good to a depth of about 365 mbsf. Below 365 mbsf the velocities measured by the sonic tool are lower than the core measurements, which may be due to the difference in scale between the two types of measurements. The sonic tool measures velocity over a 0.61-m interval, whereas shipboard measurements are made on 1- to 2-cm samples. Formation microscanner images from nearby Hole 858F ("Downhole Logging" section, "Site 858" chapter) shows that below 365 mbsf there are some large vertical cracks in the sediments. Comparison of density measurements at Hole 857C below 365 mbsf reveals that the downhole logging values fall about 0.1 to 0.2 g/cm^3 below the shipboard measurements.

Photoelectric Absorption Index

The variation of the photoelectric absorption index through the sedimentary section is shown in Figure 85. Zones of enhanced photoelectric absorption may reflect the increased abundance of barium (in barite), which has a large neutron-capture cross section. The increases in photoelectric absorption index correlate well with the resistivity curve, which suggests that higher barium content may be associated with coarser grained turbidites. On the other hand, increases in natural gamma-ray activity (Fig. 85) are associated with the clay rich zones.

Basalt Sills and Sediment Complex

The lower part of Hole 857C was drilled through a sequence of basaltic sills interbedded with sediments. All parameters measured by the logs respond to the changes in density and chemistry of the igneous sills, which were first intersected at 469 mbsf (Fig. 86). Six discrete sills were detected—the thickest is about 8 m thick and the thinnest is less than 1 m thick. The resistivity log which provides the deepest measurement in the hole may have detected the top of a seventh sill. The interbedded sediments have similar thicknesses to the sills except for the very bottom of the hole where a 20 m thick layer of sediment was drilled.

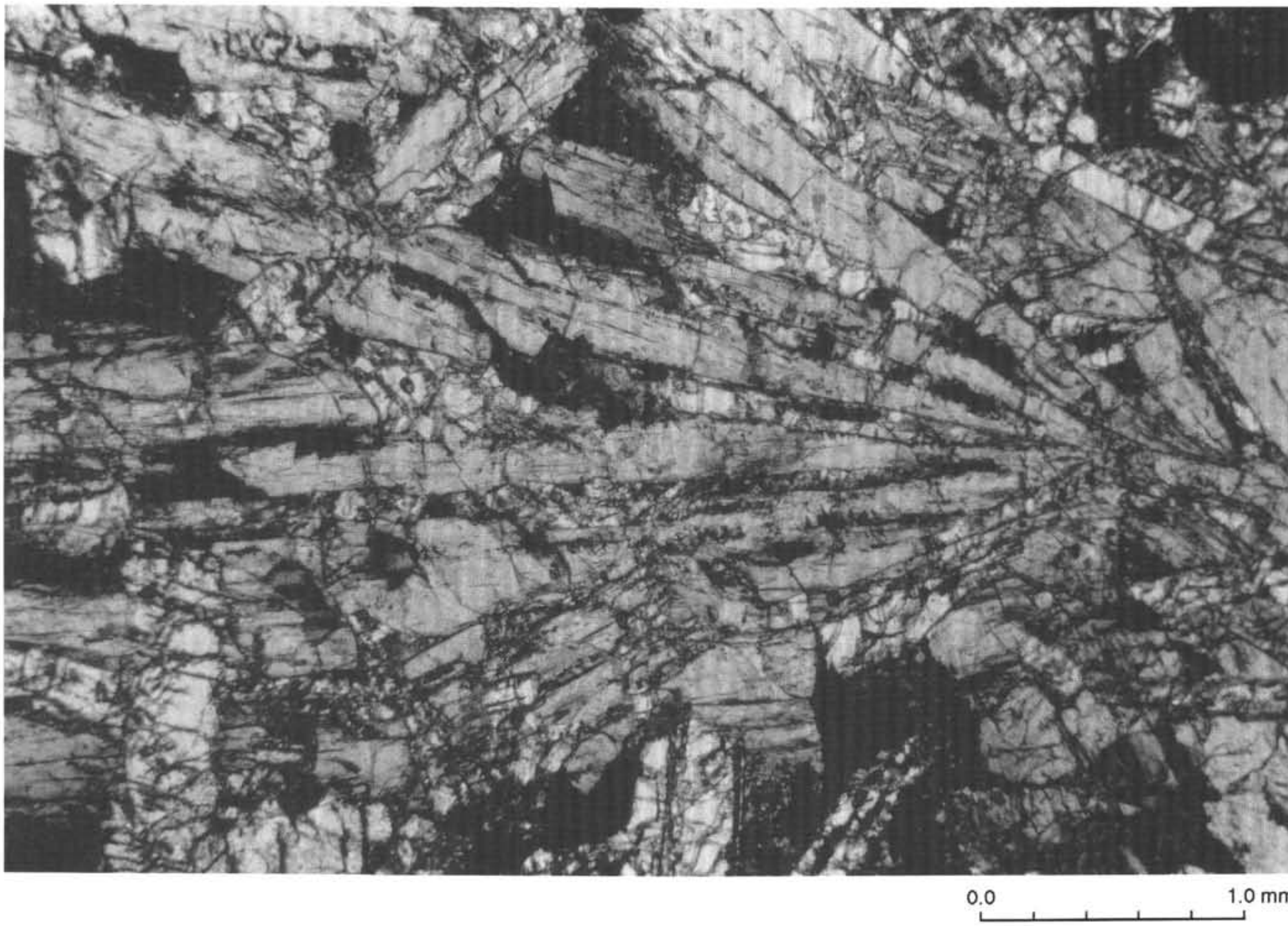

Figure 55. Photomicrograph showing spherulitic texture in clinopyroxene, characteristic of the medium-grained diabase from the sills. Sample 139-857C-68R-2, Piece 1, 8–10 cm, plane transmitted light, ×2.5.

Schlumberger Logging Results in Hole 857D

Three different tool strings were run in the 362 m of open hole in Hole 857D (Table 44); the seismic stratigraphy string, the lithoporosity string, and the formation microscanner string. During the time these logs were being run there was a large sea swell, and the ship was heaving 3 to 5 m with a period of about 6 s. We did not have a wireline heave-compensation system on Leg 139, and as a consequence the tool strings oscillated up to 5 m the hole. Oscillations of this amplitude and period undoubtedly resulted in the logging tool actually reversing its direction of motion during raising or lowering. These motions seriously compromised the resolution of logs made in Hole 857D. This motion also resulted in serious damage to the formation microscanner when the extendable arms of the tool took the full weight of the string during a downward heave of the ship. One of the arms was bent outward and the sensor pad bent nearly 90° so that it could not be retracted fully. As a consequence, much of the FMS data was seriously degraded. The bent arm on the FMS string also prevented it from being pulled up into the pipe after the logging runs were complete, making a pipe trip necessary for recovery.

Resistivity, Gamma-ray, and Spontaneous Potential Logs

All of the open hole below casing at Hole 857D is in the interbedded sill and sediment complex. The gamma-ray log (NGT) proved to be the most effective measurement for delineating volcanic units in the complex because of the very low counts in the basalts. The NGT can detect variations in activity behind the casing so that a complete gamma-ray log of the complex between 465 and 920 was obtained (Fig. 87). Thirty distinct volcanic units can be identified; two additional basaltic layers between 920 and 934 mbsf were imaged by the FMS tool. The combined thickness of basaltic layers drilled is over 165 m, which represents about 36% of the total thickness of the sill and sediment complex. The caliper log, which is shown alongside the NGT log in Figure 87, shows that the thicker volcanic units form ledges in the hole between intervals of sediment which are more easily washed out during the drilling process despite their indurated nature.

The resistivity data are useful only in open hole below the casing, and they reveal two features of interest. First, the average level of resistivity is relatively high (2–4 ohm-m), which is consistent with the large percentage of igneous rock and the low porosity of the sediment. Second, there are positive resistivity peaks which we interpret as corresponding to volcanic units (Fig. 87). The boundaries between the high and low resistivity units are smeared because of the large oscillations of the tool in the hole.

The most striking features of the resistivity log are two zones of very low resistivity between 607 and 625 mbsf and 675 and 690 mbsf. The resistivity in theses zones approaches that of seawater (about 0.2 ohm-m). The spontaneous potential log shows prominent minima in these zones as well. These minima correspond to two locations where water that is flowing down the hole is inferred to be diverted into the formation ("Special Downhole Measurements" section, this chapter).

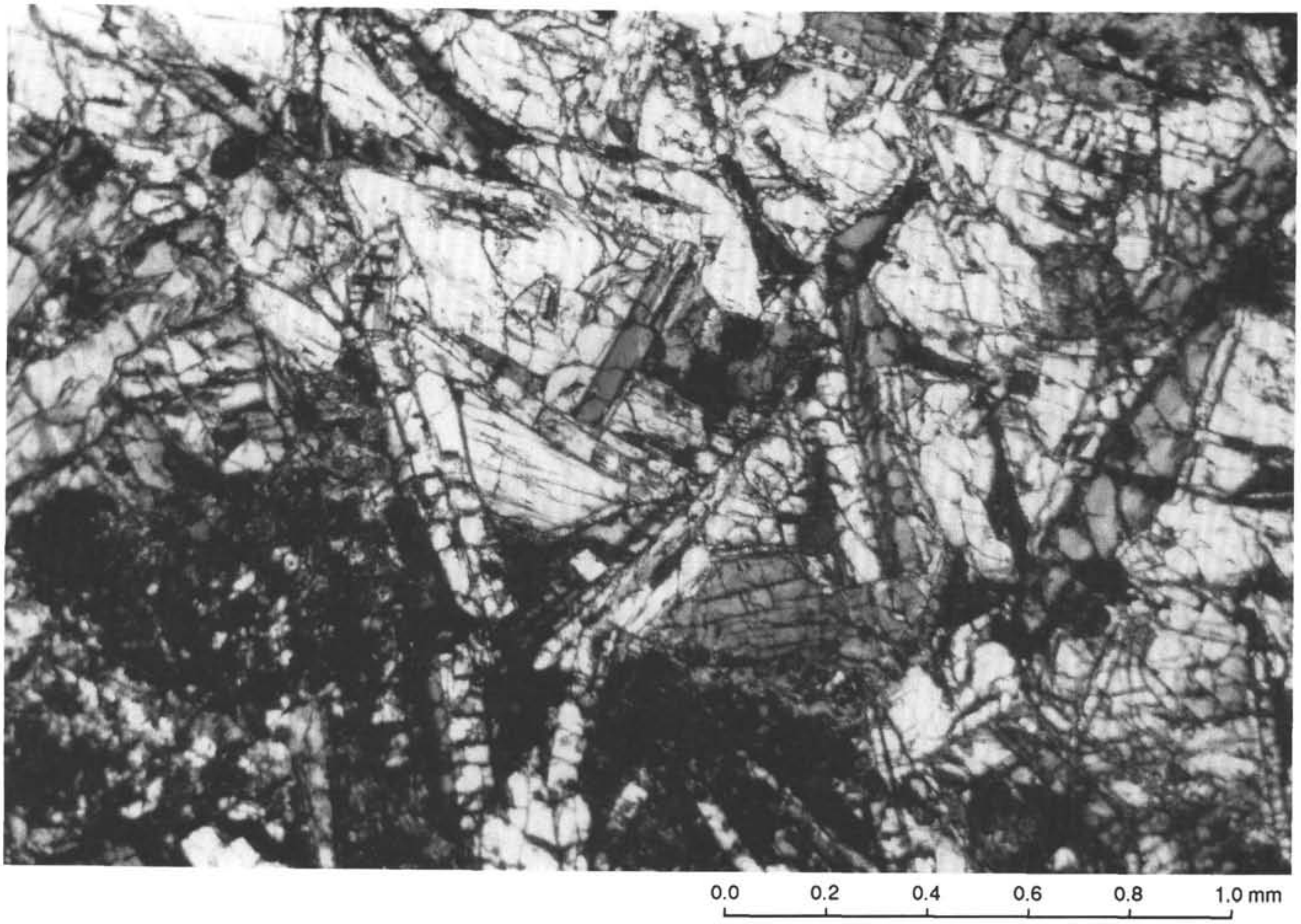

Figure 56. Photomicrograph showing poikilitic texture characteristic of the coarse-grained sill centers. Sample 139-857C-63R-1, Piece 4, 51–53 cm, polarized transmitted light, ×5.

Table 25. Visual estimates of modal proportions in thin sections from Hole 857D.

Core, section:	4R-1	12R-1	18R-1	20R-1	25R-1	27R-1	36R-1
Interval (cm):	59–61	61–64	55–58	62–65	71–73	78–81	140–142
Piece number:	9	10	4	8	11	11	21
Texture:	Isotropic	Fine-grained	Poikilitic	Poikilitic	Subophitic	Ophitic	Intergranular
Primary minerals (%)							
Plagioclase	35	17	45	39	45	30	34
Clinopyroxene	25	o.p.	34	30	35	31	33
Oxide	5	1	3	2	5	3	4
[a]Mesostasis		o.p.				o.p.	15
Secondary minerals (%)							
Smectite						5	5
Chlorite	20	35	6	10	10	10	5
Sulfides	5	5	3	1	tr	10	4
Actinolite	5	20		10	3	1	
Epidote	5		5	5	1	2	
Sphene	tr		1	tr			
Zeolites + prehnite		5		3		8	
Quartz		15	1				1
Albite			3				tr

Notes: tr = trace; o.p. indicates that phase was originally present, now totally replaced. Some of the plagioclase occur as phenocrysts. Possible prehnite is included with zeolite volume.
[a]Interstitial or matrix glass.

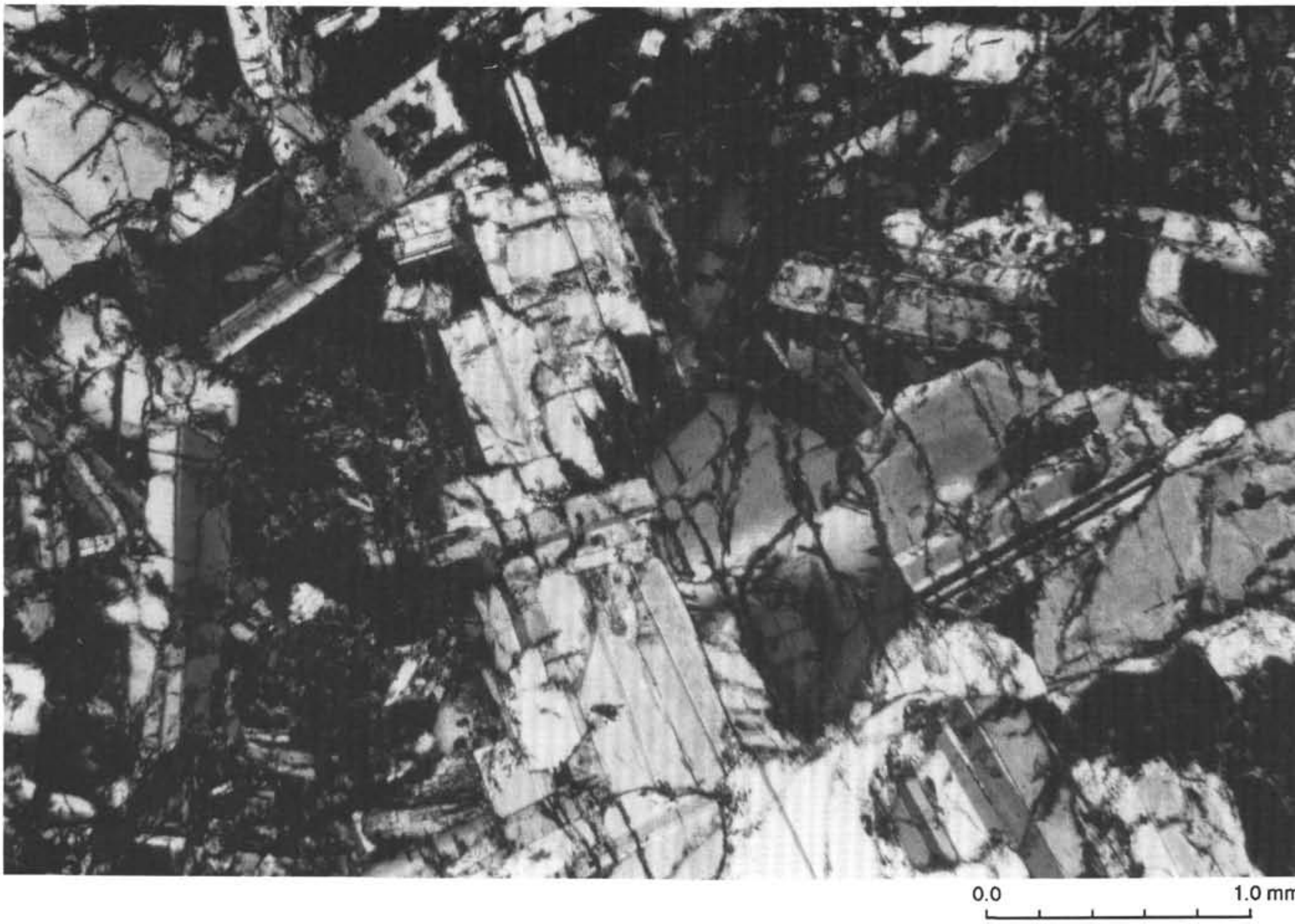

Figure 57. Photomicrograph of Sample 139-857D-3R-1, Piece 2B, 25–27 cm. This sample contains an abundance of embayed and broken calcic plagioclase (An_{80}) xenocrysts. Note the concentric zonation and sodic rims (An_{20-40}), polarized transmitted light, 2.5×.

The spontaneous potential anomalies are probably associated with this influx, perhaps as a result of the chemical reactions caused by the introduction of a large quantity of cold seawater into the altered rock and sediment that was at high temperature. A third zone of inferred high relative permeability and water influx, between 620 and 645 mbsf, has mixed resistivity and spontaneous potential results.

Formation Microscanner

Despite operational problems, useful images of the wallrock were obtained, especially in the lower part of the hole which was logged before the tool was damaged. The volcanic units can be clearly identified based on the character and density of gray of the image (Fig. 88; also see FMS images presented on microfiche in the back of this volume). The higher resistivity volcanic units are a lighter gray shade and exhibit a network of fractures or veins that are displayed as irregular, branching dark lines. Most of these fractures or veins appear to be naturally occurring. Many of the volcanic units and some of the superadjacent or subadjacent sedimentary units have long, ragged, vertical fractures which were probably formed by thermal stresses that resulted from the introduction of cold circulation water into the wall rock that was at a temperature of about 300°C. These vertical fractures have a consistent orientation of between 340° and 355° (see Fig. 88), which is consistent with an east-west direction of maximum horizontal extensional stress if these fractures are induced by thermal stresses. The sedimentary units are distinguished by much darker gray images and frequent banding or layering. The banding is often dipping at steep angles relative to the borehole. The FMS images in the zones where other evidence shows that water is flowing into the formation at a high rate were examined carefully; no unusual or anomalous features were found, although the quality of the images in this part of the hole is poor.

Sonic Logs

The sonic log results in Hole 857D are very poor quality because of the amount of movement of the tool in the hole, which caused a great deal of noise as well as ambiguities in the location of the transmitter receiver pairs. The density log is also of poor quality because the sensing pad, which is on an extendable arm, failed to extend against the hole wall due to exposure to excessively high temperatures at the bottom of the hole.

Summary

In general, the quality of the data from the logging program at Hole 857C is excellent. The thicker layers of sandy and silty turbidites are clearly displayed by variations in many of the parameters measured by the logs. Further analysis of the logs in the sedimentary section will provide an accurate measurement of the proportions and frequency of the large turbidite layers. There is general agreement between the log-derived values of velocity and the vertical component of velocity measured on discrete core samples to a depth of 365 mbsf. The logged values of density fall below those measured on core samples, which in part may be explained by the different scale of the two measurement techniques.

Figure 58. Close-up photograph of Sample 139-857D-12R-1, Piece 8, 42–54 cm. Fine-grained equigranular diabase near chilled margin with prominent chlorite veins, surrounded by wallrock alteration.

Temperature measurements in open hole in Hole 857C were made while the hole was still recovering from the drilling disturbance, and thus lie below the estimated equilibrium profile shown in Figure 80. Temperatures are believed to be recovering normally toward an equilibrium conductive profile, however. The deepest measured temperature at 476 mbsf sets a minimum equilibrium temperature of 222°C. The extrapolation of the conductive gradient measured higher in the section probably represents an upper limit estimate of about 260°C at this depth.

A temperature log in Hole 857D after it was drilled to 936 m was nearly isothermal at bottom-water temperature to 620 mbsf. This is the result of a very strong drawdown of water into the hole. Flowmeter tests and the resistivity and self-potential logs indicate that most of the water that flows down the hole enters the formation in relatively narrow zones between 605 and 625 mbsf and 680 to 690 mbsf.

The gamma-ray log defined the volcanic units within the sill and sediment complex in the bottom 474 m of Hole 857D very clearly. There are 32 separate basaltic units of thicknesses varying from less than 1 m to 25 m.

HEAT FLOW

Operations

The WSTP and APC tools were deployed a total of 13 times at Site 857 with nine successful measurements of *in-situ* temperatures (Table 45; Figs. 89 and 90). The first and third runs with the APC tool in Hole 857A (Cores 139-857A-4H and -8H, 31.9 and 69.4 mbsf, respectively) were unsuccessful; the batteries died during the first run, and an intermittent power loss caused a tool failure during the third. The final run with the WSTP in Hole 857A (following Core 139-857A-14P, 113.3 mbsf) was unsuccessful because the tool flooded. WSTP data records are noisier, overall, than are the APC tool records, but bench and bottom-water calibrations indicate that the WSTP provided accurate measurements.

Data from all successful deployments in Hole 857A are presented in Figures 89 and 91. Measurements of temperatures near mudline during all deployments were either greater than or within 0.1°C of the previously measured temperature of 1.7°C (Davis and Villinger, this volume). Because we failed to collect temperature data from the upper 50 m of the sediments in Hole 857A (and because we did not recover the mudline with Core 139-857A-1H), Hole 857B was drilled with a negligible offset from Hole 857A to collect three additional cores and measure sediment temperatures. Core 139-857B-1H recovered the mudline, and Cores 139-857B-2H and -3H included the APC tool; both runs were successful (Figs. 89 and 92). All data were processed by fitting measured temperatures to theoretical decay curves (Fig. 93; "*In-situ* Temperatures" section, "Explanatory Notes" chapter, this volume).

The processed data (Fig. 93) resulted in a calculated thermal gradient in Holes 857A and 857B that is lower than was intended for the reentry hole at this site (Fig. 94; see discussion below), so the ship was offset about 180 m to the east (closer to the peak of the local heat flow high; Davis and Villinger, this volume) before spudding Hole 857C. The WSTP was run four times in Hole 857C, with three successful measurements at 37.6, 57.6, and 77.2 mbsf (Table 45; Figs. 90 and 95). Measured temperatures never rose beyond 10°C above bottom-water temperature during the fourth deployment (at 96.3 mbsf), suggesting that the probe split the formation upon insertion. As the formation appeared to be too hard to allow penetration of the probe without cracking, no additional measurements were attempted.

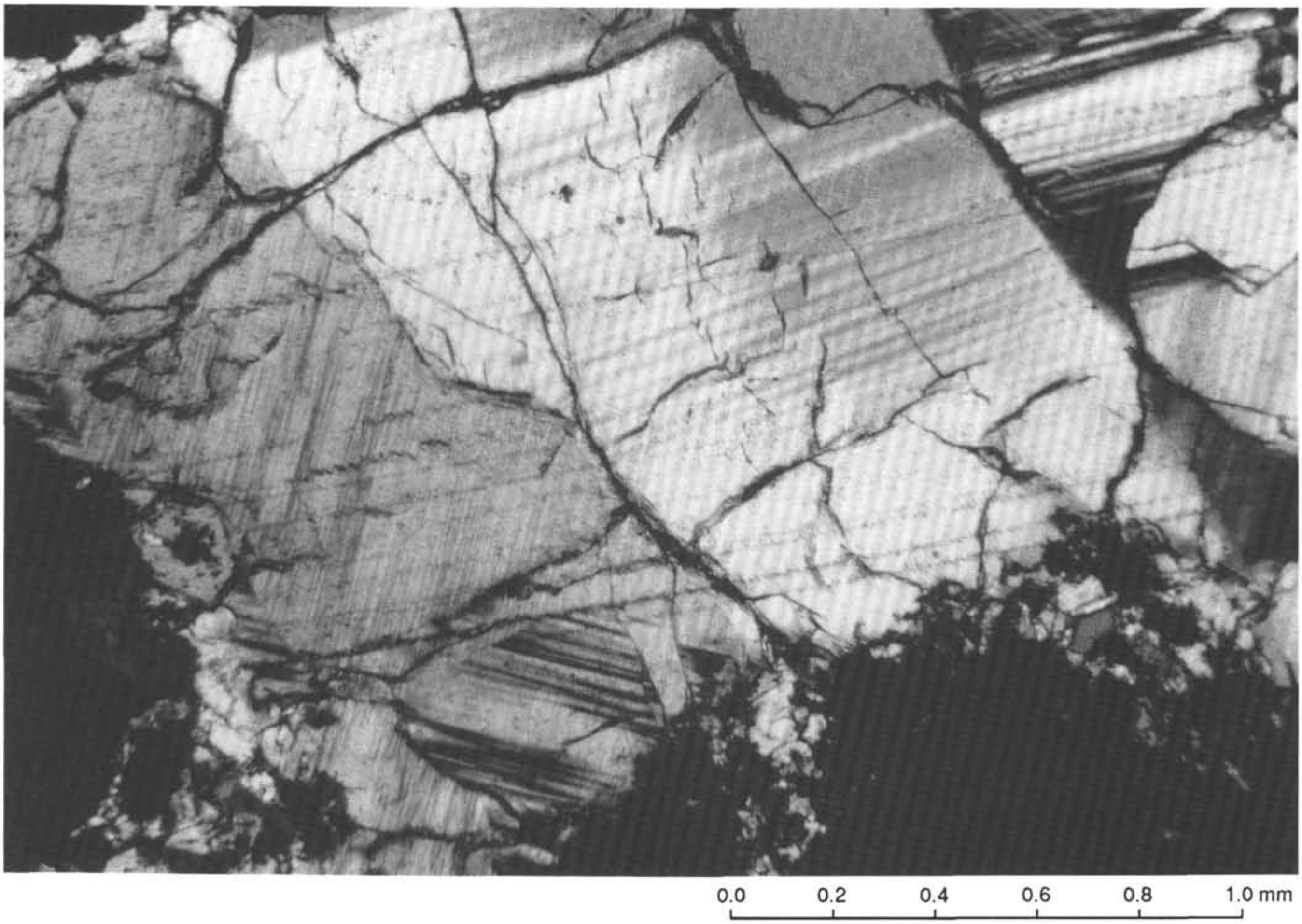

Figure 59. Photomicrograph of vein containing twinned wairakite, sphalerite, and euhedral quartz. Sample 139-857D-1R-1, Piece 8D, 68–70 cm, polarized transmitted light, 5×.

The data from runs following recovery of Cores 139-857C-2W and -3W required special handling, as the data logger malfunctioned during these stations. Inconsistent digital offsets were recorded intermittently throughout the deployments. One component of these offsets (which shifted the least significant word of each two-word digital value) was easily identifiable, but the exact nature of another shift (which most strongly affected the results of the deployment following Core 139-857C-3W) remains unresolved. We believe that the data from the measurement following Core 139-857C-2W have been fully corrected (Fig. 95A), but we were unable to apply a complete correction to the data from the measurement following Core 139-857C-3W (Fig. 95B). For the latter measurement we therefore give a range of possible *in-situ* temperatures, based on our understanding of the behavior of the data logger.

Interpretations

Final temperatures from Holes 857A and 857B (Fig. 93) yield an average gradient of 0.612°C/m (Fig. 94A) when all successful measurements are fit using a linear, least-squares regression forced to pass through 1.7°C at mudline. A Bullard plot of temperature vs. cumulative thermal resistance (as determined from shipboard measurements of thermal conductivity; see "Physical Properties" section, this chapter) yields a heat flow of 709 mW/m^2 over the upper 76 mbsf (Fig. 94B).

A linear regression of final temperatures from Hole 857C (Fig. 96), when forced through a bottom-water value of 1.7°C, results in a calculated gradient of about 0.71°C/m down to 77 mbsf (Fig. 97A). A Bullard plot of these data indicates a heat flow of 803 mW/m^2 over the same interval (Fig. 97B). The consistency of the data from Hole 857C suggests that the higher temperature is probably correct for the measurement following Core 139-857C-3W (Figs. 97A and 97B).

The Bullard plots from Site 857 data are nearly linear over the extent of the data, indicating that heat flow through the upper sediment column is dominantly conductive. The calculated heat flow values are consistent with nearby measurements (Davis and Villinger, this volume).

SPECIAL DOWNHOLE EXPERIMENTS

An extensive program of logging and downhole experiments was conducted in Hole 857D after it had been cased to 574 mbsf and deepened to 936 mbsf. This program included standard Schlumberger logging and temperature logging described in the "Downhole Logging" section (this chapter) and several special experiments designed to assess the hydrogeological and thermal state of the section penetrated in Hole 857D. The latter included standard packer experiments to determine bulk permeability and average formation fluid pressure, a flowmeter log conducted in conjunction with the packer to assess the fine-scale distribution of permeability, and the emplacement of a long-term instrumented borehole seal or "CORK." Methods for the packer and flowmeter experiments are summarized in the "Special Downhole Experiments" section, "Explanatory Notes" chapter (this volume), and the CORK is described by Davis et al. (this volume). The data from the packer and flowmeter experiments require analyses that could not be completed in the brief time

Figure 60. Close-up photograph of Sample 139-857C-60R-1, Piece 3, 34–60 cm. Surface view of a chlorite-pyrite vein, illustrating large, coarse-grained pyrite aggregates surrounded by chlorite.

Figure 61. Close-up photograph of Sample 139-857D-3R-1, Piece 6A, 56–63 cm. Vein cuts coarse-grained rock at center of sill. Note open vugs filled with euhedral quartz and epidote crystals. Light-colored aureole adjacent to vein is enriched in quartz, epidote, and chlorite.

remaining during Leg 139, and the CORK will provide no data or samples until revisited with the submersible *Alvin* shortly after Leg 139. Therefore, this section comprises a summary of operations during these experiments and a qualitative assessment of the results of the packer and flowmeter experiments.

Packer and Flowmeter Experiments

The packer and flowmeter experiments were conducted as described in the "Special Downhole Experiments" section, "Explanatory Notes" chapter (this volume) with one important modification: the packer was deployed with two inflation elements instead of one, to double its mechanical and hydraulic holding power when inflated in casing. The two elements were separated by only about 0.5 m, so the packer acted essentially as a double-seal single packer that isolated the zone between the entire packer assembly and the bottom of the hole. Four go-devils were deployed, and the packer was inflated six times (including two repeats of failed inflations) at two depths during a 27-hr sequence of normal permeability experiments and the flowmeter experiment.

First Go-devil (Packer at 96 mbsf)

After reentry, the packer assembly was positioned at 96 mbsf in order to test the permeability of the section between the casing shoe at 574 mbsf and the bottom of Hole 857D at 936 mbsf. The go-devil was deployed with one mechanical Kuster K-3 pressure recorder and one electronic GRC ERPG-300 recorder; the pressure record from the latter is shown in Figure 98. After the go-devil landed, the packer was twice inflated at 1500 psi but inadvertently deflated due to heave motion. A third inflation at 1500–1700 psi held for the duration when the weight placed on the packer by the drill-string heave compensator to hold the inflation control sleeve in place was increased from 20 to 30 klb.

With the packer successfully inflated, three slug tests were attempted. These gave indications of surprisingly low permeability, given that circulation had been lost during drilling ("Operations" section, this chapter) and a temperature log suggested flow of bottom water down the hole and into the formation ("Downhole Logging" section, this chapter). However, when the go-devil was retrieved, it was found to be plugged with rust and grease, with no downhole signal of the apparent slug tests (Fig. 98). Thus this testing sequence provided no information about the permeability of the formation. Nevertheless, the pressure record does show clear evidence of an underpressure (relative to cold hydrostatic) of about 1 MPa in the isolated zone once it was sealed by the packer.

Second Go-devil (Packer at 96 mbsf)

As the plugged first go-devil prevented essential permeability information from being collected, a "pig" was pumped down the pipe to clean it of rust, and the packer experiment was repeated at the same inflation depth. A second go-devil was deployed with redressed Kuster and GRC pressure recorders, and the packer was inflated without problem at 1800 psi, with 30 klb of weight to hold it set. Figure 99 shows the pressure record collected with the GRC recorder during the ensuing test sequence. Two slug tests were attempted, but the pressure pulses decayed extremely rapidly and can barely be distinguished on the downhole pressure record. This indicated that

Table 26. Compilation of geochemical data from Holes 857C and 857D.

Hole, core, section:	857C-59R-1	857C-59R-2	857C-59R-3	857C-60R-1	857C-62R-1	857C-62R-2	857C-O64R-1	857C-64R-2	857C-66R-1
Interval (cm):	106–108	138–139	101–103	13–15	46–48	60–62	63–66	33–35	114–116
SiO_2	50.88	51.61	52.16	48.74	49.72	49.84	49.28	52.11	47.26
TiO_2	1.70	1.72	1.64	1.72	1.41	1.68	1.42	1.15	2.28
Al_2O_3	15.29	15.18	15.55	15.43	16.12	15.35	15.69	14.76	16.75
Fe_2O_3	10.03	9.67	10.14	10.46	10.73	10.18	9.65	10.71	11.99
MnO	0.19	0.189	0.17	1.27	0.31	0.24	0.23	0.28	0.22
MgO	7.24	7.71	7.73	8.12	12.58	10.13	8.35	11.32	7.92
CaO	12.59	12.43	10.46	12.45	8.09	10.47	12.28	7.72	12.16
Na_2O	2.11	1.99	2.04	2.33	1.84	1.84	2.06	1.56	1.88
K_2O	0.02	0.01	0.01	0.03	0.00	0.00	0.01	0.00	0.03
P_2O_5	0.19	0.20	0.19	0.20	0.13	0.17	0.14	0.10	0.27
Total	100.24	100.709	100.09	100.75	100.93	99.9	99.11	99.71	100.76
LOI	1.64	1.36	1.31	1.77	4.76	3.5	2.71	3.81	2.51
Rb	1	1	0	1	1	0	0	1	1
Sr	206	199	198	201	148	161	144	101	157
Y	33	33	32	33	27	33	28	23	41
Zr	167	166	158	165	115	147	118	91	191
Nb	5	5	4	5	2	3	4	3	12
Ni	67	69	86	69	115	76	84	94	121
Cr	288	310	309	290	371	334	343	404	343
V	290	291	277	291	244	284	264	239	347
Zn	55	55	54	43	111	112	97	120	98
Ba	35	42	21	25	21	19	13	24	30

Table 26 (continued).

Hole, core, section:	857C-66R-1	857C-68R-1	857C-68R-1	857C-68R-2	857C-68R-2	857C-68R-2	857D-1R-1	857D-1R-2	857D-2R-1	857D-2R-1
Interval (cm):	25–27	108–111	26–29	11–13	11–13	144–146	2–4	82–84	73–75	77–79
SiO_2	40.68	49.39	42.15	47.58	47.69	49.63	49.33	46.43	48.08	48.67
TiO_2	2.81	1.64	2.34	1.64	1.65	1.59	1.84	1.82	1.62	1.63
Al_2O_3	20.46	16.83	17.48	17.39	17.56	16.27	15.28	17.38	17.64	17.44
Fe_2O_3	14.32	10.79	16.31	10.83	10.91	10.73	11.42	11.59	10.16	9.80
MnO	0.33	0.35	0.51	0.31	0.31	0.32	0.30	0.28	0.20	0.19
MgO	13.99	9.45	13.28	8.39	8.49	9.26	8.71	9.23	7.89	7.62
CaO	5.83	10.72	6.20	12.36	12.38	12.28	10.97	11.58	12.60	12.69
Na_2O	2.02	1.33	0.79	1.72	1.82	1.56	1.62	1.81	1.65	1.68
K_2O	0.04	0.02	0.01	0.03	0.03	0.01	0.01	0.00	0.00	0.00
P_2O_5	0.32	0.17	0.22	0.17	0.17	0.18	0.17	0.14	0.14	0.14
Total	100.8	100.69	99.29	100.42	101.01	101.81	99.66	100.29	99.98	99.86
LOI	6.78	3.13	5.37	3.34	3.34	2.57	2.81	3.42	2.68	2.43
Rb	1	1		0	0	0	1	0	0	0
Sr	134	110	68	129	129	115	96	117	111	112
Y	48	33	41	33	33	32	38	36	35	35
Zr	213	123	147	127	127	118	136	138	123	123
Nb	14	7		8	8	6	5	5	3	3
Ni	150	109	77	106	106	87	81	89	72	66
Cr	413	362	492	292	292	305	203	389	326	294
V	354	313	414	323	323	289	340	327	293	274
Zn	367	84	1250	152	152	102	73	144	62	55
Ba	45	21	0	33	33	15	20	24	32	15

the formation was indeed very permeable on average, so constant-rate injection tests were attempted. Injection was started at 38 strokes per minute, or spm (1 spm = 5 gallons/min = 18.93 L/min), but no pressure rise was observed on the surface gauges, so the pump rate was gradually increased. After the injection rate reached 80 spm, a small pressure rise was observed, so the pumps were held constant at this rate for 10 min and then the hole was shut in, as in a standard constant-rate injection test. Pressure decayed immediately at the surface, and two more injection tests were conducted at rates of 100 and 140 spm. Although the latter was close to the maximum that the ship's pumps could deliver, Figure 99 shows that the downhole pressure increase was quite small compared to the difference between the formation pressure and the cold hydrostat in the borehole. The small pressure increases at large injection rates, and immediate pressure decays on shut-in after pumping, indicate that the average permeability of the formation is very large, probably orders of magnitude greater than any value previously measured in any DSDP or ODP hole. This go-devil also gave a more reliable indication of the underpressure of the formation, which was on the order of 0.9 MPa relative to the cold hydrostat in the hole. Analysis of the injection tests to calculate the bulk permeability will require careful correction for the effects of this underpressure.

Table 26 (continued).

Hole, core, section: Interval (cm):	857D-3R-2 67–69	857D-3R-2 94–96	857D-4R-1 9–11	857D-7R-1 16–18	857D-8R-1 73–75	857D-8R-1 73–75	857D-15R-1 58–60	857D-18R-2 84–87	857D-20R-1 64–67	857D-21R-1 62–65
SiO_2	48.29	48.96	48.83	50.97	39.04	47.82	47.45	49.21	49.23	51.54
TiO_2	1.59	1.58	1.57	1.96	1.92	1.73	1.85	1.7	1.49	1.58
Al_2O_3	17.99	17.34	17.78	14.68	22.18	15.41	17.26	15.64	13.58	15.18
Fe_2O_3	9.87	9.56	10.26	11.64	13.99	10.84	14.04	11.15	11.66	10.59
MnO	0.24	0.22	0.26	0.25	0.29	0.33	0.28	0.23	0.21	0.19
MgO	8.08	7.89	8.16	7.54	14.28	8.37	13.98	8.19	11.99	7.37
CaO	12.46	11.85	11.99	11.50	6.49	11.51	5.19	12.15	11.11	12.94
Na_2O	1.78	1.74	1.63	1.86	1.21	1.53	0.94	2.12	1.37	2.01
K_2O	0.01	0.01	0.00	0.01	0.00	0.00	0.02	0.02	0.01	0.03
P_2O_5	0.14	0.14	0.18	0.15	0.15	0.16	0.16	0.14	0.16	0.15
Total	100.45	99.29	100.62	100.59	99.55	97.7	101.17	100.55	100.81	101.58
LOI	2.1	2.87	2.19	1.81	6.42	0	6.84	2.68	3.07	1.38
Rb	1	1	0	1	1	1	0	0	1	1
Sr	113	109	107	107	66	66	62	118	100	122
Y	33	34	33	42	41	41	36	33	34	32
Zr	120	120	118	145	109	109	120	115	120	119
Nb	3	3	3	5	3	3	4	4	4	4
Ni	71	67	70	64	142	142	86	67	177	57
Cr	288	304	274	153	597	597	369	299	353	191
V	273	285	283	364	351	351	337	347	271	315
Zn	102	79	121	92	177	177	192	112	108	63
Ba	10	9	18	31	16	16	15	11	20	17

Table 26 (continued).

Hole, core, section: Interval (cm):	857D-22R-1 52–55	857D-24R-1 112–115	857D-32R-1 60–65
SiO_2	47.18	51.96	52.21
TiO_2	1.61	1.48	2.00
Al_2O_3	16.34	16.20	14.17
Fe_2O_3	10.20	9.87	10.52
MnO	0.23	0.22	0.23
MgO	8.59	7.87	6.89
CaO	12.29	11.93	11.80
Na_2O	1.93	2.25	2.15
K_2O	0.03	0.04	0.01
P_2O_5	0.15	0.15	0.19
Total	98.55	101.97	100.17
LOI	3.09	1.9	1.99
Rb	1	0	0
Sr	149	151	138
Y	34	29	41
Zr	129	124	155
Nb	5	6	6
Ni	68	60	66
Cr	217	268	195
V	321	279	358
Zn	80	71	71
Ba	19	20	27

Third Go-devil and Flowmeter Experiment (Packer at 96 mbsf)

The extreme permeability of the formation provided nearly ideal conditions for the flowmeter/injection experiment, which had been partially tested during Leg 137 (Becker, Foss, et al., 1992). The packer was left uninflated in position in the casing, logging sheaves were rigged, and the flowmeter logging tool, sinker bar, and logging cable go-devil were run into the hole. After a pressure calibration stop at 2410.1 mbsf, the go-devil was run to the packer and the packer was successfully inflated. Pump pressure was then increased to shear the release pins in the go-devil and free the logging cable so that the flowmeter tool could be run into the section of hole isolated by the packer.

The flowmeter tool was lowered to near the bottom of casing, at which point the ship's pumps were used to calibrate the spinner reading at known flow rates. Heave introduced significant noise in the spinner readings, particularly at low flow rates—a situation which probably could have been mitigated had the wireline heave compensator been available.

The flowmeter tool was then run into the hole for stationary measurements at 5- to 10-m intervals while the mud pumps were turned up to the maximum steady injection rate, 150 spm. Within 60 m below the bottom of the casing, the flowmeter readings dropped so low relative to the noise introduced by heave that no reliable information would have been collected by continuing any deeper. The tool was then raised back into the casing, stopping at two depths not logged before. The flowmeter was then recalibrated within casing at a pump rate of 150 spm, and the packer was deflated.

As soon as the packer deflated, the spinner reading more than tripled, indicating that the formation was so underpressured that it was drawing bottom water at roughly three times the maximum rate that the ship's pumps could deliver! The estimated rate at which the formation was naturally drawing fluids is equivalent to 400–500 spm, or the order of 10,000 L/min. This rate is nearly two orders of magnitude greater than the rates of similar downhole flows observed in DSDP Holes 395A and 504B (Becker et al., 1983, 1984; Kopietz et al., 1990).

Given that the formation was drawing bottom water so strongly, the packer and ship's pumps were actually unnecessary for the experiment, and the log was repeated at intervals of 10–20 m utilizing the induced flow down the hole. With the larger injection rate, the flowmeter gave valid readings down to about 120 m below the base of the casing, by which point most of the massive downhole flux had been diverted into the formation. The flowmeter was then pulled back into the casing for a final calibration, and the experiment was ended.

At each station, flow, pressure, and caliper were logged. These three parameters are necessary to convert the variation in flow rates to a permeability "log" of the formation. Calculating the variation of permeability with depth will require considerable post-cruise analysis, but comparing the variation in flow readings immediately pinpoints the zones into which the downhole flow is directed (Fig. 100). It is clear from this comparison that the great majority of the downhole

Table 27. Normative compositions of igneous rocks from Holes 857C and 857D.

Hole, core, section:	857C-59R-1	857C-59R-2	857C-59R-3	857C-60R-1	857C-62R-1	857C-62R-2	857C-64R-1	857C-64R-2	857C-66R-1	857C-68R-1	857C-68R-2
Interval (cm):	106–108	138–139	101–103	13–15	46–48	60–62	63–66	33–35	114–116	108–111	11–13
Apatite	0.42	0.44	0.42	0.44	0.28	0.36	0.31	0.22	0.59	0.37	0.37
Ilmenite	3.27	3.27	3.14	3.32	2.68	3.26	2.75	2.25	4.33	3.12	3.13
Orthoclase	0.06	0.06	0.06	0.18	0.00	0.00	0.06	0.00	0.24	0.12	0.18
Albite	17.75	16.85	17.38	19.72	15.56	15.28	17.72	12.93	15.60	11.27	14.62
Anorthite	32.43	32.47	33.48	31.85	35.70	35.00	34.10	33.72	37.50	39.96	39.82
Corundum	0.00	0.00	0.00	0.00	0.00	0.00	0.00	0.00	0.00	0.00	0.00
Magnetite	1.32	1.28	1.35	1.42	1.42	1.36	1.30	1.45	1.58	1.43	1.44
Hematite	0.00	0.00	0.00	0.00	0.00	0.00	0.00	0.00	0.00	0.00	0.00
Diopside	23.92	22.87	14.45	24.14	2.99	13.44	22.01	3.72	17.56	10.07	17.00
Hypersthe	18.72	19.50	24.61	11.42	35.67	31.24	19.50	41.08	16.06	32.16	16.08
Quartz	2.08	3.26	5.11	0.00	0.00	0.00	0.00	4.62	0.00	1.49	0.00
Forsterite	0.00	0.00	0.00	4.44	3.86	0.04	1.39	0.00	3.71	0.00	4.33
Fayalite	0.00	0.00	0.00	3.07	1.84	0.02	0.87	0.00	2.82	0.00	3.03
Total	100.00	100.00	100.00	100.00	100.00	100.00	100.00	100.00	100.00	100.00	100.00

Table 27 (continued).

Hole, core, section:	857C-68R-2	857D-1R-1	857D-1R-2	857D-2R-1	857D-2R-1	857D-3R-2	857D-3R-2	857D-4R-1	857D-7R-1	857D-8R-1	857D-18R-2	857D-20R-1
Interval (cm):	144–146	2–14	82–84	73–75	77–79	67–69	94–96	9–11	16–18	73–75	84–87	64–67
Apatite	0.35	0.37	0.37	0.31	0.29	0.31	0.31	0.30	0.39	0.33	0.31	0.35
Ilmenite	2.97	3.53	3.48	3.10	3.12	3.03	3.05	3.02	3.74	3.32	3.24	2.84
Orthoclase	0.12	0.06	0.00	0.06	0.00	0.06	0.06	0.06	0.06	0.00	0.12	0.06
Albite	14.16	13.82	15.41	15.22	14.73	15.11	14.94	14.13	16.53	15.44	18.00	11.61
Anorthite	36.37	34.60	39.55	40.37	40.15	41.20	40.06	41.07	31.46	42.03	33.21	30.91
Corundum	0.00	0.00	0.00	0.00	0.00	0.00	0.00	0.00	0.00	0.00	0.00	0.00
Magnetite	1.39	1.53	1.54	1.36	1.30	1.31	1.28	1.36	1.53	1.43	1.48	1.54
Hematite	0.00	0.00	0.00	0.00	0.00	0.00	0.00	0.00	0.00	0.00	0.00	0.00
Diopside	18.82	15.74	14.12	17.48	18.51	16.33	15.33	14.66	20.22	11.74	21.65	18.93
Hypersthe	23.88	28.33	12.14	18.03	21.77	18.27	24.20	23.82	22.66	18.39	17.71	29.24
Quartz	0.00	2.02	0.00	0.00	0.00	0.00	0.77	0.00	3.42	0.00	0.00	0.00
Forsterite	1.19	0.00	8.00	2.41	0.08	2.65	0.00	0.95	0.00	4.34	2.47	2.94
Fayalite	0.75	0.00	5.37	1.67	0.05	1.72	0.00	0.64	0.00	2.99	1.80	1.58
Total	100.00	100.00	100.00	100.00	100.00	100.00	100.00	100.00	100.00	100.00	100.00	100.00

Table 27 (continued).

Hole, core, section:	857D-21R-1	857D-22R-1	857D-24R-1	857D-32R-1	857C-8R-1	857C-8R-1	857C-8R-1	857C-8R-2
Interval (cm):	62–65	52–55	112–115	60–65	108–111	2–4	73–75	84–87
Apatite	0.33	0.35	0.35	0.42	0.37	0.40	0.36	0.29
Ilmenite	2.98	3.13	2.79	3.83	3.15	3.54	3.40	3.27
Orthoclase	0.18	0.18	0.24	0.06	0.06	0.06	0.00	0.12
Albite	16.88	18.32	18.10	18.31	11.16	13.88	13.37	16.66
Anorthite	32.07	35.60	33.80	29.18	39.87	34.83	36.33	34.06
Corundum	0.00	0.00	0.00	0.00	0.00	0.00	0.00	0.00
Magnetite	1.39	1.37	1.30	1.40	1.43	1.53	1.48	1.48
Hematite	0.00	0.00	0.00	0.00	0.00	0.00	0.00	0.00
Diopside	25.23	20.37	19.65	23.48	10.26	15.73	17.73	21.32
Hypersthe	18.74	11.02	22.10	18.09	32.33	28.40	26.65	20.18
Quartz	2.21	0.00	1.68	5.23	1.36	1.63	0.68	0.00
Forsterite	0.00	5.91	0.00	0.00	0.00	0.00	0.00	1.53
Fayalite	0.00	3.75	0.00	0.00	0.00	0.00	0.00	1.11
Total	100.00	100.00	100.00	100.00	100.00	100.00	100.00	100.00

flow is diverted into the formation at a depth of 610–615 mbsf; this is the same section into which circulation was lost when the drill suddenly broke through hard formation above ("Operations" section, this chapter). Accounting for possible relative depth errors of ±5 m, this zone clearly corresponds to a 3- to 5-m section with anomalous spontaneous potential (SP) readings and very low resistivity immediately below a sill with higher resistivity ("Downhole Logging" section, this chapter). Thus, the sill must act as a cap rock over an extremely permeable and underpressured formation; in fact, this zone accepts so much fluid that the concept of its "permeability" may be of questionable validity. Unfortunately, core recovery was very poor in this zone, and its composition is unclear.

Sufficient downhole flow continued past this formation to allow a qualitative assessment of the variation of permeability in the 50–75 m below it (Fig. 100). The steady decrease in the flowmeter count between 620 and 645 mbsf suggests a significant permeability for this zone, whereas the relatively steady count between 645 and 680 mbsf suggests a lower permeability. The decrease in flowmeter count between 680 and 695 mbsf indicates another permeable zone. In fact, this section includes a zone of anomalous SP reading and low resistivity similar to that of the highly permeable zone at 610–615 mbsf, except that there is no overlying sill.

Fourth Go-devil (Packer at 756 mbsf)

The flowmeter experiment had shown that most of the downhole flow is diverted into the upper section of open hole, so it was decided to run the packer below this zone and measure the permeability of the deeper section of open hole. The packer was run to 756 mbsf, 180 m above the bottom of the hole, and inflated at the center of the thickest

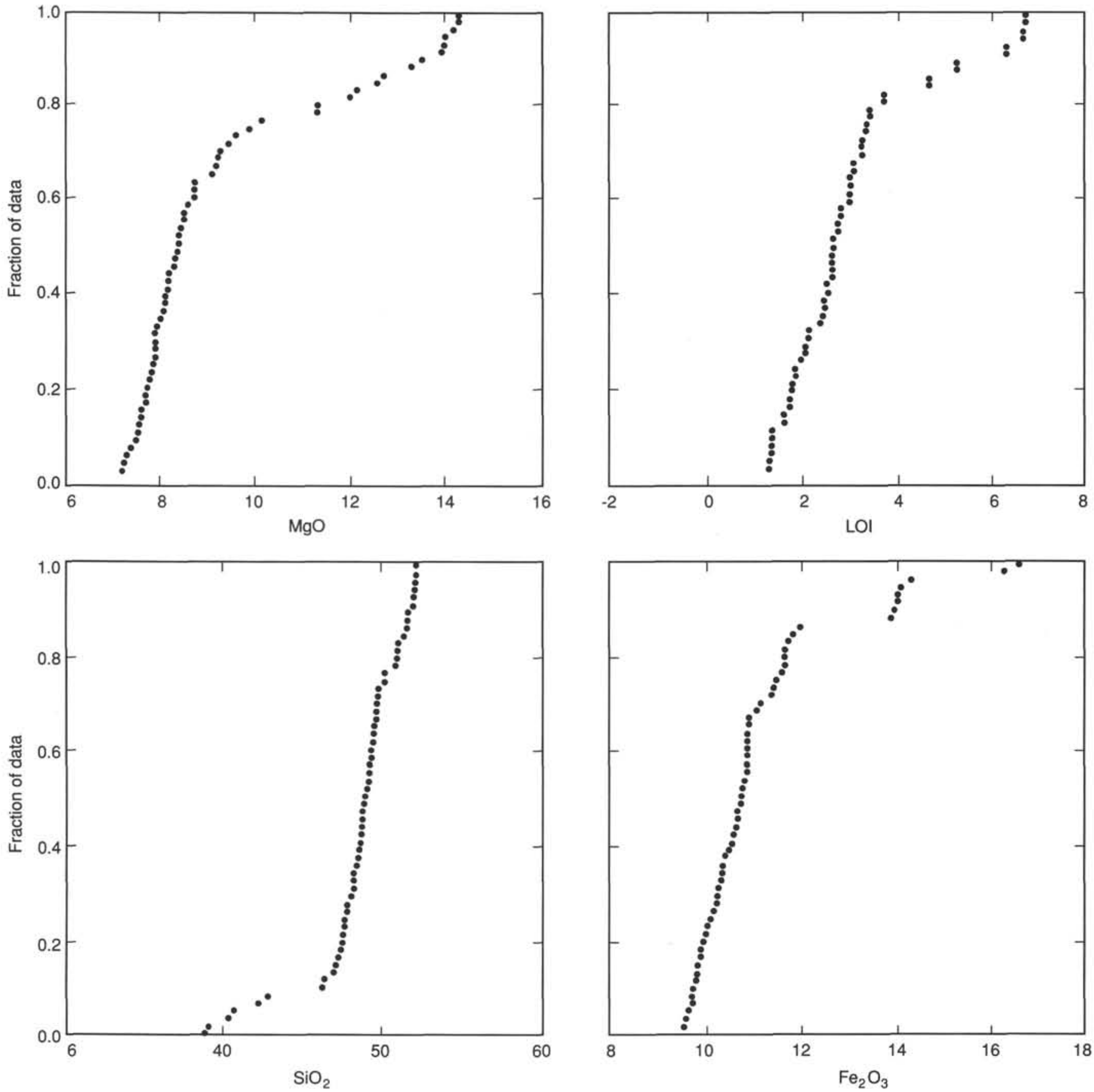

Figure 62. Cumulative frequency plots of selected major elements and loss on ignition (LOI) for all Site 857 data. Major breaks in slope indicate different populations of data.

sill cored in Hole 857D. Previous logs had indicated that this interval is particularly smooth and round. Figure 101 shows the record of testing during this packer inflation. Three slug tests were attempted, including the slug test that automatically occurs when the packer is inflated. Pressure readings at the surface decayed quickly, and two constant-rate injection tests were conducted. The injection tests showed that this section of hole is significantly less permeable than the formations in the upper part of open hole, although it is still roughly as permeable as the upper sections of basement in DSDP Holes 504B and 395A (Anderson and Zoback, 1982; Becker, 1990).

When the downhole gauges were recovered, they showed longer decay periods for both the slug tests and injection tests than the rapid decays seen on the surface gauges, because of the difference between hydrostatic pressure in the borehole and the pressure of the formation. As this pressure differential is probably quite large, the fact that the downhole flow does not appear to extend at any significant rate to this depth supports the conclusion that this section is significantly less permeable than the upper 100 m of open hole. The first slug test and the second injection test (Fig. 101) both appear to be of excellent quality for determining the permeability of the lower section of the hole; calculating this value will require careful analyses, accounting for the effects of the formation underpressure and the large variations in fluid properties due to the steep thermal gradient in this section of the hole taken into account.

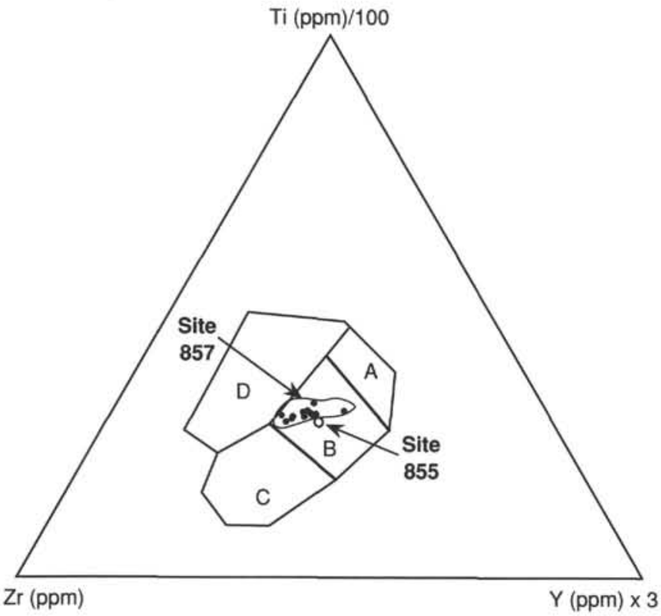

Figure 63. Plot of Ti-Zr-Y for all "unaltered" samples (see text). Note the broad distribution of data relative to Site 855. Ti data are divided by 100, Y data are multiplied by 3. Ocean-floor tholeiite compositions are in field B. Low-potassium tholeiite is in fields A and B, continental basalt in field D, and calc-alkali basalt in fields C and B. Field boundaries from Pearce and Cann (1973).

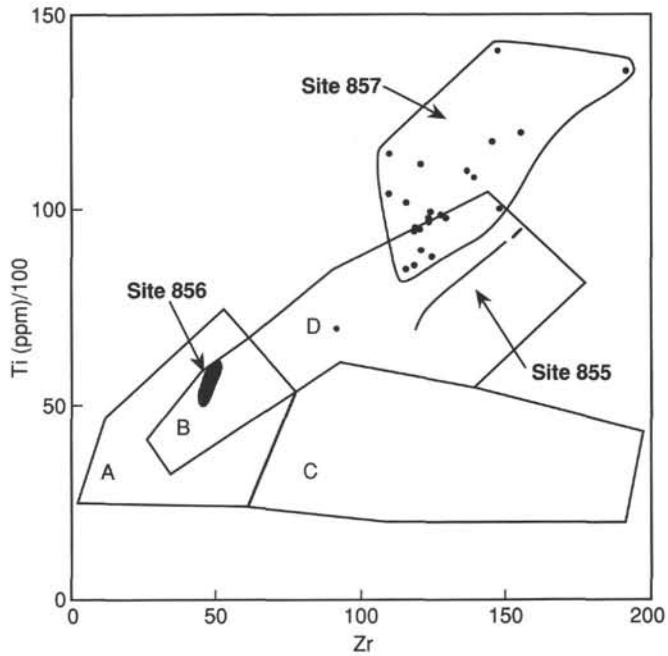

Figure 64. Plot of Zr vs. Ti content of samples from Site 857. Note the broad scatter of data, in contrast with for Sites 855 and 856. The moderate positive trend of the data, and its excursion away from the fields for basalt, indicate fractional crystallization.

Instrumented Borehole Seal or CORK

At the end of operations at Site 857, Hole 857D was sealed with the CORK and instrumented with a thermistor string, pressure sensor, fluid sampling tubing, and long-term data logger (see Davis et al., this volume). Figure 102 shows the configuration of the instrumentation deployed. This was the first complete deployment of the instrumented borehole seal, and the operations proceeded remarkably smoothly, requiring several hours fewer than budgeted. Only one problem was encountered, that being two severe twists of the Teflon tubing near the top of the sensor string. These bends threatened to break downhole and were repaired by splicing new tubing in place with Swagelok fittings made of Inconel, the same material as the sinker bar. On the basis of this experience, it was decided that during future deployments of the instrumented borehole seal the fluid sampling tubing should be attached to the thermistor cable as the cable is being run into the hole. Data and samples from the CORK were scheduled to be collected from the submersible *Alvin* about 10 days after the end of Leg 139, roughly three weeks after the deployment of the instrumentation.

SUMMARY AND CONCLUSIONS

Site 857 is located 5.2 km west of Site 855 and the normal-fault scarp that forms the eastern boundary of Middle Valley. It is located on the major thermal anomaly in this part of the valley, 1.6 km south of the high-temperature discharge zone at Site 858. Within this anomaly, conductive heat flow through the seafloor exceeds 0.8 W/m^2 over an area 1 km wide by 15 km long that is elongate parallel to the axis of the rift. The main objective of drilling at this site was to test the hypothesis that there is a high-temperature hydrothermal reservoir at depth that is thermally and chemically well mixed and is supplying hot water to the vents at Site 858.

Four holes were drilled in order to meet this objective. APC/XCB Hole 857A was drilled and cored to refusal at 112 mbsf. Hole 857B was mainly washed to make additional temperature measurements. Because the conductive heat flow of 0.71 W/m^2 determined from these measurements was lower than desired, RCB Hole 857C was drilled 180 m to the east, closer to the axis of the thermal anomaly, to a depth of 568 mbsf. The temperature gradient measured in this hole indicates that heat flow is conductive at 0.80 W/m^2. Hole 857D is a reentry hole 50 m northeast of Hole 857C. It was drilled without coring to 581 mbsf, cased, and then continuously cored to 936 mbsf. These holes penetrated interbedded turbidites and hemipelagic sediment to about 470 mbsf, followed by basaltic sills alternating with sediment to the maximum depth drilled. Hole 857D bottomed in highly altered and indurated sediment.

Sediment at Site 857 is divided into two lithostratigraphic units that are similar to those at Sites 856 and 858. Unit I is silty clay of Holocene to late Pleistocene age and extends to 25 mbsf in Hole 857A, the only hole in which the base of the unit was sampled. It contains several thin layers that are presumed to be turbidites, but is mainly hemipelagic.

Unit II is interbedded turbidites and hemipelagic sediment that is divided into three subunits based on degree of induration and hydrothermal alteration. Subunit IIA extends to about 100 mbsf and shows little or no induration. It commonly contains carbonate nodules and cement, as well as disseminated and nodular pyrite and, more rarely and at deeper levels, barite and anhydrite. Subunit IIB is moderately indurated because it is cemented by carbonate. It extends to 462 mbsf, just above the first sill, and becomes increasingly sandy with depth, especially below 284 mbsf. Like Subunit IIA, it contains carbonate nodules and disseminated and nodular pyrite. Below about 400 mbsf it also uncommonly contains pyrrhotite, chalcopyrite, and sphalerite, both in fractures and in rare clasts of massive sulfide at the base of turbidites. Subunit IIC occurs in layers interbedded with mafic sills that were first encountered at 471 mbsf in Hole 857C and 463.5 mbsf in Hole 857D. The unit was sampled below 471 mbsf in Hole 857C and below 581 mbsf in Hole 857D. The uppermost sill in Hole 857D occurs at a depth of 463.5 m in the interval of the hole that was drilled without coring in order to set casing. Sediment in this subunit completely lacks carbonate and is cemented instead with quartz. It is highly deformed and displays soft-sediment deformation, high-angle normal and reverse microfaults, tight isoclinal folds and other evidence of plastic flow, and nearly vertical or overturned bedding. Fracture fillings include various combinations of quartz, chlorite,

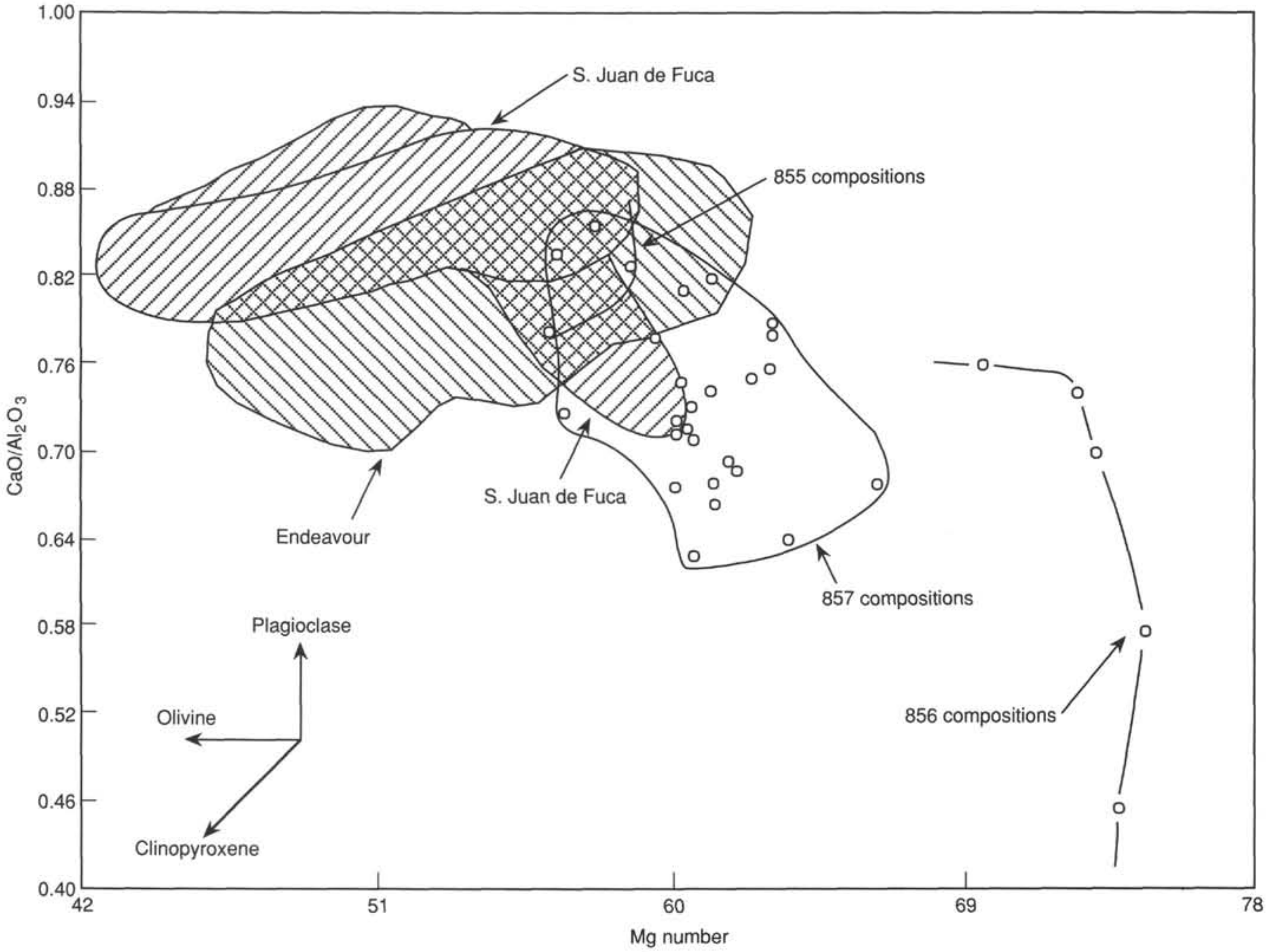

Figure 65. Plot of CaO/Al_2O_3 vs. Mg number. Field boundaries from Karsten et al. (1990). The compositions of samples from Site 857 form a poorly defined linear trend that extends well away from the normal MORB fields for Juan de Fuca Ridge basalts. Compositions are not corrected for plagioclase accumulation.

epidote, zoisite, zeolite, pyrite, pyrrhotite, and sphalerite. Epidote is abundant in sandstones near contacts with the sills.

Compositional variation in the sediment reflects primary differences that are related to grain size, and secondary differences that result from hydrothermal alteration and metasomatism. At depths above 150 mbsf, chemical covariation is dominated by the relative abundances of (1) a coarse clastic component comprising mainly quartz and plagioclase and causing covariation in SiO_2, CaO, and Na_2O; and (2) a clay component comprising chlorite and illite and causing covariation in TiO_2, Al_2O_3, Fe_2O_3, MgO, K_2O, H_2O, Rb, Cu, and Zn. The only systematic change with depth over this interval is a two-fold or more decrease in $CaCO_3$. Between 150 mbsf and the depth of the first sill, the effects of hydrothermal metasomatism are most obvious for Na_2O. Between 150 and 230 mbsf, Na_2O doubles from about 2 to 4 wt%, while CaO remains constant, whether adjusted for carbonate content or not, as do the other major oxides. Na_2O decreases between 300 and 400 mbsf to its original concentration of about 2%, then increases again to about 500 mbsf, then decreases yet again with increasing depth. Below the depth of the first sill, K_2O and Rb virtually disappear from the sediment, possibly by conversion of illite to chlorite. Barium and Cu are also heavily leached, while Zn decreases slightly and SiO_2 increases substantially. Many of these changes, especially the increase in Na_2O centered at about 300 mbsf, are complementary to changes in the composition of the sediment pore water.

Foraminifers are abundant to common at depths above 85 mbsf; below this depth, recovery of sediment was poor and both foraminifers and calcareous nannofossils are poorly preserved. About half of the samples below 85 mbsf are barren of foraminifers, about one-quarter are barren of calcareous nannofossils. Two extensive barren intervals characterize Hole 857C: 240–328 mbsf and 394–471 mbsf. Hole 857C also had the most diverse nannofossil species and nannofossils to the greatest depth (390 mbsf). Foraminifers and calcareous nannofossils are completely absent in Hole 857D.

Sediment of Holocene age was found in all three of the holes in which samples were collected immediately below the seafloor. The samples are assigned to foraminiferal Zone CD1 of Lagoe and Thompson (1988). The Holocene-Pleistocene boundary lies within the first core from each hole, and in Hole 857B lies above 3.4 mbsf. A single sample that might be from the penultimate interglacial was tentatively assigned to Zone CD3 of Lagoe and Thompson (1988). All other samples were assigned to the late Pleistocene Zones CD2 and CD4. The *Emiliania huxleyi* Acme Zone was recognized in all of the three shallow holes at Site 857. Based on the presence of this calcareous nannofossil zone, sedimentation rates are estimated to be 242 m/m.y. for Hole 857A and 177 to 415 m/m.y. for Hole 857B. The mean sedimentation rate determined from three paleontological datums is 220 m/m.y., which is considerably faster than the Holocene to latest Pleistocene rates estimated from ^{14}C data. It is, however, similar to average rates calculated for the Pleistocene section at Site 174 on the

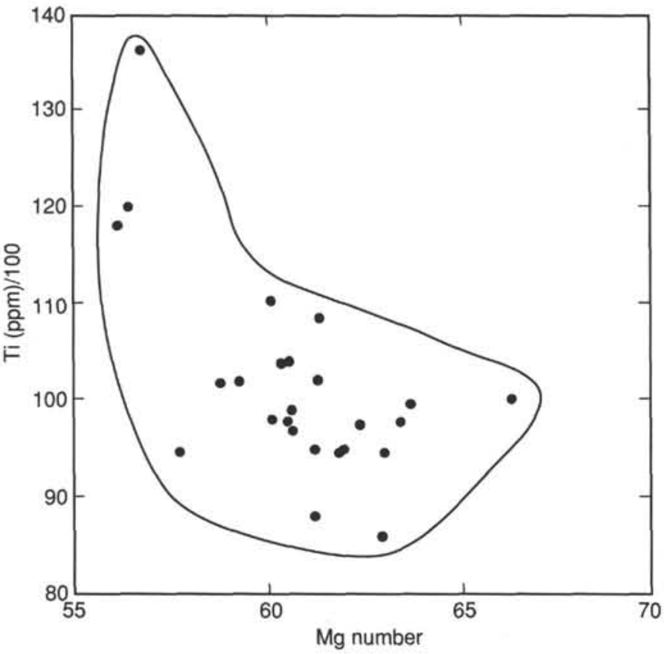

Figure 66. Plot of Mg number vs. Ti contents of samples from Site 857. Note the upward-negative trend, with a few unusually titanium-rich samples, indicating extreme fractional crystallization or accumulation of ilmenite. The fractionation could have occurred *in situ* or within a crustal magma chamber.

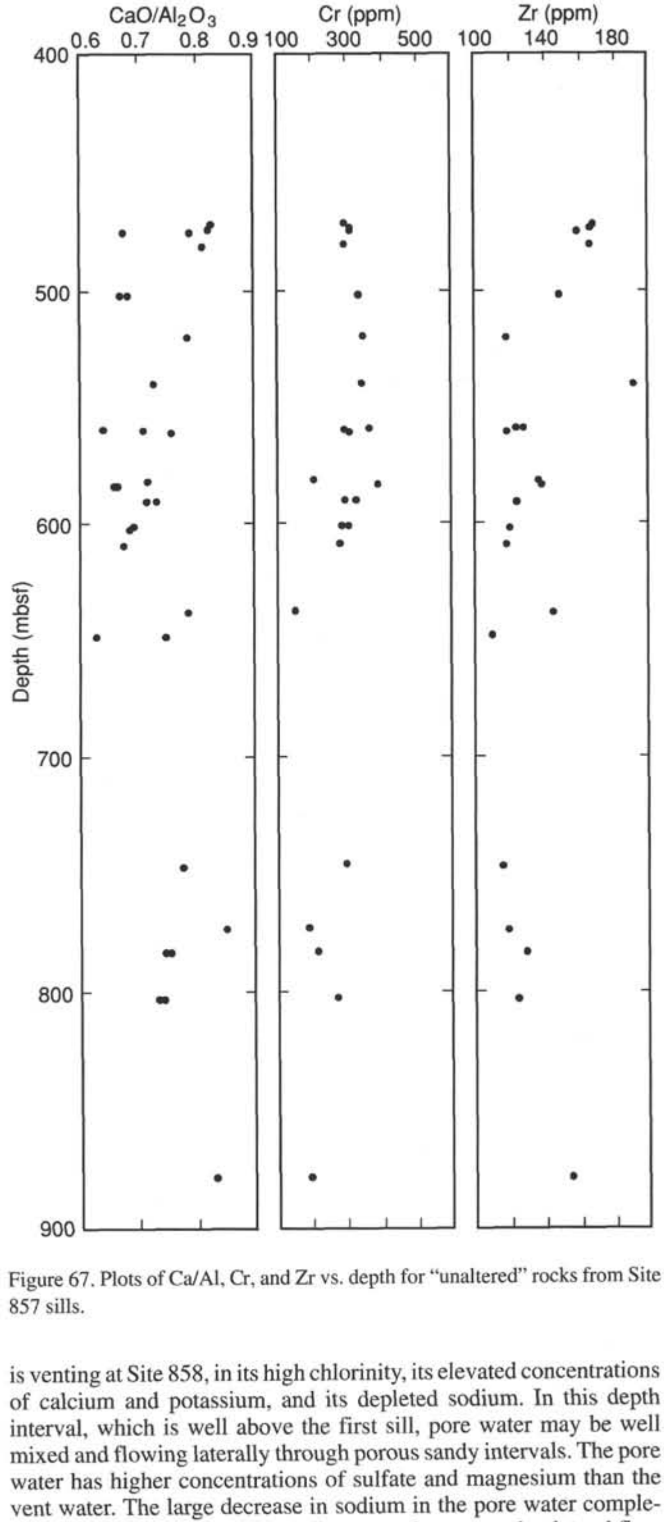

Figure 67. Plots of Ca/Al, Cr, and Zr vs. depth for "unaltered" rocks from Site 857 sills.

Astoria Fan. The age of the crust and the thickness of sediment penetrated at Site 857 imply that sedimentation rates were much higher before 125 ka.

Measurements of magnetic properties indicate that the zone of lower magnetic intensity and susceptibility found at Site 856 is also present at Site 857, at 15 to 24 mbsf in Hole 857A. In Hole 857C, the magnetic intensity and susceptibility of the sediment decrease with depth, apparently as a result of increasing alteration of detrital magnetite. The magnetization of the igneous rock in the sill complex also decreases sharply with depth from the top of the first sill. The average intensity is extremely low compared with fresh young oceanic basalt. It is even low compared with hydrothermally altered sheeted dikes from DSDP Hole 504B. Susceptibility of the igneous rocks is highest near the top of the sill complex and decreases with depth to values below that observed at the dike-lava transition zone in Hole 504B. Paleomagnetic results from igneous rocks from Hole 857D are scattered and suggest that a stable thermoremanent magnetization may have been acquired during drilling by contact of cold drilling fluid with the hot rock within the distorted magnetic field at the end of the core barrel. A sample subjected to thermal demagnetization was estimated to have a Curie temperature of 500°C. It is from a horizon in which titanomagnetite is visibly altered to sphene or rutile. The low central magnetic anomaly of Middle Valley can be explained by the low magnetic intensity of the hydrothermally altered sediment and sills. No petrographic evidence was found for high-temperature oxidation and exsolution of ilmenite lamellae; however, high-temperature deuteric oxidation could produce the high measured Curie temperature.

The chemical composition of pore water has been changed from that of bottom seawater by early diagenesis, as well as by water-rock reaction at temperatures that exceed 250°C. These processes include bacterial degradation of organic matter, reaction with detrital silicates and basaltic sills, recrystallization of biogenic carbonates and silicates, hydration of silicates, and transport processes. Chlorinity profiles require either a non-steady-state condition or lateral flow, probably at several depths; we prefer the latter explanation. Pore water from 300 to 400 mbsf closely resembles the 276°C water that is venting at Site 858, in its high chlorinity, its elevated concentrations of calcium and potassium, and its depleted sodium. In this depth interval, which is well above the first sill, pore water may be well mixed and flowing laterally through porous sandy intervals. The pore water has higher concentrations of sulfate and magnesium than the vent water. The large decrease in sodium in the pore water complements a large increase in the sediment, and suggests that lateral flow through this depth interval has a significant history. Below 400 mbsf, the trends in pore-water composition generally reverse. There is no evidence for vertical fluid flow at Site 857.

The variations in amount and composition of gases observed downhole at Site 857 appear to reflect *in-situ* downhole temperatures. Exponential increases in methane, ethane, and propane occur from 200 to 300 mbsf at Site 857, consistent with thermogenic sources either *in situ* or at depth. The temperature range of this zone, 150° to 200°C, falls within the gas generation portion of the petroleum

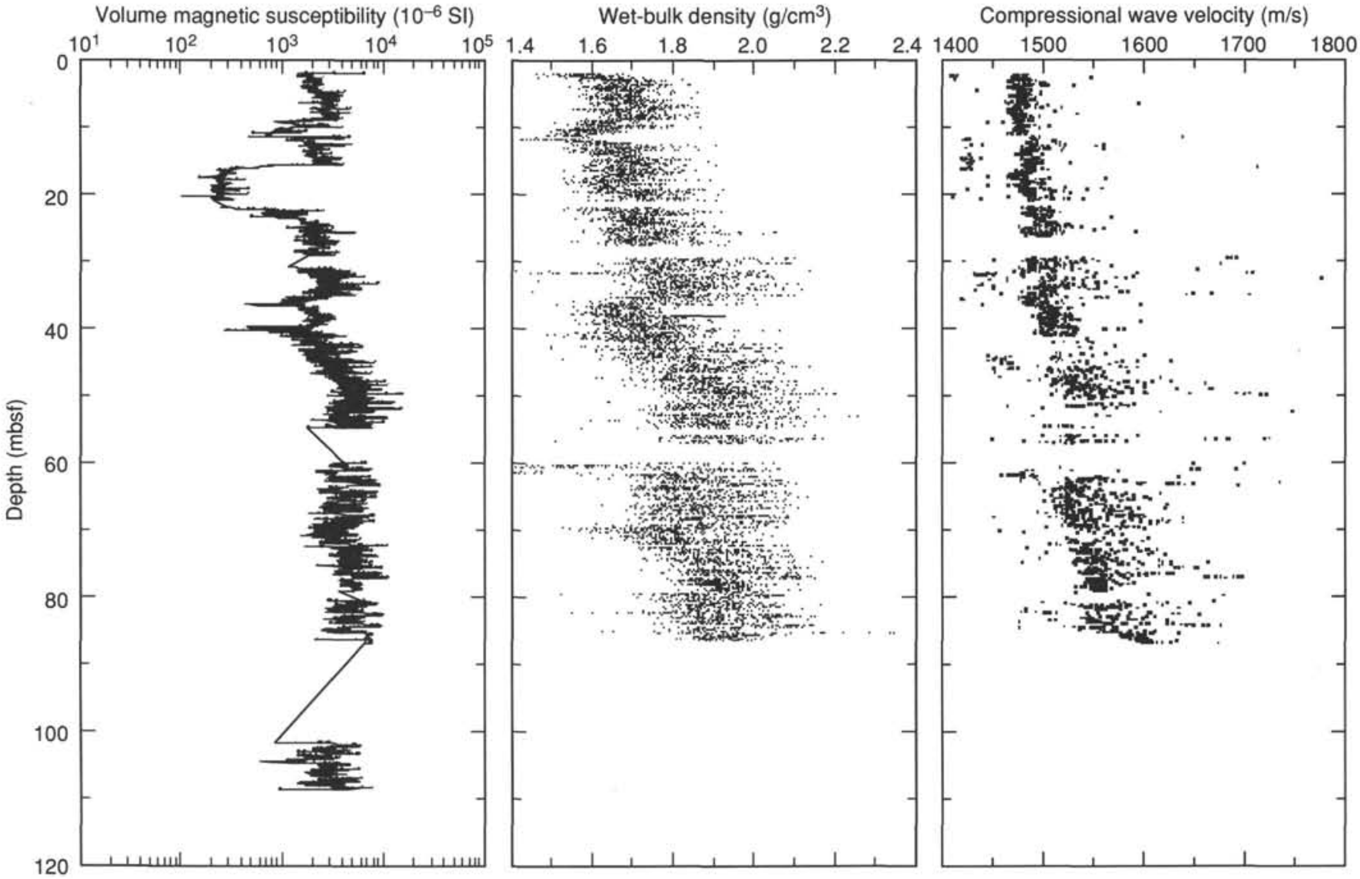

Figure 68. Magnetic susceptibility, GRAPE bulk density, and PWL compressional wave velocity in Hole 857A. Data gaps reflect low core recovery.

thermal window, consistent with an *in-situ* thermal source from kerogen. The total organic carbon concentrations, 0.3% to 0.55%, are too low for efficient petroleum generation and primary expulsion, suggesting cracking of both kerogen and bitumens to gas at higher temperatures. The leveling out of methane, ethane, and propane observed from about 300 to 450 mbsf in Hole 857C could be caused by (1) a depletion of the gas generation capability of the *in-situ* kerogen and bitumen, (2) a steady-state condition where the rates of gas generation and expulsion into shallower zones from a specific depth interval are approximately equaled by the rate of upward gas migration from deeper and hotter zones, or (3) a decrease in geothermal gradient in deeper intervals, where the temperature either remains constant or decreases below 300 mbsf. Alternatively, the methane profile (but not ethane or propane) is similar to that of calcium, so that diffusional processes could be important for this gas. Carbon dioxide is also a ubiquitous gas in these sediments to all depths and, considering the low amounts of calcium carbonate, may also have a kerogen source in Site 857 sediments.

The concentration levels of extractable organic matter are extremely low throughout, based on color and fluorescence intensities, consistent with low petroleum-generating potential. The amounts gradually decrease with depth. This low yield, together with low total organic carbon values, indicate that migrated bitumens are not important and the hydrocarbon signatures can be utilized as indicators for *in-situ* alteration conditions. The gradual decrease with depth may indicate thermal alteration (oxidation) of the organic matter, possibly to CO_2. Changes in composition of specific hydrocarbons diagnostic of maturation, such as the carbon preference index, are consistent with this interpretation.

The extrapolation of present-day subsurface temperatures leads to the surprising result that the higher molecular weight compounds ($>C_{14}$) are surviving in these sediments to temperatures considerably beyond those considered normal for the oil-generation window. Thus, the thermal alteration and destruction of these typical aliphatic petroleum hydrocarbons is not complete up to temperatures of 270°C at 433 mbsf in Hole 857C. Their gradual thermal destruction, together with that of the remaining residual kerogen, is a potential source for the C_1 to C_3 hydrocarbons and of the CO_2 found in these sediments. It is possible that survival of C_{14+} hydrocarbons to depths and temperatures well beyond those generally considered "normal" for the oil window is due to the young age of the sediments. Alternatively, as suggested by the organic geochemical data, the actual maximum temperatures experienced by sediment below 300 mbsf in Hole 857C may be less than the values estimated from the surface heat flow.

Total carbon varies from about 0.5% to 1% in Hole 857A and 0.4% to 0.7% in Hole 857C, comparable to the general range observed at Sites 855 and 856. Except for a few intervals rich in carbonate, the total carbon is about equally divided between organic and inorganic carbon. A series of peaks and valleys in the H, N, and S percentage curves can be observed below 300 m in Hole 857C at about the same depth at which the concentrations of the C_1 to C_3 gases level off and at which a maximum is observed in pore-water calcium. All of these phenomena may be related to lateral fluid flow through the sediment at this depth and below.

Igneous rock was recovered from Holes 857C and 857D as a series of mafic sills 1 to 25 m thick, interlayered with sediment. In Hole 857C, mafic sills were encountered between 471 and 568 mbsf, and a cumulative total of 20.6 m of igneous rock was recovered. In Hole 857D,

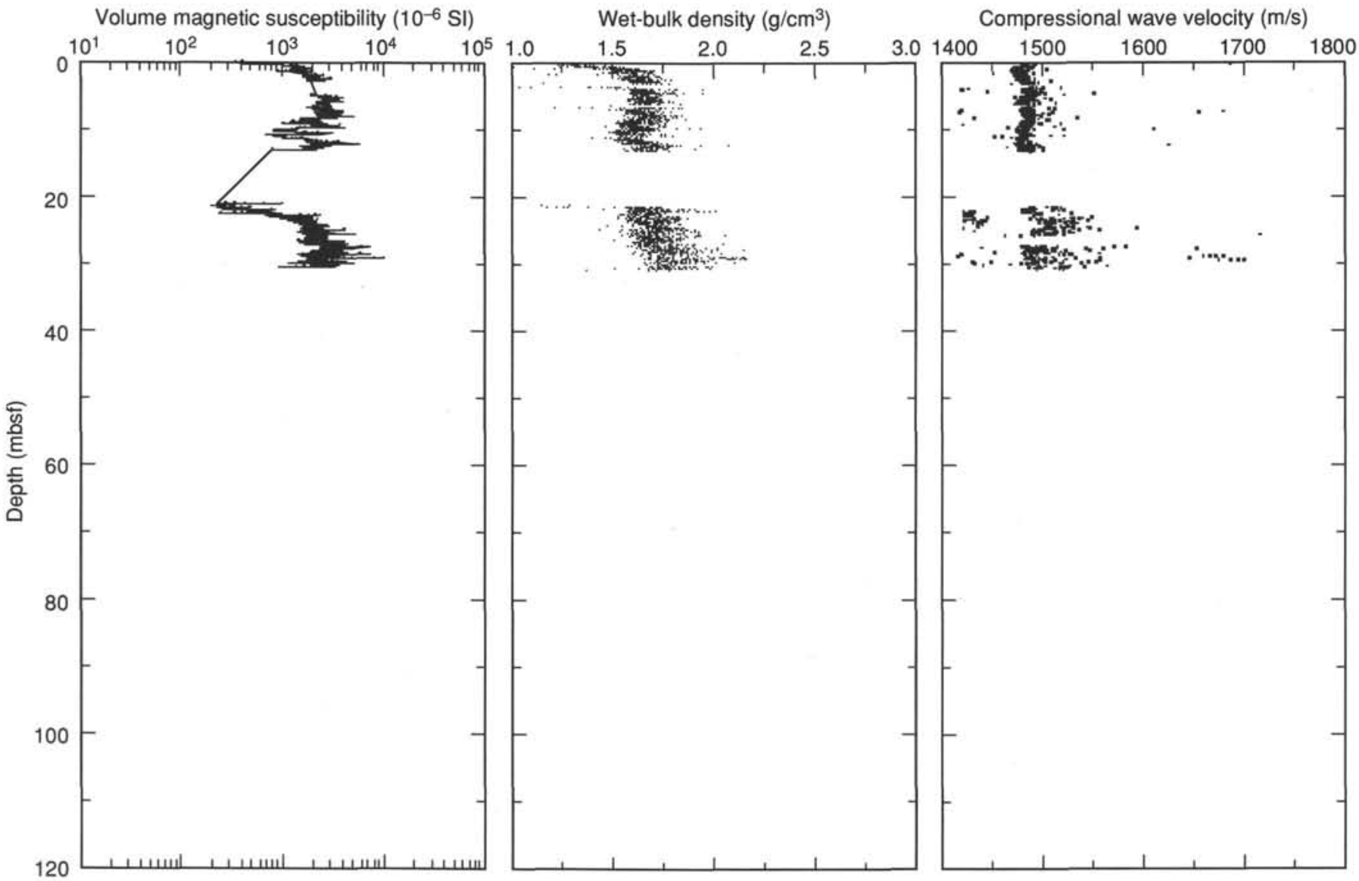

Figure 69. Magnetic susceptibility, GRAPE bulk density, and PWL compressional wave velocity in Hole 857B. Data gaps reflect low core recovery.

mafic sills and interlayered sediment were cored between 581 and 936 mbsf, and 30.7 m of igneous rock were recovered. Many of the cored sills are characterized by chilled margins against the adjacent sedimentary units, and by a gradual change in grain size from fine-grained margins to coarse-grained, gabbroic interiors. The chilled margins are extensively metamorphosed and the adjacent fine-grained rock is heavily veined and vesicular. A resistivity log from Hole 857D reveals conspicuous highs associated with the sills and lows associated with sediment. This log correlates well with the rocks recovered.

Plagioclase is the dominant phenocryst in the finer grained rocks. In Hole 857D large (1–2 mm) plagioclase phenocrysts are observed as embayed, glomerocrystic aggregates. These large crystals are broken, corroded, strongly zoned, and have sodic overgrowths, all characteristic of xenocrysts. The interiors of the larger sills are extremely coarse-grained and are composed of plagioclase poikilitically intergrown with clinopyroxene, plus ilmenite, magnetite, and residual mesostasis. Textures are heterogeneous and as coarse as microgabbroic to gabbroic. The bulk chemistry of the sills indicates that they are the products of extensive fractionation and crystal accumulation from a normal MORB parent melt. All of the sills were probably derived from a similar magmatic source.

The alteration observed in Holes 857C and 857D is of upper zeolite to greenschist facies and consists of three types: (1) static replacement of phenocrysts and mesostasis by epidote, chlorite, albite, and actinolite; (2) vein-filling and associated wall-rock alteration; and (3) deposition of sulfide minerals. Metasomatism is extensive in the sill margins and includes uptake of Mg as magnesian chlorite and loss of Ca and Na. Mineralization has enriched the sills in Zn and, to a lesser extent, copper. Disseminated pyrite is abundant, in the interiors as well as the margins of the sills. Typical vein fillings include chlorite, sphalerite, chalcopyrite, quartz, zeolites (most notably wairakite), and epidote.

Physical properties were measured on hemipelagic and turbiditic sediment from Hole 857A, and on sediment and fresh to altered diabase sills from Holes 857C and 857D. Down to 250 mbsf, the volume magnetic susceptibility (VMS) of the sediment at this site is relatively high and the bases of the turbidites are well defined, probably because of a higher magnetite content. Below 250 mbsf, the VMS decreases by an order of magnitude, due to the alteration of magnetite. The metadiabase sills have a VMS that is only slightly higher than the sediment at that depth. The VMS in the sills decreases from unit to unit with depth, to values that are two orders of magnitude lower than that of typical fresh MORB.

The high degree of sediment induration is apparent in the general increase in velocity and bulk density with depth and the accompanying decrease in porosity and water content. Grain density stays approximately constant. Velocity, bulk density, and grain density of the sills are higher than that of the sediment, and porosity and water content are lower.

The increase in thermal conductivity with depth correlates with decreases in porosity and water content. The indurated sediments have conductivities similar to those of the igneous rocks, perhaps due to high-temperature diagenetic cementation of clay and coarser grained particles. The sill complex in the lower 96 m of Hole 857C is characterized by an average thermal conductivity of 1.91 W/(m·K), with little contrast between the sediment and igneous rock at this level. Sediment and igneous rock show an inverted contrast in the deeper section cored in Hole 857D with the average conductivity of the sediments increasing to 2.37 W/(m·K).

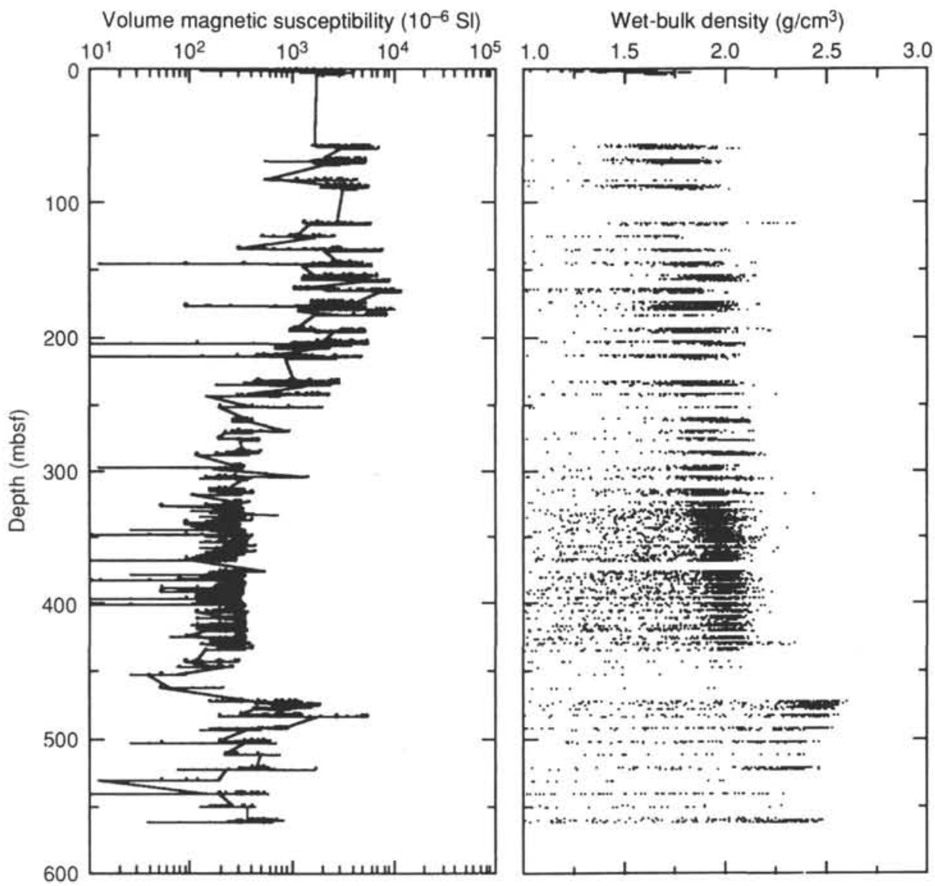

Figure 70. Magnetic susceptibility and GRAPE bulk density in Hole 857C. Data gaps reflect low core recovery.

Vertical seismic velocities measured on sediment samples from this site increase systematically with depth from about 1500 m/s near the seafloor to about 2500 m/s at the level of the first sill. Horizontal velocities increase more rapidly with depth; at a depth of 450 m, anisotropy reaches a level of 25%. Velocities in the beds between sills are as high as 4500 m/s. Velocities of the igneous rocks in the sill complex range from below 4000 m/s to over 5500 m/s.

Logging at Site 857 was done with the seismic stratigraphy and lithoporosity strings and, in Hole 857D, the formation microscanner. Many of the parameters measured by the logs clearly show the thicker sandy and silty layers of the turbidites, and all show the thicknesses and properties of the interbedded sills. Thirty-two distinct igneous units were identified, with a combined thickness of over 165 m, or about 36% of the total thickness of the sill and sediment sequence drilled. The sills range from <1 to 25 m thick, and are separated by sediment interbeds of similar thickness. The gamma-ray log proved to be the most effective log for delineating the sills. The sills are also clearly distinguishable in the resistivity logs and in the formation microscanner images, despite the latter's poor quality caused by ship's heave in the absence of a heave compensator.

The logs in sediment show generally positive correlations among velocity, density, and resistivity, and a negative correlation with porosity. Zones of high velocity, density, and resistivity, and low porosity, correspond to relatively thick silty and sandy turbidite layers in the sediment sequence. Velocity and density from the logs agree well with vertical velocity and density determined on core samples to a depth of 365 mbsf; below that depth the log values are lower, probably because of the difference in scale of the measurements. The velocity profile shows a general, though nonmonotonic, increase with depth due to increasing sediment compaction and alteration, but there is only a small increase in resistivity over the same interval. The effects on bulk resistivity of the reduction of porosity with depth in the sediment probably is counterbalanced by the effect of the strong increase in temperature at this site. Porosity derived from the lithodensity log agrees with that measured on core samples. The difference between this density-derived porosity and neutron porosity, which is a measure of the abundance of hydrogen atoms, gives an estimate of the amount of water bound up in clay minerals. This difference correlates well with the resistivity log.

An unusual feature of the resistivity log is two intervals at 607–625 mbsf and 675–690 mbsf which have resistivities nearly as low as that of seawater. The spontaneous potential log shows prominent minima here as well. As demonstrated by downhole flowmeter measurements, seawater is flowing down the hole and into the formation within these two intervals.

Temperature was measured with the GRC high-temperature logging tool in Holes 857C and 857D while they were still recovering from drilling disturbance. Values measured in the open holes lie below the conductive temperature profile extrapolated from measurements made in the soft sediment within the upper 80 mbsf of Hole 857C. The open-hole temperatures appear to be recovering normally toward an equilibrium conductive profile. The highest temperature measured in Hole 857C was 222°C at 476 mbsf. Extrapolation of the shallower conductive gradient to this depth yields a temperature of 260°C, which probably represents a maximum estimate for this depth. The low temperatures and slow thermal recovery observed in the open boreholes demonstrate that there is no significant flux of hot water into the holes. Two profiles measured in Hole 857D indicate instead

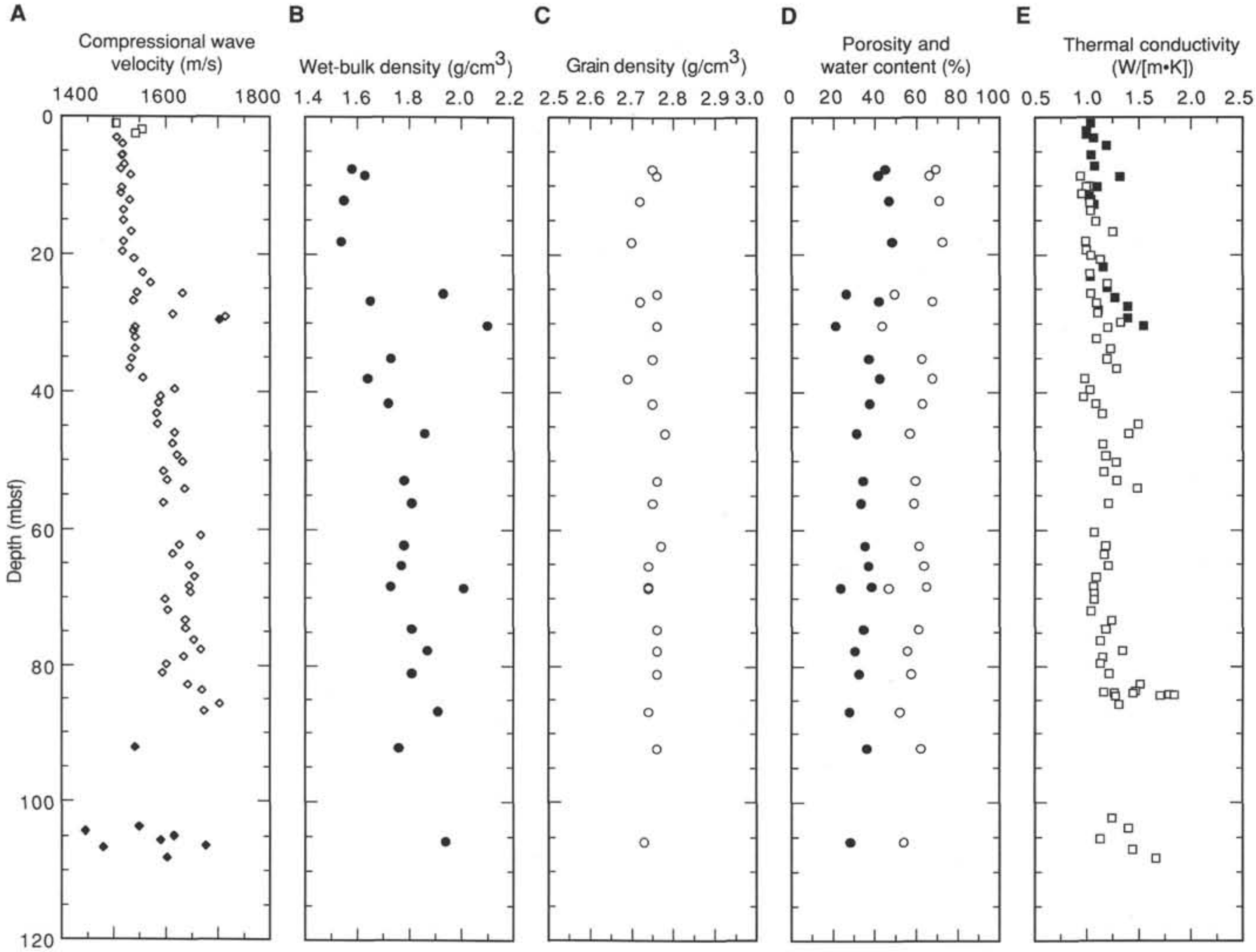

Figure 71. Compressional wave sonic velocity (**A**), wet-bulk density (**B**), grain density (**C**), porosity and water content (**D**), and thermal conductivity (**E**) vs. depth in Holes 857A and 857B (where measured). The three velocity measurements made on Hole 857B samples with the digital sediment velocimeter (DSV) are indicated by open squares in (A). Open diamonds in (A) are Hole 857A velocities measured by the DSV; solid diamonds are data from the Hamilton frame velocimeter (HFV). Open circles in (D) are porosities and solid circles are water content data. Thermal conductivities in (E) are given by open squares for Hole 857A and by solid squares for Hole 857B.

that water was being drawn down into this hole. The first was made in the cemented and plugged casing before deeper drilling and suggested that the casing was not well bonded to the formation and was allowing water to flow down between the outside of the casing and the wall of the hole. The second, completed after the hole was deepened below the casing, was nearly isothermal to a depth of 620 mbsf and suggested major drawdown to depths of up to 700 mbsf.

Temperature in soft sediment within the upper 92 mbsf at Site 857 was measured successfully in nine attempts out of 13 using the WSTP and APC tools. Six measurements in Holes 857A and 857B yielded an average gradient of 0.612°C/m and a heat flow of 709 mW/m^2, lower than was intended for the reentry hole at this site. For this reason Holes 857C and 857D were drilled farther to the east, where heat flow was known to be higher. Two measurements in Hole 857C yielded a gradient of 0.71°C/m and a heat flow of 803 mW/m^2. The Bullard plots for Site 857 are nearly linear, indicating that heat flow through the upper sediment column is dominantly conductive.

Special experiments in Hole 857D included packer experiments to determine bulk permeability and formation fluid pressure, a flowmeter log to measure downhole flow and, when used with the packer, to assess the fine-scale distribution of permeability, and the long-term instrumented borehole seal, or CORK. The packer was deployed six times (including two repeats of failed inflations) as a double-seal single packer at two depths during a 27-hr sequence of permeability and flowmeter measurements.

The packer was first deployed at 96 mbsf to test the permeability of the section between the casing shoe at 574 mbsf and the bottom of the hole at 936 mbsf. Two slug tests produced pressure pulses that decayed extremely rapidly and could barely be distinguished on the downhole pressure record. Constant-rate injection tests were made at increasing pump rates up to the maximum that could be delivered by the ship, resulting in only a small pressure increase that decayed immediately after pumping stopped and the hole was shut in. These results indicate that the average permeability of the formation is very large, probably orders of magnitude greater than any value previously measured in any hole in the seafloor.

The extreme permeability of Hole 857D provided ideal conditions for the flowmeter/injection experiment. The packer was set in the

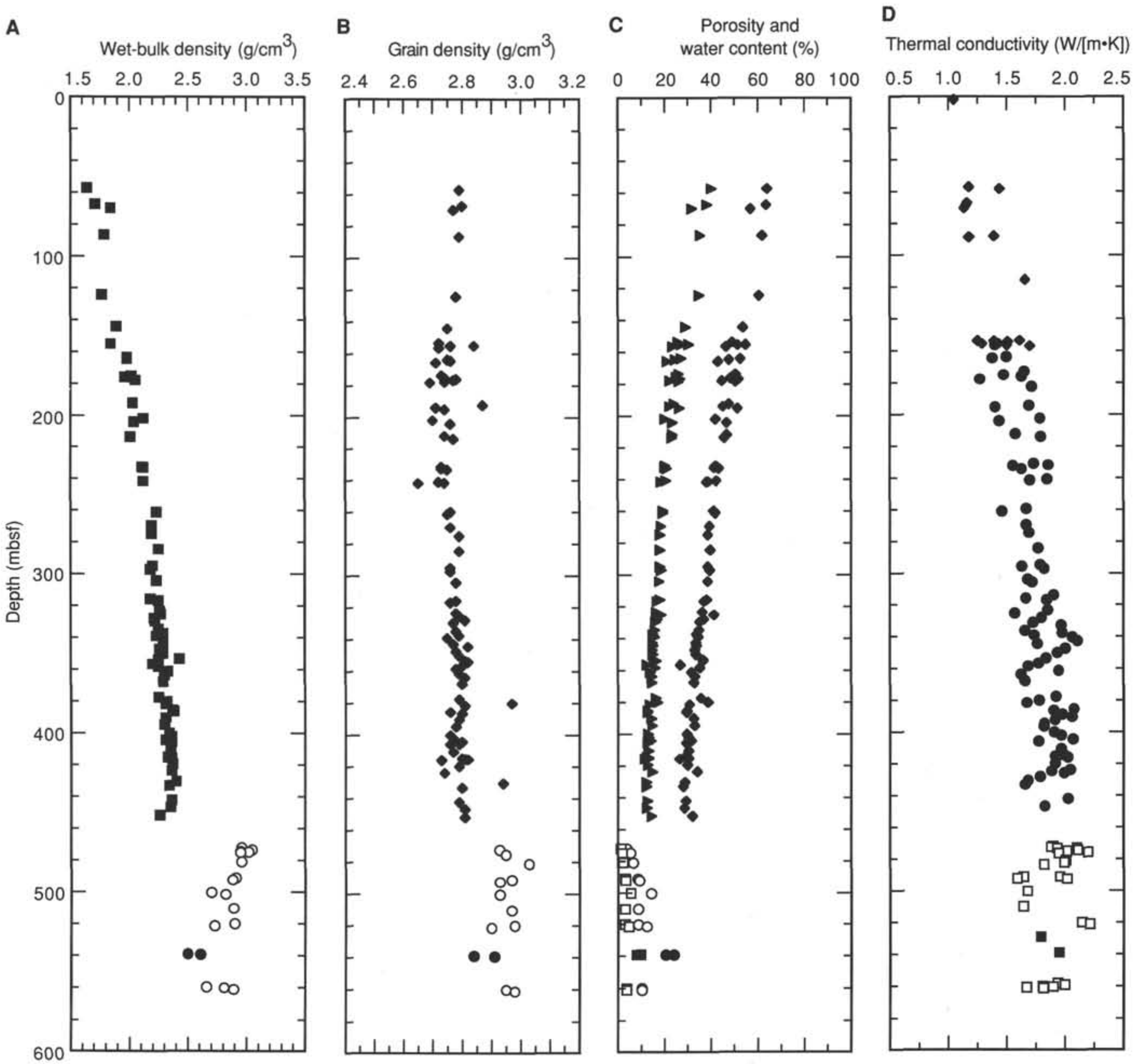

Figure 72. Wet-bulk density (**A**), grain density (**B**), porosity and water content (**C**), and thermal conductivity (**D**) vs. depth in Hole 857C. Solid squares in (A) are wet-bulk densities of sediments above the sill complex; solid circles are densities of sediment interbeds in the sill complex and open circles are densities of igneous rocks constituting the sills. Solid diamonds in (B) represent grain densities of sediments above the sill complex; solid circles are densities of sediment interbeds and open circles are grain densities in igneous rocks. Porosities in (C) from sediments above the sill complex are indicated by solid diamonds; data from sediment interbeds in the sills are presented as solid circles and igneous rock porosities are denoted by open circles. Water content data in (C) are represented by solid triangles for sediments above the sill complex, solid squares for sediments interbeds within the sills, and open squares for igneous rock values. Thermal conductivity data in (D) for sediments above sills are given by solid diamonds for full-space measurements and by solid circles for half-space measurements. Half-space conductivity data in sediments in the sill complex are indicated by solid squares; half-space data for igneous rocks are identified by open squares.

casing at 96 mbsf, isolating the hole below, and the flowmeter was lowered into it. Stationary measurements were made at 5- to 10-m intervals while the mud pumps were turned up to a maximum steady injection rate. Within 60 m below the bottom of the casing, the flowmeter reading dropped below the noise level introduced by heave. The flowmeter was raised into the casing and the packer was deflated, at which point the spinner reading more than tripled relative to its speed at the maximum pumping rate. This indicated that the formation was drawing bottom water at a rate three times the maximum rate that the ship's pumps could deliver. We estimate the natural drawdown to be on the order of 10,000 L/min. This is two orders of magnitude greater than the downhole flows observed in DSDP Holes 395A and 504B. The flowmeter log (flow, pressure, and caliper) was then repeated using only the induced flow down the hole. The results indicate that most of the flow was diverted into the formation at 610–615 mbsf, a horizon immediately below one of the igneous sills. We failed to recover core from this zone and so could not determine its nature directly. The packer and flowmeter experiments were

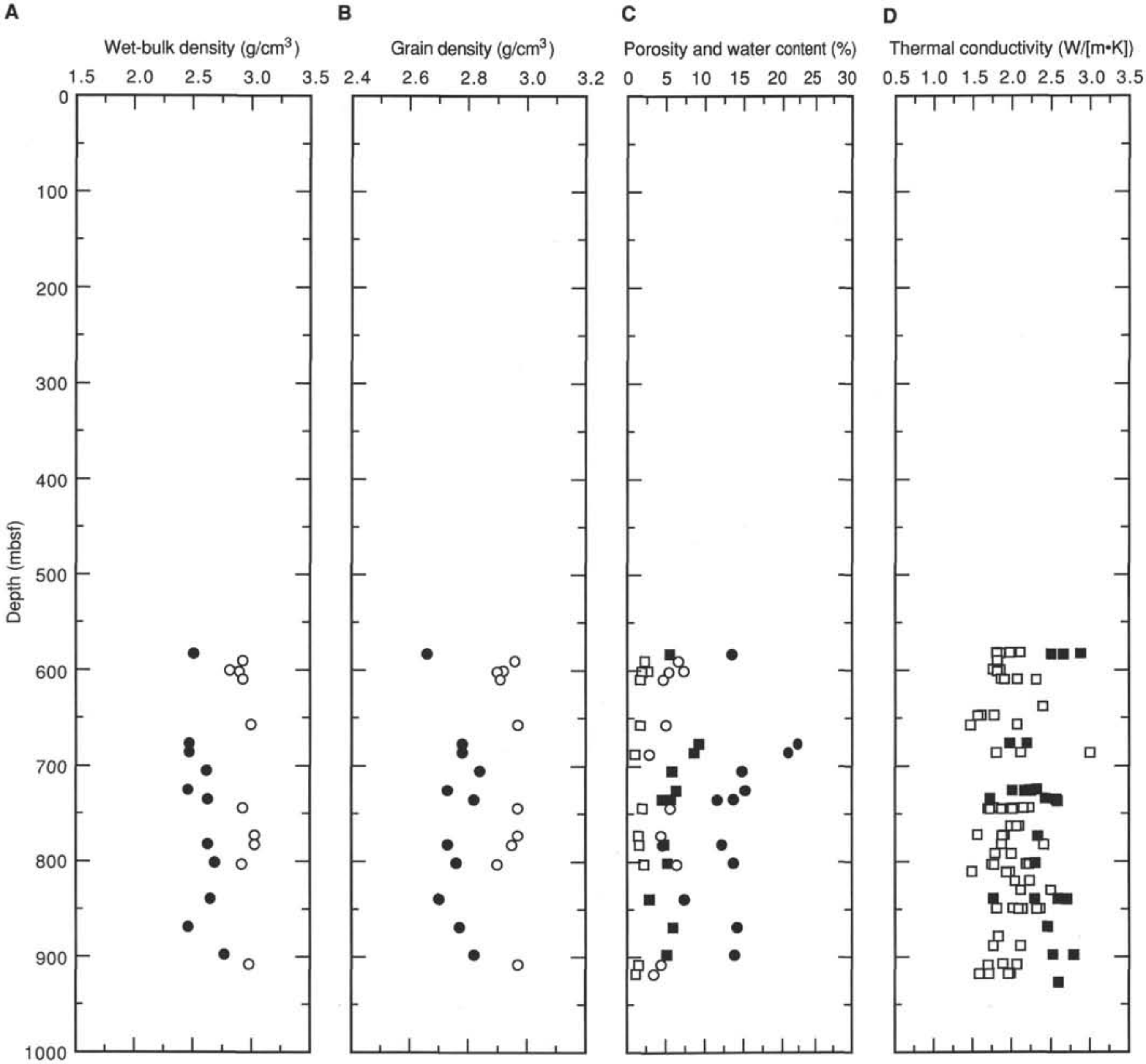

Figure 73. Wet-bulk density (**A**), grain density (**B**), porosity and water content (**C**), and thermal conductivity (**D**) vs. depth in the sill complex of Hole 857D. Solid circles in (A) are wet-bulk densities of samples from sediment interbeds; open circles are data from igneous sills; grain density symbols in (B) follow the same convention. Porosities in (C) are given as solid circles for sediments and as open circles for igneous rock; water content data are presented as solid squares for sediments and as open squares for igneous samples. Similarly, half-space thermal conductivity data in (D) are given by solid squares for sediments and by open squares for igneous rock.

repeated at 756 mbsf, below the highly permeable zones that were detected with the flowmeter log. The results suggest that the deeper formation is significantly less permeable, but is still roughly as permeable as the upper sections of basement in DSDP Holes 504B and 395A.

At the end of operations in Hole 857D, the hole was sealed with a CORK that will allow long-term monitoring of downhole temperature and pressure, and perhaps periodic fluid sampling (see Davis et al., this volume).

REFERENCES

Anderson, R. N., and Zoback, M. D., 1982. Permeability, underpressures, and convection in the oceanic crust near the Costa Rica Rift, eastern equatorial Pacific. *J. Geophys. Res.*, 87:2860–2868.

Bandy, O. L., 1960. The geological significance of coiling ratios in the foraminifer *Globigerina pachyderma* (Ehrenberg). *J. Paleontol.*, 34:671–681.

Becker, K., 1990. Measurements of the permeability of the upper oceanic crust at Hole 395A, ODP Leg 109. *In* Detrick, R., Honnorez, J., Bryan, W. B., Juteau, T., et al., *Proc. ODP, Sci. Results,* 109: College Station, TX (Ocean Drilling Program), 213–222.

Becker, K., Foss, G., et al., 1992. *Proc. ODP, Init. Repts.,* 137: College Station, TX (Ocean Drilling Program).

Becker, K., Langseth, M. G., and Hyndman, R. D., 1984. Temperature meas-ure-ments in Hole 395A, ohr, Leg 78B. *In* Hyndman, R. D., Salisbury, M. H., et al., *Init. Repts. DSDP,* 78B: Washington (U.S. Govt. Printing Office), 689–698.

Becker, K., Langseth, M. G., Von Herzen, R. P., and Anderson, R. N., 1983. Deep crustal geothermal measurements, Hole 504B, Costa Rica Rift. *J. Geophys. Res.,* 88:3447–3457.

Bergen, F. W., and O'Neil, P., 1979. Distribution of Holocene foraminifera in the Gulf of Alaska. *J. Paleontol.,* 53:1267–1292.

Bischoff, J. L., and Henyey, T. L., 1974. Tectonic elements of the central part of the Gulf of California. *Geol. Soc. Am. Bull.,* 85:1893–1904.

Bleil, U., and Petersen, N., 1983. Variations in magnetization intensity and low-temperature titanomagnetite oxidation of ocean floor basalts. *Nature,* 301:384–388.

Brassell, S. C., Eglinton, G., Marlowe, I. T., Pflaumann, U., and Sarnthein, M., 1986. Molecular stratigraphy: a new tool for climatic assessment. *Nature,* 320:129–133.

Carmichael, R. S., 1982. Magnetic Properties of Minerals and Rocks. *In* Carmichael, R. S. (Ed.), *Handbook of Physical Properties of Rocks* (Vol. 2): Boca Raton, FL (CRC Press), 273–274.

Claypool, G. E., 1975. *Manual on Pollution-Prevention and Safety* (3rd ed.). *JOIDES* J.

Curray, J. R., Moore, D. G., et al., 1982. *Init. Repts. DSDP,* 64 (Pt. 1): Washington (U.S. Govt. Printing Office).

Davis, E. E., and Lister, C.R.B., 1977. Tectonic structures on the northern Juan de Fuca Ridge. *Geol. Soc. Am. Bull.,* 88:346–363.

Davis, E. E., and Riddihough, R. P., 1982. The Winona Basin: structure and tectonics. *Can. J. Earth Sci.,* 19:767–788.

Farrimond, P., Poynter, J. G., and Eglinton, G., 1990. A molecular stratigraphic study of Peru Margin sediments, Hole 686B, Leg 112. *In* Suess, E., von Huene, R., et al., *Proc. ODP, Sci. Results,* 112: College Station, TX (Ocean Drilling Program), 547–553.

Franklin, J. M., 1986. Volcanogenic massive sulphide deposits-an update. *In* Andrew, C. J., Crowe, R.W.A., Finlay, S., Pennell, W. M., Pyne, J. F. (Eds.), *Geology and Genesis of Mineral Deposits in Ireland.* Irish Assoc. Econ. Geol., 49–65.

Gartner, S., Jr., 1977. Calcareous nannofossils biostratigraphy and revised zonation of the Pleistocene. *Mar. Micropaleontol.,* 2:1–25.

Gieskes, J., and Peretsman, G., 1986. Water chemistry procedures aboard *JOIDES Resolution*—some comments. *Tech. Note No. 5,* Ocean Drilling Program.

Goodfellow, W. D., and Blaise, B., 1988. Sulfide formation and hydrothermal alteration of hemipelagic sediment in Middle Valley, Northern Juan de Fuca Ridge. *Can. Mineral.,* 26:675–696.

Grimalt, J., and Albaiges, J., 1987. Sources and occurrence of C_{12}–C_{22} *n*-alkane distributions with even carbon-number preference in sedimentary environments. *Geochim. Cosmochim. Acta,* 51:1379–1384.

Hunt, J. M., 1979. *Petroleum Geology and Geochemistry:* San Francisco (W. H. Freeman).

Johnson, H. P., Franklin, J. M., and Currie, R. G., in press. SeaMARC IA acoustic imagery of the Middle Valley Area, northern Juan de Fuca Ridge. *Open-File Rep., Geol. Surv. Can.*

Karsten, J. L., Delaney, J. R., Rhodes, J. M., and Liias, R. A., 1990. Spatial and temporal evolution of magmatic systems beneath the Endeavour segment, Juan de Fuca Ridge: tectonic and petrological constraints. *J. Geophys. Res.,* 95:19235–19256.

Kopietz, J., Becker, K., and Hamano, Y., 1990. Temperature measurements at Site 395, ODP Leg 109. *In* Detrick, R., Honnorez, J., Bryan, W. B., Juteau, T., et al., *Proc. ODP, Sci. Results,* 109: College Station, TX (Ocean Drilling Program), 197–203.

Lagoe, M. B., and Thompson, P. R., 1988. Chronostratigraphic significance of Late Cenozoic planktonic foraminifera from the Ventura Basin, California: potential for improving tectonic and depositional interpretation. *J. Foraminiferal Res.,* 18:250–266.

Larson, P. A., Mudie, J. D., and Larson, R. L., 1972. Magnetic anomalies and fracture zone trends in the Gulf of California. *Geol. Soc. Am. Bull.,* 83:3361–3368.

Levi, S., and Riddihough, R., 1986. Why are marine magnetic anomalies suppressed over sedimented spreading centers? *Geology,* 14:651–654.

Marlowe, I. T., Brassell, S. C., Eglinton, G., and Green, J. C., 1984. Long chain unsaturated ketones and esters in living algae and marine sediments. *Org. Geochem.,* 6:135–141.

Martini, E., 1971. Standard Tertiary and Quaternary calcareous nannoplankton zonation. *In* Farinacci, A. (Ed.), *Proc. 2nd Planktonic Conf. Roma:* Rome (Ed. Tecnosci.), 2:739–785.

Pearce, J. A., and Cann, J. R., 1973. Tectonic setting of basic volcanic rocks determined using trace element analyses. *Earth Planet. Sci. Lett.,* 19: 290–300.

Petersen, N., Eisenach, P., and Bleil, U., 1979. Low temperature alteration of the magnetic minerals in ocean floor basalts. *In* Talwani, M., Harrison, C.G.A., and Hayes, D. E. (Eds.), *Deep Drilling Results in the Atlantic Ocean: Ocean Crust.* Am. Geophys. Union, Maurice Ewing Ser., 2:169–209.

Poynter, J. G., Farrimond, P., Brassell, S. C., and Eglinton, G., 1989. Molecular stratigraphic study of sediments from Holes 658A and 660A, Leg 108. *In* Ruddiman, W., Sarnthein, M., et al., *Proc. ODP, Sci. Results,* 108: College Station, TX (Ocean Drilling Program), 387–394.

Prahl, F. G., and Wakeham, S. G., 1987. Calibration of unsaturation patterns in long-chain ketone compositions for paleotemperature assessment. *Nature,* 330:367–369.

Raff, A. D., and Mason, R. G., 1961. Magnetic survey off the west coast of North America, 40°N latitude to 52°N latitude. *Geol. Soc. Am. Bull.,* 72:1267–1270.

Rohr, K. M., Davis, E. E., and Hyndman, R. D., 1992. Multichannel seismic reflection profiles across Middle Valley, northern Juan De Fuca Ridge. *Geol. Surv. Can. Open-File Rep.* 2476.

Seyfried, W. E., Jr., and Bischoff, J. J., 1979. Low temperature basalt alteration by seawater: an experimental study at 70° and 150°C. *Geochim. Cosmochim. Acta,* 43:1937–1947.

Simoneit, B.R.T., 1977. Diterpenoid compounds and other lipids in deep-sea sediments and their geochemical significance. *Geochim. Cosmochim. Acta,* 41:463–476.

————, 1978. The organic chemistry of marine sediments. *In* Riley, J. P., and Chester, R. (Eds.), *Chemical Oceanography* (Vol. 7) (2nd ed.): New York (Academic Press), 233–311.

Simoneit, B.R.T., Goodfellow, W. D., and Franklin, J. M., in press. Hydrothermal petroleum at the seafloor and organic matter alteration in sediments of Middle Valley, northern Juan de Fuca Ridge. *Applied Geochem.*

Smith, G. M., and Banerjee, S. K., 1986. Magnetic structure of the upper kilometer of the marine crust at Deep Sea Drilling Project Hole 504B, eastern Pacific Ocean. *J. Geophys. Res.,* 91:10337–10354.

Steiner, A., 1955. Wairakite, the calcium analogue of analcime, a new zeolite mineral. *Mineral. Mag.,* 30:691.

Verbeek, J. W., 1990. Late Quaternary Calcareous Nannoplankton Biostratigraphy for the Northern Atlantic Ocean. *In* Van Amerom, H.W.J. (Ed.), *Mededelingen Rijks Geologisch Dienst,* 44-2: Heerlan, Netherlands (Rijks Geol. Dienst), 13–33.

Ms 139A-107

NOTE: For all sites drilled, core description forms ("barrel sheets") and core photographs have been printed on coated paper and bound as Section 3, near the back of the book, beginning on page 573. Forms containing smear slide data are bound as Section 4, beginning on page 933. Thin-section data are given in Section 5, beginning on page 949.

Formation microscanner images for this site are presented on microfiche in the back of the book.

Table 28. Index properties, Hole 857A.

Core, section, interval (cm)	Depth (mbsf)	Wet-bulk density (g/cm^3)	Grain density (g/cm^3)	Wet porosity (%)	Wet water content (%)	Void ratio
139-857A-						
1H-4, 119–123	7.59	1.58	2.75	69.4	45.0	2.27
1H-5, 56–60	8.46	1.63	2.76	66.2	41.6	1.95
2H-1, 74–77	12.14	1.55	2.72	71.0	46.8	2.44
2H-5, 76–79	18.16	1.54	2.70	72.6	48.4	2.65
4H-3, 80–84	25.70	1.93	2.76	49.4	26.2	0.98
4H-4, 39–43	26.79	1.65	2.72	67.6	41.8	2.08
4H-6, 94–98	30.34	2.10	2.76	43.3	21.1	0.76
5H-3, 75–77	35.15	1.73	2.75	62.6	37.1	1.67
5H-5, 59–61	37.99	1.64	2.69	67.7	42.3	2.10
6H-1, 73–77	41.63	1.72	2.75	62.8	37.4	1.69
6H-4, 59–61	45.99	1.86	2.78	56.8	31.3	1.31
7H-3, 64–66	52.86	1.78	2.76	59.4	34.2	1.47
7H-6, 44–46	56.12	1.81	2.75	58.7	33.2	1.42
8H-2, 89–91	62.29	1.78	2.77	61.1	35.2	1.57
8H-4, 84–86	65.24	1.77	2.74	63.6	36.8	1.75
8H-6, 88–92	68.28	1.73	2.74	64.9	38.5	1.85
8H-6, 112–122	68.52	2.01	2.74	46.6	23.7	0.87
9H-4, 63–67	74.53	1.81	2.76	60.9	34.5	1.56
9H-6, 74–77	77.64	1.87	2.76	55.5	30.4	1.25
10H-2, 66–68	81.05	1.81	2.76	57.4	32.4	1.35
10H-6, 35–38	86.75	1.91	2.74	52.0	27.9	1.08
12X-CC, 29–32	92.19	1.76	2.76	62.2	36.2	1.64
13X-3, 113–117	105.63	1.94	2.73	53.8	28.3	1.16

Table 29. Compressional wave velocity (DSV), Hole 857A.

Sample (cm)	Depth (mbsf)	DSV velocity (m/s)
139-857A-		
1H-1, 116	3.06	1506
1H-2, 56	3.96	1518
1H-3, 63	5.53	1518
1H-3, 73	5.63	1516
1H-4, 56	6.96	1521
1H-4, 120	7.60	1514
1H-5, 62	8.52	1533
1H-6, 92	10.32	1516
1H-7, 20	11.10	1514
2H-1, 75	12.15	1531
2H-2, 68	13.58	1519
2H-3, 73	15.13	1519
2H-4, 80	16.70	1534
2H-5, 76	18.16	1519
2H-6, 72	19.62	1518
2H-7, 24	20.64	1539
4H-1, 80	22.70	1556
4H-2, 80	24.20	1570
4H-3, 71	25.61	1544
4H-3, 82	25.72	1632
4H-4, 41	26.81	1538
4H-5, 86	28.76	1613
4H-5, 118	29.08	1714
4H-6, 122	30.62	1541
4H-7, 28	31.18	1538
5H-1, 74	32.14	1541
5H-2, 83	33.73	1541
5H-3, 76	35.16	1534
5H-4, 71	36.61	1531
5H-5, 60	38.00	1556
5H-6, 73	39.63	1617
5H-7, 25	40.65	1590
6H-1, 75	41.65	1586
6H-2, 77	43.17	1583
6H-3, 81	44.71	1584
6H-4, 60	46.00	1617
6H-5, 65	47.55	1613
6H-6, 85	49.25	1621
6H-7, 31	50.21	1632
7H-2, 85	51.57	1595
7H-3, 65	52.87	1602
7H-4, 54	54.16	1636
7H-6, 45	56.13	1595
8H-1, 104	60.94	1667
8H-2, 90	62.30	1627
8H-3, 70	63.60	1613
8H-4, 85	65.25	1646
8H-5, 100	66.90	1655
8H-6, 90	68.30	1646
8H-7, 35	69.25	1647
9H-1, 85	70.25	1599
9H-2, 95	71.85	1604
9H-3, 88	73.28	1638
9H-4, 64	74.54	1638
9H-5, 80	76.20	1653
9H-6, 75	77.65	1667
9H-7, 27	78.67	1634
10H-1, 89	79.79	1601
10H-2, 65	81.05	1593
10H-3, 92	82.82	1642
10H-4, 25	83.65	1669
10H-5, 80	85.70	1703
10H-6, 36	86.76	1673

Table 30. Compressional wave velocity (HFV), Hole 857A.

Core, section, interval (cm)	Depth (mbsf)	Direction (a, b, c)	HFV velocity (m/s)
139-857A-			
4H-6, 16–18	29.56	c	1702
12X-CC, 29–31	92.19	c	1541
13X-2, 66–68	103.66	c	1549
13X-2, 129–131	104.29	c	1445
13X-3, 46–48	104.96	c	1616
13X-3, 106–108	105.56	c	1590
13X-4, 31–33	106.31	c	1677
13X-4, 61–63	106.61	c	1480
13X-5, 56–58	108.06	c	1602

Table 31. Thermal conductivity, Hole 857A.

Sample (cm)	Depth (mbsf)	Thermal conductivity (W/[m·K])
139-857A-		
1H-1, 70	2.60	0.90
1H-2, 70	4.10	0.99
1H-3, 75	5.65	1.03
1H-4, 75	7.15	0.89
1H-5, 70	8.60	0.94
1H-6, 60	10.00	1.02
1H-6, 75	10.15	1.00
1H-7, 22	11.12	0.95
2H-1, 100	12.40	1.02
2H-2, 68	13.58	1.04
2H-3, 75	15.15	1.09
2H-4, 75	16.65	1.25
2H-5, 68	18.08	0.99
2H-6, 40	19.30	1.00
2H-6, 120	20.10	1.04
2H-7, 30	20.70	1.13
4H-1, 78	22.68	1.03
4H-2, 75	24.15	1.19
4H-3, 75	25.65	1.04
4H-4, 60	27.00	1.09
4H-5, 52	28.42	1.10
4H-6, 43	29.83	1.32
4H-6, 116	30.56	1.20
5H-1, 75	32.15	1.09
5H-2, 75	33.65	1.23
5H-3, 75	35.15	1.19
5H-4, 68	36.58	1.28
5H-5, 60	38.00	0.98
5H-6, 70	39.60	1.03
5H-7, 25	40.65	0.97
6H-1, 75	41.65	1.09
6H-2, 75	43.15	1.15
6H-3, 70	44.60	1.50
6H-4, 60	46.00	1.40
6H-5, 65	47.55	1.15
6H-6, 85	49.25	1.18
6H-7, 30	50.20	1.28
7H-2, 85	51.57	1.16
7H-3, 65	52.87	1.28
7H-4, 30	53.92	1.48
7H-6, 45	56.13	1.21
8H-1, 45	60.35	1.07
8H-2, 90	62.30	1.18
8H-3, 70	63.60	1.16
8H-4, 85	65.25	1.21
8H-5, 100	66.90	1.09
8H-6, 90	68.30	1.07
8H-7, 35	69.25	1.07
9H-1, 80	70.20	1.07
9H-2, 95	71.85	1.04
9H-3, 82	73.22	1.24
9H-4, 62	74.52	1.18
9H-5, 80	76.20	1.12
9H-6, 75	77.65	1.34
9H-7, 20	78.60	1.15
10H-1, 60	79.50	1.13
10H-2, 62	81.02	1.21
10H-3, 75	82.65	1.51
10H-4, 25	83.65	1.46
10H-4, 40	83.80	1.16
10H-4, 50	83.90	1.27
10H-4, 60	84.00	1.44
10H-4, 70	84.10	1.79
10H-4, 80	84.20	1.84
10H-4, 90	84.30	1.70
10H-4, 100	84.40	1.27
10H-5, 80	85.70	1.31
13X-1, 75	102.25	1.24
13X-2, 75	103.75	1.40
13X-3, 75	105.25	1.12
13X-4, 75	106.75	1.44
13X-5, 50	108.00	1.66

Note: All measurements were made in the full-space configuration.

Table 32. Electrical resistivity, Hole 857A.

Sample (cm)	Depth (mbsf)	Electrical resistivity, seawater readings	Electrical resistivity, sample readings	Formation factor
139-857A-				
1H-1, 120	3.10	0.025	0.033	1.32
1H-2, 70	4.10	0.026	0.032	1.23
1H-3, 53	5.43	0.025	0.035	1.40
1H-4, 68	7.08	0.025	0.036	1.44
1H-5, 90	8.80	0.025	0.030	1.20
1H-6, 100	10.40	0.028	0.028	1.00
2H-1, 90	12.30	0.028	0.028	1.00
2H-2, 63	13.53	0.025	0.032	1.28
2H-3, 90	15.30	0.025	0.033	1.32
2H-4, 80	16.70	0.025	0.036	1.44
2H-5, 70	18.10	0.025	0.032	1.28
2H-6, 85	19.75	0.025	0.033	1.32
4H-1, 80	22.70	0.025	0.037	1.48
4H-2, 75	24.15	0.025	0.039	1.56
4H-3, 40	25.30	0.025	0.035	1.40
4H-3, 80	25.70	0.025	0.035	1.40
4H-4, 40	26.80	0.025	0.035	1.40
4H-5, 60	28.50	0.025	0.034	1.36
4H-5, 116	29.06	0.025	0.050	2.00
4H-6, 16	29.56	0.025	0.040	1.60
4H-6, 96	30.36	0.025	0.040	1.60
4H-6, 67	30.07	0.025	0.038	1.52
4H-6, 126	30.66	0.025	0.035	1.40
5H-1, 108	32.48	0.025	0.040	1.60
5H-2, 54	33.44	0.025	0.037	1.48
5H-2, 130	34.20	0.025	0.045	1.80
5H-3, 75	35.15	0.025	0.040	1.60
5H-4, 68	36.58	0.025	0.036	1.44
5H-5, 70	38.10	0.025	0.039	1.56
5H-6, 80	39.70	0.025	0.036	1.44
6H-1, 70	41.60	0.025	0.037	1.48
6H-1, 112	42.02	0.022	0.035	1.59
6H-2, 80	43.20	0.025	0.045	1.80
6H-2, 97	43.37	0.025	0.045	1.80
6H-3, 60	44.50	0.023	0.036	1.57
6H-3, 93	44.83	0.023	0.062	2.70
6H-5, 60	47.50	0.022	0.040	1.82
6H-5, 120	48.10	0.022	0.044	2.00
6H-7, 30	50.20	0.022	0.045	2.05
7H-2, 80	51.52	0.023	0.035	1.52
7H-4, 52	54.14	0.022	0.046	2.09
7H-6, 70	56.38	0.023	0.037	1.61
8H-1, 113	61.03	0.015	0.040	2.60
8H-2, 103	62.43	0.015	0.042	2.75
8H-3, 60	63.50	0.015	0.037	2.39
8H-4, 94	65.34	0.015	0.043	2.78
8H-5, 112	67.02	0.014	0.045	3.13
8H-6, 113	68.53	0.015	0.044	2.93
8H-7, 30	69.20	0.015	0.041	2.79
9H-1, 86	70.26	0.016	0.043	2.71
9H-2, 95	71.85	0.016	0.043	2.66
9H-3, 88	73.28	0.017	0.043	2.56
9H-4, 64	74.54	0.016	0.043	2.65
9H-5, 80	76.20	0.016	0.043	2.65
9H-6, 75	77.65	0.016	0.045	2.78
9H-7, 27	78.67	0.017	0.043	2.53
10H-1, 89	79.79	0.016	0.037	2.33
10H-3, 92	82.82	0.017	0.045	2.65
10H-4, 25	83.65	0.017	0.042	2.41

Table 33. Thermal conductivity, Hole 857B.

Sample (cm)	Depth (mbsf)	Thermal conductivity (W/[m·K])
139-857B-		
1H-1, 90	0.90	1.03
1H-2, 50	2.00	0.99
1H-2, 100	2.50	1.00
1H-3, 8	3.08	1.06
2H-1, 75	4.15	1.19
2H-2, 60	5.50	1.04
2H-3, 75	7.15	1.08
2H-4, 75	8.65	1.32
2H-5, 68	10.08	1.10
2H-6, 60	11.50	1.02
2H-6, 110	12.00	1.04
2H-7, 30	12.70	1.07
3H-1, 75	21.75	1.16
3H-2, 68	23.18	1.03
3H-3, 75	24.75	1.19
3H-4, 75	26.25	1.27
3H-5, 50	27.50	1.39
3H-5, 100	28.00	1.11
3H-6, 70	29.20	1.39
3H-7, 30	30.30	1.55

Note: All measurements were made in the full-space configuration.

Table 34. Compressional wave velocity (DSV), Hole 857B.

Sample (cm)	Depth (mbsf)	DSV velocity (m/s)
139-857B-		
1H-1, 102	1.02	1505
1H-2, 43	1.93	1555
1H-2, 100	2.50	1543

Table 35. Index properties, Hole 857C.

Core, section, interval (cm)	Piece number	Depth (mbsf)	Wet-bulk density (g/cm^3)	Grain density (g/cm^3)	Wet porosity (%)	Wet water content (%)	Void ratio
139-857C-							
2R-1, 67–69		57.17	1.64	2.79	64.0	40.0	1.78
3R-1, 86–88		67.36	1.71	2.80	63.6	38.2	1.75
3R-3, 34–36		69.84	1.84	2.77	56.9	31.8	1.32
6R-1, 30–32		86.50	1.79	2.79	61.9	35.4	1.63
10R-1, 39–41		124.49	1.77	2.78	60.6	35.1	1.54
12R-1, 74–78		144.24	1.89	2.75	53.5	29.0	1.15
13R-2, 44–48		155.04	1.84	2.84	54.7	30.4	1.21
14R-2, 23–26		164.53	1.98	2.76	47.6	24.6	0.91
15R-3, 54–56		176.04	1.96	2.78	48.4	25.3	0.94
15R-4, 84–86		177.84	2.05	2.74	44.6	22.3	0.80
18R-2, 111–113		204.21	2.04	2.76	46.7	23.4	0.87
19R-2, 84–86		213.64	2.01	2.77	45.7	23.2	0.84
21R-2, 38–40		232.48	2.11	2.73	41.4	20.1	0.71
22R-1, 127–129		241.57	2.12	2.65	38.2	18.5	0.62
24R-2, 37–39		261.07	2.23	2.75	41.7	19.2	0.71
25R-1, 50–51		269.30	2.19	2.76	39.3	18.4	0.65
26R-1, 38–40		274.88	2.19	2.79	38.6	18.1	0.63
27R-1, 17–19		284.27	2.25	2.79	39.6	18.0	0.66
28R-1, 96–98		294.76	2.20	2.76	38.6	18.0	0.63
28R-3, 28–30		297.08	2.18	2.76	39.5	18.6	0.65
29R-1, 62–64		304.02	2.23	2.78	38.6	17.8	0.63
30R-2, 100–102		315.60	2.18	2.78	38.2	18.0	0.62
30R-3, 61–63		316.71	2.25	2.76	37.0	16.8	0.59
31R-1, 73–75		323.43	2.26	2.78	36.3	16.5	0.57
31R-2, 91–93		325.11	2.27	2.79	41.3	18.6	0.70
32R-1, 23–25		327.83	2.21	2.81	36.9	17.1	0.58
32R-2, 46–48		329.56	2.22	2.77	35.2	16.2	0.54
33R-2, 75–77		334.65	2.25	2.78	34.9	15.9	0.54
34R-1, 91–93		337.41	2.29	2.79	33.8	15.1	0.51
34R-2, 95–97		338.95	2.23	2.75	34.5	15.8	0.53
35R-1, 136–140		342.66	2.29	2.77	33.6	15.0	0.51
35R-3, 10–12		344.40	2.29	2.82	33.8	15.1	0.51
36R-1, 114–115		347.24	2.26	2.78	33.1	15.0	0.49
36R-3, 88–90		349.98	2.29	2.79	33.6	15.1	0.51
37R-2, 112–114		353.42	2.43	2.81	36.6	15.5	0.58
37R-3, 3–5		353.83	2.25	2.82	36.6	16.6	0.58
38R-1, 79–81		356.59	2.20	2.80	26.9	12.5	0.37
38R-2, 100–102		358.30	2.25	2.78	35.3	16.1	0.54
39R-1, 80–82		361.20	2.33	2.79	31.7	13.9	0.46
39R-3, 30–32		363.70	2.30	2.81	33.1	14.7	0.50
40R-2, 77–79		367.67	2.29	2.80	32.7	14.6	0.49
41R-2, 89–91		377.29	2.25	2.79	35.6	16.2	0.55
42R-1, 25–27		379.95	2.32		38.7	17.1	0.63
42R-2, 19–21		381.39	2.31	2.81	30.7	13.6	0.44
43R-1, 64–66		385.34	2.37	2.76	29.7	12.8	0.42
43R-2, 13–15		386.33	2.38	2.80	29.5	12.7	0.42
44R-1, 44–46		390.14	2.31	2.79	32.6	14.4	0.48
45R-1, 18–20		394.48	2.30	2.78	33.0	14.7	0.49
46R-1, 91–93		399.91	2.34	2.76	29.7	13.0	0.42
46R-2, 146–148		401.96	2.36	2.77	30.3	13.2	0.43
47R-1, 24–26		404.24	2.31	2.80	31.7	14.1	0.46
47R-2, 3–5		405.53	2.36	2.79	30.0	13.0	0.43
47R-2, 13–15		405.63	2.35	2.76	29.4	12.8	0.42
48R-2, 19–21		410.39	2.35	2.77	30.4	13.3	0.44
49R-1, 81–83		414.51	2.34	2.80	28.8	12.6	0.40
49R-1, 126–128		414.96	2.33	2.81	30.2	13.3	0.43
49R-2, 2–4		415.22	2.34	2.82	30.5	13.3	0.44
49R-2, 48–50		415.68	2.36	2.73	26.5	11.5	0.36
50R-1, 124–126		419.54	2.37	2.79	29.9	12.9	0.43
51R-1, 31–33		423.71	2.36	2.74	34.1	14.8	0.52
52R-CC, 10–12		430.25	2.40		28.8	12.3	0.40
53R-1, 20–22		433.00	2.34	2.80	28.1	12.3	0.39
55R-1, 5–7		442.05	2.36	2.79	29.3	12.7	0.41
56R-1, 25–27		446.75	2.35	2.81	28.6	12.5	0.40
57R-1, 8–9		451.78	2.26	2.81	32.0	14.5	0.47
59R-1, 102–104	8	472.12	2.96	2.93	03.9	01.4	0.04
59R-2, 91–93	7	473.51	3.05	*	*	*	*
59R-3, 33–35	1	474.35	2.95	*	*	*	*
59R-3, 88–90	4	474.90	3.02	*	*	*	*
59R-3, 105–107	5	475.07	2.95	2.95	05.6	01.9	0.06
60R-1, 17–19	1	480.97	2.96	3.03	06.8	02.4	0.07
61R-1, 68–70	2A	491.18	2.91	2.97	08.5	03.0	0.09
61R-2, 45–47	5	492.31	2.88	2.93	09.3	03.3	0.10
62R-1, 42–44	3	500.42	2.70	2.93	14.4	05.5	0.17

Table 35 (continued).

Core, section, interval (cm)	Piece number	Depth (mbsf)	Wet-bulk density (g/cm^3)	Grain density (g/cm^3)	Wet porosity (%)	Wet water content (%)	Void ratio
63R-1, 56–58	4	510.26	2.89	2.97	08.7	03.1	0.09
64R-1, 68–70	6	520.08	2.90	2.98	08.7	03.1	0.10
64R-2, 38–40	4	521.28	2.73	2.90	12.4	04.7	0.14
66R-1, 12–14	2	538.92	2.50	2.84	24.1	09.9	0.32
66R-1, 38–40	5B	539.18	2.61	2.91	20.6	08.1	0.26
68R-2, 58–60	6	560.08	2.81	2.95	10.4	3.8	0.12
68R-3, 23–25	3	561.23	2.89	2.98	10.3	3.7	0.11

Note: Asterisk (*) denotes paleomagnetic cubes; dry analyses not made.

Table 36. Compressional wave velocity (DSV), Hole 857C.

Core, section, interval (cm)	Depth (mbsf)	DSV velocity (m/s)
139-857C-		
1R-1, 61	0.61	1505
1R-2, 70	2.20	1567
3R-1, 30	66.80	1599
3R-2, 30	68.30	1510
3R-3, 35	69.85	1593

Table 37. Compressional wave velocity (HFV), Hole 857C.

Core, section, interval (cm)	Piece number	Depth (mbsf)	Direction (a, b, c)	HFV velocity (m/s)
139-857C-				
2R-1, 66–68		57.16	c	1625
2R-2, 59–60		58.59	c	1703
3R-1, 86–88		67.36	c	1648
3R-3, 107–109		70.57	c	1728
6R-1, 89–91		87.09	c	1610
6R-2, 23–25		87.93	c	1556
9R-1, 9–11		114.59	c	2012
9R-1, 26–28		114.76	c	1699
9R-1, 38–40		114.88	c	2372
10R-1, 37–39		124.47	c	1702
10R-1, 71–73		124.81	c	1699
11R-1, 41–43		134.21	c	1746
11R-1, 129–131		135.09	c	1727
12R-1, 84–86		144.34	c	1798
12R-1, 93–95		144.43	c	1841
12R-2, 12–14		145.12	c	1784
12R-2, 49–51		145.49	c	1820
12R-2, 76–78		145.76	c	1841
13R-1, 33–35		153.43	c	1876
13R-1, 110–112		154.20	c	1854
13R-2, 18–20		154.78	c	1860
13R-2, 95–97		155.55	c	1874
13R-3, 29–31		156.39	c	1908
14R-1, 101–103		163.81	c	1929
14R-2, 37–39		164.67	c	2032
15R-1, 53–55		173.03	c	1933
15R-2, 118–120		175.18	c	1946
15R-3, 47–49		175.97	c	1907
15R-4, 94–96		177.94	c	2292
15R-5, 38–40		178.88	c	1998
16R-1, 13–16		182.33	c	2096
17R-1, 77–79		192.67	c	1945
17R-2, 81–84		194.21	c	2112
17R-3, 31–34		195.21	c	1973
18R-1, 71–73		202.31	c	2033
18R-2, 116–118		204.26	c	2092
19R-1, 105–107		212.35	c	2078
19R-2, 103–105		213.83	c	1936
21R-1, 50–53		231.10	c	2117
21R-1, 124–126		231.84	c	2015
21R-2, 79–81		232.89	c	2204
21R-3, 19–21		233.79	c	2146
21R-3, 88–90		234.48	c	2206
22R-1, 39–41		240.69	c	2236
22R-1, 83–85		241.13	c	2104
22R-1, 123–125		241.53	c	2210
24R-1, 19–21		259.39	c	2409
24R-2, 23–25		260.93	c	2315
25R-1, 46–48		269.26	c	2296
25R-1, 50–51		269.30	a	1943
25R-1, 50–51		269.30	b	2070
25R-1, 50–51		269.30	c	2289
25R-1, 52–54		269.32	c	2280
25R-1, 89–91		269.69	c	2346
26R-1, 38–40		274.88	a	2021
26R-1, 38–40		274.88	b	2427
26R-1, 38–40		274.88	c	2350
26R-1, 41–43		274.91	c	2330
27R-1, 12–14		284.22	c	2380
27R-1, 17–19		284.27	a	1994
27R-1, 17–19		284.27	b	2418
27R-1, 17–19		284.27	c	2432
27R-2, 59–61		286.19	c	2442
28R-1, 96–98		294.76	a	2039
28R-1, 96–98		294.76	b	2466
28R-1, 96–98		294.76	c	2493
28R-1, 103–105		294.83	c	2362
28R-2, 65–67		295.95	c	2485
28R-3, 21–23		297.01	c	2308
28R-3, 28–30		297.08	a	2005
28R-3, 28–30		297.08	b	2337
28R-3, 28–30		297.08	c	2404
29R-1, 57–59		303.97	c	2277
29R-1, 62–64		304.02	a	2113

Table 37 (continued).

Core, section, interval (cm)	Piece number	Depth (mbsf)	Direction (a, b, c)	HFV velocity (m/s)
29R-1, 62–64		304.02	b	2363
29R-1, 62–64		304.02	c	2391
29R-2, 73–75		305.63	c	2317
30R-1, 54–56		313.64	c	2399
30R-2, 100–102		315.60	c	2499
30R-2, 100–102		315.60	a	1967
30R-2, 100–102		315.60	b	2520
30R-2, 100–102		315.60	c	2505
30R-3, 56–58		316.66	c	2738
30R-3, 61–63		316.71	a	2088
30R-3, 61–63		316.71	b	2587
30R-3, 61–63		316.71	c	2609
31R-1, 54–56		323.24	c	2648
31R-1, 73–75		323.43	a	2038
31R-1, 73–75		323.43	b	2690
31R-1, 73–75		323.43	c	2651
31R-2, 91–93		325.11	a	2064
31R-2, 91–93		325.11	b	2555
31R-2, 91–93		325.11	c	2604
31R-2, 97–99		325.17	c	2616
32R-1, 23–25		327.83	a	2131
32R-1, 23–25		327.83	b	2429
32R-1, 23–25		327.83	c	2531
32R-1, 24–26		327.84	c	2503
32R-2, 46–48		329.56	c	2560
32R-2, 46–48		329.56	a	2080
32R-2, 46–48		329.56	b	2487
32R-2, 46–48		329.56	c	2548
32R-3, 40–42		331.00	c	2548
33R-1, 36–38		332.76	c	2519
33R-2, 75–77		334.65	c	2643
33R-2, 75–77		334.65	a	2100
33R-2, 75–77		334.65	b	2587
33R-2, 75–77		334.65	c	2580
33R-3, 78–80		336.18	c	2580
34R-1, 91–93		337.41	a	2216
34R-1, 91–93		337.41	b	2474
34R-1, 91–93		337.41	c	2450
34R-1, 94–96		337.44	c	2421
34R-2, 95–97		338.95	a	2211
34R-2, 95–97		338.95	b	2426
34R-2, 95–97		338.95	c	2406
34R-2, 99–101		338.99	c	2441
34R-3, 54–56		340.04	c	2465
35R-1, 138–140		342.68	a	2495
35R-1, 138–140		342.68	b	2575
35R-1, 138–140		342.68	c	2475
35R-1, 139–141		342.69	c	2539
35R-3, 9–11		344.39	c	2600
35R-3, 10–12		344.40	a	2164
35R-3, 10–12		344.40	b	2675
35R-3, 10–12		344.40	c	2638
36R-1, 114–115		347.24	a	2424
36R-1, 114–115		347.24	b	2524
36R-1, 114–115		347.24	c	2486
36R-1, 115–117		347.25	c	2550
36R-3, 88–90		349.98	a	2219
36R-3, 88–90		349.98	b	2665
36R-3, 91–93		350.01	c	2811
37R-2, 108–110		353.38	c	2740
37R-2, 112–114		353.42	a	2145
37R-3, 3–5		353.83	a	2151
37R-3, 3–5		353.83	b	2635
37R-3, 3–5		353.83	c	2685
37R-3, 7–9		353.87	c	2453
38R-1, 79–81		356.59	c	2676
38R-1, 79–81		356.59	a	2255
38R-1, 79–81		356.59	b	2649
38R-1, 79–81		356.59	c	2714
38R-2, 100–102		358.30	a	2255
38R-2, 100–102		358.30	b	2648
38R-2, 100–102		358.30	c	2718
38R-2, 103–105		358.33	c	2720
39R-1, 80–82		361.20	c	2671
39R-1, 80–82		361.20	a	2358
39R-1, 80–82		361.20	b	2809

Table 37 (continued).

Core, section, interval (cm)	Piece number	Depth (mbsf)	Direction (a, b, c)	HFV velocity (m/s)
39R-1, 80–82		361.20	c	2754
39R-3, 30–32		363.70	c	2560
39R-3, 30–32		363.70	a	2308
39R-3, 30–32		363.70	b	2691
39R-3, 30–32		363.70	c	2649
40R-2, 73–84		367.63	c	2575
40R-2, 77–79		367.67	a	2361
40R-2, 77–79		367.67	b	2534
40R-2, 77–79		367.67	c	2514
41R-2, 89–91		377.29	a	1970
41R-2, 89–91		377.29	b	2550
41R-2, 89–91		377.29	c	2332
41R-2, 90–102		377.30	c	2688
42R-1, 25–27		379.95	a	1970
42R-1, 25–27		379.95	b	2380
42R-1, 25–27		379.95	c	2441
42R-1, 28–30		379.98	c	2610
42R-2, 19–21		381.39	a	2076
42R-2, 19–21		381.39	b	3034
42R-2, 23–25		381.43	c	2762
42R-3, 42–44		383.07	c	2710
43R-1, 64–66		385.34	a	2402
43R-1, 64–66		385.34	b	2887
43R-1, 64–66		385.34	c	2854
43R-1, 69–71		385.39	c	2807
43R-2, 6–8		386.26	c	2913
43R-2, 13–15		386.33	a	2390
43R-2, 13–15		386.33	b	2964
43R-3, 86–88		388.56	c	2815
44R-1, 44–46		390.14	a	2636
44R-1, 44–46		390.14	b	3231
44R-1, 44–46		390.14	c	3132
44R-1, 48–50		390.18	c	2844
44R-2, 88–90		392.06	c	2839
45R-1, 18–20		394.48	a	2465
45R-1, 18–20		394.48	b	2959
45R-1, 18–20		394.48	c	3045
45R-1, 22–24		394.52	c	2622
45R-2, 43–45		396.23	c	2610
46R-1, 91–93		399.91	c	3328
46R-1, 92–94		399.92	a	2665
46R-1, 92–94		399.92	b	3228
46R-1, 92–94		399.92	c	3406
46R-1, 134–136		400.34	c	3377
46R-2, 67–69		401.17	c	2810
46R-2, 145–147		401.95	c	3369
46R-2, 145–147		401.95	a	2646
46R-2, 145–147		401.95	b	3540
46R-2, 145–147		401.95	c	3395
47R-1, 24–26		404.24	a	2393
47R-1, 24–26		404.24	b	2761
47R-1, 24–26		404.24	c	2814
47R-1, 26–28		404.26	c	2961
47R-2, 3–5		405.53	a	2327
47R-2, 3–5		405.53	b	2949
47R-2, 3–5		405.53	c	2877
47R-2, 11–13		405.61	c	2899
47R-2, 13–15		405.63	a	2364
47R-2, 13–15		405.63	b	2900
47R-2, 13–15		405.63	c	2908
48R-2, 19–21		410.39	a	2444
48R-2, 19–21		410.39	b	2713
48R-2, 19–21		410.39	c	2790
48R-2, 30–32		410.50	c	2590
49R-1, 81–83		414.51	a	2306
49R-1, 81–83		414.51	b	3032
49R-1, 81–83		414.51	c	3093
49R-1, 83–85		414.53	c	3130
49R-1, 123–125		414.93	c	2872
49R-1, 126–128		414.96	a	2380
49R-1, 126–128		414.96	b	2788
49R-1, 126–128		414.96	c	2829
49R-2, 2–4		415.22	a	2413
49R-2, 2–4		415.22	b	2714
49R-2, 2–4		415.22	c	2756
49R-2, 3–5		415.23	c	2691

Table 37 (continued).

Core, section, interval (cm)	Piece number	Depth (mbsf)	Direction (a, b, c)	HFV velocity (m/s)
49R-2, 48–50		415.68	a	2613
49R-2, 48–50		415.68	b	2765
49R-2, 48–50		415.68	c	2857
50R-1, 124–126		419.54	c	3151
50R-1, 124–126		419.54	a	2449
50R-1, 124–126		419.54	b	3175
50R-1, 124–126		419.54	c	3160
51R-1, 30–32		423.70	c	3037
51R-1, 31–33		423.71	a	2390
51R-1, 31–33		423.71	b	3030
51R-1, 31–33		423.71	c	3090
51R-1, 120–122		424.60	c	3003
51R-2, 92–94		425.82	c	3049
52R-1, 19–21		427.99	c	2963
52R-CC, 10–12		430.25	a	3191
52R-CC, 10–12		430.25	b	2446
52R-CC, 10–12		430.25	c	3103
52R-CC, 20–22		430.35	c	3122
53R-1, 18–20		432.98	c	3097
53R-1, 20–22		433.00	a	2488
53R-1, 20–22		433.00	b	3109
53R-1, 20–22		433.00	c	3116
55R-1, 5–7		442.05	c	2943
55R-1, 5–7		442.05	a	2468
55R-1, 5–7		442.05	b	3000
55R-1, 5–7		442.05	c	3010
56R-1, 25–27		446.75	a	2436
56R-1, 25–27		446.75	b	3086
56R-1, 25–27		446.75	c	3107
59R-1, 102–104	8	472.12	a	4875
59R-1, 102–104	8	472.12	c	5018
59R-2, 91–93	7	473.51	a	4905
59R-2, 91–93	7	473.51	b	4927
59R-2, 91–93	7	473.51	c	5121
59R-3, 33–35	1	474.35	a	4984
59R-3, 33–35	1	474.35	b	5026
59R-3, 33–35	1	474.35	c	5215
59R-3, 88–90	4	474.90	a	4631
59R-3, 88–90	4	474.90	b	4568
59R-3, 88–90	4	474.90	c	4518
59R-3, 105–107	5	475.09	a	4426
59R-3, 105–107	5	475.09	b	4881
59R-3, 105–107	5	475.09	c	4718
60R-1, 17–19	1	480.97	a	4329
60R-1, 17–19	1	480.97	b	4529
60R-1, 17–19	1	480.97	c	4538
61R-1, 68–70	2A	491.18	a	4377
61R-1, 68–70	2A	491.18	b	4200
61R-1, 68–70	2A	491.18	c	4602
61R-2, 45–47	5	492.31	a	3653
61R-2, 45–47	5	492.31	b	4231
61R-2, 45–47	5	492.31	c	3756
62R-1, 42–44	3	500.42	a	3502
62R-1, 42–44	3	500.42	b	3688
62R-1, 42–44	3	500.42	c	3816
63R-1, 56–58	4	510.26	a	4051
63R-1, 56–58	4	510.26	b	4346
63R-1, 56–58	4	510.26	c	4076
64R-1, 68–70	6	520.08	a	4432
64R-1, 68–70	6	520.08	b	4552
64R-1, 68–70	6	520.08	c	4915
64R-2, 38–40	4	521.28	a	4002
64R-2, 38–40	4	521.28	b	4038
64R-2, 38–40	4	521.28	c	4326
66R-1, 12–14	2	538.92	a	2779
66R-1, 12–14	2	538.92	b	3179
66R-1, 12–14	2	538.92	c	3283
66R-1, 38–40	5B	539.18	a	3484
66R-1, 38–40	5B	539.18	b	3589
66R-1, 38–40	5B	539.18	c	3329
68R-2, 58–60	6	560.08	a	3719
68R-2, 58–60	6	560.08	b	3890
68R-2, 58–60	6	560.08	c	3443
68R-3, 23–25	3	561.23	a	4320
68R-3, 23–25	3	561.23	b	4331
68R-3, 23–25	3	561.23	c	4337

Table 38. Thermal conductivity, Hole 857C.

Sample (cm)	Piece number	Depth (mbsf)	Full-space/ half-space (F/H)	Thermal conductivity (W/[m·K])
139-857C-				
1R-1, 110		1.10	F	1.32
1R-2, 70		2.20	F	1.05
2R-1, 70		57.20	F	1.18
2R-2, 35		58.35	F	1.44
3R-1, 80		67.30	F	1.16
3R-2, 75		68.75	F	1.15
3R-3, 90		70.40	F	1.14
6R-2, 36		88.06	F	1.39
6R-2, 85		88.55	F	1.18
6R-2, 110		88.80	F	1.18
9R-1, 95		115.45	F	1.66
13R-1, 50		153.60	F	1.61
13R-1, 80		153.90	F	1.25
13R-1, 105		154.15	F	1.39
13R-1, 132		154.42	F	1.51
13R-2, 75		155.35	F	1.18
13R-2, 80		155.40	H	1.41
13R-2, 105		155.65	F	1.29
13R-3, 10–18		156.20	H	1.40
13R-3, 35		156.45	F	1.50
13R-3, 95		157.05	F	1.70
14R-1, 96–107		163.76	H	1.50
14R-2, 30–46		164.60	H	1.38
15R-1, 52–58		173.02	H	1.65
15R-2, 114–128		175.14	H	1.47
15R-3, 39–57		175.89	H	1.63
15R-4, 85–102		177.85	H	1.27
15R-5, 36–43		178.86	H	1.34
16R-1, 7–17		182.27	H	1.71
17R-2, 80–100		194.20	H	1.69
17R-3, 30–38		195.20	H	1.40
18R-1, 67–75		202.27	H	1.79
18R-2, 114–123		204.24	H	1.44
19R-1, 100–112		212.30	H	1.58
19R-2, 109–116		213.89	H	1.79
21R-1, 42–60		231.02	H	1.73
21R-1, 118–132		231.78	H	1.86
21R-2, 27–35		232.37	H	1.55
21R-3, 79–99		234.39	H	1.63
22R-1, 34–45		240.64	H	1.85
22R-1, 120–128		241.50	H	1.70
24R-1, 5–10		259.25	H	1.67
24R-2, 30–37		261.00	H	1.46
25R-1, 73–80		269.53	H	1.67
26R-1, 5–14		274.55	H	1.69
27R-1, 7–18		284.17	H	1.77
28R-1, 95–109		294.75	H	1.79
28R-2, 57–73		295.87	H	1.63
28R-3, 16–27		296.96	H	1.82
29R-1, 50–67		303.90	H	1.68
29R-2, 73–75		305.63	H	1.72
30R-1, 48–63		313.58	H	1.90
30R-2, 97–109		315.57	H	1.67
30R-3, 52–63		316.62	H	1.84
31R-1, 48–61		323.18	H	1.85
31R-2, 90–104		325.10	H	1.57
32R-1, 21–30		327.81	H	1.80
32R-3, 38–45		330.98	H	1.73
33R-1, 34–42		332.74	H	1.97
33R-3, 75–83		336.15	H	1.66
34R-1, 90–102		337.40	H	1.98
34R-2, 94–108		338.94	H	1.74
34R-3, 56–72		340.06	H	2.07
35R-1, 127–142		342.57	H	2.11

Table 38 (continued).

Sample (cm)	Piece number	Depth (mbsf)	Full-space/ half-space (F/H)	Thermal conductivity (W/[m·K])
35R-3, 1–15		344.31	H	1.76
36R-1, 112–122		347.22	H	2.01
36R-3, 84–98		349.94	H	1.94
37R-2, 104–110		353.34	H	1.84
38R-1, 74–84		356.54	H	1.78
38R-2, 100–110		358.30	H	1.69
39R-1, 75–88		361.15	H	1.95
39R-3, 26–36		363.66	H	1.63
40R-2, 73–84		367.63	H	1.66
41R-2, 90–102		377.30	H	1.92
42R-1, 23–34		379.93	H	1.78
42R-2, 18–30		381.38	H	1.67
43R-1, 65–73		385.35	H	2.08
43R-2, 1–13		386.21	H	1.90
43R-3, 81–95		388.51	H	1.98
44R-1, 42–55		390.12	H	2.06
44R-2, 73–95		391.91	H	1.92
45R-1, 16–28		394.46	H	1.82
45R-2, 38–46		396.18	H	1.82
46R-1, 88–100		399.88	H	1.91
46R-2, 129–149		401.79	H	1.97
47R-1, 21–29		404.21	H	2.07
47R-2, 1–26		405.51	H	1.77
48R-2, 18–35		410.38	H	1.97
49R-1, 80–95		414.50	H	2.00
49R-1, 119–130		414.89	H	1.92
49R-2, 2–15		415.22	H	1.93
49R-2, 48–53		415.68	H	2.03
50R-1, 119–137		419.49	H	1.92
51R-1, 24–36		423.64	H	2.05
51R-1, 108–126		424.48	H	1.89
51R-2, 80–108		425.70	H	1.99
52R-1, 17–30		427.97	H	1.79
52R-CC, 8–26		430.23	H	1.69
53R-1, 17–25		432.97	H	1.66
55R-1, 3–9		442.03	H	2.03
56R-1, 23–27		446.73	H	1.83
59R-1, 84–98	7	471.94	H	1.90
59R-1, 135–148	11	472.45	H	1.88
59R-2, 22–33	3	472.82	H	2.10
59R-2, 65–89	6	473.25	H	1.93
59R-3, 40–65	2	474.42	H	2.11
59R-3, 98–113	5	475.00	H	2.02
59R-4, 33–47	2	475.85	H	2.20
59R-4, 82–94	7	476.34	H	1.95
60R-1, 1–19	1	480.81	H	2.00
60R-1, 20–35	2	481.00	H	2.01
60R-2, 1–24	1	482.19	H	2.00
60R-2, 126–141	15	483.44	H	1.82
61R-1, 60–71	2A	491.10	H	1.95
61R-1, 71–88	2B	491.21	H	1.64
61R-2, 45–60	5	492.31	H	1.59
61R-2, 68–81	7	492.54	H	2.02
62R-1, 31–49	3	500.31	H	1.68
62R-1, 67–78	5	500.67	H	1.47
63R-1, 42–57	4	510.12	H	1.64
64R-1, 54–70	6	519.94	H	2.15
64R-2, 29–40	4	521.19	H	2.21
65R-1, 4–15	2	529.14	H	1.79
66R-1, 9–18	2	538.89	H	1.95
68R-1, 17–27	4	558.17	H	1.94
68R-1, 107–114	17	559.07	H	2.00
68R-2, 46–61	6	559.96	H	1.81
68R-2, 85–98	9	560.35	H	1.90
68R-3, 1–16	1	561.01	H	1.70
68R-3, 24–35	3	561.24	H	1.81

Table 39. Electrical resistivity, Hole 857C.

Sample (cm)	Depth (mbsf)	Electrical resistivity, seawater readings	Electrical resistivity, sample readings	Formation factor
139-857C-				
1R-1, 61	0.61	0.026	0.034	1.32
1R-2, 70	2.20	0.021	0.037	1.78
2R-1, 60	57.10	0.022	0.048	2.19
2R-2, 53	58.53	0.022	0.050	2.28
2R-2, 60	58.60	0.023	0.048	2.09
2R-2, 66	58.66	0.022	0.051	2.35
3R-1, 80	67.30	0.020	0.045	2.25
11R-1, 140	135.20	0.019	0.066	3.47
12R-2, 76	145.76	0.020	0.093	4.65
13R-1, 30	153.40	0.019	0.087	4.58
14R-1, 100	163.80	0.019	0.089	4.68
15R-1, 75	173.25	0.019	0.095	5.00
17R-2, 75	194.15	0.022	0.154	6.97

Table 40. Index properties, Hole 857D.

Core, section, interval (cm)	Piece number	Depth (mbsf)	Wet-bulk density (g/cm^3)	Grain density (g/cm^3)	Wet porosity (%)	Wet water content (%)	Void ratio
139-857D-							
1R-1, 125–127	13	582.75	2.51	2.66	13.5	5.5	0.60
2R-1, 73–75	12	590.33	2.93	2.96	6.6	2.3	0.07
3R-1, 130–132	13	600.60	2.82	2.92	7.3	2.7	0.08
3R-2, 67–69	6	601.44	2.90	2.90	5.4	1.9	0.06
4R-1, 88–90	11	609.78	2.93	2.91	4.7	1.7	0.05
9R-1, 32–34	6	657.22	3.00	2.97	5.0	1.7	0.05
11R-1, 47–49	7	676.67	2.47	2.78	22.3	9.2	0.29
12R-1, 31–33	6	686.21	2.47	2.78	20.8	8.6	0.26
12R-2, 33–35	5	687.63	3.00	2.95	2.9	1.0	0.03
14R-1, 18–20	4	705.28	2.62	2.84	14.8	5.8	0.17
16R-1, 75–77	6B	725.25	2.46	2.73	15.2	6.3	0.18
17R-1, 68–70	7B	734.58	2.52	2.75	13.7	5.6	0.16
17R-1, 122–124	11	735.12	2.63	2.82	11.6	4.5	0.13
18R-1, 59–61	4B	744.19	2.93	2.97	5.6	2.0	0.06
21R-1, 65–67	6B	772.85	3.03	2.97	4.4	1.5	0.05
22R-1, 17–19	4	781.97	2.63	2.73	12.2	4.8	0.14
22R-1, 89–91	13	782.69	3.03	2.95	4.6	1.6	0.05
24R-1, 28–30	5	801.48	2.69	2.76	13.7	5.2	0.16
24R-2, 32–34	5	803.02	2.92	2.90	6.4	2.2	0.07
28R-1, 33–35	6	839.23	2.65	2.70	7.4	2.9	0.08
31R-1, 27–29	6	868.77	2.46	2.77	14.2	5.9	0.16
34R-1, 14–16	5	897.64	2.77	2.82	13.8	5.1	0.16
35R-1, 70–72	10	907.90	2.98	2.97	4.4	1.5	0.05
36R-1, 82–84	13	917.72	3.03	2.98	3.5	1.2	0.04

Table 41. Compressional wave velocity (HFV), Hole 857D.

Core, section, interval (cm)	Piece number	Depth (mbsf)	Direction (a, b, c)	HFV velocity (m/s)
139-857D-				
1R-1, 4–6	1	581.54	c	5092
1R-1, 27–29	4	581.77	c	4226
1R-1, 36–38	5	581.86	c	3711
1R-1, 42–44	6	581.92	c	3253
1R-1, 65–67	8C	582.15	c	3550
1R-1, 72–74	8D	582.22	c	3136
1R-1, 104–106	11	582.54	c	3226
1R-1, 125–127	13	582.75	a	4080
1R-1, 125–127	13	582.75	b	4496
1R-1, 125–127	13	582.75	c	4695
1R-1, 126–128	13	582.76	c	3945
1R-1, 136–138	14	582.86	c	4749
1R-1, 147–149	15	582.97	c	3840
1R-2, 23–25	4	583.23	c	4133
1R-2, 62–64	10	583.62	c	4504
1R-2, 80–82	11D	583.80	c	4961
2R-1, 2–4	1	589.62	c	4543
2R-1, 12–14	3	589.72	c	5159
2R-1, 32–34	7	589.92	c	4533
2R-1, 49–51	9	590.09	c	4221
2R-1, 67–69	11	590.27	c	5167
2R-1, 73–75	12	590.33	a	5141
2R-1, 73–75	12	590.33	b	5071
2R-1, 73–75	12	590.33	c	4393
2R-1, 75–77	12	590.35	c	4422
2R-1, 103–105	16	590.63	c	4561
3R-1, 3–5	1	599.33	c	4906
3R-1, 14–16	2A	599.44	c	5294
3R-1, 41–43	4	599.71	c	5161
3R-1, 67–69	6B	599.97	a	4789
3R-1, 67–69	6B	599.97	b	4906
3R-1, 67–69	6B	599.97	c	5221
3R-1, 95–97	9A	600.25	c	5066
3R-1, 130–132	13	600.60	a	5080
3R-1, 130–132	13	600.60	b	5258
3R-1, 130–132	13	600.60	c	4856
3R-1, 142–144	15	600.72	c	5185
3R-2, 14–16	2B	600.91	c	4850
3R-2, 62–64	8	601.39	c	5015
3R-2, 84–91	11	601.61	c	4742
3R-2, 112–114	14	601.89	c	4502
3R-2, 125–127	16	602.02	c	4140
4R-1, 20–22	3	609.10	c	3900
4R-1, 47–49	7	609.37	c	5438
4R-1, 66–68	9	609.56	c	4746
4R-1, 80–82	10	609.70	c	4343
4R-1, 88–90	11	609.78	a	5080
4R-1, 88–90	11	609.78	b	4899
4R-1, 88–90	11	609.78	c	5275
4R-1, 89–91	11	609.79	c	5091
4R-1, 98–100	12	609.88	c	4624
4R-1, 133–135	17	610.23	c	4362
4R-1, 140–142	18	610.30	c	4642
4R-2, 25–27	6	610.65	c	5230
4R-2, 45–47	9	610.85	c	4544
4R-2, 61–63	12	611.01	c	4206
5R-1, 7–9	2	618.67	c	4032
5R-1, 29–31	7	618.89	c	4865
6R-1, 7–8	3	627.97	c	4108
6R-1, 13–15	4	628.03	c	4820
6R-1, 19–21	5	628.09	c	4634
7R-1, 2–4	1	637.62	c	4246
7R-1, 10–12	3	637.70	c	5042
7R-1, 15–17	4	637.75	c	4904
7R-1, 20–22	5	637.80	c	5493
7R-1, 24–26	6	637.84	c	4943
7R-1, 32–34	8	637.92	c	5321
7R-1, 40–42	10	638.00	c	4967
7R-1, 46–48	11	638.06	c	5416
8R-1, 7–9	1	647.37	c	3461
8R-1, 34–36	5A	647.64	c	4079
8R-1, 42–44	5B	647.72	c	3846
8R-1, 61–63	8	647.91	c	4197
8R-1, 75–77	10	648.05	c	3160

Table 41 (continued).

Core, section, interval (cm)	Piece number	Depth (mbsf)	Direction (a, b, c)	HFV velocity (m/s)
8R-1, 82–84	11	648.12	c	5313
8R-1, 87–89	12	648.17	c	5443
8R-1, 97–99	14	648.27	c	5481
9R-1, 5–7	1	656.95	c	5600
9R-1, 20–22	4	657.10	c	5057
9R-1, 27–29	5	657.17	c	4623
9R-1, 32–34	6	657.22	a	5862
9R-1, 32–34	6	657.22	b	5531
9R-1, 32–34	6	657.22	c	5663
9R-1, 34–36	6	657.24	c	5085
9R-1, 53–55	10	657.43	c	4970
9R-1, 66–68	12	657.56	c	4768
9R-1, 119–121	21	658.09	c	4323
10R-1, 12–14	2	666.72	c	3615
10R-1, 25–27	4	666.85	c	3348
11R-1, 16–18	3	676.36	c	3830
11R-1, 42–44	6	676.62	c	3972
11R-1, 47–49	7	676.67	a	3575
11R-1, 47–49	7	676.67	b	4331
11R-1, 47–49	7	676.67	c	3666
11R-1, 49–51	7	676.69	c	4009
12R-1, 25–27	5	686.15	c	3478
12R-1, 31–33	6	686.21	a	3175
12R-1, 31–33	6	686.21	b	3385
12R-1, 31–33	6	686.21	c	3299
12R-1, 32–34	6	686.22	c	3566
12R-1, 55–57	9	686.45	c	3430
12R-1, 63–65	10	686.53	c	3776
12R-1, 75–77	11	686.65	c	4291
12R-1, 106–108	14	686.96	c	3067
12R-2, 2–4	1	687.32	c	4031
12R-2, 18–20	4	687.48	c	5232
12R-2, 33–35	5	687.63	a	6141
12R-2, 33–35	5	687.63	b	6141
12R-2, 33–35	5	687.63	c	6046
12R-2, 41–43	5	687.71	c	5233
14R-1, 18–20	4	705.28	a	3907
14R-1, 18–20	4	705.28	b	3644
14R-1, 18–20	4	705.28	c	3746
15R-1, 1–3	1	714.81	c	3965
15R-1, 7–9	2	714.87	c	3549
15R-1, 15–17	4	714.95	c	3176
15R-1, 26–28	6	715.06	c	3168
15R-1, 32–34	7	715.12	c	3372
15R-1, 41–43	9	715.21	c	5254
15R-1, 54–56	12	715.34	c	4123
15R-1, 59–61	13	715.39	c	3782
15R-1, 67–69	15	715.47	c	4191
15R-1, 72–74	16	715.52	c	2624
15R-1, 78–80	17	715.58	c	3925
16R-1, 14–16	3	724.64	c	3688
16R-1, 18–20	4	724.68	c	3513
16R-1, 26–28	4	724.76	c	3486
16R-1, 42–44	5	724.92	c	3733
16R-1, 51–53	6A	725.01	c	3559
16R-1, 59–61	6A	725.09	c	3391
16R-1, 67–69	6A	725.17	c	3449
16R-1, 75–77	6B	725.25	a	3115
16R-1, 75–77	6B	725.25	b	3714
16R-1, 75–77	6B	725.25	c	3690
16R-1, 78–80	6B	725.28	c	3567
16R-1, 86–88	6B	725.36	c	3643
16R-1, 93–95	6B	725.43	c	3466
16R-1, 116–118	9A	725.66	c	3539
16R-1, 127–130	9B	725.77	c	3512
16R-2, 4–6	1	725.90	c	3776
16R-2, 11–13	2	725.97	c	3676
16R-2, 18–20	3	726.04	c	3639
16R-2, 48–52	9	726.34	c	4129
16R-2, 61–63	11	726.47	c	4108
16R-2, 110–112	18	726.96	c	4397
17R-1, 3–5	1	733.93	c	3582
17R-1, 7–9	2A	733.97	c	3736
17R-1, 15–17	2B	734.05	c	3427
17R-1, 22–24	2C	734.12	c	3118
17R-1, 29–31	3A	734.19	c	3290

Table 41 (continued).

Core, section, interval (cm)	Piece number	Depth (mbsf)	Direction (a, b, c)	HFV velocity (m/s)
17R-1, 36–38	4	734.26	c	2906
17R-1, 41–43	5	734.31	c	2784
17R-1, 49–51	6	734.39	c	3569
17R-1, 59–61	7A	734.49	c	4191
17R-1, 68–70	7B	734.58	a	3397
17R-1, 68–70	7B	734.58	b	4051
17R-1, 68–70	7B	734.58	c	4073
17R-1, 69–71	7B	734.59	c	3421
17R-1, 77–79	7B	734.67	c	3308
17R-1, 88–90	8	734.78	c	2885
17R-1, 96–98	9	734.86	c	2984
17R-1, 106–108	10	734.96	c	3850
17R-1, 120–122	11	735.10	c	4461
17R-1, 122–124	11	735.12	a	4144
17R-1, 122–124	11	735.12	b	4758
17R-1, 122–124	11	735.12	c	4925
17R-1, 131–133	12	735.21	c	4162
17R-1, 143–145	13	735.33	c	4126
17R-2, 3–5	1	735.43	c	4257
17R-2, 16–18	2A	735.56	c	3723
17R-2, 21–23	2A	735.61	c	3801
17R-2, 27–29	2A	735.67	c	3218
17R-2, 36–38	2B	735.76	c	3051
17R-2, 44–46	3	735.84	c	3244
17R-2, 52–54	4	735.92	c	3643
17R-2, 58–60	5	735.98	c	3604
17R-2, 67–69	6	736.07	c	3934
17R-2, 75–77	7	736.15	c	3744
17R-2, 84–86	8	736.24	c	3874
17R-2, 90–92	9	736.31	c	4022
17R-2, 96–98	10	736.36	c	3824
17R-2, 106–108	11	736.46	c	4482
17R-2, 120–122	12	736.60	c	4549
17R-2, 130–132	13	736.70	c	4429
17R-2, 140–142	14	736.80	c	4488
17R-3, 7–9	1	736.91	c	3981
17R-3, 25–27	3	737.09	c	4467
17R-3, 33–35	4	737.17	c	3882
17R-3, 40–42	5	737.24	c	4184
17R-3, 68–70	10	737.52	c	4655
17R-3, 91–93	13	737.75	c	4485
18R-1, 8–10	1A	743.68	c	5285
18R-1, 25–27	1B	743.85	c	5410
18R-1, 37–39	2	743.97	c	5028
18R-1, 49–51	4A	744.09	c	5584
18R-1, 58–60	4B	744.18	c	5121
18R-1, 59–61	4B	744.19	a	5467
18R-1, 59–61	4B	744.19	b	5516
18R-1, 59–61	4B	744.19	c	5551
18R-1, 74–76	5	744.34	c	5208
18R-1, 92–94	7	744.52	c	5291
18R-1, 106–108	8	744.66	c	5360
18R-1, 125–127	10	744.85	c	5448
18R-1, 134–136	11	744.94	c	5607
18R-2, 4–6	1	745.06	c	5386
18R-2, 14–16	2A	745.16	c	4513
18R-2, 44–46	4	745.46	c	4701
18R-2, 58–60	6	745.60	c	5277
18R-2, 73–75	8A	745.75	c	4505
18R-2, 83–85	9	745.85	c	4854
19R-1, 2–4	1	752.82	c	4923
19R-1, 16–18	4	752.96	c	5525
19R-1, 26–28	6	753.06	c	5062
20R-1, 27–29	4	762.77	c	4554
20R-1, 43–45	6	762.93	c	4849
20R-1, 50–52	7	763.00	c	4810
20R-1, 65–67	8	763.15	c	4801
20R-1, 72–74	9	763.22	c	4896
20R-1, 82–84	10	763.32	c	4779
20R-1, 116–118	16	763.66	c	4461
21R-1, 4–6	1	772.24	c	3230
21R-1, 10–12	3	772.30	c	2854
21R-1, 14–16	4	772.34	c	4591
21R-1, 26–28	5	772.46	c	5452
21R-1, 37–39	5	772.57	c	5457
21R-1, 49–51	6A	772.69	c	5376

Table 41 (continued).

Core, section, interval (cm)	Piece number	Depth (mbsf)	Direction (a, b, c)	HFV velocity (m/s)
21R-1, 58–60	6A	772.78	c	5545
21R-1, 63–65	6B	772.83	c	5907
21R-1, 65–67	6B	772.85	a	6361
21R-1, 65–67	6B	772.85	b	6063
21R-1, 65–67	6B	772.85	c	6277
21R-1, 70–72	6B	772.90	c	5773
21R-1, 77–79	6B	772.97	c	5569
21R-1, 86–88	6B	773.06	c	5664
21R-1, 94–96	7	773.14	c	5135
21R-1, 120–122	11	773.40	c	2958
21R-1, 126–128	12	773.46	c	2932
21R-1, 130–132	13	773.50	c	3507
21R-1, 141–143	15	773.61	c	3486
21R-2, 10–12	2	773.80	c	3085
21R-2, 17–19	3	773.87	c	2988
21R-2, 24–26	4	773.94	c	3156
22R-1, 7–9	2	781.87	c	5525
22R-1, 28–30	5	782.08	c	3455
22R-1, 39–41	7	782.19	c	3748
22R-1, 56–58	9	782.36	c	4805
22R-1, 68–70	10	782.48	c	4135
22R-1, 89–91	13	782.69	a	6403
22R-1, 89–91	13	782.69	b	6186
22R-1, 89–91	13	782.69	c	5614
22R-1, 90–92	13	782.70	c	3732
23R-1, 42–44	8	791.92	c	5628
23R-1, 52–54	9	792.02	c	5364
23R-1, 61–63	10	792.11	c	5714
23R-1, 81–83	13	792.31	c	5481
24R-1, 32–34	6	801.52	a	6183
24R-1, 32–34	6	801.52	b	5628
24R-1, 32–34	6	801.52	c	5231
24R-1, 34–36	6	801.54	c	3577
24R-1, 40–42	7	801.60	c	3500
24R-1, 52–54	9	801.72	c	3885
24R-1, 90–92	17	802.10	c	5290
24R-1, 112–114	20A	802.32	c	6358
24R-1, 130–132	22A	802.50	c	6092
24R-2, 3–5	1	802.73	c	5736
24R-2, 11–13	2	802.81	c	5758
24R-2, 18–20	3	802.88	c	4800
24R-2, 32–34	5	803.02	c	5694
24R-2, 40–42	5	803.10	c	5345
24R-2, 52–54	7	803.22	c	5623
24R-2, 62–64	8	803.32	c	5683
24R-2, 71–73	9	803.41	c	5629
24R-2, 78–80	10	803.48	c	5510
24R-2, 135–137	19B	804.05	c	5549
24R-3, 2–4	1	804.11	c	5436
24R-3, 10–12	2	804.19	c	5313
24R-3, 25–27	4A	804.34	c	5872
25R-1, 3–5	1	810.83	c	6219
25R-1, 10–12	2	810.90	c	5992
25R-1, 20–22	3	811.00	c	5649
25R-1, 29–31	4	811.09	c	5632
25R-1, 37–39	5	811.17	c	5440
25R-1, 48–50	7	811.28	c	5648
25R-1, 55–57	8	811.35	c	5407
25R-1, 65–67	10	811.45	c	5724
25R-1, 72–74	11	811.52	c	5484
25R-1, 78–80	12	811.58	c	5661
25R-1, 87–89	13	811.67	c	5101
26R-1, 3–5	1	820.33	c	6102
26R-1, 10–12	2	820.40	a	6490
26R-1, 10–12	2	820.40	b	6456
26R-1, 10–12	2	820.40	c	6469
26R-1, 10–12	2	820.40	c	5891
26R-1, 18–20	3	820.48	c	5870
26R-1, 32–34	4C	820.62	c	6005
26R-1, 56–58	6	820.86	c	5738
26R-1, 67–69	7	820.97	c	5597
26R-1, 74–76	8	821.04	c	5159
26R-1, 93–94	10	821.23	c	6110
27R-1, 2–4	1	829.62	c	4188
27R-1, 11–12	2	829.71	c	3072
27R-1, 51–53	7	830.11	c	3778

Table 41 (continued).

Core, section, interval (cm)	Piece number	Depth (mbsf)	Direction (a, b, c)	HFV velocity (m/s)
27R-1, 57–59	8	830.17	c	3808
27R-1, 63–65	9	830.23	c	5271
27R-1, 69–71	10	830.29	c	5009
27R-1, 76–78	11	830.36	c	5303
27R-1, 83–85	12	830.43	c	5199
27R-1, 94–96	14	830.54	c	5693
27R-1, 108–110	16	830.68	c	5005
28R-1, 3–5	1	838.93	c	5299
28R-1, 8–9	2	838.98	c	3487
28R-1, 18–20	4	839.08	c	3490
28R-1, 25–26	5	839.15	c	3090
28R-1, 32–34	6	839.22	c	4553
28R-1, 33–35	6	839.23	a	4644
28R-1, 33–35	6	839.23	b	4891
28R-1, 33–35	6	839.23	c	4667
28R-1, 40–41	7	839.30	c	4289
28R-1, 46–48	8	839.36	c	4466
28R-1, 53–55	9	839.43	c	4252
28R-1, 65–67	11	839.55	c	3900
28R-1, 75–76	12	839.65	c	4401
28R-1, 80–82	13	839.70	c	4405
29R-1, 12–14	3	848.52	c	4564
29R-1, 16–18	4	848.56	c	4234
29R-1, 20–21	5	848.60	c	4957
29R-1, 29–31	7	848.69	c	4337
29R-1, 37–39	9	848.77	c	4945
29R-1, 43–45	10	848.83	c	5529
29R-1, 56–58	12	848.96	c	5302
29R-1, 75–77	14	849.15	c	5561
29R-1, 86–88	15	849.26	c	5647
29R-1, 104–106	18	849.44	c	5665
29R-1, 112–113	19	849.52	c	5976
29R-1, 117–119	20A	849.57	c	5830
29R-1, 124–126	20B	849.64	c	5785
29R-1, 132–133	21	849.72	c	5802
29R-1, 137–138	22A	849.77	c	5248
29R-1, 142–144	22B	849.82	c	5645
29R-2, 10–12	2	850.00	c	5645
29R-2, 24–26	3	850.14	c	5664
29R-2, 35–37	4A	850.25	c	5847
30R-1, 56–58	15	859.46	c	4728
31R-1, 14–16	4	868.64	c	3669
31R-1, 21–23	5	868.71	c	3575
31R-1, 26–28	6	868.76	c	3631
31R-1, 27–29	6	868.77	a	3530
31R-1, 27–29	6	868.77	b	3554
31R-1, 27–29	6	868.77	c	3457
31R-1, 41–43	8	868.91	c	3196
31R-1, 105–107	21	869.55	c	5864
32R-1, 2–4	1	878.12	c	4832
32R-1, 61–63	13	878.71	c	5208
33R-1, 34–36	6	888.14	c	5027
33R-1, 48–50	8	888.28	c	4928
33R-1, 65–67	11	888.45	c	4564
33R-1, 73–75	12	888.53	c	4002
33R-1, 82–84	13	888.62	c	5066
34R-1, 9–11	3	897.59	c	4181
34R-1, 24–26	5	897.74	c	4644
34R-1, 37–39	7	897.87	c	4923
34R-1, 53–55	9	898.03	c	4657
34R-1, 85–87	13	898.35	c	3295
35R-1, 2–4	1	907.20	c	5923
35R-1, 29–31	5	907.49	c	5753
35R-1, 37–39	6	907.57	c	5214
35R-1, 55–57	9	907.75	c	5306
35R-1, 63–65	10	907.83	c	5839
35R-1, 65–67	10	907.85	c	5986
35R-1, 68–70	10	907.88	c	5789
35R-1, 70–72	10	907.90	a	5626
35R-1, 70–72	10	907.90	b	5629
35R-1, 70–72	10	907.90	c	5597
35R-1, 72–74	10	907.92	c	5574
35R-1, 89–91	13	908.09	c	5448
35R-1, 99–101	14A	908.19	c	5851
35R-1, 102–104	14A	908.22	c	5797
35R-1, 105–107	14A	908.25	c	5581

Table 41 (continued).

Core, section, interval (cm)	Piece number	Depth (mbsf)	Direction (a, b, c)	HFV velocity (m/s)
35R-1, 107–109	14A	908.27	c	5505
35R-1, 119–121	14B	908.39	c	5596
35R-1, 121–123	14B	908.41	c	5888
35R-1, 124–126	14B	908.44	c	6018
35R-1, 128–130	14C	908.48	c	5843
35R-1, 131–133	14C	908.51	c	5695
35R-1, 132–134	14C	908.52	c	6101
35R-1, 139–141	15	908.59	c	5602
36R-1, 2–4	1	916.92	c	5611
36R-1, 16–18	3	917.06	c	5272
36R-1, 23–24	4	917.13	c	4795
36R-1, 28–30	5B	917.18	c	5228
36R-1, 36–39	6	917.26	c	5161
36R-1, 50–51	8	917.40	c	5800
36R-1, 56–58	9	917.46	c	6076
36R-1, 70–72	11	917.60	c	5476
36R-1, 82–84	13	917.72	a	6192
36R-1, 82–84	13	917.72	b	5265
36R-1, 82–84	13	917.72	c	6441
36R-1, 82–84	13	917.72	c	5471
36R-1, 94–96	14	917.84	c	5492
36R-1, 103–105	15	917.93	c	5602
36R-1, 112–114	17	918.02	c	5772
36R-1, 120–122	18	918.10	c	5884
36R-1, 127–129	19	918.17	c	5833
37R-1, 2–4	1	926.52	c	2436
37R-1, 18–19	4	926.68	c	6273
37R-1, 21–23	5	926.71	c	4868
37R-1, 26–28	6	926.76	c	5273
37R-1, 36–38	8A	926.86	c	4273
37R-1, 43–45	9	926.93	c	4836

Table 42. Thermal conductivity, Hole 857D.

Core, section, interval (cm)	Piece number	Depth (mbsf)	Thermal conductivity (W/[m·K])
139-857D-			
1R-1, 1–9	1	581.51	2.11
1R-1, 1–9	1	581.51	1.81
1R-1, 23–31	4	581.73	1.97
1R-1, 70–76	8D	582.20	1.85
1R-1, 70–76	8D	582.20	1.81
1R-1, 119–132	13	582.69	2.88
1R-2, 17–28	4	583.17	2.50
1R-2, 17–28	4	583.17	2.66
2R-1, 30–38	7	589.90	1.82
3R-1, 7–20	2A	599.37	1.76
3R-1, 35–48	4	599.65	1.85
3R-2, 54–72	8	601.31	1.82
4R-1, 14–26	3	609.04	1.86
4R-1, 58–74	9	609.48	2.07
4R-1, 75–86	10	609.65	1.90
4R-1, 130–138	17	610.20	2.31
7R-1, 45–51	11	638.05	2.40
8R-1, 1–13	1	647.31	1.77
8R-1, 1–13	1	647.31	1.61
8R-1, 38–48	5B	647.68	1.56
9R-1, 1–7	1	656.91	2.07
9R-1, 63–70	12	657.53	1.47
11R-1, 38–45	6	676.58	1.97
11R-1, 38–45	6	676.58	2.19
12R-1, 22–30	5	686.12	2.11
12R-1, 46–54	8B	686.36	1.80
12R-1, 71–79	11	686.61	3.00
15R-1, 53–57	12	715.33	2.28
16R-1, 18–30	4	724.68	2.32
16R-1, 53–72	6A	725.03	2.23
16R-1, 111–123	9A	725.61	2.01
16R-1, 124–134	9B	725.74	2.25
16R-2, 16–23	2	726.02	2.16
17R-1, 10–20	2B	734.00	2.43
17R-1, 44–54	6	734.34	1.72
17R-1, 101–114	10	734.91	2.57
17R-2, 123–134	14	736.63	2.58
18R-1, 4–20	2A	743.64	2.23
18R-1, 20–32	2B	743.80	1.76
18R-1, 56–69	4B	744.16	2.15
18R-1, 97–115	8	744.57	2.00
18R-1, 120–130	10	744.80	1.87
18R-1, 130–141	11	744.90	1.70
18R-2, 1–12	1	745.03	2.01
18R-2, 41–49	4	745.43	1.72
18R-2, 54–62	6	745.56	1.87
20R-1, 47–57	7	762.97	2.10
20R-1, 68–77	9	763.18	1.98
20R-1, 78–87	10	763.28	2.06
21R-1, 26–40	5	772.46	1.56
21R-1, 48–63	6A	772.68	1.90
21R-1, 90–104	7	773.10	1.88
21R-2, 13–22	3	773.83	2.33
22R-1, 51–65	9	782.31	1.87
22R-1, 88–95	13	782.68	2.41
23R-1, 40–47	8	791.90	1.79
23R-1, 57–66	10	792.07	2.00
24R-1, 49–55	9	801.69	2.30
24R-1, 110–115	20A	802.30	2.23
24R-2, 28–43	5	802.98	2.19
24R-2, 48–57	7	803.18	2.22
24R-2, 58–66	8	803.28	1.75
24R-2, 76–84	10	803.46	1.78
25R-1, 19–25	3	810.99	1.49
25R-1, 26–35	4	811.06	1.97
25R-1, 70–75	11	811.50	1.93
25R-1, 85–91	13	811.65	1.93
26R-1, 15–23	3	820.45	2.23
26R-1, 49–63	6	820.79	2.04
27R-1, 73–79	11	830.33	2.50
27R-1, 81–87	12	830.41	2.12
28R-1, 14–23	4	839.04	1.76
28R-1, 27–37	6	839.17	2.59
28R-1, 50–56	9	839.40	2.29
28R-1, 62–72	11	839.52	2.71
29R-1, 53–63	12	848.93	2.02
29R-1, 81–91	15	849.21	1.81
29R-1, 121–130	20B	849.61	2.36
29R-1, 139–147	22B	849.79	2.13
29R-2, 6–15	2	849.96	2.32
29R-2, 18–30	3	850.08	2.09
31R-1, 18–25	5	868.68	2.46
32R-1, 57–64	13	878.67	1.83
33R-1, 63–70	11	888.43	1.76
33R-1, 71–79	12	888.51	2.11
34R-1, 20–29	5	897.70	2.53
34R-1, 34–42	7	897.84	2.79
35R-1, 26–33	5	907.46	1.88
35R-1, 96–109	14A	908.16	2.07
35R-1, 117–126	14B	908.37	1.70
36R-1, 12–21	3	917.02	1.97
36R-1, 53–59	9	917.43	1.99
36R-1, 67–79	11	917.57	1.59
36R-1, 80–87	13	917.70	1.96
36R-1, 89–100	14	917.79	1.71
37R-1, 41–47	9	926.91	2.60

Note: All measurements were made in the half-space configuration.

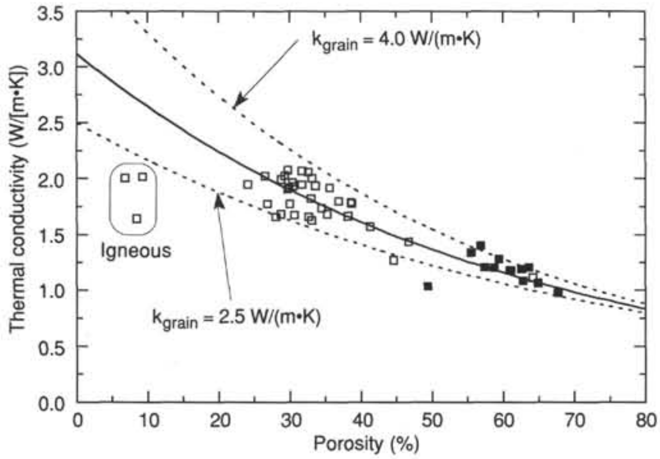

Figure 74. Correlation of porosity with thermal conductivity in Holes 857A (solid squares) and 857C (open squares). Dashed lines are the calculated geometric-mean thermal conductivities for two different grain thermal conductivities. The solid line is a best-fit geometric mean with a calculated grain thermal conductivity of 3.12 W/(m·K). A value of 0.6 W/(m·K) is used as the thermal conductivity of seawater.

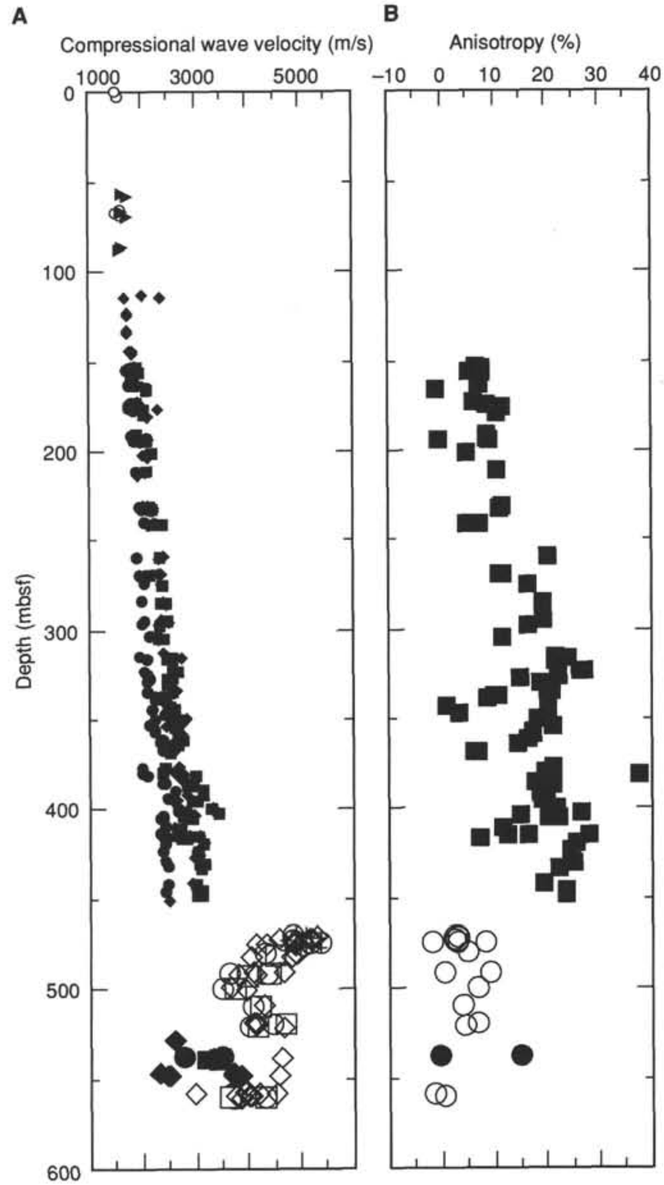

Figure 75. **A.** Compressional wave velocity vs. depth in Hole 857C. Small dotted circles are vertical ("a" direction) velocities measured with the DSV; all other measurements were made with the HFV. Small solid triangles are horizontal velocities ("c" direction) measured through the liner on sediments above the sill; small solid diamonds are velocities measured without a liner for deeper sediments above the sills. Small solid circles are vertical velocities obtained from cubes of these sediments; small solid squares are horizontal velocities (average of b- and c-directional velocities) for these cubes. Large symbols represent velocities in the sill complex. No liner horizontal velocity data (in the c direction) are indicated by solid diamonds for sediment interbed samples and by open diamonds for igneous rock samples. Cube data are presented as follows: solid circles are vertical velocities in the sediment interbeds, open circles are vertical velocities in igneous rock, solid squares are horizontal velocities (average of b and c directions) in the sediment interbeds, and open squares are horizontal velocities from igneous rock. **B.** Velocity anisotropy vs. depth for cube samples of sediment and basalt in Hole 857C. The sediment was lithified enough for cubes to be cut from below 153.5 mbsf. Solid squares represent data from the sediment column above the sill complex. Solid circles are data from sediment interbed samples and open circles are values from igneous rock samples.

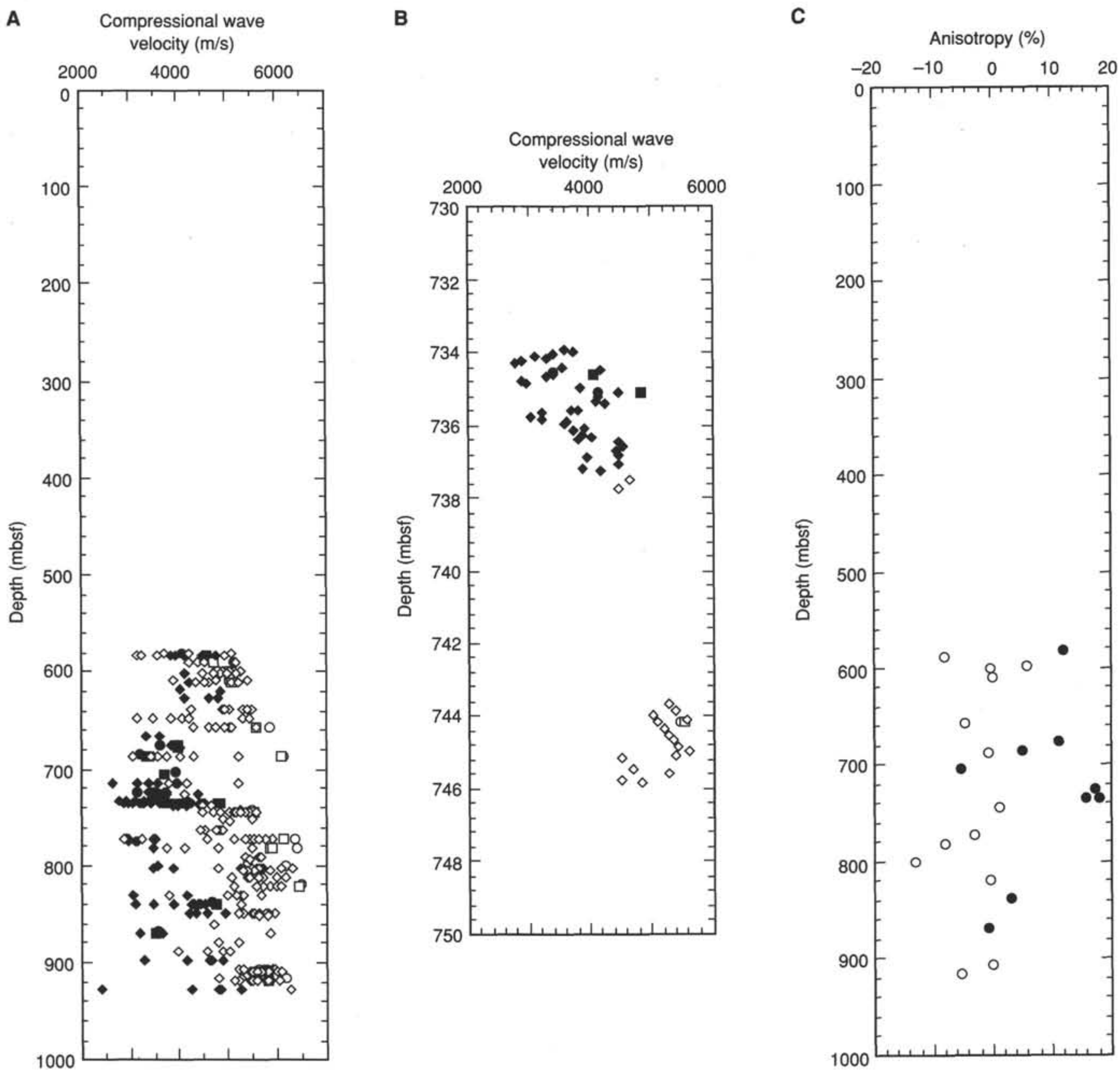

Figure 76. **A.** Compressional wave velocity vs. depth in Hole 857D. All measurements were made with the HFV. No-liner horizontal velocity data (in the c direction) are indicated by solid diamonds for sediment interbed samples and by open diamonds for igneous rock samples. Cube data are presented as follows: solid circles are vertical velocities in the sediment interbeds, open circles are vertical velocities in igneous rock, solid squares are horizontal velocities (average of b and c directions) in the sediment interbeds and open squares are horizontal velocities in igneous rock. **B.** Enlargement of the interval from 730.0 to 750.0 mbsf in (A) shows the range of values obtained from closely spaced measurements on working-half pieces of sediment and igneous rock were made for Hole 857D. Cubes were cut at less frequent intervals. Symbols are as described in (A). The range of velocities is greater in the sediment samples than in the igneous rocks, as is the range of anisotropy (Fig. 76C); the cube data agree well with the working-half piece values. **C.** Velocity anisotropy vs. depth for cube samples of sediment and basalt in Hole 857D. Solid squares represent data from the sediment column above the sill complex. Solid circles are anisotropy data from sediment interbed samples and open circles are values from igneous rock samples.

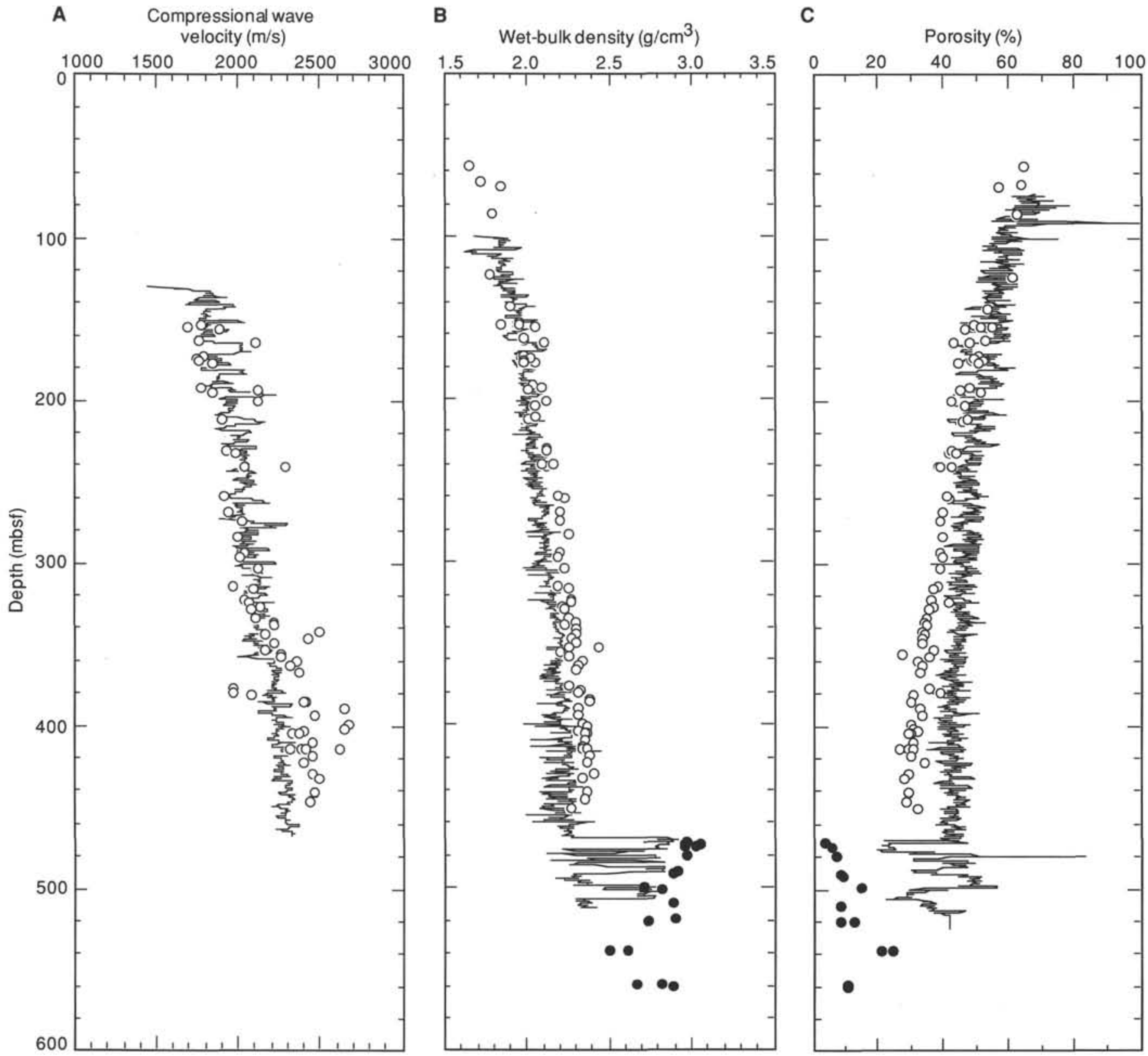

Figure 77. **A.** Comparison of velocities measured in the laboratory with logging data for Hole 857C from about 270 mbsf to about 445 mbsf. Solid line represents smoothed velocities from the long-spaced sonic tool. Open circles are velocities in the vertical direction measured on sample cubes with the HFV. The interval shown represents the deep, highly indurated sedimentary section; raw logging data are unreliable in the sill complex below 471.1 mbsf and are therefore not compared to laboratory data. **B.** Comparison of the density profile obtained with the lithodensity logging tool and wet-bulk density values measured in the laboratory. The logging data, shown by the solid line, represent the entire borehole interval logged in Hole 857C. Open circles are wet-bulk density data from index properties samples. **C.** Comparison of the porosity profile obtained with the compensated neutron porosity logging tool and porosity values measured in the laboratory. The logging data, shown by the solid line, represent the entire borehole interval logged in Hole 857C. Open circles are porosity data from index properties samples.

Table 43. Summary of logging operations in Hole 857C.

Logging run	Begin/End (Date [1991], Time [PST])	Tool string	Tools[a]	Interval logged (mbsf)
1	29 July, 1347 29 July, 1616	High-temperature	GRC	Bottom-hole temp. at 202 mbsf
2	30 July, 0659 30 July, 1010	High-temperature	GRC	Bottom-hole temp. at 288 mbsf
3	2 Aug., 1428 2 Aug., 2146	Seismic stratigraphy	LSS/DIT/NGT	129–541
4	3 Aug., 0700 3 Aug., 1300	Lithoporosity	HDLT/CNT/NGT	101–524
5	3 Aug., 1400 4 Aug., 1200	[b]Formation microscanner	FMS/NGT/GPIT	—
6	8 Aug., 1010 8 Aug., 1214	High-temperature	GRC	107–193
7	9 Aug., 0146 9 Aug., 0345	High-temperature	GRC	272–321
8	9 Aug., 0607	High-temperature	GRC	Bottom-hole temp. at 476 mbsf

[a]See "Explanatory Notes" chapter (this volume) for definitions of acronyms.
[b]The formation microscanner string became jammed in the bottom of the drill pipe and the run had to be aborted without collecting any useful data.

Table 44. Summary of logging operations in Hole 857D.

Logging run	Begin/End (Date [1991], Time [PST])	Tool string	Tools[a]	Interval logged (mbsf)
1	23 Aug., 1745 23 Aug., 2248	Wireline high-temperature	PTF/GSC	8–510
2	29 Aug., 1094 29 Aug., 1428	Wireline high-temperature	PTF/GSC	475–936
3	30 Aug., 0555 30 Aug., 1250	Seismic stratigraphy	LSS/DIT/NGT	46–936
4	30 Aug., 1405 30 Aug., 2000	[b]Formation microscanner	FMS/NGT/GPIT	574–936 (pass 1) 574–830 (pass 2)
5	1 Sept., 0443 1 Sept., 0650	Lithoporosity	HDLT/NGT	565–750 (pass 1) 565–662 (pass 2)

[a]See "Explanatory Notes" chapter (this volume) for definition of acronyms.
[b]The formation microscanner was badly damaged due to heave and became jammed in the bottom of the drill pipe while trying to pull through the bit after the runs. Some of the record is badly degraded due to damage to the pads.

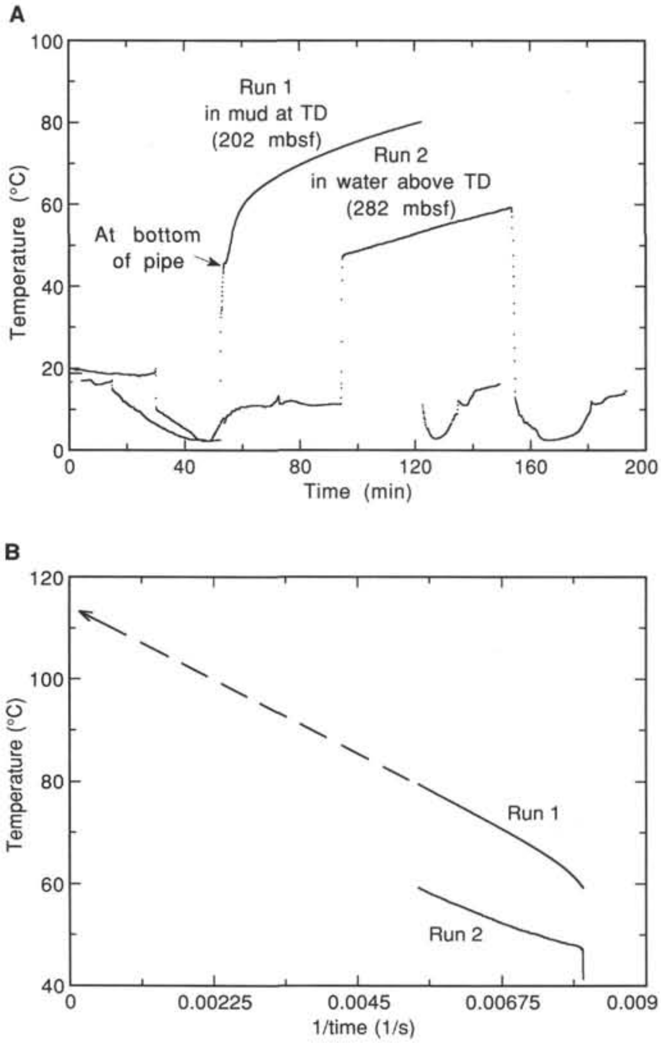

Figure 78. **A.** Temperature histories of two downhole temperature measurements with the GRC high-temperature tool. The records show the history from turn on of the instrument to turn off. The long period of nearly uniform temperature between 60 and 95 min during run 2 resulted from the probe being stuck in the bottom of the pipe. **B.** The temperature record of runs 1 and 2 in the bottom of the hole vs. reciprocal time.

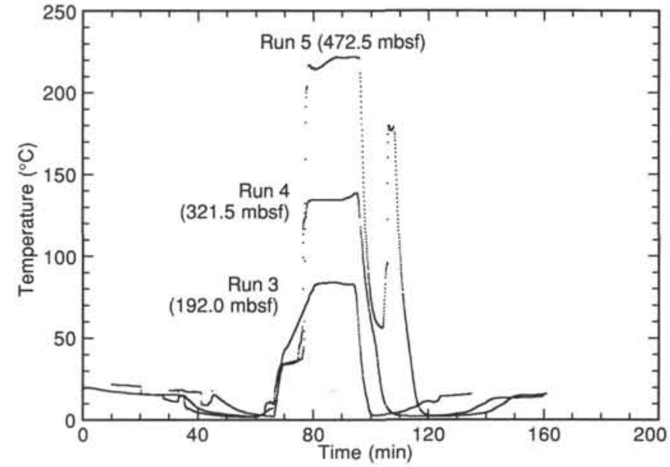

Figure 79. Temperature histories for three open hole measurements (runs 3–5) in Hole 857C.

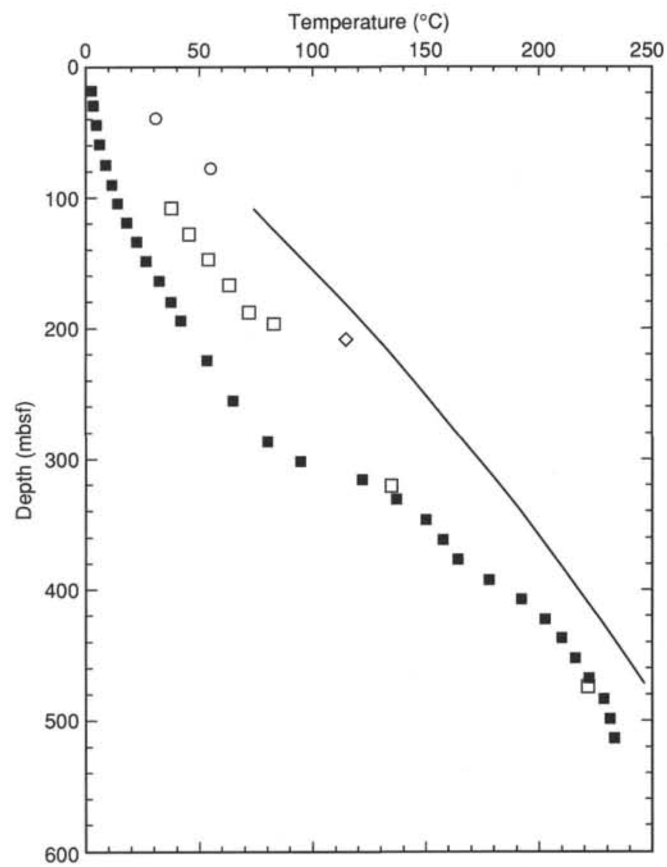

Figure 80. Summary plot of temperature measurements in Hole 857C. Open circles denote measurements with the WSTP tool, which are the best measure of undisturbed *in-situ* temperatures in the figure. Open squares denote open-hole measurements made on runs 3–5 (see Fig. 79). The open diamond denotes the estimated equilibrium temperature for run 1. Small solid squares denote the temperature profile in casing at nearby Hole 857D. The solid line is the estimated temperature profile based on heat flow and conductivity measurements and assuming one-dimensional conductive heat transfer.

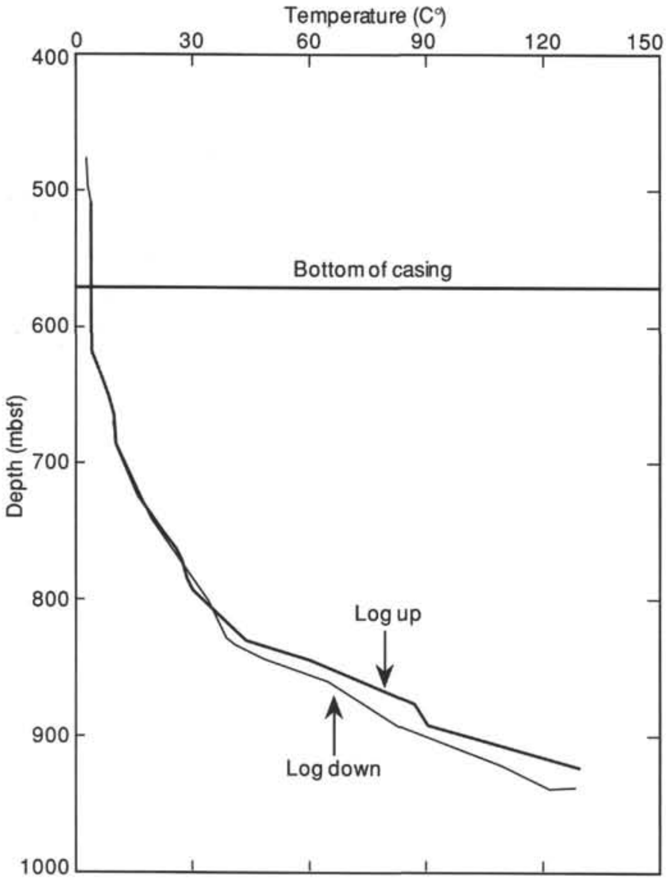

Figure 81. Temperature profile measured in Hole 857D after it had been drilled to 936 mbsf. The temperature tool was left at the bottom of the hole for about 35 min and temperatures in the interval from 820 to 936 mbsf increased significantly during this time, but remain nearly constant over the remainder of the hole.

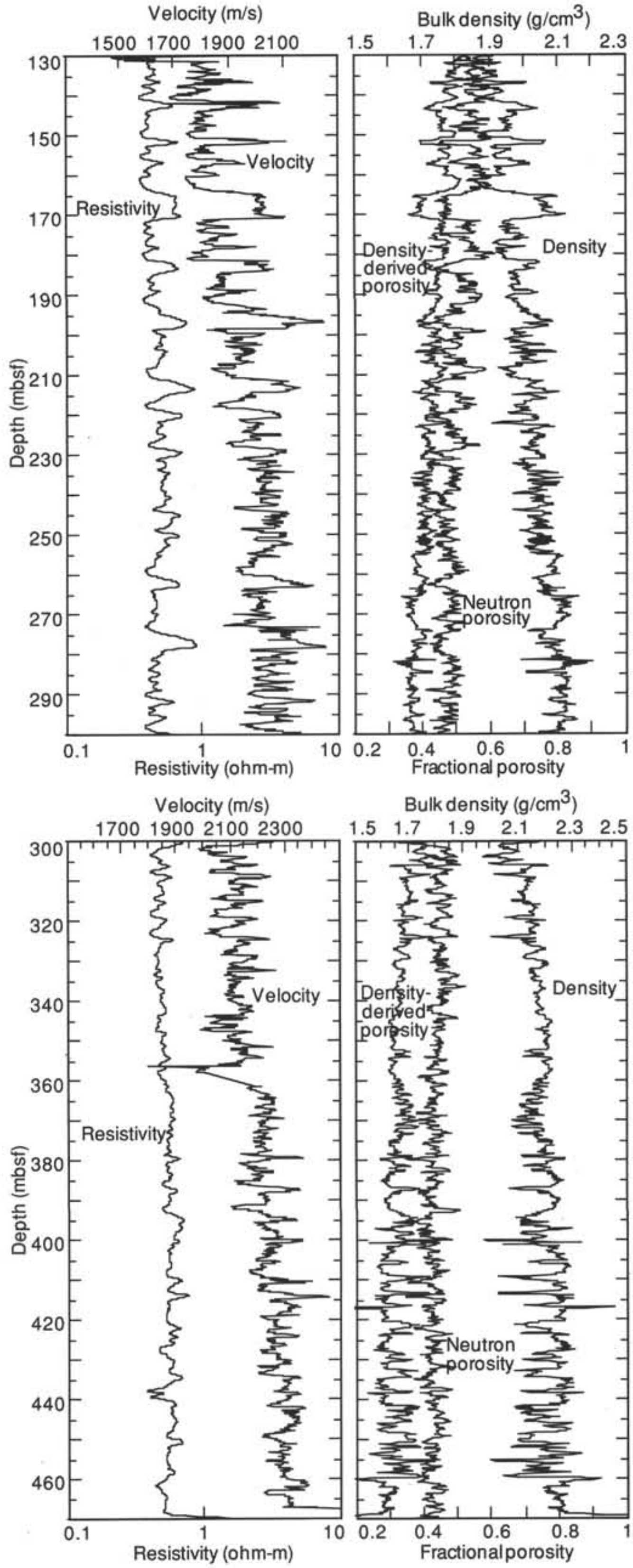

Figure 82. Profiles of porosity-related properties in the sedimentary section of Hole 857C.

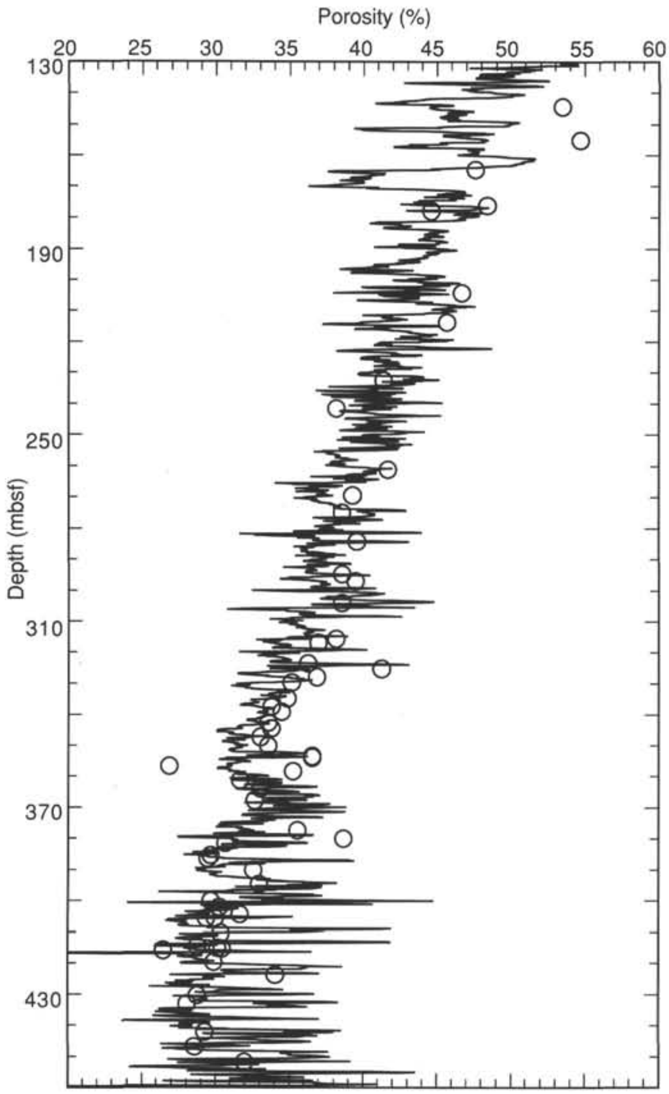

Figure 83. Comparison of shipboard porosity measurements on discrete core samples (open circles) with the density-derived porosity from the downhole logs for Hole 857C.

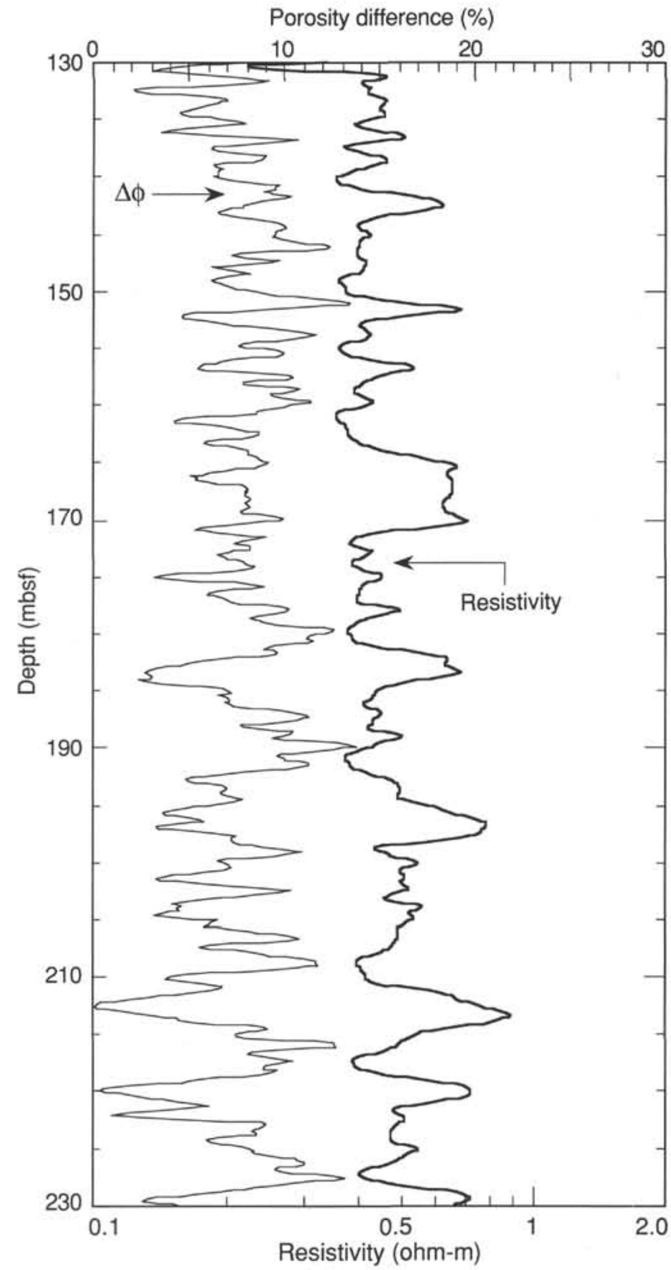

Figure 84. Comparison of the difference between neutron porosity and density-derived porosity with resistivity for Hole 857C. The general negative correlation indicates that the more resistive zones are associated with low clay content.

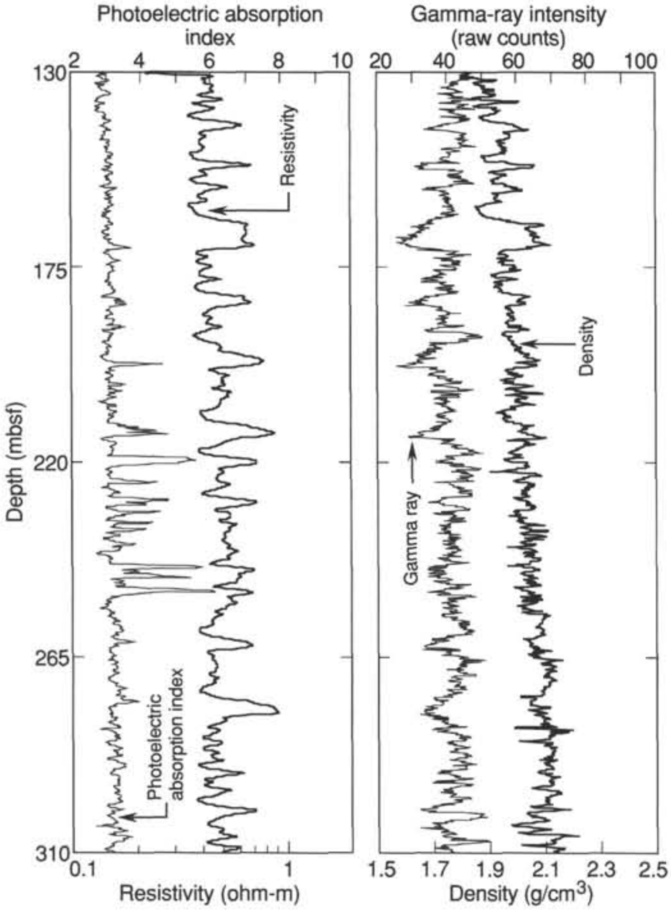

Figure 85. Profiles of photoelectric absorption index and resistivity, and profiles of total gamma-ray intensity and density for Hole 857C. In this plot the negative correlation shows that lower densities are associated with more clay-rich layers.

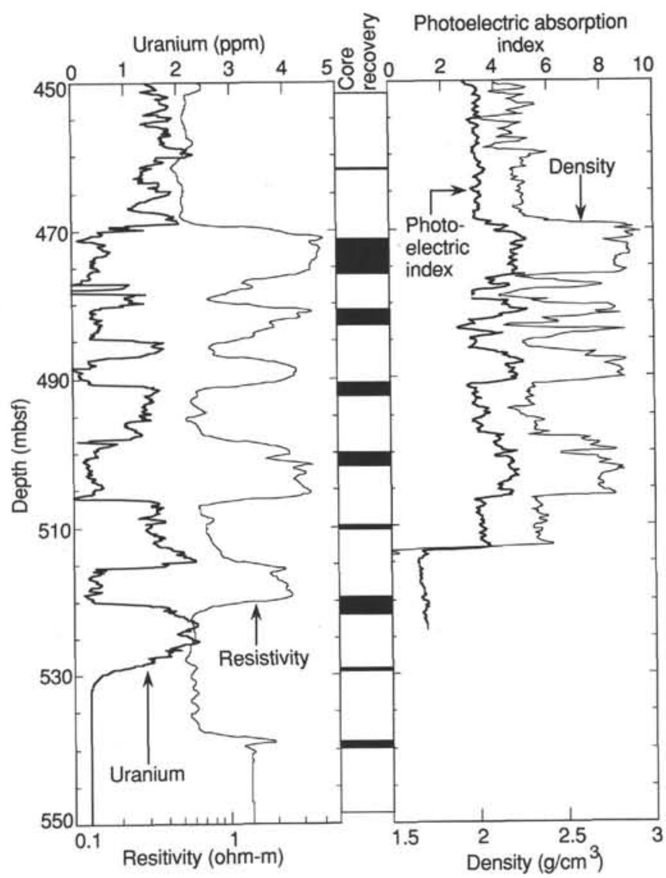

Figure 86. Downhole variation of uranium abundance, resistivity, photoelectric absorption index, and density in the sill and sediment complex of Hole 857C. Black bars indicate core recovery.

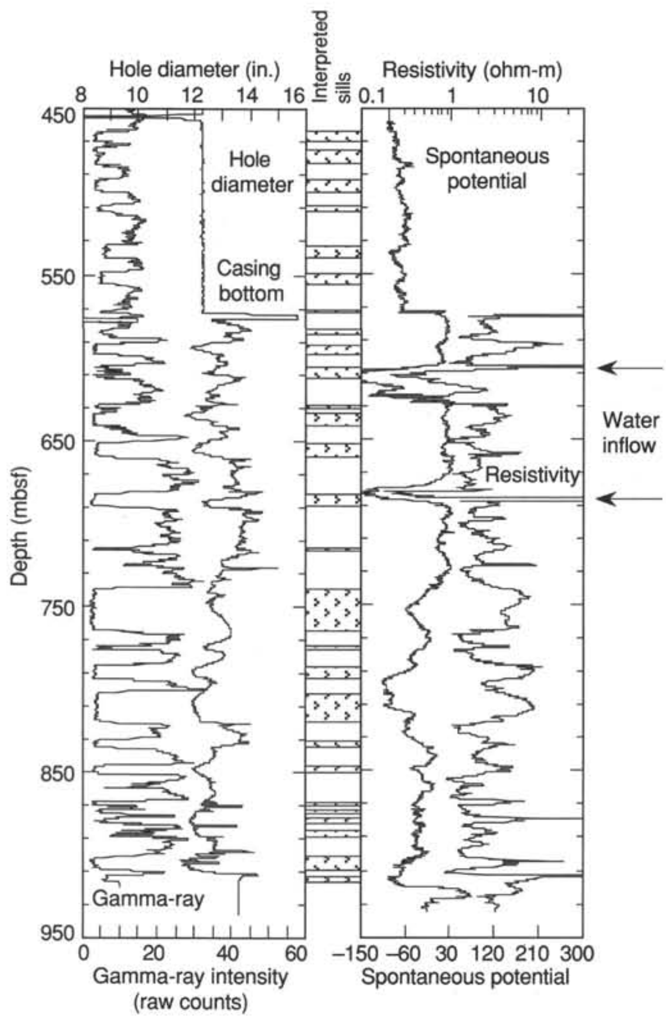

Figure 87. Logging results between 440 and 930 mbsf in Hole 857D. The bars between the two tracks indicate the inferred location of basaltic units (based on correlation with low gamma-ray counts). The two zones where water is flowing into the hole are also indicated. Note the strong response of the spontaneous potential and the resistivity logs in these zones.

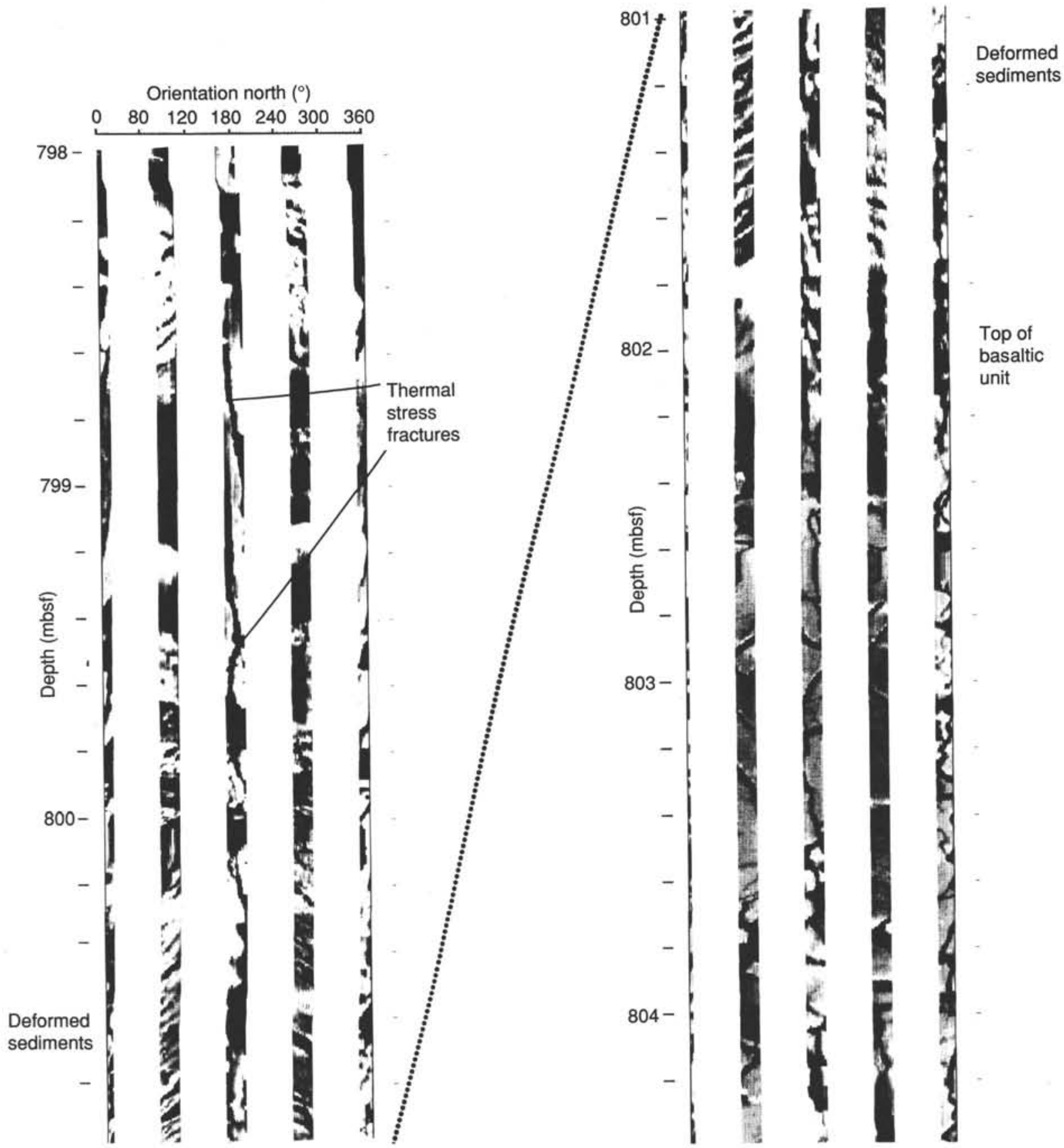

Figure 88. Section of the formation microscanner record from Hole 857D.

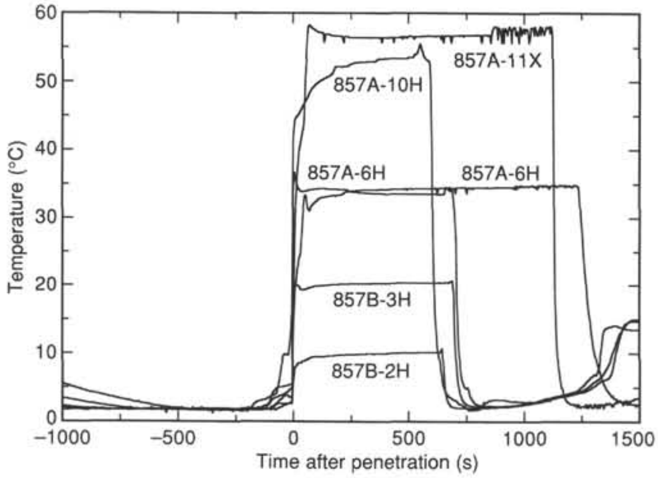

Figure 89. Sediment temperatures plotted against time, following penetration of the WSTP or APC tools in Holes 857A and 857B. WSTP measurements were made following collection of cores, while APC-tool measurements were made during collection of cores.

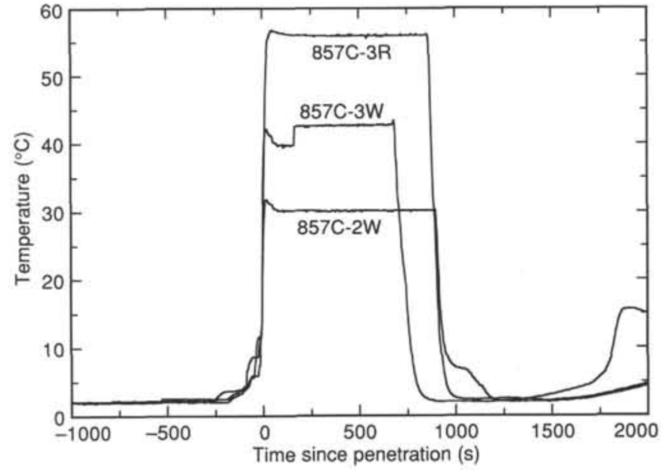

Figure 90. Sediment temperatures plotted against time, following penetration of the APC tool in Hole 857C.

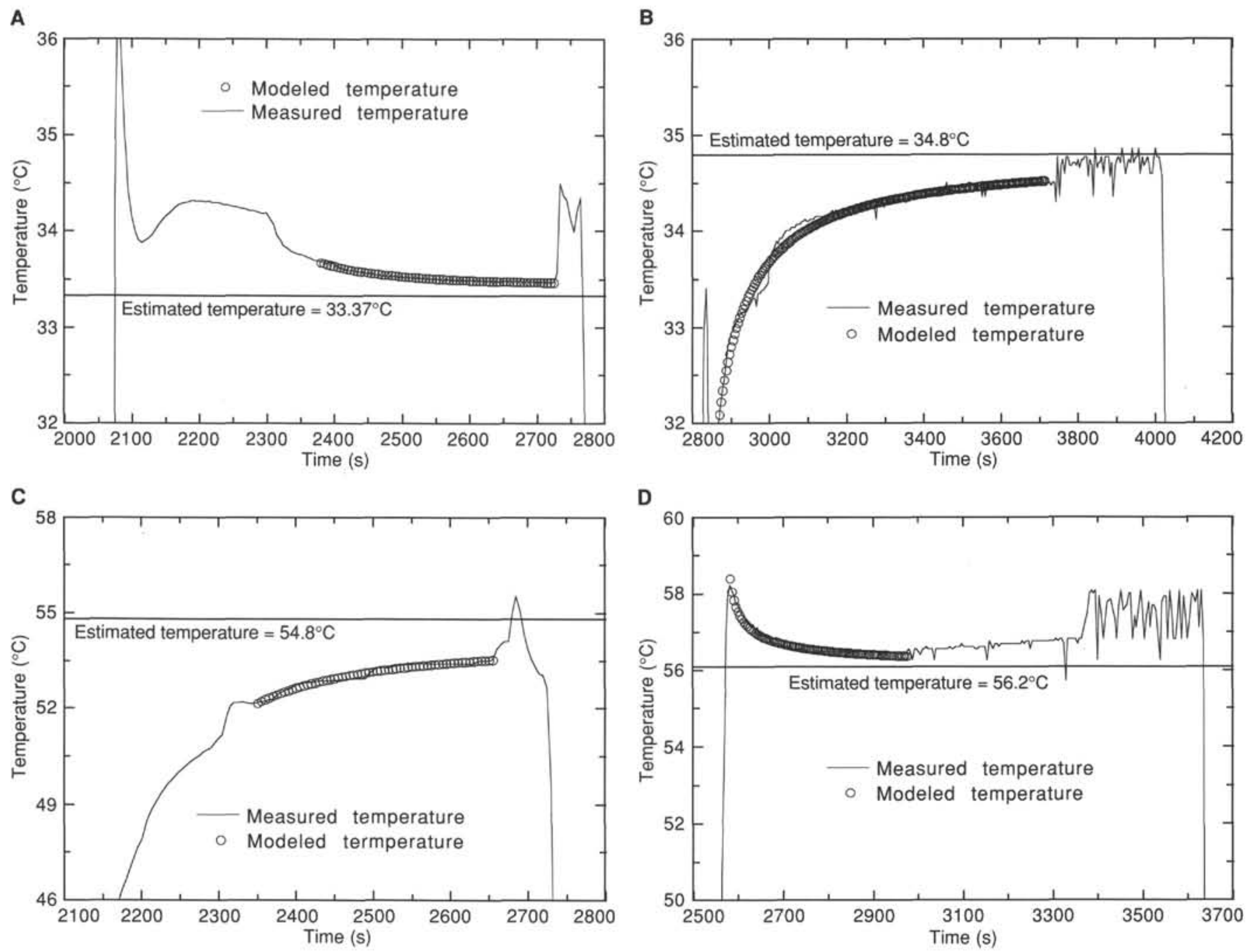

Figure 91. **A.** APC-tool measured and modeled temperatures vs. time for Core 139-857A-6H (50.4 mbsf). **B.** WSTP measured and modeled temperatures vs. time following recovery of Core 139-857A-6H (51.5 mbsf). **C.** APC-tool measured and modeled temperatures vs. time for Core 139-857A-10H (86.9 mbsf). **D.** WSTP measured and modeled temperatures vs. time following recovery of Core 139-857A-11X (92.2 mbsf).

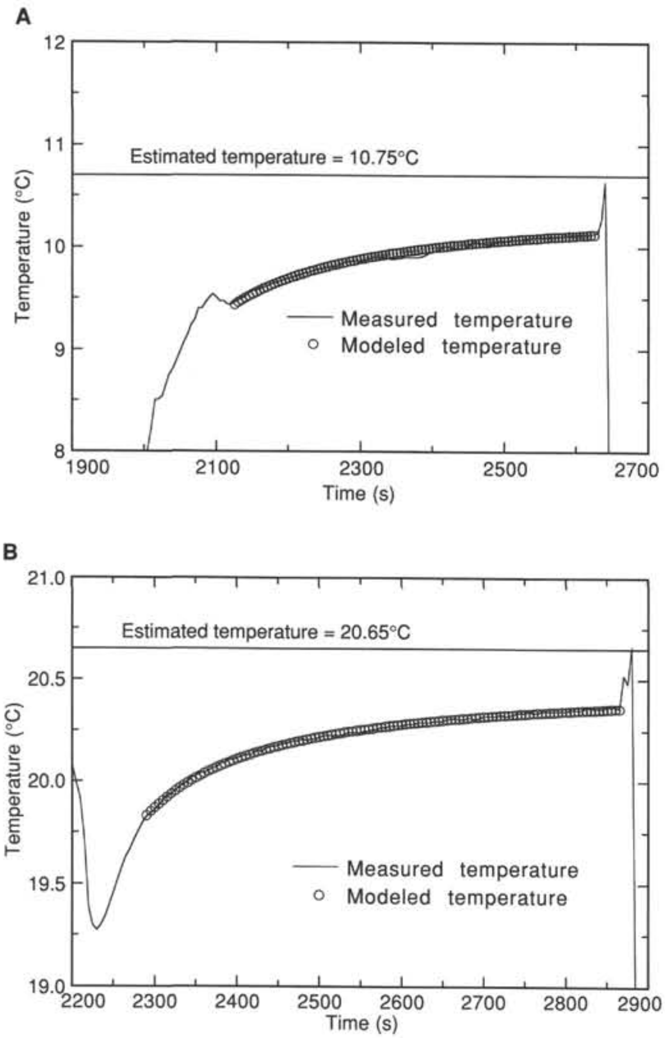

Figure 92. **A.** APC-tool measured and modeled temperatures vs. time for Core 139-857B-2H (12.9 mbsf). **B.** APC-tool measured and modeled temperatures vs. time for Core 139-857B-3H (31.5 mbsf).

Table 45. *In-situ* temperature tool deployments at Site 857.

Core	Depth (mbsf)	Tool	Quality[a]	Temperature[b] (° C)
139-857A-				
4H	31.9	APC	Battery failure	—
6H	50.4	APC	Excellent	33.4 ± 0.2
6H	51.5	WSTP	Excellent	34.8 ± 0.2
8H	69.4	APC	Tool failure	—
10H	86.9	APC	Excellent	58.4 ± 0.2
11X	92.2	WSTP	Good	56.2 ± 0.3
14P	113.3	WSTP	Tool flooded	—
139-857B-				
2H	12.9	APC	Excellent	10.75 ± 0.2
3H	30.5	APC	Excellent	20.65 ± 0.2
139-857C-				
2W	37.6	WSTP	Good	30.1 ± 0.2
3W	57.6	WSTP	Poor	[c]38.5–42.9
3R	77.2	WSTP	Good	55.6 ± 0.3
6R	96.3	WSTP	Tool split formation?	—

Notes: WSTP measurements were made after the specified core; for all WSTP measurements, the depth listed is 1.1 m greater than the maximum depth of this core.
[a]Quality is subjective and based on interpretations described in the text.
[b]Estimated error is based on a subjective assessment of deployment operations and how well-recovered data fit a theoretical model.
[c]Temperature is a range because the record is ambiguous. See discussion in text and Figure 95B.

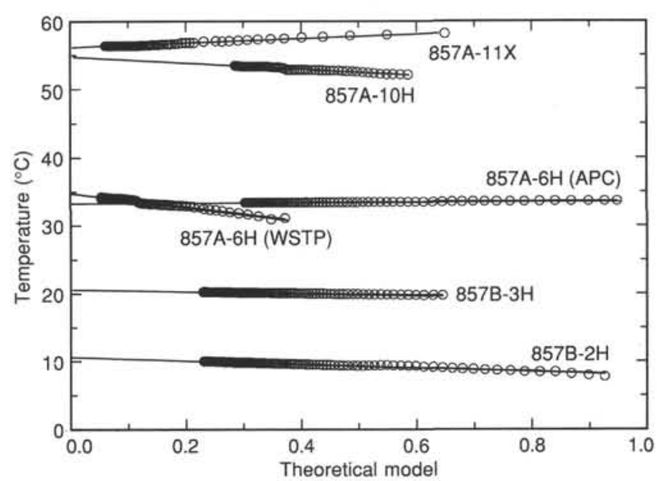

Figure 93. Temperatures measured in Holes 857A and 857B vs. the appropriate theoretical function that describes the approach with time of the annular APC cutting shoe or cylindrical WSTP to *in-situ* temperatures. The theoretical function is proportional to reciprocal time and therefore the estimated *in-situ* temperatures are given by intercepts of the extrapolations of the linear trends of the measured data.

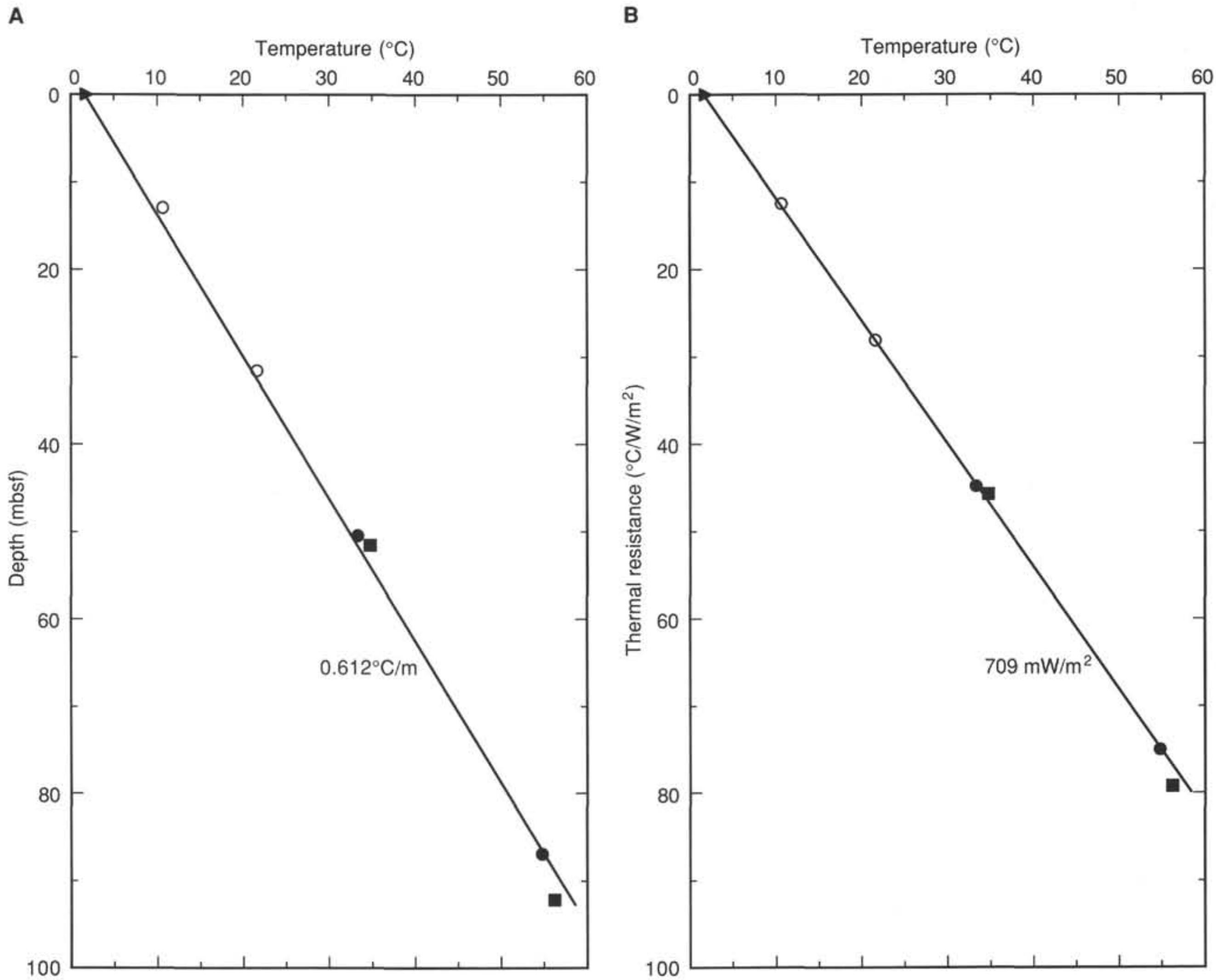

Figure 94. **A.** Estimated temperatures vs. depth in Holes 857A and 857B. The least-squares, best-fitting linear gradient through all data (APC/Hole 857A = solid circles; WSTP/Hole 857A = solid squares; APC/Hole 857B = open circles), forced to pass through a bottom-water temperature of 1.7°C at mudline (triangle), is shown. **B.** Bullard plot of temperature vs. cumulative thermal resistance, Holes 857A and 857B. Symbols as in (A).

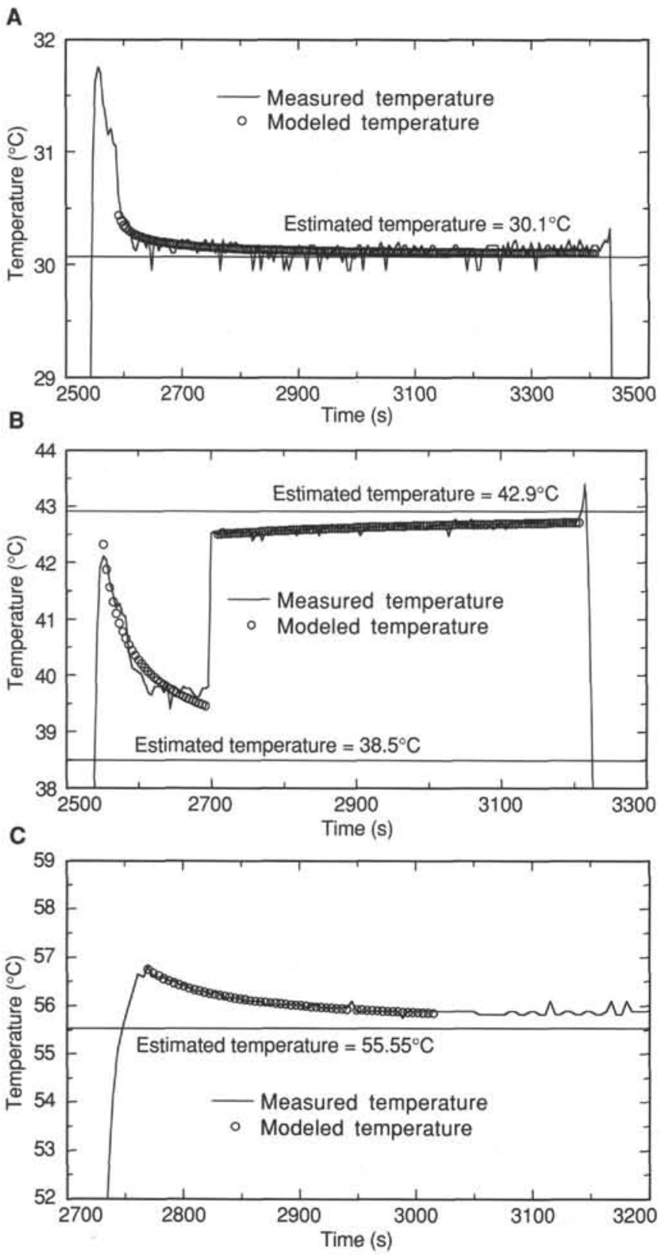

Figure 95. **A.** WSTP measured and modeled temperatures vs. time following recovery of Core 139-857C-2W (37.6 mbsf). **B.** WSTP measured and modeled temperatures vs. time following recovery of Core 139-857C-3W (57.6 mbsf). Digital shifts in the data (near 2700 s) make the equilibrium temperature ambiguous, although the higher of the two predicted temperatures (42.9°C) is more consistent with nearby data. **C.** WSTP measured and modeled temperatures vs. time following recovery of Core 139-857C-3R (77.2 mbsf).

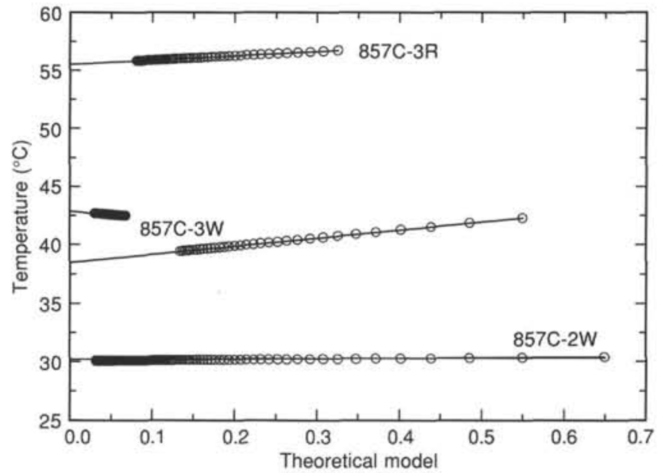

Figure 96. Temperatures vs. theoretical decay for all WSTP measurements in Hole 857C. Circles are measured temperatures and lines are modeled temperatures, projected to their equilibrium values.

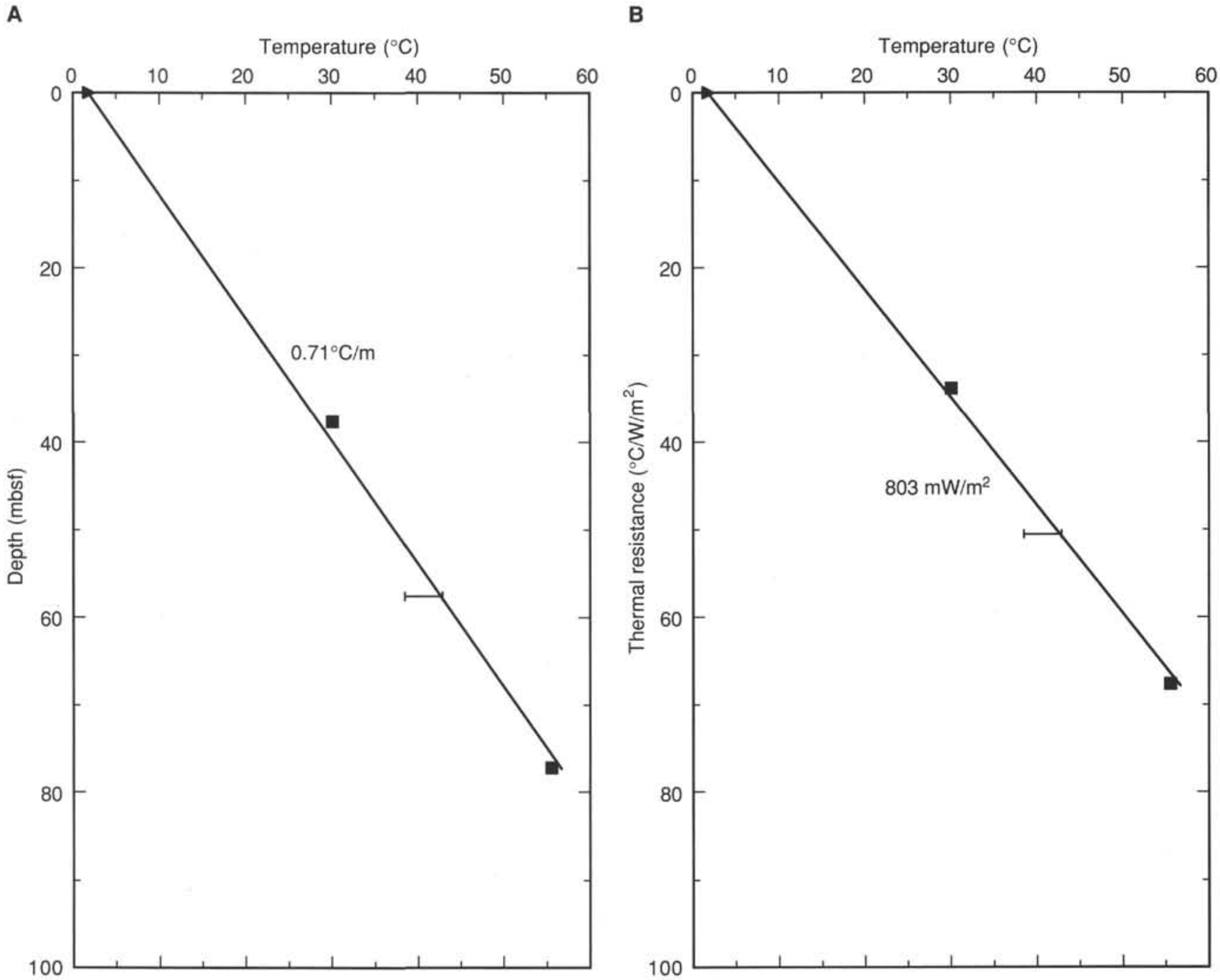

Figure 97. **A.** Estimated sediment temperatures vs. depth in Hole 857C. The range of temperatures shown for the measurement at 57.6 mbsf extends between the two values predicted by different portions of the temperature-time curve shown in Figure 95B. The least-squares, best-fitting linear gradient through the remaining two WSTP temperatures (squares), forced to pass through the bottom-water temperature of 1.7°C at mudline (triangle), is shown. This gradient passes through the higher of the two most likely temperatures at 57.6 mbsf. **B.** Bullard plot of temperature vs. cumulative thermal resistance, Hole 857C.

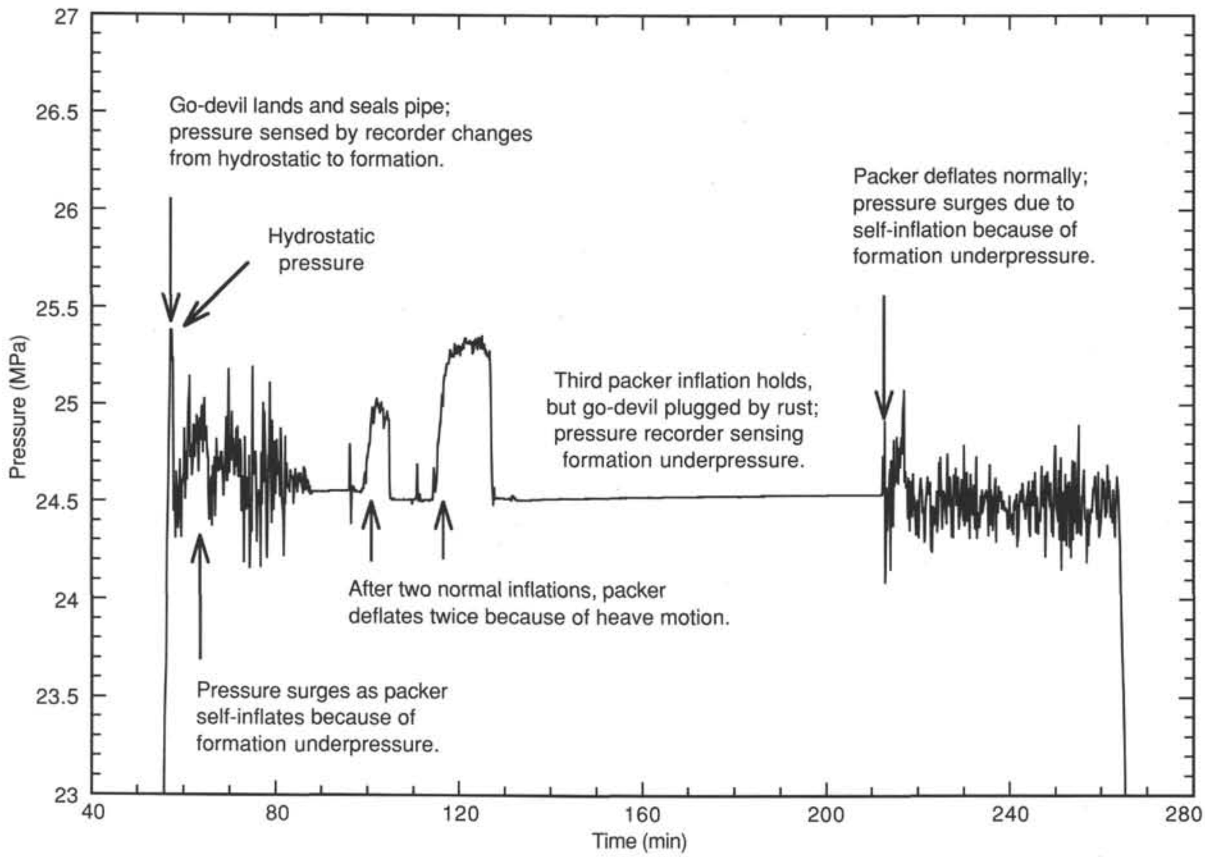

Figure 98. Annotated downhole pressure-time record collected with a GRC ERPG-300 recorder deployed within the first go-devil, with the packer set in casing at 96 mbsf in Hole 857D.

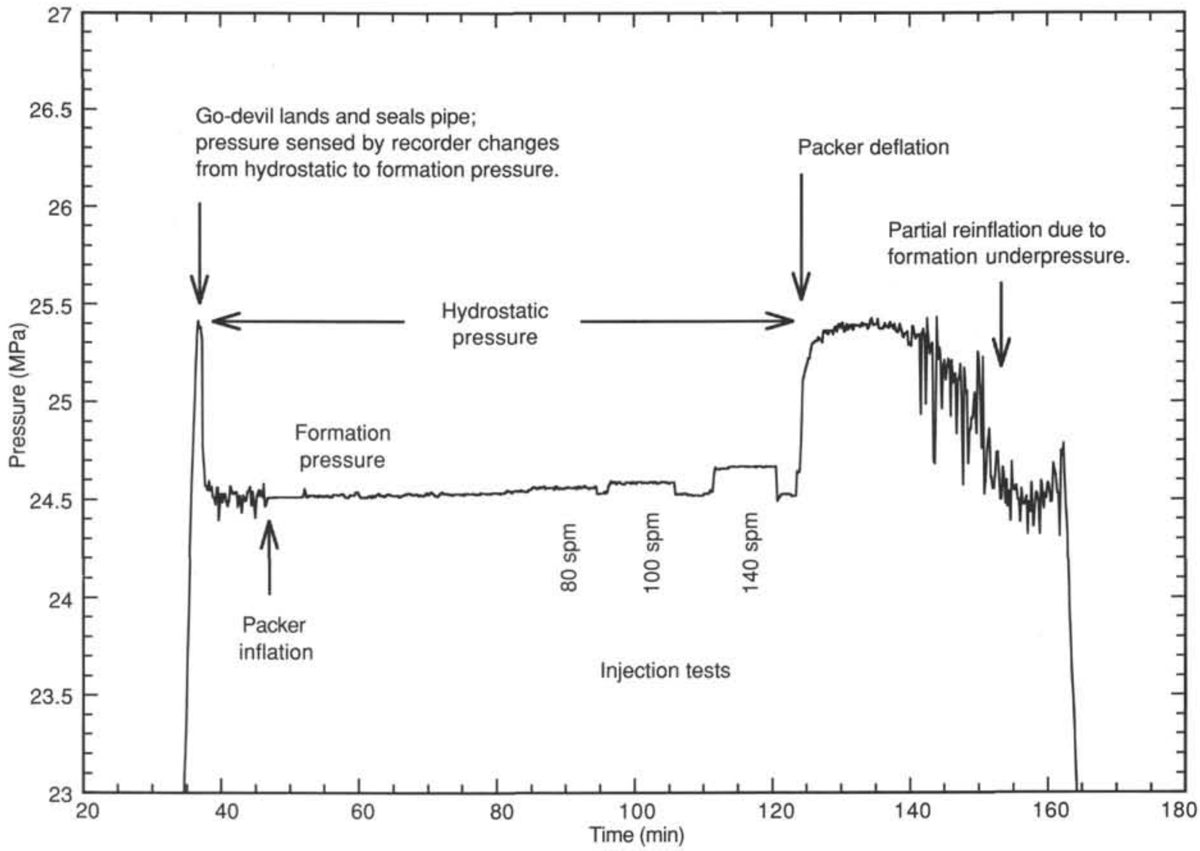

Figure 99. Annotated downhole pressure-time record collected with a GRC ERPG-300 recorder deployed within the second go-devil, with the packer set in casing at 96 mbsf in Hole 857D.

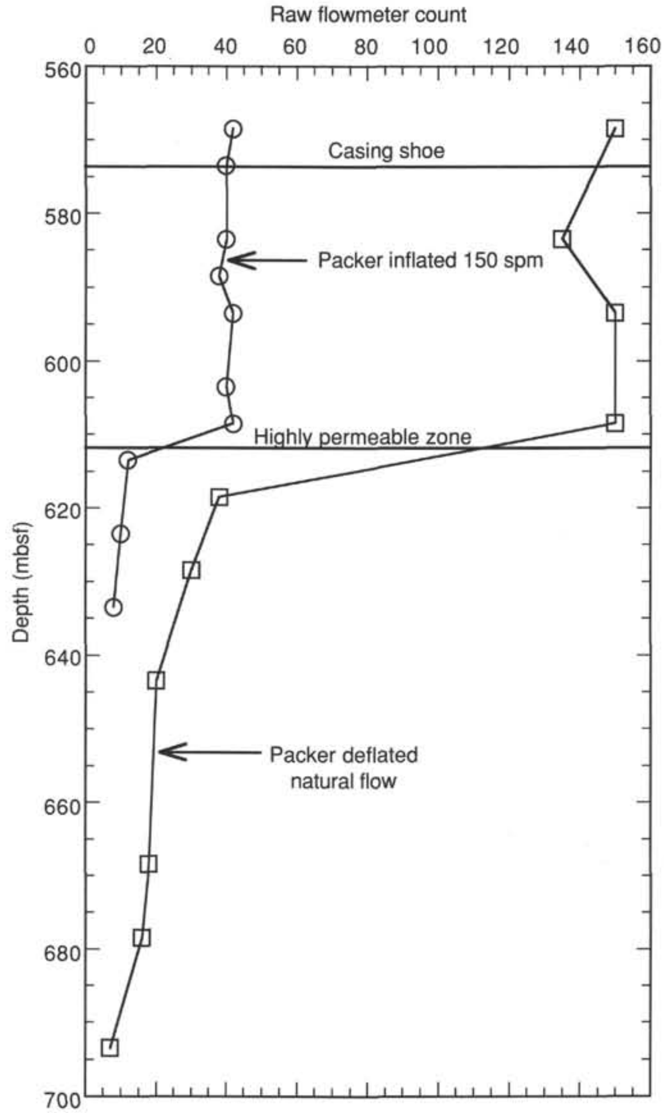

Figure 100. Preliminary determination of the variation of downhole flow readings collected during the flowmeter experiment.

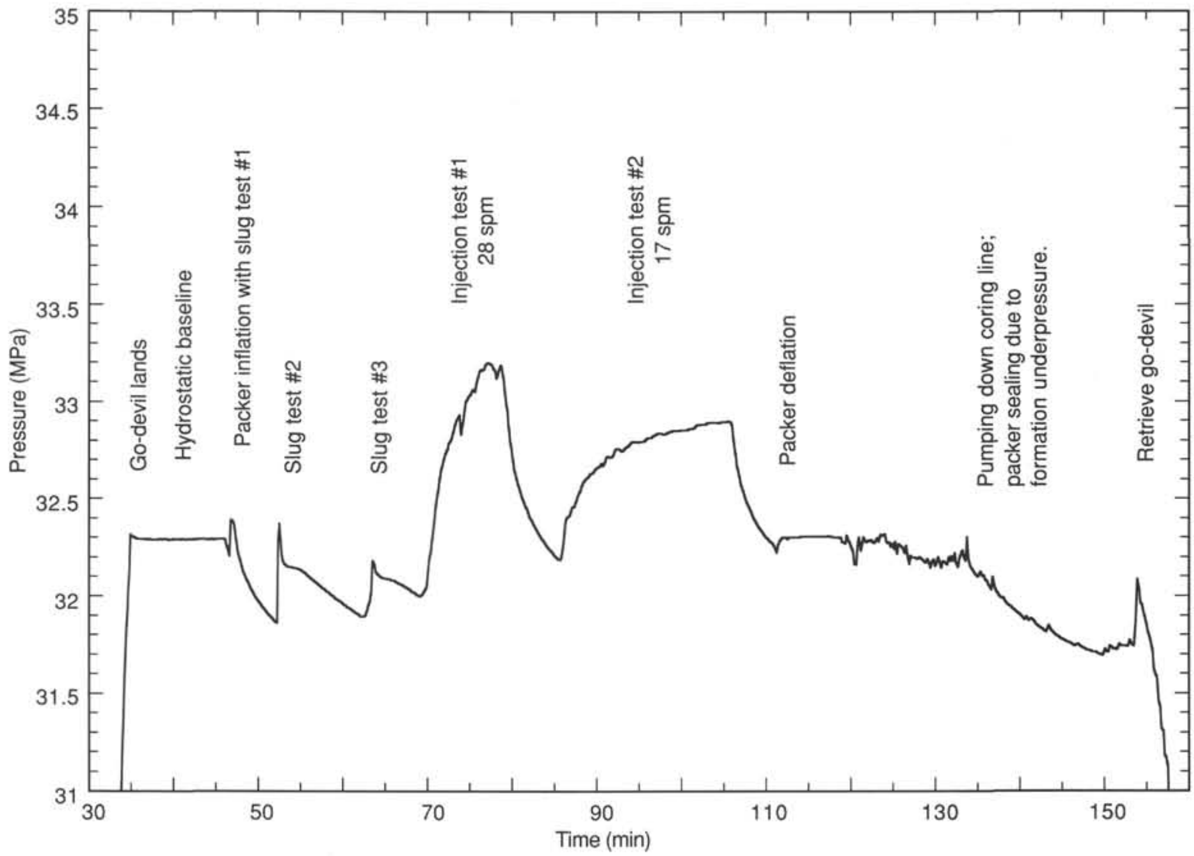

Figure 101. Annotated downhole pressure-time record collected with a GRC ERPG-300 recorder deployed within the fourth go-devil, with the packer set in the formation at 756 mbsf in Hole 857D.

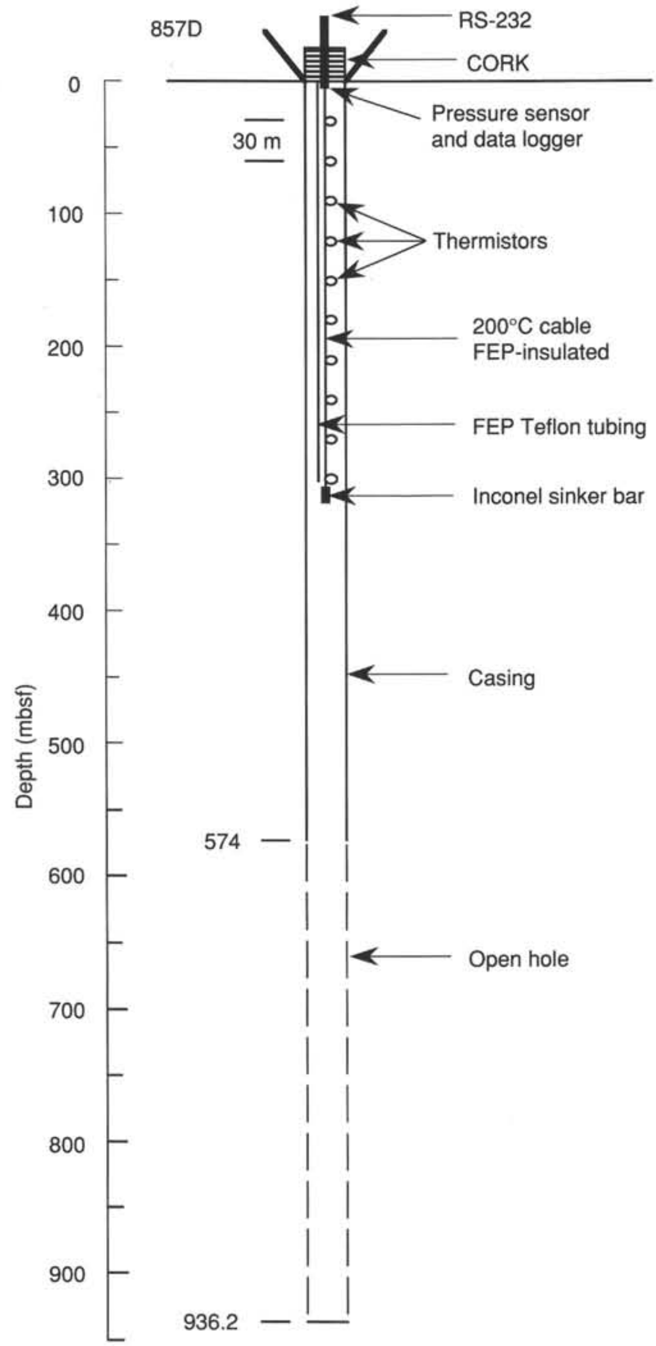

Figure 102. Schematic of the long-term instrumented borehole seal deployed in Hole 857D at the end of operations in the hole.

Hole 857C: Density-Natural Gamma Ray Log Summary

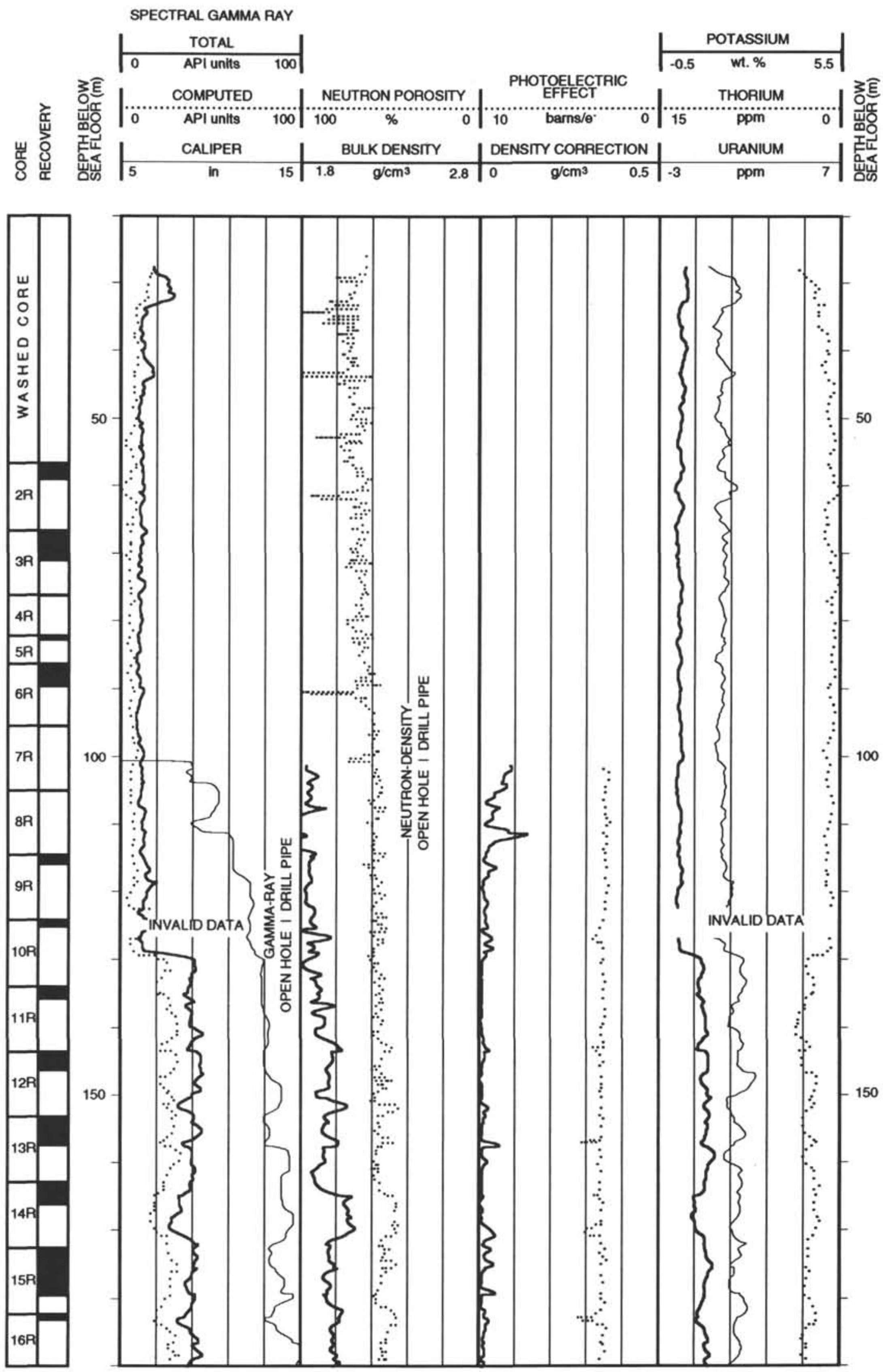

Hole 857C: Density-Natural Gamma Ray Log Summary (continued)

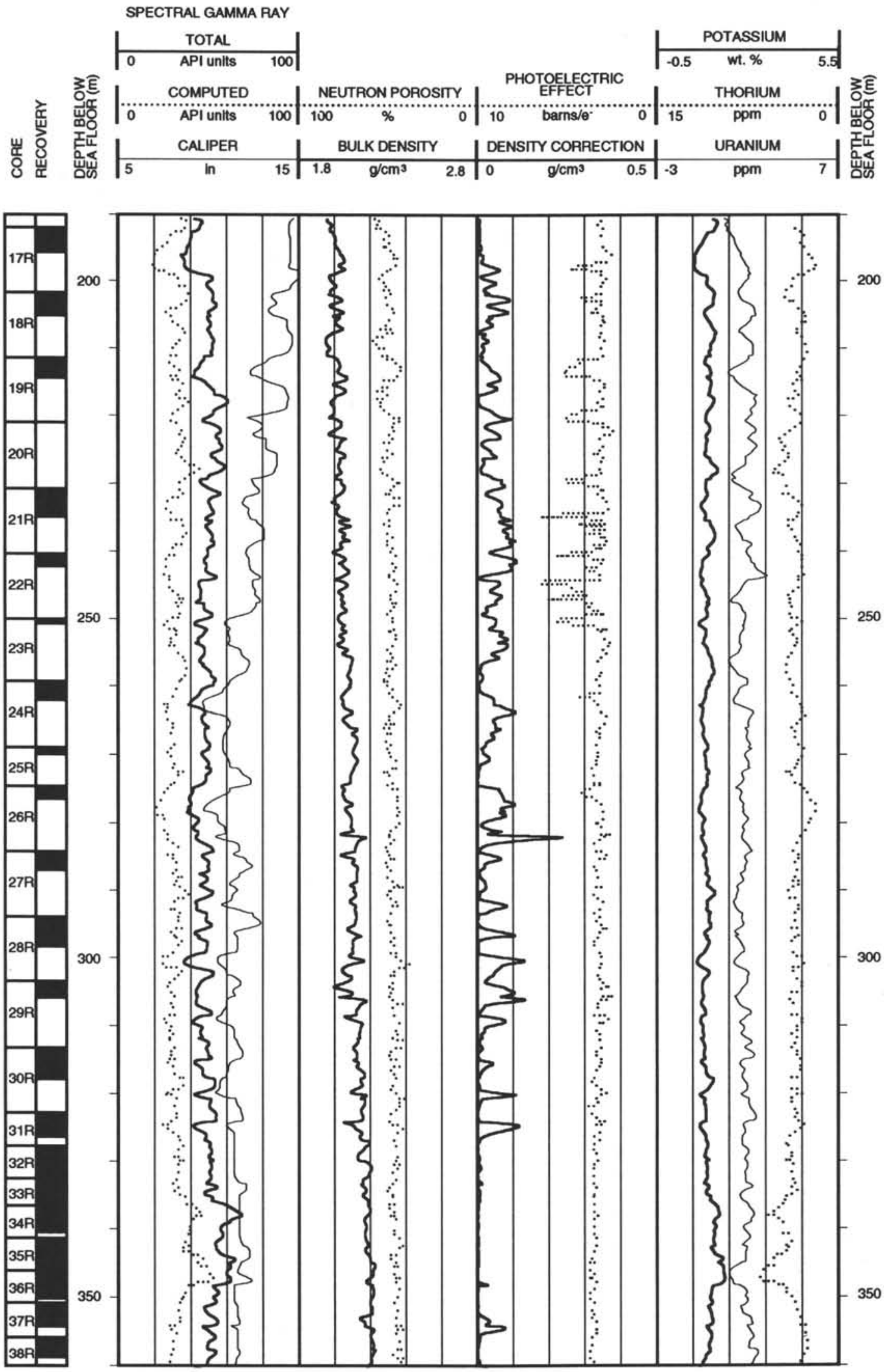

Hole 857C: Density-Natural Gamma Ray Log Summary (continued)

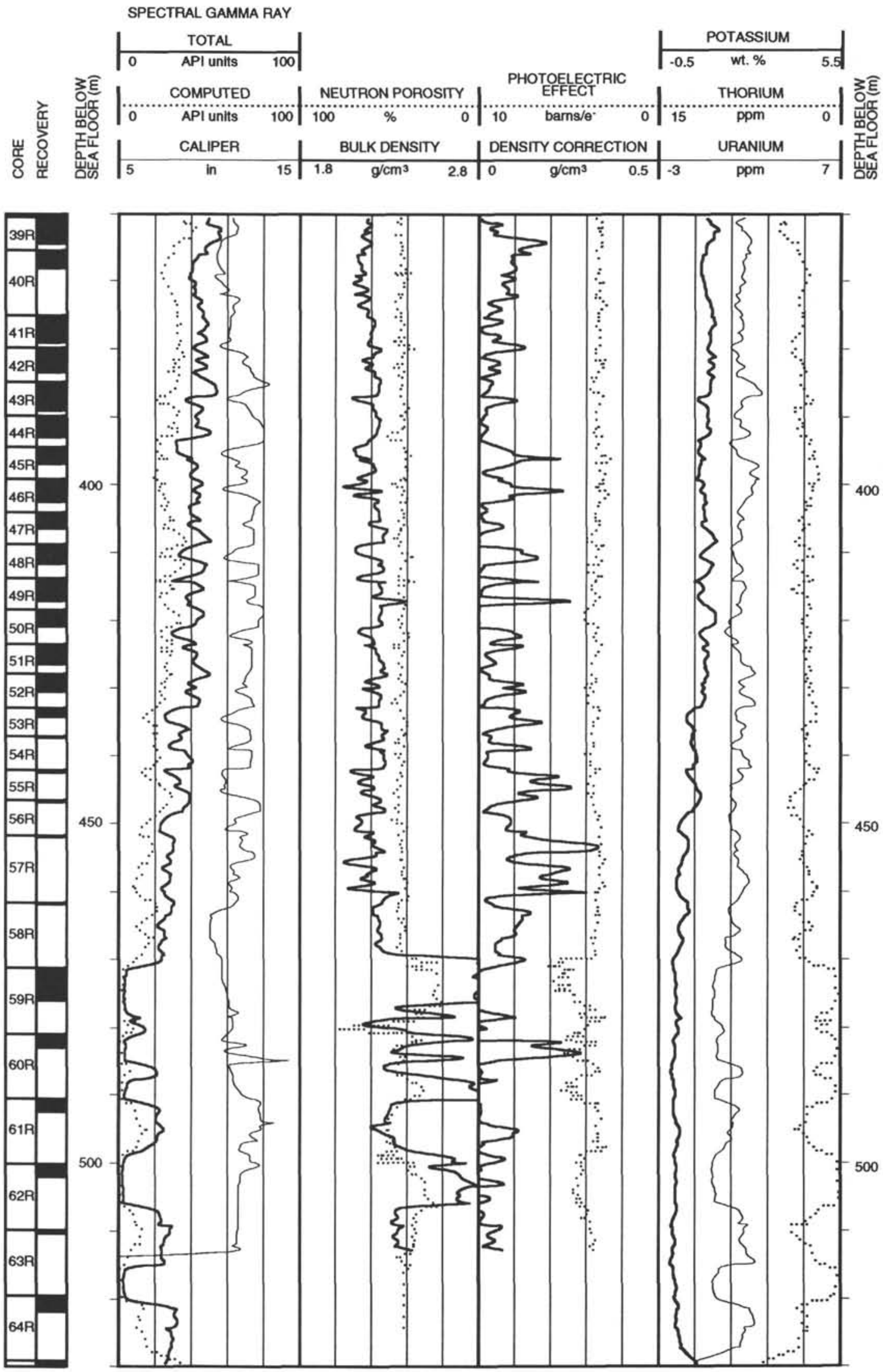

Hole 857C: Resistivity-Sonic-Natural Gamma Ray Log Summary

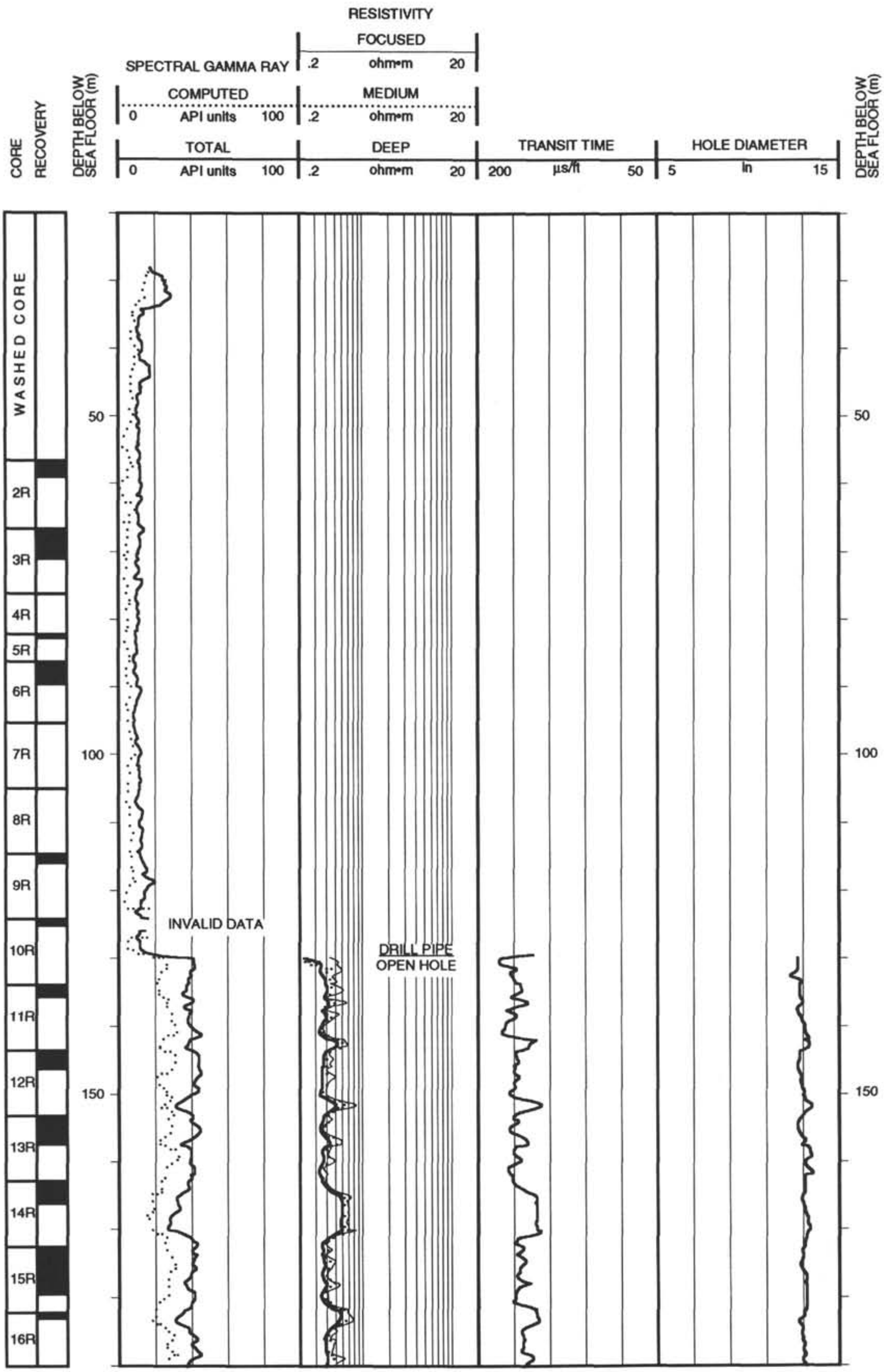

Hole 857C: Resistivity-Sonic-Natural Gamma Ray Log Summary (continued)

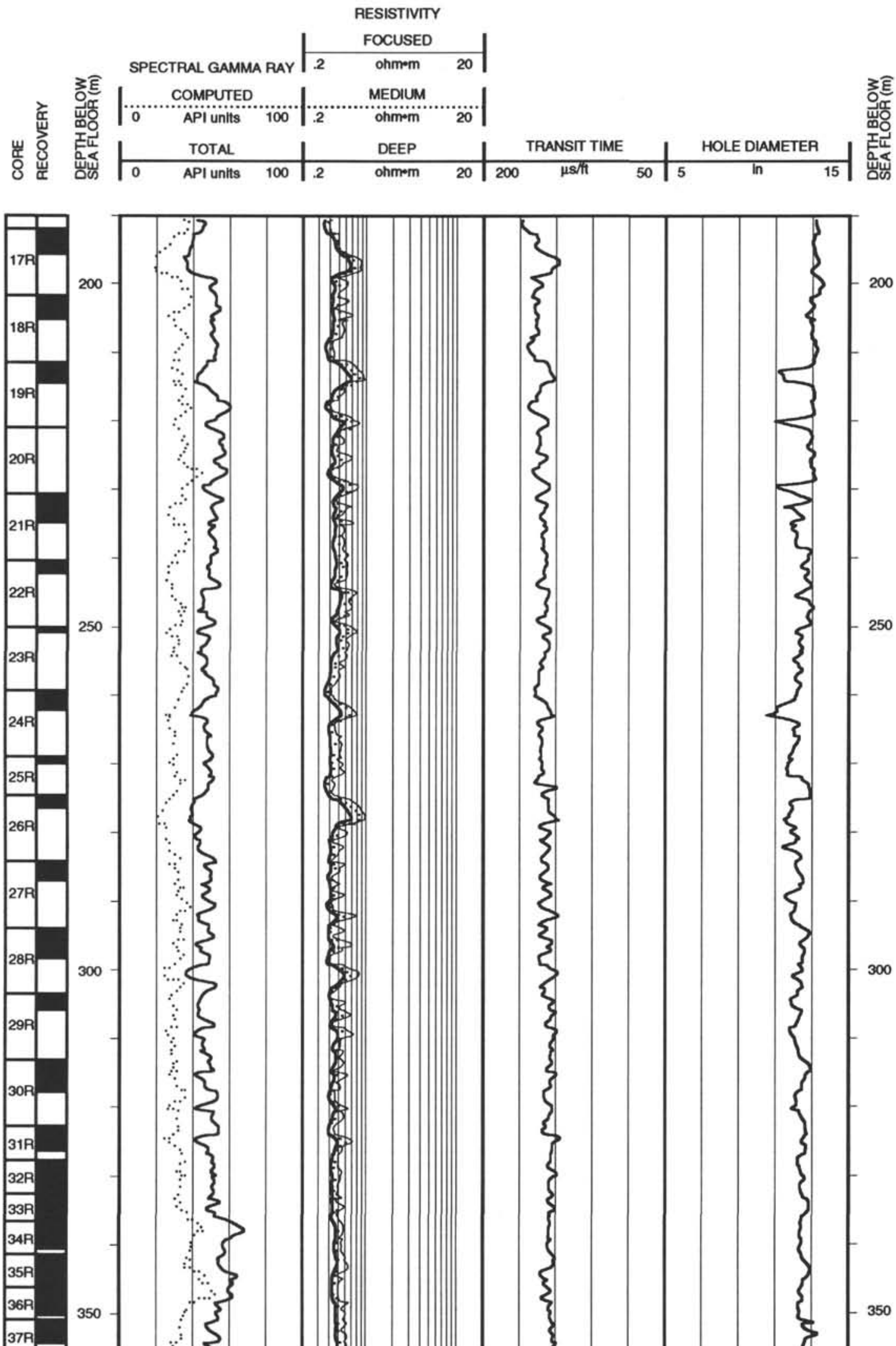

Hole 857C: Resistivity-Sonic-Natural Gamma Ray Log Summary (continued)

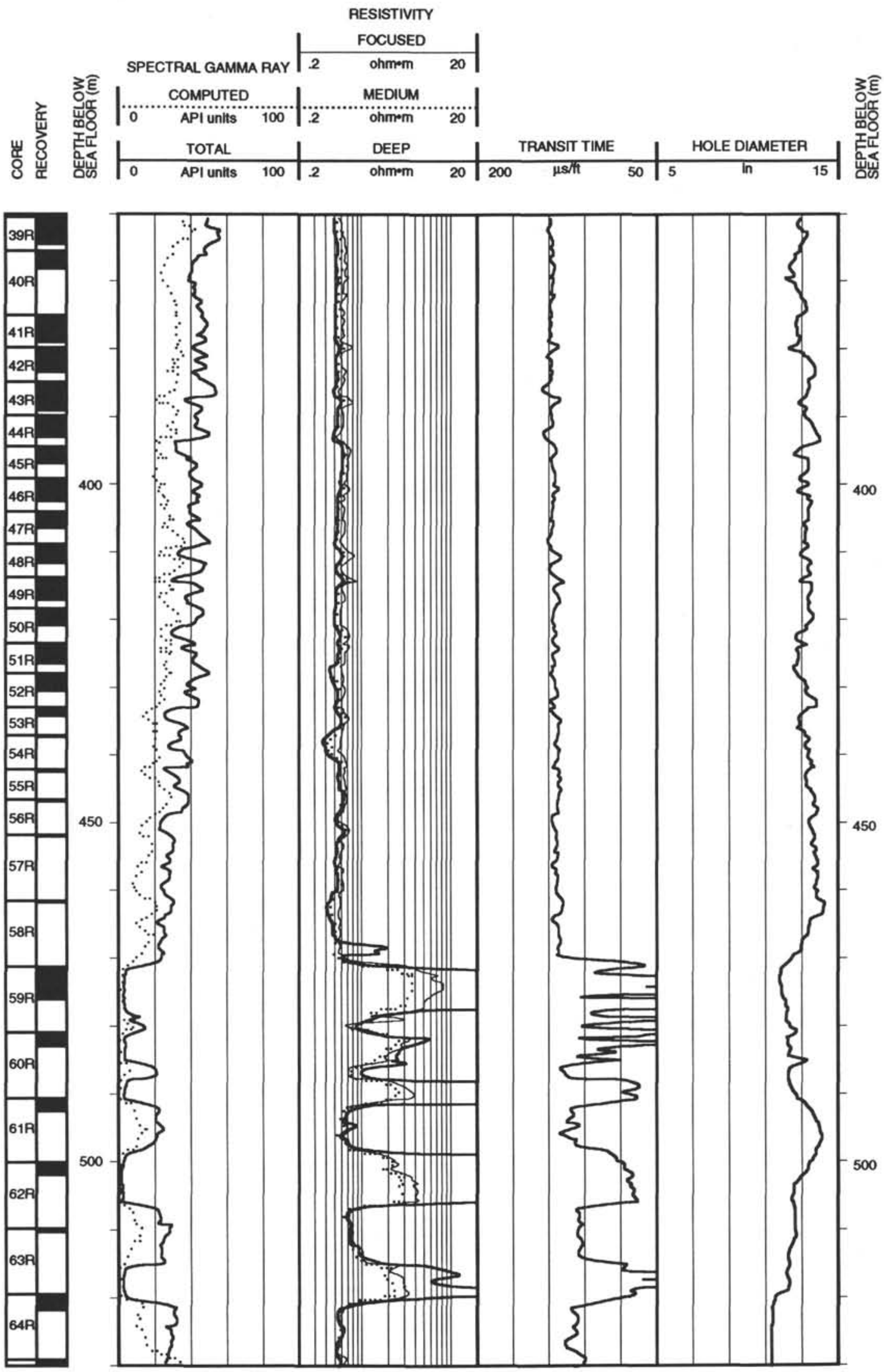

Hole 857C: Resistivity-Sonic-Natural Gamma Ray Log Summary (continued)

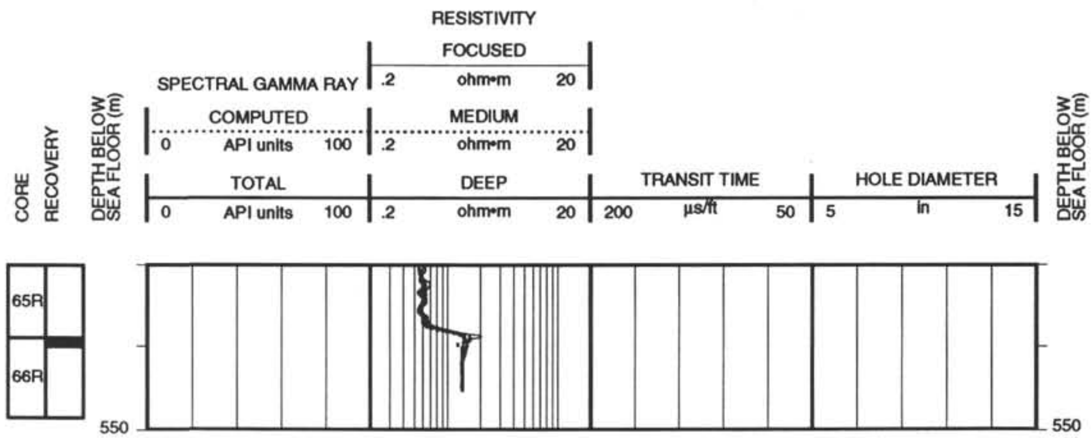

Hole 857D: Porosity-Natural Gamma Ray Log Summary

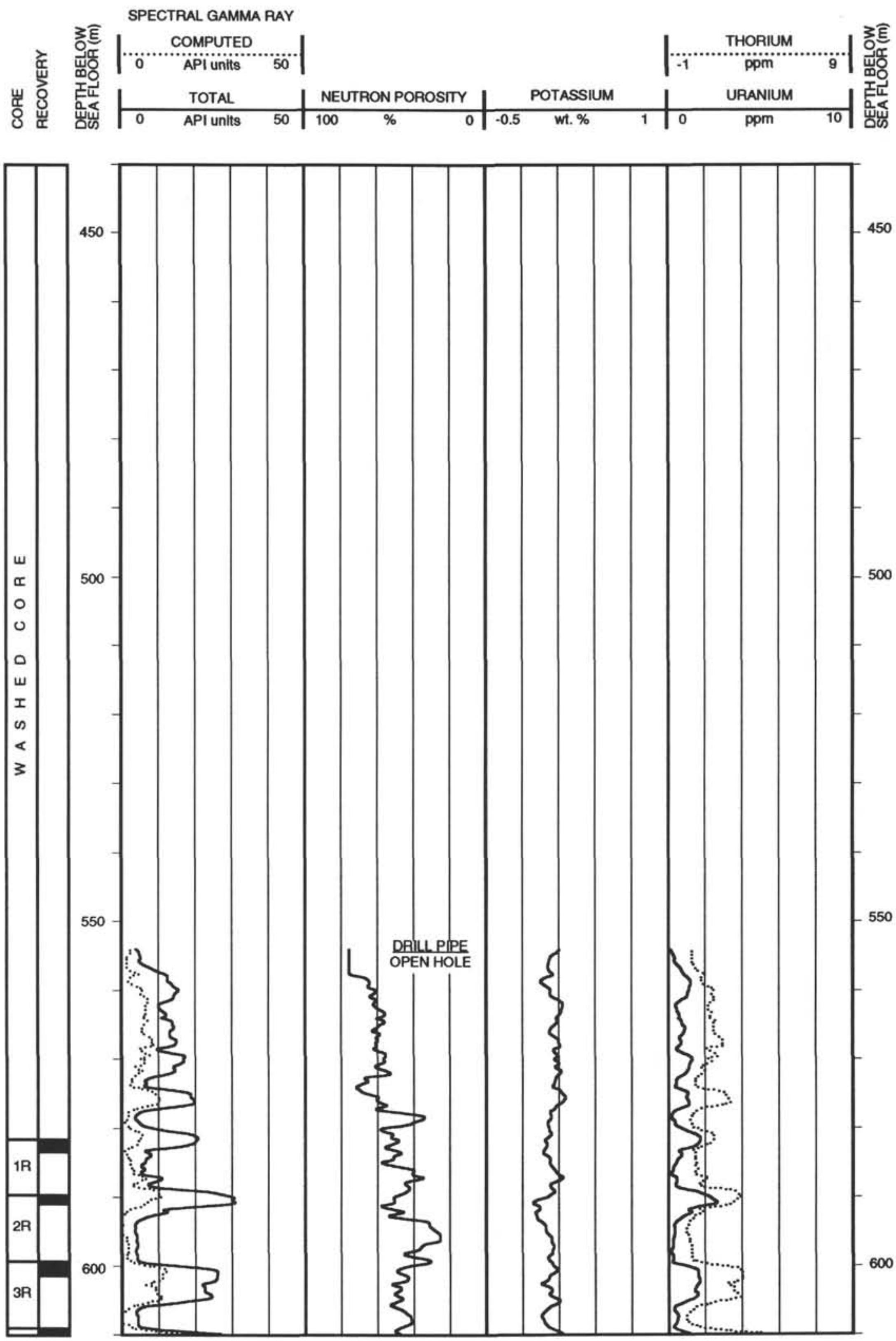

Hole 857D: Porosity-Natural Gamma Ray Log Summary (continued)

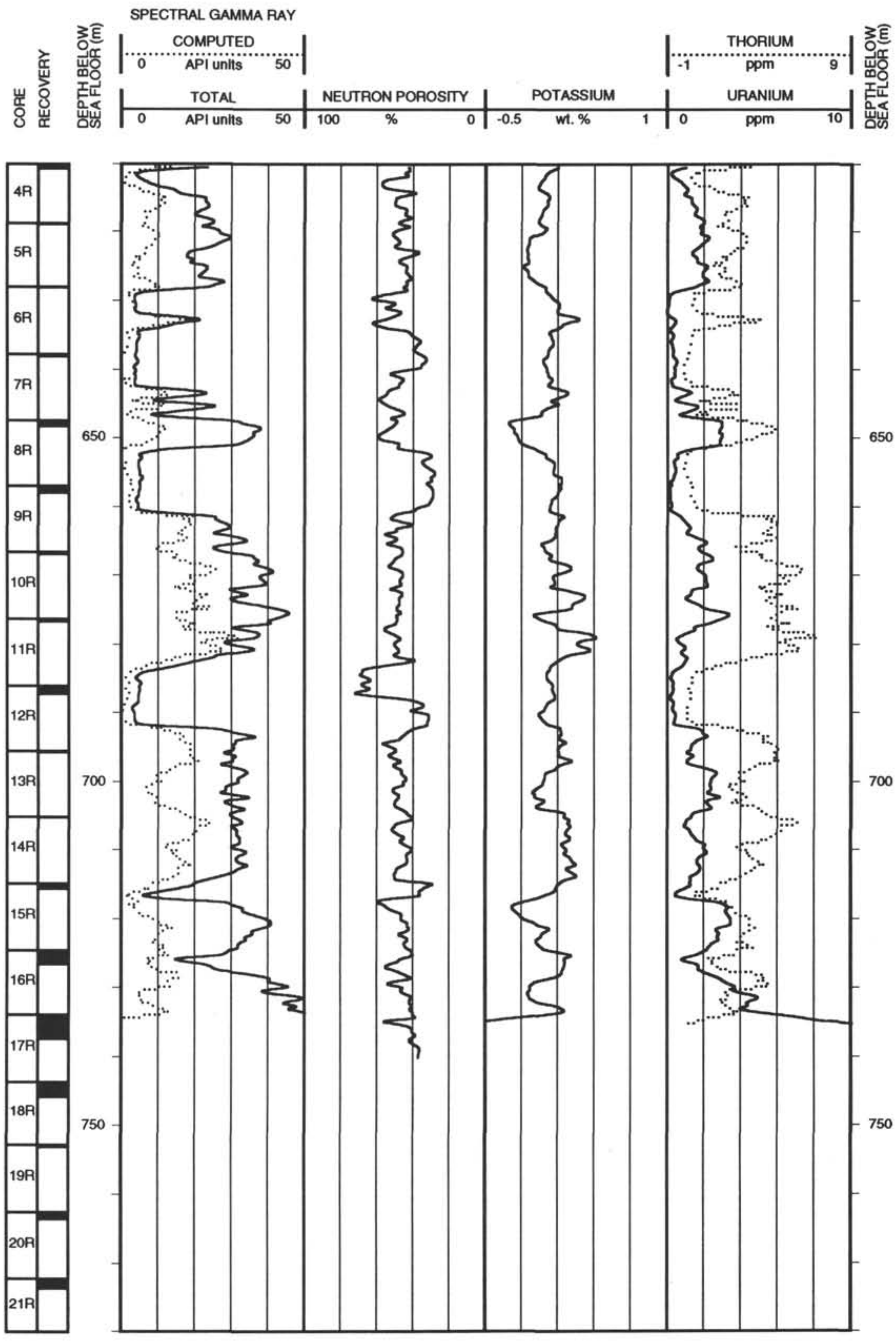

Hole 857D: Resistivity-Natural Gamma Ray Log Summary

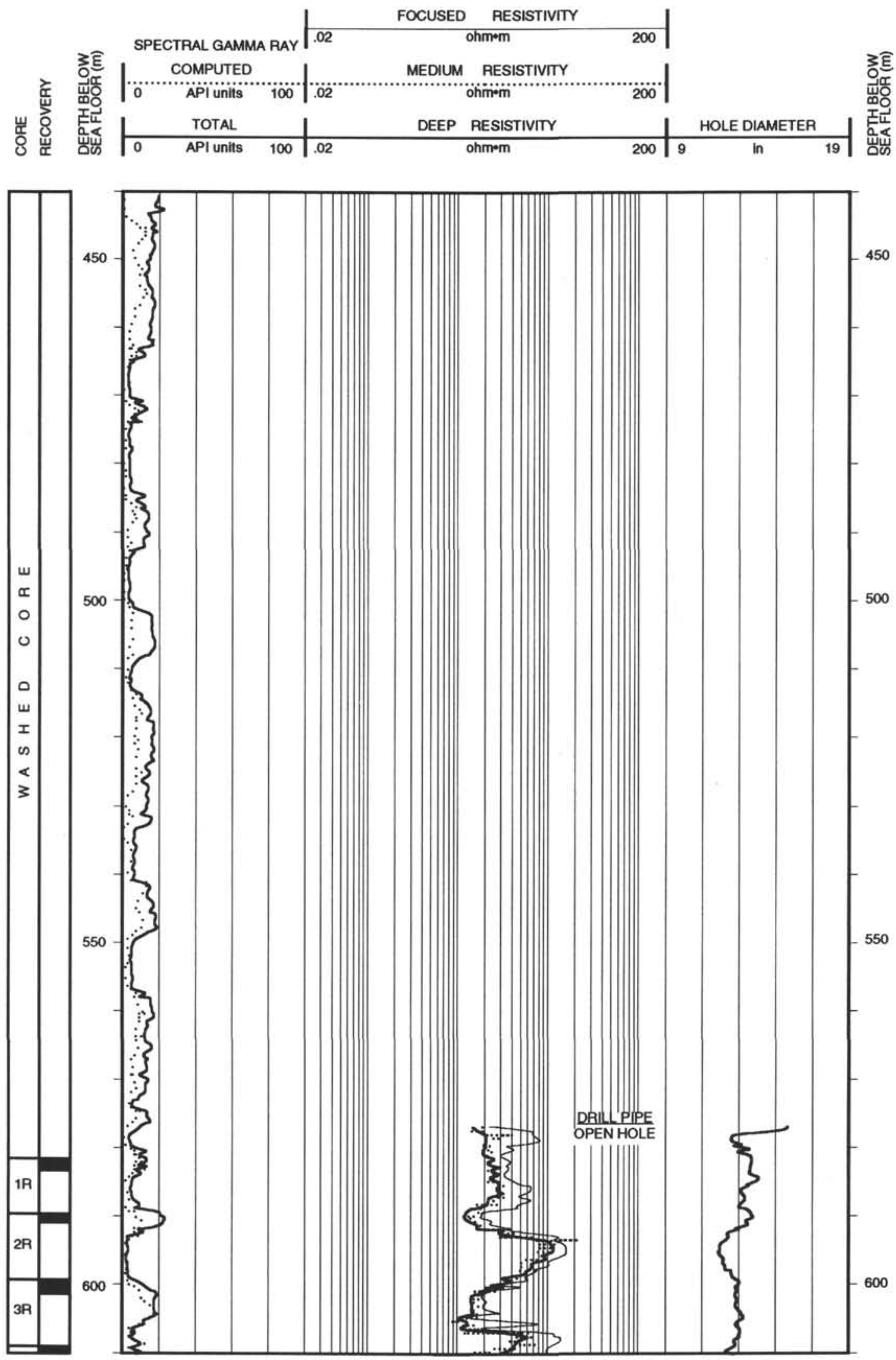

Hole 857D: Resistivity-Natural Gamma Ray Log Summary (continued)

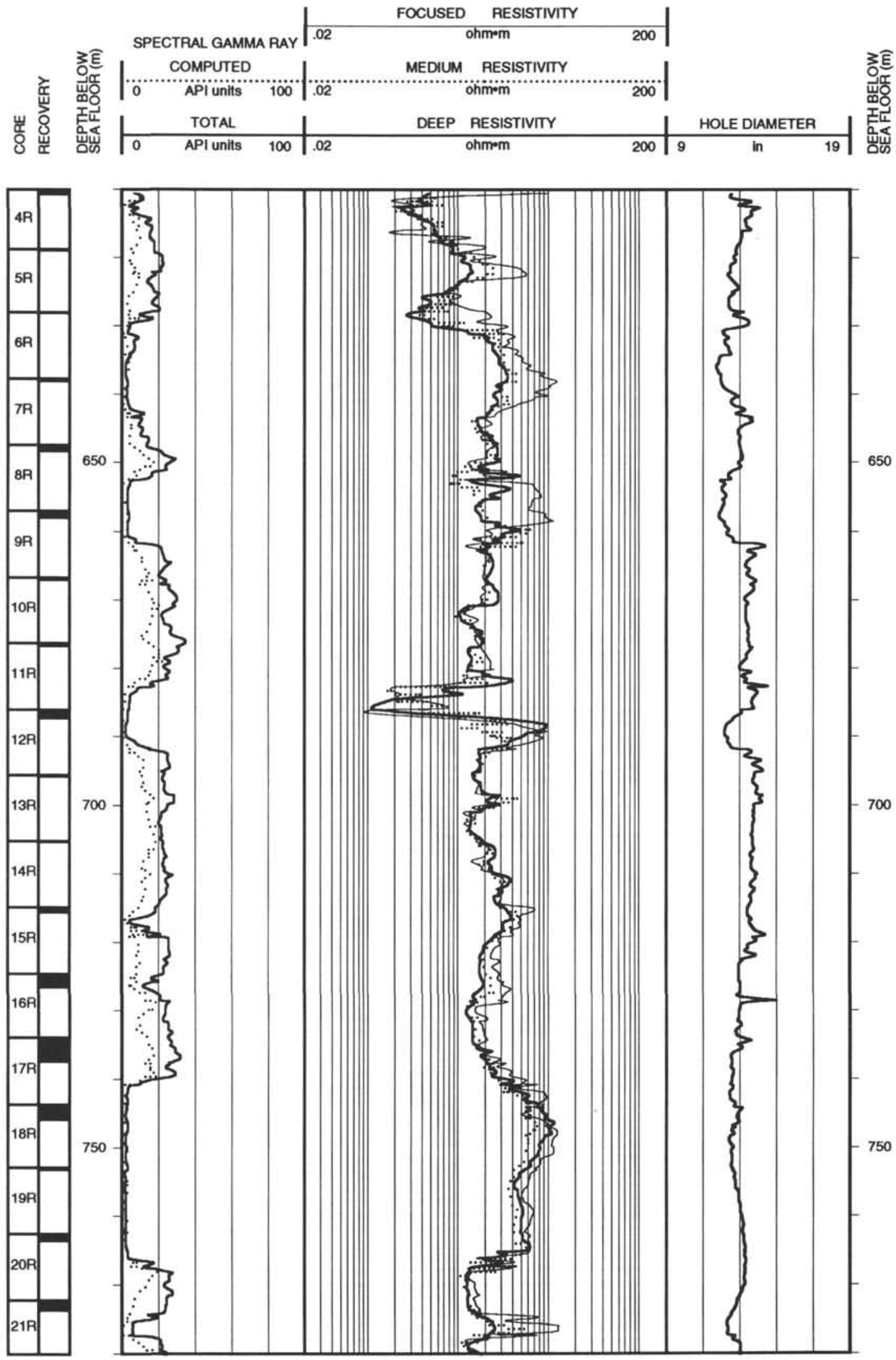

Hole 857D: Resistivity-Natural Gamma Ray Log Summary (continued)